HABILITATION À DIRIGER DES RECHERCHES

Spécialité :

Astrophysique

Présentée par :

Jérôme RODRIGUEZ

Sujet :

ASTRONOMIE ET ASTROPHYSIQUE DES BINAIRES X GALACTIQUES : DE LA NATURE DES SOURCES X À LA PHYSIQUE DES PHÉNOMÈNES LIÉS À L'ACCRÉTION

Soutenue le 13 Janvier 2010, au CEA-Saclay

Devant le jury composé de :

Mr. Didier Barret	Directeur de recherches, CNRS	Rapporteur
Mr. Christian Motch	Directeur de recherches, CNRS	Rapporteur
Mr. Etienne Parizot	Professeur, Univ. Paris Diderot	Rapporteur interne
Mr. Gilles Henri	Professeur, Univ. J. Fourier	Examinateur
Mr. Peter Kretschmar	Directeur des operations scientifiques, ESA	Examinateur
Mr. Michel Tagger	Directeur de recherches, CEA	Examinateur

Remerciements

Les travaux présentés dans ce document n'auraient pu être réalisés sans les contributions diverses et variées d'un grand nombre de collègues et collaborateurs. Sans les nommer tous, ce qui serait long et laborieux, ce sont toutes ces personnes que je tiens à remercier : des collègues instrumentalistes qui permettent à de formidable instruments de fonctionner et d'apporter des données de qualité extraordinaire, aux scientifiques pour les échanges d'idées, les dicussions, les conseils qui permettent à chacun une progression nette dans sa recherche personnelle.

Je voudrais remercier chaleureusement les membres du jury, Etienne, Didier, Christian, Gilles, Peter et Michel, pour avoir accepté de lire, évaluer et participer au jury de cette HDR. Dans mon travail de tous les jours j'aimerais dire un grand merci à Michel, Stéphane, Peggy, Claude qui sont là depuis le début de mon aventure scientifique, et avec qui c'est toujours un grand plaisir (que j'espère partagé) d'interagir. Merci à Claude, Philippe, et Marion, pour plein de choses (discussions sur le foot, courses, ski, etc, la liste est longue), et aussi pour avoir accepté le rôle laborieux de relecteur des premières versions de ce manuscrit.

Enfin merci à mes proches et ma famille de me supporter, je sais que ça peut être dur. Une speciale mention donc à Dr. Ana, qui elle en plus vit cela au quotidien. You got guts my dear !

Table des matières

Table des figures

Liste des tableaux

Liste des acronymes

La plupart des acronymes que nous utilisons couramment sont en anglais. En raison de la généralisation de leur emploi, je les conserve dans cette langue tout au long de ce document, et j'en donne ici une traduction possible

2MASS : *2-Micron All Sky Survey point source* Catalogue du ciel à 2 μm pour les sources ponctuelles
2MASX : *2-Micron All Sky survey eXtended* Catalogue du ciel à 2 μm pour les sources étendues
AGN : *Active Galactic Nucleus* / Noyau actif de galaxie
AIM : Astrophysique et Interactions multi-échelles (UMR)
AO : *Announcement of Opportunity* / Appel d'offre pour du temps d'observation
ASCA : *Advanced Satellite for Cosmologie and Astrophysics* / Satellite d'observations X japonais
ASM : *All Sky Monitor* / Moniteur voute céleste
BAT : *Burst Alert Telescope* / Telescope d'alerte de sursauts (gamma) embarqué sur *Swift*
CC : *Color-Color Diagram* / Diagramme couleur-couleur
CEA : Commissariat à l'énergie atomique
Co-I : *Co-Investigateur* / Collaborateur à un projet
CS : *Compton Shoulder* / "Epaule" Compton
DDT : *Director Discretionary Time* / Temps discrétionnaire directeur
EPIC : *European Photon Imaging Camera* / Camera embarquées sur *XMM–Newton*
ESA : *European Space Agency* / Agence spatiale Européenne
FSC : *French Science Centre* / Centre scientifique Français (SVOM)
GCDE : *Galactic Centre Deep Exposure* / Exposition profonde du centre Galactique (*INTEGRAL*)
GO : *Guest Observer* / Observeur invité
GPS : *Galactic Plane Scan* / Balayage du plan Galactique (*INTEGRAL*)
GRB : *Gamma-Ray Burst* / Sursaut gamma
HEXTE : *High Energy Timing Experiment* / Experience temporelle de haute énergie, instrument embarqué sur *RXTE*
HMXB : *High Mass X-ray Binary* / Binaire X de forte masse
HR : *Hardness Ratio* / Rapport de dureté
IAU : *International Astronomical Union*
IBIS : *Imager onBoard the INTEGRAL Satellite* / Imageur embarqué sur *INTEGRAL*
IGR : *INTEGRAL Gamma-Ray Source* / Source gamma (découverte par) *INTEGRAL*
INTEGRAL : *INTErnational Gamma-Ray Astrophysics Laboratory* / Observatoire européen dédié aux observations des sources célestes de rayons gamma
ISDC : *INTEGRAL Science Data Centre* / Centre de données d'*INTEGRAL*
ISGRI : *IBIS Soft Gamma-Ray Imager* / L'imager gamma mou d'IBIS
JEM-X : *Joint European X-ray Monitor* / Moniteurs X embarqués sur *INTEGRAL*
JJM : Jour Julien Modifié
LEPCHE : *Laboratoire d'Etudes des Phénomènes Cosmiques de Haute énergie*
LMXB : *Low Mass X-ray Binary* / Binaire X de faible masse
NASA : *National Aeronautic and Space Agency* / Agence spatiale Américaine

NED : *NASA Extragalactic Database* / Base de donnée extragalactique de la NASA
PCA : *Proportional Counter Array* / Matrice de compteurs proportionnels, instrument embarqué sur *RXTE*
PI : *Principal Investigator* / Chef de projet
POSS : *Palomar Observatory Sky Survey* / Catalogue céleste de l'observatoire Palomar
QLA : *Quick Look Analysis* / Analyse prompte
QPO : *Quasi-Periodic Oscillation* / Oscillations quasi-périodiques
RXTE : *Rossi X-ray Timing Explorer* / Observatoire américain dédié aux études temporelles en X
SPI : *SPectrometer aboard INTEGRAL* / Spectromètre embarqué sur *INTEGRAL*
SCW : *SCience Window* / Fenêtre d'observation scientifique (*INTEGRAL*)
SiSOC : *Simbol-X Science Operation Centre* / Centre d'opération scientifique de Simbol-X
TAC : *Time Allocation Committee* / Comité d'allocation du temps
ToO : *Target of Opportunity* / Cible d'opportunité
UMR : Unité Mixte de Recherche
USNO : *United States Naval Observatory* / Observatoire naval US
UVOT : *UV-Optical Telescope* / Telescope UV-Visible embarqué sur *Swift*
XMM(-Newton) : *X-ray Multi-Mirror Mission* / Mission X multi-miroirs
XRT : *X-Ray Telescope* / Telescope à rayons X embarqué sur *Swift*

Curriculum vitae et autres informations administratives

Jérôme Rodriguez

Nationalité : Française
Date de naissance : 25 Octobre 1974
Tél : : +33-(0)1 69 08 98 08
Fax : +33-(0)1 69 08 65 77
jrodriguez@cea.fr

CEA Saclay
DSM/IRFU/SAp
91191 Gif sur Yvette Cedex
France

Expérience Professionnelle de Recherche et d'Enseignement

- Depuis 2004 : Chercheur permanent employé par le CEA
  Membre du Laboratoire d'Étude des Phénomènes Cosmiques de Haute Énergie
- 2002-2004 : Ingénieur de recherche CNRS
  Détaché à l'INTEGRAL Science Data Centre, Versoix Suisse
  Représentant pour le CEA de l'instrument IBIS
- 2000-2002 : Enseignements Université de Versailles–St Quentin
  2000–2001 : 44 heures de cours de TD de physique en DEUG B première année
  2001–2002 : 22 heures de cours de TP optique en première année de science pour l'ingénieur
  2001–2002 : 22 heures de cours de TD de physique en DEUG B première année
  2001–2002 : 6 heures de cours d'électronique en amphithéâtre

Cursus et diplômes

- 1999–2002 : Thèse de doctorat
  Université Pierre et Marie Curie (Paris-VI), Paris, France
  Sujet : Etudes spectro-temporelles de microquasars : oscillations quasi périodiques et couplage accrétion éjection
  Directeur : Philippe Durouchoux
- 1999 : DEA Méthodes instrumentales en astrophysique et leurs applications spatiales
  Université Paris-VI, Paris, France
  Obtenu mention Bien
  Stage de recherche : Etudes en rayons X de l'éruption de XTE J1550−564
  Directeur : Philippe Durouchoux
- 1998 Maîtrise de Physique Fondamentale
  Université Paris-VI, Paris, France
  Obtenue mention assez-bien
  Stage de recherche : Etude de la diffusion de la lumière dans le système solaire par des poussières
  Directeur : Annie-Chantal Levasseur-Regourd
- 1997 Licence de Physique Fondamentale
  Université Paris-VI, Paris, France
  Obtenue mention assez bien
- 1992 Baccalaureat série C
  Lycée Jean Zay, Aulnay s/s Bois, France
  Obtenu mention bien

Responsabilités et comités scientifiques

- Co-I français de l'ISDC
- Membre du Simbol-X Science Operation Centre Working Group (Juin 2008-Mars 2009)
- Membre du SVOM French Science Centre
- Co-I SVOM (science hors-sursaut)
- 2009-2013 : Membre élu du conseil de laboratoire de l'UMR Astrophysique et Intéractions Multi-échelles (AIM)
- 2007-2008 : Membre du comité d'allocation du temps pour INTEGRAL
  Chargé d'évaluer les demandes de temps des AO 5 et 6 panel objets compacts
- 2007-2008 : Membre du comité d'allocation du temps pour XMM-Newton
  Chargé d'évaluer les demandes de temps des AO 8 et 9 panel objets compacts
- 2008-2010 : Membre du comité d'allocation du temps ESA pour Suzaku
  Chargé d'évaluer les demandes de temps des AO 3 et 4

Edition et évaluation

- 2009 : Co-éditeur des minutes du 2nd symposium Simbol-X
  Minutes publiées par American Institute of Physics, Editeurs Philippe Ferrando et Jérôme Rodriguez
- 2002 : Co-éditeur des minutes du 4ème workshop Microquasars
  Minutes publiées par Centre of Physics, Editeurs Philippe Durouchoux, Y. Fuchs et Jérôme Rodriguez
- Depuis 2003 : régulièrement référant pour les revue suivantes : Astronomy & Astrophysics, The Astrophysical Journal, Monthly Notices of the Royal Astronomical Society, Publications of the Astronomical Society of Japan, Advances in Space Research

Langues

Français : langue maternelle
Anglais : courant
Espagnol : courant
Suédois : notions

Autres–loisirs

- Sports :
  Judo : Ceinture noire 2ème dan. Pratique régulière en club/compétition.
  Footing : pratique régulière loisir.
  Musculation : pratique régulière loisir.

Liste des publications

- Nombre de publications dans des revues à comité de lecture : 65, dont 16 en premier, 12 en second et 12 en 3ème auteur (Août 2009).
- h-indice : 19 (Août 2009)
- 45 Télegrammes astronomiques et circulaires IAU
- Invité dans 3 conférences/ateliers internationaux

Publications dans des revues à comité de lecture

- 2009 :
  - **Swift follow-up observations of 17 INTEGRAL sources of uncertain or unknown nature**
    J. Rodriguez, J.A. Tomsick, S. Chaty *2009, A&A, 494, 417*
  - **The early phase of a H1743-322 outburst observed by INTEGRAL, RXTE, Swift, and XMM/Newton**
    L. Prat, J. Rodriguez, M. Cadolle Bel, E. Kuulkers, M. Hanke, J. Tomsick, S. Corbel, M. Coriat, J. Wilms, A. Goldwurm *2009, A&A, 494, L21*
  - **An XMM-Newton spectral and timing study of IGR J16207-5129 : an obscured and non-pulsating HMXB**
    J.A. Tomsick, S. Chaty, J. Rodriguez, R. Walter, P. Kaaret, G. Tovmassian *2009, ApJ, 694, 344*
  - **Chandra Localizations and Spectra of INTEGRAL Sources in the Galactic Plane : The Cycle 9 Sample**
    J.A. Tomsick, S. Chaty, J. Rodriguez, R. Walter, P. Kaaret, *2009, accepted in ApJ arXiV 0906.2577*
  - **Detailed Radio to Soft Gamma-ray Studies of the 2005 Outburst of the New X-ray Transient XTE J1818-245**
    M. Cadolle Bel, L. Prat, J. Rodriguez, et al. *2009, A&A, 501, 1*
  - **Quasi-Periodic oscillation frequency-color radius connection in GRS 1915+105 : a possible turnover supporting accretion-ejection instability predictions**
    V.J. Mikles, P. Varnière, S.S Eikenberry, J. Rodriguez, D. Rothstein *2009, ApJ, 694, L132*
  - **Identifications of Five INTEGRAL Sources via Optical Spectroscopy**
    S. Butler, J.A. Tomsick, S. Chaty, J.A. Zurita Heras J. Rodriguez, R. Walter, P. Kaaret, E. Kalemci, M. Ozbey *2009, accepted in ApJ arXiV 0903.1302*
  - **Broad-Band Spectrum of The Black Hole Candidate IGR J17497-2821 Studied with Suzaku**
    A. Paizis, K. Ebisawa, H. Takahashi, T. Dotani, T. Kohmura, M. Kokubun, J. Rodriguez et al. *2009, PASJ 61, 107*

- 2008 :
  - **Two years of INTEGRAL monitoring of GRS 1915+105 Part 1 : multiwavelength coverage with INTEGRAL, RXTE, and the Ryle radio Telescope**
    J. Rodriguez, D.C. Hannikainen, S.E Shaw, et al. *2008, ApJ, 675, 1436*

- **Two years of INTEGRAL monitoring of GRS 1915+105 Part 2 : X-ray spectro-temporal analysis**
  J. Rodriguez, S.E Shaw, D.C. Hannikainen et al. *2008, ApJ, 675, 1449*
- **Swift Follow-up Observations of INTEGRAL Sources of Unknown Nature**
  J. Rodriguez, J.A. Tomsick, S. Chaty *2008, A&A, 482, 731*
- **Peering through the stellar wind of IGR J19140+0951 with simultaneous INTEGRAL/RXTE observations**
  L. Prat, J. Rodriguez, D.C. Hannikainen, S.E Shaw *2008, MNRAS, 389, 301*
- **Chandra Localizations and Spectra of INTEGRAL Sources in the Galactic Plane**
  J.A. Tomsick, S. Chaty, J. Rodriguez, R. Walter, P. Kaaret *2008, ApJ, 685, 1143*
- **Galactic hard X-ray sources discovered by INTEGRAL brought to light by multi-wavelengths observations**
  S. Chaty, F. Rahoui, C. Foellmi, J.A. Tomsick, J. Rodriguez, R. Walter *2008, A&A, 484, 783*
- **TeV J2032+4130 : a not-so-dark Accelerator ?**
  Y. Butt, J. Drake, J. Combi, A. Konopelko, J. Finley, M. Lister, J. Rodriguez, D. Shepherd *2008, MNRAS, 385, 1784*

– 2007 :

- **The discovery outburst of the X-ray transient IGR J17497-2821 observed with RXTE and ATCA**
  J. Rodriguez, M. Cadolle Bel, J. A. Tomsick, S. Corbel, C. Brocksopp, A.Paizis, S. E. Shaw, A.Bodaghee *2007, ApJL, 655, L97*
- **Simultaneous mutliwavelength observations of the Low/Hard state of the transient source Swift J1753.5-0127**
  M. Cadolle Bel, M. Ribo, J. Rodriguez, S. Chaty, S. Corbel et al. *2007, ApJ, 659, 549*
- **A description of sources detected by INTEGRAL during the first 4 years of observations**
  A. Bodaghee, T. Courvoisier J. Rodriguez, et al. *2007 A&A, 467, 585*
- **Hunting the nature of IGR J17497-2821 with X-ray and NIR observations**
  A. Paizis, M. Nowak, S. Chaty, J. Rodriguez et al. *2007 ApJL, 657, L109*
- **The nature of the infrared counterpart of IGR J19140+0951**
  D.C. Hannikainen, M.G. Rawlings, P. Muhli, O. Vilhu, J. Schultz, J. Rodriguez *2007, MNRAS, 380, 665*
- **The XMM-Newton/INTEGRAL monitoring campaign of IGR J16318-4848**
  A.Ibarra, G. Matt, M. Guainazzi, E. Kuulkers, E. Jimenez-Bailon, J. Rodriguez, F. Nicastro, R. Walter *2007, A&A, 465, 501*
- **Hard X-ray emission of the microquasar GX 339-4 in the low/hard state**
  A. Joinet, E. Jourdain, J. Malzac, J.P. Roques, S. Corbel, J. Rodriguez, E. Kalemci *2007 ApJ, 657, 400*

– 2006 :

- **INTEGRAL and XMM-Newton observations of the X-ray pulsar IGR J16320-4751/AX J1631.9-4752**
  J. Rodriguez, A. Bodaghee, P. Kaaret, J.A. Tomsick, E. Kuulkers, et al. *MNRAS 2006, 366, 274*

- **The faint 2005 hard state outburst of Aquila X-1 seen by INTEGRAL and RXTE**
  J. Rodriguez, S.E. Shaw, S. Corbel *2006, A&A 451, 1045*
- **Identifications of Four INTEGRAL Sources in the Galactic Plane via Chandra Localizations**
  J.A Tomsick, S. Chaty, J. Rodriguez, L. Foschini, R. Walter, P. Kaaret *2006 ApJ 647, 1309*
- **The high energy spectrum of Cygnus X-1 as measured by INTEGRAL**
  M. Cadolle Bel, P. Sizun, A. Goldwurm, J. Rodriguez, P. Laurent, et al. *2006, A&A, 446, 591*
- **XMM-Newton observations of PSR B1259-63 near the 2004 periastron passage**
  M. Chernyakova, A. Neronov, A. Lutovinov J. Rodriguez, S. Johnston *2006, MNRAS, 367, 1083*
- **INTEGRAL observation of the high mass X-ray transient V 0332+53 during the 2005 outburst decline**
  N. Mowlavi, I Krekeynbohm, S.E. Shaw, K Pottschmidt, J. Wilms, J. Rodriguez, et al. *2006, A&A, 451, 187*
- **A torque reversal of 4U 1907+09**
  S. Fritz, I. Kreykenbohm, J. Wilms, R. Staubert, F. Bayazit, K. Pottschmidt, J. Rodriguez, A. Santangelo *2006, A&A, 458, 893*
- **Bimodal spectral variability of Cygnus X-1 in an intermediate state**
  J. Malzac, P.O. Petrucci, E. Jourdain, M. Cadolle, P. Sizun, G. Pooley, C. Cabanac, S. Chaty, T. Belloni, J. Rodriguez, et al. *2006, A&A, 448, 1125*
- **Average hard X-ray emission from NS LMXBs : Observational evidence of different spectral states in NS LMXBs**
  A. Paizis, R. Farinelli, L. Titarchuk, T.J.-L. Courvoisier, A. Bazzano, V. Beckmann, F. Frontera, P. Goldoni, E. Kuulkers, S. Mereghetti, J. Rodriguez, O. Vilhu *2006 A&A, 459, 187*

– 2005 :

- **Unveiling the nature of the high energy source IGR J19140+0951**
  J. Rodriguez, C. Cabanac, D.C. Hannikainen, V. Beckmann, S.E. Shaw, J. Schultz *2005, A&A, 432, 235*
- **Characterizing a new class of variability in GRS 1915+105 with simultaneous INTEGRAL/RXTE observations**
  D.C. Hannikainen, J. Rodriguez, O. Vilhu, L. Hjalmarsdotter, A.A. Zdziarski, et al. *2005, A&A, 435, 995*
- **Discovery of X-ray pulsations from IGR J16320-4751 = AX J1631.9-4752**
  A. Lutovinov, J. Rodriguez , M. Revnivtsev, P. Shtykovskiy *2005, A&A, 433, L41*
- **Discovery and study of the accreting pulsar 2RXP J130159.6-635806**
  M. Chernyakova, A. Lutovinov, J. Rodriguez, M. Revnivtsev *2005 MNRAS, 364, 455*
- **Discovery of the INTEGRAL X/γ-ray transient IGR J00291+5934 : a Comptonised accreting ms pulsar ?**
  S.E. Shaw, N. Mowlawi, J. Rodriguez, P. Ubertini, F. Capitanio, et al. *2005, A&A, 432, L13*
- **Resolving the Hard X-ray Emission of GX 5-1 with INTEGRAL**

A. Paizis, K. Ebisawa, T. Tikkanen, J. Rodriguez, J. Chenevez, E. Kuulkers, O. Vilhu, T. J.-L. Courvoisier *2005, A&A, 443, 599*

- **Chandra and RXTE spectroscopy of the accreting msec pulsar IGR J00291+5934**
  A. Paizis, M. A. Nowak, J. Wilms, T.J.-L. Courvoisier, K. Ebisawa, J. Rodriguez , P. Ubertini, *2005, A&A, 444, 357*
- **Swift, INTEGRAL, RXTE, and Spitzer reveal IGR J16283-4838**
  V. Beckmann, J. Kennea, C.B. Markwardt, A. Paizis, S. Soldi, J. Rodriguez, et al. *2005, ApJ, 631, 506*
- **Investigating the EGRET-radio galaxies link with INTEGRAL : the case of 3EG J1621+8203 and NGC 6251**
  L. Foschini, M. Chiaberge, P. Grandi, I.A. Grenier, M. Guainazzi, W. Hermsen, G.G.C. Palumbo, J. Rodriguez, et al. *2005, A&A, 433, 515*

– 2004
- **Spectral Properties of Low Frequency Quasi Periodic Oscillations in GRS 1915+105**
  J. Rodriguez, S. Corbel, D.C. Hannikainen, T. Belloni, A. Paizis, O. Vilhu *2004, ApJ, 615, 416*
- **An X-ray Timing Study of XTE J1550−564 : Evolution of the Low Frequency QPO for the Complete 2000 Outburst**
  J. Rodriguez, S. Corbel, E. Kalemci, J.A. Tomsick, M.Tagger *2004, ApJ, 612, 1018*
- **High Energy Observations of the State Transition of the X-ray Nova and Black Hole Candidate XTE J1720−318**
  M. Cadolle Bel, J. Rodriguez, P. Sizun, R. Farinelli, M. del Santo et al. *2004, A&A, 426, 659*
- **Discovery of a new INTEGRAL source : IGR J19140+0951**
  D.C. Hannikainen, J. Rodriguez, C. Cabanac, J. Shultz, N. Lund, O. Vilhu, P.O. Petrucci, G. Henri *2004, A&A, 423, L17*
- **XMM-Newton Observations of the Ultraluminous Nuclear X-ray Source in M33**
  L. Foschini, J. Rodriguez, Y. Fuchs, L. C. Ho, M. Dadina, et al. *2004, A&A, 416, 529*
- **INTEGRAL Observations of the PSR B1259-63/SS2883 system after the 2004 periastron passage**
  S.E. Shaw, M. Chernyakova, J. Rodriguez, R. Walter, P. Kretschmar, S. Mereghetti *2004, A&A, 426, L33*
- **Magnetic Floods : a scenario for the variability of the microquasar GRS 1915+105**
  M. Tagger, P Varniere, J. Rodriguez, R. Pellat *2004, ApJ, 607, 410*

– 2003 :
- **An XMM-Newton Observation of IGR J16320-4751=AX J1631.9-4752**
  J. Rodriguez, J.A. Tomsick, L. Foschini, R. Walter, A. Goldwurm, S. Corbel, P. Kaaret *2003, A&A, 407, L41*
- **Spectral evolution of the microquasar XTE J1550-564 over its entire 2000 outburst**
  J. Rodriguez, S. Corbel, J.A. Tomsick *2003, ApJ, 595, 1032*
- **First Results from the IBIS/ISGRI Data Obtained During the Galactic Plan**

Scan. II The Vela Region

J. Rodriguez, M. Del Santo, F. Lebrun, G. Bellanger, M. Cadolle-Bel, et al. *2003, A&A, 411, L373*

- **Simultaneous Multi-wavelength Observations of GRS 1915+105**

  Y. Fuchs, J. Rodriguez, I.F. Mirabel, S. Chaty, M. Ribo, et al. *2003, A&A, 409, L35*
- **XMM-Newton study of the persistent X-ray source 1E1743.1-2843 located in the Galactic Center direction**

  D. Porquet, J. Rodriguez, S. Corbel, P. Goldoni, R.S. Warwick, A. Goldwurm, A. Decourchelle *2003, A&A, 406, 299*
- **IBIS Performances During the Galactic Plane Scan. I The Cygnus Region**

  M. Del Santo, J. Rodriguez, P. Ubertini, A. Bazzano, A.J. Bird, et al. *2003, A&A, 411, L369*
- **INTEGRAL discovery of a bright highly obscured galactic X-ray binary source IGR J16318-4848**

  R. Walter, J. Rodriguez, L. Forschini, J. de Plaa, S. Corbel, et al. *2003, A&A, 411, L427*
- **First INTEGRAL observations of GRS 1915+105**

  D.C. Hannikainen, O. Vilhu, J. Rodriguez, S. Brandt, N.J. Westergaard, et al. *2003, A&A, 411, L415*
- **INTEGRAL-RXTE Observations of Cyg X-1**

  K. Pottschmidt, J. Wilms, M. Chernyakova, M.A. Nowak, J. Rodriguez, et al. *2003, A&A, 411, L383*
- **The INTEGRAL/IBIS System Point Spread Function and Source Location Accuracy**

  A. Gros, A. Goldwurm, M. Cadolle-Bel, P. Goldoni, L. Foschini, J. Rodriguez, et al. *2003, A&A, 411, L179*
- **First INTEGRAL Observations of Eight Persistent Neutron Star Low Mass X-ray binaries**

  A. Paizis, V. Beckmann, T. J.-L. Courvoisier, O. Vilhu, A. Lutovinov, K. Ebisawa, D. C. Hannikainen, M. Chernyakova, J. A. Zurita Heras, J. Rodriguez, et al. *2003, A&A, 411, L363*

– 2002 :

- **Energy Dependence of a low Frequency QPO in GRS 1915+105**

  J. Rodriguez, P. Durouchoux, F. Mirabel, Y. Ueda, M. Tagger, K. Yamaoka *2002, A&A, 386, 271*
- **Accretion-ejection instability and QPO in black hole binaries I. Observations**

  J. Rodriguez, P. Varnière, M. Tagger, P. Durouchoux *2002, A&A, 387, 487*
- **Accretion-ejection instability and QPO in black-hole binaries.II. Relativistic effects**

  P. Varnière, J. Rodriguez, M. Tagger *2002, A&A, 387, 497*
- **Study of the Largest Multiwavelength Campaign of the Microquasar GRS 1915+105**

  Y. Ueda, K. Yamaoka, C. Sanchez-Fernandez, V. Dhawan, S. Chaty, J.E. Grove, M. McCollough, A.J. Castro-Tirado, F. Mirabel, K. Kohno, M. Feroci, P. Casella, S.A. Trushkin, H. Castaneda, J. Rodriguez, et al. *2002, ApJ, 571, 978*

Encadrement d'étudiants

Je décris ici les activités d'encadrement d'étudiants lors de leurs stages de recherche et/ou thèses. Pour ces derniers je distinguerai les encadrements "officieux" pour lesquels j'ai participé et/ou collaboré sur des parties spécifiques des projets sans nécessairement être officiellement identifié comme tel (si ce n'est par la co-écriture d'articles de recherche).

Encadrements officiels d'étudiants

Thèses de doctorat

- Lionel Prat :
  2007-2010 : "Etudes de microquasars à haute énergie"
  Université Paris Diderot
  1 publication LP premier auteur (Prat et al. 2009), une publication LP 2nd auteur (Cadolle Bel et al. 2009)

Stages de Master

- Lionel Prat :
  Stage master II 2007 : "Etudes de haute énergie de la binaire X IGR J19140+0951"
  Université Paris VI
  1 publication LP premier auteur (Prat et al. 2008)

Participation à encadrements

- Arash Bodaghee :
  Soutenue en 2007 : "Multi-wavelength observations of INTEGRAL sources & the parameters space occupied by soft γ-ray emitting objects"
  Université de Genève. Directeur de thèse T. Courvoisier
  Large participation dans l'encadrement/direction notamment concernant les sources INTEGRAL :
  1 publication AB premier auteur dans A&A (Bodaghee et al. 2007), une publication AB 2nd auteur (Rodriguez et al. 2006a) dans MNRAS
  Participation de AB dans la mise à jour du site web "INTEGRAL sources"
- Ada Paizis :
  Soutenue en 2004 : "High energy emission from the Galaxy : a study with INTEGRAL and Chandra"
  Université de Genève. Directeur de thèse T. Courvoisier
  Large participation dans l'encadrement/direction notamment concernant les binaires X de faibles masses :
  Plusieurs publications AP première auteure dans A&A, ApJ (Paizis et al. 2003, 2005a,b, 2006), collaboration de AP à Rodriguez et al. (2003b, 2004a, 2006a).
  Collaboration à demandes de temps (acceptées) INTEGRAL et Chandra
- Marion Cadolle Bel :
  Soutenue en 2006 : "Etude des émissions à haute énergie des trous noirs stéllaires accrétants"

Université Paris Diderot. Directeur de thèse A. Goldwurm

Collaboration à l'encadrement :

Plusieurs publications MCB première auteure dans A&A (Cadolle Bel et al. 2006, 2004)

Collaboration à demande de temps (acceptées) INTEGRAL, RXTE

Programmes d'observations "Guest Observer" acceptés

Je décris ici les divers programmes pour lesquels j'ai obtenu du temps d'observation. Je ne décris ici que les programmes que j'ai menés en tant que PI (*Principal Investigator*). Hormis ceux-ci, je suis CoI (*Co-Investigator*) des demandes de temps acceptées suivantes :
–Chandra : 2 programmes couvrant plusieurs AO (*Announcement of Opportunity*) pour des suivis de sources *INTEGRAL* (localisation et caractérisation, PIs Tomsick et Paizis)
– *XMM–Newton* : mesure de variations de l'absorption le long de l'orbite dans des binaires X de forte masse (PI Zurita-Heras).
– *XMM–Newton* : campagne simultanée *INTEGRAL-XMM–Newton*/ d'observation de IGR J16320−4751 (PI Foschini).
– *INTEGRAL* : obervations de trous noirs (PI Cadolle Bel principalement) ou d'étoiles à neutrons (PI Paizis principalement).

En outre Lionel Prat, mon étudiant, a obtenu les droits pour des données *INTEGRAL* sur 17 trous noirs, lors des balayages du plan et du centre de la Galaxie lors de l'AO 6. Cette proposition a été soumise de nouveau pour l'AO 7 (5 Juillet 2009).

Observations *INTEGRAL*

- AOs 2–6 : monitorage de GRS 1915+105.
  AOs 2–3 : la campagne consistait en six pointés de 100 ks répartis sur la période de visibilité de la source (2×3 mois par an).
  AOs 4–6 : nous observons maintenant la source en moyenne une fois par semaine tout au long de la période de visibilité pendant 20 ks.
- AO 7 : Co-PI d'un programme large sur Cyg X-1 et GRS 1915+105
- AO 5 : monitorage d'un trou noir nouvellement découvert au long de son éruption. ToO jamais déclenchée

Observations *RXTE*

- AOs 8–9 : suivi simultané du monitorage de GRS 1915+105
- AOs 9–10 : monitorage de IGR J19140+0951 simultanément à *INTEGRAL*.
- AOs 10–12 : observation d'un maximum de 4 sources nouvellement détectées par *INTEGRAL*. Observations de type ToO, déclenchées 4 fois.
- AO 13–14 : le programme d'observation de 4 potentielles nouvelles sources *INTEGRAL* est incorporé dans le *Core Program* de cet AO. 1 déclenchement sur IGR J19294+1816, article soumis à A&A

Observations *Swift*

- AO 3 : observations d'un maximum de 4 sources nouvellement détectées par *INTEGRAL* en simultané avec *RXTE*. Observations de type ToO.
- AO 4–5 : observations d'un maximum de 2 sources nouvellement détectées par *INTEGRAL* en simultané avec *RXTE* tant que ce dernier sera maintenu en opérations. Observations de type ToO.

Organisation d'événements scientifiques et édition

Participation à l'organisation de 6 congrès/symposium, ateliers, et/ou écoles. Deux en tant qu'organisateur principal, les quatre autres en tant que co-organisateur. Co-éditeur des minutes publiées de deux des évenement. Cyber-éditions (cd-rom) des minutes de deux des écoles.

Organisation

En tant qu'organisateur principal

- **2nd Simbol-X Symposium : focusing on the hard X-ray Universe**
  Paris, 2-5 Décembre 2008
- **Observing the X- and Gamma-ray sky summer school**
  Ecole thématique : Cargèse 6-14 Avril 2006

En tant que co-organisateur

- **Multiwavelength Astronomy international school**
  Ecole thématique : Paris 29 juin-10 Juillet 2009
  Organisateur principal : S. Corbel
- **The violent Universe**
  Ecole thématique : Les Houches 2007
  Organisateur principal : F. Lebrun
- **Black holes in the Universe**
  Ecole thématique : Cargèse Mai 2003
  Organisateur principal : J. Paul
- **The 4^{th} microquasar workshop**
  Cargèse Mai 2002
  Organisateur principal : Ph. Durouchoux

Edition scientifique

Sous forme de livre : minutes

- **2nd Simbol-X Symposium : focusing on the hard X-ray Universe**
  "Simbol-X : focusing on the hard X-ray Universe", AIP, 2009
  Eds. Ph. Ferrando & J. Rodriguez
- **4^{th} microquasar workshop**
  "New views on microquasars", 2002, Centre for Physics, Kolkata
  Eds : Ph. Durouchoux, Y. Fuchs, J. Rodriguez

Sous forme de cd-rom : cours d'écoles thématiques

- **The Violent Universe**
  Production et "publication" du cd-rom
- **Observing the X- and Gamma-ray sky**
  Production et "publication" du cd-rom

Exposé synthétique des recherches

Chapitre 1
Introduction : les objets compacts, enjeux, questions ouvertes et moyens mis en jeu pour y répondre

1.1 Introduction

Depuis toujours l'homme regarde le ciel et se demande quelle est l'origine de ces nébuleuses et points lumineux qu'il y voit. Pendant des siècles ces observations étaient restreintes au seul domaine visible qui n'est qu'une portion infime du spectre électromagnétique. Le vingtième siècle est probablement celui où l'on peut considérer que l'astronomie professionnelle est devenue astrophysique, c'est-à-dire une science dont le but est de comprendre les mécanismes physiques responsables du fonctionnement des sources stellaires et de notre Univers en général. Cette ouverture s'est faite de concert avec l'extension du domaine spectral observable. Nous pourrions comparer l'astronome pre-vingtième siècle à un aveugle qui n'aurait accès qu'à une partie (par le toucher) d'un chameau[1] ; impossible alors pour lui de décrire l'animal en entier ! Ce n'est que par une approche globale (en touchant/observant toutes ses parties) que l'animal pourra être décrit précisément. Il en est de même dans notre domaine. Les nouvelles fenêtres spectrales ont permis la découverte de nouveaux objets, mais elles ont aussi ouvert nos yeux aux émissions des astres connus dans tout le spectre électromagnétique. Il devenait ainsi possible de confronter totalement théories physiques et résultats observationnels.

[1] Cette analogie a été présentée à une conférence hautes énergies ; le chameau était choisi pour ses deux bosses, parallèles des deux bosses du spectre multi-longueur d'onde des AGN.

L'astronomie X et gamma[2] est extrêmement récente puisqu'elle a nécessité l'avénement des observations à partir de ballons stratosphériques et, encore mieux, à partir d'observatoires spatiaux. A la fin des années soixante le ciel X connu ne compte tout au plus qu'une dizaine de sources : les plus brillantes. C'est le cas de Sco X-1 la première source X extra-solaire jamais détectée (Giacconi et al. 1962), et Cyg X-1 (Giacconi et al. 1967) le premier objet identifié comme un potentiel trou noir. Le premier catalogue du ciel X est publié à partir des observations Uhuru, à la fin des années soixante-dix. 339 sources X y sont recensées.

Aujourd'hui, 40 ans après la découverte de Cyg X-1, les catalogues X mous (< 10 keV) contiennent des centaines de milliers d'objets (par exemple Watson et al. 2009) et le nombre total d'objets ayant été détectés dans les X-durs ($20 - 100$ keV) n'excède pas 2000. L'extrême sensibilité des télescopes X-mous (par exemple $Rosat$, *Chandra* et *XMM–Newton*) a permis d'observer tout type de sources et même certaines étoiles émettant une partie (certes infime) de leur luminosité sous ~ 2 keV. Au-delà de 5 keV le nombre d'objets décroît drastiquement, et l'on entre dans le domaine des objets compacts : naines blanches, étoiles à neutrons et trous noirs. Et même si différents processus peuvent expliquer les flux importants de rayons X et gamma détectés, le dernier catalogue de source *INTEGRAL*/IBIS (Bird et al. 2007) contient une majorité de binaires X et d'AGN, ainsi que des variables cataclysmiques (Bodaghee et al. 2007). En d'autres termes la majorité du ciel X (aujourd'hui) détecté à 20 keV est dû aux phénomènes d'accrétion de matière par des objets compacts.

Ces objets, et plus particulièrement les binaires X galactiques, sont au cœur de ma recherche. Je présente, dans cette habilitation à diriger des recherches, les travaux que j'ai effectués depuis la fin de ma thèse. Je me focalise sur deux types particuliers de binaires X : les systèmes de grandes masses, et les microquasars. Avant de présenter les résultats obtenus au cours de ces sept années de recherche je vais introduire quelques notions utiles à la compréhension de ces objets, ainsi que certaines des grandes questions relatives.

1.2 Accrétion dans les binaires X : comment et pourquoi ?

1.2.1 Grandes lignes du fonctionnement des binaires X

Les binaires X sont des systèmes binaires serrés dont l'une des composantes, au moins, est un objet compact de type étoile à neutrons ou trou noir. En raison de la proximité des deux composantes, une partie de la matière de l'étoile compagnon est attirée par l'intense champ gravitationnel de cet objet compact. L'energie gravitationnelle de la matière en chute peut être convertie sous forme lumineuse selon $L_{acc} = 2\eta GM\dot{M}/R_{oc}$ (Frank et al. 2002), où R_{oc} est le rayon de l'objet compact, M la masse de cet objet, $\dot{M}$ le taux d'accrétion, et η l'efficacité de conversion qui vaut environ 10% ($\eta \sim 0.15$ pour une étoile à neutron et ~ 0.47 pour un trou noir en rotation maximale). Avec un taux d'accrétion typique de 1.5×10^{-10} $M_\odot$/an, on obtient une luminosité typique de 10^{35} erg/s (pour $\eta = 0.1$) pour un objet compact de 1 $M_\odot$ et de rayon 10 km.

Il est naturel de s'attendre à un spectre thermique notamment lorsque la matière impacte la surface de l'étoile à neutron et relache alors une partie de son énergie. Toutes les observations X d'énergie supérieure à environ 5 keV ont cependant montré la présence de composantes additionnelles à un spectre purement thermique. La plus importante est une composante en loi de puissance, avec une possible coupure exponentielle vers 100 keV, et pouvant s'étendre dans certains cas jusqu'à 1 MeV, voire 10 MeV dans Cyg X-1. Cette composante est, depuis assez longtemps, généralement

[2]dans tout le reste du document le rayonnement gamma sous-entendra les rayonnements d'énergie maximum 10 MeV. Je ne traite pas des rayons gamma de hautes énergie (>GeV), même si aujourd'hui les observatoires Fermi, HESS, MAGIC et VERITAS apportent d'énormes découvertes sur cette astronomie de l'extrême.

attribuée à un phénomène de comptonisation inverse des photons directement issus de l'accrétion sur des électrons énergétiques présents à proximité de l'objet compact (Sunyaev & Titarchuk 1980). Le milieu responsable de la comptonisation, que nous appelerons couronne, est très peu connu. Sa géométrie, son origine, son énergétique sont au cœur de plusieurs modèles concurrents. Dans les microquasars, cette interprétation fait, de plus, débat aujourd'hui. Certains remettent en question l'existence de cette couronne, et proposent que la 'queue' de haute énergie dans les spectres soit plutôt due à l'émission synchrotron d'un jet dans les microquasars (par exemple Markoff et al. 2003).

1.2.2 Utilité de l'étude des binaires X

Les grandes lignes, ainsi que certains détails relativement précis (comme nous le verrons dans les sections suivantes) sont donc aujourd'hui connus. Pourquoi est-il donc important d'étudier ces objets, et qu'est-ce-qui suscite cet engouement ?
Tout d'abord ils excitent notre curiosité. Ces objets sont relativement récents, et ils peuvent apporter les premières preuves observationnelles de l'existence d'objets aussi mystiques que les trous noirs !
Ensuite, scientifiquement parlant, ils nous permettent d'observer des phénomènes difficilement reproductibles sur Terre : chute de matière en champ gravitationnel extrême, plasma de températures élevées ($\gtrsim 10^6$ K $= 0.1$ keV), éjections relativistes à des vitesses proches de c, champ magnétiques intenses ($10^8 - 10^{14}$ G). En observant les binaires X (et les objets compacts en général) nous avons donc accès à des expériences extrêmes apportant toujours plus de contraintes à nos modèles, et notre connaissance de la physique.
Enfin, d'un point de vue plus astrophysique, les binaires X concentrent des phénomènes qui se rencontrent dans d'autres objets. Il est, par exemple, extrêmement important de remarquer qu'il est communément admis/observé que toutes les sources de jets possèdent un disque (noyaux actifs de galaxies (AGN dans la suite), proto-étoiles, sursauteurs gamma (GRB dans la suite), microquasars). Cette constatation implique donc un lien très fort entre disque d'accrétion et mécanismes d'éjections.
L'avantage d'observer des microquasars est multiple :

- ils sont proches (contrairement aux AGNou aux GRB)
- ils sont très brillants à toutes longueurs d'onde (contrairement aux proto-étoiles)
- L'émission du disque se trouve principalement en X et donc est peu affectée par l'absorption (contrairement aux AGN par exemple)
- Ils varient sur des temps courts et l'on peut donc analyser leur temps caractéristiques d'évolution (contrairement aux AGN et proto-étoiles).
- Ils subissent des éruptions pas trop courtes qui permettent des suivis relativement faciles (contrairement aux GRB).

1.3 Deux grandes familles de binaires X

1.3.1 L'accrétion dans les binaires X de grandes masses

Les HMXB (*High Mass X-ray Binaries*) sont des binaires X dont le compagnon est une étoile de grande masse : une étoile en séquence principale de type Be (Be-HMXB par la suite) dont la caractéristique est un disque équatorial important, ou une étoile supergéante (sg-HMXB par la suite), qui possède un fort vent isotrope. L'accrétion s'y fait de manière radiale (c'est à dire en chute libre).

Dans le cas où le système contient un pulsar (l'extrême majorité des sources connues), à proximité de l'objet compact la matière va suivre les lignes du champ magnétique. Pour un taux d'accrétion

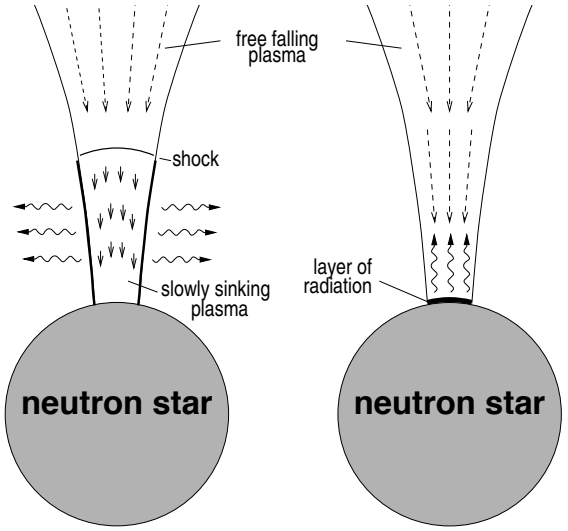

FIG. 1.1 – Représentation schématique de l'accrétion polaire sur un pulsar. A gauche dans le cas d'un taux d'accrétion fort, avec présence d'un choc dans le flot. A droite à taux d'accrétion faible la matière vient heurter la surface du pulsar. Adapté de Caballero (2009, thèse de doctorat).

(luminosité) faible, elle va heurter la surface de l'étoile à neutrons aux pôles magnétiques. Une partie de l'énergie d'accrétion est alors libérée sous forme thermique (fig. 1.1, droite). Certains des photons X mous ainsi émis vont subir un processus compton-inverse sur les électrons énergétiques environnant l'objet. Ce modèle est en assez bon accord avec les observations en spectroscopie X, puisque le continuum de ces objets est en général bien ajusté avec des modèles de comptonisation thermique auquel se superpose parfois une émission de type corps noir.

Dans certains cas, comme par exemple le système Be V0332+53 que nous avons suivi avec *INTEGRAL* et *RXTE* (Mowlavi et al. 2006), on peut détecter des raies d'absorption dans la région 15–100 keV. Celles-ci sont des raies de résonance cyclotron dont l'origine vient du "piégeage" des électrons de la colonne d'absorption sur des niveaux de résonnance quantique (dits de Landau) dans le champ magnétique intense. Comme pour une raie d'absorption d'un élément chimique, les photons d'énergie égale à l'énergie du niveau de Landau seront absorbés. L'énergie du centre de la raie d'absorption permet alors une mesure (la seule directe) du champ magnétique de l'objet puisque d'après la formule suivante (Pottschmidt et al. 2005, et les références s'y trouvant) :

$$E_{c,n} = \frac{2nE_F}{1+z}(1+\sqrt{1+2n\frac{E_F}{m_e c^2}sin^2\theta})^{-1} \sim \frac{nE_F}{1+z}$$

où l'énergie de la raie fondamentale est E_F =(11.6 keV) $(B/10^{12}$ G). Dans l'équation précédente n est le numéro d'harmonique, z le décalage spectral gravitationnel (~ 0.3 pour une étoile à neutrons de 1.4 $M_\odot$ de rayon 10 km), θ l'angle entre la direction du champ magnétique et celle du vecteur d'onde du photon incident.

A forte luminosité (fort taux d'accrétion), un choc peut se produire dans la colonne d'accrétion (fig. 1.1, gauche). Dans ce cas une partie du rayonnement X est produit au choc. Le lieu (hauteur dans la colonne d'accrétion) où se produit le choc est fortement dépendant de la luminosité de l'objet. Comme premier corollaire à ce modèle, et puisque le champ suit $B \propto r^{-3}$ (r distance au pulsar), l'énergie des raies cyclotrons devrait être anti-corrélée à la luminosité X. Si ce phénomène

est effectivement observé dans plusieurs pulsars, il ne l'est cependant pas dans tous et pose donc la question de l'origine de ces divergences.

Enfin, les observations X de ces objets ont montré, dans un grand nombre de systèmes, la présence d'un excès mou, souvent modélisé par un corps noir, dont l'origine n'est pas le point chaud de la surface de l'etoile à neutrons (par exemple Haberl et al. 1989). Cet excès est très souvent observé dans les HMXB très absorbées ($N_H \gtrsim 10^{23}$ cm^{-2}), et il peut avoir différentes origines selon le système considéré (Hickox et al. 2004). Les HMXB très absorbées focalisent une partie de ma recherche, surtout depuis qu'*INTEGRAL* a permis la découverte d'un grand nombre de ces systèmes. Mentionnons aussi la présence de raie(s) d'émission fine(s) attribuée(s) au fer, très souvent présente(s) autour de 6,4 keV.

Bien qu'à travers mes observations j'ai abordé la plupart des aspects présentés dans cette section, je me concentrerai, dans cette HDR (notamment au chapitre 10) sur les questions relatives à la forte absorption, à l'origine des raies du fer, et à l'excès mou. Nous verrons que ces propriétés permettent de caractériser le vent de l'étoile compagnon. Les rayons X produits par l'accrétion de matière fournissent, en quelque sorte, une radiographie des systèmes.

1.3.2 Binaires X de faibles masses

Les objets les plus brillants sont les binaires X dont le compagnon est une étoile de faible massse qui remplit et déborde son lobe de Roche (la surface d'équipotentielle gravitationnelle entre les deux composantes). La conservation du moment cinétique assure alors la création d'un disque d'accrétion dont le rôle est de permettre la chute de matière sur l'objet compact par la libération locale d'énergie (sous forme de chaleur) et de moment cinétique. Dans le modèle le plus couramment admis pour les disques d'accrétion, dit modèle de disque α, c'est la viscosité turbulente qui est responsable du transport de moment cinétique. Elle est paramétrée selon $\nu = \alpha C_s H$ (Shakura & Sunyaev 1973; Frank et al. 2002), où C_s est la vitesse du son dans le plasma, et H l'épaisseur du disque supposée faible devant sa taille. Ces objets, LMXB (*Low Mass X-Ray Binaries*) sont bien souvent transitoires (notamment ceux à trous noirs), extrêmement brillants. La plupart des trous noirs se trouvent dans de tels systèmes.

Contrairement aux HMXB qui sont en majorité des sources faibles et persistentes[3], l'extrême variabilité des LMXB dans leur ensemble a conduit à un grand nombre de classification en fonction de leurs états de luminosité, du types de source etc. Je ne rentrerai pas dans les détails des diverses familles de LMXB à étoiles à neutrons (Z-sources, Atoll-sources, pulsars milliseconde accrétants, bursters, ...) et je me concentrerai, ici, plus particulièrement sur les trous noirs accrétants. La zoologie des différents états spectraux, les connexions spectro-temporelles et multi-longueurs d'onde de ces objets sont présentées plus loin, à la section 1.5.

1.4 Etoiles à neutrons vs. trous noirs

Le type même de l'objet compact a une influence particulière sur les phénomènes observés, et ce notamment en raison de la présence ou non d'un fort champ magnétique (pouvant se manifester par la présence de pulsations), ou encore la présence ou non d'une surface (flash de fusion thermonucléaire de l'océan d'hydrogène ou d'hélium). Ainsi, l'observation de l'un ou l'autre de ces deux derniers phénomènes (pulsations périodiques et/ou flash thermonucléaire) assure de la présence d'une

[3]Exception faite des cas où un disque d'accrétion se forme, comme dans Cyg X-1 qui sont brillantes, ou les Be à très longue période orbitale comme V0332+53 qui sont transitoires.

étoile à neutrons au sein du système. Nous ajouterons à cela la présence de paires de QPO dans le domaine de fréquence du kHz, qui est aussi l'apanage des étoiles à neutrons. Nous ne pourrons conclure si aucune de ces signatures n'est observée.

Il est souvent difficile de trouver la contrepartie visible et/ou infrarouge d'une binaire. Or l'identification du type du compagnon et la mesure de la fonction de masse d'un système est, à l'heure actuelle, le seul moyen de distinguer clairement entre étoile à neutrons et trou noir. L'une des grandes questions de ces dernières décennies a été de tenter de trouver un ou plusieurs critères permettant de toujours pouvoir distinguer les étoiles à neutrons des trous noirs à partir des observations en X. Bien que par le passé plusieurs auteurs aient cru avoir identifié un tel critère, il faut bien avouer qu'aujourd'hui nous n'avons pas vraiment découvert cette pierre de Rosette de l'astronomie X. Les études systématiques des binaires X, en particulier les 13 ans de bons et loyaux services de *RXTE*, ont permis de trouver quelques critères possibles (mais pas définitifs) de distinction. Par exemple la luminosité des étoiles à neutrons à haute énergie (20–200 keV) est, semble-t-il, moindre que celle des trous noirs (par exemple Barret et al. 1996; Di Salvo et al. 2001). Un trou noir à flux X donné (et dans l'état dur) brille généralement plus en radio (par exemple Corbel et al. 2000, 2003; Gallo et al. 2003). Il semble que les spectres de puissance temporels des trous noirs n'aient quasiment aucun signal au-delà de 50 Hz, contrairement aux étoiles à neutrons ("faiblement" magnétisées, c'est-à-dire où B$\sim 10^8$ G, Sunyaev & Revnivtsev 2000).
Tous ces diagnostics ne restent cependant qu'indicatifs, et aucun n'apporte une preuve définitive en faveur d'un trou noir. Certains objets, comme nous allons le voir, ont des comportements de trous noirs clairs du point de vue d'une majorité de ces points, mais peuvent aussi ressembler à des étoiles à neutrons selon certains autres critères. C'est le cas de IGR J17497−2721 (chap. 6) dont quasiment toutes les signatures pointent vers un trou noir, mais qui est sous-lumineux (pour ces objets) en radio.

1.5 Microquasars : processus de rayonnement, états spectraux, et modèles d'accrétion-éjection

1.5.1 Processus de rayonnement

Les observations large-bande (0.1–200 keV) ont permis de mettre en exergue plusieurs composantes additionnelles au disque d'accrétion dans les spectres en énergie. La plus notable est une queue de haute énergie avec parfois une coupure exponentielle autour de 100 keV, mais qui peut s'étendre jusqu'au MeV (Grove et al. 1998; Cadolle Bel et al. 2006; Joinet et al. 2007), voire même jusqu'à 10 MeV dans Cyg X-1 (McConnell et al. 2002) sans coupure apparente. L'origine de cette queue ne fait, aujourd'hui, toujours pas consensus ; certains l'attribuent à un processus Compton inverse des photons mous du disque (Sunyaev & Titarchuk 1980) sur des électrons présents dans une couronne. D'autres pensent à une contribution du jet (par exemple Markoff et al. 2001, 2003) via un processus synchrotron. Nous verrons (notamment au chapitre 11) si ces différentes explications sont en accord avec les observations, et, le cas échéant, comment nous pouvons les insérer dans un modèle plus global.

En plus de ces deux composantes majeures des spectres X de microquasars nous pourrons, dans certaines sources, détecter une raie du fer dans la région $6 - -7$ keV, ainsi qu'une composante de reflexion entre 10 et 20 keV.

1.5.2 Approche temporelle

Les phénomènes d'accrétion ne se déroulant pas à flot constant, une variabilité intrinsèque des flux émis peut-être attendue. Ainsi, dès 1973, R. Sunyaev imaginait qu'un "point" (une bulle de matière) localement plus chaud du disque d'accrétion pouvait donner lieu à un phénomène d'oscillation quasi-périodique du flux (Sunyaev 1973). Même si, en raison de la forte rotation différentielle des régions internes du disque, une telle bulle ne pourrait pas subsister longtemps en tant que telle, des QPO de toutes fréquences sont vus dans les objets compacts accrétants. Plus généralement, la variabilité des objets compacts est très complexe, et est due à plusieurs composantes. L'origine de ces variabilités est, à l'heure actuelle, très mal connue, même si les études spectro-temporelles (c'est-à dire l'analyse temporelle contrainte par la spectroscopie) permises en particulier par l'avènement de *RXTE* en 1996, ont permis d'avancer peu à peu dans cette direction.

L'origine de la quasi-période ou, en d'autres termes, de la faible cohérence du signal périodique ($\nu/\Delta\nu \sim 10$ pour des QPO typiques) peut avoir plusieurs origines (van der Klis 2006, pour une revue). Un phénomène de fréquence faiblement variable autour de la fréquence moyenne, ou un phénomène périodique mais temporaire donneront, en effet, un QPO. La grande inconnue concerne l'origine même de cette pulsation quasi-périodique. Plusieurs modèles prédisent l'origine des QPO. Mais, comme nous le verrons dans cette HDR (chap. 11 et 13), il est aujourd'hui clair que phénomènes spectraux et temporels sont liés. Un bon modèle de QPO devra donc aussi répondre aux questions liées aux processus spectraux.

RXTE lancé en 1996 est un satellite dédié aux études temporelles. Ses capacités spectrales en font un instrument de premier ordre pour apporter des contraintes fortes sur les propriétés des QPO. Plusieurs auteurs se sont penchés sur la question. Voici un résumé des principaux résultats utiles aux analyses que je présente dans cette HDR :

- La fréquence des QPO est corrélée à la température du disque (Muno et al. 1999)
- La fréquence des QPO est corrélée au rayon du disque, mais de manière non-triviale (Rodriguez et al. 2002b)
- La fréquence des QPO est corrélée au flux X-mou (sous 10 keV) dans GRS 1915+105 et XTE J1550−564 (Rodriguez et al. 2002a, 2004b)
- La fréquence des QPO est corrélée (de manière non-triviale) à l'indice de photon de la loi de puissance des spectres (Vignarca et al. 2003)
- La puissance des QPO est corrélée à la contribution relative de la couronne, et anti-corrélée à la contribution relative du disque (Homan & Belloni 2005; McClintock & Remillard 2006; van der Klis 2006, par exemple)
- La fréquence des QPOs dans GRS 1915+105 est anticorrélée à la puissance radio, et à l'épaisseur optique (indice spectral du spectre radio) du jet (Muno et al. 2001). Notons cependant que Migliari et al. (2005) semblent remarquer une tendance contraire dans GX 339−4.
- Les QPO ont des spectres en énergie durs : leur amplitude croît avec l'énergie (par exemple Morgan et al. 1997; Rodriguez et al. 2002a)

La première conclusion qu'il est possible de tirer de ces observations est qu'il semble bien que la fréquence du QPO soit réglée par le disque, même si une composante de comptonisation forte est nécessaire pour que la puissance de l'oscillation soit élevée. Il est d'ailleurs relativement clair que le QPO n'est pas émis par le disque lui-même, ou du moins n'est pas reliée au flux thermique issu du disque. Ceci a pour conséquence d'exclure tout modèle basé sur des oscillations mécaniques du disque, puisqu'alors le QPO aurait un spectre similaire à celui du disque. Au-delà de la physique même de l'oscillation il est intéressant de remarquer que les différentes caractéristiques du QPO semblent indiquer qu'une forte interaction disque-couronne puisse être nécessaire à sa présence.

1.5.3 États spectraux

On distinguera différents états spectraux en fonction de la contribution relative et des paramètres des deux principales composantes spectrales (le disque et la couronne) au spectre global d'une source (McClintock & Remillard 2006), ainsi qu'en fonction du comportements temporel rapide (Homan & Belloni 2005) :

- **État dur :** Cet état est caractérisé par une dominance d'une loi de puissance de pente dure ($\Gamma < 2$) et bien souvent une coupure exponentielle à ~ 100 keV. Le disque est froid (< 0.5 keV). Les spectres de puissances temporels sont complexes, et en général représentés par plusieurs Lorentziennes larges, avec une forte variabilité (30–40% RMS, pour $Root\ Mean\ Square$) et des QPO de basses fréquences ($\lesssim 1$ Hz).
- **État mou :** Dans cet état le disque domine totalement le spectre ($F_{disque} > 75\% F_{total}$). La couronne est absente ou très faible et à une pente forte ($\Gamma \gtrsim 2,5$). Le spectre de puissance montre très peu de variabilité (quelques % RMS) et le "bruit" de la source est en loi de puissance d'indice ~ 1.

Entre ces deux états canoniques, nous pourrons avoir des mélanges plus ou moins dominés par l'une ou l'autre des composantes. Dans l'état intermédiaire dur la loi de puissance est forte et relativement pentue ($\Gamma \sim 2.$), le disque est relativement chaud (~ 1 keV), et les spectres de puissance montrent encore une variabilité importante (10–20 % RMS) avec la présence de QPO (1–10 Hz). Dans l'état intermédiaire mou le spectre est plus mou, même si la loi de puissance est toujours présente. La variabilité est faible, mais des QPO de hautes fréquences peuvent apparaître (~ 100 Hz).

1.5.4 Modélisation des éruptions et connexions accrétion éjection

Les microquasars, lors de leur éruption vont pouvoir transiter entre les différents états. Les mécanismes physiques donnant lieu aux transitions d'états sont très peu connus. Le paramètre principal régissant l'évolution d'un microquasar est le taux d'accrétion $\dot{M}$[4]. Il est cependant clair aujourd'hui que ce paramètre seul n'est pas suffisant pour expliquer les variations spectrales de ces objets (Homan et al. 2001). Notamment le phénomène d'hysteresis, c'est-à-dire le fait que la transition état dur→état mou lors de la montée de l'éruption s'éffectue à luminosité plus importante que la transition inverse lors de la décroissance (Miyamoto et al. 1995), est en désaccord avec un paramètre unique régissant les transitions spectrales. Les éruptions en général sont phénoménologiquement assez bien décrites par un "Q", ou une tête de tortue, lorsque l'évolution d'une source est reportée sur un diagramme dureté-intensité, comme celui représenté sur la figure 1.2. Les connexions spectro-temporelles et accrétion-éjection délimitent aussi des régions claires sur ce diagramme, qui sont identifiées aux différents états spectraux.

L'évolution d'une source sur ce diagramme peut s'interpréter relativement aisément, même si tous les détails ne font pas consensus. Les grandes lignes font intervenir un disque dont le bord interne et la température maximale fluctuent, et une couronne plus ou moins refroidie par l'afflux de photons thermiques du disque (fig. 1.2). Dans l'état dur le disque est froid, la couronne forte (comptonisation thermique), dans l'état mou le disque est chaud, la couronne faible ou absente. Ces caractéristiques s'accompagnent de signatures temporelles et radio claires. Dans l'état dur un fort jet compact est présent (par exemple Fender 2001), et est absent dans l'état mou (par exemple Fender et al. 1999a). Ce jet a été résolu, grâce au VLA, dans deux systèmes : Cyg X-1 (Stirling et al. 2001) et GRS 1915+105 (Fuchs et al. 2003). La transition entre état dur et état mou s'accompagne d'une éjection discrète pouvant atteindre jusqu'à plus de 90% de la vitesse de la lumière dans certaines

[4]Notons que ce paramètre est aussi le paramètre de base régissant les variations de luminosité de toutes les binaires X en général.

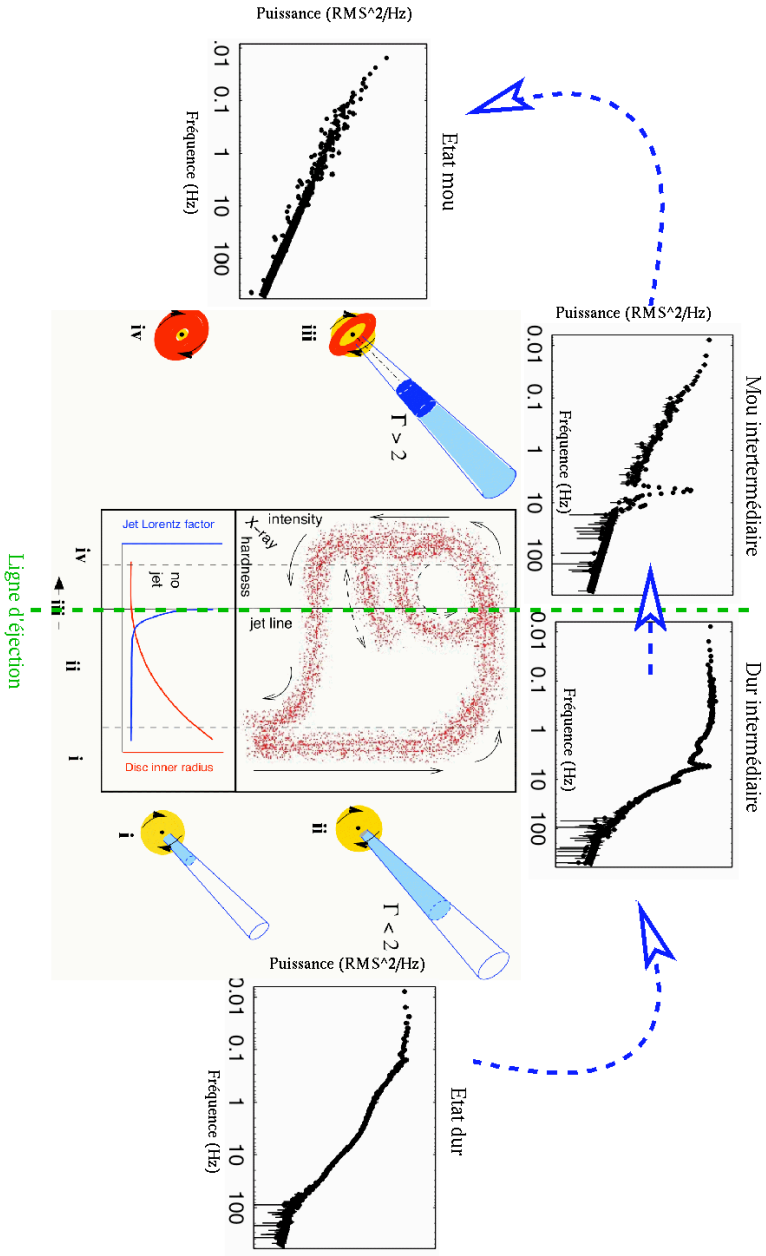

FIG. 1.2 – Diagramme dureté-flux représentant schématiquement l'évolution spectrale et temporelle d'un microquasar au cours de son éruption. Les états spectraux sont aussi représentés en termes de taille de disque et/ou présence de jet. La ligne de jet marquant la transition entre les deux états intermédiaires, moment des éjections discrètes. Source Fender et al. (2004); Homan & Belloni (2005).

sources (par exemple Mirabel & Rodriguez 1994).

Les raisons de ces connexions accrétion-éjections ne sont pas claires du tout. En particulier si l'évolution entre les différents états spectraux semble liée à la taille et température du disque d'accrétion, son influence sur la présence de jets est débattue. Ce débat est d'autant plus relancé depuis la controverse sur la taille des disques dans les états durs. Certains auteurs prétendent en effet détecter des disques froids pouvant aller jusqu'à leur dernière orbite stable (par exemple, Rykoff et al. 2007, dans le cas de XTE J1817−330) ; d'autres, analysant parfois les mêmes données, y voient plutôt un effet dû à une absorption locale variable (Cabanac et al. 2009).

Il est clair que les modèles basiques de disque comme le disque-α, et l'instabilité magnéto-rotationnelle (*Magneto-Rotational Instability*, MRI dans la suite Balbus & Hawley 1991) développée pour expliquer le transport d'énergie et de moment cinétique dans le disque, ne sont pas valides dans les cas autres que l'état mou. Les connexions entre accrétion de matière et jets, posent la question du transfert d'énergie et de moment cinétique depuis la matière accrétée (direction radiale, coplanaire du disque) vers la matière éjectée (direction verticale, perpendiculaire au disque). La MRI prédit en effet un transport de moment cinétique purement radial et coplanaire au disque. Plusieurs modèles concurrents existent comme par exemple le *CENtrifugal BOundary Layer* (CENBOL, Chakrabarti 1996), le modèle de jet lancé par le disque (JED-SAD, Ferreira et al. 2006), ou encore l'instabilité d'accretion éjection (*Accretion-Ejection Instability*, AEI, Tagger & Pellat 1999).

1.6 Les grandes questions liées aux binaires X

Le décor est planté, et le schéma général de fonctionnement des binaires X est relativement clair. L'origine de l'énergie et des radiations est l'accrétion de matière par un objet compact. Comme nous l'avons vu dans cette introduction, un grand nombre d'aspects ne fait toujours pas consensus, certains sont même relativement énigmatiques. Rappelons certaines des grandes questions relatives aux objets compacts et binaires X :

- Objets compacts, types et populations de sources
  - Les trous noirs existent-ils vraiment ?
  - Quelle est l'equation d'état des étoiles à neutrons ?
  - Quelle est la répartition des populations contenant l'un ou l'autre des objets compacts ?
  - Comment, grâce à l'étude des populations de sources, peut-on contraindre les modèles d'évolution stellaire ? Et en système binaires serrés ?
  - La répartition spatiale des différents types de systèmes peut il nous apporter des contraintes sur l'évolution de notre Galaxie ?
- Questions liées aux systèmes binaires en général
  - Quelle est l'origine des variabilités de tous types dans les binaires X ?
  - D'où provient l'émission due au fer dans les binaires X et les différences notables entre HMXB et LMXB ?
  - Quelles sont la nature et la géométrie du milieu émetteur de la composante spectrale de haute énergie : couronne sphérique, couronne grumeleuse, colonne d'accrétion, jet ?
  - Quels sont les liens entre les différents milieu émetteurs ?
  - Dans les LMXB quelle relation de causalité existe-t-il entre disque et couronne ? et le jet dans les microquasars ?
- Processus de rayonnement et leur origine
  - Quelle est l'origine de la forte absorption dans les binaires X (principalement de fortes masses) ?
  - Quelle est l'origine des variations de l'absorption locale dans les sg-HMXB ?

  - Quelle est l'origine de l'excès X-mou dans les sg-HMXB (aussi vu dans certains AGN), et le lien très probable avec la forte absorption ?
  - Quelle est l'origine de la queue de haute énergie vue dans les LXMB (y compris celles contenant une étoile à neutron) : comptonisation, effet synchrotron, les deux ?
- Liens accrétion-éjection
  - Quelle est l'origine de la matière éjectée dans les microquasars ?
  - Comment l'énergie d'accrétion peut-elle servir à accélerer les jets, ou bien existe-t-il une autre source d'énergie pour les jets ?
  - Quelle est l'origine des transitions spectrales dans les binaires X (principalement de faibles masses), et la nature du paramètre additionel au taux d'accrétion ?
  - Quels liens ont les QPO avec les phénomènes d'accrétion-éjection ?
  - Le disque est-il réellement tronqué, et les variations de flux X sont elles liées aux variations de rayon interne et température ?

Certaines questions peuvent recevoir des élements de réponse, comme par exemple la première. Si l'on admet qu'aucun astre compact de masse supérieure à 3 $M_\odot$ ne peut être soutenu par aucune pression de dégénérescence, alors on accepte l'existence d'un trou noir, un astre tellement dense que rien n'empêche son effondrement. Bien entendu celui-ci a de fortes chances de ne pas ressembler au trou noir théorique de Schwarzschild.

Ces questions s'insèrent dans un cadre plus vaste servant à la compréhension des phénomènes physiques régissant la matière en champs forts, et les plasma en général. Le seul moyen de "sonder" les trous noirs est d'étudier ce qui est dans leur entourage immédiat. De même l'observation des plasmas astrophysiques (par exemple le disque d'accrétion) et des liens et phénomènes y étant rattachés (existence/présence de jets par exemple) peut nous permettre de mieux comprendre l'évolution de ces entités.

Il n'est évidemment pas questions de répondre à toutes ces questions dans ce document, et je ne me suis d'ailleurs pas penché sur toutes. Je présente, ici, mes démarches, mes projets, et les analyses que j'ai faites et qui, *in-fine*, m'ont permis d'avancer un tant soit peu dans la compréhension de ces objets, en apportant des éléments de réponses à certaines de ces questions.

1.7 Moyens utilisés/mis en œuvre et justification du plan de ce document

Avant de se jeter dans l'analyse physique de ces objets, il nous faut remarquer qu'il arrive souvent, lorsque nous pointons un télescope vers une source, que nous découvrions d'autres sources stellaires dans le même champ de vue. Alors, comme R. Giacconi en 1962, la question préliminaire à toute analyse concerne la nature de cet émetteur. Le premier travail consiste donc en une étude des propriété du nouvel objet afin de l'identifier.

En raison de mon implication dans les observations du satellite gamma *INTEGRAL*, j'ai été, au cours de ces dernière années, souvent confronté à cet aspect de découverte de nouvelle source. J'ai alors développé des programmes de suivis afin d'identifier les sources en question. Plutôt donc que de séparer ce document en deux parties, chacune traitant de familles de binaires différentes, j'ai choisi de présenter mes travaux d'une manière plus évolutive, pour faire ressortir l'aspect d'astronome lié aux découvertes et identifications des nouvelles sources X et gamma. Ce document est séparé en trois parties au cours desquelles nous aborderons tout d'abord l'étude des sources X d'un point de vue purement astronomique, et rentrerons peu à peu, dans l'interprétation et l'analyse physique donnant lieu aux phénomènes observés. J'ai choisi ce plan car il me semble qu'il représente bien mon approche du travail d'astrophysicien observateur mais aussi parce qu'il me permet de présenter mes travaux

d'une manière logique et originale.

Pour caractériser les nouvelles sources, c'est-à-dire trouver la nature de l'émetteur, la première étape consiste à trouver des contreparties à d'autres longueurs d'ondes. Ceci permet d'affiner la connaissance de l'objet, en en donnant une identification possible. C'est cet aspect d'astronome (observation du ciel, photométrie élémentaire, associations multi-longueurs d'onde) que j'ai voulu souligner dans la première partie de ce document. J'y présente l'outil, le satellite *INTEGRAL* qui a permis les découvertes de sources, quelques résultats basiques de balayages du centre et du plan galactiques, ainsi que certains résultats de suivis multi-longueurs d'onde obtenus à partir des programmes de suivis que j'ai mis en place.

Notre but est de comprendre la physique dans les systèmes binaires X donc les mécanismes menant aux émissions observées. L'approche précédente n'est, évidemment, pas suffisante pour aboutir à ce but. De manière générale, le physicien aime classer les résultats (observables) d'une expérience ou d'un phénomène dans différentes catégories selon leurs valeurs. La définition de ces catégories peut être arbitraire. Néanmoins, lorsqu'un grand nombre d'événements est identifié et une classification claire établie, une étape importante vers la compréhension d'un phénomène est alors effectuée. L'avantage, de cette approche, purement phénoménologique, est qu'aucun modèle physique n'est alors invoqué. Les résultats sont donc, *a-priori*, indépendants du choix du contexte physique. C'est ce type de démarche que j'ai voulu illustrer dans la seconde partie : une fois les contreparties des sources trouvées, différents paramètres sont obtenus, qui, par comparaison avec d'autres sources connues, nous permettrons alors de classifier plus précisément les objets en question. Ceci est aussi valable pour des sources dont le type est connu, mais pour laquelle les processus physiques restent grandement mystérieux. La classification "phénoméno-zoologique" permet de regrouper des phénomènes similaires, que l'on tentera ensuite de comprendre en tant que groupes. Je montrerai aussi, à travers l'étude du microquasar GRS 1915+105 (chap. 7), comment une approche purement phénoménologique peut permettre une interprétation élémentaire des mécanismes physiques en jeu.

Enfin, les outils d'observation aujourd'hui mis à notre disposition nous permettent d'obtenir de nombreux diagnostics sur la physique des sources observées. Les études spectrales et temporelles et leur interprétation apportent des contraintes aux modèles théoriques, tant par la finesse des paramètres observés que par la présence de signatures précises (oscillations quasi-périodiques, présence de raies, connexions avec les jets, flux et saveur spectrale, ...). Ces derniers donnent alors des pistes de recherches et de compréhension des objets observés. Cette confrontation entre résultats, interprétation et théorie est illustrée dans la dernière partie de ce documents.

Tous les chapitres et les différentes approches sont fondés et se réfèrent à des articles publiés. Dans la réalité, astronomie et astrophysique sont évidemment intimement liées. Donc, bien que chaque article soit choisi pour illustrer au mieux un chapitre ou une section donnée, le lecteur y trouvera en général des aspects décrits dans les trois grandes parties de ce document. Aussi, de manière à bien illustrer l'aspect évolutif de la caractérisation et de la compréhension des objets, nous suivrons en particulier quelques sources bien identifiées qui serviront d'exemples et de fils directeurs. Celles-ci sont IGR J16318−4848, IGR J16320−4751 dans le bras de Norma, et IGR J19140+0951 et GRS 1915+105 dans la constellation de l'Aigle. Evidemment d'autres exemples ponctuels seront présentés de manière à montrer au lecteur la reproductibilité de certains phénomènes, ainsi que pour appuyer les conclusions concernant l'interprétation physique proposée.

Première partie

Astronomie X et Gamma : découverte et identification des sources

Chapitre 2
L'observatoire : *INTEGRAL*

2.1 Introduction

INTEGRAL (acronyme de *INTErnational Gamma-Ray Astrophysics Laboratory*, Winkler et al. (2003)) est un observatoire Européen dont la charge utile scientifique est constituée de quatre télescopes. Les deux principaux, constituant en quelque sorte l'âme de l'observatoire, sont l'imageur IBIS (*Imager onBoard the INTEGRAL Satellite*, Ubertini et al. (2003)), et le spectromètre SPI (*SPectrometer aboard INTEGRAL*, Vedrenne et al. (2003)), qui couvrent le domaine des rayons X durs (au-delà de 20 keV) jusqu'aux rayons gamma d'énergie 10 MeV. À plus basse énergie, *INTEGRAL* embarque deux moniteurs X regroupés sous l'appelation JEM-X (*Joint European X-ray Monitor*, Lund et al. (2003)), ainsi qu'un télescope visible, l'OMC (*Optical Monitoring Camera*, Mas-Hesse et al. (2003)) fonctionnant dans la bande V. N'ayant pas utilisé ce dernier, je me focaliserai sur les 3 télescopes X/Gamma sus-mentionnés. La figure 2.1 montre une représentation du satellite, ainsi que l'emplacement des ces quatre télescopes.

Une partie du temps garanti d'*INTEGRAL* a consisté en des balayages systématiques des régions centrales de la Galaxie (le GCDE pour *Galactic Centre Deep Exposure*) et de son plan (GPS pour *Galactic Plane Scan*). Il y a de nombreuses raisons scientifiques justifiant ces programmes, comme la surveillance de l'activité des sources Galactiques accrétantes qui sont hautement variables (changement d'état spectral, éruption, ..). La grande sensibilité dans les rayons X durs/gamma mous (notamment entre $\sim$ 20 et $\sim$ 500 keV) couplée au grand champ de vue ont permis la découverte d'un grand nombre de sources X dures. Elles sont nommées IGR J$RA\pm Dec$. Par la suite, j'utiliserai l'acronyme IGR pour désigner l'ensemble ou un sous-ensemble des sources découvertes par *INTEGRAL*. C'est cet aspect de suivis astronomiques et découvertes de sources que j'ai souhaité mettre en avant en présentant *INTEGRAL* en chapitre introductif de la première partie de ce document.

2.2 L'ISDC et ma participation à *INTEGRAL*

Le centre de données d'*INTEGRAL* (ISDC pour *INTEGRAL Science Data Centre*) est considéré comme le cinquième instrument d'*INTEGRAL*. Contrairement à *XMM–Newton*, par exemple pour

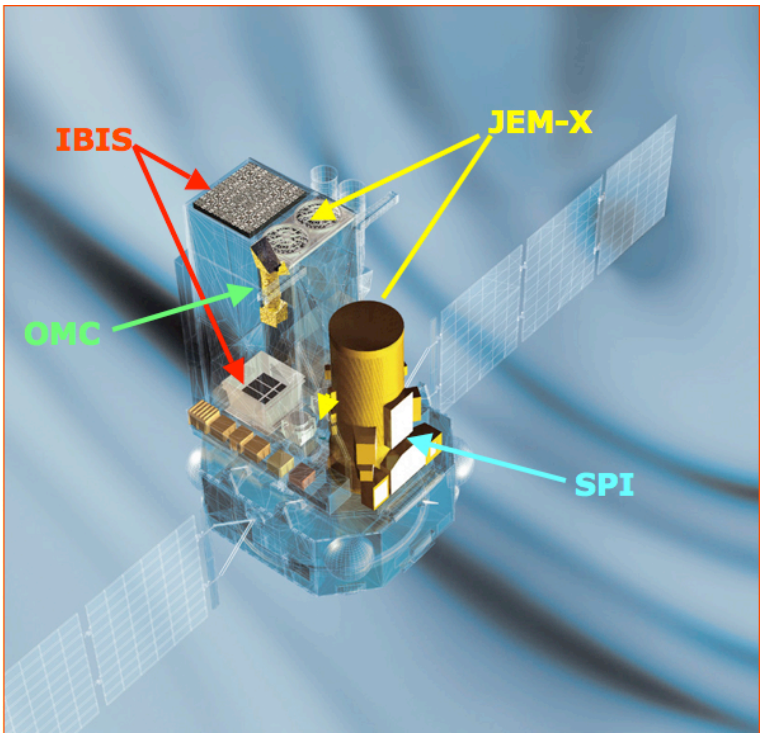

FIG. 2.1 – Représentation du satellite *INTEGRAL* montrant l'emplacement des quatres télescopes embarqués. Crédits ESA/ESAC.

lequel le centre de donnée est fourni par l'Agence Spatiale Européene, l'ISDC est un consortium extérieur dirigé par la Suisse, et dont la sélection est passée, comme pour tous les autres instruments, par un processus d'appel d'offre. Outre sa fonction d'archivage, et de distribution des données et des logiciels, l'ISDC collecte les données en temps quasi-réel, afin d'en faire une première analyse rapide (QLA pour *Quick Look Analysis*). Ce QLA à plusieurs raisons d'être ; on y vérifie en particulier l'état des détecteurs (effet des radiations, température, pixels bruyants, ...). C'est aussi lors du QLA que l'état du ciel (l'activité des sources connues, la présence de GRB (*Gamma-Ray Bursts*), ou de nouvelles sources) est étudié. Les observations d'*INTEGRAL* sont découpées en sous-pointés (SCW pour *SCience Windows*) d'environ une heure. Une nouvelle image du ciel apparaît sur les écrans de QLA pour chaque SCW durant la période d'observation (environ 2,5 jours/orbite de 3 jours). Ceci permet alors un premier suivi du ciel X et Gamma sur cette base temporelle.

Je suis arrivé à l'ISDC moins d'un mois après le lancement d'*INTEGRAL*, en tant que représentant de l'instrument IBIS. Je ne rentrerai pas ici dans toutes les tâches plutôt instrumentales auxquelles j'ai participées alors, mais me concentrerai sur ce qui est relatif à la suite de ce document : la surveillance du ciel X-dur. Lors des phases de routine j'ai ainsi participé aux tâches de QLA durant des périodes d'astreinte. Pendant celles-ci, et grâce à mes propres programmes d'observations, j'ai pu avertir la communauté scientifique lors du réveil de certaines sources X (par exemple Aql X-1 Rodriguez et al. 2004c) ; j'ai aussi participé et contribué à la découverte d'un grand nombre de nouvelles sources, par exemple IGR J17544−2619 (Sunyaev et al. 2003). Le fait d'être géographiquement localisé au centre de données m'a, de plus, permis d'être averti promptement de l'état du ciel X et de pouvoir réagir en fonction de celui-ci, en déclenchant, en particulier, des programmes d'observations dédiés. Très

tôt j'ai développé le site web des sources IGR[1] que je présente succintement au chapitre 8, ainsi que les courriers d'alertes électroniques allant de pair.

Je suis aujourd'hui Co-I de l'ISDC, et à ce titre participe à sa vie scientifique, ainsi qu'à son évolution future, et post-*INTEGRAL*. L'expérience que j'ai acquise dans la participation à la vie d'un centre de données est aujourd'hui mise à contribution. Je fais en effet partie du FSC (*French Science Centre*) de SVOM (future mission Franco-Chinoise dédiée aux GRB), et suis CoI de cette mission avec un fort intérêt pour la science hors sursaut. Je fus aussi membre du groupe de travail de définition du SiSOC (*Simbol-X Science Operation Centre*) (tâches, organisation, préparation, moyens) avant l'arrêt de la mission Simbol-X en mars 2009.

2.3 IBIS

IBIS est certainement l'instrument d'*INTEGRAL* que j'ai le plus utilisé. Il est aussi celui qui, pour la communauté étudiant les objets compacts accrétant (et j'inclus ici les noyaux actifs de galaxies), a permis de produire le plus de résultats. C'est un télescope fonctionnant sur la technique du masque codé, qui permet de remonter à la position des sources stellaires par déconvolution de l'image du masque qu'elles projettent sur le détecteur.

Son plan détecteur est composé de deux instruments : ISGRI (*IBIS Soft Gamma-Ray Imager*, Lebrun et al. (2003)) est le plan supérieur et est efficace dans la région spectrale ∼15–500 keV ; PiCSIT (*Pixellated Imaging Caesium Iodide Telescope*, Labanti et al. (2003)) est efficace dans la région ∼ 200–10000 keV. Ce dernier fonctionnant dans un domaine d'énergie où les sources sont faibles et le bruit de fond fort, n'a, à ce jour, détecté qu'une poignée de sources. Cet instrument m'est donc d'un usage restreint.

ISGRI a une surface de 2800 cm^2 composée de 16384 pixels de semi-conducteur de tellure de cadmium (CdTe), permettant à IBIS d'avoir une résolution angulaire de 12 arcmin. Le télescope possède en outre des capacités photométriques et spectroscopiques. Il a une résolution temporelle de 61 μs et un pouvoir de séparation en spectroscopie de 9 keV à 100 keV. Le lecteur intéressé par plus de détails sur IBIS pourra lire Ubertini et al. (2003), Lebrun et al. (2003), et Labanti et al. (2003). Les principales caractéristiques du télescope sont reportées dans la table 2.1.

La fonction première d'IBIS est de faire une carte du ciel dans le domaine des rayons X-durs. Le but premier est d'obtenir une position fine des objets célestes. La précision de localisation d'IBIS est dépendante de l'intensité de la source observée, et donc de la significativité de sa détection. Cette dépendance a été étudiée par A. Gros et al. en se basant notamment sur différents pointés effectués sur des sources brillantes (avec donc différents temps d'exposition et valeurs d'angles hors-axe). Gros et al. (2003) ont établi que l'incertitude à 90 % sur la position d'une source en arcmin suit $\Delta_{pos} = 22.1 \times SNR^{-0.95} + 0.16$ où SNR est le rapport signal à bruit de la détection. Cette fonction est représentée en figure 2.2.

2.4 JEM-X

JEM-X est composée de deux télescopes à masques codés identiques. Les unités détectrices sont composées de chambres à gaz à haute pression (90% de xénon et 10% de méthane à 1.5 bars). Comme pour IBIS ses principales caractéristiques scientifiques sont rappelées dans la table 2.1. Sa couverture spectrale dans les rayons X plutôt mous (sous 20 keV en particulier) en fait un instrument extrêmement utile pour l'étude des sources accrétantes, puisque c'est dans ce domaine spectral que les composantes thermiques (disque d'accrétion, surfaces d'étoiles à neutrons) ont leur pic de

[1] http ://isdc.unige.ch/∼rodrigue/html/igrsources.html

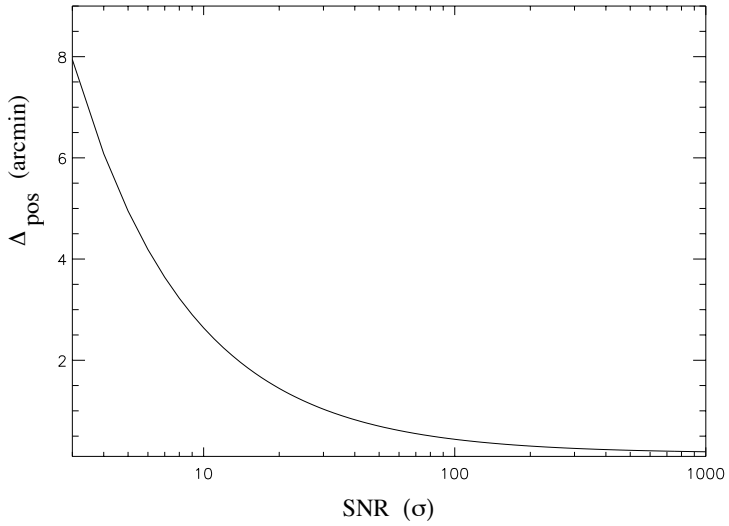

FIG. 2.2 – Dépendance de la précision de localisation d'IBIS en fonction du rapport signal à bruit de la détection, obtenue à partir d'un ajustement des données (Gros et al. 2003).

	JEM-X	IBIS	SPI
Domaine spectral	3–35 keV	15–10000 keV	18–8000 keV
Résolution spatiale	$3'$	$12\,'$	$2.5°$
Précision de localisation	$1'(15\sigma)$	$3'(10\sigma)$	$< 1.3°$
Résolution spectrale	1.3 keV (à 10 keV)	8 keV (à 100 keV)	2.2 keV (à 1.3 MeV)
Résolution temporelle	122 μs	61 μs	129 μs
Champ de vue (totalement codé)	$4.8°$	$8.3°\times8.0°$	$14°$

TAB. 2.1 – Principales caractéristiques des trois télescopes X/gamma embarqués sur *INTEGRAL*.

luminosité. La réussite de ce détecteur est cependant toute relative. Afin de préserver l'instrument d'une dégradation rapide, une seule des deux caméras est maintenue en fonctionnement lors des observations. De plus, l'instrument est peu sensible : sur le nombre de sources découvertes par *INTEGRAL* JEM-X n'en a découverte qu'une. La plupart, même, des sources découvertes par IBIS ne sont pas détectés par JEM-X. Cet instrument sera donc d'une faible utilité et aura peu d'influence dans cette partie. Il sera exploité pleinement lors de certaines études de GRS 1915+105 (présentées en parties II et III). Pour bien plus de détails sur cet instrument, je renvoie le lecteur intéressé à Lund et al. (2003).

2.5 SPI

Comme les autres instruments de haute énergie d'*INTEGRAL*, SPI est un télescope à masque codé. Comme son nom l'indique sa fonction principale est d'établir la spectrométrie des sources X et Gamma. Pour cela il est doté d'une matrice de 19 détecteurs au germanium à haute pureté. Ces détecteurs sont refroidis à une température de 85 K. La résolution spectrale de 2,2 keV à 1.3 MeV est inégalée dans ce domaine spectral. En raison de la dégradation de ses capacités, un "recuit" c'est-à-

dire un rechauffement des détecteurs est effectué régulièrement. C'est après deux de ces recuits que deux unités de germanium cessèrent de fonctionner. On a longtemps pensé à une relation entre la perte de détecteurs et le recuit (même si de telles pertes ne s'étaient pas reproduites), jusqu'à très récemment (février 2009) lorsqu'un troisième détecteur a été perdu, et ce sans rapport avec aucun recuit. Les principales caractéristiques sont reportées dans la table 2.1. Le lecteur intéressé par plus de détails pourra lire Vedrenne et al. (2003).

La faible résolution spatiale et moins bonne sensibilité de SPI dans l'intervalle 20–200 keV par rapport à IBIS en fait un instrument d'un usage marginal pour la découverte de sources et même pour le suivi des sources variables. Les images de SPI ne sont notamment pas systématiquement analysées lors des QLA.

Chapitre 3
Découverte de nouvelles sources de rayonnement X et gamma mou

3.1 Balayages et suivis des régions centrales et du plan de la Galaxie

Comme je le mentionne au chapitre précédent, les balayages galactiques d'*INTEGRAL* ont tout d'abord permis de suivre l'activité des sources connues. On détectera, par exemple, les sources transitoires entrant en éruption, ainsi que tout changement de comportement (état spectral, flash de fusion d'hydrogène, etc...). Les résultats des tous premiers GPS effectués dans la region du Cygne et celle de la Voile sont décrits dans Del Santo et al. (2003) et Rodriguez et al. (2003b).

De manière toute aussi importante, ces balayages devaient permettre de trouver de nouvelles sources (Fig. 3.1), notamment des transitoires entrant en éruption. Et, en effet, une myriade de nouvelles sources ont été découvertes. Nous recensons environ 250 IGR aujourd'hui. Parmis celles-ci l'apport d'*INTEGRAL* est d'avoir mis au jour une population assez importantes de HMXB relativement faibles, et surtout très absorbées. Toutes ces sources semblent être des systèmes contenant des étoiles supergéantes. Ce résultat a une grande importance puisqu'avant le lancement d'*INTEGRAL* les HMXB à supergéantes (sg-HMXB par la suite) étaient un sous ensemble faible des HMXB, ce qui n'est plus le cas aujourd'hui. Cet aspect doit donc être pris en compte dans les modèles de synthèse de populations galactiques et d'évolution des binaires serrées. Je présente, en section 2, l'exemple de la région tangente au bras de Norma, dans laquelle un grand nombre de ces sources furent découvertes. J'y détaille notamment la découverte de la première source *INTEGRAL*, IGR J16318−4848 (Walter et al. 2003).

Je suis PI et CoI d'un certain nombre d'observations permettant des suivis réguliers de certaines portion du ciel dans lesquelles se trouvent des sources d'interêt. C'est le cas de GRS 1915+105, se trouvant dans la région de l'Aigle, et pour laquelle je suis PI d'une campagne de suivis depuis 2003. Grâce à cette campagne, et profitant du grand champ de vue d'*INTEGRAL* je veille, depuis 2003, sur Aquila X-1, LMXB transitoire contenant une étoile à neutron, et communique alors sur son état d'activité (Rodriguez et al. 2004c, 2005b; Rodriguez & Shaw 2005; Rodriguez et al. 2007b,c, 2009a,

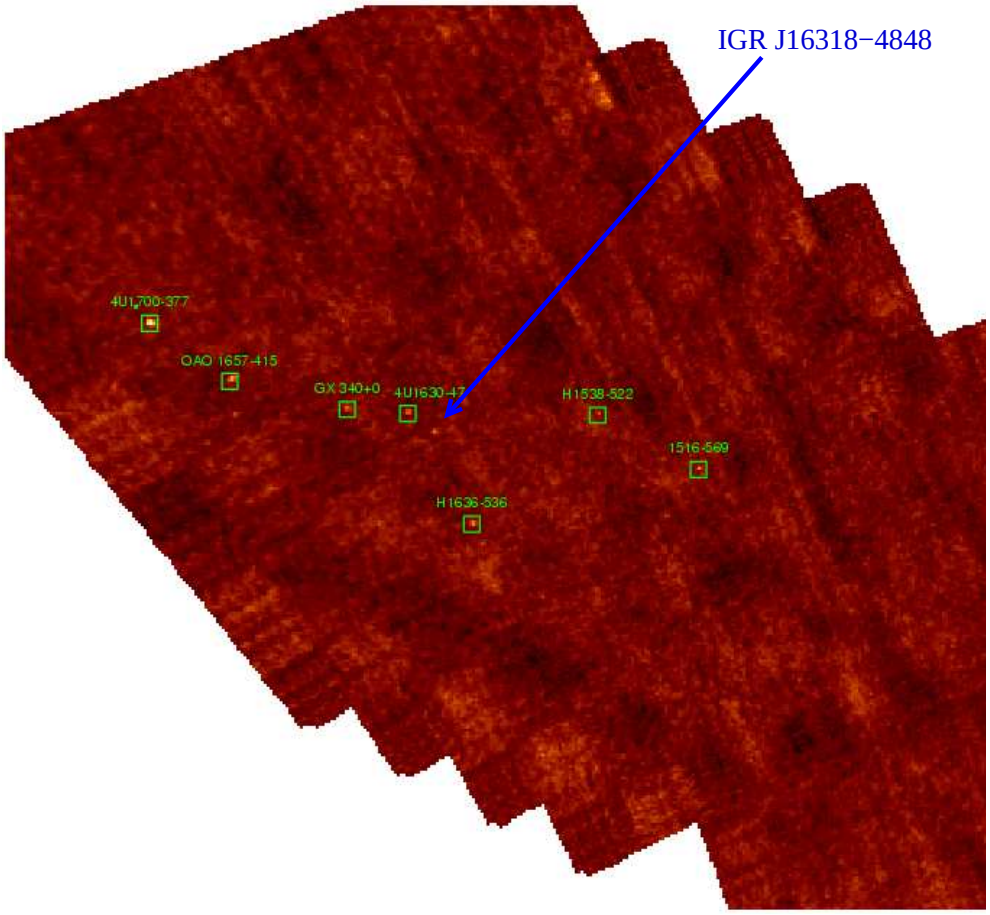

FIG. 3.1 – Premier GPS de la region de Norma. De nombreuses sources connues sont clairement détectées (en vert). Non loin du candidat trou noir 4U 1630−47, nous avons découvert IGR J16318−4848 (Courvoisier et al. 2003; Walter et al. 2003), indiqué par une flèche. Crédit image : "INTEGRAL Picture of the Month" J. Rodriguez et A. Bazzano, ESA, 2003.

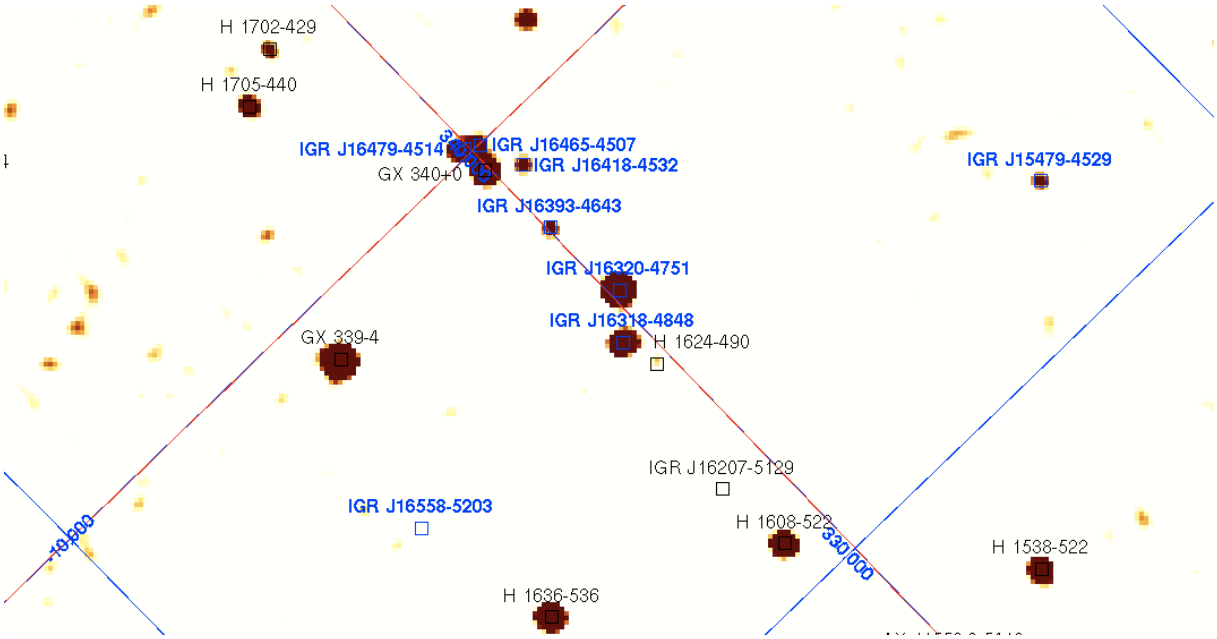

FIG. 3.2 – Mosaique de la région de Norma, prise entre 20 et 40 keV, pour une exposition d'environ 100 ks. On y voit clairement apparaître en bleu les IGR.

ATels 280,464,660,1079,1229,1977). Les résultats obtenus lors de l'éruption de 2006 sont publiés dans Rodriguez et al. (2006b). Cette région a aussi révélé de nombreuses sources dont la dernière en date fut trouvée par nos soins en mars 2009 (Tuerler et al. 2009). J'illustre et résume toutes ces années de suivis de la région de l'Aigle en section 3.3.

Notons qu'en plus de ces régions particulières, Lionel Prat, étudiant en thèse sous ma direction, suit activement l'activité de 17 trous noirs connus. Cela nous a, en particulier, permis d'étudier l'éruption de H1743−322 avec *INTEGRAL*, et à l'aide d'autres satellites X (Prat et al. 2009), sans oublier le domaine radio (Coriat et al. 2009 en préparation).

3.2 Le bras de Norma

La région de direction tangente au bras de Norma (référencée dans SIMBAD[1] à RA=16h 00m et Dec=-50° equinoxe J2000) est certainement la région du ciel où le plus grand nombre de source *INTEGRAL* Galactiques a été trouvé (Bodaghee et al. 2007). Comme nous le verrons par la suite pour certains cas particuliers, il s'est vite avéré qu'une grande partie de ces sources étaient des HMXBs contenant des pulsars. Ceci n'est, *in fine*, pas vraiment surprenant vu que les bras galactiques sont des régions d'intense formation d'étoiles ; comme les HMXBs sont des systèmes jeunes qui n'ont pas vraiment eu le temps de migrer à travers la Galaxie, nous les retrouvons à proximité de leur région de naissance. Une mosaique d'environ 100 ks d'exposition totale est montrée comme exemple en Figure 3.2.

[1] http ://simbad.u-strasbg.fr/simbad/

3.2.1 IGR J16318−4848 la première source découverte par *INTEGRAL*

IGR J16318−4848 a suscité un énorme intérêt lors de sa découverte. Tout d'abord elle fut découverte le 29 janvier 2003, extrêmement tôt après le début du programme d'observation général, durant le premier GPS couvrant la région de Norma (Courvoisier et al. 2003, Fig. 3.1). La ToO faite avec *XMM–Newton* a montré que cette source était très probablement une HMXB bien particulière : son spectre est tout d'abord extrêmement absorbé ($N_H$vaut quelques 10^{24} cm^{-2}) ; son émission X est complètement obscurcie sous ∼4 keV. De plus d'énormes raies de fluorescence respectivement attribuées au Fer (raies K_α et K_β) et au Nickel (raie K_α) sont clairement visibles. Une "épaule Compton" (CS pour *Compton shoulder*), résultant de l'interaction des photons de fluorescence avec les électrons du milieu absorbant, est aussi possiblement détectée (Matt & Guainazzi 2003). Si elle était confirmée, cette CS serait d'une importance capitale pour la compréhension de la nature du matériel absorbant dans cette source (Matt 2002; Watanabe et al. 2003). La résolution spectrale d'*XMM–Newton* n'est, à mon avis, pas suffisante pour totalement confirmer la présence du CS, et surtout pour contraindre ses paramètres. L'article (Walter et al. 2003, A&A, 411, L427), qui relate les principaux résultats des observations *XMM–Newton* et *INTEGRAL* est inclu à la fin de la partie I au chapitre 5.

3.2.2 Une moisson de nouvelles sources

Les observations répetées ont permis la découverte de nombreuses sources dans la région de Norma. Je mentionnerai IGR J16320−4751, découverte lors d'un ToO sur le trou noir 4U 1630−47 (Tomsick et al. 2003) que nous suivrons tout au long de ce document (Rodriguez et al. 2003c,d,e, 2006a, et aux chapitres 4,6, 10). Le tableau 3.1 reporte toutes les sources découvertes dans cette région après presque sept années d'observations (sources Bird et al. 2004, 2006, 2007; Bodaghee et al. 2007; Krivonos et al. 2007, et les références y étant reportées[2]). Notons la forte proportion de HMXB parmis ces 20 sources : 9 sont des HMXB confirmées, et 3 autres sources sont des candidats HMXB.

3.3 Le suivi de la région de l'Aigle : IGR J19140+0951 et autres sources

La région de la constellation de l'Aigle (région tangente au bras du Sagitaire) que je centrerai arbitrairement sur la source transitoire Aql X-1 (RA=19h 11m 16.0s, Dec=+00° 35′ 06″) a elle aussi bénéficié d'un temps d'exposition total relativement important. Une mosaique d'environ 900 ks, prise lors des toutes premières observations de cette région (mars–juin 2003) est représentée en figure 3.3. En ce qui me concerne directement, cette région contient le microquasar GRS 1915+105, que nous (en étroite collaboration avec D. Hannikainen de l'observatoire radio Metsahövi en Finlande) monitorons depuis le lancement d'*INTEGRAL*. Nous avons obtenu un grand nombre de résultats sur cet objet (Fuchs et al. 2003; Hannikainen et al. 2003b, 2005; Rodriguez et al. 2004a, 2008a,b), dont je détaillerai une partie dans la suite (chapitres 7, 11, et 12).

Le suivi de la région de l'Aigle nous a permis d'y découvrir, dès la première observation, IGR J19140+0951 (Hannikainen et al. 2003a). Dès lors, D. Hannikainen et moi-même nous sommes particulièrement intéressés à cette source. Sa position à $\sim 1.1°$ de GRS 1915+105 nous assurait de

[2]Voir aussi le site web dédié aux IGR http ://idsc.unige.ch/∼rodrigue/html/igrsources.html

Source	type	RA	Dec	erreur
IGR J15479-4529	CV/IP	15h 48m 14.7s	$-45°\ 28'\ 40.4''$	$3.5''$
IGR J15529-5029	CV ?	15h 52m 46.56s	$-50°\ 29'\ 52.3''$	$4.9''$
IGR J16167-4957	CV/IP	16h 16m 37.74s	$-49°\ 58'\ 44.5''$	$0.6''$
IGR J16185-5928	Sey 1	16h 18m 26.38s	$-59°\ 28'\ 45.27''$	$5''$
IGR J16195-4945	HMXB	16h 19m 32.20s	$-49°\ 44'\ 30.7''$	$0.6''$
IGR J16207-5129	HMXB	16h 20m 46.26s	$-51°\ 30'\ 06.0''$	$0.6''$
IGR J16248-4603	?	16h 24.8m	$-46\ °\ 03'$	4.7'
IGR J16283-4838	HMXB ?	16h 28m 10.7s	$-48°\ 38'\ 55''$	$5''$
IGR J16287-5021	HMXB ?	16h 28m 26.85s	$-50\ °\ 22'\ 39.6''$	$0.64''$
IGR J16293-4603*	AGN ou XRB particulière	16h 29m 12.87s	$-46°\ 02'\ 50.9''$	$0.6''$
IGR J16318-4848	HMXB	16h 31m 48.6s	$-48°\ 49'\ 00''$	$4''$
IGR J16320-4751	HMXB	16h 32m 01.9s	$-47°\ 52'\ 27''$	$3''$
IGR J16328-4726	?	16h 32.8m	$-47°\ 26'$	4.5'
IGR J16351-5806	Sey 2	16h 35m 13.17s	$-58°\ 04'\ 49.68''$	$5.1''$
IGR J16358-4726	HMXB ?	16h 35m 53.8s	$-47°\ 25'\ 41.1''$	$0.6''$
IGR J16393-4643	HMXB	16h 39m 05.4s	$-46°\ 42'\ 12''$	$4''$
IGR J16418-4532	HMXB	16h 41m 51.0s	$-45°\ 32'\ 25''$	$4''$
IGR J16465-4507	HMXB	16h 46m 35.5s	$-45°\ 07'\ 04''$	$4''$
IGR J16479-4514	HMXB	16h 48m 06.6s	$-45°\ 12'\ 08''$	$4''$
IGR J16493-4348	HMXB	16h 49m 26.92s	$-43°\ 49'\ 08.96''$	$0.6''$

TAB. 3.1 – Liste des sources découvertes dans le bras de Norma, c'est à dire dans un rayon d'environ 10° autour de la position donnée dans SIMBAD (RA=16h 00, Dec=-50°). Un ? après un type indique que la source est un candidat de ce type. *Kuiper et al. 2008 ATel 1774.

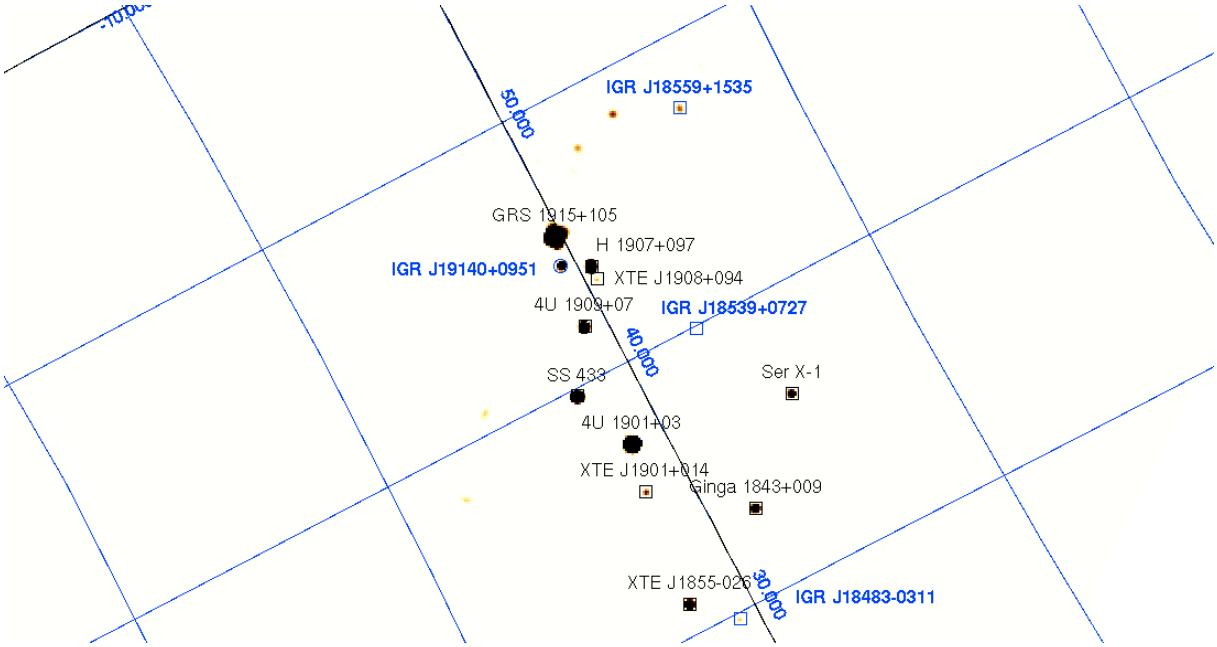

FIG. 3.3 – Mosaique de la région de l'Aigle, prise entre 20 et 40 keV, pour une exposition d'environ 900 ks. Les IGR y apparaissent en bleu.

Source	type	RA	Dec	erreur
IGR J18259-0706	AGN/Sey 1	18h 25m 57.58s	-07° 10′ 22.8″	0.64″
IGR J18284-0345	?	18h 28m 30.0s	-03° 45′ 43.2″	4″
IGR J18307-1232	CV	18h 30m 49.6s	-12° 32′ 18″	8″
IGR J18325-0756	HMXB	18h 32m 28.32s	-07° 56′ 41.7″	0.64″
IGR J18406-0539	HMXB	18h 40m 55s	-05° 39′	3′
IGR J18450-0435	HMXB	18h 45m 01.4s	-04° 33′ 57.7″	2″
IGR J18462-0223	HMXB	18h 46.9m	-02° 23′ 12″	2′
IGR J18483-0311	HMXB	18h 48m 17.17s	-03° 10′ 15.54″	3.3″
IGR J18485-0047	AGN ?	18h 48m 25.67s	-00° 46′ 33.3″	4.9″
IGR J18490-0000	PWN	18h 49m 01.6s	-00° 01′ 18″	3.7″
IGR J18539+0727	BHC	18h 53.9m	+07° 27′	3′
IGR J18559+1535	AGN, Sey 1	18h 56m 00.6	+15° 37′ 58″	3.6”
IGR J19048-1240	?	19h 04.8m	-12° 40′	4.2′
IGR J19112+1358	?	19h 11m 12.6s	+13° 58′ 52″	4′
IGR J19140+0951	HMXB	19h 14m 4.232s	+09° 52′ 58.29″	0.6″
IGR J19267+1325	CV/IP	19h 26m 26.98s	+13° 22′ 05.1″	0.64″
IGR J19284+0107	?	19h 28.4m	+01° 07′ 08″	1.3′
IGR J19294+1816	HMXB	19h 29m 55.9s	+18° 18′ 39″	3.5″
IGR J19308+0530	XRB ou CV	19h 30m 50.9s	+05° 30′ 57″	4.3″
IGR J19378-0617	AGN/Sey 1.5	19h 37m 33.1s	−06° 13′ 04″	3.5″

Tab. 3.2 – Liste des sources découvertes dans la région de l’Aigle. J’ai arbitrairement mentionné les sources trouvées à moins de 15° d’Aql X-1.

l’avoir toujours dans le champ totalement codé de IBIS, et dans le champ de vue de JEM-X lors des observations de GRS 1915+105. Nous avons immédiatement monté un programme d’observations de haute énergie avec *RXTE* (en simultaneité avec *INTEGRAL*), puis des observations dans l’infra rouge. Nous suivrons cet objet au fil de ce document, et verrons comment nous en avons affiné la compréhension jusqu’à en obtenir un modèle basique (chap. 10).

L’article “Discovery of a new INTEGRAL source : IGR J19140+0951” (Hannikainen et al. 2004, A&A, 423, L17), qui est reporté à la fin de cette partie au chapitre 5, résume la découverte et donne les résultats obtenus lors des premières observations de cet objet avec *INTEGRAL* et *RXTE*. En dépit de l’absence de position fine ne permettant pas l’identification de contrepartie à d’autres longueurs d’onde, les paramètres spectraux et le comportement général de la source suggérait, dès alors que cet objet était galactique et très probablement une XRB à étoile à neutrons.

IGR J19140+0951 n’est évidemment pas le seul objet découvert dans cette région, et, comme pour le bras de Norma, les observations profondes ont permis, en plus d’objets relativement brillants, de détecter des objets faibles (Molkov et al. 2004; Bird et al. 2004, 2006, 2007; Krivonos et al. 2007). Ajoutons aussi les transitoires détectées par nos soins, dont la toute récente IGR J19294+1816 Tuerler et al. (2009).

La liste de toutes les nouvelles sources découvertes dans cette région est reportée en table 3.2. J’ai arbitrairement choisi d’y faire figurer toutes les sources se trouvant à moins de 15° de Aql X-1. Dans cette région encore, les HMXB semblent constituer la majorité des 20 IGR.

3.4 Conclusions du chapitre

À ce jour, parmis les quelques 500 sources détectées par IBIS au-delà de 20 keV, nous pouvons en dénombrer environ 250 comme nouvellement détectées. La répartition des sources vues par IBIS sur le plan du ciel est representée sur la Figure 3.4 (source Bodaghee et al. 2007). En dévoilant un grand nombre de nouvelles sg-HMXB, *INTEGRAL* a permis de ré-équilibrer la répartition sg-HMXB contre HMXB contenant une étoile Be (Be-HMXB par la suite) ce qui apporte de nouvelles contraintes sur la synthèse de population, et les modèles d'évolution stellaire. Un nouveau type d'objet a aussi été découvert : il s'agit de sg-HMXB à sursauts très courts. Ici, l'avantage d'*INTEGRAL* réside dans sa plage spectrale permettant de lever le problème de l'absorption obscurcissant les Sg-HMXB à basse énergie, et son grand champ de vue permettant la détection d'évenements courts et fortuits.

Mieux connaître une famille de sources est capital si l'on veut bien comprendre leur comportement général (éruptions, transitions de classes de luminosité, lien avec leur environnement), leur origine (par exemple lieu de naissance, et liens avec les propriétés locales de la Galaxie) et leur évolution (influence de l'environnement, du compagnon dans les binaires, ...). La figure 3.4 montre, par exemple, que les HMXB sont plutôt réparties dans le disque galactique, à proximité des bras spiraux. Ce résultat s'explique facilement lorsque l'on sait que les HMXB sont jeunes et n'ont donc pas eu le temps de migrer loin de leur lieu de formation que sont les bras spiraux. L'analyse physique (spectres, courbes de lumière) nous aidera alors à cerner les processus physiques qui sont à l'origine des rayonnements émis. Bien que tous ces aspects aient une importance capitale pour notre compréhension du ciel, l'identification de la nature des sources de ces rayonnements en est un préalable fondamental. A partir des seules données *INTEGRAL* cela est dans une vaste majorité des cas impossible. C'est l'aspect identification et les différents moyens et programmes que j'ai mis en route que je décris au chapitre suivant.

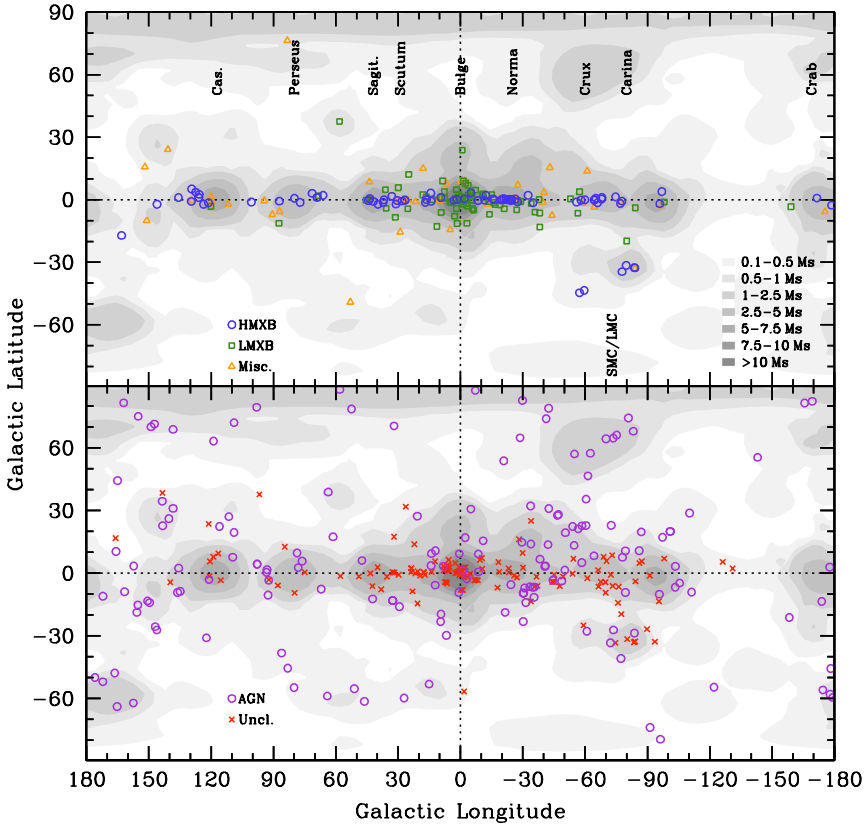

FIG. 3.4 – Répartition des sources de types Galactiques (en haut) et extraGalaciques et de type inconnu (en bas) vues par IBIS sur le plan du ciel en coordonnées Galactiques (source Bodaghee et al. 2007).

Chapitre 4
Suivis des nouvelles sources à différentes longueurs d'ondes

4.1 Introduction

INTEGRAL ne permet pas de connaître avec exactitude le type d'un objet nouvellement détecté. Le moyen le plus certain, est d'observer l'objet à d'autres longueurs d'onde afin de découvrir ses contreparties (ex. galaxie, type d'étoile, présence de jet radio, etc). Bien que possédant une résolution angulaire inégalée au-delà de 20 keV, les boîtes d'erreur d'*INTEGRAL* (chap. 2 Gros et al. 2003) sont encore trop grandes, puisque elles englobent de nombreuses contreparties potentielles, en particulier dans les régions centrales de la Galaxie, régions où, bien entendu, *INTEGRAL* a découvert une grande partie de ses nouvelles sources.

Malgré la présence de nombreuses contreparties possibles dans la boîte d'erreur, il existe certains cas pour lesquels peu de doutes subsistent quand à l'identification de la probable contrepartie, et donc du type l'objet ; le cas le plus évident concerne la présence d'une galaxie, ou mieux, d'un noyau actif de galaxie (AGN, *Active Galactic Nucleus*) connu dans la boîte d'erreur. Il est communément admis alors que l'objet de haute énergie est probablement un AGN. N. Masetti de l'INAF de Bologne va même un peu plus loin ; il estime que dans les régions centrales et dans le disque Galactique, la présence d'une supergéante ou d'une étoile massive de type Be, permet de classifier la source *INTEGRAL* comme une HMXB. Il mène depuis plusieurs années une campagne de suivis en spectroscopie visible des étoiles massives se trouvant dans la boîte d'erreur des IGRs et a possiblement identifié de nombreuses sources (Masetti et al. 2004, 2006b,d,a,c, 2008, 2009). Bien que cette dernière méthode n'ait pas complètement été mise en défaut, elle est extrêment imprécise, et peut être source d'erreur. Un exemple concerne la source IGR J05009−7047, dont la boîte d'erreur *INTEGRAL* contient un AGN. On aurait alors pu penser que l'objet était effectivement une galaxie active. L'affinement de la boîte d'erreur suite à une observation avec *Chandra* a permis d'associer l'objet à une étoile de forte masse dans le grand nuage de Magellan.

Nous (J. Tomsick, S. Chaty et moi-même) préférons commencer par affiner la position X de ces

objets avant d'en mener des campagnes d'observations multi longueurs-d'onde. L'étape primordiale consiste donc à pointer un télescope X à haut pouvoir séparateur (*XMM–Newton*,*Chandra*, ou *Swift*), afin d'obtenir des positions précises à l'arcseconde. Les contreparties peuvent ensuite être identifiées dans des catalogues, ou bien grâce à des observations dédiées (en infrarouges, visibles, UV et/ou radio) afin d'en déterminer le type (Rodriguez et al. 2003e; Tomsick et al. 2006; Rodriguez et al. 2008d; Tomsick et al. 2008; Chaty et al. 2008; Rodriguez et al. 2009b; Tomsick et al. 2009b; Butler et al. 2009).

Je décris dans ce chapitre cet aspect purement astronomique de l'identification des sources. Ici donc, comme on le verra, les IGRs seront classées en AGN, LXMB, HMXB (ou CV) selon qu'une galaxie, une étoile de faible masse, ou bien une étoile de forte masse aura été trouvée dans la boîte d'erreur. Malgré la finesse de la position, il reste des cas pour lesquelles il existe plusieurs contreparties possibles. Nous discutons ces cas à partir d'arguments simples. Pour aller plus loin dans la détermination, puis la compréhension de ces objets, nous ferons appel aux études des variabilités temporelles et à la spectroscopie X, qui seront présentées dans les parties ultérieures lorsque la physique des objets sera discutée plus en détails. Sur ces aspects, je mène, depuis plusieurs années, une double campagne *Swift* et *RXTE* d'observations simultanées de nouvelles IGR ayant pour but la détermination de la position fine (quelques secondes d'arc), l'établissement d'un spectre large bande (0.5–150 keV), et l'étude des propriétés temporelles rapides (de la milliseconde à quelques centaines de secondes).

4.2 Positions X fines et quelques identifications "faciles"

4.2.1 Les observations *Swift*

Swift est observatoire dédié à l'observation des sursauts Gamma (GRB pour *Gamma-Ray Burst*). Il embarque un moniteur X-dur grand champ qui balaye le ciel constamment (BAT pour *Burst Alert Telescope*). En cas d'alerte pour un GRB la plateforme arrête son balayage et pointe vers la direction du sursaut. Ceci permet au GRB d'entrer dans le champ de vue du télescope X-mou (XRT pour *X-ray Telescope*) dont le but est de donner des boîtes d'erreur fine. Ce repointage peut aussi permettre au sursaut d'être détecté par le télescope UVOT (pour *UV Optical Telescope*). En dehors des observations de GRB, l'observatoire pointe diverses sources, pour lesquelles des appels d'offre sont émis, mais aussi des sources d'intérêt général (par exemple des sources nouvellement détectées par d'autres observatoires dont des IGR) dans le cadre de programme d'observations générales (par opposition au programme principal se focalisant sur les GRB).

En plus des programmes ToO dont je suis PI sur *Swift*, j'ai analysé toute les observations de sources *INTEGRAL* pour lesquelles aucune position fine (c'est-à-dire inférieure à 10″) n'existait (en août 2008). Le but était d'obtenir une position X assez fine pour pouvoir chercher des contreparties à d'autres longueurs d'onde en commençant avec l'UV grâce au moniteur UVOT embarqué, puis, dans les catalogues et archives, et tenter de déterminer le type de la source. Comme toujours les possibilités d'études spectroscopiques du XRT devaient aussi permettre d'affiner les identifications.

4.2.2 Quelques résultats

L'échantillon de sources détectées s'élève à 29. Il n'est donc pas question ici de faire un résumé des résultats pour chacune, ce qui serait long, laborieux et ennuyeux pour le lecteur. La table 4.1 donne un résumé des identifications que je suggère dans ces travaux.

Un cas d'identification "facile" est illustré par la source IGR J09025−6814. L'observation de *Swift* dévoile la présence d'une source unique dans la boîte d'erreur d'*INTEGRAL*. Bien que cette

Nom (IGR)	Type & Commentaires
J02343+3229	Sey 2
J03184−0014	sources *INTEGRAL* et *Swift* ne sont pas liées
J03532−6829	BL Lac
J05319−6601	probable XRB in LMC
J05346−5759	CV
J09025−6814	AGN, poss. Compton épaisse, Sey 2
J09523−6231	Sey 1.5
J10101−5654	HMXB
J10147−6354	possible Sey 2
J11187−5438	?
J13000+2529	AGN
J13020−6359	HMXB contenant un pulsar
J13149+4422	Sey 2
J14579−4308	Sey 2
J15161−3827 #1	Liner/Sey 2
#2	?
#3	YSO
#4	?
J15479−4529	CV/IP
J16287−5021	possible HMXB
J16385−2057	Sey 1
J17353−3539	possible HMXB
J17476−2253	possible XRB
J18214−1318	probable HMXB (supergéante ?)
J18490−0000	possible XRB
J18559+1535	Sey 1
J19267+1325	Source Galactique
J19308+0530	XRB avec étoile à neutrons ou CV
J19378−0617	Sey 1.5
J20286+2544 #1	Sey 2
#2	possible Sey 2
J23206+6431	Sey 1
J23524+5842	?

TAB. 4.1 – Résumé des types des sources *INTEGRAL* dont nous avons identifié une contrepartie *Swift*. Les identifications obtenues dans certains cas sont aussi indiquées. Sources Rodriguez et al. (2008d, 2009b), et les références citées dans ces travaux.

source soit relativement faible, nous avons pu en obtenir une position précise à $RA_{J2000}=09^h\ 02^m\ 39.4^s$ $\delta_{J2000}=-68^\circ\ 13'\ 38.7''$ avec une incertitude de 4.8″. Les images prises avec UVOT montre que cette position coïncide exactement avec le noyau d'une galaxie spirale vue par la tranche (Fig. 4.1). Cette source est aussi reportées dans le catalogue *2-Microns All-Sky Survey Extended Source* (2MASX), elle-même indiquée comme une galaxie à z=0.013 dans le *NASA Extragalacic Database* (NED). Evidemment une association due à la chance n'est pas à exclure, notamment entre la source *INTEGRAL* et la galaxie. Cependant le fait que l'on ne trouve qu'une source X dans la boîte d'erreur *INTEGRAL*, *a-fortiori* faible, et la compatibilité des spectres X et Gamma avec ceux des AGN renforce les diverses associations. Tous les résultats que j'ai obtenus à partir des observations *Swift*

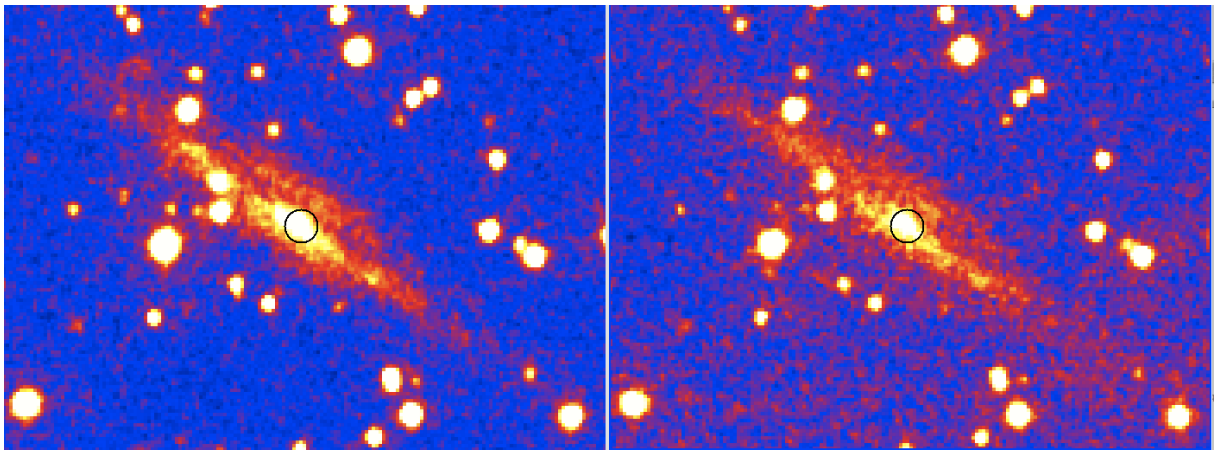

FIG. 4.1 – $2.9' \times 2.13'$ images en bande U (gauche) et UW1 (gauche) du champ autour de la meilleure position de IGR J09025−6814 obtenue avec *Swift*. Le boîte d'erreur tombe sur le centre d'une galaxie suggérant que l'objet de haute énergie est un AGN.

sont reportés dans Rodriguez et al. (2008d, A&A, 482, 731) et Rodriguez et al. (2009b, A&A, 494, 417) et qui sont inclus au chapitre 5 en fin de partie I.

4.3 Un cas plus complexe IGR J16320−4751

Je prends comme exemple, ici, IGR J16320−4751, la deuxième source découverte par *INTEGRAL* (Tomsick et al. 2003) le 1^{er} février 2003. La recherche de contrepartie dans des catalogues X a montré que cette source faisait partie du catalogue des sources faibles d'*ASCA* (Sugizaki et al. 2001), et qu'elle avait alors été nommée AX J1631.9-4752. Immédiatement après sa (re-)découverte j'ai demandé et obtenu une ToO de type DDT avec *XMM–Newton*. Le but de l'observation était d'utiliser la grande précision de localisation des caméra EPIC de ce télescope X (environ 2″pour les caméras MOS) pour affiner et pouvoir identifier des contreparties à d'autres longueurs d'ondes. Les capacités de spectroscopie et de photométrie de cet observatoire devaient aussi permettre d'identifier plus précisemment le type de l'objet.

Notre réaction rapide nous a permis de donner la position *XMM–Newton* et une possible contrepartie de la source X rapidement à travers deux circulaires IAU (Rodriguez et al. 2003c,d). Dans le même temps, je préparais un article présentant et détaillant bien plus les observations et résultats. Cet article (Rodriguez et al. 2003e, A&A, 407, L41), résumé ci-dessous, est inclus au chapitre 5.

L'observation *XMM–Newton* eut lieu le 4 Mars 2003 pour un total de 25 ks. Cependant, en raison d'un bruit de fond (protons solaires) important, seules environ 5 ks purent être utilisées pour

l'analyse scientifique. En fait, comme nous le verrons dans la seconde partie de ce document, ce filtrage est surtout nécessaire pour l'analyse spectrale. La recherche de pulsations périodiques est moins affectée par l'afflux de protons solaires. Malgré ces restrictions j'ai déterminé la position X la plus fine à $RA_{J2000}=16^h\ 32^m\ 01.9^s$, $\delta_{J2000}=-47^\circ\ 52'\ 29''$ avec une incertitude à 90% de $\pm 4''$.

Fort de cette position fine, j'ai pu alors identifié deux contreparties infrarouges possibles dans le catalogue 2MASS, qui apparaissent aussi dans le catalogue POSS. La première source, dont je favorise l'association avec la source de haute énergie, est située à $RA_{J2000}=16^h\ 32^m\ 01.75^s$, $\delta_{J2000}=-47^\circ\ 52'\ 28.9''$. L'autre est plus excentrée dans la boîte d'erreur de *XMM–Newton*. Les magnitudes dérougies en supposant une absorption $N_H=2.1\times10^{22}$ cm^{-2} (la valeur de l'absorption due au HI sur la ligne de visée Dickey & Lockman 1990) suggèrent que la deuxième source est une étoile de type M de température ∼3000 K, alors qu'avec la même valeur d'absorption pour la première source un clair excès infrarouge est visible. Avec une absorption interstellaire plus forte ($N_H=5\times10^{22}$ cm^{-2}), les magnitudes dérougies pourraient suggérer une géante de type K ou même une supergéante. Ces deux suppositions sont en accord avec la forte extinction locale obtenues des ajustements des spectres X ($N_H=21\times10^{22}$ cm^{-2}). Enfin, l'analyse spectrale de la source X montre un spectre de Comptonization typique des sources galactiques accrétantes. La comparaison avec les résultats *ASCA* et des observations d'archives de *Beppo-SAX* montre des fortes variations de l'absorption et de la pente spectrale. Cette dernière peut prendre des valeurs très basses (en valeur absolue), typique des pulsars, alors que les variations de N_H sont relativement typiques des HMXB contenant une supergéante (cf. Partie III). En conclusion, je favorisais une HMXB contenant un pulsar orbitant autour d'une étoile supergéante. Nous verrons par la suite si ces prédictions furent ou non vérifiées et comment.

Source	Nature du système	Type Spectral
IGR J16320−4751	HMXB	O8 I
IGR J16358−4726	HMXB	B[e] I
IGR J16393−4643	HMXB	BIV-V ?
IGR J16418−4532	HMXB	OB I
IGR J16426+6536	Sey 1.5	
IGR J16479−4514	HMXB	O8.5 I
IGR J16558−5203	AGN	
IGR J17091−3624	LMXB	?
IGR J17252−3616	HMXB	O8.5 I
IGR J17391−3021	HMXB	OB I
IGR J17597−2201	LMXB	?
IGR J18027−2016	HMXB	OB I
IGR J18214−1318	HMXB	O9 I
IGR J18308−1232	CV	
IGR J18483−0311	HMXB	B0.5 Ia
IGR J19140+0951	HMXB	B0.5 I
IGR J19267+1325	CV/IP	
IGR J22292+6647	Sey 1	

TAB. 4.2 – Nature et type spectral du compagnon (lorsqu'il est connu) obtenu à partir de nos programmes de suivis infrarouges. Sources Chaty et al. (2008); Butler et al. (2009); Hannikainen et al. (2007); Rahoui et al. (2008).

4.4 Observations visibles et infrarouges dédiées

Même si l'on peut parfois obtenir le type du compagnon de manière relativement simple, seule une approche photométrique et/ou spectroscopique infrarouge ou visible apportera un diagnostic relativement certain. Même si je n'ai pas dirigé personnellement ces travaux, cette approche fait partie de suivis systématiques des IGR depuis les X jusqu'à l'infrarouge et/ou radio dont je suis CoI. Je mentionnerai donc les programmes de S. Chaty, J. Tomsick et D. Hannikainen, qui nous ont permis d'obtenir les types de respectivement 13, 5 et 1 IGR (Chaty et al. 2008; Butler et al. 2009; Hannikainen et al. 2007). Toutes les identifications obtenues à partir de ces travaux sont reportées dans la table 4.2.

4.5 Conclusions du chapitre et de la première partie

J'ai présenté dans cette partie la découverte de sources X et gamma avec *INTEGRAL*, et les premiers suivis multi-longueurs d'ondes mis en œuvre afin de déterminer le type de ces objets. Cette aspect purement astronomique prélude à toute étude ultérieure, qu'elle soit une analyse physique des processus de rayonnement, ou bien une étude des populations de sources en tant que familles. J'ai personnellement travaillé sur les données *XMM–Newton* et *Swift* de 31 sources IGR pour lesquelles j'ai obtenu des résultats positifs. Dans une quinzaine d'autres cas les observations obtenues avec l'un ou l'autre de ces deux satellites n'ont pas abouti à une détection ; c'est le cas de IGR J19112+1358 qui n'a été détectée ni avec *Swift*, ni à l'aide de *RXTE* (Rodriguez et al. 2008c).

Le suivi des sources à de multiples longueur d'onde est certainement le moyen le plus sur d'obtenir une identification de celles-ci. Ceci permet, en outre, d'établir les répartitions spectrales d'énergies sur la bande spectrale la plus large possible. Nous obtiendrons ainsi de plus grandes contraintes sur la modélisation spectrale, et nous pourrons donc, mieux comprendre la physique en jeu dans ces systèmes. J'aborderai cet aspect dans la partie III de ce document, en me focalisant notamment sur les rayons X, et la radio.

L'organisation de ces suivis multi-longueurs d'onde est cependant une chose assez ardue, et il suffit pour cela de comparer le nombre de sources que j'ai pu observer en X (grâce par exemple à *Swift*, mais aussi dans le cadre de nos programmes *Chandra* (Tomsick et al. 2006, 2008, 2009a)), et le nombre de sources que nous avons observées en infrarouge lors d'observations dédiées. Dans une majorité de cas, il nous faut nous contenter des observations X, et des diagnostics que celles-ci nous apportent. Dans un futur immédiat, j'ai prévu de continuer les travaux d'analyses systématiques des données *Swift* en étudiant notamment toutes les sources ayant été observées depuis Rodriguez et al. (2009b), ainsi que celles, non détectées, ayant eu de nouvelles observations.

Chapitre 5

Articles de recherche liés à la partie I

5.1 Découverte de IGR J16318−4848 : Walter et al. 2003, A&A, 411, L427

A&A 411, L427–L432 (2003)
DOI: 10.1051/0004-6361:20031369

Astronomy & Astrophysics

INTEGRAL discovery of a bright highly obscured galactic X-ray binary source IGR J16318−4848

R. Walter[1,2], J. Rodriguez[3,1], L. Foschini[4], J. de Plaa[5], S. Corbel[3,6], T. J.-L. Courvoisier[1,2], P. R. den Hartog[5], F. Lebrun[3], A. N. Parmar[7], J. A. Tomsick[8], and P. Ubertini[9]

[1] *INTEGRAL* Science Data Centre, Chemin d'Écogia 16, 1290 Versoix, Switzerland
[2] Observatoire de Genève, Chemin des Maillettes 51, 1290 Sauverny, Switzerland
[3] CEA Saclay, DSM/DAPNIA/SAp (CNRS FRE 2591), Bât. 709, 91191 Gif-sur-Yvette Cedex, France
[4] IASF/CNR Section of Bologna, via Pietro Gobetti 101, 40129 Bologna, Italy
[5] SRON National Institute for Space Research, Sorbonnelaan 2, 3584 CA Utrecht, The Netherlands
[6] Université Paris VII (Fédération APC), 91191 Gif-sur-Yvette, France
[7] Astrophysics Missions Division, Research and Scientific Support Department of ESA, ESTEC, PO Box 299, 2200 AG Noordwijk, The Netherlands
[8] CASS, Code 0424, University of California San Diego, La Jolla, CA 92093-0424, USA
[9] IASF/C.N.R. Section of Roma, Area di Ricerca di Tor Vergata, via del Fosso del Cavaliere, 00133 Roma, Italy

Received 14 July 2003 / Accepted 4 September 2003

Abstract. *INTEGRAL* regularly scans the Galactic plane to search for new objects and in particular for absorbed sources with the bulk of their emission above 10−20 keV. The first new *INTEGRAL* source was discovered on 2003 January 29, 0.5° from the Galactic plane and was further observed in the X-rays with *XMM-Newton*. This source, IGR J16318−4848, is intrinsically strongly absorbed by cold matter and displays exceptionally strong fluorescence emission lines. The likely infrared/optical counterpart indicates that IGR J16318−4848 is probably a High Mass X-Ray Binary neutron star or black hole enshrouded in a Compton thick environment. Strongly absorbed sources, not detected in previous surveys, could contribute significantly to the Galactic hard X-ray background between 10 and 200 keV.

Key words. X-rays: individuals: IGR J16318-4848 – X-rays: binaries – X-rays: diffuse background

1. Introduction

X-ray binaries (where the compact object is a neutron star or black hole) can become strong hard X-rays emitters when accretion takes place. Among the ∼300 known X-ray binaries in our Galaxy and the Magellanic clouds, a few systems show strong intrinsic photo-electric absorption: GX 301–2 (Swank et al. 1976), Vela X–1 (Haberl & White 1990), CI Cam (Boirin et al. 2002). Moderate absorption was also detected in a few X-ray bursters (Natalucci et al. 2000). We report here on the discovery of IGR J16318−4848, a Compton thick X-ray binary in which the X-ray obscuring matter has a column density as large as the inverse of the Thomson cross section.

2. High energy observations and data analysis

IGR J16318−4848 was discovered using the *INTEGRAL* imager *IBIS/ISGRI* (Ubertini et al. 2003; Lebrun et al. 2003) on 2003 January 29 (Courvoisier et al. 2003a) and was regularly observed for two months. Figure 1 shows the 15−40 keV *ISGRI* sky image around the source with an accumulation time of 508 ksec. The position of the source (RA = $16^{\rm h}31.8^{\rm m}$ and Dec = $-48°48'$) was determined with an accuracy of $2'$. IGR J16318−4848 is detected up to 80 keV with a mean 20−50 keV flux of 6×10^{-11} erg cm^{-2} s^{-1}. Significant ($>5\sigma$) intensity variations occur on time scales as short as 1000 s.

We selected 70 pointings of the *INTEGRAL* core program between revolution 36 and 50 in which IGR J16318−4848 was located at less than 5° from the center of the field of view. Since IGR J16318−4848 is often below the detection level, further selection was applied on the luminosity of the source. We selected pointings where the source was detected by the IBIS analysis software (Goldwurm et al. 2003) and out of them only 8 pointings (from 2003 March 3 to 2003 March 14) for which we were able to produce spectra of sufficient quality. This resulted in a 17.5 ksec average spectrum that is displayed in Fig. 2. The current *ISGRI* energy correction and response matrices are preliminary. Throughout this analysis we used an

Send offprint requests to: R. Walter,
e-mail: Roland.Walter@obs.unige.ch

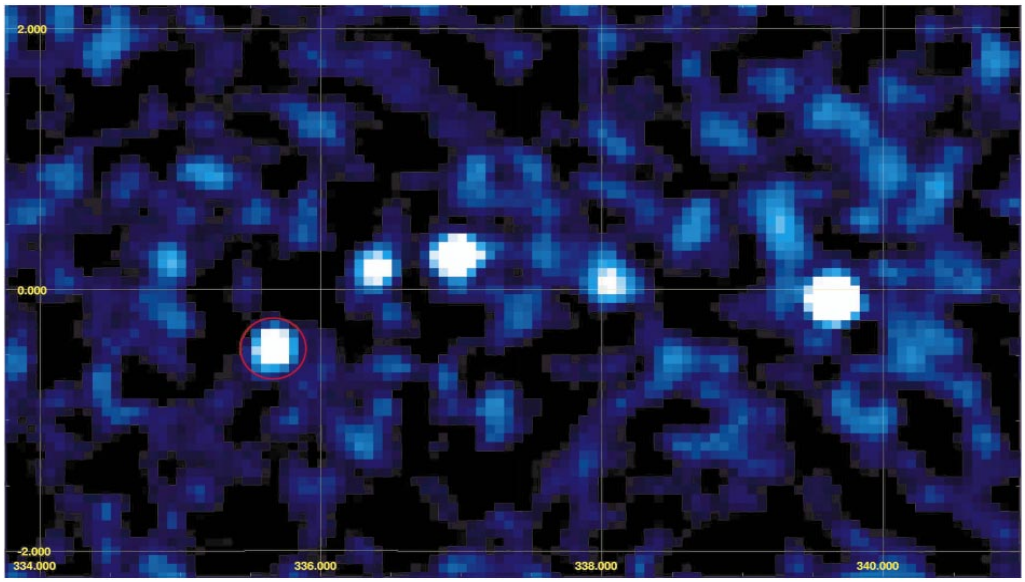

Fig. 1. *INTEGRAL ISGRI* 15−40 keV sky image of the Norma region in Galactic coordinates. This image accumulates 508 ksec of *INTEGRAL* core program data. The red circle indicates IGR J16318−4848.

ISGRI ancillary response that was modified to obtain a good fit to the spectrum of the Crab Nebula. The *ISGRI* spectrum of IGR J16318−4848 could be represented by a power law with a photon index, $\Gamma = 2.7^{+1.2}_{-0.8}$ and a flux $F_{20-100\ \mathrm{keV}} = 1.6 \times 10^{-10}$ erg cm^{-2} s^{-1}.

IGR J16318−4848 was observed for 28 ksec by *XMM-Newton* on 2003 February 10. A single X-ray source was found within the *INTEGRAL* uncertainty circle in the *EPIC PN* and *MOS* cameras (Strüder et al. 2001; Turner et al. 2001) at a position of RA = $16^{\mathrm{h}}31^{\mathrm{m}}48.6^{\mathrm{s}}$ and Dec = −48°49′00″ with a 4″ uncertainty (Schartel et al. 2003). The X-ray spectrum was immediately recognized as exceptional featuring strong photo-electric absorption, the associated Fe absorption edge at 7.1 keV and fluorescence line emission of mostly neutral Fe Kα (6.4 keV), Fe Kβ (7.1 keV) and Ni Kα (7.5 keV). The *XMM-Newton* spectrum of IGR J16318−4848, presented by Matt & Guainazzi (2003) is significantly flatter than the *ISGRI* spectrum.

All spectral uncertainties are given at 90% confidence for a single interesting parameter, unless indicated otherwise. The abundances of Anders & Grevesse (1989) and the photo-electric cross section of Verner et al. (1996) are used throughout.

To analyze the *ISGRI* and *EPIC* data together we extracted *EPIC* spectra using version 5.4.1 of the *XMM* Science Analysis System (SAS) software. The data were first screened for enhanced variable background by filtering out the time intervals where the count rate above 10 keV was higher than the threshold count rate (18 for *MOS2* and 60 for *PN* per 100 s bin). The total exposure after screening resulted in 24 ksec for *MOS2* and 21 ksec for *PN*. Source events were subsequently extracted from a 25″ radius circle centered on the source. A second circle with the same radius was fixed on a comparable region on the detector to serve as background. Standard SAS tools were used to calculate the instrumental response and the effective area for the extracted spectra.

The simultaneous fit of the *EPIC PN* and *MOS2* and *ISGRI* spectra of IGR J16318−4848 using an absorbed power-law continuum, free Fe abundance and three Gaussian emission line model (model 1) resulted in a reduced χ^2 of 1.04 for 322 degrees of freedom (d.o.f.). A normalization constant C_{ISGRI} was introduced in the model and was left as a free parameter in the fit in order to account for cross calibration uncertainties and the non simultaneity of the *ISGRI* and *EPIC* observations. The best fit parameters, listed in Table 1 are compatible with those of Matt & Guainazzi (2003). The powerlaw flux in Table 1 is corrected for the effects of photoelectric absorption but not for the effects of Compton scattering. The line fluxes are observed fluxes, not corrected for any absorption effect.

Examination of the residuals of model 1 shows that the spectral model is systematically flatter than the *ISGRI* spectrum. In addition as the *ISGRI* spectrum represents the high state of the source and the *EPIC* data correspond to a mix of different levels we would expect C_{ISGRI} to be >0.67, the value derived using our *ISGRI* response matrix and the *EPIC/ISGRI* inter-calibration obtained on 3C273 (Courvoisier et al. 2003b), in contrast to the best fit value of 0.43.

Matt & Guainazzi (2003) noted that the spectral slope was weakly constrained by the *EPIC* data alone as it correlates with the absorbing column density. C_{ISGRI} correlates with the

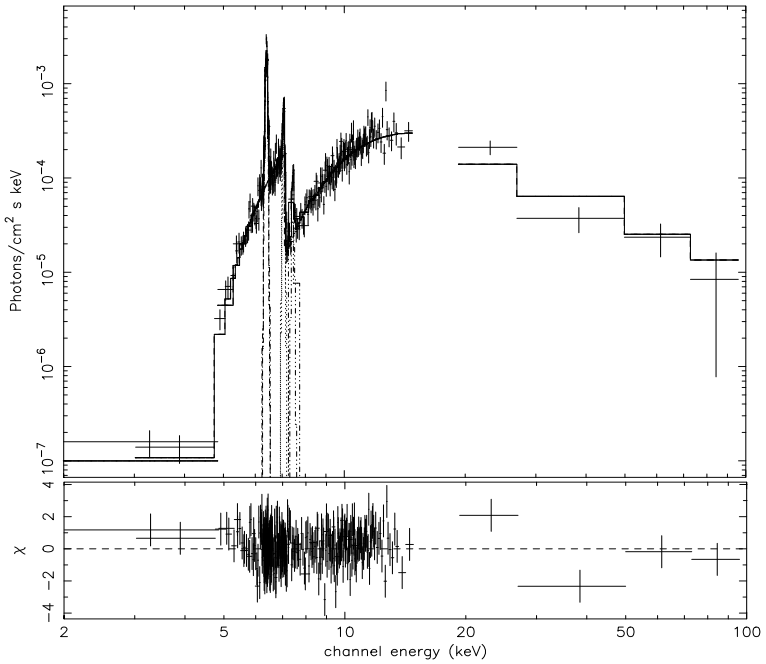

Fig. 2. The *EPIC PN*, *EPIC MOS2* and *ISGRI* photon spectra of IGR J16318−4848 along with the best fit model and residuals for C_{ISGRI} fixed to 0.67. The fit gave a reduced χ^2 of 1.04 for 323 d.o.f. (Table 1).

Table 1. Best fit parameters (90% confidence). All parameters are free in model 1. C_{ISGRI} is fixed to 0.67 in model 2.

Parameter	Model 1	Model 2	Unit
χ^2/d.o.f.	333 / 322	336 / 323	
C_{ISGRI}	$0.43^{+0.14}_{-0.23}$	0.67 (fixed)	
$N_{\rm H}$	1.96 ± 0.07	2.07 ± 0.10	10^{24} cm^{-2}
Γ	1.6 ± 0.3	1.97 ± 0.17	
Pwl $I_{1\ \rm keV}$	0.08 ± 0.03	0.12 ± 0.03	ph/kev cm^2 s
$Fe_{\rm abs}$	0.82 ± 0.05	0.79 ± 0.04	$Z_\odot$
Fe Kα E.	6.405±0.003	6.405 ± 0.003	keV
Fe Kα Flux	1.84 ± 0.09	1.75 ± 0.06	10^{-4} ph/cm^2 s
Fe Kβ E.	7.07 ± 0.01	7.07 ± 0.01	keV
Fe Kβ Flux	0.32 ± 0.08	0.30 ± 0.07	10^{-4} ph/cm^2 s
Ni Kα E.	7.46 ± 0.02	7.46 ± 0.02	keV
Ni Kα Flux	0.09 ± 0.03	0.09 ± 0.03	10^{-4} ph/cm^2 s
Intr. line width	<20	<20	eV

power-law index as well. Constraining C_{ISGRI} to be >0.67 gives $\Gamma = 1.9\pm0.2$ and a column density $N_{\rm H} = (2.1\pm0.1)\times10^{24}$ cm^{-2}. The photon index is consistent with that derived from the fit to the *ISGRI* spectrum alone. Table 1 gives the best fit parameter for a model with C_{ISGRI} fixed to 0.67 (model 2), the photon spectrum and the residuals are shown in Fig. 2.

An exponential cutoff power-law continuum model also fits the data well providing a χ^2 of 328 for 322 d.o.f. with a flat power-law and a cutoff energy of 15 ± 5 keV. Simultaneous spectral observations performed below and above 20 keV are necessary to constraint better the spectral model.

The observed ratio of the intensities of Fe Kβ and Fe Kα (0.17 ± 0.09) is consistent with the expected value of 0.14 (Kaastra & Mewe 1993). The intensity ratio between Ni Kα and Fe Kα of 0.05 ± 0.02 is close to the solar abundance ratio of 0.03–0.045 (Molendi et al. 2003). The strength of the Fe edge at 7.1 keV also corresponds to that expected from a solar abundance.

The centroids of the Fe Kα and Kβ lines corresponds to Fe that is ionized between 2 to 6 times (1σ level) (House 1969) and to a ionisation parameter $\Xi \approx 0.05$ erg cm s^{-1} that is expected to be variable across the absorbing matter. The position of the Fe absorption edge also indicates the presence of Fe that is ionized less than 2 times. Note that the systematic uncertainty on the line and edge energies is 10 eV.

In contrast to Matt & Guainazzi (2003), we did not find that the presence of a Compton shoulder to the Fe Kα line was required by the data. This could be related to data selection and reduction. A firm detection of the Compton shoulder should be confirmed by future observations. The absence of detection of the Compton shoulder is however consistent with the conclusion of Matt & Guainazzi that the average $N_{\rm H}$ on which fluorescence takes place could be smaller than that on the line of

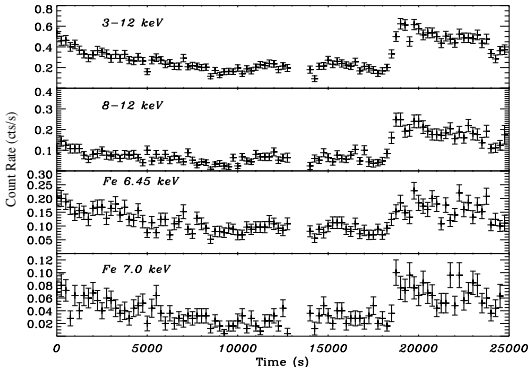

Fig. 3. *EPIC PN* light curves accumulated in different energy ranges for IGR J16318−4848. The Fe Kα light curve has been accumulated between 6.2 and 6.6 keV. The 8−12 keV light curve is unaffected by line emission.

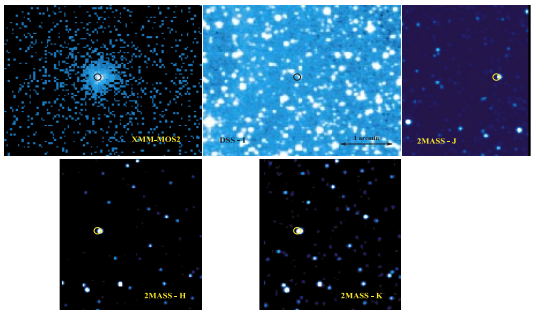

Fig. 4. *EPIC MOS*, *2MASS* (J, H, K) and *DSS* images of the counterpart of IGR J16318−4848. All images have the same scale. The *XMM* error circle (4″ radius) is shown on each image.

sight. We consider the flux of the Compton shoulder derived by Matt & Guainazzi (2003) as an upper limit.

We also did not find evidence for an excess of emission below 5 keV which could be explained by the steeper continuum derived from the *INTEGRAL* data when compared with the use of XMM data alone. Our data do not therefore show evidence for reflection as could be inferred from the low energy excess. A pure transmission geometry, with in-homogeneously distributed absorbing mater is sufficient.

Matt & Guainazzi (2003) noted that the source flux variations were intrinsic to the source (and not related to absorption). We extracted X-ray light curves for the continuum and for the Fe Kα line (Fig. 3) using time bins of 200 s. During the fast continuum rise (around time 19 000 s in Fig. 3) the count rate varies significantly in 200 s and a cross correlation analysis between the 6.2−6.6 keV light curve (strongly dominated by the Fe Kα line) and the 8−12 keV continuum light curve indicates that any differences in mean arrival time of the continuum and Fe Kα line emission are smaller than 200 s. The ratio between the Fe Kα and continuum shows however some significant variations which, as pointed out by Matt & Guainazzi (2003), could indicate variations of the properties of the cold matter on time scales of 10^4 s.

3. Discussion

3.1. X-ray variability

The variability time scale and the maximum delay observed between the Fe Kα line and the continuum variations limit the size of the zone in which fluorescent emission takes place and its distance to the X-ray source to 10^{13} cm. It is therefore very unlikely that IGR J16318−4848 is an extragalactic source such as a Seyfert II galaxy or an Ultra Luminous Infra Red Galaxy as the width of a fluorescence line (given by the Keplerian velocity) emitted at a distance of 10^{13} cm would be orders of magnitude larger than observed.

Following the *INTEGRAL* discovery of IGR J16318−4848, a re-analyis of archival data showed that IGR J16318−4848 had been weakly detected in 1994 September by ASCA (Murakami et al. 2003), with similar flux and $N_{\rm H}$ as observed in 2003. The ASCA spectrum suggested the presence of a strong Fe Kα line (Revnivtsev et al. 2003). However, the *Beppo-SAX* Wide Field Camera (WFC), that observed the field almost continuously for 6 months each year between October 1996 and 2002, has never detected the source. This indicates that it was ∼10 times fainter on average during those periods (In't Zand 2003). This suggests that IGR J16318−4848 was active in 1994 and 2003 and that it has been quiet over periods of many months. It is remarkable that the flux and the absorption observed in the active states in 1994 and 2003 are very similar.

3.2. Counterpart

A possible counterpart to IGR J16318−4848 in the Digitized Sky Survey (DSS–II/USNO-B1.0), Two Microns All Sky Survey (2MASS), and Midcourse Space Experiment (MSX) data was reported by Foschini et al. (2003). The respective images are shown in Fig. 4. In the 2MASS, the counterpart has J = 10.2, H = 8.6, K = 7.6 and an uncertainty of ±0.3 mag. It is also clearly detected in the I band of the second DSS and also in the R band (USNO-B1). The R magnitude is reported to vary over an interval of 50 years between 17.3 ± 0.3 and 18.4 ± 0.3. The flux density in the MSX A band is 0.46 Jy.

Radio observations were performed with the Australia Telescope Compact Array (ATCA). Observations have been conducted at 4.8 and 8.6 Ghz (with a total bandwidth of 128 MHz) on 2003, February 9, starting at 18:00 and finishing at 04:00 the following day, with a total of 1.33 hours (spread over the full ATCA run) on IGR J16318−4848. No source was detected with a 1σ upper limit of 0.1 mJy both at 4.8 and 8.6 GHz.

The near infrared spectral energy distribution corrected for the effect of various possible values of the galactic absorption (Lutz et al. 1996) was analyzed. The visual extinction factor derived from the galactic $N_{\rm H}$ along the line of sight is $A_{\rm V}$ = 11. The absorption could however be smaller if the source is nearby

or larger as the radio measurements have limited spatial resolution. The maximum reddening compatible with an infrared spectrum not flatter than a black body spectral component ($A_V = 20$) is two orders of magnitude smaller than the absorption observed in the X-rays. We conclude that the source of the IR/optical emission is located at $>10^{13}$ cm from the X-ray source.

If the reddenning is low ($A_V \leq 11$) the infrared companion of IGR J16318−4848 is a low mass red giant star with a luminosity of 100 $d^2_{\rm kpc}\ L_\odot$. If the reddening is strong ($A_V \approx 20$) the companion is a massive supergiant star of luminosity $10^5\ d^2_{5\ \rm kpc}\ L_\odot$. In the rest of this discussion we will assume that the infrared/optical counterpart and IGR J16318−4848 are a binary system. This however remains to be verified.

If the system is a Low Mass X-Ray Binary (*LMXRB*) located at 1 kpc, the unabsorbed 20−50 keV luminosity of 3×10^{34} erg s^{-1} corresponds to the quiescent state of those systems. In that state, neutron star systems emit thermal emission ($kT \approx 100$ eV) that dominates the hard tail below 3 keV (Rutledge et al. 2002) which is not detected in IGR J16318−4848. Black hole *LMXRB* systems in quiescence have lower luminosities (Kong et al. 2002) and do not show strong absorption.

Alternatively, if IGR J16318−4848 is a High Mass X-ray Binary (*HMXRB*) located at 5 kpc, the unabsorbed 20 − 50 keV luminosity of 7×10^{35} erg s^{-1} indicates that moderate (wind) accretion is taking place. Strong Fe Kα lines have been observed in other *HMXRB* systems. In Vela X-1, large line equivalent widths were observed during eclipses when only scattered X-rays are observed, the absorbing $N_{\rm H}$ remained however smaller than observed in IGR J16318−4848 (Pan et al. 1994). In GX 301–2, the $N_{\rm H}$ and the equivalent width of the Fe Kα line are variable and correlated. White & Swank (1984) explained this behavior by variations of the stellar wind velocity and density along the orbit of the compact source. The Fe Kα equivalent width and the $N_{\rm H}$ observed from IGR J16318−4848 match the extreme of the correlation found in GX 301–2. This suggests that the stellar wind accreting onto the compact source of IGR J16318−4848 could form a dense spherical shell in which fluorescence and absorption takes place. This possibility was also proposed by Revnivtsev et al. (2003). Note that the exponential cutoff powerlaw model that was used to represent the data is rather typical for accreting X-ray pulsars.

The ionisation parameter derived from our observations can be used to estimate the distance between the fluorescing material and the X-ray source $D = (a/D)\ L/\Xi\ N_{\rm H} = 10^{13}\ (a/D)$ cm where a is the shell thickness. This distance is also compatible with the line variability. This distance compares better with the companion star radius than with the accretion radius (unless the stellar wind velocity is small).

We searched unsuccesfully for the presence of pulsations that would be a clear signature of a neutron star in the system. The counting rate of the source during the XMM observation does not allow any definitive answer as the upper limit on the relative amplitude for a rather broad 0.15 Hz quasi periodic oscillation (QPO) (e.g. $\nu_{\rm centroid}/FWHM = 3$) is ∼30% at the 3 σ confidence level, which is not constraining. An 8000 s observation with the Proportional Counter Array (PCA) onboard *RXTE* did not find evidence for QPO either (Swank & Markwardt 2003).

3.3. Contribution to the X-ray background

Absorbed sources could contribute significantly to the Galactic high energy background. Valinia et al. (2000a) modeled the Galactic background emission observed by the PCA on *RXTE* and OSSE on *CGRO* using a specific spectral component dominating between 10 and 200 keV. The flux of that component (2.5×10^{-11} erg cm^{-2} s^{-1} deg^{-2} at 40 keV) is variable indicating that an important fraction of that emission comes from point sources. The spectral shape of IGR J16318−4848 roughly correspond to the empirical spectral model used to represent the Galactic background. The intensity of the background emission could be explained by 0.4 sources per square degree at the level of IGR J16318−4848 in a band of a width of few degrees around the Galactic plane.

The hard X-ray background also displays a strong Fe Kα emission line which is attributed to the thermal diffuse emission dominating below 10 keV (Valinia et al. 2000b). A population of intrisically absorbed sources similar to IGR J16318−4848 would only contribute at a level of 10% to the background line intensity.

In spite of the *BeppoSAX* WFC long term monitoring of the Galactic center only few strongly absorbed sources have been discovered so far (Ubertini et al. 1999). *INTEGRAL* is able to make sensitive search for highly absorbed sources (Lebrun et al. 1999) such as IGR J16318−4848, IGR J16320−4751 (Rodriguez et al. 2003) and IGR 16358−4726 (Revnivtsnev et al. 2003). Figure 1 shows the detection by *INTEGRAL* of one point source per degree of Galactic longitude in the Norma region. Those sources could indeed explain a significant fraction of the Galactic diffuse emission.

Acknowledgements. This work is based on observations obtained with *INTEGRAL* and *XMM-Newton*, two ESA science missions with instruments, science data centre and contributions funded by the ESA member states with the participation of the Czeck Republic, Poland, Russia and the USA.

We thank S. Chaty, M. Del Santo, R. Fender, W. Hermsen, J. S. Kaastra, P. Laurent, M. Mendez, T. Tzioumis, J. J. M. In't Zand and J. Zurita. JR acknowledges financial support from the French Space Agency (CNES). LF acknowledges the hospitality of the ISDC during part of this work and the financial support from the Italian Space Agency (ASI).

This publication makes use of data products from the Two Micron All Sky Survey, which is a joint project of the University of Massachusetts and the Infrared Processing and Analysis Center/California Institute of Technology, funded by the NASA and the National Science Foundation.

This research has made use of The Digitized Sky Surveys that were produced at the Space Telescope Science Institute under U.S. Government grant NAG W-2166.

References

Anders, E., & Grevesse, N. 1989, Geo. Cosm. Acta, 53, 197

Courvoisier, T., Beckmann V., Bourban, G., et al. 2003b, A&A, 411, L343

Courvoisier, T., Walter, R., Rodriguez, et al. 2003a, IAU Circ., 8063
Boirin, L., Parmar, A. N., Oosterborek, T., et al. 2002, A&A, 394, 205
Endo, T., Ishida, M., Masai, K., et al. 2002, ApJ, 574, 879
Foschini, L., Rodriguez, J., & Walter, R. 2003, IAU Circ., 8076
Goldwurm, A., David, P., Foschini, L., et al. 2003, A&A, 411, L223
Haberl, F., & White, N. 1990, ApJ, 361, 225
House, L. L. 1969, ApJS, 18, 21
In't Zand, J. J. M., Ubertini, P., Capitano, F., et al. 2003, IAU Circ., 8077
Kaastra, J., & Mewe, R. 1993, A&AS, 97, 443
Kong, A. K. H., McClintock, J. E., Garcia, M. R., et al. 2002, ApJ, 570, 277
Lebrun, F., Goldoni, P., Goldwurm, A., et al. 1999, ApL&C, 38, 457
Lebrun, F., Leray, J. P., Lavocat, P., et al. 2003, A&A, 411, L141
Lutz, D., Feuchtgruber, H., Genzel, R., et al. 1996, A&A, 315, L269
Matt, G. 2002, MNRAS, 377, 147
Matt, G., & Guainazzi, M. 2003, MNRAS, 341, L13
Molendi, S., Bianchi, S., & Matt, G. 2003, MNRAS, 343, L1
Murakami, H., Dotani, T., & Wijnands, R. 2003, IAU Circ., 8070
Natalucci, L., Bazzano, A., Cocchi, M., et al. 2000, ApJ, 543, L73
Pan, H. C., Kretschmar, P., Skinner, G., et al. 1994, ApJS, 92, 448
Revnivtsev, M., Tuerler, M., Del Santo, et al. 2003, IAU Circ., 8097
Revnivtsev, M., Sazonov, S., Gilfanov, M., et al. 2003, AL, in press
Rodriguez, J., Tomsick, J. A., Foschini, L., et al. 2003, A&A, 407, L41
Rutledge, R. E., Bildstein, L., Brown, E. F., et al. 2002, ApJ, 577, 346
Schartel, N., Ehle, M., Breitfellner, M., et al. 2003, IAU Circ., 8072
Strüder, L., Briel, U., Dennerl, K., et al. 2001, A&A, 365, L18
Swank, J. H., Becker, R. H., Boldt, E. A., et al. 1976, ApJ, 209, L57
Swank, J. H., & Markwardt, C. B. 2003, aTel, 128
Turner, M. J. L., Abbey, A., Arnaud, M., et al. 2001, A&A, 365, L27
Ubertini, P., Bazzano, A., Cocchi, M., et al. 1999, ApL&C, 38, 301
Ubertini, P., Lebrun, F., Di Cocco, G., et al. 2003, A&A, 411, L131
Valinia, A., Kinzer, R. L., & Marshall, F. E. 2000a, ApJ, 534, 277
Valinia, A., Tatischeff, V., Arnaud, K., et al. 2000b, ApJ, 543, 733
Verner, D. A., Ferland, G. J., Korista, K. T., & Yakovlev, D. G. 1996, ApJ, 465, 487
White, N. E., & Swank, J. H. 1984, ApJ, 287, 856

5.2 Découverte de IGR J19140+0951 : Hannikainen et al. 2004, A&A, 423, L17

A&A 423, L17–L20 (2004)
DOI: 10.1051/0004-6361:200400021

Astronomy & Astrophysics

Discovery of a new *INTEGRAL* source: IGR J19140+0951⋆

D. C. Hannikainen[1], J. Rodriguez[2,3], C. Cabanac[4], J. Schultz[1], N. Lund[5], O. Vilhu[1], P. O. Petrucci[4], and G. Henri[4]

[1] Observatory, PO Box 14, 00014 University of Helsinki, Finland
e-mail: diana@astro.helsinki.fi
[2] Centre d'Études de Saclay, DAPNIA/Service d'Astrophysique (CNRS FRE 2591), Bât. 709, Orme des Merisiers, Gif-sur-Yvette Cedex 91191, France
[3] *INTEGRAL* Science Data Center, Chemin d'Écogia 16, 1290 Versoix, Switzerland
[4] Laboratoire d'Astrophysique, Observatoire de Grenoble, BP 53X, 38041 Grenoble, France
[5] Danish Space Research Institute, Juliane Maries Vej 30, 2100 Copenhagen Ø, Denmark

Received 17 May 2004 / Accepted 1 July 2004

Abstract. IGR J19140+0951 (formerly known as IGR J19140+098) was discovered with the *INTEGRAL* satellite in March 2003. We report the details of the discovery, using an improved position for the analysis. We have performed a simultaneous study of the 5–100 keV JEM-X and ISGRI spectra from which we can distinguish two different states. From the results of our analysis we propose that IGR J19140+0951 is a persistent Galactic X-ray binary, probably hosting a neutron star although a black hole cannot be completely ruled out.

Key words. X-rays: binaries – X-rays: IGR J19140+0951 – gamma-rays: observations

1. Introduction

The European Space Agency's INTErnational Gamma-Ray Astrophysical Laboratory (*INTEGRAL*) was successfully launched on 2002 Oct. 17. The *INTEGRAL* payload consists of two gamma-ray instruments, two X-ray monitors and an optical monitor.

The Imager on Board the *INTEGRAL* spacecraft (IBIS, Ubertini et al. 2003) is a coded mask instrument designed for high angular resolution (12 arcmin, but source location down to 1 arcmin) imaging in the energy range from ∼20 keV to ∼10 MeV. Its total total field of view is $29° \times 29°$ for zero response with a uniform sensitivity within the central $\sim 10° \times 10°$. The *INTEGRAL* Soft Gamma-Ray Imager (ISGRI, Lebrun et al. 2003) is the top layer of the IBIS detection plane, and covers the energy range from 13 keV to a few hundred keV.

The Joint European X-ray monitor, JEM-X (Lund et al. 2003), consists of two identical coded mask instruments designed for X-ray imaging in the range 3–35 keV with an angular resolution of 3 arcmin and a timing accuracy of 122 μs. During our observation only the JEM X-2 unit was being used.

Since the start of normal observations in early 2003, *INTEGRAL* has discovered a number of new transient gamma- and X-ray sources. IGR J19140+0951 was discovered in the region tangent to the Sagittarius spiral arm during observations targeted on GRS 1915+105 performed from 2003 March 6 through 7 (Hannikainen et al. 2003a). The position of the source (Hannikainen et al. 2003b) obtained with an early version of the *Offline Scientific Analysis* software (OSA) was within the error contour of a weak X-ray source EXO 1912+097 (Lu et al. 1996). A ToO performed on IGR J19140+0951 with the *Rossi X-ray Timing Explorer* allowed the absorption column density $N_{\rm H}$ to be estimated to $\sim 6 \times 10^{22}$ cm^{-2} (Swank & Markwardt 2003). Recently a (likely orbital) period of 13.55 days has been obtained from re-analysis of the *RXTE/All Sky Monitor* (Corbet et al. 2004), suggesting a binary nature of the source.

In this letter we report the details of the discovery of the source with *INTEGRAL*, study its temporal variability as well as spectral evolution on timescale ∼30 min over this observation. In Sect. 2 we give the details of the data reduction methods that are employed in the course of this analysis. We then present our results in Sect. 3, giving in particular the most accurate position of the source (Cabanac et al. 2004), and discuss our findings in the last part of the letter.

2. Observations and data reduction

The *INTEGRAL* observation was undertaken using the hexagonal dither pattern (Courvoisier et al. 2003): this consists of a hexagonal pattern around the nominal target location (1 source on-axis pointing, 6 off-source pointings, each 2 degrees apart). The entire duration of a pointing (science window) is 2200 s,

⋆ Based on observations with *INTEGRAL*, an ESA project with instruments and science data center funded by ESA and member states (especially the PI countries: Denmark, France, Germany, Italy, Switzerland, and Spain), the Czech Republic, and Poland and with the participation of Russia and the US.

but after applying a good time interval correction the effective exposure time is ∼1700 s. The observations were continuous, except for a short slew between each science window.

The JEM X-2 data were reduced using OSA 3.0 software, following the standard procedure explained in the cookbook. This was especially useful for the spectral extraction. In this case we forced the extraction of data products for IGR J19140+0951, giving to the software the updated position of the source discussed in this letter. The resultant spectra were grouped so that each new bin contained a minimum of 60 counts, and systematic uncertainties (P. Kretschmar, priv. comm.) have been applied as follows: 10% between channels 59 and 96 (4−7.04 keV), and 2% above channel 97 (>7.04 keV).

The IBIS/ISGRI data were reduced using pre-OSA 4.0 version of the software. This new software includes the same core as OSA 3.0 except updated patches for ibis_isgr_energy (v5.1), ibis_isgr_deadtime (v4.2), ii_shadow_build (v1.4), ii_shadow_ubc (v2.7), ii_skyimage (v6.7.2) & ii_spectra_extract (v2.2), which fix many of the OSA3.0 known issues. We made two runs of the software up to the IMA level, i.e. production of images. During the first run we extracted images from individual science windows in two energy ranges (20–40 keV, and 40–80 keV), as well as a mosaic in the same energy range. Figure 1 shows a zoomed IBIS/ISGRI image of the field of the new transient. The standard ISDC catalogue v13 was given as an input, and the software was let free to find the most significant peaks in the images. This provided us with the best position for the source which was used (together with the JEM-X position) to update the entry of IGR J19140+0951 in the standard catalogue. This first run was also used to identify the sources clearly seen during our observation (only 7 were detected in the 20–40 keV mosaic). We then created a second catalogue containing only those sources. This second catalogue was given as the input for the second run, and we forced the software to extract the source count rate in every science window at the position of the catalogue. Note that the same process was re-applied in the 20–40 keV and 40–80 keV energy ranges, to obtain the "true" lightcurves of the source. They are shown in Fig. 2. We then extracted spectra from each science window with the Least Square Method. A preliminary Crab-corrected response matrix rebinned to 16 spectral channels was used in the extraction process and then in the subsequent fitting process. The resultant spectra were further grouped so that each new bin had a minimum of 20 counts, while 5% systematics have been applied to all channels (Goldwurm et al. 2003). The spectra were then fitted in XSPEC v11.3, with a newly available ancillary response file (P. Laurent, priv. comm.). We retained the energy channels between 5 and 25 keV for JEM X-2 and those between 20 and 100 keV for ISGRI.

3. Results

3.1. Refining the position of IGR J19140+0951

The source was discovered soon after the observation began (Hannikainen et al. 2003b) in near real time data, using an early version of the software (OSA1.0). It was first

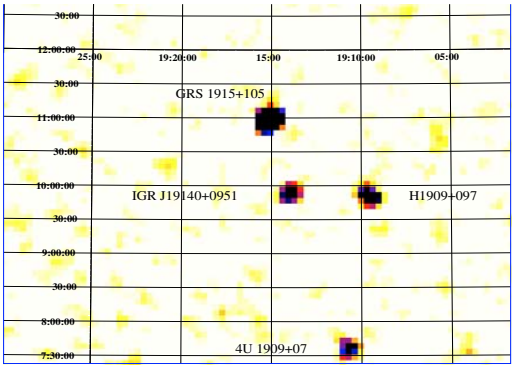

Fig. 1. The IBIS/ISGRI 20–30 keV image, showing the new source and three other sources in the field-of-view. GRS 1915+105 is bright in this energy range. The image is ∼7° width and ∼5°.3 height. North is up and East is to the left. The other sources in the field are dealt with in Molkov et al. (2004).

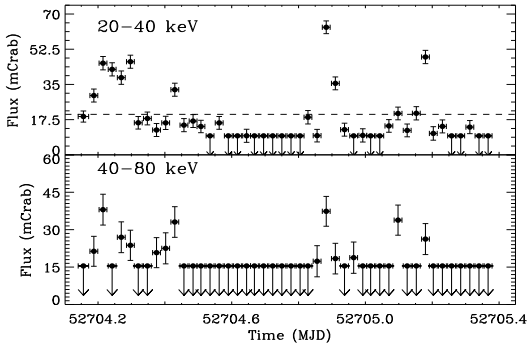

Fig. 2. The 20–40 keV (*top*) and 40–80 keV (*bottom*) ISGRI lightcurves. Each symbol represents a science window. The 3-sigma upper limits are denoted with an arrow. The dashed line in the upper panel indicates the 20 mCrab level.

spontaneously detected in science window 3 at a level of ∼3 cts/s in the 20–40 keV (26 mCrab), and reached a level of ∼6 cts/s (∼52 mCrab) in the following science window. In the latter it was even detected above 40 keV, at a level of 2.4 cts/s (∼35 mCrab). The source position had been obtained using only those science windows where the source was spontaneously detected by the software in ISGRI. Concerning the JEM X-2 data reduction, we used the "JEM-X offline software" (Lund et al. 2004) to constrain with more accuracy the new position.

We have refined the position using both JEM X-2 and ISGRI data. IGR J19140+0951 is clearly detected in nine independent science windows of the whole observing programme. Among them, the source was detected in two energy bands (8.4–14 keV and 14–35 keV) three times, thus we used those 12 independent detections to derive a best (JEM-X) weighted mean position of (J2000, errors at 1.64 σ):
RA = $19^{h}14^{m}01^{s} \pm 9$ s and Dec = $9°53'21'' \pm 1.3'$.

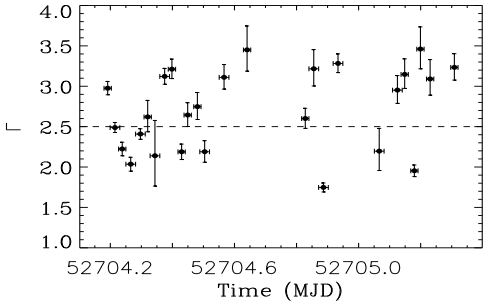

Fig. 3. The powerlaw photon index for the science windows for which a good fit was obtained. The horizontal dashed line shows the $\Gamma = 2.5$ level.

In the same way IGR J19140+0951 is clearly detected in IBIS/ISGRI mosaics (Fig. 1) in both energy ranges. We can derive a best (ISGRI) position of (J2000):
RA = $19^h14^m02.7^s \pm 2'$ and Dec = $9°53'13'' \pm 2'$ (all errors are at the 90% confidence level, see e.g. Gros et al. 2003). From these two independent data sets we can estimate the most accurate (weighted mean) position of the source of :
RA = $19^h14^m02^s$ and Dec = $9°53.3'$ ($1.3'$ error at 90%, Cabanac et al. 2004). The source is $5.2'$ away from EXO 1912+097 (Lu et al. 1996). As the *EXOSAT* error box is $6'$ it is possible that the *EXOSAT* detection represents an earlier outburst of the source seen by *INTEGRAL*. The *EXOSAT* source was discovered using the demodulation technique (Lu et al. 1996), but besides this detection nothing is known about this source.

3.2. Temporal variability

Figure 2 shows the 20–40 keV and 40–80 keV lightcurves during Revolution 48. It is immediately apparent that the source is variable on the timescale of 2200 s (typical duration of a science window) during the observation. In the 20–40 keV range the source is detected at a flux higher than the 3-σ limit of 9−10 mCrab in 70% of the science windows. It is found at a level of ∼20 mCrab in the 20–40 keV range 50% of the time, and undergoes flares on rather short timescales up to a level of 70 mCrab on one occasion. The flares in the 20–40 keV range are accompanied by flaring also in the 40–80 keV range, reaching levels of ∼38 mCrab.

3.3. Spectral analysis

To begin our spectral analysis, we extracted spectra from each one of the 46 science windows from both JEM X-2 and ISGRI, as explained in Sect. 2. Based on the lightcurve shown in Fig. 2, we selected only the science windows where IGR J19140+0951 is clearly detected at a significance level greater than 3σ in the 20–40 keV range. We then fitted the JEM X-2 and ISGRI spectra simultaneously, with a simple model consisting of an absorbed power law. The value of N_H, was frozen to the value obtained with *RXTE* (Swank & Markwardt 2003), i.e. 6×10^{22} cm^{-2}, since the useful energy range of JEM X-2 does not allow us to obtain a better constraint on this parameter. We did a first run with a multiplicative constant to account for cross-calibration of the instruments, but it was found to be very close to 1 in each spectrum. Therefore, in a second run no such constant was included. Figure 3 shows the results obtained for the science windows for which a good fit was achieved. This excludes three science windows.

To increase our statistics, we further averaged all the spectra from the science windows in which IGR J19140+0951 is found at a flux up to ∼20 mCrab between 20 and 40 keV (Fig. 2; hereafter this spectrum is referred to as "faint"). In addition we also averaged together all the spectra where the source was found to be at a level of >20 mCrab (referred to as "bright"). The FTOOL MATHPHA was used to compute the true weighted average spectrum (K. Ebisawa, priv. comm.). Figure 4 shows the spectra obtained after the averaging processes. Although a simple model fits the single spectra well, it gives a relatively poor reduced chi square for the the average spectra (1.55 for 65 d.o.f. in the case of the "faint" spectrum, and 1.48 for 73 d.o.f., in the case of the "bright" spectrum).

Faint spectrum. Adding a blackbody to the simple powerlaw improves the fit to a reduced $\chi^2 = 1.19$ (63 d.o.f.). An F-test indicates that the blackbody component is required at a level greater than 99.99%. The temperature is $kT = 1.27^{+0.07}_{-0.08}$ keV and $\Gamma = 2.39 \pm 0.11$. The 2–20 keV (20–100 keV) unabsorbed flux is 9.80×10^{-10} erg s^{-1} cm^{-2} (1.96×10^{-10} erg s^{-1} cm^{-2}). Figure 4 (left) shows the faint spectrum with the best-fit model.

Bright spectrum. The blackbody is only marginally required with an F-test probability of 92%. However, adding a high energy cutoff to the simple powerlaw improved the fit to a reduced $\chi^2 = 0.93$ which leads to an F-test probability of >99.99%. The powerlaw photon index is 2.03 ± 0.04. The cutoff energy is 49 ± 3 keV and the folding energy is 16^{+4}_{-7} keV. Since the cutoff in a powerlaw is attributed to thermal Comptonization we also fitted the bright spectrum with comptt (Fig. 4, right). Given the energy range, the temperature of the input photons was frozen to 0.5 keV. The electron temperature is $15.1^{+2.5}_{-1.6}$ keV and the optical depth of the plasma is $2.1^{+0.2}_{-0.3}$. The reduced χ^2 is 1.07 for 71 d.o.f. The 2–20 keV (20–100 keV) unabsorbed flux is 1.01×10^{-9} erg s^{-1} cm^{-2} (5.39×10^{-10} erg s^{-1} cm^{-2}). Adding a blackbody and fixing its parameters to those of the faint spectrum leads to a very bad fit, ruling out a constant blackbody emission.

4. Discussion

The refined position has allowed us to perform an improved analysis of IGR J19140+0951 using both JEM-X and ISGRI data. In particular, this has enabled us to obtain the true ISGRI lightcurve on a timescale of ∼2000 s as well as individual JEM X-2 and ISGRI spectra. The ISGRI lightcurve shows that the source is variable on the timescale of a science window, so this would imply a maximum size of the emitting region of $\sim 7 \times 10^{13}$ cm, i.e. ∼4 AU. This, together with the newly-discovered period of 13.55 days, implies the Galactic

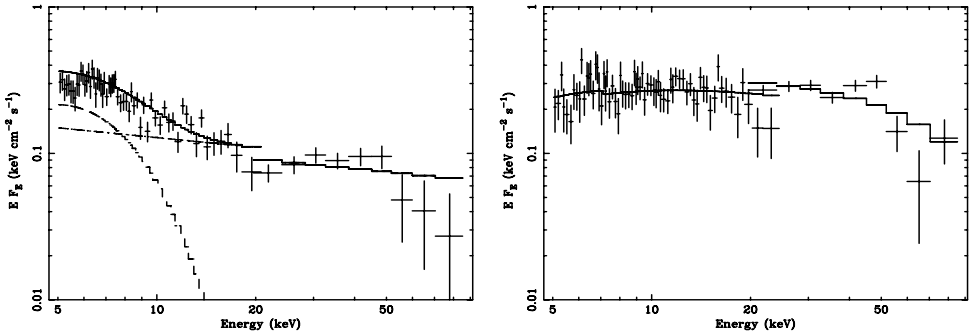

Fig. 4. The faint (*left*) and bright (*right*) spectra with the best-fit model superimposed, a blackbody + powerlaw for the faint spectrum and comptt for the bright spectrum.

origin of IGR J19140+0951. It is interesting to note that throughout the 100 ks observation, the source went from being undetectable in the *INTEGRAL* instruments to a level of 80 mCrab in the 20–40 keV ISGRI range. The variations appear to be not only related to a global change in luminosity but rather reflect changes in the emitting media – for example the appearance and possible disappearance of a blackbody component in the spectra. This is reminiscent of X-ray binaries (e.g. Tanaka & Shibazaki 1996) and the newly-discovered period of 13.55 days (Corbet et al. 2004) strongly points to the binary nature of IGR J19140+0951.

The spectral parameters obtained for this object could be consistent with both types for the primary, i.e. either a neutron star or a black hole. In fact, although neutron stars usually have a lower energy cutoff in their spectra, some black holes can show a cutoff as low as 30 keV (e.g. XTE J1550−564, Rodriguez et al. 2003). However, in the latter the low energy of the cutoff is accompanied by the very bright emission of soft X-rays (close to 1 Crab in the 1–10 keV range) which is not the case here. In addition, the main difference between a neutron star and a black hole in thermal Comptonization is related to the temperature of the electrons (Barret 2001). In the first phenomenological model we used, it is usually admitted that it is more the folding energy which is close to the electron temperature rather than the cutoff energy. In that case, IGR J19140+0951 manifests the expected difference for a neutron star compared to a black hole such as XTE J1550−564. This and the persistence of the source would point to a neutron star rather than a black hole. However, a black hole cannot be dismissed since the variations of the photon index (Fig. 3) are similar to those seen in GRS 1915+105 (e.g. Markwardt et al. 1999).

The high energy tail would represent the Comptonization of the soft photons on relativistic electrons. And indeed, the averaged bright spectrum is well fitted with a thermal Comptonization model. In addition to a variation in the blackbody, or thermal, component, the variations may also indicate transitions between thermal Comptonization and non-thermal or hybrid thermal-non-thermal Comptonization. The quality of our data does not allow us to answer more precisely these points; a longer accumulation of data in time is currently underway with the aim to increase the statistics at especially the higher energies which in turn will allow us to address this question and the true nature of the compact object.

Further analysis of this source will be deferred to a later paper which will include the remaining *INTEGRAL* observations from both the Open Time programme and the Galactic Plane Scans of the Core Programme, plus multiwavelength coverage including e.g. the Nordic Optical Telescope and the VLA.

Acknowledgements. D.C.H. gratefully acknowledges a Fellowship from the Academy of Finland. J.R. acknowledges financial support from the French space agency (CNES). J.S. acknowledges the financial support of Vilho, Yrjö and Kalle Väisälä foundation. O.V. and J.S.H. are grateful to the Finnish space research programme Antares and TEKES. The authors wish to thank Ken Ebisawa for useful suggestions, and Aleksandra Gros and Marion Cadolle Bel for providing us with the most recent IBIS products. The authors also wish to thank the referee for useful comments.

References

Barret, D. 2001, Adv. Space Res., 28, 307
Cabanac, C., Rodriguez, J., Hannikainen, D., et al. 2004, ATel, 272
Corbet, R. H. D., Hannikainen, D. C., & Remillard, R. 2004, ATel, 269
Courvoisier, T. J.-L., Walter, R., Beckmann, V., et al. 2003, A&A, 411, L53
Goldwurm, A., David, P., Foschini, L., et al. 2003, A&A, 411, L223
Gros, A., Goldwurm, A., Cadolle-Bel, M., et al. 2003, A&A, 411, L179
Hannikainen, D. C., Rodriguez, J., & Pottschmidt, K. 2003a, IAUC, 8088
Hannikainen, D. C., Vilhu, O., Rodriguez, J., et al. 2003b, A&A, 411, L415
Lebrun, F., Leray, J.-P., Lavocat, P., et al. 2003, A&A, 411, L141
Lu, F. J., Li, T. P., Sun, X. J., Wu, M., & Page, C. G. 1996, A&AS, 115, L395
Lund, N., Budtz-Jørgensen, C., Westergaard, N. J., et al. 2003, A&A, 411, L231
Lund, N., et al. 2004, Proc. of the 5th INTEGRAL Workshop
Markwardt, C. B., Swank, J. H., & Taam, R. E. 1999, ApJ, 513, L37
Rodriguez, J., Corbel, S., & Tomsick, J. A. 2003, ApJ, 595, 1032
Swank, J. H., & Markwardt, C. B. 2003, ATel, 128
Tanaka, Y., & Shibazaki, N. 1996, ARA&A, 34, 607
Ubertini, P., Lebrun, F., Di Cocco, G., et al. 2003, A&A, 411, L131

5.3 Suivis d'IGRs avec *Swift* : Rodriguez et al. 2008, A&A, 482, 731 ; Rodriguez et al. 2009, A&A, 494, 417

A&A 482, 731–737 (2008)
DOI: 10.1051/0004-6361:20079208

Astronomy & Astrophysics

Swift follow-up observations of INTEGRAL sources of unknown nature

J. Rodriguez[1], J. A. Tomsick[2], and S. Chaty[1]

[1] Laboratoire AIM, CEA/DSM – CNRS – Université Paris Diderot, DAPNIA/SAp, 91191 Gif-sur-Yvette, France
e-mail: jrodriguez@cea.fr
[2] Space Sciences Laboratory, 7 Gauss Way, University of California, Berkeley, CA 94720-7450, USA

Received 6 December 2007 / Accepted 16 February 2008

ABSTRACT

Context. Since its launch in 2002, *INTEGRAL* has discovered many new hard X-ray sources. A lot of them still lack sufficient positional accuracy, for finding counterparts at other wavelengths. Their true nature is, therefore, still unknown.
Aims. The goal of this study is to give an accurate X-ray position for 12 of these sources so as to further identify their counterpart at optical, infrared, and radio wavelengths, and to unveil their true nature. We also make use of the X-ray spectral parameters to tentatively distinguish between the various possible types.
Methods. We made use of X-ray observations with the X-ray telescope on-board the *Swift* observatory to refine the X-ray position to 3–5″ accuracy, and performed 0.1–10 keV spectral analysis. We then searched the online catalogues (e.g. NED, SIMBAD, 2MASS, 2MASX, and NVSS) to search for counterparts at other wavelengths.
Results. For all sources, we give a refined X-ray position, provide X-ray spectral parameters, identify infrared counterparts, and give magnitudes at optical and ultra violet wavelengths seen with UVOT when observations are available. We confirm the nature of six sources formerly suspected to be AGN (IGR J02343+3229, J13149+4422, J14579−4308, J16385−2057, J18559+1535, J19378−0617). Our analysis first leads us to suggest that IGR J09523−6231 and IGR J10147−6354 are AGN. While the former has recently been confirmed as a Seyfert 1.5 AGN, we suggest the latter is a Seyfert 2. All other sources may be Galactic sources, in which case their spectral shape may suggest that they are X-ray binaries. In one case (IGR J19308+0530), the Galactic nature is confirmed through the identification of an F8 star as the counterpart. We favour a distance to the source not greater than 1 kpc. The source is likely to be a neutron star XRB or a CV. We also report the discovery of six serendipitous sources of unknown nature.

Key words. astrometry – stars: binaries: close – galaxies: Seyfert – X-rays: binaries – X-rays: galaxies

1. Introduction

Since its launch on October 17, 2002, the INTErnational Gamma-Ray Astrophysical Laboratory (*INTEGRAL*, Winkler et al. 2003) has detected about 250 sources that had previously never been seen or serendipitously detected once, and not studied. This has been made possible mainly thanks to the high sensitivity, the wide field of view (FOV) and high imaging resolution of the IBIS Soft Gamma-Ray Imager (ISGRI, Lebrun et al. 2003) sensitive in the 20–300 keV energy range. These sources are named with the acronym IGR JRA±Dec and we will hereafter refer to them as IGRs[1]. Understanding the nature of those sources has a great importance and implication for several astrophysical questions. The identification of sources allows us to perform statistics on families of sources and source population studies, while individual studies of new sources allows us to better understand the physics of the emission of high energy radiation. This, in turn, can help us answer questions regarding the evolution of stars, galaxies, and/or have cosmological implications while studying Galactic or extra-galactic sources such as AGN and other quasars.

In a recent paper, Bodaghee et al. (2007) collected all the known parameters (such as the absorption column density N_H, or the pulse period for Galactic sources, the redshift for AGN, etc.) of all sources detected by *INTEGRAL* during the first four years of activity, and tried to understand the different families of sources by testing and searching correlations between those parameters. Their catalogue, however, contains a large number of sources whose high energy position is accurate just at the arcmin level, the best accuracy achievable with *INTEGRAL*/ISGRI. In most cases this level of accuracy is not sufficient to unveil the nature of the source through the identification of counterpart at other wavelengths. In some cases, a tentative identification is given, mainly when an AGN is found within the *INTEGRAL*/ISGRI error box, but this is far from being secure as other possible counterpart usually lie in the few arcmin ISGRI error box.

Since the discovery of the first source by *INTEGRAL*, secure identification has been possible only through follow-up observations with softer X-ray telescopes, either by refinement of the X-ray position and identification of the optical/infrared counterpart (e.g. Rodriguez et al. 2006; Tomsick et al. 2006; Chaty et al. 2008), or by discovery of X-ray pulsations in the case of pulsars (e.g. Lutovinov et al. 2005). Here, we report the results of several pointed observations made with the *Swift* observatory (Gehrels et al. 2004), on a total of 12 sources that lacked precise localisation at soft X-ray energies. We start by introducing the observations and method of data reduction, before giving the results on each source, i.e., refined position, identification of the

[1] An up-to-date online catalogue of all IGRs can be found at http://isdc.unige.ch/$\sim$rodrigue/html/igrsources.html

Table 1. Log of the *Swift* observations analysed in this paper.

Name (IGR)	*Swift* Sequence Number	Observation Date	Exp.⋆ (s)	Offset† (′)
J02343+3229	00037105001	2007-07-03	2481	5.4
	00037105002	2007-07-04	4265	5.4
	00037105004	2007-07-07	6402	5.1
	00037105006	2007-07-07	6821	5.1
J09523-6231	00030927001	2007-05-12	1027	1.9
	00030927002	2007-06-08	2123	1.0
	00030927003	2007-06-14	1867	2.4
J10147-6354	00037048001	2007-11-01	4538	0.8
J11187-5438	00037051001	2007-09-26	6905	7.0
	00037051002	2007-09-30	16062	2.9
J13149+4422	00037093001	2007-06-03	11493	7.8
	00037093002	2007-09-19	1228	4.8
	00037093003	2007-09-20	2449	7.1
J14579-4308	00036621001	2007-09-21	10725	8.0
	00036621002	2007-09-25	6401	7.8
	00036621003	2007-09-25	4552	7.4
J16385-2057	00036649001	2007-10-07	4554	6.1
	00036649002	2007-10-08	4606	6.3
J18490-0000	00035092001	2006-03-05	8432	3.0
	00035092002	2006-03-09	3828	2.0
J18559+1535	00036651001	2007-07-20	3848	2.5
	00036651002	2007-07-29	1309	2.2
	00036651003	2007-10-03	593	4.0
	00036651004	2007-10-18	5130	6.5
J19308+0530	00035357002	2006-04-13	2120	1.3
	00035357004	2006-05-19	4477	1.2
J19378-0617	00036652001	2007-08-07	408	7.2
	00036652003	2007-09-26	5713	4.3
J23524+5842	00037065001	2007-06-09	5901	0.9

⋆ XRT exposure time.
† Offset between the direction of the *Swift* pointing and the best *INTEGRAL* position for the given source.

counterpart, and X-ray spectrum. We discuss and summarise the results in the last part of the paper.

2. Observations and data reduction

Among all the *Swift* pointed observations of IGRs, we first restricted our analysis to sources whose fine (less than ∼10″) soft X-ray position was not published anywhere. We, then, disregarded the sources that were not detected in single pointings, because a non detection can have several reasons (absorption, under-exposures, variability, transience, etc.) that does not help in unraveling the type of a source. We also rejected the sources that were not observed in photon mode by the XRT, as no fine position can be obtained. In the remaining sample, we focused on sources for which either a secure identification was not given in Bodaghee et al. (2007) or those for which we found a mismatch between the X-ray position and the proposed association. Our analysis contains a sample of twelve sources. The observing log for these sources is reported in Table 1. All our results are first based on observations made with the XRT (Burrows et al. 2005) and UVOT (Roming et al. 2005) telescopes onboard the *Swift* observatory. The XRT is a focusing X-ray telescope with an effective area of 110 cm^2, and a FOV of about 23′. It has an imaging resolution of 18″ between 0.1 and 10 keV, and has a location accuracy for point source as low as ∼3″.

The XRT data were reduced within the `HEASOFT` package v. 6.3.2. We produced level 2 data with the `xrtpipeline` v0.11.5 that processes the raw data to obtain clean data products, i.e. images, spectra and light curves used for the scientific analysis. For each pointing, we estimated the X-ray position of the X-ray sources with the task `xrtcentroid` v.0.2.7. In the various cases where several pointings were available for the same source the final position is the mean of all positions obtained from the individuals pointings. As the error computed by this task includes various effects (especially some systematic effects and satellite misalignment), the error we report here is also the average of all individual errors.

Spectra and light curves were extracted with `xselect` v2.4. The source spectra and light curves were obtained from a circle of 20 pixels (∼47″) radius centred on the best source position. This ensures that 90% of the PSF is enclosed in this region. Background spectra and light curves were extracted from a region of the detector free of sources and of 40 pixels radius. Exposure maps were produced with `xrtexpomap` and summed within `XIMAGE`. The ancillary response files were generated with the tool `xrtmkarf` v0.5.5, and corrected with the exposure maps at the position of the source. The resultant spectra were rebined so as to at least have 20 counts per channel allowing the chi-statistics to be used in `xspec` v11.3.2ag. If this criterion was not achievable, the Cash-statistic was used instead. In the cases where several pointings are available the spectra were averaged together unless large variability was seen in the light curve. The spectra were fitted between 0.5 keV and ∼8 keV depending on the quality of the high energy bins.

The UVOT is an UV/optical telescope, whose design is based on the OM onboard the *XMM-Newton* observatory. It has a 17′ × 17′ FOV with an angular resolution of about 2″ depending of the filter used. It can observe a given field through several filters, or grisms to perform spectroscopy. The UVOT data (when available) discussed in this paper were obtained through one or more of the following filters: *V* (5000–6000 Å), *B* (3800–5000 Å), *U* (3000–4000 Å), *UVW1* (2200–4000 Å), *UVM2* (2000–2800 Å) and *UVW2* (1800–2600 Å). The UVOT individual exposures of a single observation were summed with `uvotimsum` while magnitudes and upper limits were estimated at the best X-ray position obtained with XRT with `uvotsource` as explained in the UVOT analysis thread[2] by comparison with a region free of sources taken as background reference. Note that, as indicated in the UVOT analysis threads, regions of, respectively, 6″ radius for the *U*, *B*, and *V* filters and 12″ radius, for the *UVW*1, *UVW*2, *UVM*2 filters, where given as an input to `uvotsource` for the computation of the magnitudes. The typical errors are 0.2 mag.

3. Results

The main results, X-ray position, presence of an infrared counterpart and its type are reported in Table 2, the IR, optical magnitudes found in the literature, and the magnitudes obtained from the analysis of the UVOT data when available are reported in Table 3. The spectral results are reported in Table 4. All errors are given at the 90% confidence level. The luminosities reported in Table 4 are estimated at a distance of 1 kpc for sources of unknown type. For the confirmed AGNs, we used the redshift reported in Table 2 and H_0 = 65 km s^{-1} Mpc^{-1} to estimate it. Note that for all sources, the *Swift*/XRT position falls well within the 90% confidence *INTEGRAL* error box. In all cases there is a single source within the *INTEGRAL* error box, and except where further discussed below, there are no other bright sources in the

[2] http://swiftsc.gsfc.nasa.gov/docs/swift/analysis/threads/uvot_threads.html

Table 2. X-ray position (equatorial and Galactic), presence of an IR counterpart and reddshift of the 12 sources studied with *Swift*/XRT.

Name (IGR)	RA (J2000)	Dec (J2000)	Error (″)	l (°)	b (°)	Counterpart (infrared)	Type	Comment
J02343+3229	$02^h34^m19.9^s$	+32°30′20″	3.8	146.865	−25.540	yes/extended	Sey 2	$z = 0.016$
J09523−6231	$09^h52^m20.5^s$	−62°32′37″	4.4	283.854	−6.507	yes (Fig. 1)	Sey 1.5	$z = 0.252^\star$
J10147−6354	$10^h14^m15.2^s$	−63°51′50″	4.2	286.638	−6.083	yes/point	Sey 2 (?)	
J11187−5438	$11^h18^m21.1^s$	−54°37′32″	3.7	289.640	+5.826	yes/point	?	
J13149+4422	$13^h15^m17.3^s$	+44°24′26″	3.8	108.983	+72.069	yes/extended	Sey 2	$z = 0.035$
J14579−4308	$14^h57^m41.3$	−43°07′57″	3.8	326.114	+13.984	yes/extended	Sey 2	$z = 0.016$
J16385−2057	$16^h38^m31.1^s$	−20°55′25″	3.6	357.728	+17.020	yes/extended	Sey 1	$z = 0.027$
J18490−0000	18^h49^m 01.6^s	−0°01′18″	3.7	32.646	+0.510	faint IR/point	XRB (?)	
J18559+1535	$18^h56^m00.6^s$	+15°37′58″	3.6	47.409	+6.072	yes/point	Sey 1	$z = 0.084$
J19308+0530	$19^h30^m50.9^s$	+05°30′57″	4.3	42.381	−6.186	yes/point	neutron star XRB or CV	F8 star
J19378−0617	$19^h37^m33.1^s$	−06°13′04″	3.5	32.591	−13.074	yes/extended	Sey 1.5	$z = 0.011$
J23524+5842	$23^h52^m22.0^s$	+58°45′31″	4.5	115.323	−3.238	yes/point	?	

⋆ From Masetti et al. (2008).

Table 3. IR, Optical and UV apparent magnitudes obtained from the literature and online catalogues, and, when available, from the analysis of the UVOT data. Upper limits are given at the 5-σ level.

Source (IGR)	Magnitudes IR	Optical	UV
J02343+3229	$J = 10.021$, $H = 9.184$, $K = 8.772$	$B = 13.7$	$U = 17.7$, $UVW2 = 18.3$
J09523−6231			$U = 18.6$,$UVM2 > 19.3$, $UVW1 > 19.0$
J10147−6354	$J = 14.831$, $H = 13.874$, $K = 12.53$		$UVW2 = 16.3$
J11187−5438	$J = 15.534$, $H = 14.869$, $K = 14.455$		
J13149+4422	$J = 12.248$, $H = 11.624$, $K = 10.821$	$B = 16.5$	$UVM2 = 16.9$, $UVW1 = 16.7$
J14579−4308	$J = 10.745$, $H = 9.918$, $K = 9.578$	$B = 15$	
J16385−2057	$J = 12.527$, $H = 11.644$, $K = 11.106$		
J18490−0000	$K = 14.159$	$V > 20.2$	
J18559+1535	$J = 13.639$, $H = 12.584$, $K = 11.438$		$UVM2 > 19.4$, UVW2> 20.2
J19308+0530	$J = 9.617$, $H = 9.245$, $K = 9.130$	$V = 11.0$, $B = 11.3$	$U < 11.9$, $UVM2 = 12.5$, $UVW2 = 13.7$
J19378−0617	$J = 10.88$, $H = 10.141$, $K = 9.666$	$V = 15.35$, $B = 16.12$	$UVW1 = 14.4$
J23254+5842	$J = 16.127$, $H = 15.059$, $K = 13.9155$		$U > 20.7$

FOV, although there may be some slight excesses in some of the fields. The infrared (IR) counterparts are either found in the 2MASS point source catalogue, or the 2MASX extended source catalogue. Below, we discuss some individual properties for each source.

3.1. IGR J02343+3229

IGR J02343+3229 was discovered with *INTEGRAL* by Burenin et al. (2006) and Krivonos et al. (2007), and promptly associated with NGC 973 a likely Sey 2 AGN (Burenin et al. 2006). The average XRT position is 3.7″ away from the reported position for NGC 973. The angular size of the galaxy is 3.98′, which renders the association of the X-ray source and the Galaxy very likely. We found a possible counterpart in the 2MASX catalogue of extended sources. 2MASX J02342010+3230200 is 2.0″ away from the centre of the *Swift*/XRT error box. Both objects fall well within the XRT error, further increasing the probability that IGR J02343+3229 is an AGN. This AGN is at $z = 0.016$ as reported in NED from various sources. We examined the UVOT data of the third exposure that contains coverage in the *U* and *UVW2* filters. The best XRT position of IGR J02343+3229 clearly contains the nucleus of a galaxy detected in both filters. The magnitudes obtained at the best XRT position within the recommended 6″and 12″radius regions of extraction are reported in Table 3.

We remark the presence of an additional source and another possible faint excess in the field. Both features are outside the *INTEGRAL* error box. The position of the source (named SWIFT J023405.1+322707) is reported in Table 5. It lies 2.5″ from HD 15896 (=2MASS J02340529+3227074) a K0 star, with

Table 4. Spectral parameters of the 12 sources studied with *Swift*/XRT.

Name (IGR)	N_H $\times 10^{22}$ cm^{-2}	Γ	Flux⋆	Lumin.†
J02343+3229	2.2 ± 0.4	1.3 ± 0.2	1.0×10^{-11}	6.7×10^{42}
J09523−6231	8^{+5}_{-4}	$2.3^{+1.3}_{-1.1}$	9.1×10^{-12}	1.5×10^{43}
J10147−6354	$2.0^{+1.6}_{-1.1}$	$1.7^{+0.9}_{-0.8}$	2.1×10^{-12}	2.5×10^{32}
J11187−5438	$0.28^{+0.08}_{-0.07}$	1.5 ± 0.14	3.4×10^{-12}	4.1×10^{32}
J13149+4422	$5.2^{+1.5}_{-1.0}$	$1.7^{+0.4}_{-0.3}$	1.2×10^{-11}	4.1×10^{43}
J14579−4308	20 ± 4	2.9 ± 0.6	1.8×10^{-11}	1.2×10^{43}
J16385−2057	0.21 ± 0.04	2.1 ± 0.1	7.7×10^{-12}	1.4×10^{43}
J18490−0000	5 ± 2	$1.8^{+0.7}_{-0.6}$	6.4×10^{-12}	7.6×10^{32}
J18559+1535	0.7 ± 0.1	1.6 ± 0.1	1.4×10^{-11}	2.5×10^{44}
J19308+0530	$<0.3^\ddagger$	$3.0^{+1.4}_{-0.5}$	8.2×10^{-14}	9.8×10^{30}
J19378−0617	0.15 ± 0.05	2.5 ± 0.2	4.4×10^{-11}	1.3×10^{43}
J23524+5842	6^{+4}_{-2}	2 *frozen*	2.9×10^{-12}	3.4×10^{32}

⋆ 2–10 keV unabsorbed (erg cm^{-2} s^{-1}).
† 2–10 keV unabsorbed luminosity (erg s^{-1}).
‡ 90% upper limit.

Table 5. Best XRT positions of serendipitous sources found in this study.

Name (SWIFT)	RA_{J2000}	Dec_{J2000}	Error ($''$)
J023405.1+322707	$02^h34^m05.1^s$	$+32°27'07''$	4.1″
J095238.4−622316	$09^h52^m38.4^s$	$-62°23'16''$	4.1″
J145704.4−430020	$14^h57^m04.4^s$	$-43°00'20''$	3.8″
J145729.9−430231	$14^h57^m29.9^s$	$-43°02'31''$	4.0″
J145746.9−430056	$14^h57^m46.9^s$	$-43°00'56''$	4.2″
J145702.3−430128	$14^h57^m02.3^s$	$-43°01'28''$	4.0″

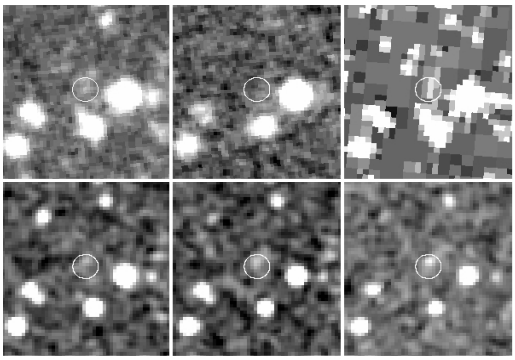

Fig. 1. ~46″×59″ finding charts of the field around IGR J09523−6231. *From left to right and top to bottom* DSS II infrared, red, blue images, and 2MASS *J*, *H* and *K*-band images. In all images, the small circle represents the *Swift*/XRT error box.

$B = 8.74$, $V = 7.65$, $J = 5.754$, $H = 5.259$, $K = 5.087$, which may suggest the source has a Galactic origin.

We combined the four observations to perform a spectral analysis of IGR J02343+3229. The average spectrum has 1437 cts for a total of 19 910 s exposure. An absorbed power law fits the data well with a reduced χ^2 (hereafter χ^2_ν) of 1.11 for 63 degrees of freedom (d.o.f.). The parameter values are reported in Table 2. The value of N_H is about 40 times higher than the mean absorption along the line of sight, which indicates that IGR J02343+3229 is an intrinsically absorbed AGN. Note that intrinsic absorption is expected in the case of a Sey 2 AGN.

3.2. IGR J09523−6231

IGR J09523−6231 was first reported in the third edition of the IBIS catalogue (Bird et al. 2007). The source was only detected in the 20–40 keV energy range at a low significance of 5.3σ over 290 ks of observation (Bird et al. 2007). Only one X-ray source is found in the *INTEGRAL* error box. It is, however, extremely weak and the positions obtained from the three *Swift*/XRT pointings can differ by few arcsec (up to 4). There is nothing reported in the various online catalogue at less than 10″ from the average X-ray position. Figure 1 shows the DSS II R-band and infrared, and the 2MASS *J*, *H*, and *K*-band images. As can be seen in Fig. 1, a weak source is found within the *Swift* error box in the 2MASS and DSS II images. The source may even be blended or extended as seen from the infrared images. We examined the UVOT data for the presence of a possible counterpart at the position of the source. A faint source is visible in the *U*-band only (Table 3).

We remark the presence of another X-ray source in the *Swift*/XRT FOV. It is well outside the *INTEGRAL* error box. Its position is reported in Table 5. This additional source (named SWIFT J095238.4-622316) is within the 14″ *ROSAT* error box of 1RXS J095237.2-622310, which suggests the two sources are the same. A counterpart with $m_{UVM2} = 17.2 \pm 0.2$ is found in the XRT error box of SWIFT J095238.4-622316. This source is unfortunately outside the UVOT FOV of the pointings made with the *U* and *UVW*1 filters.

We combined the three observations to perform a spectral analysis. The spectrum has 215 cts for a total of 5017 s exposure. An absorbed power law fits the data well ($\chi^2_\nu = 0.9$ for 6 d.o.f.). The fitted value of N_H is about 40 times higher than the average value of the absorption along the line of sight, which indicates that IGR J09523−6231 is intrinsically absorbed. The detection of the source in the *U*-filter and the high X-ray absorption first led us to think the object was a Sey 2 AGN, since in those objects, the optical emission is thought to be produced outside of the absorbing matter affecting the X-ray emission. This despite the position of the source close to the Galactic plane (Table 2) which may have rather pointed towards a Galactic source, as AGN tend to statistically be found at high Galactic latitudes. In a very recent work, Masetti et al. (2008), showed through optical spectroscopy, that IGR J09523−6231 was indeed an AGN. They refined the type to a Sey 1.5.

3.3. IGR J10147−6354

IGR J10147−6354 was first reported by Bird et al. (2007). The source was detected in the 40–100 keV energy range at a significance of 4.9σ during 1340 ks of observation. The best XRT position is well within the ISGRI error box of 5′.

There is a single source in the 2MASS point source catalogue within 5″ from the XRT position. 2MASS J10141554-6351500 is at 2.1″ away from the centre of the *Swift* error box. It is also well detected in the UVOT *UVW2* filter.

The XRT spectrum has 93 cts for a total exposure of 4538 s. An absorbed power law fits the data well, with a C-statistic value = 32.6 for 29 bins. The value of N_H is a factor about 7.3 times higher than the average value of the absorption along the line of sight which indicates that the absorption is mostly intrinsic to the source. The detection of a bright UV counterpart, as for the former source, suggests either a very close Galactic or a far and bright extragalactic object. Again, the low Galactic latitude would rather tend to point towards a Galactic source rather than an extragalactic one. Dereddening the magnitudes with the absorption on the line of sight does, however, not lead to any known stellar spectral type for a Galactic source. This, the detection in the UV-band, and the intrinsic absorption of the source would tend to favour a Sey 2 AGN.

3.4. IGR J11187−5438

IGR J11187−5438 was first reported by Bird et al. (2007). The source was detected at a 18–60 keV significance of 6.3σ during 1016 ks of observations. There is a single source in the 2MASS point source catalogue within 5″ from the XRT position. 2MASS J11182121-5437286 is at 3.5″ away from the centre of the *Swift* error box. The source is also visible in the DSS II IR and *R*-Band images, although it is quite weak in the latter. The UVOT was not operating during either of the observations.

We combined the two observations to perform a spectral analysis. The average spectrum has 1328 cts for a total of 21 888 s exposure. An absorbed power law fits the data well ($\chi^2_\nu = 0.91$ for 55 d.o.f.). The value of the absorption is compatible with the Galactic absorption along the line of sight, which may mean that the source is not intrinsically absorbed.

3.5. IGR J13149+4422

IGR J13149+4422 was first reported in Sazonov et al. (2007) and Krivonos et al. (2007). The latter give an IBIS position of $RA_{J2000} = 13^h14^m58^s$ $Dec_{J2000} = +44°23'$ with a 1-σ uncertainty as high as 2.1′. It was then tentatively identified with Mrk 248 a Sey 2 AGN at $z = 0.037$ (Sazonov et al. 2007). The best *Swift*/XRT position is 3.56′ from the IBIS position, therefore within the 90% confidence error box. It is compatible with the best reported position of UGC 8327 NED02 (at $RA_{J2000} = 13^h15^m17.270^s$, $Dec_{J2000} = +44°24'25\farcs60$ according to the latest measurements available in NED, thus at 0.13″ from the centre of the *Swift* error box). Note that this is also at 16.″8 from the position reported in Bodaghee et al. (2007), and in SIMBAD for Mrk 248. We remark that SIMBAD reports an earlier measurement than NED, and also mentions Mrk 248 as being UGC 8327, a pair of interacting galaxies (UGC 8327). NED, on the other hand, associates Mrk 248 with one of the components of the pair of interacting galaxies (UGC 8327 NED02). Mrk 248 is also reported in the 2MASS extended source catalogue as 2MASX J13151725+4424259 whose best position is at only 0.64″ away from the best X-ray position. The 2MASS source is also classified as an emission line galaxy in SIMBAD. An extended or blended source is also clearly visible in the UVOT UVM2 and UVW1 images within the XRT error box. The spatial coincidence between all sources likely indicates that IGR J13149+4422 is a Sey 2 AGN.

We extracted a spectrum from three pointings. The spectrum has 964 cts for a total of 15116 s. It is well fitted by an absorbed power law ($\chi^2 = 1.11$ for 32 d.o.f.). We note the presence of positive residuals at low energy. The value of N_H is about 430 times higher than the average absorption along the line of sight, which indicates that the source is an intrinsically absorbed AGN as would be expected in the case of a Sey 2 AGN.

3.6. IGR J14579−4308

IGR J14579−4308 was first reported by Kalemci et al. (2005) from an IBIS/ISGRI observation of SN 1006. It was promptly suggested to be an AGN due to its positional coincidence with VV 780 a Sey 2 AGN. Revnivtsev et al. (2006) later reported the presence of the source from a survey of the Galactic Crux arm tangent. The XRT images show that the field is crowded with about five bright sources in the field of view (Fig. 2). Only the brightest source is, however, found within the maximum of 6′ error box of ISGRI (Revnivtsev et al. 2006). It is labeled 1 in Fig. 2. The best XRT position is 42″ away from the reported position of IC 4518/ VV 780 which rules out an association between the X-ray source and the AGN. Bird et al. (2007) suggested a possible association of the INTEGRAL source with IC 4518A, a Sey 2 galaxy as inferred from optical spectroscopy (Masetti et al. 2007), also the western component of a pair of interacting galaxies named MCG-07-31-001. The best *Swift* position is, indeed, just 1.48″ away from the position of IC 4518A (also named VV 780 NED01) as reported in NED. Our *Swift* analysis, therefore, strengthens the association of both objects,

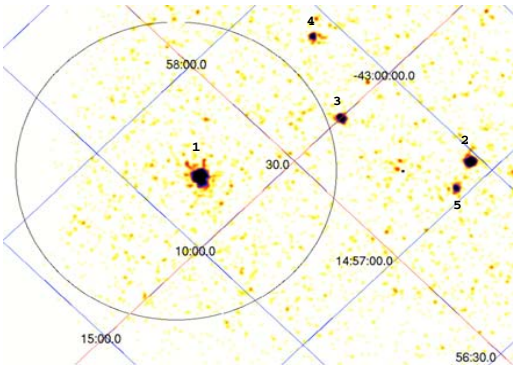

Fig. 2. *Swift* XRT image of the field around IGR J14579−4308. The 5 sources are indicated with numbers. Source 1 is the X-ray counterpart to IGR J14579−4308. The big circle is the maximum IBIS error box of 6′ reported in Revnivtsev et al. (2006).

and we confirm that IGR J14579−4308 is a Sey 2 galaxy. Note that, as for IGR J13149+4422, the position of IGR J14579−4308 reported in Bodaghee et al. (2007) and in SIMBAD is that of the pair of interacting galaxies, while we identify here one of the components of this double system as the best counterpart to the *INTEGRAL* source thanks to the refined position. The best positions for the other sources are reported in Table 5. Only source 2 in Fig. 2 has an infared counterpart reported in 2MASS. 2MASS J14570433−4300187 indeed lies 1.″5 from SWIFT J145704.4−430020. No UVOT data are available from any of the observing sequences.

We combined the three observations to perform a spectral analysis. The average spectrum of IGR J14579−4308 has 703 cts for a total of 21685 s exposure. A simple absorbed power law does not fit the data well ($\chi^2_\nu = 2.88$ for 29 d.o.f.). A large excess is visible below 2 keV. Adding a black body to the model improves the fit to $\chi^2_\nu = 1.25$ for 27 d.o.f. The black body radiation is not absorbed and has a temperature of $0.28^{+0.11}_{-0.06}$ keV. The best parameters of the other spectral components (power law and N_H) are reported in Table 2. Replacing the black body by a disc model (`diskpn` in XSPEC) provides a good description of the spectrum ($\chi^2_\nu = 1.28$ for 27 d.o.f.). The inner disc temperature is $0.5^{+0.7}_{-0.2}$ keV. The high value of the absorption indicates that the object is intrinsically highly absorbed, as would be expected in a Sey 2 AGN. Further spectral results will be reported in Kalemci et al. (in prep.).

3.7. IGR J16385−2057

IGR J16385−2057 was first reported by Bird et al. (2007). Based on a positional coincidence with 1RXS J163830.9−205520 and Oph J163830−2055, it was suggested to be the X-ray counterpart to those objects. Optical spectra allowed Masetti et al. (2006a) to tentatively classify it as a Sey 1 at $z = 0.027$. The *Swift*/XRT position is 2.5″ away from the position of 2MASX J16383091−2055246 an AGN at $z = 0.026$ (Hasegawa et al. 2000). This object is also compatible with Oph J163830−2055, and therefore the tentative identification as a Sey 1 seems confirmed by the refined XRT position. Note that the *Swift* position is also 5.73″ from 1RXS J163830.9−205520, well within the ROSAT error box (7″). No UVOT data are available for this source.

We combined the two observations to perform a spectral analysis. The average spectrum of IGR J16385−2057 has 2195 cts for a total of 9168 s exposure. An absorbed power law fits the data well ($\chi^2_\nu = 1.27$ for 85 d.o.f.). The value of the absorption is a factor of two higher than the total absorption along the line of sight. This may indicate that a part of the absorbing material is intrinsic to the object.

3.8. IGR J18490−0000

IGR J18490−0000 was first reported by Molkov et al. (2004) from a survey of the Sagittarius Arm tangent region. Nothing more is known about this source. There is a single 2MASS point source within the *Swift*/XRT error box. 2MASS J18490182-0001190 lies 3.55″ from the centre of the *Swift* error box. It has a well-measured magnitude only in the *K*-band, while it is not detected in the UVOT *V*-filter.

We extracted an average spectrum from the two pointings. The spectrum has 441 counts for a total of 12 208 s and is well fitted by an absorbed power law ($\chi^2_\nu = 0.40$ for 17 d.o.f.). The value of $N_{\rm H}$ is about 3 times higher than the average value of the absorption along the line of sight. This may indicate that IGR J18490−0000 is intrinsically absorbed. This source is likely a Galactic X-ray binary because of the presence of a point source *K*-band counterpart, its spectrum intrinsically absorbed and typical of an XRB, and its position towards the Sagittarius Arm.

3.9. IGR J18559+1535

The first mention of an *INTEGRAL* detection of this source is reported in Bird et al. (2006), as 2E 1853.7+1534, a Sey 1 AGN. The *Swift*/XRT position is about 12″ away from the best reported position for 2E 1853.7+1534/2MASX J18560128+1538059. There are no extended sources or NED objects within 10″ of the best position. In the XRT error box there are, however, a 2MASS point source, 2MASS J18560056+1537584 at 0.7″ and a *ROSAT* source 1RXH J185600.4+153757 at 2.89″. The positional coincidence of these two sources probably indicates that they are related. We do not detect any source in the UVOT *UVM2* and *UVW2*-filters at the best XRT positions. Masetti et al. (2006a) and Bikmaev et al. (2006) performed optical follow-up observations of the field of this object. Masetti et al. (2006a) suggested an association of this gamma-ray source with the *ROSAT* source, which allowed them to perform optical spectroscopy of the object. They identified it as a Sey 1 galaxy at $z = 0.084 \pm 0.001$. Bikmaev et al. (2006) obtained an optical position exactly coincident with the *Swift* position of IGR J18559+1535. They also refine the redshift to $z = 0.0844 \pm 0.0002$. Our X-ray refined position strongly confirms the identification of the high energy source as a Sey 1 galaxy.

We extracted an average spectrum from the four pointings. The spectrum has 1572 cts for a total exposure of 8378 s. The spectrum is well fitted with an absorbed power law ($\chi^2_\nu = 0.90$ for 68 d.o.f.). The value of $N_{\rm H}$ is about twice the value of the absorption along the line of sight which could indicate that the object has some intrinsic absorption, although at a low level, as would be expected from a Sey 1 AGN.

3.10. IGR J19308+0530

IGR J19308−0530 was first reported by Bird et al. (2006). It was detected at a 20–60 keV significance of 6.6σ for a total of 949 ks of observing time. Within the *Swift*/XRT error box lies a known star, TYC 486-295-1 also reported in the 2MASS catalogue as 2MASS J19305075+0530582. The average *Swift*/XRT position is just 2.5″ away from the best position of TYC 486-295-1 = 2MASS J19305075+0530582 a F8 star. This positional coincidence may suggest IGR J19308+0530 is a Low Mass/Intermediate Mass X-ray Binary. However, all DSII and 2MASS images are saturated at the position of TYC 486-295-1/2MASS J19305075+0530582, and we do not exclude that this is actually a blend of sources.The source saturates the UVOT images in the *U*, *B* and *V*-filters, and is clearly detected in the other filters (Table 3).

We extracted an average spectrum from the two pointings. The source is quite weak, with a 82 cts spectrum for a total exposure of 6556 s. The spectrum is well fitted by an absorbed power law (C-statistic value 20.7 for 22 bins). The value of $N_{\rm H}$ is compatible with the value of the absorption along the line of sight. This indicates that the object is not intrinsically absorbed. As can be seen in Table 2 the power law photon index is quite soft. As such a steep power law may be indicative of a thermal spectrum, we replaced it by an absorbed absorbed black body. The fit is rather good (C-statistic value 26 for 23 bins). The best parameters are $N_{\rm H} < 0.15 \times 10^{22}$ cm^{-2} (90% upper limit) and $kT = 0.26 \pm 0.5$ keV. Note that a bremsstrahlung also fits the spectrum well.

We dereddened the data with the value of $N_{\rm H}$ obtained from the spectral fit (Table 2) and the value of Galactic value of the absorption along the line of sight ($\sim 0.2 \times 10^{22}$ cm^{-2}). We then estimated the distance to the source assuming the optical/infrared counterpart is an F8 star, corresponding to the 2MASS source. Typical parameters of an F8 star favour a low absorption (0.2×10^{22} cm^{-2}) at a distance not greater than 1 kpc. At this distance the 2–10 keV unabsorbed luminosity is $\sim 4 \times 10^{31}$ erg s^{-1} for the 0.2 keV black body. These parameters suggest that IGR J19308+0530 is most probably a neutron star XRB in quiescence, or a CV. If it is much closer than 1 kpc, and although an F8 companion may be a quite extreme case, the source would rather be a CV.

3.11. IGR J19378−0617

A first mention of an *INTEGRAL* source at this position is given in Molkov et al. (2004). They suggested that the source of the hard X-ray emission was SS 442 (1H 1934−063). The authors, however, suspected the presence of a new source given the 5.6′offset of their position of the IBIS source and that of SS 442. IGR J19378−0617 was then reported by Bird et al. (2007) at a position slightly different than that of Molkov et al. (2004). It was detected at a 18–60 keV SNR of 5.7σ. It was promptly suspected to be a Sey 1 AGN. Within the *Swift*/XRT error box lies an extended 2MASS source. 2MASX J19373299-0613046 is at 1.0″ from the best *Swift* position. Note that this source is also associated with SS 422/1H 1934−063 mentioned in the catalogue of Molkov et al. (2004). It is a Seyfert 1.5 galaxy at $z = 0.011$. The 2MASS source is also reported in several catalogues, while it is clearly detected in the *UVW1*-filter in the UVOT data. It is a known radio source (NVSS J193733-061304) and a known X-ray source (1RXS J193732.8-061305).

We extracted an average spectrum from the two pointings. The spectrum has 4222 cts for a total exposure of 2910 s which may indicate that pile up is not negligible. To avoid pile up effect we extracted the source spectrum from an annular region centred on the best source position excluding the 10 central pixels. The outer radius of the annulus was set to 40 pixels. The resultant spectrum has 1201 cts. An absorbed power law fits the spectrum

well (χ^2_ν = 1.1 for 45 d.o.f.). The value of $N_{\rm H}$ is compatible with the average value of the absorption along the line of sight, which indicates that IGR J19378−0617 is a Sey 1.5 which is not intrinsically absorbed.

3.12. IGR J23254+5842

IGR J23254+5842 was first reported in the third edition of the IBIS catalogue (Bird et al. 2007). It was detected in both the 20–40 keV and 40–100 keV energy ranges, and the 18–60 significance of its detection was 6.3σ out of a total of 1780 ks of observations. Within the *Swift*/XRT error box lies a single 2MASS source. 2MASS J23522211+5845307 is 0.92″ away from the centre of the *Swift* error box, and it is also bright in the DSS I & II images. Although a very faint source may be present in the U-filter of the UVOT data, we cannot precisely determine its magnitude.

We extracted a spectrum from the single *Swift*/XRT pointing. The source is very weak with a 70 cts spectrum for a total of 5902 s exposure. A simple power law fits the spectrum well (C-statistic value = 19.5 for 13 bins). Adding an absorbing component improves the statistic to 16.3 for 14 bins. Note that when all parameters are left free to vary they are poorly constrained. We therefore froze the power law photon index to 2. The prefered value of $N_{\rm H}$ may indicate that the absorption is intrinsic to the source, but the poor quality of the data prevents us any firm conclusion on that matter.

4. Discussion and conclusions

We analysed *Swift*/XRT observations of 12 IGRs that previously lacked X-ray position at several arcsec accuracy. This lack of fine positions at X-ray energy either prevented a confirmation of the supposed type of the object or simply prevented nature of the object to be found. The refinement of the X-ray positions allowed us to identify potential counterparts at infrared, optical and UV wavelengths for all of them. We also report the detection of six serendipitous sources of unknown nature although in the case of SWIFT J023405.1+322707, a K0 star is the likely counterpart and thus suggests the source has a galactic origin. All IGRs that were formerly suspected to be AGN were confirmed through our analysis as indeed being so. This shows that although the error box of *INTEGRAL* can contain several candidate counterparts, when an AGN is found inside it is usually also at the origin of the hard X-ray emission. This is especially true for sources that have high galactic latitude (>10°). We confirm that IC 4518A is the counterpart to IGR J14579−4308, and therefore that this source is a Sey 2. We also truly identify IGR J19378−0617 as a Sey 1.5 galaxy, with known infrared, radio and X-ray counterparts. In IGR J14579−4308 we detected a soft excess in the X-ray spectrum. Soft excesses have been detected in a large number of X-ray spectra of AGNs (e.g. Porquet et al. 2004). The estimated luminosity of this soft excess is 7.9×10^{40} erg s^{-1}, which is compatible with an origin intrinsic to the AGN. When fitting with a `diskpn` model instead of a black body, we obtain a lower limit on the inner radius of the disk $R_{\rm in} > 6\,R_{\rm G}$.

For the other sources, we either found in the optical and infrared surveys, faint sources within the *Swift* error box. In two cases these counterparts may be extended or a blend of sources, which prevents an identification to be given. In two cases U and UVW2 counterparts were found. For IGR J09523−6231 we first proposed a tentative Sey 2 identification. The AGN nature of the source has recently been confirmed. It is, however, a Sey 1.5 (Masetti et al. 2008). For IGR J10147−6354 the identification as an AGN, possibly a Sey 2, seems more secure. We, however, stress that only through optical spectroscopy of the counterpart shall the identification be firmly given. For the others, the fact that these objects have point sources as optical/infrared counterparts may suggest that they are Galactic sources, although this is not a definite proof. Only in some specific cases this is, however, strongly supported by some additional facts. IGR J19308+0530 has an F8 star as the most likely counterpart. It spectrum is indicative of little intrinsic absorption (which may also suggest that it is a close object), and is very soft. IGR J18490−0000 has a *K*-band counterpart. Its spectrum is intrinsically absorbed and resembles that of an XRB. Its position in the direction of the Sagittarius Arm tangent would strengthen its Galactic nature, as the arms of the Galaxy are sites with high-density of sources. Note that these sources lie at Galactic latitudes <7° which may suggest that they are associated with the Galactic Plane, further supporting a Galactic origin. In all those cases (but IGR J19308+0530), the power law photon index returned by the spectral fit may suggest they are XRBs, although a more definite identification would require optical spectroscopy of the counterpart, and study of the temporal variability of the X-ray source.

Acknowledgements. J.R. thanks A. Maury for very useful suggestions on early versions of this paper. The authors thank Emrah Kalemci for communications of preliminary results on VV 780 prior to publication. We also warmly thank N. Masetti and I. Bikmaev for pointing us more precise results concerning some of the sources, and the anonymous referee for a very useful report which helped us to improve the paper. We acknowledge the use of data collected with the *Swift* observatory. This research has made use of the SIMBAD database, operated at CDS, Strasbourg, France. It also makes use of data products from the Two Micron All Sky Survey, which is a joint project of the University of Massachusetts and the Infrared Processing and Analysis Center/California Institute of Technology, funded by the National Aeronautics and Space Administration and the National Science Foundation. This research has made use of the NASA/IPAC Extragalactic Database (NED) which is operated by the Jet Propulsion Laboratory, California Institute of Technology, under contract with the National Aeronautics and Space Administration. We acknowledge the use of NVSS, DSS online catalogues.

References

Bikmaev, I. F., Sunyaev, R. A., Revnivtsev, M. G., & Burenin, R. A. 2006, Astron. Lett., 32, 221
Bird, A. J., Barlow, E. J., Bassani, L., et al. 2006, ApJ, 636, 765
Bird, A. J., Malizzia, A., Bazzano, A., et al. 2007, ApJS, 170, 175
Bodaghee, A., Courvoisier, T. J.-L., Rodriguez, J., et al. 2007, A&A, 467, 585
Burenin, R., Mescheryokov, A., Sazonov, S., et al. 2006, ATel, 883
Burrows, D. N., Hill, J. E., Nousek, J. A., et al. 2005, SSRv, 120, 165
Chaty, S., Rahoui, F., Foellmi, C., et al. 2008, A&A, in press
Gehrels, N., Chincarini, G., Giommi, P., et al. 2004, ApJ, 611, 1005
Hasegawa, T., Wakamatsu, K., Malkan, M., et al. 2000, MNRAS, 316, 326
Kalemci, E., Boggs, S. E., & Lund, N. 2005, ATel, 410
Krivonos, R, Revnivtsev, M., Lutovinov, A., et al. 2007, A&A, 475, 775
Lebrun, F., Leray, J. P., Lavocat, P., et al. 2003, A&A, 411, L141
Lutovinov, A., Rodriguez, J., Revnivtsev, M., & Shtykovskiy, P. 2005, A&A, L41
Masetti, N., Malizia, A., Dean, A. J., Bazzano, A., & Walter, R. 2006a, ATel, 957
Masetti, N., Mason, E., Bassani, L., et al. 2006b, A&A, 448, 547
Masetti, N., Morelli, L., Cellone, S. A., et al. 2007, ATel 1033
Masetti, N., Mason, E., Morelli, L. et al. 2008, A&A, 482, 113
Molkov, S. V., Cherepaschuk, A. M., Lutovinov, A. A., et al. 2004, Astron. Lett., 30, 534
Porquet, D., Reeves, J. N., O'Brien, P., & Brinkmann, W. 2004, A&A, 422, 85
Revnivtsev, M. G., Sazonov, S. Yu., Molkov, S. V., et al. 2006, Astron. Lett., 32, 145
Rodriguez, J., Bodaghee, A., Kaaret P., et al. 2006, MNRAS, 366, 274
Roming, P. W. A., Kennedy, T. E., Mason, K. O., et al. 2005, SSRv, 120, 95
Sazonov, S., Revnivtsev, M., Krivonos, R., Churazov, E., & Sunyaev, R. 2007, A&A, 462, 57
Tomsick, J. A., Chaty, S., Rodriguez, J., et al. 2006, ApJ, 647, 1309
Winkler, C., Courvoisier, T. J.-L., Di Cocco, G., et al. 2003, A&A, 411, L1

A&A 494, 417–428 (2009)
DOI: 10.1051/0004-6361:200810773

Astronomy & Astrophysics

Swift follow-up observations of 17 INTEGRAL sources of uncertain or unknown nature

J. Rodriguez[1], J. A. Tomsick[2], and S. Chaty[1]

[1] Laboratoire AIM, CEA/DSM - CNRS - Université Paris Diderot, IRFU/SAp, Centre de Saclay, 91191 Gif-sur-Yvette, France
e-mail: jrodriguez@cea.fr
[2] Space Sciences Laboratory, 7 Gauss Way, University of California, Berkeley, CA 94720-7450, USA

Received 8 August 2008 / Accepted 25 November 2008

ABSTRACT

Context. The positional accuracy of the IBIS telescope on-board *INTEGRAL*, albeit unprecedented in the >20 keV range, is still not good enough to identify many hard X-ray sources discovered by *INTEGRAL*. This indeed prevents counterparts from being found at other wavelengths, which is the only way to unveil the true nature of these sources.
Aims. We continue the work of trying to reveal the nature of these hard X-ray sources. This is done by analysing X-ray data collected via focusing X-ray telescopes, with the primary goal of discovering soft X-ray counterparts of the *INTEGRAL* sources to provide an accurate X-ray position. With a few arcsec accuracy, we can identify counterparts at infrared and optical wavelengths.
Methods. We analysed data from observations of 17 *INTEGRAL* sources made with the *Swift* satellite. The X-ray images obtained by the X-ray Telescope instrument allowed us to refine the position of the hard X-ray sources to an accuracy of a few arcsec. We then browsed the online catalogues (e.g., NED, SIMBAD, 2MASS, 2MASX, USNO) to search for counterparts at other wavelengths. We also made use of the X-ray spectral parameters to further distinguish between the various possibilities.
Results. For 13 sources, we find the X-ray counterpart without any ambiguity. For these, we provide the position with arcsec accuracy, identify possible infrared and optical counterparts (when found), give the magnitudes in those bands and in the optical and UV as seen with the *Swift*UVOT telescope when observations are available. We confirm the previously suggested associations and source types for IGR J03532−6829, J05346−5759, J10101−5654, J13000+2529, J13020−6359, J15479−4529, J18214−1318, and J23206+6431. We identify IGR J09025−6814 as an AGN for the first time, and we suggest that it may be a Seyfert 2. We suggest that IGR J05319−6601, J16287−5021, J17353−3539, and J17476−2253 are X-ray binaries, with J05319−6601 located in the LMC and the other three possibly being HMXBs in our Galaxy. For IGR J15161−3827 and J20286+2544, we find several possible X-ray counterparts in the IBIS error region, and we discuss which, if any, are the likely counterparts. Both are likely AGNs, although the latter could be a blend of two AGNs. For IGR J03184−0014 and J19267+1325, we find X-ray sources slightly outside the IBIS error circle. In the former, we do not favour an association of the *Swift* and *INTEGRAL* source, while it is very likely that IGR J19267+1325 and the *Swift* source are the same.

Key words. astrometry – binaries: close – galaxies: Seyfert – X-rays: binaries – X-rays: galaxies

1. Introduction

Since its launch, the INTErnational Gamma-Ray Astrophysics Laboratory (*INTEGRAL*) has detected about 500 sources as reported in a recent version of its source catalogue (Bird et al. 2007; Bodaghee et al. 2007). A large number of the sources had either not been well-studied or had not been detected prior to *INTEGRAL*. In this paper, we refer to them as "IGRs"[1]. Although ∼arcmin accuracy is achieved for source positions with IBIS/ISGRI (Lebrun et al. 2003), a level that is unprecedented in the >20 keV range, this is not sufficient to unveil counterparts at other wavelengths (optical, infrared (IR), and radio), which is the best way to reveal the true nature of the IGRs.

In a recent paper, Bodaghee et al. (2007) collected known parameters (e.g., the absorption column density, $N_{\rm H}$, the pulse period for Galactic sources with X-ray pulsations, the redshift for AGN, etc.) of all sources detected by *INTEGRAL* during the first four years of activity. Their catalogue, however, contains a large number of IGRs whose high-energy position is accurate at just the arcmin level, which therefore prevents their true nature from being known. In some cases, a tentative identification is given, mainly when an AGN is found within the *INTEGRAL*/ISGRI error circle, but this is far from being secure, as other possible counterparts usually lie in the few arcmin ISGRI error regions.

In this paper, we continue our work of identifying the unknown IGRs that we started soon after the discovery of the first IGRs. A first step is to provide an ∼arcsec position with soft X-ray telescopes such as *XMM-Newton*, *Chandra* (e.g., Rodriguez et al. 2003, 2006; Tomsick et al. 2006, 2008a), and also *Swift* (Rodriguez et al. 2008, hereafter paper 1). We then search for counterparts at a position consistent with the refined X-ray position of a given source. In the case of HMXBs, we also have follow-up programmes from ground-based facilities that permit us to further understand the nature of a large number of systems (Chaty et al. 2008; Rahoui et al. 2008). In paper 1, we focused on sources that were easily detected with *Swift*/XRT (Gehrels et al. 2004; Burrows et al. 2005), i.e., sources that were bright enough to be detected during single pointings lasting a few ks. In this paper, we report on the analysis of *Swift* observations (XRT imaging and spectral analysis and UVOT imaging) of seventeen IGRs that either lacked precise arcsec X-ray positions or whose Chandra

[1] An up-to-date online catalogue of all IGRs can be found at http://isdc.unige.ch/~rodrigue/html/igrsources.html

Table 1. Journal of the *Swift* observations analysed in this paper.

Source Id (IGR)	Id	Date Obs	Tstart (UTC)	Exposure (s)
J03184−0014	00030995001	2007–11–07	00:12:58	9192
J03532−6829	00037303001	2008–07–02	13:59:56	2405
J05319−6601	00036094001	2007–01–07	07:16:32	1395
	00036094002	2008–01–01	00:05:08	17 649
J05346−5759	00037120001	2007–11–13	01:29:04	5926
	00037120002	2007–12–25	12:08:50	2762
	00037120003	2007–12–31	15:41:50	6966
J09025−6814	00037312001	2008–02–07	20:00:42	1054
	00037312002	2008–03–02	00:46:22	4119
	00037312003	2008–03–18	02:23:28	2529
	00037312004	2008–05–08	07:25:07	2269
J10101−5654	00030356001	2006–01–12	08:07:43	1201
J13000+2529	00036818001	2008–02–23	09:56:41	558
	00036818002	2008–02–22	06:43:11	744
J13020−6359	00030966001	2007–07–07	14:35:41	2705
	00030966002	2007–07–09	13:27:01	5126
	00030966003	2007–07–11	07:09:27	5512
	00030966004	2007–07–13	16:49:45	5951
J15161−3827	00036663001	2008–01–25	23:38:01	7808
	00036663002	2008–01–27	01:21:41	5309
J15479−4529	00037149001	2007–06–23	14:49:57	346
	00037149002	2007–06–24	00:28:26	3968
	00037149003	2007–06–26	00:41:28	983
	00037149004	2008–01–25	01:01:51	4758
	00037149005	2008–06–25	01:19:05	2580
	00037149006	2008-06-26	07:50:53	1685
J16287−5021	00037074001	2008–07–11	17:20:34	1944
J17353−3539	00311603004	2008–05–28	00:38:42	4540
	00311603005	2008–06–04	23:56:39	184
	00311603006	2008-06-05	06:14:18	4368
	00311603008	2008–06–14	03:48:37	3869
	00311603009	2008–07–12	04:49:18	8713
J17476−2253	00036656001	2008–07–03	20:16:28	1142
J18214−1318	00035354001	2006–02–11	15:30:34	6285
J19267+1325	00037062001	2007–07–20	11:15:50	4312
J20286+2544	00030722001	2006–06–03	14:44:55	6876
	00035276001	2005–12–16	01:19:43	4525
	00035276002	2006–03–23	00:23:43	4597
	00035276003	2006–03–28	01:20:05	921
J23206+6431	00031026001	2007–11–24	00:05:08	3978

refined X-ray position was very recently published by us (Tomsick et al. 2008a,b). We also present the identification of IR and optical counterparts obtained from online catalogues such as SIMBAD, the United States Naval Observatory (USNO), the 2 Micron All Sky Survey point source and extended source catalogues[2] (2MASS and 2MASX, Skrutskie et al. 2006), and the NASA/IPAC Extragalactic Database (NED[3]). It should be noted that although the presence of a bright *Swift* source within a given *INTEGRAL* error circle renders very likely the association between the two sources, there is a slight probability that the two sources are not associated. This is, in particular, exemplified by the few cases where several *Swift* sources are found within the *INTEGRAL* error circle. Note that this remark is also true for the association between the *Swift* sources and the proposed counterpart at other wavelengths. We cannot give a general statement about this issue, that would hold for all cases, as there is a wide range of association probabilities from possible associations to nearly certain associations. For all sources, we discuss the likelihood of association between the *INTEGRAL*, *Swift*, and counterparts at other wavelengths. Dubious cases (as, e.g., multiple possible counterparts) are discussed in more detail.

We start by introducing the *Swift* observations and briefly presenting the data reduction techniques in Sect. 2. Then, in Sect. 3, we describe the results for each source (position, counterparts, and spectral properties) and discuss their possible nature. We conclude the paper by summarising the results in Sect. 4.

2. Observations and data reduction

Among all the *Swift* pointed observations of IGRs, we mainly restricted our analysis to sources whose fine position and/or *Swift* observations were not published anywhere else[4]. We used only the pointings during which the XRT instrument was in photon counting mode since this is the only mode that provides a fine position. We also included in our study sources for which a *possible* identification had been given, e.g., based on the presence of an AGN in the IBIS error region in existing catalogues (see, e.g., Bodaghee et al. 2007). The observing log for our sample of seventeen sources is reported in Table 1.

We reduced the *Swift* data with the `HEASoft V6.5` software package and the calibration files issued on 2008 May 1 and 2008 June 25 for the UVOT and XRT instruments, respectively. The reduction steps are identical to those presented in paper 1, and follow the standard steps described in the XRT users guide and UVOT software guides[5]. More specifically, we ran the `xrtpipeline` tool with standard screening criteria to produce level 2 (i.e., cleaned) event files from the level 1 data products. The positions of the sources were obtained with `xrtcentroid`. We co-added all individual pointings of a given source with `xselect`, before estimating the source position from the resulting mosaic. We extracted spectra and light curves with `xselect` from a circular region with a radius of 20 pixels centred on the best position, while we obtained the background products from a source-free circular region with a radius of 40 pixels (see also paper 1). Due to the presence of columns of dead pixels in the XRT, we produced "true" exposure maps to further correct the ancillary response files (see also paper 1). We rebinned the spectra to have at least 20 counts per channel which allows for χ^2-minimization in the fitting with `XSPEC 11.3.2ag`. When this criterion was not achievable, the Cash statistic (hereafter C-statistic, Cash 1976) was used instead.

When available, we analysed the UVOT level 2 data obtained from the *Swift* data archive. We first corrected the aspect for each individual UVOT exposure with the `uvotskycorr` tool, calculating the aspect correction via comparison to the USNO-B1.0

[2] `http://www.ipac.caltech.edu/2mass/`
[3] `http://nedwww.ipac.caltech.edu/index.html`
[4] with the exceptions of IGR J10101−5654, J18214−1318, J16287-5021, and J19267+1325 whose *Chandra* positions have very recently been published by Tomsick et al. (2008a,b)
[5] both available at `http://heasarc.gsfc.nasa.gov/docs/swift/analysis/`

catalogue[6] (Monet et al. 2003). Then, we summed the aspect-corrected individual exposures with `uvotimsum`, and performed the UVOT photometry and astrometry with the `uvotdetect` tool.

3. Results

The refined X-ray positions of the sources detected by *Swift* are reported in Table 2. For each source, we searched the 2MASS, 2MASX and the USNO-B1.0 online catalogues for the presence of infrared and/or optical counterparts within the *Swift*/XRT error circle. Infrared counterparts that are newly identified from this search are reported in Table 3. The typical positional accuracy for the 2MASS sources is 0.5″ (Skrutskie et al. 2006), while that of the USNO-B1.0 sources is typically 0.2″ (Monet et al. 2003). The magnitudes and UV positions of the optical and UV counterparts are reported in Table 4. The USNO-B1.0 photometric accuracy is typically 0.3 mag (Monet et al. 2003).

We fitted the source spectra with a simple model of an absorbed power law. This provided an acceptable representation of the spectra in the large majority of the cases. The spectral parameters we obtained are reported in Table 5. The errors on the X-ray spectral parameters (including upper limits) are at the 90% confidence level. We discuss in the following subsections the results obtained for each of the sources, including the few cases where a simple absorbed power law is not sufficient, or not appropriate to represent the spectra well. To estimate the luminosity of the candidate AGN we used $H_0 = 75$ km s^{-1}Mpc^{-1} to convert the redshift (of the suggested counterpart) to distance. The lower limits on the *UVOT* magnitudes are given at the 3σ level. The UVOT positional uncertainties are dominated by a 0.5″ systematic uncertainty (90% confidence) for each source. All X-ray fluxes and luminosities are corrected for absorption. The absorption due to intervening material along the line of sight is first obtained with the `nh` tool based on the measurements of H I made by Dickey & Lockman (1990). It is also compared to the values obtained from the Leiden/Argentine/Bonn (LAB) surveys of Galactic H I in the Galaxy. The LAB Survey is the most sensitive Milky Way H I survey to date, with the most extensive coverage both spatially and kinematically and an angular resolution of 0.6 degrees (Kaberla et al. 2005). For each source, the two values are reported in Table 5 for comparison.

3.1. Confirmations of previously suggested associations

IGR J03532−6829:
Masetti et al. (2006a) suggested an association of the IGR source with PKS 0352−686, a blazar of BL Lac type at $z = 0.087$, based on its location inside the IBIS error circle (Götz et al. 2006) as well as the fact that these objects are known to be strong emitters of X- and gamma-rays. The source detected by *Swift*/XRT is 1.14″ from the position of PKS 0352−686 reported in NED, further strengthening the classification of the IGR source as a BL Lac. The extended 2MASX source that lies within the XRT error circle (Table 3) has already been associated with the BL Lac. There is also one USNO-B1.0 source and a single UVOT source within the *Swift* error circle (Table 4). The USNO-B1.0 and UVOT sources are at positions consistent with the BL Lac object given the ∼30″ extension of the 2MASX source. The *Swift* source is coincident with 1RXS 035257.7−683120 which is classified as being a cluster of galaxies in SIMBAD.

[6] http://tdc-www.harvard.edu/software/catalogs/ub1.html

An absorbed power-law represents the *Swift*/XRT spectrum well with $\chi^2_\nu = 0.98$ for 63 degrees of freedom (d.o.f.). The value of the absorption (Table 5) is compatible with the value of Galactic absorption along the line of sight. This indicates that the source is not significantly locally absorbed. This further argues in favour of the hard X-ray source being the blazar as these objects do not usually show significant intrinsic absorption. At $z = 0.087$, the 2–10 keV luminosity of the source is $\sim 2.5 \times 10^{44}$ erg/s. We note that the extrapolated 20–40 keV flux of the *Swift* spectrum is about twice as high as the *INTEGRAL* flux of 0.6 mCrab reported in Götz et al. (2006). If the extrapolation of the power-law is valid, then this indicates variability, as expected in a BL Lac.

IGR J05346−5759:
Based on positional coincidence and the good agreement between the *INTEGRAL* and *ROSAT* spectral shape, Götz et al. (2006) suggested that IGR J05346−5759 is the hard X-ray counterpart to TW Pic, a cataclysmic variable (CV). There is a unique and quite bright XRT source within the IBIS error circle. TW Pic is the only source given in SIMBAD that is within the XRT error circle, where it is also associated with the 2MASS source listed in Table 3. The single source that is found in the USNO-B1.0 catalogue is positionally coincident with the single detected UVOT source (see Table 4), indicating that they are the same source. We note that the UVOT magnitudes were obtained from pointing #2 for the *UVW1* filter and pointings #1 and #3 for the other two filters. The values obtained in the latter two are compatible (within the 0.2 mag errors) and we report the mean of the two in Table 4. These spatial coincidences strengthen the association of the XRT source with the CV. The fact that CVs are known X-ray emitters, and that an increasing number have been seen at X-ray energies >20 keV, makes the suggested associations between IGR J05346−5759 and TW Pic very likely and secure.

We first checked the XRT count rates for variability between the different pointings. The source shows some variability between high flux states (up to ∼0.45 cts/s) and lower flux states (down to ∼0.11 cts/s). We extracted a single spectrum from one of each of the three pointings. An absorbed power-law[7] fits the data well in all cases (χ^2_ν=1.19 for 89 d.o.f., 1.29 for 14 d.o.f. and 1.26 for 98 d.o.f., for pointings #1, 2 and 3, respectively). The best spectral parameters of all three pointings are reported in Table 5, and they are in good agreement with those obtained by Götz et al. (2006) from a *ROSAT* observation of TW Pic. In addition, no cut-off is seen in the XRT spectrum (which extends to higher energy than the *ROSAT* spectrum). The extrapolation of the XRT spectral model to the 20–40 keV range leads to a flux that is compatible with the flux measured by *INTEGRAL* (0.9 mCrab). All these points (including the spatial coincidences discussed above) further confirm that IGR J05346−5759 is TW Pic, including the spectral variability of IGR J05346−5759 as TW Pic is known to be variable. This variability has been used by Norton et al. (2000) to refute the intermediate polar (IP) type for this source. We therefore conclude that IGR J05346−5759 is the hard X-ray counterpart to TW Pic, and thus, is a CV.

[7] Note that we chose to use a simple power-law rather than the more sophisticated models usually used to fit CV spectra in order to compare the XRT spectral parameters to those mentioned in the literature. In particular, Götz et al. (2006) showed that the extrapolation at hard X-rays of spectrum obtained with *ROSAT* was compatible with the *INTEGRAL*/IBIS one. A discussion of the emission processes at work in CVs is beyond the scope of this paper.

Table 2. X-ray position (equatorial and Galactic) of the X-ray counterparts to the 17 sources studied with *Swift*/XRT.

Name (IGR)	RA (J2000)	Dec (J2000)	Error (″)	l (°)	b (°)
J03184−0014†	$03^h18^m17.6^s$	−00°17′48.1″	5.7	181.8112	−45.7082
J03532−6829	$03^h52^m57.4^s$	−68°31′18.0″	3.5	282.8102	−40.7968
J05319−6601†	$05^h31^m52.6^s$	−65°59′40.2″	4.7	275.9037	−32.6650
J05346−5759	$05^h34^m50.5^s$	−58°01′39.3″	3.5	266.4230	−32.7788
J09025−6814†	$09^h02^m39.4$	−68°13′38.7″	4.8	284.1738	−14.1567
J10101−5654⋆	$10^h10^m11.9^s$	−56°55′31.6″	4.3	282.2567	−0.6719
J13000+2529†	$12^h59^m55.0^s$	+25°28′08.8″	6.9	352.2816	+87.4774
J13020−6359	$13^h01^m59.2^s$	−63°58′06.0″	3.5	304.0891	−1.1202
J15161−3827‡ #1	$15^h15^m59.3^s$	−38°25′48.3″	4.3	331.6935	+16.2381
#2	$15^h16^m\ 29.6^s$	−38°26′56.5″	4.6	331.7689	+16.1681
#3†	$15^h16^m12.7^s$	−38°31′02.4″	4.7	331.6819	+16.1411
#4†	$15^h15^m45.8^s$	−38°27′36.2″	4.7	331.6380	+16.2370
J15479−4529	$15^h48^m14.7^s$	−45°28′40.4″	3.5	332.4403	+7.0228
J16287−5021°	$16^h28^m27.2^s$	−50°22′38.3″	4.4	334.1093	−1.1261
J17353−3539	$17^h35^m23.5^s$	−35°40′13.8″	3.5	353.1445	−1.7401
J17476−2253	$17^h47^m30.0^s$	−22°52′43.2″	4.8	5.3999	+2.7813
J18214−1318⋆	$18^h21^m19.7^s$	−13°18′38.2″	3.5	17.6813	+0.4856
J19267+1325°	$19^h26^m27.0^s$	+13°22′03.4″	3.7	48.8032	−1.5059
J20286+2544‡ #1	$20^h28^m34.9^s$	+25°43′59.7″	3.9	67.0045	−7.5713
#2	$20^h28^m28.7^s$	+25°43′22.5″	4.4	66.9825	−7.5582
J23206+6431	$23^h20^m36.8^s$	+64°30′42.8″	3.8	113.3539	+3.3424

† Source is very faint, just a very slight excess (very few photons) within IBIS error; ⋆ consistent with the *Chandra* position published by Tomsick et al. (2008a); ‡ several sources within IBIS error; ° consistent with the *Chandra* position published by Tomsick et al. (2008b).

Table 3. List of newly identified infrared counterparts in the 2MASS and 2MASX catalogues.

Name (IGR)	Counterpart	Magnitudes J	H	K_s	Offset from the XRT position (″)
J03184−0014	2MASS J03181753−0017502			15.2 ± 0.1	2.4
J03532−6829	2MASX J03525755−6831167	13.22 ± 0.04	12.50 ± 0.05	12.07±0.08	1.5
J05346−5759	2MASS J05345057−5801406	14.77 ± 0.04	14.34 ± 0.05	14.11 ± 0.06	1.4
J09025−6814	2MASX J09023946−6813365	10.24 ± 0.01	9.50 ± 0.01	9.19 ± 0.02	2.1
J13000+2529	2MASS J12595533+2528101	10.39 ± 0.02	9.80 ± 0.03	9.68 ± 0.02	4.7
J15161−3827 #1	2MASX J15155970−3825468	12.55 ± 0.03	11.83 ± 0.03	11.34 ± 0.06	4.9
#3	2MASS J15161246−3831041	10.45 ± 0.02	10.21 ± 0.02	10.13 ± 0.02	3.5
J15479−4529	2MASS J15481459−4528399	13.22 ± 0.03	12.75 ± 0.03	12.53 ± 0.03	1.2
J17353−3539	2MASS J17352361−3540128	10.23 ± 0.02	9.03 ± 0.02	8.63 ± 0.03	1.6
J17476−2253	2MASS J17472972−2252448			13.00 ± 0.07	4.2
J20286+2544 #1	2MASX J20283506+2544001	11.31 ± 0.02	10.39 ± 0.02	9.93 ± 0.03	2.3
#2	2MASX J20282884+2543241	10.05 ± 0.01	9.23 ± 0.01	8.87 ± 0.01	2.6

IGR J10101−5654:
A refined *Chandra* position for this object has recently been published by Tomsick et al. (2008a). The XRT position is 0.55″ from the 0.64″ accurate *Chandra* position (Tomsick et al. 2008a) and therefore both positions are compatible. We further confirm all the suggested associations for this object, and the fact that it is a very likely HMXB (Masetti et al. 2006c; Tomsick et al. 2008b). There are no UVOT data available for this pointing.

The spectrum is well-fitted with an absorbed power-law (C = 19.9 for 14 bins). The spectral parameters reported in Table 5 are fully consistent with those reported from the *Chandra* observation of this source (Tomsick et al. 2008a). Although the poor statistical significance of the parameters we obtain does not allow us to constrain the possible spectral variability for this source, the flux we obtain from the *Swift* observation is about five times higher than during the *Chandra* observation (Tomsick et al. 2008a). This may indicate significant variation of the mass accretion rate.

IGR J13000+2529:
Based on the spatial coincidence between the two objects, Bassani et al. (2006) suggested an association of IGR J13000+2529 with MAPS-NGP O-379-0073388, an AGN

Table 4. Magnitudes and UVOT position of the newly identified optical and UV counterparts in the USNO-B1.0 catalogue (*I*, *R* and *B* bands) and *Swift*/UVOT detector (*V*, *U*, *UVW1*, *UVM2*, and *UVW2* bands). The *B* magnitudes are those obtained from the USNO-B1.0 catalogue, except where indicated. The long dashes indicate the absence of corresponding data.

Name	Optical counterpart	UVOT position		Magnitudes							
(IGR)	(USNO-B1.0)	RA	Dec	*I*	*R*	*V*	*B*	*U*	*UVW1*	*UVM2*	*UVW2*
J03532−6829	0214-0026031	$03^h52^m57.5^s$	−68° 31′ 17.4″	12.7	12.3	–	13.7	–	–	–	17.28 ± 0.02
J05346−5759	0319-0039890	$05^h34^m50.6^s$	−58° 01′ 40.8″	13.8	15.2	–	14.9	–	13.886 ± 0.004	13.182 ± 0.006‡	12.909 ± 0.001‡
J09025−6814	0217-0159098⋆	$09^h02^m39.5^s$	−68° 13′ 38.2″	–	8.6	–	9.7	16.6	16.61 ± 0.02‡	17.63 ± 0.03	–
J13000+2529	1154-0199710	$12^h59^m55.3^s$	25° 28′ 10.5″	10.6	11.3	–	13.0	–	15.51 ± 0.02	17.61 ± 0.06	–
J15161−3827#1	0515-0356635	–	–	10.7	10.6	–	10.6	–	–	–	–
#2	0515-0357047	–	–	18.2	18.3	–	19.0	–	–	–	–
#3	7822-02179-1	–	–	10.9	11.3	–	11.0	–	–	–	–
#4	0515-0356459	–	–	–	18.5	–	18.9	–	–	–	–
J15479−4529	–	$15^h48^m14.6^s$	−45° 28′ 39.9″	–	–	–	–	–	–	–	14.501 ± 0.003‡
J17353−3539	0543-0510755	–	–	10.9	–	11.9	–	–	>20.3	>20.2	–
J17476−2253	0671-0618341	–	–	15.3	17.0	–	19.1	–	–	>19.3	–
J18214−1318	–	–	–	–	–	>19.3	>19.8°	>19.9	>20.6	>20.5	>20.9
J19267+1325	–	$19^h26^m27.0^s$	13° 22′ 05.1″	–	–	–	–	–	–	–	20.54 ± 0.07
J20286+2544 #1†	1157-0462303⋆	$20^h28^m35.1^s$	25° 43′ 59.5″	–	10.1	15.06 ± 0.01‡	11.4	18.03 ± 0.05‡	20.5 ± 0.1‡	>21.1	20.6 ± 0.1*
#2	1157-0462166	$20^h28^m28.9^s$	25° 43′ 24.6″	8.9	8.7	12.897 ± 0.007‡	10.3	15.41 ± 0.01‡	16.83 ± 0.02‡	>21.1	19.15 ± 0.05‡
J23206+6431	1545-0296864	–	–	17.9	19.1	–	20.9	>21.1	–	–	–

‡ Values averaged over multiple pointing; ⋆ there are two possible USNO-B1.0 sources in the XRT error circle. This is the closest to the IR source; † the UVOT positional accuracy is dominated by a statistical uncertainty of 1.1″; ◇ *B* magnitude obtained from *Swift*/UVOT; * average value obtained with `uvotsource`.

listed in the NED database. The XRT position is consistent with that of MAPS-NGP O-379-0073388, which provides further confirmation that the high energy source and the AGN are the same. We found a single 2MASS source within the XRT error circle, and although the source is not reported as extended it lies only 0.9″ from the position of the AGN reported in NED, which indicates the two objects are probably the same. A single source is also found within the XRT error circle in the USNO-B1.0 catalogue and UVOT images (Table 4).

As the source is very weak, we extracted an average spectrum from the two *Swift* pointings. The spectrum has too few counts for a spectral analysis to be possible. Although this source is the faintest from our sample that we detect with XRT, and the very low flux could indicate a lower probability that it is associated with the IGR source, the good spatial coincidence with the AGN along with the fact that this is the only XRT source in the IBIS error circle that we detect make IGR J13000+2529 a strong AGN candidate.

IGR J13020−6359:

This source was first mentioned in Bird et al. (2006) and was classified as a pulsar/HMXB in Bird et al. (2007), probably based on the positional coincidence with 2RXP J130159.6−635806, which indeed is an HMXB containing a pulsar (Chernyakova et al. 2005). Bodaghee et al. (2007) further report a distance to the source of about 5.5 kpc. We find a single XRT source within the IBIS error circle at a position compatible with that of 2RXP J130159.6−635806. This renders the association even more likely. It is unfortunate that due to its off-axis position (the pointings were aimed at PSR B1259−63), none of the UVOT exposures contains the source. There is no USNO-B1.0 source within the *Swift* error circle. We estimate a lower limit $V \gtrsim 21$ for the magnitude of an optical counterpart. Chernyakova et al. (2005) mention the presence of a $J \sim 13$, $H = 12.0$ and $K_s = 11.3$ 2MASS source at a position compatible with that of the pulsar, that they consider as its likely counterpart.

As the source may be significantly variable (Chernyakova et al. 2005), we fitted each spectrum from each independent pointing separately. An absorbed power-law fits all spectra rather well (χ^2_ν in the range 0.6 to 1.40 for 30 to 13 d.o.f.). Since the absorption is poorly constrained and given that Chernyakova et al. (2005) mention a relatively stable value of 2.48×10^{22} cm^{-2}, we froze N_H to this value in all our fits. Note that for all pointings the value obtained for N_H when it is allowed to vary is in good agreement, or compatible with Chernyakova et al. (2005). The spectral results reported in Table 5 show some slight variability especially between the first pointing and the following ones, which are slightly softer. The spectral parameters are those expected for an accreting pulsar and, assuming a distance of 5.5 kpc, lead to a 2–10 keV luminosity of about 8–9 × 10^{34} erg/s, typical for these objects.

IGR J15161−3827:

Based on the positional coincidence of IGR J15161−3827 and LEDA 2816946, Masetti et al. (2006b) suggested that the latter, an AGN, is the counterpart of the high energy source. The AGN type is intermediate between a Liner and a Sey 2 at $z = 0.0365$ (Masetti et al. 2006b). The *Swift* mosaic image revealed four possible X-ray counterparts within the IBIS error circle of IGR J15161−3827. Swift J151559.3−382548, Swift J151630.0−382656, Swift J151612.2−383102, and Swift J151545.8−382738 are labeled source #1, #2, #3, and #4, respectively in Tables 2 and 3. It is a priori not possible to say which

Table 5. X-ray spectral analysis. Errors and upper limits are all given at the 90% level.

Name (IGR)	Net number ă of counts	Galactic $N_{\rm H}$ (LAB/DL)‡ $\times10^{22}$ cm^{-2}	$N_{\rm H}$ $\times10^{22}$ cm^{-2}	Γ	2–10 keV flux erg cm^{-2} s^{-1}
J03184−0014	19	0.05/0.06	$0.06^{\dagger}$	$1.4^{+0.8}_{-0.7}$	$5.3^{+0.5}_{-0.3}\times10^{-14}$
J03532−6829	1650	0.06/0.06	$0.09^{+0.04}_{-0.04}$	$1.9^{+0.1}_{-0.1}$	$1.75^{+0.14}_{-0.18}\times10^{-11}$
J05319−6601	19	0.12/0.06	$0.12^{\dagger}$	$1.55^{+0.89}_{-0.77}$	$5^{+4}_{-3}\times10^{-14}$
J05346−5759	2172	0.04/0.05	<0.05	$1.22^{+0.1}_{-0.09}$	$1.7^{+0.2}_{-0.1}\times10^{-11}$
	378		<0.15	$1.75^{+0.3}_{-0.3}$	$5.7^{+1.2}_{-1.0}\times10^{-12}$
	2516		$0.05^{+0.03}_{-0.03}$	$1.34^{+0.09}_{-0.09}$	$1.7^{+0.1}_{-0.1}\times10^{-11}$
J09025−6814	17	0.05/0.07	9^{+123}_{-7}	<3.2	$<9.2\times10^{-12}$
J10101−5654	86	1.35/1.77	$3.3^{+2.5}_{-1.7}$	$1.3^{+0.9}_{-0.8}$	$1.2^{+0.3}_{-0.6}\times10^{-11}$
J13020−6359	337	1.40/1.53	$2.48^{\dagger}$	$0.9^{+0.3}_{-0.3}$	$2.3^{+0.3}_{-0.9}\times10^{-11}$
	670		$2.48^{\dagger}$	$1.2^{+0.2}_{-0.2}$	$2.6^{+0.2}_{-0.4}\times10^{-11}$
	471		$2.48^{\dagger}$	$1.1^{+0.2}_{-0.2}$	$2.3^{+0.3}_{-0.5}\times10^{-11}$
	574		$2.48^{\dagger}$	$1.1^{+0.2}_{-0.2}$	$2.3^{+0.3}_{-0.5}\times10^{-11}$
J15161−3827 #1	48	0.06/0.07	22^{+17}_{-9}	$2.0^{\dagger}$	$1.2^{+0.5}_{-0.5}\times10^{-12}$
#2	32	0.07/0.07	<0.2	$1.2^{+0.7}_{-0.5}$	$<1.3\times10^{-13}$
#3	18	0.07/0.07	<1.9	>2.8	$<1\times10^{-13}$
#4	13	0.06/0.07	$0.065^{\dagger}$	$2.0^{+1.0}_{-0.9}$	$3^{+5}_{-2}\times10^{-14}$
J16287−5021	75	1.37/1.55	$2.6^{+2.1}_{-1.6}$	$0.9^{+0.8}_{-0.8}$	$6.5^{+2.2}_{-3.0}\times10^{-12}$
J17353−3539	416	0.69/0.63	$0.7^{+0.4}_{-0.3}$	$2.2^{+0.4}_{-0.4}$	$5.0^{+0.9}_{-0.5}\times10^{-12}$
	803		$0.8^{+0.2}_{-0.2}$	$2.1^{+0.3}_{-0.3}$	$1.2^{+0.1}_{-0.1}\times10^{-11}$
J17476−2253	45	0.30/0.38	$1.9^{+1.7}_{-1.1}$	$2.6^{+1.4}_{-1.0}$	$5^{+2}_{-3}\times10^{-12}$
J18214−1318	1866	1.21/1.54	$3.5^{+0.8}_{-0.5}$	$0.4^{+0.2}_{-0.2}$	$6.7^{+0.7}_{-0.4}\times10^{-11}$
J19267+1325	461	0.95/0.93	<0.6	$1.1^{+0.3}_{-0.3}$	$8.1^{+1.6}_{-0.7}\times10^{-12}$
J20286+2544 #1	171	0.20/0.26	61^{+23}_{-20}	$2.5^{+1.6}_{-1.4}$	$2.1^{+1.6}_{-1.2}\times10^{-11}$
#2	53	0.20/0.26	93^{+80}_{-61}	$2.7^{+3.1}_{-3.1}$	$<1.6\times10^{-11}$
J23206+6431	244	0.78/0.90	$0.9^{+1.0}_{-0.7}$	$1.6^{+0.7}_{-0.5}$	$5.5^{+1.3}_{-1.0}\times10^{-12}$

‡ Values of weighted average Galactic $N_{\rm H}$ respectively obtained from Leiden/Argentine/Bonn (LAB) and Dickey & Lockman (DL) surveys of Galactic H I in the Galaxy; † unconstrained parameter that was fixed during the spectral fit.

(if any) is the true counterpart. Two of these are compatible with IR counterparts found in the 2MASS and 2MASX catalogues, although 2MASX J15155970−3825468 is 4.9″ from the *Swift* position and therefore is slightly outside the XRT error circle of source #1. It is, however, an extended source, and the XRT error circle still contains a significant part of the source. This source is the one suggested by Masetti et al. (2006b) as the counterpart to the IGR source. A USNO-B1.0 source lies at 5.4″ from the XRT position, at a position compatible with the 2MASX source (offset by 0.7″), given the extension of the latter. Source #3 has a position compatible with an IR point source, which is consistent with being TYC 7822-2179-1 catalogued as a star in SIMBAD and also reported in the USNO-B1.0 catalogue (Table 4). There are USNO-B1.0 counterparts for the other two sources as well, although the source #4 counterpart does not have measurement in the *I*-band (Table 4). There are no UVOT data available for either of the two XRT pointings.

We extracted an average spectrum from the two pointings for each of the four sources. The spectrum of source #1 has a low statistical quality. The spectrum was fitted with an absorbed power-law (C = 38.5 for 15 bins). When all parameters are left free to vary, they are very poorly constrained (Table 5). Although only an upper limit can be obtained from the absorption, visual inspection of the spectrum shows that the source may show significant absorption. Fig. 1 represents the contour plot of Γ vs. $N_{\rm H}$. It is clear from this figure that the value of $N_{\rm H}$ is tightly correlated to that of Γ as expected. This figure, however, shows that for $\Gamma \geq 0.5$, a value typical for most high energy sources, this source is significantly (intrinsically) absorbed as would be expected from a Sey 2. We note that, to obtain the 20–40 keV flux of 0.5 mCrab seen with *INTEGRAL* (Bird et al. 2007), a harder power-law ($\Gamma \sim 0.7$) is needed. Even in that case,

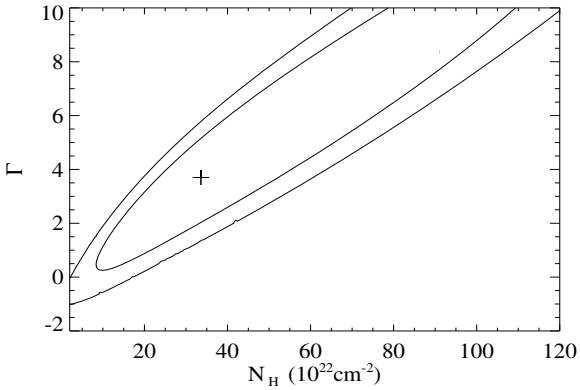

Fig. 1. Contour plot of the power-law photon index Γ vs. $N_{\rm H}$ in IGR J15161−3827 source #1. The contours represent ΔC = 2.30 and 4.61.

significant absorption is implied by the fit. The 2–10 keV luminosity at $z = 0.0365$ is $5.6 \pm 0.5 \times 10^{42}$ erg/s, compatible with the luminosity of an AGN.

An absorbed power-law provides a good fit to the spectrum of source #2 ($C = 7.6$ for 15 bins). The spectrum is consistent with little or no absorption in this source. The absence of significant absorption in the spectrum of the source argues in favour of a nearby object. The extrapolated 20–40 keV flux is well below the *INTEGRAL* flux. A hard power-law with a photon index $\lesssim$0.35 would be needed to reach the 20–40 keV flux observed by *INTEGRAL*. These last points argue against an association of source #2 with the IGR source.

The X-ray spectrum of source #3 is well-fitted with an absorbed power-law ($C = 7.7$ for 14 bins). The quite steep power-law and the low flux obtained with the lower limit of Γ, may indicate that the spectrum is thermal. Replacing the power-law by a black-body also gives a good fit ($C = 7.5$ for 15 bins). Note that since the value of $N_{\rm H}$ is poorly constrained, it was frozen to the value of Galactic $N_{\rm H}$. The black-body temperature is 0.2 ± 0.1 keV for a luminosity of $9 \times (D_{10}^2) \times 10^{32}$ erg/s, with D_{10} the distance in units of 10 kpc. The probable low value of the absorption and the bright IR and optical counterparts argue in favour of a nearby object. In that case, the rather flat SED, black-body shape and temperature of the X-ray spectrum indicate that this is probably a young stellar object (YSO), e.g. a T Tauri star. The softness of the source renders it difficult to reconcile the emission of this object with that at energies >20 keV. A very hard photon index of ~1.0 would be needed to be compatible with the 20–40 keV flux. Such a power-law slope is incompatible with the XRT spectrum. We conclude that this object is certainly not related to the IGR source.

As for the 2 previous objects, the X-ray spectrum of source #4 is well-fitted with an absorbed power-law ($C = 4.7$ for 15 bins). A quite absorbed source with a very steep power-law seems to be favoured here. We note, however, that a simple power-law (with no absorption) leads to more physical results for this source. As a compromise the value of absorption was frozen to the Galactic $N_{\rm H}$. A $0.6^{+0.3}_{-0.2}$ keV black-body also fits the data well ($C = 6.2$ for 15 bins). In any case, the extrapolation of the spectra to the *INTEGRAL* range falls well below the 20–40 keV flux. A power-law with a value of the photon index incompatible with the XRT spectrum ($\Gamma \lesssim 0.5$) would be needed. This shows that this source and the IGR source are very probably not related.

To conclude, the broad band (counterpart and X-ray) analysis of the four *Swift* objects found within the IBIS error circle of IGR J15161−3827 leads us to conclude that the IGR source is very probably associated with the Liner/Sey 2 object LEDA 2816946.

IGR J15479−4529:
Based on the presence of a *ROSAT* source (also detected by *XMM-Newton*) within the IBIS error circle, Tomsick et al. (2004) suggested an association between 1RXS J154814.5−452845, and the IGR source. 1RXS J154814.5−452845 is a CV, more precisely an Intermediate Polar (IP) with a pulse period of 693 s and an orbital period of 562 mn (Barlow et al. 2006). The refined position we obtained with *Swift* is only 5″ from the *ROSAT* position (Haberl et al. 2002), indicating that the two positions are compatible. There is a single source listed in SIMBAD within 3′ of the XRT position. This source has several names, one of which is V ⋆ Ny Lup indicating that it is a variable star (Samus et al. 2004). Clearly the coincidence of the *Swift* and *ROSAT* sources renders their association likely. The fact that it is an IP, which are known hard X-ray emitters, strengthens the associations with the *INTEGRAL* source. We therefore confirm all suggested association, and the fact that IGR J15479−4529 is very probably an IP. A bright source is found within the XRT error circle with the *UVOT UVW2*-filter (Table 4). Its position is consistent with the 2MASS source. We note that this UV counterpart may show some variability from one pointing to the other, from $UVW2 = 14.0$ to 15.0, which further confirms the variable nature of the source.

Table 6. Spectral parameters obtained from the fits to the XRT spectra of IGR J15479−4529.

Pointing #	kT_{bb} (keV)	Γ	χ^2_ν (d.o.f.)	Flux (erg cm^{-2} s^{-1})
2	$0.12^{+0.03}_{-0.02}$	$0.9^{+0.06}_{-0.15}$	1.0 (59)	$2.1^{+0.2}_{-0.2} \times 10^{-11}$
4	$0.12^{+0.01}_{-0.01}$	$0.89^{+0.1}_{-0.09}$	1.0 (93)	$2.8^{+0.2}_{-0.2} \times 10^{-11}$
5	$0.11^{+0.01}_{-0.01}$	$0.9^{+0.1}_{-0.1}$	1.1 (58)	$3.3^{+0.3}_{-0.3} \times 10^{-11}$
6	$0.13^{+0.02}_{-0.01}$	$0.8^{+0.2}_{-0.2}$	0.8 (43)	$3.4^{+0.4}_{-0.5} \times 10^{-11}$

As the source may show some variability, we extracted a spectrum from each of the six pointings. Pointings #1 and #3 are quite short (<1 ks) so we do not consider them further. An unabsorbed power-law provides acceptable fits to pointings #2 and 4 (χ^2_ν between 1.3 for 61 d.o.f. and 1.6 for 95 d.o.f.), but not to pointings #5 and #6, where a significant excess is detected at soft X-rays. Haberl et al. (2002) also mention the need for a black-body to account for a soft excess in their *XMM* spectra. Adding a black-body to the power-law improves the fits greatly. We point out that Haberl et al. (2002) used a much more sophisticated model, but given the lower quality of our data, we only use the simple phenomenological models. However, since they report some absorption in the spectra we also included an absorption component. The resulting model is therefore `phabs*(bbody+powerlaw)` in the `XSPEC` terminology. When left free to vary, $N_{\rm H}$ tends toward very low values, although the 90% upper limit is (marginally) compatible with $\sim 0.14 \times 10^{22}$ cm^{-2} (Haberl et al. 2002). We therefore fixed $N_{\rm H}$ to this value in our fits. The results are reported in Table 6. The variations of the flux do not seem to be related to spectral changes, but they are more probably due to slight variations of the accretion rate.

IGR J18214−1318:
Tomsick et al. (2008a) recently reported a refined X-ray position with *Chandra* for this object. The accuracy of their position is 0.64″. The XRT position is 1.1″ away from the *Chandra* position, and the XRT error box (Table 2) contains the Chandra source. No counterpart is detected in any of the *UVOT* filters. We refer to Tomsick et al. (2008a) for the identification of counterparts. An absorbed power-law fits the XRT spectrum well ($\chi^2_\nu = 0.96$ for 83 d.o.f.). The value of $N_{\rm H}$ is higher than the Galactic value along the line of sight (Table 5), which confirms that there is intrinsic absorption in this source (Tomsick et al. 2008a). Our value of 3.5×10^{22} cm^{-2} is, however, significantly lower than the value of 11.7×10^{22} cm^{-2} obtained with *Chandra* observations (Tomsick et al. 2008a). Fixing $N_{\rm H}$ to the latter value does not lead to a good fit ($\chi^2_\nu = 2.4$ for 84 d.o.f.). This indicates that the variations of $N_{\rm H}$ are genuine for this source. This further argues in favour of an HMXB (possibly a supergiant system) since significant variability of $N_{\rm H}$ has been reported for several systems (e.g., Prat et al. 2008, in the case of IGR J19140+0951).

Note that the very hard spectrum may then indicate the presence of a pulsar.

IGR J19267+1325:
No X-ray source is found within the 3.7′ IBIS error circle. A bright X-ray source is, however, found 4.5′ away from the center of the IBIS error circle, and is, therefore, marginally compatible (within the 3σ error circle) with the *INTEGRAL* position. The *Swift* position is 1.7″away from the very recent 0.64″ *Chandra* position reported by Tomsick et al. (2008b). The positions given by the two satellites are therefore entirely compatible. Tomsick et al. (2008a) report the presence of a single IR and optical counterpart within the *Chandra* error circle of this object. We detect a single source in the UVOT detector (Table 4). It is well within the XRT and *Chandra* error circles (at 0.3″ from the best *Chandra* position).

An absorbed power-law provides an acceptable, although not perfect, fit ($\chi^2_\nu = 1.7$ for 18 d.o.f.) to the XRT spectrum. The value of the absorption is below the Galactic value on the line of sight, and we obtain an upper limit consistent with the value of 2.1×10^{22} cm^{-2} obtained with *Chandra* (Tomsick et al. 2008b). Landi et al. (2007) mentioned the presence of black-body emission in the spectrum. We added such a component in our spectral fits (both with and without absorption), but in no case did it provide a noticeable improvement over the absorbed power-law fit. The extrapolated 20–40 keV flux of $\sim 2.3^{+1.7}_{-1.1}$ mCrab is higher than the IBIS 20–40 keV flux of 0.7 mCrab reported by Bird et al. (2007). This may argue in favour of an association of this source with the *INTEGRAL* source, suggesting that it undergoes significant flux variations. The hard power-law index, low value of the absorption and position on the plane of the sky close to the Sagittarius arm would tend to suggest this object has a Galactic origin. Optical observations allowed Steeghs et al. (2008) to detect a possible counterpart within the *Chandra* error box of this source. Optical spectroscopy of this source permitted Steeghs et al. (2008) to further conclude that this source is a CV, probably containing a magnetic white dwarf (see also Butler et al., submitted to ApJ).

IGR J20286+2544:
Based on the presence of MCG+04-48-002 in the IBIS error circle of the *INTEGRAL* source Bassani et al. (2006) suggested an association between the two objects. Masetti et al. (2006a) added that although this Compton thick $z = 0.013$ Sey 2 was most probably the true counterpart to the IGR source, contribution from the nearby $z = 0.01447$ galaxy NGC 6921 could not be excluded. Our *Swift* mosaic image reveals 2 sources (Swift J202834.9+254359, source #1, and Swift J202828.7+254322, source #2), whose positions match those of the two galaxies. There are two possible USNO-B1.0 sources within the *Swift* position of source #1. Only one has well-estimated magnitudes in the *B* and *R* bands. As it is the closest in position to the 2MASX source (0.9″), it is the one we report in Table 4. Both sources are quite well-detected with the *UVOT* as extended sources in the *B*, *U*, *V*, *UVW1* and *UVW2* filters (Fig. 2). The UVOT counterpart to source #1 is not spontaneously found by `uvotdetect`, although it is clearly visible in Fig. 2. In this case, we used `uvotcentroid` to obtain an *estimate* of the source position[8], while the magnitudes at the best position of the source were obtained with `uvotsource`. The positions of all counterparts of source #2 are compatible with being within the extension of the 2MASX sources. We note, however, a large discrepancy between the *B* magnitude obtained by the *UVOT* (14.3) and that of the USNO-B1.0 source reported in Table 4. This may indicate that all *UVOT* magnitudes are overestimated, possibly because of the extension of the source.

As both sources are rather faint, we accumulated average spectra from the four pointings. The spectrum of source #1 is not well-fitted by an absorbed power-law ($C = 43$ for 14 bins). Significant residuals are found at low energy. Such soft excesses have been reported in a number of AGN (e.g., paper 1 and references therein). Adding an unabsorbed black-body greatly improves the fit ($C = 8.0$ for 14 d.o.f.). The black-body has a temperature of $0.4^{+0.2}_{-0.1}$ keV, and a 0.5–10 keV luminosity of $1.5^{+0.75}_{-0.5} \times 10^{40}$ erg/s assuming a distance $z = 0.013$. The other parameters are reported in Table 5. The source is strongly absorbed, but not Compton-thick. The extrapolated 20–40 keV flux is 4.5 times lower than the 20–40 keV IBIS flux of 2.6 mCrab reported by Bird et al. (2007).

As for source #1, a simple absorbed power-law does not provide a good description of the spectrum of source #2. It in particular gives negative values for the power-law index. Even fixing the latter to a fiducial value of 2 does not help. We used a similar model as for source #1, and this led to a good fit ($C = 11.7$ for 14 bins). The value of the photon index is poorly constrained (Table 5). In subsequent runs it was fixed to 2.0. Even in those cases, the source is highly absorbed and could be a Compton-thick object with $N_{\rm H} \sim 83 \times 10^{22}$ cm^{-2}. In this latter case, the extrapolated 20–40 keV flux is 8.2 times lower than the IBIS flux of IGR J20286+2544.

Although the flux of source #2 highly depends on the value of the photon index, our results indicate that IGR J20286+2544, the source seen by *INTEGRAL*, is probably a blend between Swift J202834.9+254359 and Swift J202828.7+254322, with a stronger contribution from the former. We also note that the high flux obtained by *INTEGRAL* may indicate significant variability in those sources. It has to be noted that the high absorption in source #2 would argue in favour of the source being a Sey 2, similar to source #1.

IGR J23206+6431:
This source was associated with 2MASX J23203662+6430452 by Bikmaev et al. (2008) based on the observation made with *Swift*. They did not provide any fine X-ray position, however. The position reported in Table 2 is fully compatible with that of the IR counterpart. They measured a value of $z = 0.0717$ from optical spectroscopy of this counterpart, and classified it as a Sey 1. The source is not detected by the *UVOT* *U*-filter with a 3σ lower limit $U > 21.1$.

An absorbed power-law fits the spectrum well ($\chi^2_\nu = 0.3$ for 8 d.o.f.). The 2–10 keV luminosity at $z = 0.0717$ is $5.4^{+1.3}_{-1.0} \times 10^{43}$ erg/s, which is typical for this type of object. The low value of the absorption is also compatible with the source being a Sey 1.

3.2. IGR J03184−0014

The position of the *Swift* source we found is 4.4′ away from the best IBIS position, and is, therefore, slightly outside the 4.0′ 90% IBIS error circle reported in Bird et al. (2007). Given the compatibility of the 3σ error circles of both the *INTEGRAL* and *Swift* sources, we first consider the possibility that the two

[8] `uvotcentroid` obtains mean coordinates by running a series of Monte-Carlo simulations of the source's pixel distribution on a 20 × 20″ sub-image centred on the best position

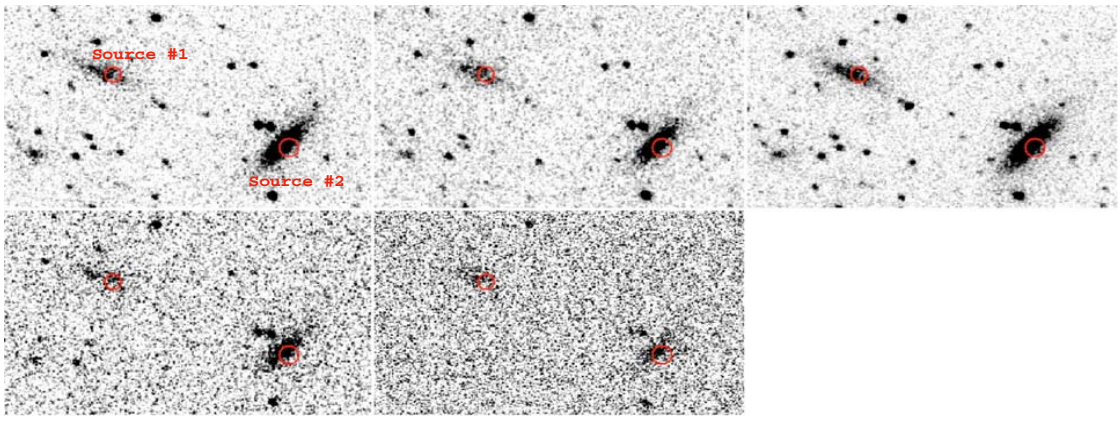

Fig. 2. *From top to bottom and left to right* 2.9′×1.7′ $B, U, V, UVW1, UVW2$ images of the field of IGR J20286+2544. The circles represent the *Swift* error circles for the two possible counterparts.

sources are associated. Its IR counterpart has a well-measured magnitude in the K_s band only. There is no USNO-B1.0 source within the *Swift* error circle with $V \gtrsim 21$. The UVOT telescope observed the field in the $UVW1$ filter. The `uvotdetect` tool did not yield a detection of a source within the XRT error circle. The presence of a bright $UVW1 = 13$ source at 23.8″ from the candidate counterpart renders, however, the detection of a possible counterpart difficult (the source is so bright that part of its flux is within the XRT error circle). Keeping this caveat in mind, we can roughly estimate a 3σ upper limit $UVW1 > 21.95$ based on the faintest source detected (at a confidence level greater than 3σ) with `uvotdetect`.

The *Swift* spectrum extracted from the single pointing available has 19 cts. An absorbed power-law is a good representation of the spectrum ($C = 10.4$ for 14 bins). As the value of the absorption is very poorly constrained ($<1.3 \times 10^{22}$ cm^{-2} at 90% confidence if left free to vary) we fixed it to the Galactic value along the line of sight. The spectral parameters are reported in Table 5. A fit with a black-body instead of the power-law also provides a good description of the data although statistically worse ($C = 12.0$ for 14 bins). The black-body has a temperature of $1.0^{+0.7}_{-0.3}$ keV, and a luminosity of $1.5^{+1.5}_{-0.7} \times 10^{33}$ erg/s at a distance of 10 kpc. The extrapolated 20–40 keV flux (3.5×10^{-13} erg cm^{-2} s^{-1}) is ∼100 times below the IBIS flux reported in Bird et al. (2007). We, therefore, conclude that this source (Swift J031818.0−001748) and IGR J03184−0014 are probably not related.

Given the faintness of the source, it is quite difficult to unveil its true nature. The fact that it is well-detected in the K band only, and that it has no counterpart in the optical and UV bands either points to a very distant object or a faint Galactic source. If we assume the source is an AGN, with a luminosity of 6×10^{42} erg/s (the luminosity of the faintest AGN detected in Paper 1), this implies a distance $z = 0.144$. The only source that was farther than this in paper 1 (IGR J09523−6231) was not significantly detected in the IR, but had, on the other hand, a well detected U-band counterpart compatible with the emission from the accretion disc of the AGN. The absorption on the line of sight for the latter object was also much higher than in the case of IGR J03184−0014, which suggests that, if IGR J03184−0014 was an AGN it would probably be detected with the UVOT. We conclude that it is unlikely that this object is an AGN. In the case of a Galactic object, the spectral parameters, while being very poorly constrained, may be compatible with the source being either an active star, a CV, or a neutron star X-ray Binary. At 8 kpc, the 2–10 keV power-law luminosity would be 1.1×10^{34} erg/s. These again point towards the *Swift* and *INTEGRAL* sources not being related.

3.3. IGR J05319−6601

A weak source is found in the XRT ∼20 ks mosaic image at a position consistent with that of IBIS (Götz et al. 2006). The XRT position is also consistent with that of RX J0531.8−6559. There are no IR or optical counterparts reported in the 2MASS, 2MASX, USNO-B1.0 catalogues with $K_s \gtrsim 16.2$, and $V \gtrsim 21$. There are no sources detected in the $UVOT$ U, V, $UVM2$ and $UVW2$ filters compatible with the XRT position. As in the case of IGR J03184−0014, the presence of a bright UV source at ∼10″ from the centre of the XRT error box renders the estimate of upper limits difficult due to possible contamination at the position of IGR J05319−6601. In a similar manner as for the previous source, we can estimate $U > 19.43$, $V > 19.33$, $UVW1 > 19.81$, and $UVM2 > 14.87$.

An absorbed power-law is a good representation of the *Swift* spectrum ($C = 7.4$ for 14 bins). As the value of the absorption is very poorly constrained ($<2.7 \times 10^{22}$ cm^{-2} at 90% confidence if it is left free to vary), we fixed it to the Galactic value along the line of sight. The spectral parameters are reported in Table 5. A fit with a black-body instead of the power-law also provides a good description of the data ($C = 6.53$ for 14 bins). The black-body has a temperature of $0.8^{+0.4}_{-0.3}$ keV, and a luminosity $6.6/D^{2+4.5}_{10-2.9} \times 10^{32}$ erg/s, where D_{10} is the distance in units of 10 kpc. The extrapolated 20–40 keV flux (based on the power-law model) is within 9.6×10^{-15}–1.9×10^{-13} erg cm^{-2} s^{-1}, which is more than 40 times lower than the IBIS 20–40 keV flux of 0.9 mCrab reported in Götz et al. (2006). We note, however, that during a second observing campaign, the same team did not

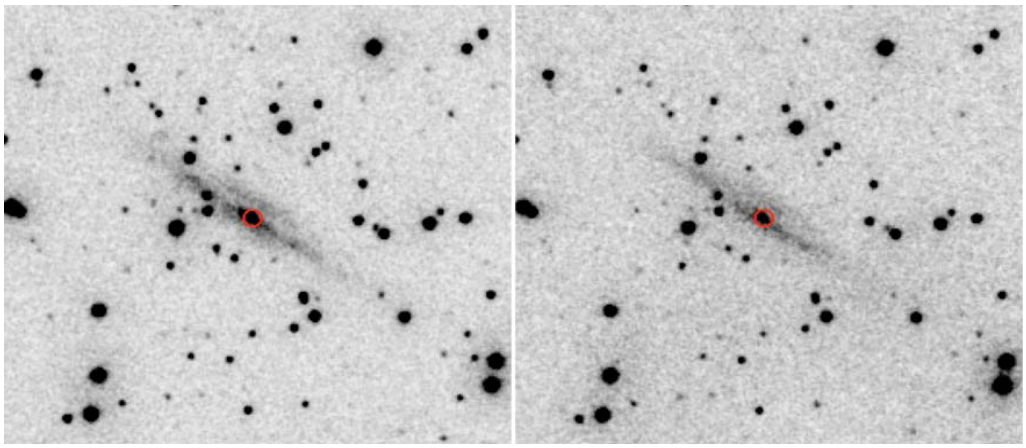

Fig. 3. 4.3′×4.1′ U (*left*) and UVW1 (*right*) UVOT images of the field around IGR J09025−6814. The best X-ray position is represented by the circle.

detect the source with *INTEGRAL*, which may indicate significant variability.

Götz et al. (2006) suggested the IGR source may be an X-ray binary in the LMC. In fact this assumption is in good agreement with the fact that no counterparts are reported in any of the optical and IR catalogues which may be due to the large distance to the source. Assuming the source is at the distance of the LMC, the 2–10 keV luminosity is $1.6^{+0.5}_{-0.3}\times10^{34}$ erg/s, which is therefore compatible with this hypothesis.

3.4. IGR J09025−6814

A very weak XRT excess is found within the IBIS error circle. The XRT position contains a 2MASX source (Table 3). It also contains two USNO-B1.0 sources. The one that is reported in Table 4 is the closest to the position of the 2MASX source (1.1″ away). It also has well-defined B and I magnitudes while the second source does not. The 2MASX source is reported in the NED database as ESO 60-24/NGC 2788A, a $z = 0.013$ galaxy. The detection of the source at X-ray energies with *INTEGRAL* and *Swift* suggests it is an AGN. The X-ray position falls right on the nucleus of the Galaxy as can be seen in the *UVOT U* and *UVW*1 images of the field (Fig. 3).

The XRT source is too weak to study any possible variability. We therefore extracted an averaged spectrum from the four pointings. An absorbed power-law seems to be a good representation of the spectrum. If we allow all parameters to be free to vary, they are, however, very poorly constrained ($C = 23$ for 14 bins, $N_{\rm H} < 52\times10^{22}$ cm^{-2} and $-2.5 < \Gamma < 3$). In order to try and have a more constraining range of values, we refitted the spectrum forcing $\Gamma \geq 0$.. An equally good fit is obtained with $C = 24$ for 14 bins. The values are reported in Table 5. The source may be intrinsically absorbed, and this may point towards a Sey 2 object, as intrinsic absorption is expected in this case. As the source is a Sey candidate, and to obtain a reasonable estimate of its flux, we fixed the power law photon index to 2.0. The 2–10 keV unabsorbed flux is $2.7^{+1.7}_{-1.5}\times10^{-12}$ erg cm^{-2} s^{-1}, which translate into a 2–10 keV luminosity of $8.7^{+1.7}_{-1.5}\times10^{41}$ erg/s. This value lies in the usual range for Seyfert galaxies.

3.5. IGR J16287−5021

The XRT position is well within the 4.4′ IBIS error circle, and is compatible with the very recent *Chandra* position reported by Tomsick et al. (2008b) (the *Chandra* positional accuracy is 0.64″. The *Swift* position is 3.6″ away from the *Chandra* position). There are no infrared and optical counterparts reported in the 2MASS, 2MASX, USNO-B1.0 catalogues. There is no source within the XRT error circle in the *UVOT UVM*2-filter image with $UVM2 > 20.0$.

The XRT spectrum is well-fitted by an absorbed power-law ($C = 8.5$ for 14 bins). The value of the absorption is not very well-constrained (Table 5), but may indicate little intrinsic absorption. Following Tomsick et al. (2008b), we also fitted the data with a non-absorbed power-law. The fit has a worse C-statistic value of 19.5 for 14 bins, which indicates that absorption is required in the fit. A good fit is also obtained when fixing $N_{\rm H}$ to the Galactic value along the line of sight ($C = 9.15$ for 14 bins). The spectrum is then much harder (0.4 ± 0.4) and is not consistent with the very hard photon index of -0.9 ± 0.4 obtained with *Chandra* (Tomsick et al. 2008b). Such a hard spectrum may indicate that the source is an HMXB.

3.6. IGR J17353−3539

As for the previous sources, a single X-ray source is found within the ∼ 3′ IBIS error circle. Our best position is within 3.1″ of 1RXH J173523.7−354013, indicating that the two sources are the same. Note that the position of 1RXH J173523.7−354013 reported in SIMBAD is at ∼9″ from the position reported in the online *ROSAT* catalogue[9]. In addition to the 2MASS source listed in Table 3, the XRT error circle also contains two USNO-B1.0 objects. Both have positions that are compatible with the position of the IR source. The closest (at 0.2″ from the 2MASS source) is the one reported in Table 4. No source is detected in the $UVM2$ and $UVW1$ filters of the UVOT telescope.

Since we see some variability, we extracted spectra from all pointings and analysed them separately. We report here only the

[9] http://www.xray.mpe.mpg.de/cgi-bin/rosat/src-browser

two extreme cases, as the others have parameters that are intermediate between those two. An absorbed power-law fits both spectra well (χ^2_ν = 0.75 and 0.88 for 16 and 34 d.o.f., respectively). The value of $N_{\rm H}$ is consistent with the Galactic value on the line of sight, which indicates the object is not highly intrinsically absorbed. The position of the source towards the Galactic Bulge may indicate a Galactic source. We note that the absence of a UV counterpart with the presence of a possible optical counterpart is also more compatible with a Galactic source as, in case of an AGN, the optical would be also completely absorbed, while a Galactic stellar component could have significant emission in optical and not in the UV domain (see, e.g., paper 1). The compatibility of $N_{\rm H}$ with the Galactic value may indicate that the source lies at a significant distance. The 2–10 keV luminosity of the highest state (Table 5) is 14.4 ± 0.1 /$D^2_{10} \times 10^{34}$ erg/s (where D_{10} is the distance in units of 10 kpc), which, combined with the spectral shape, may indicate the source is an HMXB.

3.7. IGR J17476−2253

A single bright X-ray source is found within the IBIS error circle. A single source is reported in the 2MASS catalogue (Table 3), while 2 USNO-B1.0 sources are found in the XRT error circle. The latter two are at, respectively, 1.7 and 2.9″ from the 2MASS source, and we consider the first (reported in Table 4) as just marginally compatible. The second is very probably not related to the IR source. No source is found in the $UVM2$-filter image of the UVOT telescope.

The XRT spectrum is well-fitted with an absorbed power-law (C = 4 for 15 bins). The value of the absorption is not well-constrained, and it may indicate that some intrinsic absorption occurs in this source. We, however, note that it is marginally compatible with the Galactic value along the line of sight. Fixing $N_{\rm H}$ to the Galactic value also provides a good description of the spectrum (C = 11.2 for 15 bins). In this case, the photon index is harder ($\Gamma = 1.2 \pm 0.4$). In this latter case, the 20–40 keV extrapolated flux is in good agreement with the 20–40 keV *INTEGRAL* flux of 1.3 mCrab (Bird et al. 2007). This may further argue in favour of an association between the *Swift* and *INTEGRAL* sources, although the flux obtained when all parameters are left free to vary is lower than that obtained with *INTEGRAL*. We, in addition, note that an absorbed black-body also gives a good representation of the data. It has a temperature of $0.9^{+0.1}_{-0.2}$ keV and a luminosity of 6×10^{34} erg/s at 10 kpc. Bird et al. (2007) tentatively classify this source as an AGN. We do not find strong evidence of this possibility, as the spectral parameters are also compatible with a Galactic X-ray binary. Here again, the position towards the Galactic bulge may favour a Galactic source. We note that the absence of a UV counterpart with the presence of a possible optical one is also more compatible with a Galactic source as, in case of an AGN, the optical would be also completely absorbed, while a Galactic stellar component could have significant emission in optical and not in the UV domain.

4. Summary and conclusions

In this paper, we reported the X-ray analysis of seventeen hard X-ray sources discovered by *INTEGRAL*. The refined X-ray positions provided by the *Swift* observations (Table 2) allowed us to pinpoint the possible IR and optical counterparts in most of the cases. Table 7 reports the conclusions of our analysis concerning the possible type of each of the seventeen sources. We confirm the associations and types previously suggested for five sources:

- IGR J03532−6829 is a BL Lac;
- IGR J05346−5759 and J15479−4529 are CVs, the latter is an IP;
- IGR J10101−5654 is very likely an HMXB;
- IGR J18214−1318 is a probable HMXB;
- IGR J13000+2529 and J23206+6431 are AGNs. The latter is a Sey 1;
- IGR J13020−6359 is an HMXB containing a pulsar.

In 2 cases, we detected several X-ray counterparts in the IBIS error circle. In these cases, the spectral analysis of each of those sources allowed us to suggest that Swift J151559.3−382548 is a probable Sey 2 AGN, which is the likely counterpart to IGR J15161−3827. In the case of IGR J20286+2544, the *Swift* error circle contains two AGNs, and the *INTEGRAL* source seems to be a blend of those two objects, although Swift J202834.9+254359 (=MCG+04-48-002) is brighter and therefore contributes more to the hard X-ray emission.

In one case (IGR J19267+1325), we do not detect any X-ray source within the IBIS error circle. A bright source, however, has a position that is marginally consistent, and, although it is slightly outside the IBIS error circle, our analysis leads us to suggest that both sources are related. We could not unambiguously unveil its true nature, although we favoured a Galactic source. Of the six remaining source:

- IGR J05319−6601 is compatible with being an X-ray binary in the LMC;
- We identified IGR J09025−6814 with the nucleus of a galaxy, and provided the first identification of this source as an AGN and a possible Sey 2;

Table 7. Summary of the possible type for each counterpart of the seventeen sources, obtained through the analysis presented in this paper.

Name (IGR)	Type and Comment
J03184−0014	IGR and Swift sources not related
J03532−6829	z = 0.087 BL Lac
J05319−6601	probable XRB in LMC
J05346−5759	CV (not an IP?)
J09025−6814	AGN, poss. Compton thick, Sey 2(?)
J10101−5654	HMXB
J13000+2529	AGN
J13020−6359	HMXB with pulsar
J15161−3827 #1	AGN, Liner/Sey 2
#2	?
#3	YSO
#4	?
J15479−4529	CV/IP
J16287−5021	HMXB (?)
J17353−3539	HMXB (?)
J17476−2253	XRB (?)
J18214−1318	probable HMXB (sg star?)
J19267+1325	Galactic source
J20286+2544 #1	AGN, Sey 2
#2	AGN, Sey 2 (?)
J23206+6431	AGN, Sey 1

- We suggest that IGR J16287−5021, J17353−3539 and J17476−2253 are probable X-ray binaries and possibly HMXBs;
- We find an X-ray source slightly outside the IBIS error circle of IGR J03184−0014, but our analysis does not favour any association between the *Swift* and *INTEGRAL* objects.

Acknowledgements. J.R. thanks the Swift help desk for their great help and rapid answer. J.A.T. acknowledges partial support from a NASA INTEGRAL Guest Observer grant NNX07AQ13G. We warmly thank the anonymous referee for his/her very constructive comments, that really helped to improve to quality of this paper. We acknowledge the use of data collected with the *Swift* observatory. This research has made use of the USNOFS Image and Catalogue Archive operated by the United States Naval Observatory, Flagstaff Station (http://www.nofs.navy.mil/data/fchpix/). This research has made use of the SIMBAD database, operated at CDS, Strasbourg, France. It also makes use of data products from the Two Micron All Sky Survey, which is a joint project of the University of Massachusetts and the Infrared Processing and Analysis Center/California Institute of Technology, funded by the National Aeronautics and Space Administration and the National Science Foundation. This research has made use of the NASA/IPAC Extragalactic Database (NED) which is operated by the Jet Propulsion Laboratory, California Institute of Technology, under contract with the National Aeronautics and Space Administration.

References

Barlow, E. J., Knigge, C., Bird, A. J., et al. 2006, MNRAS, 372, 224
Bassani, L., Molina, M., Malizia, A., et al. 2006, ApJ, 636, L65
Bikmaev, I., Revnivstev, M., Burenin, R., et al. 2008, ATel 1363
Bird, A. J., Barlow, E. J., Bassani, L., et al. 2006, ApJ, 636, 765
Bird, T. A. J., Malizzia, A., Bazzano, A., et al. 2007, ApJS, 170, 175
Burrows, D. N., Hill, J. E., Nousek, J. A., et al. 2005, SSRv, 120, 165
Bodaghee, A., Courvoisier, T. J.-L., Rodriguez, J., et al. 2007, A&A, 467, 585
Cash, W. 1976, A&A, 52, 307
Chaty, S., Rahoui, F., Foellmi, C., et al. 2008, A&A, 484, 783
Chernyakova, M., Lutovinov, A., Rodriguez, J., & Revivtsev, M. 2005, MNRAS, 364, 455
Corbel, S., Kaaret, P., Fender, R. P., et al. 2005, ApJ, 632, 504
Dickey, J. M., & Lockman, F. J. 1990, ARA&A, 28, 215
Götz, D., Mereghetti, S., Merlini, D., Sidoli, L., & Belloni, T. 2006, A&A, 448, 873
Gehrels, N., Chincarini, G., Giommi, P., et al. 2004, ApJ, 611, 1005
Haberl, F., Motch, C., & Zickgraf, F.-J. 2002, A&A, 387, 201
Kalberla, P. M. W., Burton, W. B., Hartmann, D. et al. 2005, A&A, 440, 775
Landi, R., Masetti, N., Sguera, V., et al. 2007, ATel 1323
Lebrun, F., Leray, J. P., Lavocat, P., et al. 2003, A&A, 411, L141
Masetti, N., Bassani, L., Bazzano, A., et al. 2006a, A&A, 455, 11
Masetti, N., Malizia, A., Dean, A. J., Bazzano, A., & Walter, R. 2006b, ATel 957
Masetti, N., Morelli, L., Palazzi, E., et al. 2006c, A&A, 459, 21
Monet, D. G., Levine, S. E., Canzian, B., et al. 2003, AJ, 125, 984
Norton, A. J., Beardmore, A. P., Retter, A., & Buckley, D. A. H. 2000, MNRAS, 312, 362
Prat, L., Rodriguez, J., Hannikainen, D. C., & Shaw, S. E. 2008, MNRAS, 389, 301
Rahoui, F., Chaty, S., Lagage, P.-O., & Pantin, E. 2008, A&A, 484, 801
Rodriguez, J., Tomsick, J. A., Foschini, L., et al. 2003, A&A, 407, L41
Rodriguez, J., Bodaghee, A., Kaaret P., et al. 2006, MNRAS, 366, 274
Rodriguez, J., Tomsick, J. A., & Chaty, S. 2008, A&A, 482, 731, paper 1
Samus, N. N., Durlevich, O. V., et al. 2004, Combined General Catalogue of Variable Stars
Skrutskie, M. F., Cutri, R. M., Stiening, R., et al. 2006, AJ, 131, 1163
Steeghs, D., Knigge, C., Drew, J., et al. 2008, ATel 1653
Tomsick, J. A., Lingenfelter, R., Corbel, S., Goldwurm, A., & Kaaret, P. 2004, ATel 224
Tomsick, J. A., Chaty, S., Rodriguez, J., et al. 2006, ApJ, 647, 1309
Tomsick, J. A., Chaty, S., Rodriguez, J., Walter, R., & Kaaret, P. 2008a, ApJ, 685, 1143
Tomsick, J. A., Rodriguez, J., Chaty, S., Walter, R., & Kaaret, P. 2008b, ATel 1649

5.4 Premier suivi de IGR J16320−4751 avec *XMM–Newton* Rodriguez et al. 2003, A&A, 407, L41

A&A 407, L41–L45 (2003)
DOI: 10.1051/0004-6361:20031093

Astronomy & Astrophysics

An XMM-Newton observation of IGR J16320−4751 = AX J1631.9−4752

J. Rodriguez[1,2], J. A. Tomsick[3], L. Foschini[4,2], R. Walter[2], A. Goldwurm[1], S. Corbel[5,1], and P. Kaaret[6]

[1] CEA Saclay, DSM/DAPNIA/SAp (CNRS FRE 2591), 91191 Gif-sur-Yvette Cedex, France
[2] Integral Science Data Center, Chemin d'Ecogia, 16, 1290 Versoix, Switzerland
[3] Center for Astrophysics and Space Sciences, Code 0424, University of California at San Diego, La Jolla, CA 92093, USA
[4] IASF/CNR, sezione di Bologna, via Gobetti 101, 40129 Bologna, Italy
[5] Université Paris VII, Fédération APC, 2 place Jussieu, 75251 Paris Cedex 05, France
[6] Harvard-Smithsonian Center for Astrophysics, 60 Garden Street, Cambridge, MA 02138, USA

Received 7 April 2003 / Accepted 3 July 2003

Abstract. The hard X-ray sensitivity and arcminute position accuracy of the recently launched International Gamma-Ray Laboratory (INTEGRAL) has lead to the (re-)discovery of a class of heavily absorbed hard X-ray sources lying in the Galactic plane. We report on the analysis of an XMM observation of such a source IGR J16320−4751 = AX J1631.9−4752. Our analysis allowed us to obtain the most accurate X-ray position to date (Rodriguez et al. 2003), and to identify a likely infrared counterpart (Tomsick et al. 2003). We present the detailed analysis of the IGR J16320−4751 XMM spectra. The PN spectrum can be well represented by a single powerlaw or a comptonized spectrum with a high equivalent absorption column density of $\sim 2 \times 10^{23}$ cm^{-2}. The current analysis and the comparison with the properties of other sources favor the possibility that the source is a Galactic X-Ray Binary (XRB). The identification of two candidate IR counterparts is in good agreement with this identification. The hard spectrum previously seen with ASCA, and the brightness of the candidate counterparts indicate that IGR J16320−4751 is most probably a highly absorbed High Mass X-ray Binary, hosting a neutron star.

Key words. accretion, accretion disk – stars: individual: IGR J16320−4751 – X-rays: binaries – X-rays: general

1. Introduction

The International Gamma-Ray Laboratory (INTEGRAL) has been launched on October 17, 2002. Since then, the high sensitivity and position accuracy of the IBIS imager has allowed for detections and determinations of arcminute positions for faint hard X-ray sources (e.g. IGR J16318−4848, Courvoisier et al. 2003; IGR J16358−4726, Revnivtsev et al. 2003, in addition to IGR J16320−4751). It is interesting to note that these sources belong to a class of highly absorbed low luminosity X-ray sources, which renders their detection in the soft X-rays (≤10 keV) difficult. In fact, some of them were missed with the All Sky Monitors of past X-ray missions, especially those sensitive in the 1−10 keV spectral range. As a result, these sources have remained poorly studied until the advent of INTEGRAL, and there may be many more than previously realized. In that view the IBIS/ISGRI detector on board INTEGRAL appears perfectly suited since it works in a spectral range (≥15 keV) not affected by absorption. Once such a source is detected, given the good position accuracy of the IBIS/ISGRI detector, it is possible to use highly sensitive soft (1−10 keV) X-ray telescopes, such as XMM-Newton or CHANDRA, to 1) obtain a more precise position and allow for counterpart search, and 2) obtain a soft X-ray spectrum and try to identify the type of the source. Such studies should then allow for a better understanding of the nature of these highly absorbed sources and the physics underlying the emission/absorption processes (e.g. Revnivtsev et al. 2003b).

IGR J16320−4751 was detected on Feb. 1.4 UT (Tomsick et al. 2003a), as a hard X-ray source with the IBIS/ISGRI detector (Lebrun et al. 2001) on board INTEGRAL at RA_{J2000} = $16^h32^m.0$, δ_{J2000} = −47°51′ (±2′), during an observation of the Galactic Black Hole Candidate (BHC) 4U 1630−47 (PI Tomsick). The source was observed to vary significantly in the 15−40 keV energy range on time-scale of ∼1000 s, and was detected in some occasions above 60 keV (Tomsick et al. 2003a). This source has a position consistent with that of AX J1631.9-4752, which was observed with ASCA in 1994, and 1997. The ASCA spectrum was fitted with a powerlaw with a hard photon index (0.2 ± 0.2, Sugizaki et al. 2001), which may suggest that the source belongs to the High Mass X-ray Binary (HMXB) class. Analysis of archival BeppoSAX-WFC data revealed that this source was persistent for at least 8 years (in't Zand et al. 2003). Their 2−28 keV spectral analysis shows a quite different result, since they obtain a soft photon index (2.5 ± 0.3) for the powerlaw. This evolution and the persistence of the source may indicate the presence of an absorbed

Send offprint requests to: J. Rodriguez,
e-mail: jrodriguez@cea.fr

XRB. Two possible infrared counterparts have been identified (Tomsick et al. 2003b).

We report here the detailed spectral analysis of an XMM public Target of Opportunity (ToO) observation of IGR J16320−4751, and compare it to the former observations of the source. In Sect. 2 we provide details about the XMM observation and data reduction methods that were employed for the analysis. We describe the spectral analysis in Sect. 3, and present results on the time variability of the source in Sect. 4. The infrared counterparts will be discussed in Sect. 5, and the results of our analysis will be discussed in the last section of this paper.

2. XMM data reduction and analysis

IGR J16320−4751 was observed with XMM-Newton on March 4, during a public ToO pointing on the INTEGRAL position that started around 21 h UTC. The data were processed using the Science Analysis Software v.5.4.1. Images were then obtained both from the EPIC MOS (Turner et al. 2001) and EPIC PN (Strüder et al. 2001) cameras. The EPIC-PN was operating in imaging mode with large window and a medium filter, the EPIC MOS2 in imaging mode with a full window and a medium filter. The EPIC-MOS1 was operating in timing mode (medium filter). During the processing, the data were screened by rejecting periods of high background, and by filtering the bad pixels. Correction for vignetting (Lumb 2002) has not been applied, because the source is close to the center of the field of view (<2′). One source was detected by the MOS2 within the 1 arcmin INTEGRAL error circle. The source position (obtained following the procedures given in the Introduction to XMM-Newton Data Analysis[1]) is $\alpha_{J2000} = 16^{h}\ 32^{m}\ 01.9^{s}$ and $\delta_{J2000} = -47^{\circ}\ 52'\ 29''$ (±4″ at the 90% confidence level, Rodriguez et al. 2003). It should be noted that this position is also consistent with the ASCA (at 0.4′ from the XMM position with an uncertainty of 1′), and BeppoSAX (at 0.7′ from the XMM position, uncertainty of 1.7′) positions of AX J1631.9−4752.

Due to soft proton flares during this observation, the MOS2 data are not usable for spectral and timing analysis, and only ∼4.9 ks out of a total of 25 ks are exploitable for scientific (spectral and timing) studies with the PN camera. The spectrum and light curve for the source were extracted from a circular region centered on the source with a radius of 45″ (which gives an encircled energy fraction of about 85%). The background spectrum and light curve were extracted from a source free region, with a radius of 2 arcmin. The response matrices were generated with the SAS package (arfgen, rmfgen). The spectrum was grouped with a minimum of 25 counts per channels and was fitted with the XSPEC v11.2 package.

3. Spectral studies

The PN spectrum was fitted with different models. In a first run, only single component models were tested. An absorbed powerlaw gives a good representation of the spectrum, with a reduced χ^2 of 0.81 (Rodriguez et al. 2003 and Fig. 1). An absorbed blackbody or disc blackbody give acceptable fits, with a reduced χ^2 of 0.81 (bbody) and 0.83 (diskbb), but the temperature returned from the fits (kT = 2.1 keV for the bbody and 3.8 keV for the diskbb) is a bit higher (especially for the diskbb component) than what is observed in general for accreting compact objects, even during the high luminosity states where a thermal component contributes strongly to the spectrum (see Tanaka & Shibazaki 1996 for a review). Furthermore, the detection of the source at higher energies (≥15 keV, Tomsick et al. 2003a) indicates the need for an additional component to account for this hard part. A comptonized spectrum (comptt, Titarchuk 1994) gives a good representation of the spectrum, with a reduced χ^2 of 0.83. The spectral parameters are not well constrained, however, if they are all left free. Fixing the electron temperature to 10 keV (which is an reasonable value, Barret 2001), leads to a reduced χ^2 of 0.84, with spectral parameters compatible with what is commonly observed in accreting neutron stars (Table 1 and Barret 2001). Since both models are strongly correlated to $N_{\rm H}$, the 68% and 90% confidence intervals are shown in Fig. 2, for the photon index and the absorption column density.

We have re-analysed the publicly available ASCA data, and fitted the SIS and GIS energy spectra simultaneously in

[1] Snowden et al. http://xmm.vilspa.esa.es/external/xmm_sw_cal/sas_frame.shtml

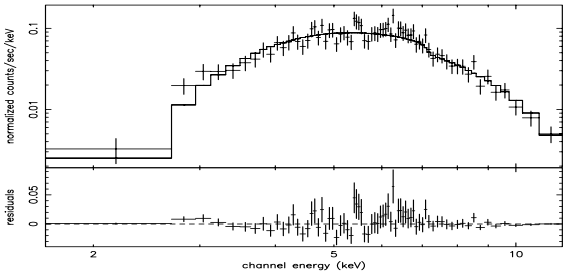

Fig. 1. EPIC-PN spectrum of IGR J16320−4751 and residuals to the absorbed powerlaw model.

Table 1. Spectral fit parameters. The given fluxes are corrected for an encircled energy fraction of 85%. The errors are the 1σ confidence level.

Power-law Model	
$N_{\rm H}$	$21^{+4}_{-1} \times 10^{22}$ cm^{-2}
Γ	$1.6^{+0.2}_{-0.1}$
χ^2	55.9 (69 d.o.f.)
2−10 keV unabsorbed flux	1.7×10^{-11} erg/s/cm^2
Comptt	
$N_{\rm H}$	$14 \pm 2 \times 10^{22}$ cm^{-2}
$kT_{\rm seed}$	$1.6^{+0.5}_{-0.3}$ keV
$kT_{\rm e}$	10 keV fixed
τ	≤3.35 (3 σ)
χ^2	56.2 (68 d.o.f.)
2−10 keV unabsorbed flux	1.1×10^{-11} erg/s/cm^2

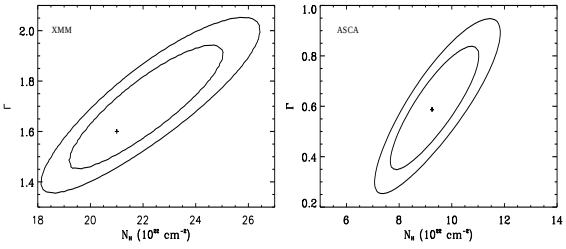

Fig. 2. Left: error contours for the column density ($N_{\rm H}$), and the photon index (Γ) obtained from the XMM-Newton observation. The cross marks the location of the best fit values, and the 68% ($\Delta\chi^2 = 2.30$) and 90% ($\Delta\chi^2 = 4.61$) contours are shown. **Right:** same plot for the ASCA observation.

XSPEC, with a simple model of an absorbed powerlaw. Our best result gives an equivalent absorption column density of $N_{\rm H} = (9.2 \pm 1.1) \times 10^{22}$ cm^{-2}, and a photon index of $\sim 0.6 \pm 0.2$ (errors at 1σ), somewhat softer than that obtained by Sugizaki et al (2001). The error contour plot is shown in Fig. 2, allowing for a direct comparison with that of the XMM observation. The BeppoSAX spectrum was fitted with an absorbed powerlaw of photon index 2.5, and $N_{\rm H} = 20 \times 10^{22}$ cm^{-2} (in't Zand et al. 2003).

4. Timing behavior

The PN light curve is displayed in Fig. 3. The source shows variability on a time scale of ∼50−100 s. A slow decrease and a period of relatively quiet emission is first observed until ∼2000 s. Then, the source undergoes two flares: the first starts at 2000 s after time 0 (begining of the good time intervals), reaches its maximum about 300 s later. The flux increases by a factor of 2.3 in the mean time. This flare lasts for ∼900 s. The second flare starts around 3050–3100 s, and reaches the maximum around 3450 s, the flux increases by a factor of ∼3.3, during this time. A third flare may start around 4500 s, but our observation stops soon after, and does not allow us to follow it.

We produced light curves in two different energy bands (2−5 keV and 5−12 keV, Fig. 3), and the hardness ratio between these two. The flare episodes occur in the two ranges in a similar manner (Fig. 3). With the time binning of 200 s, the flux increases by a factor of ∼4 between 2 and 5 keV, and ∼3 between 5 and 12 keV during a time interval of 400 s (first flare), and by a factor of ∼3 between 2 and 5 keV, and ∼2 between 5 and 12 keV during 400 s (second flare)[2] This similarity indicates that the flares are related to broadband flux increase rather than variations of the absorption (since the hard band would be much less affected in this case). The hardness ratio does not show significant changes between the low flux periods and the flares. The same behavior is observed if the light curves are produced in other energy bands (e.g. 2−3 keV and 2−4 keV).

[2] Note that the differences of the variation rates compared to those of the total range light curve, are simply due to the different time binnings used for the light curves.

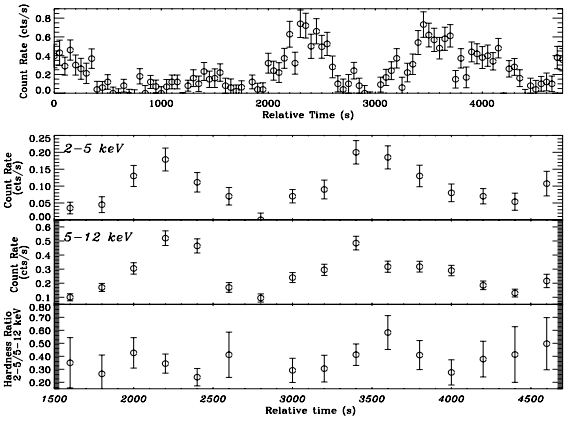

Fig. 3. Upper panel: 0.5–12 keV PN light curve of IGR J16320−4751 measured after background subtraction. The time sampling is 50 s, which shows the fast rise during the flare episodes. The lower panels represent a zoom on the region of the flares (starting around relative time 1500 s). The 2–5 keV, 5–12 keV and hardness ratio between 2–5 and 5–12 keV are shown. The time sampling is 200 s.

We searched for pulsations and quasi-periodic oscillations in the power spectra of the source. However, the low counting statistics and short exposure time does not enable us to obtain strong constraints. Indeed taking into account a net average counting rate of 0.22 cts/s for the source, and 0.16 cts/s for the background, during a 4.8 ks observation, leads to a 3σ upper limit on the amplitude of a periodic signal between ∼5 mHz and 10 Hz (where the power spectrum is dominated by Poissonian noise) of 12.25%. The 3σ upper limit for QPOs is higher than this value in the given frequency range (due to the non-zero width of the QPO).

5. Infrared counterpart

From the improved position obtained with XMM−Newton (Rodriguez et al. 2003), two candidate infrared counterparts have been identified (Tomsick et al. 2003b, Fig. 4). The first one is located at $\alpha_{J2000} = 16^{\rm h}\ 32^{\rm m}\ 01\overset{\rm s}{.}75$, $\delta_{J2000} = -47°\ 52'\ 28\overset{''}{.}9$ (1″ uncertainty) with magnitudes[3] $K_{\rm s} = 10.99 \pm 0.03$, $H = 13.03 \pm 0.04$, $J > 14.08$ (97 % confidence). The second source ($K_{\rm s} = 10.82 \pm 0.04$, $H = 11.24 \pm 0.03$, $J = 12.13 \pm 0.02$) is on the southeast edge of the X-ray error circle. From the Palomar Observatory Sky Survey (POSS) epoch I and II, we can derive $R > 21$ for the first source, and $R = 14.6$ (±0.3, 1σ error POSS epoch I, period 1949–1965) and $R = 15.4$ (±0.3, 1σ error POSS epoch II, period 1985–2000), for the second one (note that the evidence for variability is only marginal). To estimate the equivalent absorption column density along the line of sight we used a web-based tool that uses data from Dickey & Lockman (1990). For the position

[3] the magnitudes come from the "2MASS All-Sky Point Source Catalog" `http://www.ipac.caltech.edu/2mass/`

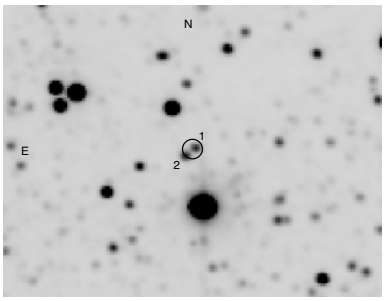

Fig. 4. 2-MASS K-band $2.5 \times 2'$ image of IGR J16320−4751 field, the XMM error circle is superimposed. One can clearly see the two possible counterparts. 1 stands for the most probable one, and 2 for the second.

of IGR J16320−4751, the average value is $\sim 2.1 \times 10^{22}$ cm^{-2}. Then, assuming $A_V = 5.6 \times 10^{-22} \times N_{\rm H}$ (Predehl & Schmitt 1995), we derived $A_V = 11.7$. With this value, we can calculate the dereddened fluxes in the three bands, and compare them to tabulated objects. The second source appears to be a star with a peak in the J band. The colors $(J - H) = 0.9$ and $(H - K) = 0.4$ are typical for a M−type star with a temperature around 3000 K.

With this visual extinction, the first source, the faintest and most probable counterpart, presents some very interesting features. The dereddened flux increases toward radio wavelenghts (from J to K band) and the colors $(J - H) > 3.1$ and $(H - K) = 2.0$ suggest an infrared excess that is likely to be due to circumstellar matter (probably hot plasma or warm dust). However, the absorption column density along the line of sight may be different from this value. The $N_{\rm H}$ returned from XMM spectral fits leads to an extinction of $A_V = 106$, giving a dereddened $K_{\rm s}$ magnitude close to 0 for both objects. In addition, some molecular clouds and inhomogeneities in the ISM can make the A_V increase. If, for example, we take a value of $A_V = 30$ (i.e. $N_{\rm H} = 5 \times 10^{22}$ cm^{-2}), the dereddened magnitudes would suggest a K-giant or supergiant, rendering the object more usual. Furthermore, the wavelength dependence of the interstellar extinction is poorly constrained when studying sources close to the Galactic ridge. We thus cannot exclude other types for the companion star. We remark for example that the color, and magnitude of the second candidate counterpart could indicate a high mass star (O or B spectral type).

6. Discussion

From their analysis of ASCA data, Sugizaki et al. (2001) suggested that AX J1631.9−4752 was an HMXB with a pulsar, given the flat spectrum they obtained. Our best model, a powerlaw or a comptt spectrum, is also consistent with the source being a Galactic XRB. A comptonized spectrum would not be surprising for such an object, but alone it is not a sufficient argument since extragalactic sources have similar X-ray spectra. For a distance range of 5−15 kpc (the latter giving an upper limit on the distance for the object to be Galactic), the powerlaw model leads to unabsorbed 2−10 keV isotropic luminosities of $0.5-4.5 \times 10^{35}$ erg/s, which may be compatible with the observe luminosity of either a neutron star or a black hole in a low hard state. The spectral parameters we obtain are also compatible with those commonly observed for this kind of objects (e.g. Tanaka & Shibazaki 1996). The persistence of the source over 8 years (in't Zand et al. 2003), and the evolution of the spectral parameters resembles the spectral transitions seen in XRBs.

It is interesting to note the similarities of IGR J16320−4751 with the persistent X-ray source 1E 1743.1−2843 whose primary type is still a matter of debate. Both sources are persistent, heavily absorbed, and undergo XRB-like spectral transitions between hard states (Porquet et al. 2003), and softer ones (Cremonesi et al. 1999). Although for 1E 1743.1−2843 the neutron star hypothesis could not be ruled out, Porquet et al. (2003) have suggested that this object might be a black hole in a hard state. In the case of IGR J16320−4751, the BeppoSAX and XMM observations alone would rather indicate a persistent black hole undergoing spectral transitions between hard states and softer ones. However, the low value of the photon index during the ASCA observation, and its large variations between ASCA (Sugizaki et al. 2001), BeppoSAX (in't Zand et al. 2003), and XMM (current study) observations are rather unusual for a black hole. On the other hand, such very hard photon indices and large variations (from 0 to 2.4) have already been observed in the neutron star system Sco X−1 (D'Amico et al. 2001), but also in some other sources (Sugizaki et al. 2001). In addition, the powerlaw model gives extrapolated 1−20 keV luminosities (between 5−15 kpc), of $0.93-8.4 \times 10^{35}$ erg/s, and extrapolated 20−200 keV luminosities of $0.23-2.1 \times 10^{36}$ erg/s (the comptt model leads to slightly lower values). With these values, the source would lie in the neutron star box in Fig. 1 of Barret et al. (1996). The relatively good fit obtained with the comptt model is compatible with a Comptonization of soft photons on hot electrons surrounding the compact object. However, the lack of data above 12 eV, does not allow us to obtain a good constraint on the cut-off energy. The detection of hard emission with INTEGRAL (Tomsick et al. 2003a) appears in good agreement with a comptonized spectrum. The hard photon index obtained during the ASCA observation, however, is not easy to understand in the framework of thermal Comptonization.

The identification of the infrared counterpart remains difficult given the proximity of the two candidates. The faintest one (number 1 in Fig. 4), however, is more likely related to the X-ray source. This candidate could either favor a reprocessing of high energy photons by a cloud or some dust, or the emission from a supergiant or K-giant star depending on the visual extinction on the line of sight. Both hypothesis are in good agreement with the high absorption obtained from the X-ray spectrum, and the spectral parameters obtained from our fits, which are similar to those observed in the case of HMXB (e.g. GX 301−2, Saraswat et al. 1996, 4U1700−37, Boroson et al. 2003), although we do not detect lines in IGR J16320−4751 with a 3σ upper limit on the equivalent width of a narrow 6.4 keV Iron (emission) line of 112 eV. The position of IGR J16320−4751 in the Galactic plane, and along a spiral arm (the Norma arm), a region of star

formation, where a number of young (massive) stars can be found, appear in good agreement with the system being an HMXB. It is interesting to note the change of equivalent absorption density between the different observations, (from $\sim 9 \times 10^{22}$ cm^{-2} to $\sim 20 \times 10^{22}$ cm^{-2}). This strongly favors an absorption intrinsic to the source, similar to what observed in heavily absorbed sources (e.g. Revnivtsev et al. 2003 and reference therein). In the case of a Galactic XRB, the absorption could be due to the accretion flow, and the changes could be associated with variations of the accretion rate.

Although the source appears more likely to be a Galactic XRB (given its similarities with known neutron stars or black holes XRB) we can not exclude totally an extragalactic source, e.g. an ULX seen through the Galactic plane. Assuming a typical luminosity of 10^{40} erg/s (Foschini et al. 2002), the simple power law model would lead to a distance to the source of about 2.2 Mpc. Although compatible with an extragalactic origin, this hypothesis appears not to be favored given such a short distance. Longer X-ray observations and more multiwavelength studies (e.g. infrared spectra), should allow for more precise answers to all the above mentioned points. Note that a better X-ray position would be useful to select a unique IR counterpart, allowing for a better understanding of the nature of the source.

Acknowledgements. J.R. thanks D. Barret, S. Chaty, Y. Fuchs, A. Paizis, and M. Revnivtsev, for useful discussions and careful reading of the manuscript. The authors thanks the anonymous referee for useful comments which allowed to improve the quality of the paper. J.R. acknowledges financial support from the French spatial agency (CNES). J.A.T. acknowledges partial support from NASA grant NAG5-12703. This work is based on observations obtained with XMM-Newton, an ESA science mission with instruments and contributions directly funded by ESA Member States and the USA (NASA). This publication makes use of data products from the Two Micron All Sky Survey, which is a joint project of the University of Massachusetts and the Infrared Processing and Analysis Center/California Institute of Technology, funded by the NASA and the National Science Foundation. This reasearch has made use of The Digitized Sky Surveys that were produced at the Space Telescope Science Institute under U.S. Government grant NAG W-2166.

References

Barret, D., McClintock, J. E, & Grindlay, J. E. 1996, ApJ, 473, 963
Barret, D. 2001, Adv. Space Res., 28, 307
Boroson, B., Vrtilek, S. D., Kallman, T., & Corcoran, M. 2003, ApJ, submitted [astro-ph/0303277]
Courvoisier, T., Walter, R., Rodriguez, J., et al. 2003, IAUC, 8063
Cremonesi, D. I., Mereghetti S., Sidoli L., Israel G. L. 1999, A&A, 345, 826
D'Amico, F., Heindl, W. A., Rotschild, R. E., et al. 2001, Adv. Space Res., 28, 389
Dickey, J. M., & Lockman, F. J. 1990, ARA&A, 28, 215
Foschini, L., Di Cocco, G., Ho, L. C., et al. 2002, A&A, 392, 817
in't Zand, J. J. M, Ubertini, P., Capitanio, F., Del Santo, M. 2003, IAUC, 8077
Kong, A. K. H., McClintock, J. E., Garcia, M. R., et al. 2002, ApJ, 570, 277
Lebrun, F., et al. 2001, Proceedings of the 4th INTEGRAL Workshop, ed. A. Gimenez, V. Reglero, & C. Winkler
Lumb, D. H. 2002, Proc. Symp. New Visions of the X-ray Universe in the XMM-Newton and Chandra Era, ed. F. Jansen, ESA SP488 [astro-ph/0203278]
Predehl, P., & Shmitt, J. H. M. 1995, A&A, 293, 889
Porquet, D., Rodriguez, J., Corbel, S., et al. 2003, A&A, 406, 299
Revnivtsev, M., Turler, M., Del Santo, M., et al. 2003, IAUC, 8097
Revnivtsev, M., Sazonov, S., Gilfanov, M., & Sunyaev, R 2003b, Astr. Lett., accepted [astro-ph/0304353]
Rodriguez, J., Tomsick, J. A., Foschini, L., et al. 2003, IAUC, 8096
Saraswat, P., Yoshida A., Mihara T., et al. 1996, ApJ, 463, 726
Strüder, L. et al. 2001, A&A, 365, L18
Sugizaki, M., Mitsuda, K., Kaneda, H., et al. 2001, ApJS, 134, 77
Tanaka, Y., & Shibazaki, N. 1996, ARA&A, 34, 607
Titarchuk, L. 1994, ApJ, 434, 313
Tomsick, J. A., Lingelfelter, R., Walter, R., et al. 2003a, IAUC, 8076
Tomsick, J. A., Rodriguez, J., Foschini, L., et al. 2003b, IAUC, 8096
Turner, M., et al. 2001, A&A, 365, L27

Deuxième partie

“Astro-phénoménologie” : vers une compréhension des sources accrétantes

Chapitre 6
Astro-phénoménologie X : une approche utile pour la classification des sources astronomiques ?

6.1 Astro-phénoménologie

Il n'existe pas à proprement parler de science qui se cacherait sous ce nom quelque peu étrange. Bien souvent, néanmoins, lors d'observations de sources (de type connu ou non), nous ferons en premier lieu des analyses scientifiques basées sur une approche non pas physique, mais phénoménologique. Ceci consistera, par exemple, à étudier les rapport de dureté (les rapports entre les flux dans deux bandes d'énergie distinctes), à utiliser des lois de puissance, avec ou sans coupure exponentielle, pour ajuster les spectres en rayons X. On pourra aussi y ajouter des raies Gaussiennes, des fronts d'absorption, étudier l'absorption locale, ... Si la présence de ces composantes spectrales peut être interprétée en terme de processus physiques (par exemple Comptonisation inverse, fluorescence d'éléments chimiques, composante de reflexion, cf. Partie III), l'avantage de ces lois simples est qu'elles sont exemptes de toute dépendance à des modèles théoriques, et, cette approche est donc affranchie de tout *a-priori*. Ces modélisations phénoménologiques permettent, en outre, une comparaison directe entre des paramètres obtenus par l'ajustement d'une même loi mathématique, simple, à toute une famille de sources. Cette approche phénoménologique est, de même, applicable dans le cadre d'études temporelles.

Jusqu'à maintenant je me suis concentré sur la détermination du type des systèmes observés. Ce point est d'une importance capitale pour tout ce qui concerne la compréhension des populations de sources (en particulier galactiques), et donc a une incidence sur les modèles d'évolution stellaire, la dynamique stellaire galactique, la connaissance des sites de formation d'étoiles, etc... Le cœur de ma recherche concerne cependant plus les phénomènes physiques ayant lieu à proximité de l'objet compact et donc responsables des émissions de rayons X. Le type même de l'objet compact a une influence particulière sur les phénomènes observés, notamment en raison de la présence ou non d'une

surface et/ou d'un champ magnétique (chap. 1).

L'approche phénoménologique, nous le verrons au prochain chapitre, peut permettre une compréhension basique de certains de ces phénomènes ; elle est aussi utile pour identifier le type des nouvelles sources, et/ou la nature de l'objet compact, même si, comme nous l'avons vu au chapitre 1, la distinction entre une étoile à neutrons et un trou noir n'est pas toujours évidente ni aisée. Dans ce chapitre, en continuant l'identification des sources de rayons X, je me concentrerai sur l'aspect plus particulier de la détermination du type de l'objet compact ; nous verrons pourquoi et comment l'analyse des observations X nous permet de l'identifier dans certains systèmes. Pour cela je présente les études de IGR J16320−4751, IGR J19140+0951 et IGR J17497−2721 qui, je pense, illustrent bien ces aspects : on y identifie clairement un pulsar dans le premier, on y favorise la présence d'un pulsar dans le second, et celle d'un trou noir dans le dernier objet.

6.2 IGR J16320−4751 trahi par ses signatures temporelles

6.2.1 Une première idée due au comportement spectral : comparaison avec d'autres sources

La premère observation faite avec *XMM–Newton* et brièvement résumées au chapitre 4 a montré que le spectre de la source était relativement dur. Une modélisation à l'aide d'une loi de puissance $dN = N_0 \times E^{-\Gamma} dE$ donne un indice de photon Γ=1,6. Le spectre est relativement absorbé avec une colonne d'absorption équivalente Hydrogène N_H=21$\times 10^{22}$ cm^{-2} (Rodriguez et al. 2003e). De tels paramètres peuvent indiquer aussi bien une HMXB qu'un AGN. Les paramètres spectraux de IGR J16320−4751 sont cependant plutôt similaires à ceux de 4U 1700-37 (Haberl et al. 1989; Boroson et al. 2003) ou de GX 301−2 (Saraswat et al. 1996), deux HMXB contenant un pulsar. Des observations ASCA et Beppo-SAX de IGR J16320−4751 montrent, de plus, des variations claires de l'absorption et de l'indice de photon ; ce dernier a pu varier entre 0,2 et 2,5. La première valeur, extrêmement dure, exclue presque à coup sûr un AGN, alors que de larges variations de la colonne d'absorption sont plutôt une signature d'une HMXB contenant une supergéante (par exemple Haberl et al. 1989; Prat et al. 2008, voir chapitre 10)). L'analyse phénoménologique des premières observations X de la source, et surtout la comparaison de ces résultats avec des paramètres de sources connues, conduit donc, presque naturellement, à privilégier une HMXB (avec un pulsar) (Rodriguez et al. 2003e).

Des observations simultanées *XMM–Newton* et *INTEGRAL* ont eu lieu en 2006. Les résultats précis seront présentées au chapitre 10, en partie III. Néanmoins, l'idée d'une HMXB était, ici encore, renforcée par la présence d'un excès mou, autour de 0,5 keV et d'une raie du fer fine à 6,41 keV (Rodriguez et al. 2006a). La première de ces deux signatures est aussi bien vue dans les AGN (par exemple Porquet et al. 2004) que les HMXB (par exemple Haberl et al. 1989). La présence d'une raie fine tend elle plus à indiquer un objet galactique notamment en raison de la finesse de ladite raie. Lors de ces observations, l'extrême dureté du spectre ($\Gamma = 0.2 - 0.3$) était de nouveau plutôt indicative d'un pulsar. Les pulsars étant des objets jeunes, ils sont en général trouvés dans des systèmes jeunes, autour donc d'étoiles massives.

6.2.2 Découverte de la pulsation : un pulsar confirmé

Il faut avouer que lors des observations de 2006 plus aucun doute n'était permis quant au type de l'objet compact. En effet, lors d'une nouvelle analyse des données de 2003, en ne filtrant pas les moments de fort bruit de fond, nous (Lutovinov, Rodriguez, Revnivtsev, Shtikovskyi 2005) avions trouvé une pulsation dans le périodogramme de la source. Ceci est une charactéristique claire de la

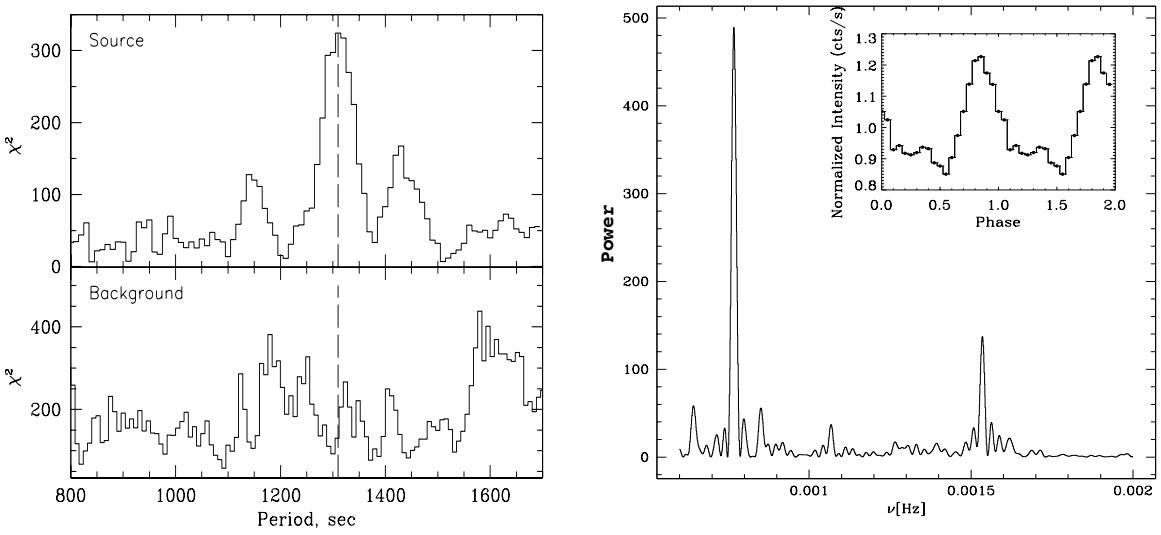

FIG. 6.1 – Périodogrammes de IGR J16320−4751. À gauche : tels qu'obtenus à partir de l'observation *XMM–Newton* de 2003. Le panneau supérieur représente la source celui du dessous le bruit de fond. Tiré de Lutovinov et al. (2005). À droite : périodogramme obtenu lors de l'observation *XMM–Newton* de 2006. L'insert représente la courbe de lumière du PN repliée à la période de 1303 s. Tiré de Rodriguez et al. (2006a).

présence d'un pulsar, puisque dans ces objets la matière accretée va être guidée le long des lignes de champ magnétique et donc tomber sur le pôle magnétique. Si plusieurs modèles concurrents prédisent le lieu de l'émission de rayons X, depuis le pôle lui même (*polar cap*) à des régions plus externes (*outer gap, slot gap*), la raison de la présence d'une pulsation est elle relié à une différence entre l'alignement de l'axe de rotation de l'étoile et celle du champ magnétique (comme sur la Terre), donnant lieu a un effet de type "phare" lors de l'observation de ces objets.

La pulsation de IGR J16320−4751 est relativement longue (1303 s) en regard des pulsations trouvées dans les pulsars ; il est, à ce titre, intéressant de noter que les pulsars découverts par *INTEGRAL* ont généralement une pulsation relativement longue (> 100 s Bodaghee et al. 2007, pour une compilation). Cette longue période explique pourquoi dans les données de 2003 filtrées du bruit (5 ks au total, Chap 4) nous ne pouvions la voir : seuls 3 cycles complets étaient présents. Il est important de remarquer que le non-filtrage des données n'a aucune incidence sur la détection d'une pulsation, puisque le bruit de fond (dû à un fort afflux de protons solaires sur les détecteurs) est non-périodique par essence. Le niveau de significativité de la pulsation est, en revanche, affecté notamment en raison du faible flux de la source relativement au fond. Ceci est illustré sur la figure 6.1 tirée de Lutovinov et al. (2005). L'observation *XMM–Newton* de 2006, de bien meilleure qualité et plus longue, nous a permis d'affiner la détermination de cette pulsation à une période de 1303.8 ± 0.9 s et 1302.0 ± 1.1 s respectivement à partir du MOS et du PN (Rodriguez et al. 2006a) pour une fraction pulsée de 18.1 ± 0.7 % (Figure 6.1). Cette pulsation est aussi vue dans *INTEGRAL* avec ISGRI à une fraction pulsée de 17 ± 4 %. L'identification d'un pulsar au sein de ce système, et la forte absorption en faisait presque irrémédiablement une HMXB ; point qui fût confirmé par les suivis infrarouges de cette source.

6.3 IGR J19140+0951 et ses états spectraux

Malheureusement déterminer le type de l'objet compact n'est pas toujours aussi simple que dans le cas précédent. La présence de pulsations et leur détection dépend de paramètres géométriques particuliers (non-alignement des axes de rotation et magnétiques), et bon alignement de l'axe magnétique par rapport à la ligne de visée. Avant la détermination du type du système IGR J19140+0951 par Hannikainen et al. (2007), les premières observations X tendaient à indiquer un système de forte masse contenant une étoile à neutron. J'ai publié les résultats de ces analyses dans Rodriguez et al. (2005a, A&A, 432, 235), article inclus au chapitre 9 à la fin de la partie II, et que je résume brièvement ici.

J'ai tout d'abord commencé par chercher de possibles pulsations et/ou des QPO kHz caractéristiques d'étoile à neutrons. Les spectres de puissance obtenus à partir des observations *RXTE* sont cependant plats (ajustés avec une constante) et cohérents avec un bruit purement Poissonnien. J'ai estimé une limite supérieure à 3 σ de 1.5 à 6 $\%$ pour l'amplitude RMS r d'un QPO de fréquence comprise entre 0.06 et 20 Hz (pour un rapport de qualité $Q = \nu/fwhm = 10$ où ν est la fréquence du QPO, et $fwhm$ sa largeur à mi-hauteur). Vu que l'amplitude r d'un QPO est telle que $r \propto \sqrt{fwhm_{pulse}}$, cette limite est valable pour toute pulsation de cohérence supérieure ($<=> Q > 10$), y compris pour une pulsation strictement périodique (même si dans ce cas elle est quelque peu conservative). Ces limites sur l'amplitude sont relativement contraignantes : QPO de basses fréquences et pulsations périodiques ont, en général, des amplitudes minimales supérieures à ces valeurs (typiquement $> 5\%$ pour un QPO, et $> 10 - 15\%$ pour une pulsation McClintock & Remillard 2006; van der Klis 2006). En revanche pour des QPO kHz les valeurs limites que j'obtiens dans IGR J19140+0951 ne sont pas contraignantes ($r_{lim} < 17.4\%$ pour un QPO à 200 Hz).

Pour étudier le comportement spectral de cette source, j'ai séparé les observations en différents états spectraux basés sur les flux vus par ISGRI entre 20 et 40 keV. Les spectres pris entre 3 et $\sim$100 keV sont bien ajustés avec les modèles standards des sources accrétantes (lois de puissance coupées et absorbées à basse énergie, ou modèles de comptonisation thermique). De grandes variations de la colonnes d'absorption N_H et de l'indice de photon Γ de la loi de puissance sont observées. Γ peut devenir relativement dur (~ 0.9), ce qui est plutôt une caractéristique des pulsars accrétants. La grande valeur de N_H et la présence d'une raie du fer fine, pointe aussi vers de l'accrétion radiale, et donc un système de forte masse. Enfin, sauf si la source est située à l'autre bout de la Galaxie, ses luminosités dans les bandes 1–20 keV et 20–200 keV la place dans la zone des étoiles à neutrons identifiée par Barret et al. (1996). Les résultats de cette étude favorisent donc une étoile à neutron dans un système de forte masse, même si nous ne pouvons être aussi catégoriques que pour IGR J16320−4751. Il faut d'ailleurs remarquer que, même si la nature du système est aujourd'hui clairement établie (Hannikainen et al. 2007), le type de l'objet compact, quant à lui, ne l'est toujours pas.

6.4 IGR J17497−2721 : un trou noir silencieux en radio ?

Un autre exemple de système relativement énigmatique est IGR J17479−2721. Les analyses des observations *INTEGRAL* ayant mené à la découverte de cette source favorisaient la présence d'un trou noir (Kuulkers et al. 2006). Notre groupe a mené de front deux campagnes d'observations en X de cet objet. L'un dans le cadre de mes programmes de suivis *RXTE*, l'autre avec *Chandra* mené par A. Paizis, dans le cadre d'un programme de suivi des sources *INTEGRAL*, que nous poursuivons depuis 5 AOs. L'article (Rodriguez et al. 2007a, ApJ, 655, L97) rapportant les résultats des observations *RXTE*, menées en quasi-simultanéité avec des observations radio est inclus au chapitre 9, à la fin de la partie II. Je présente ici le résumé des principaux résultats obtenus.

IGR J17497−2721 est resté lors de cette éruption dans un état spectral qualifié de dur, comme cela a maintenant été observé dans un grand nombre de binaires X (par exemple XTE J1550−564, ou Aql X-1). C'est-à-dire que ses spectres sont bien representés par une loi de puissance absorbée ($N_H \sim 3,5 - 410^{22}$ cm^{-2}) d'indice inférieur à 2, avec une coupure exponentielle à haute énergie (à ~ 100 keV). Un modèle de comptonisation purement thermique donne une bonne représentation physique de ces spectres. Les paramètres obtenus à partir de ces deux modèles sont conformes à ceux observés dans les trous noirs dans l'état dur. De même les spectres de puissance sont bien ajustés à l'aide de trois Lorentziennes larges, et l'amplitude totale de la variabilité est de 36 $\%$. Nous ne voyons ni QPO ni pulsations cohérentes, avec des limites supérieures (à 3 σ) sur leur amplitude relativement contraignantes : 2 % pour un QPO de largeur 2 Hz ; et de 2,4 à 1 % entre 0.4 mHz et 1Hz, et 0.9 % au-delà pour une pulsation cohérente. Il est important de noter que cet objet n'a quasiment aucune variabilité détectable au-delà de 10 Hz, ce qui en fait, outre son comportement spectral, et selon le critère temporel de Sunyaev & Revnivtsev (2000, chapitre 1), un excellent candidat trou noir.

Le point le plus intéressant, et probablement le plus énigmatique, est que cet objet est silencieux en radio, et ce contrairement à la majorité des trous noirs dans l'état dur. En effet, une forte corrélation entre le flux radio et le flux X existe dans cet état (Corbel et al. 2003; Gallo et al. 2003). Il faut néanmoins remarquer que IGR J17497−2721 n'est pas unique puisqu'il existe au moins deux autres objets ne suivant pas la corrélation : Swift J1753.5−0127 (Cadolle Bel et al. 2007), et XTE J1650−500 (Corbel et al. 2004), comme illustré sur la figure 6.2. Nous remarquerons simplement que ce dernier objet, semble cependant suivre une tendance parallèle, bien que moins brillante en radio.

Nous avons aussi récemment observé que le trou noir H 1743−322, étudié en X par L. Prat étudiant en thèse sous ma direction (Prat et al. 2009), et par mes collaborateurs en radio (Coriat, Prat, Corbel, Rodriguez, in prep.) semble être décrit par une loi de puissance de pente différente dans cette représentation. Je ne concluerai pas plus ici, d'autres observations seront nécessaires pour bien comprendre ce phénomène.

Les observations *Chandra* et infrarouge ont permis d'affiner la position X de la source et d'en trouver une contrepartie (Paizis et al. 2007). La spectroscopie infrarouge a permis de déterminer un type spectral K pour un compagnon de la classe des géantes. La conclusion principale, relative au type de ce système, tirée de ces deux études est que IGR J17497−2721 est une LMXB contenant très probablement un trou noir.

6.5 Conclusions du chapitre

Nous avons vu, à travers l'étude des ces trois objets, que l'approche phénoménologique en rayons X permettait d'avoir une idée du type de l'objet astronomique préliminaire à toute identification basée sur la spectroscopie visuelle et/ou infrarouge. Si certains cas sont relativement clairs, comme par exemple IGR J16320−4751 pour lequel la découverte de pulsations a permis l'identification d'un pulsar, il n'est, dans une large majorité des cas, pas possible de conclure avec certitude. L'astro-phénoménologie, appliquée à la détermination de la nature des sources, reste, certes extrêmement utile, mais néanmoins assez loin d'être parfaite. Et même si l'interprétation de IGR J16320−4751 et IGR J19140+0951 comme des HMXBs à étoiles à neutrons (pour la première) fut confirmée par la suite, il n'en reste pas moins que, dans le passé, de nombreux trous noirs (candidats) se révelèrent finalement être des étoiles à neutrons (Cir X-1, V0332+53, GS 1826−238, 4U 0142+61).

Mes travaux ouvrent aussi des perspectives intéressantes concernant les comportements globaux, ou bien attendus d'une famille de source. Swift J1753.5−0127, IGR J17497−2721 et H 1743−322 (à l'analyse desquels j'ai contribué) sont classés comme des trous noirs candidats. Nos travaux

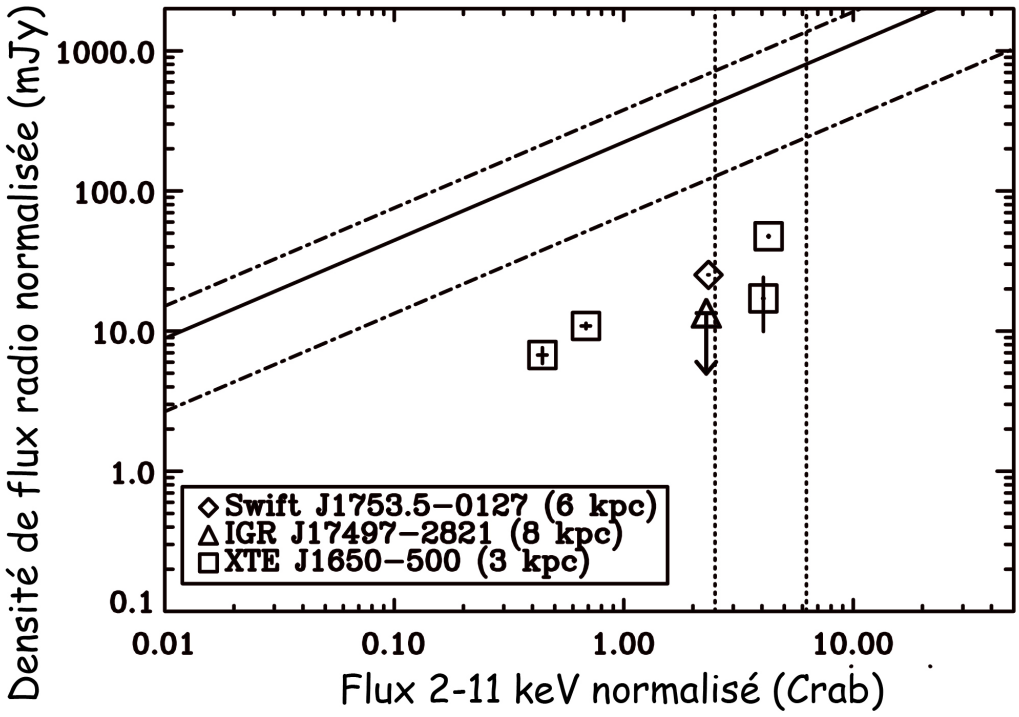

FIG. 6.2 – Flux radio en fonction du flux X pour IGR J17497−2721 (triangle) ainsi que deux autres trous noirs radio-silencieux. Les lignes représentent la corrélation habituellement vue pour les trous noirs. Source Rodriguez et al. (2007a).

montrent cependant quelques particularités au niveau de leur émission radio. Ces observations doivent maintenant être explorées plus avant pour être comprises. Elles devront aussi clairement servir de contraintes pour tout modèle d'accrétion-éjection.

Chapitre 7
Liens accrétion-éjection dans GRS 1915+105 : une première étape

7.1 GRS 1915+105 : un objet bien fascinant

Le microquasar GRS 1915+105 est sans doute l'un des objets les plus énigmatiques de notre Galaxie, et par ses comportements même est extrêmement déroutant. Cette source de haute énergie fut découverte en 1992 comme une source X transitoire grâce au moniteur WATCH à bord du satellite Russe *Granat* (Castro-Tirado et al. 1992). Les suivis multi-longueurs d'onde et surtout radio permirent rapidement de montrer que cet objet était un microquasar. Le plus important, et ce qui a suscité un énorme engouement pour cette source, fut l'observation d'un déplacement apparement superluminique des ejecta de matière (Mirabel & Rodriguez 1994). Même si cet effet est un effet de projection sur le plan du ciel de déplacements à des vitesses proche de c, il n'en reste pas moins que la vitesse corrigée des éjections est d'environ 0.98 c (Fender et al. 1999b). La distance de la source est habituellement estimée à 12 kpc, même si elle est sujette à débat. Chapuis & Corbel (2004) ont notamment montré qu'elle pouvait être aussi basse que 6 kpc. Il a enfin fallu attendre 2001 pour qu'une fonction de masse de ce système soit mesurée, menant à une masse de $14 \pm 4\ M_\odot$ pour l'objet compact (Greiner et al. 2001), excluant alors définitivement la possibilté (parfois évoquée) que GRS 1915+105 héberge une étoile à neutrons. Nous remarquerons que par une technique basée sur la corrélation entre indice de photon et fréquence de QPO, technique certes non encore complètement généralisée[1] Shaposhnikov & Titarchuk (2007) ont estimé une masse de $15.6 \pm 1.5\ M_\odot$.

Cet objet est extrêmement brillant à toutes longueurs d'onde (sauf en visible en raison de la grande extinction optique), et montre de grandes variations de luminosité. Ceci est illustré par la figure 7.1 qui montre les courbes de lumière X (1.2–12 keV) et radio (Ryle à 15 GHz). GRS 1915+105 est persistente en X depuis 1992, ce qui explique le grand nombre d'observations existant dans les bases

[1] Shaposhnikov & Titarchuk (2009) estiment la masse de 7 trous noirs par cette méthode et obtiennent un bon accord avec la mesure obtenue grâce à la fonction de masse dans 5 cas pour lesquels celle-ci est connue. Un désaccord entre les mesures obtenues par les deux méthodes existe cependant dans un cas : XTE J1650−500.

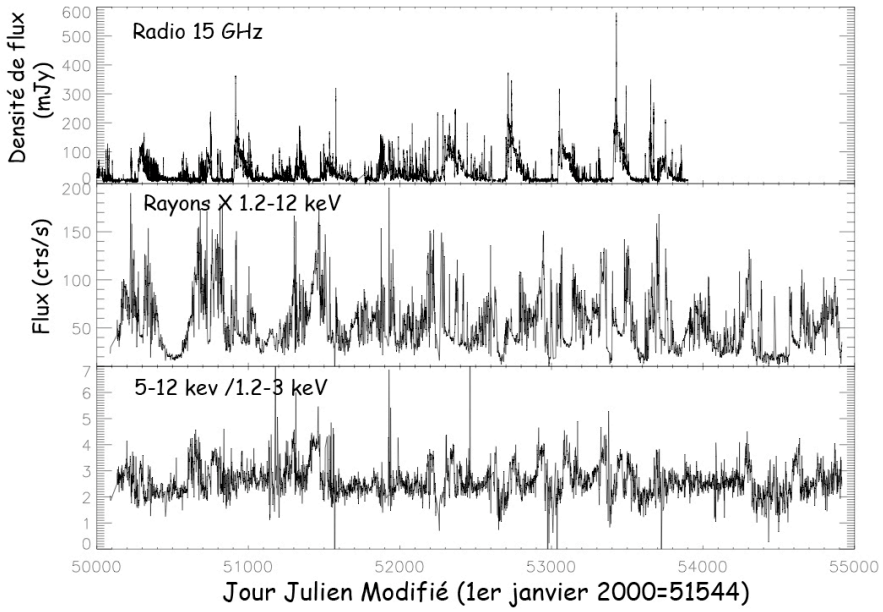

FIG. 7.1 – Courbes de lumière en radio (à 15 GHz en haut), en X (1.2–12 keV au milieu), et rapport de dureté entre les bandes 5–12 keV et 1.2–3 keV (en bas) d'environ 14 ans d'observations de GRS 1915+105.

de données (par exemple environ 1500 pointés *RXTE*). Le lecteur intéressé par une revue détaillée (bien que non totalement exhaustive vu le grand nombre de publications sur cet objet) pourra lire Fender & Belloni (2004).

7.2 GRS 1915+105 parle Grec !

L'extrême variabilité en X est clairement mise en évidence par la courbe de lumière ASM (fig. 7.1) pour des périodes de l'ordre de la journée et plus. Le rapport de dureté (HR pour *Hardness Ratio*) entre la bande dure (5–12 keV) et la bande molle (1.2–3 keV) de ce même instrument (fig. 7.1 panneau du bas) montre, de plus, que ces variations de flux s'accompagnent de changements drastiques au niveau spectral puisque l'on peut passer de périodes où la source est plutôt "molle" (HR ~ 2) à des périodes "dures" (HR > 3). Ceci montre que les variations ne sont pas simplement dues à des baisses de luminosité (dont on pense souvent qu'elles sont liées au taux d'accrétion), mais aussi à des changements au niveau de la physique des milieux émetteurs.

Morgan et al. (1997) ont montré que la variabilité de GRS 1915+105 était tout aussi extrême sur des périodes très courtes en découvrant dans cet objet des QPO à des fréquences variées, 67 mHz, autour de 1 Hz, mais aussi ce qu'ils ont déterminé comme étant le QPO de haute fréquence (QPO HF par la suite) dans ce trou noir, un QPO à 67 Hz. GRS 1915+105 est donc un objet variable à toutes échelles de temps, depuis la dizaine de millisecondes à l'année ! Si d'autres trous noirs montrent aussi de telles variabilités (QPO HF, et variations sur des périodes de l'ordre du mois), l'originalité, s'il en est une en particulière, de GRS 1915+105 réside dans ses variations de l'ordre de la dizaine de secondes, clairement visibles dans une majorité de pointés ; cette source répète en effet

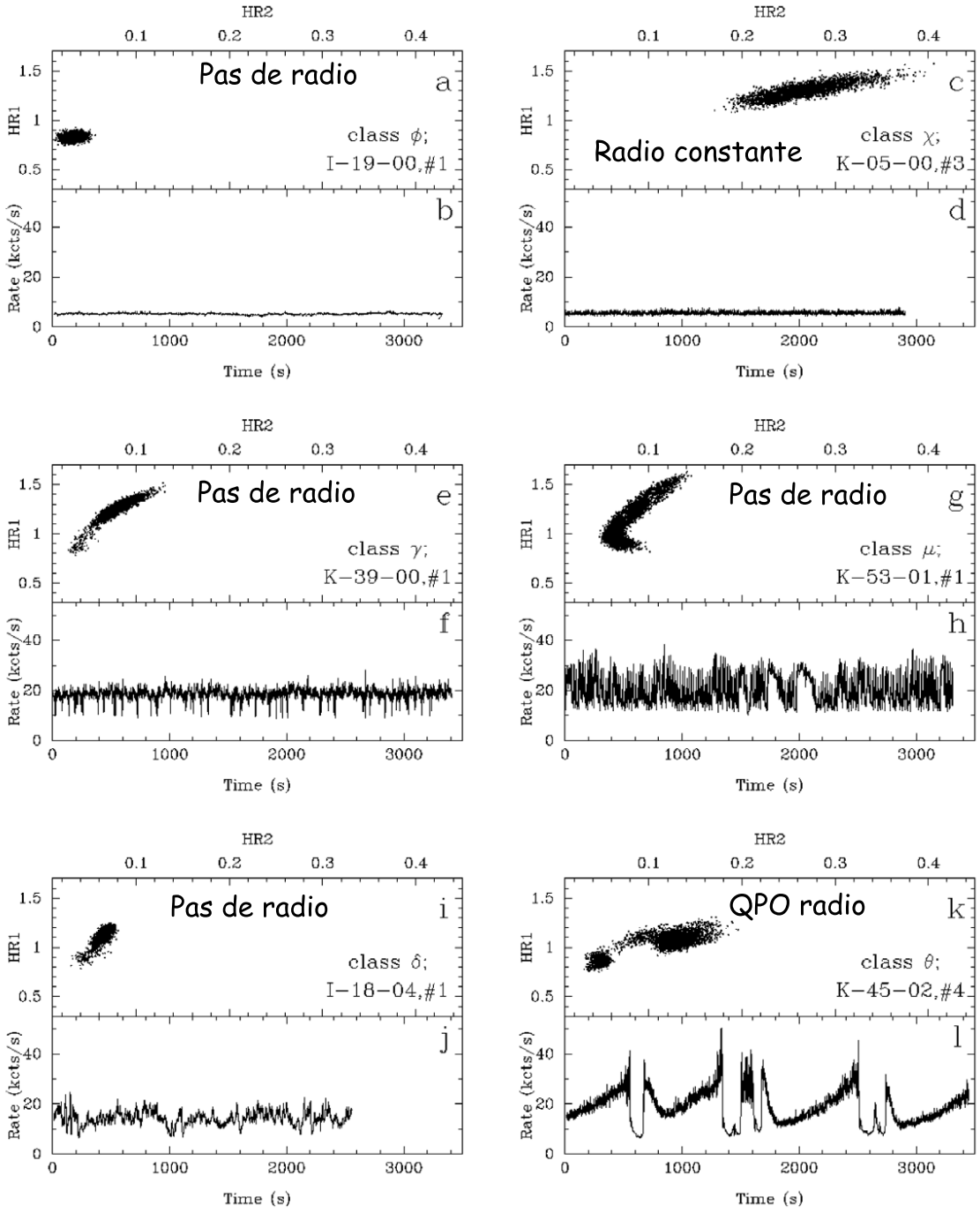

FIG. 7.2 – Courbes de lumière et CC des classes $\phi, \chi, \gamma, \mu, \delta, \theta$ selon la classification de Belloni et al. (2000). Les comportements radio sont tirés de Klein-Wolt et al. (2002).

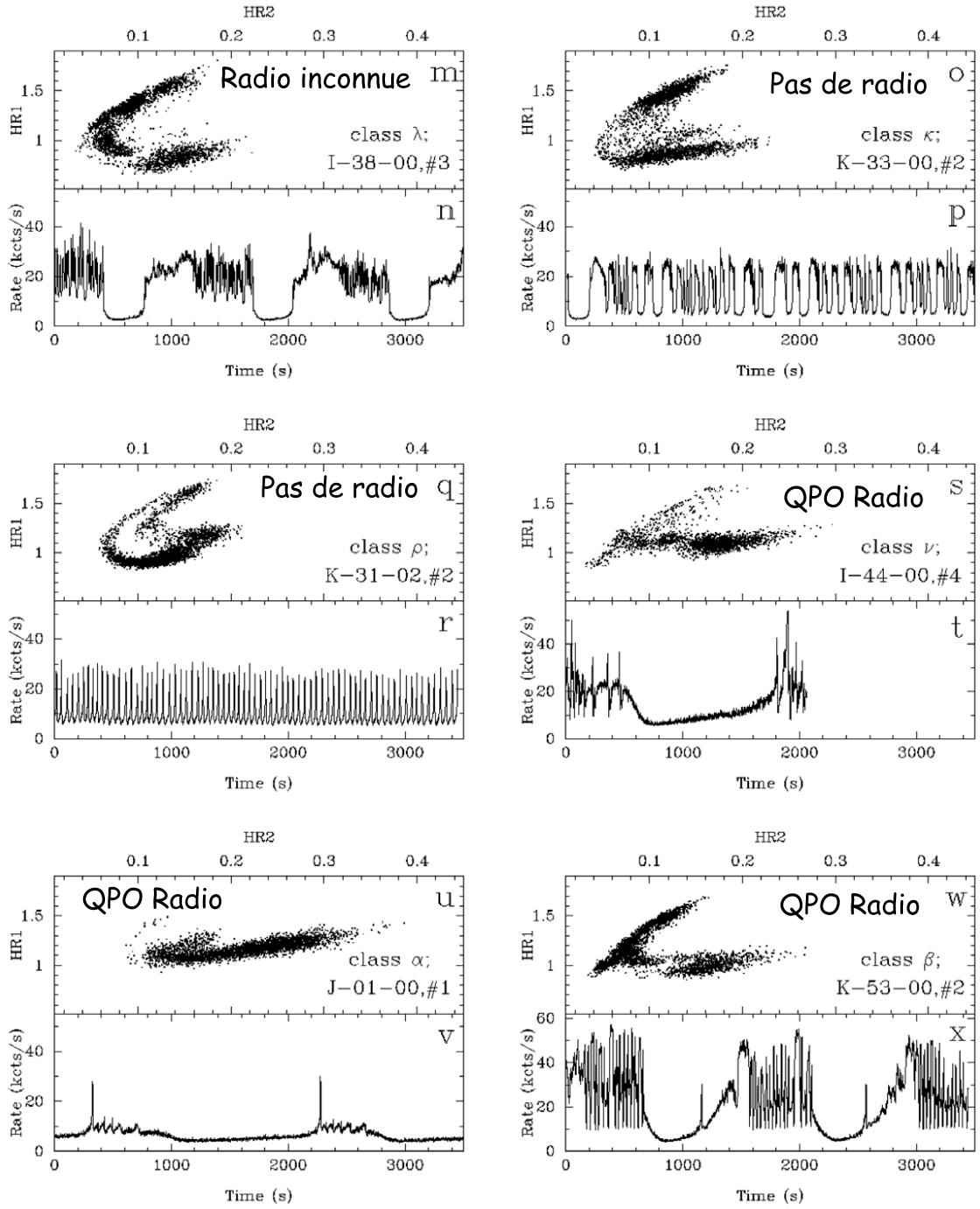

FIG. 7.3 – Courbes de lumière et CC des classes $\lambda, \kappa, \rho, \nu, \alpha, \beta$ selon la classification de Belloni et al. (2000). Les comportements radio sont tirés de Klein-Wolt et al. (2002).

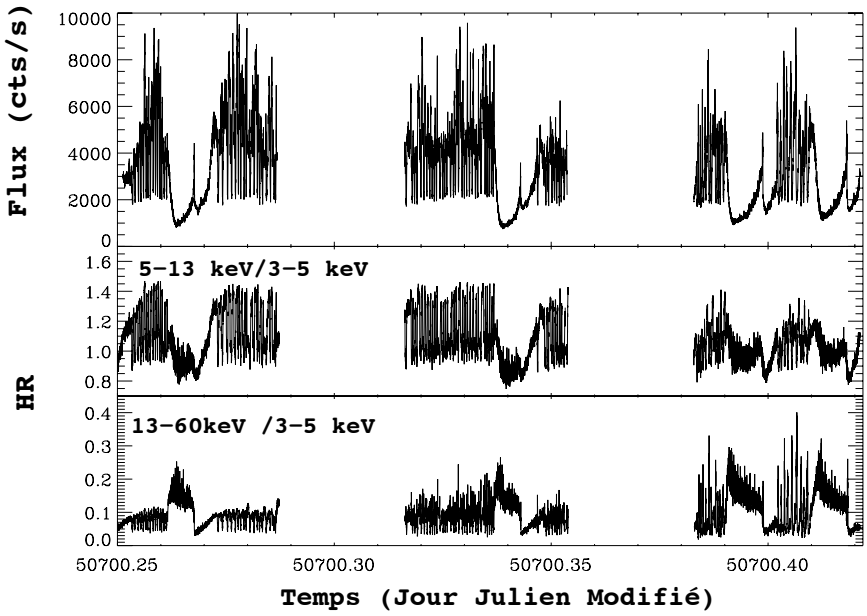

FIG. 7.4 – Courbe de lumière 2–60 keV *RXTE*/PCA de GRS 1915+105 dans l'état β (panneau du haut). On y voit la répétition de quatre cycles creux X-mous/pic/état intense et variable. HR 5–13 keV/3–5 keV (panneau du milieu) et 13–60 keV/3–5 keV (panneau du bas) montrant les évolutions spectrales de la source lors des passages dans les différents moments des cycles.

des motifs particuliers aisément identifiables dans ses courbes de lumière et diagrammes couleur-couleur (CC par la suite). Afin de comprendre, de manière modèle-indépendante, le comportement de cette source, aussi bien que pour faciliter la description de son comportement, Belloni et al. (2000) ont systématiquement analysé 163 observations *RXTE* de GRS 1915+105 ; ils ont pu regrouper les comportements vus dans les courbes de lumière et CC en 12 classes de variabilités distinctes nommées à l'aide de lettres grecques. Celles-ci sont reportées sur la figure 7.2 et 7.3. Les HR (ou couleurs) sont définis comme suit : HR1 = 5–13 keV/2–5 keV, HR2 = 13–60 keV/2–5 keV. J'indique aussi sur cette figure le comportement radio de chacune des classes tel qu'il était connu avant mes travaux (source Klein-Wolt et al. 2002, et les références y étant citées).

Penchons-nous d'abord sur les classes $\alpha, \beta, \lambda, \nu, \theta$ qui comportent toutes des périodes de creux en X mou (< 20 keV) de l'ordre de quelques centaines de secondes, durant lesquels le spectre est plutôt dur (HR> 0.15). Ces intervalles sont terminés par un brusque pic X, très mou, marquant un retour à une séquence d'activité intense et extrêmement variable. La figure 7.4 représente un exemple d'observation de type β. On y voit, grâce aux différents HR, la "saveur" (molle ou dure) des différents intervalles notables : creux, pic, et haute variabilité. Ces séquences seront par la suite appelées cycles, puisqu'en plus d'être relativement caractéristiques, elles sont récurrentes de manière quasi-périodiques (fig 7.4).

Enfin il est important de noter que nonobstant le nombre important de classes de variabilité différentes, Belloni et al. (2000) ont montré que toutes se résumaient à des transitions entre 3 saveurs spectrales nommées A, B et C. La première est extrêmement molle, la seconde très intense avec des composantes molles et dures importantes, et la dernières est plutôt dure. Il est remarquable que toutes les transitions sauf une sont observées ; GRS 1915+105 ne transite jamais directement de C à B.

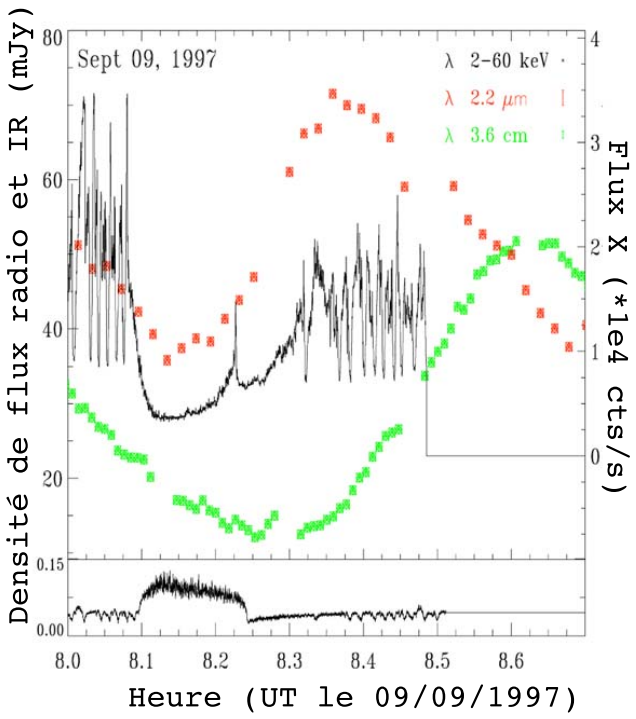

FIG. 7.5 – Zoom multi-longueurs d'onde sur le second cycle de l'observation de type β présentée sur la fig. 7.4. En noir est représentée la courbe de lumière en X, en rouge la courbe de lumière en IR, en vert la courbe de lumière radio. Le panneau du dessous représente le HR 13–60 keV/2–13 keV. Tiré de Mirabel et al. (1998).

7.3 Corrélations X-radio

La grande amplitude des variabilités en radio et en X est tout à fait remarquable dans cet objet (fig. 7.1) ; l'une des premières questions légitimes concerne l'existence d'un lien entre les variations radio et celles vues en X. Sans trop rentrer dans des détails de modélisation physique ici (ce que nous ferons en partie III), nous admettrons simplement que la radio trace la présence et l'évolution de jets de matière, alors que les rayons X sont plutôt la signature de phénomènes d'accrétion. La question précédemment posée revient alors à se demander s'il existe une connexion claire entre phénomènes d'accrétion et d'éjection. Cette question, étendue aux trous noirs en général, est au cœur d'une partie de mes travaux, comme nous le verrons plus en détails dans la partie III, au chapitre 11 en particulier.

Nous nous intéresserons ici aux comportements à relativement court terme, c'est-à-dire aux phénomènes X et multi-longueurs d'onde vus sur des périodes de l'ordre de la minute (équivalents aux durées typiques des pointés *RXTE* et *INTEGRAL*). Les phénomènes plus longs (journée et plus) sont étudiés en détails par Fender & Pooley (2000). Les premières études multi-longueurs d'ondes importantes de cet objet viennent de Pooley & Fender (1997) qui étudient les liens radio-X lors de trois cycles ν, de Mirabel et al. (1998) pour les liens radio-IR-X (Fig. 7.5) lors de cycles β et de Eikenberry et al. (1998a) pour les liens IR-X, là aussi pour une observation de type β. L'étude de référence et la plus citée reste cependant celle de Mirabel et al. (1998) qui a donc pu lier les variations X, IR et radio. Ces auteurs ont alors proposé qu'à la suite d'un phénomène soudain d'accrétion (le pic

X mou à la fin de la période dure dont ils pensaient qu'il était lié à la disparition de régions internes du disque), un bulle de matière était éjectée, et qu'au fur et à mesure de sa propagation dans le milieu interstellaire, lors de l'expansion de cette bulle, son pic d'émission se décalait progressivement vers les longueurs d'onde élevées. D'où l'apparition, tout d'abord, d'un pic IR suivi par un pic radio (fig. 7.5). Cette proposition correspond très précisemment au modèle de jet proposé par van der Laan (1966) pour expliquer les sources radio extragalactiques. La présence d'émission IR due au jet a, de plus, été confirmée par les études en spectroscopie IR de Eikenberry et al. (1998b).

Klein-Wolt et al. (2002) ont tenté une étude systématique des connexions X-radio lors de toutes les observations simultanées existantes. Les principaux résultats peuvent être résumés comme suit :

- Il n'y a pas d'éjections dans les classes $\phi, \gamma, \mu, \delta, \kappa$, et ρ, et θ
- Il y a des QPOs radio dans les classes α, β, ν
- La classe χ peut être associée à une forte émission radio de flux constant. Dans ce cas le jet est de type jet-compact comme celui vu dans d'autre microquasars dans leur état dur (par exemple GX 339−4 Fender et al. 1999a). Notons que GRS 1915+105 est l'une des deux seules sources pour lesquelles ce jet compact a été résolu avec des observations au VLA (Dhawan et al. 2000; Fuchs et al. 2003), l'autre étant Cyg X-1 (Stirling et al. 2001)
- Les QPO radio ne s'observent qu'en réponse à des creux X spectralement durs, et de durée minimum de 100 s.

Ces résultats sont importants car ils ouvrent la porte à une possible généralisation de liens entre accrétion et éjections. Néanmoins Klein-Wolt et al. (2002) n'ont pu aboutir à un tel résultat puisque le comportement radio lors de la classe λ leur est alors inconnu (fig. 7.2 et 7.3). De plus, ces auteurs gardent une approche totalement phénoménologique et ne rentrent pas dans la modélisation spectrale des observations X. Deux aspects où, notamment grâce à des approches combinées *INTEGRAL*, *RXTE*, et radio, j'ai pu approfondir la compréhension de ces connexions. Je résume l'approche phénoménologique ci-dessous, et décrirai les résultats basés sur l'analyse physique dans la Partie III, au chapitre 11.

7.4 Un modèle basique obtenu à partir de la campagne *INTEGRAL*

7.4.1 La campagne *INTEGRAL* et premiers résultats

Depuis le tout premier AO, nous (une large collaboration dont je suis PI) menons une campagne d'observation de GRS 1915+105 avec *INTEGRAL*. Les buts de cette campagne sont variés. Lors des 3 premiers AO nous pointions la source pendant de longs temps d'exposition, de manière à tenter d'obtenir un spectre s'étendant le plus haut possible en énergie. Nous voulions obtenir des contraindre sur les modèles physiques à l'origine de l'émission de la queue de haute énergie (et, espérions-nous, peut-être détecter une raie à 511 keV signant la présence de positrons). Cette approche était jointe à un suivi radio, en particulier avec le télescope Ryle, pour l'étude des connexions accrétion-éjection, et pour aussi tenter de vérifier la possible association entre queue X-dure et jet compact alors nouvellement proposée (par exemple Markoff et al. 2001, 2003). Lors des deux premiers AOs, je menais aussi une campagne de suivi simultanée avec *RXTE*, qui, outre une meilleure couverture en X mous que *INTEGRAL*/JEM-X, permettait des études spectro-temporelles précises (voir Rodriguez et al. 2004a, et le chapitre 12 dans la partie III). Enfin dans le cadre du temps garanti *INTEGRAL*, le groupe de Saclay mené par F. Mirabel, avait les droits sur deux ToO. Ces deux observations furent déclenchées et menées de front avec des observations simultanées en radio, IR, et X (avec *RXTE*). Dans ce cadre j'étais en charge de la partie haute énergie (*RXTE* et *INTEGRAL*) de cette campagne,

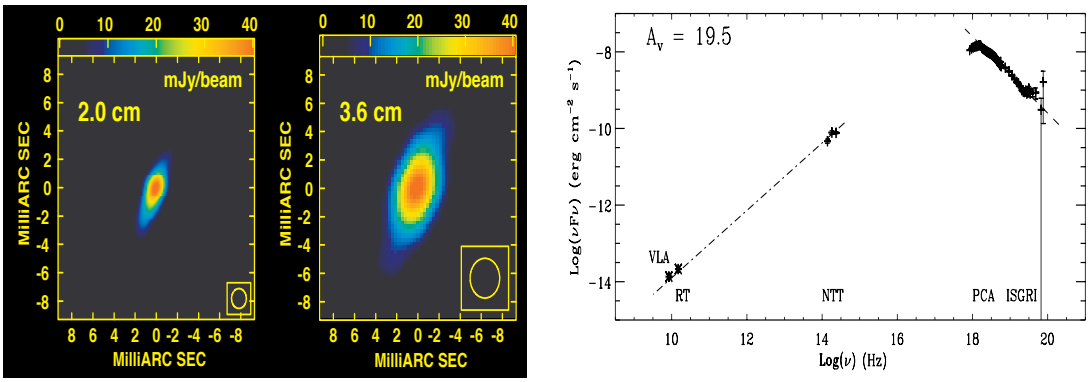

FIG. 7.6 – **Gauche :** Images obtenues au VLA à 2.0 cm et 3.6 cm montrant une structure étendue et alignée de part et d'autre de la source : le jet compact. La taille typique de cette extension est d'une centaine d'unités astronomiques à 12 kpc. **Droite :** distribution spectrale d'énergie depuis la radio jusqu'au gamma mous. Source Fuchs et al. (2003).

la compilation des résultats étant menée par Yael Fuchs.

Le résultat principal présenté dans Fuchs et al. (2003) est d'avoir pu, pour la première fois, observer de manière simultanée un grand nombre de caractéristiques de l'état dur de GRS 1915+105 (la classe χ) jusqu'alors observées de manière individuelle :

- Un fort flux radio relativement peu variable à 15 GHz avec le télescope Ryle
- Une structure radio compacte (le jet) résolue avec le VLA à 2.0 cm et 3.6 cm
- Une émission infrarouge brillante dont une partie, au moins, est associée au jet avec le NTT
- Un QPO à 2.5 Hz de puissance RMS 14% entre 2 et ∼60 keV avec *RXTE*
- Un spectre Gamma s'étendant au moins jusqu'à 400 keV avec *INTEGRAL*
- Un spectre X-Gamma dominé par une lois de puissance sans coupure avec *INTEGRAL* et *RXTE*

La figure 7.6 illustre une majorité de ces points, en montrant l'image VLA du jet compact, et la distribution spectrale d'énergie de GRS 1915+105 depuis la radio jusqu'au X. L'observation simultanée de ces différentes propriétés permet de faire un pas de plus vers une modélisation "propre" du phénomène de jet compact dans l'état dur des sources accrétantes, puisque chacune de ces caractéristiques est associée et/ou prédite dans certains modèles (cf. Partie III). Pour l'instant contentons-nous de mentionner la présence d'un jet compact (résolu), émettant clairement jusqu'en dans l'IR ; l'extension du spectre radio à l'IR passe presque exactement par les points IR obtenus au NTT comme l'on peut le voir sur la figure 7.6. Enfin tous ces aspects sont associés à un spectre X dur (et des QPOs).

7.4.2 Deux ans de suivis : des liens accrétion-éjection universels ?

Ce qui pourrait être bien plus important pour la compréhension des phénomènes physiques en action au cœur de GRS 1915+105 et des microquasars en général vient des observations régulières et répétées menées simultanément avec *INTEGRAL*, *RXTE* et le télescope Ryle et conduites lors des AO 2 et 3 d'*INTEGRAL* (octobre 2004 à décembre 2005). De manière à ne pas être biaisé par le choix d'un quelconque modèle physique (hormis d'admettre que les X tracent l'accrétion, et donc les régions proches du trou noir, et la radio trace les éjections) lors de l'interprétation de nos résultats, j'ai tout d'abord choisi d'examiner les données sous un jour purement phénoménologique, en regardant les courbes de lumière, diagrammes HR et CC. Je résume les résultats principaux ci-dessous et l'article associé (Rodriguez et al. 2008a, ApJ, 675, 1436) est inclus au chapitre 9. L'étude purement physique et modèle-dépendante est publiée dans un article compagnon (Rodriguez et al.

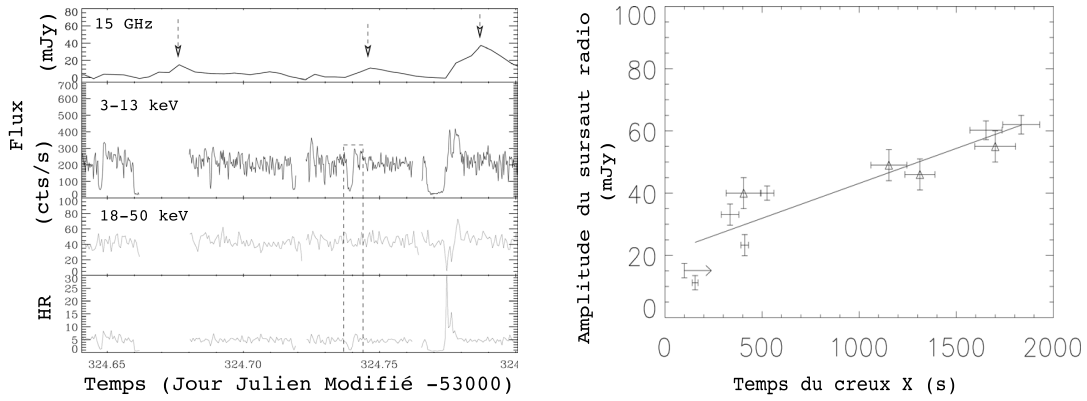

FIG. 7.7 – **Gauche :** De haut en bas : courbes de lumière à 15GHz, 3–13 keV, 18–50 keV, et rapport entre ces deux dernières pour une portion de l'observation λ. Les flèches verticales indiquent des sursauts radio indicatifs d'éjections. **Droite :** Evolution de l'amplitude du sursaut radio en fonction de la durée du creux X précédent l'éjection. La droite représente le résultat du meilleur ajustement linéaire. D'après Rodriguez et al. (2008a).

2008b, dans le même volume d'ApJ) et sera présentée en détails dans la partie III.

La première étape consiste à identifier, pour chacune des onze observations, la ou les classes de variabilité dans lesquelles GRS 1915+105 se trouve. Ceci nous permet d'observer des transitions directes entre certaines de ces classes, chose très difficilement observable avec les pointés courts ($\leq$ 4000 s) de *RXTE*. Cet aspect peut paraître relativement inintéressant au lecteur. J'insisterais, néanmoins, sur l'existence possible d'une logique au sein de la source lors de la répétition de classes, à l'identique, et ce, à des années d'écart. Nous pouvons alors nous demander s'il n'existe pas un mécanisme au sein de la source régulant la répétitivité des motifs dans les courbes de lumière. En d'autres termes il se pourrait, par exemple dans les classes à cycle, que les temps passés dans les creux X spectralement dur soient déterminés par un paramètre physique précis. il ne serait alors pas inattendu d'avoir une sorte de logique évolutive entre ces différentes classes. Cet aspect, peu développé dans l'article suivant, est au cœur d'un travail de fond que nous menons actuellement avec M. Cadolle Bel, M. Tagger et P. Varnière. Il implique l'étude des plus de 1500 observations *RXTE*, de manière à toutes les classifier, ainsi que toutes les observations *INTEGRAL* permettant de trouver des transitions directes. Je ne reviendrai pas, ni ne rentrerai plus en détails sur ce travail qui n'en est qu'à ses balbutiements (j'ai cependant déjà réduit et classé toutes les observations qui sont actuellement dans les mains de mes collaborateurs pour vérification).

Lors de cette campagne, nous observons, pour la première fois, un sursaut radio lors d'un cycle de type λ (le plus intense sur la figure 7.7). Ce sursaut, de même type que ceux observés dans les autres classes à cycles, permet d'aboutir à une première généralisation du fait que ces classes sont systématiquement associées à des éjections. En décomposant les courbes de lumières et HR de trois de ces classes (une ν et une β en plus de l'observation λ, figure 7.8), j'aboutis à une généralisation du schéma suivant : une éjection radio suit toujours une séquence d'accrétion (vue dans les rayons X) durant laquelle le flux X diminue soudainement, et devient très dur (intervalle I sur la figure 7.8), période dure qui est terminée par un brusque et plus ou moins intense pic X (intervalle II) marquant une transition vers un état particulièrement mou (intervalle III), avant que la source ne retourne dans un état de flux extrêmement variable et intense. De plus, grâce à des arguments qualitatifs basés

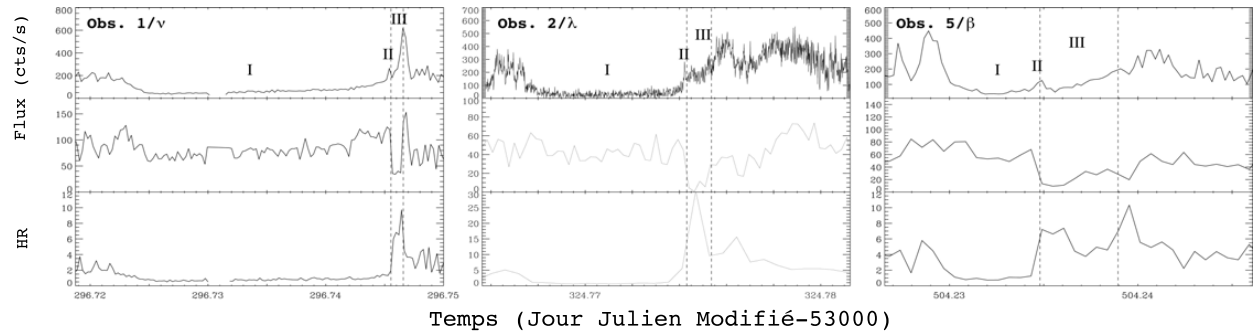

FIG. 7.8 – Courbes de lumière entre 3 et 13 keV (haut) 18–50 keV (milieu) et rapport entre les deux (bas) pour trois portions d'observations, une de type ν (gauche), une λ (milieu) et une β (droite). D'après Rodriguez et al. (2008a) .

notamment sur les délais X et radio, je montre que le pic II est probablement le moment où la matière est éjectée du système ; on peut voir le pic II comme la signature du déclencheur ou du déclenchement de l'éjection (comme l'illustre la brutale transition de saveur spectrale que l'on peut voir à chaque fois dans le HR sur la figure 7.8). Il est, ici, important de remarquer que toute cette séquence d'événement semble nécessaire pour mener à une éjection. En effet, Feroci et al. (1999) mentionne l'observation d'un creux X de spectre dur qui n'est pas suivi d'une éjection. Ceci aurait pu mettre à mal le modèle simple proposé ci-dessus, si je ne m'étais rendu compte que, dans ce cas, le creux X n'est pas terminé par un pic X de type intervalle II, qui est, dans mon interprétation, le déclencheur de l'éjection. Au final, donc, l'observation *BeppoSAX* conforte un peu plus l'interprétation que je propose.

L'observation de deux sursauts radio suivant deux creux X de faibles amplitudes (indiqués par les deux flèches de gauche sur la figure 7.7) m'a amené à me demander s'il pouvait exister une quelconque relation entre la durée des creux X et l'amplitude de l'éjection. On imagine aisément quelles implications une telle relation pourrait avoir sur la modélisation de ces phénomènes : on pourrait, par exemple, imaginer que durant le creux X la source "stocke" énergie et matière qui seront ensuite relachées lors de l'éjection. En utlisant les résultats de la campagne *INTEGRAL* et quelques observations publiées notamment dans Pooley & Fender (1997); Klein-Wolt et al. (2002) j'ai pu étudier l'évolution de l'amplitude du sursaut radio à 15 GHz en fonction de la durée du creux X sur un total de 11 cycles. Ceci est représenté sur la figure 7.7 (panneau de droite). Une corrélation semble être possible. Des tests statistiques indiquent que cette corrélation est probablement réelle, même si la relation entre les deux quantités n'est probablement pas linéaire, notamment si, comme le suggère Klein-Wolt et al. (2002), il est nécessaire d'avoir des creux X de durée supérieure à 100 s pour qu'il y ait une éjection. Remarquons tout simplement ici que cette conclusion de Klein-Wolt et al. (2002) pourrait simplement être due au manque de sensibilité du télescope Ryle à 15 GHz pour détecter des sursauts radio faibles.

7.5 Conclusions sur le chapitre

J'ai voulu montrer dans ce chapitre comment, ici encore, l'approche phénoménologique avait permis un débroussaillage important lors de l'étude d'une source au comportement compliqué. En utilisant des outils indépendants de tout modèle physique, j'ai pu généraliser une séquence d'événements liant l'accrétion et l'éjection dans GRS 1915+105. Il semble en effet que pour qu'une éjection ait lieu

dans ce système, il faille que la source entre dans un état spectral dur en rayons X (de durée >100 s), terminé par un bref flash X mou (3–20 keV) marquant un retour à un état très mou. Mes analyses indiquent que **cette séquence d'événements est la condition nécessaire et suffisante pour qu'il y ait une éjection discrète.** Le pic X est très probablement la signature et/ou le déclencheur de l'éjection dans les rayons X.

Le résultat qui, à mes yeux, semble le plus important est l'existence d'une corrélation entre l'amplitude du sursaut radio, et la durée du creux X. Cette corrélation est cependant basée sur un nombre restreint d'observations (onze), qui est loin de représenter un échantillon statistique acceptable pour pouvoir en tirer des conclusions fortes. L'étude de cet aspect est l'un des travaux que nous poursuivons actuellement avec L. Prat dans le cadre de sa thèse de doctorat. Nous avons notamment commencé à regarder toutes les observations *RXTE* pour lequel 1) il existe des observations radio à 15 GHz simultanées, et 2) lors desquelles GRS 1915+105 est dans une classe à cycle. La base de donnée à regarder est relativement vaste ; les premiers résultats sont néanmoins encourageants. Le but est de non-seulement regarder l'amplitude brute du sursaut radio, mais aussi sa fluence, ce qui nous permettra d'éviter un biais dû au fait que les éruptions radio sont de formes et de durées différentes. Enfin une fois ce travail fait nous pensons tenter la même approche à d'autres longueurs d'onde.

Chapitre 8
Etude de populations de source par l'approche phénoménologique comme conclusion de la partie II

8.1 Introduction

Nous avons vu dans cette partie comment une approche purement phénoménologique peut permettre une première compréhension des phénomènes en action au cœur des sources accrétantes (entre autres). Nous avons pu déterminer que IGR J16320−4751 était une probable HMXB avec un pulsar, que IGR J19140+0951 était une probable HMXB ; le type du système fut confirmé de manière indépendante dans les deux cas. Des analyses qualitatives du comportement du microquasar GRS 1915+105 ont permis de trouver un comportement général préludant à tout sursaut radio. En admettant que ces sursauts tracent les éjections de matière, alors ces études ont permis de mettre en avant un lien fort entre accrétion et éjection, et notamment entre les creux X spectralement durs et l'amplitude des éjections.

Bien que ces études doivent être considérées comme préliminaires à des analyses physiques poussées, elles peuvent aussi être utilisées pour étudier des familles de sources et tenter de comprendre leur comportement. Cette fois-ci l'approche sera globale plutôt que discrète, et nous tenterons alors de remonter au comportement moyen d'une famille de source en regardant un paramètre particulier. L'idée de base est de regarder des paramètres simples comme l'absorption (N_H), l'indice de loi de puissance, les valeurs de pulsations dans les pulsars, les périodes orbitales dans les systèmes binaires, etc... En explorant cet espace des paramètres, en étudiant l'existence de possibles relations des uns en fonction des autres nous pourrons (peut-être) discriminer les différents types de source. De telles relation, si elles existent, reposent sur des raisons physiques. J'ajouterai que même si mon discours, ici, semble orienté vers les HMXBs, de telles études existent aussi dans le cadre des trous noirs, microquasars, et autres objets. Je citerai par exemple les travaux de S. Corbel, R. Fender et collaborateurs qui ont permis d'identifier une corrélation forte entre flux radio et flux X dans l'état dur des microquasars (par exemple, et de manière non exhaustive Fender et al. 1999a; Corbel et al.

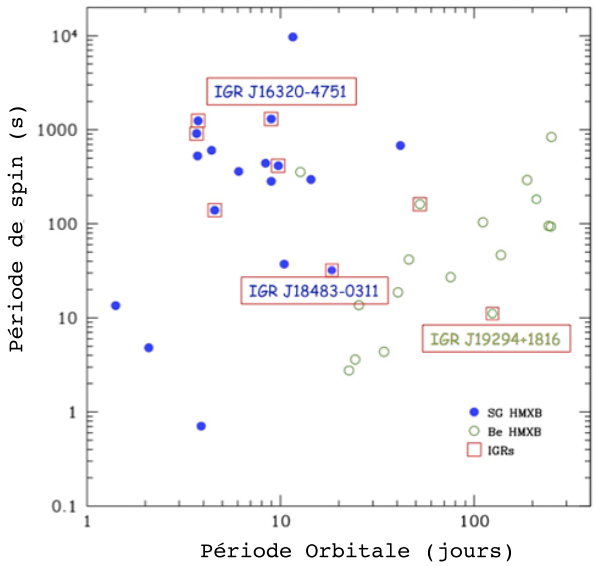

FIG. 8.1 – Diagramme de Corbet de toutes les HMXB dont les paramètres de spin et orbitaux sont connus (Mai 2009). On notera la présence de plusieurs sources *INTEGRAL* dont IGR J16320−4751, IGR J19294+1816 récemment découverte (Rodriguez et al. 2009 soumis), IGR J18483-0311, une source à la frontière entre Be et supergéante (une supergéante transitoire rapide, ou SFXT en anglais). Adapté de Bodaghee et al. (2007), Rodriguez & Bodaghee (2008), Bodaghee et al. 2009 (en préparation).

2000, 2003). Cette corrélation, tout d'abord phénoménologique, a amené à plusieurs dévellopements théoriques, dont le modèle de jet compact de S. Markoff (Markoff et al. 2001, pour n'en citer qu'un).

C'est cette démarche que nous poursuivons avec A. Bodaghee pour les cas particuliers des sources vues par *INTEGRAL* en se concentrant plus particulièrement sur les HMXB ; je résume brièvement quelques résultats de ces travaux ici en guise de conclusions de la partie II.

8.2 Période orbitale vs. pulsation : le diagramme de Corbet

Dans le cadre plus particulier des HMXB, l'approche phénoménologique la plus celèbre est probablement celle de Corbet (1986). Ce dernier a, en effet, reporté dans un diagramme P_{spin} vs. $P_{orb.}$ (couramment appelé "diagramme de Corbet") tous les systèmes pour lesquels ces paramètres étaient connus. Corbet (1986) a observé que Sg-HMXB accrétant par vent, sg-HMXB accrétant via un disque, et Be-HMXB se répartissaient dans différentes régions du diagramme (figure 8.1).

Cette répartition est compréhensible si l'on sait que les systèmes à supergéantes sont plus vieux que les systèmes Be. Né en rotation rapide, un pulsar ralentit en effet sous l'effet de la transformation de son énergie de rotation en énergie magnétique rayonnée. Les forces de marées entre les deux composantes du système binaire vont aussi contribuer à cet effet, puisqu'elle peuvent aider à synchroniser la période de spin à la période orbitale. De plus, ces systèmes accrètent le vent de leur compagnon. Ce dernier peu dense, et de densité $\rho(r) \propto r^{-2}$ (avec r la distance à l'étoile) crée un couple extrêmement peu important sur le pulsar, donc peu susceptible d'agir sur son spin. Les systèmes Be sont, en revanche, plus jeunes, et il est donc "normal" de les trouver avec, en moyenne,

une période de spin plus courte. La bonne corrélation trouvée dans le cas de ces derniers objets entre période de spin et période orbitale (fig. 8.1) peu, ici encore, s'expliquer par le mécanisme d'accrétion en jeu au sein de ces systèmes. Les Be-HMXB sont transitoires, et les périodes d'accrétions ont lieu leur de la traversée du vent équatorial dense de l'étoile par le pulsar. Ici ce "disque de décretion" à une structure telle que $\rho(r) \propto r^{-3}$, et exprime donc un couple important sur l'objet compact ayant tendance à accélerer la rotation du pulsar. Très basiquement, on comprend donc qu'un système à faible période orbitale, et donc récurrence importante, aura un pulsar plus rapide qu'un système à récurrence faible.

8.3 Au-delà du diagramme de Corbet

En 2006, durant sa thèse, l'idée suggérée par A. Bodaghee et qui obtint mon soutien appuyé, était de regarder toutes les sources détectées par *INTEGRAL*/IBIS (donc au-delà de 20 keV) après 4 années d'activité, et de tenter d'en explorer l'espace des paramètres, de manière à étudier de possibles nouvelles corrélations. Les paramètres alors pris en compte étaient multiples : position Galactique, N_H, Γ, spin, periode orbitale, ...

8.3.1 Première étape : un catalogue

En fait ce travail commença par l'établissement d'un catalogue contenant, pour chacune des sources, tous les paramètres alors connus. La première pierre de cet édifice provenait du site web crée en 2003 par mes soins (à http ://isdc.unige.ch/∼rodrigue/html/igrsources.html), qui, pour chaque nouvelle source *INTEGRAL*, recense toute information d'intérêt, et la bibliographie associée à ladite source. Ce site est né en 2003 d'un but plus ou moins avoué de me faire une base de données pour ces sources, pour éventuellement les étudier, plus tard, en tant que famille. Vu l'engouement alors suscité par ces nouvelles sources, je pensai, immédiatement, à diffuser cette base de données plutôt qu'à la garder.

Ce site a maintenant environ 6 ans, et est une référence dans la communauté. Il est effectivement régulièrement cité dans des articles, minutes de conférences, et présentations. Il contient plus de 250 sources de tous types (AGN, HMXB, LMXB, PWN, ...). Un compteur m'a permis de voir qu'il a été visité environ 4000 fois depuis le 24 avril 2007. Il est notamment utilisé comme base de la mise à jour du fichier catalogue établi par l'ISDC et nécessaire à toute réduction de données *INTEGRAL*.

J'étais loin d'imaginer la quantité de travail de maintenance et mise à jour de ce site lorque je l'ai crée. Ainsi, Arash Bodaghee m'a aidé pendant les deux dernières années de sa thèse ; cela permettait aussi de débuter le travail de fond dont je présente les résultats dans la section suivante, qui sont, principalement, dûs aux travaux de thèse d'Arash, aspect de sa thèse à laquelle j'ai activement participé.

8.3.2 Les sources détectées par *INTEGRAL* au cours de ses quatre premières années d'observations

Je ne rentrerai pas dans tous les détails des résultats obtenus et largement présentés dans Bodaghee et al. (2007) (2007, A&A, 467, p585), mais me focaliserai sur les sources accrétantes et plus particulièrement les binaires X. Dans ce cadre, un résumé relativement exhaustif de ces travaux mis à jour est présenté par Rodriguez & Bodaghee (2008). J'ajouterai que nous (A. Bodaghee, moi-même, et d'autres, dont S. Chaty, et J. Tomsick) travaillons actuellement à une mise à jour bien plus complète (comprenant toutes les sources *INTEGRAL* mais aussi les sources *Swift* de manière à uniformiser le plus possible les temps d'exposition sur la totalité de la voûte céleste) de ces travaux.

On voit alors, ici, quelle importance ont nos travaux d'identification de sources (chap. 3 et 4) placés dans un contexte plus global.

8.3.3 Binaires X et localisation Galactique

La figure 3.4, présentée au chapitre 3, présente une synthèse de la répartition des sources vues par *INTEGRAL* sur la voûte céleste. Pour toutes les sources détectées jusqu'en 2007. Evidemment la carte d'exposition *INTEGRAL* est fortement biaisée vers le plan et le centre de la Galaxie. Néanmoins, il apparaît clairement, déjà sur cette figure, que si les AGN sont trouvés de manière plutôt isotrope, il n'en est pas de même pour les binaires X. Ce résultat n'est ni neuf, ni inattendu, et les nouvelles sources et sources identifiées depuis la publication de cet article ne l'ont pas contredit.

Concernant la répartition des binaires X les résultats publiés dans Bodaghee et al. (2007) peuvent se résumer comme suit :

- Les HMXB sont plutôt groupées dans la direction de la tangente au bras spiraux galactiques, à faible latitude galactique
- Les HMXB suivent plutôt bien la distribution des traceurs de régions de formation d'étoiles.
- La plupart des LMXB sont trouvées dans le bulbe galactique et dans les amas globulaires.
- Les LMXB ont eu le temps de migrer à travers la Galaxie, et l'on peut en trouver à haute latitude Galactique.

Même si, évidemment, on trouve plus de binaires X aux faibles latitudes Galactiques, ce dernier point est relativement bien illustré par les travaux de Félix Mirabel qui a montré qu'alors Cyg X-1 (une HMXB à supergéante débordant son lobe de Roche) était très probablement née in-situ (Mirabel & Rodrigues 2003), XTE J1118+480 et GRO J1655−40 (deux microquasars, LMXBs) ont, elles, eu le temps de migrer à travers la Galaxie (Mirabel et al. 2001, 2002). La première de ces deux sources se trouve d'ailleurs relativement proche du Soleil, et à haute latitude Galactique.

Il est intéressant de noter que Bodaghee et al. (2007) remarque une possible asymétrie dans la répartition des LMXB. Or la même asymétrie semble être vue par Weidenspointner et al. (2008) dans la distribution des positrons galactiques tracés par leur émission à 511 keV, et telle que vue par *INTEGRAL*/SPI. Cette corrélation, si elle était définitivement confirmée, aurait un impact énorme sur notre compréhension de la production de positrons dans notre Galaxie (rappelons que bien que la cartographie du 511 keV ne soit pas une nouveauté, l'origine des positrons reste pour le moins spéculative). De même savoir que les LMXB sont de forts producteur de positrons permettrait de bien mieux contraindre les modèles notamment de jets (dont certains prédisent la présence de positrons).

Enfin une remarque d'importance est que notre étude concerne des sources détectées au-delà de 20 keV par un instrument relativement peu sensible (en comparaison de *Chandra* et *XMM–Newton* sous 10 keV par exemple). Même si la répartition des binaires X actives peut être considérée comme un traceur de toutes les binaires X, un biais peut être introduit ; pour en être totalement exempte, notre étude devrait prendre en compte toutes les sources, et donc les binaires X en quiescence. Même si aucun relevé total et profond de la Galaxie n'existe le relevé des sources Galactiques faibles (Sugizaki et al. 2001), les catalogues *XMM–Newton* (comme par exemple celui de Watson et al. 2009) et les études de régions ponctuelles faites avec *Chandra* (par exemple Ebisawa et al. 2005; Muno et al. 2009, pour respectivement une région "typique" du plan Galactique et le bulbe) pourraient apporter une première indication. Malheureusement le nombre de sources détectées, et surtout leur faiblesse ne permet alors pas facilement de déterminer leur type.

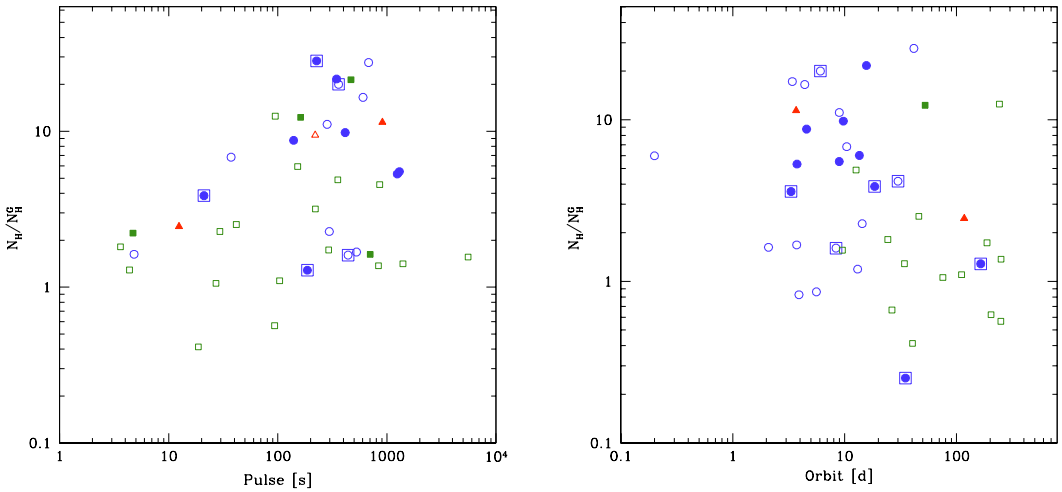

FIG. 8.2 – **Gauche :** évolution de l'absorption N_H en fonction de la période orbitale pour les systèmes pour lesquels ces paramètres sont connus. **Droite :** évolution de N_H en fonction de la période de spin. Dans les deux cas les sources en bleu sont des Sg-HMXB, les sources en vert des Be-HMXB, les triangles rouges des sources de type non-encore déterminé (incluant la récente IGR J19294+1816 qui pourrait être une SFXT ou bien une Be-HMXB, Rodriguez et al. 2009, soumis). Les sources encadrées sont des SFXT, celles avec des symboles remplis des sources découvertes par *INTEGRAL*. D'après Bodaghee et al. 2009 en préparation.

8.3.4 HMXB : les "diagrammes de Bodaghee"

La nouveauté, au niveau des HMXB, est d'étendre l'étude type diagramme de Corbet à l'absorption. On peut ainsi réprésenter l'absorption locale d'une source (normalisée par rapport à l'absorption due au HI sur la ligne de visée Dickey & Lockman 1990) en fonction de sa période orbitale, ou de sa période de spin Fig. 8.2.

Même si la discrimination entre Sg- et Be-HMXB est un peu moins claire que sur le diagramme de Corbet, il semble bien que les sources des deux types tendent à occuper des régions un peu différentes dans ces diagrammes. Les Be-HMXB sont, en particulier, moins absorbée que les Sg, tout en ayant d'une manière générale toujours une période orbitale plus longue. Ces résultats pouvaient être, à-priori, plus ou moins attendus ; les Sg-HMXB ont une orbite plus serrée où l'objet compact vit dans le vent stellaire du compagnon et donc est dans un environnement plus dense.

L'important dans ces diagrammes, est qu'ils semblent confirmer un fait : les SFXT se répartissent partout dans les diagrammes. Ceci est en fait exacerbé par deux tels objets : IGR J11215−5952 et IGR J18483−0311. Ces deux objets ont en fait des orbites excentriques bien que leur compagnon soit une supergéante.

8.4 Pour conclure : un lien Be-HMXB vers sg-HMXB ?

Récemment, très peu de temps après la découverte de IGR J19294+1816, j'ai déclenché mes programmes d'observations simultanées avec *RXTE* et *Swift*. En très peu de temps (quelques jours), la période de pulsation, la période orbitale, et la contrepartie infra rouge étaient détectées (Rodriguez et al. 2009c; Strohmayer et al. 2009; Corbet & Krimm 2009) : l'objet est une HMXB contenant un pulsar. Cette source en particulier est une excellente justification de mes programmes de suivis ; grâce

aux observations *RXTE* et *Swift* j'ai pu déterminer le type de l'objet (identification de la période de pulsation, contrepartie infrarouge), et étudier ses propriétés physiques (processus spectraux). Je pense que cette étude est un bon exemple pour conclure cette seconde partie, puisqu'elle est aussi représentative des différentes étapes que j'ai présentées depuis le début de ce document (parties I et II).

La position de cet objet dans le diagramme de Corbet, et les diagrammes de Bodaghee conduisent à la classer comme une Be-HMXB. Cependant, en scrutant toutes les observations de GRS 1915+105 dans le champ de laquelle se trouve cette source, j'ai pu découvrir deux flashs X-durs, de courtes durées, typique du comportement des SFXT. L'existence de deux autres sources à supergéantes se trouvant dans la zone des Be, pourrait réveler une famille de sources aux comportement différents : des Sg-HMXB à longue période, et donc un objet à orbite excentrique (Rodriguez et al. 2009, soumis à A&A, inclus au chapitre 9 à la fin de cette partie). Il serait alors tentant d'imaginer un lien évolutif entre les Be et certaines de ces SFXT. Remarquons qu'au moment où j'écris ces lignes, Liu et al. 2009 (en préparation) semblent être arrivés à la même conclusion après avoir étudier plus précisemment IGR J11215−5952 et IGR J18483−0311, et montrer qu'elles étaient très certainement issues de l'évolution de systèmes Be.

Au-delà même de classification, donc, l'approche phénoménologique de familles de sources, pourraient permettre de lever de nombreuses énigmes les concernant, comme ici, un possible devenir des Be-HMXB.

Chapitre 9

Articles de recherche liés à la partie II

9.1 Nature de IGR J19140+0951

A&A 432, 235–247 (2005)
DOI: 10.1051/0004-6361:20041854

Astronomy & Astrophysics

Unveiling the nature of the high energy source IGR J19140+0951

J. Rodriguez[1,2], C. Cabanac[3], D. C. Hannikainen[4], V. Beckmann[5,6], S. E. Shaw[7,2], and J. Schultz[4]

[1] Centre d'Etudes de Saclay, DAPNIA/Service d'Astrophysique (CNRS FRE 2591), Bât. 709, Orme des Merisiers, Gif-sur-Yvette Cedex 91191, France
e-mail: jrodriguez@cea.fr
[2] *INTEGRAL* Science Data Centre, Chemin d'Écogia 16, 1290 Versoix, Switzerland
[3] Laboratoire d'Astrophysique, Observatoire de Grenoble, BP 53X, 38041 Grenoble, France
[4] Observatory, PO Box 14, 00014 University of Helsinki, Finland
[5] NASA Goddard Space Flight Center, Code 661, Building 2 Greenbelt, MD 20771, USA
[6] Joint Center for Astrophysics, Department of Physics, University of Maryland, Baltimore County, MD 21250, USA
[7] School of Physics and Astronomy, University of Southampton, Southampton, SO17 1BJ, UK

Received 18 August 2004 / Accepted 21 December 2004

Abstract. We report on high energy observations of IGR J19140+0951 performed with *RXTE* on three occasions in 2002, 2003 and 2004, and *INTEGRAL* during a very well sampled and unprecedented high energy coverage of this source from early-March to mid-May 2003. Our analysis shows that IGR J19140+0951 spends most of its time in a very low luminosity state, probably corresponding to the state observed with *RXTE*, and characterised by thermal Comptonisation. In some occasions we observe variations of the luminosity by a factor of about 10 during which the spectrum can show evidence for a thermal component, besides thermal Comptonisation by a hotter plasma than during the low luminosity state. The spectral parameters obtained from the spectral fits to the *INTEGRAL* and *RXTE* data strongly suggest that IGR J19140+0951 hosts a neutron star rather than a black hole. Very importantly, we observe variations of the absorption column density (with a value as high as $\sim 10^{23}$ cm^{-2}). Our spectral analysis also reveals a bright iron line detected with both *RXTE*/PCA and *INTEGRAL*/JEM-X, at different levels of luminosity. We discuss these results and the behaviour of IGR J19140+0951, and show, by comparison with other well known systems (Vela X-1, GX 301−2, 4U 2206+54), that IGR J19140+0951 is most probably a High Mass X-ray Binary.

Key words. X-rays: binaries – X-rays: individual: IGR J19140+0951 – accretion, accretion disks – gamma-rays: observations

1. Introduction

IGR J19140+0951 was serendipitously discovered during the first INTErnational Gamma-Ray Astrophysical Laboratory (*INTEGRAL*, Winkler et al. 2003) observation of the Galactic microquasar GRS 1915+105 (Hannikainen et al. 2003). Inspection of the high energy archives showed it to be the most likely hard X-ray counterpart of the poorly studied *EXOSAT* source EXO 1912+097 (Lu et al. 1996). Soon after its discovery a Target of Opportunity (ToO) was performed on IGR J19140+0951 with the *Rossi X-ray Timing Explorer (RXTE)*. The preliminary spectral analysis of this ToO showed the source had a rather hard spectrum, fitted with a power law of photon index 1.6, and an absorption column density $N_{\rm H}$ = 6×10^{22} cm^{-2} (Swank & Markwardt 2003). Recently timing analysis of the *RXTE*/ASM data revealed an X-ray period of 13.55 days (Corbet et al. 2004). This analysis showed that the source was detected even during the early days of the *RXTE* mission, which suggests that IGR J19140+0951 is a persistent X-ray source although most of the time in a faint state. In a companion paper (Hannikainen et al. 2004a, hereafter Paper I) we used the latest version of the *INTEGRAL* software to refine and give the most accurate X-ray position of IGR J19140+0951 (see also Cabanac et al. 2004), which allowed us to obtain the most accurate X-ray/Gamma-ray spectra of the source. High energy spectral analysis of IGR J19140+0951 covering the period of its discovery, i.e. during *INTEGRAL* revolution 48, was presented for the first time. We have, in particular, shown, that during this observation, the source, although very variable, showed two distinct spectral behaviours. The first one manifests a thermal component (black body-like) in the soft X-rays, and a hard X-ray tail, whereas the second one is harder and can be interpreted as originating from thermal Comptonisation (Paper I).

Although it is very likely that IGR J19140+0951 is a Galactic object, the nature of the compact object is unclear. The spectral analysis presented in Paper I would tend to favour a neutron star, but no definite conclusion could be drawn from the data presented.

We report here observations of IGR J19140+0951 with *INTEGRAL* performed between March and May 2003, during a very well sampled and unprecedented high energy coverage of this source. To our *INTEGRAL* monitoring, we add the analysis

Table 2. Level of systematic uncertainty applied to the spectral channels of the JEM-X spectra, and energy channel correspondence.

Channel	Energy (keV)	Systematic uncertainty (%)
58–79	4.00–5.76	5
80–89	5.76–6.56	2
90–99	6.56–7.36	7
100–109	7.36–8.16	5
110–119	8.16–9.12	4
120–129	9.12–10.24	5
130–149	10.24–13.44	4
150–159	13.44–15.40	6
160–169	15.40–17.64	5
170–179	17.64–20.24	8
180–189	20.24–22.84	7
190–197	22.84–25.52	9

was in the JEM-X FOV (48, 57, 59, 62, 67, 68, 69, 70) but only included the SCWs where the source was at an offset angle less than 5°. The level of systematic uncertainty applied to each spectral channel, and the energy-channel correspondence is reported in Table 2 (P. Kretschmar & S. Martínez Núñez, priv. comm.). The IBIS/ISGRI data were reduced using version 4.1 of the OSA software. The data reduction procedure is identical to the one described in Paper I, i.e. for each revolution we first ran the software up to the production of images and mosaics in the 20–40 and 40–80 keV energy ranges. The software was here free to find the most significant sources in the images. We then created a catalogue containing only the 9 brightest sources of the field (either detected in some of the revolutions or in all), and re-ran the software forcing the extraction of the count-rate of those sources. The data products obtained through the ISGRI pipeline therefore include 20–40 keV and 40–80 keV light curves (Fig. 1), with a time bin about 2200 s (typical length of a SCW). Rather than using the standard spectral extraction, we extracted spectra from images/mosaics accumulated at different times. This non-standard method and its validity is described in Appendix A.

First of all we restricted the spectral analysis to the times when the source was both in the IBIS and JEM-X FOV, i.e. revolutions 48, 57, 59, 62, 67, 68, 69 and 70. The distinction of the different times was defined from the 20–40 keV light curve (Fig. 1), on a SCW basis in a way similar to what is presented in Paper I. The distinction of different times to accumulate the data from is solely based on the level of luminosity of the source during a SCW. Although the level on which the distinction is made is rather arbitrary, our approach allows us to try to understand the origin of the variability on the time scale of a SCW by accumulating spectra of similar (hard) luminosity. Although this approach can hide and completely miss the spectral variations on smaller time scales, it is dictated by the need to accumulate a large number of JEM-X and IBIS spectra to obtain good constraints on the spectral parameters (e.g. Paper I). Our PCA analysis (Sect. 3.2) shows that although the source can be variable on short time scales, the fitting of the average spectrum leads to a rather good representation of the physics underlying the source emission. Here due to a larger sampling of the source as compared to Paper I, it was possible to define more "states" to accumulate the spectra from, in order to understand better the origin of the variations and try to avoid possible mixture of different states together. We define here:

- The "ultra faint" state was accumulated from all SCW when the source had a 20–40 keV count rate (*CR*, measured in cts/s) < 1.
- The "faint state" has a similar definition as in Paper I and was accumulated from all SCW where $1 \leq CR < 3$.
- The "bright state" corresponds to $3 \leq CR < 6$.
- The "ultra bright state" corresponds to the bright 20−40 keV flares, i.e. $CR \geq 6$.

We caution the reader that these definition of "states" have nothing to do with the standard definition of spectral states usually employed in studies of X-ray Binaries (e.g. Tanaka & Shibazaki 1996), and that they refer to luminosity in the hard X-rays. We thus extracted the source count rate and error from 20 bin mosaics accumulated during these four intervals as described in Appendix A. 6% systematics have been added to all spectral channels. The JEM-X individual spectra were averaged together following the same time distinction.

We also tentatively extracted SPI spectra following the standard method. However, the SPI angular resolution is about 2°, which renders the analysis of IGR J19140+0951 delicate given the proximity to GRS 1915+105, which is much brighter (Hannikainen et al. 2004b; Rodriguez et al. 2004a). In fact, an analysis of the SPI spectra showed that the parameters were consistent with those of GRS 1915+105. We therefore did not include the SPI data in our analysis.

The JEM-X & ISGRI spectra were then fitted in XSPEC v11.3.1, with latest rmf file for JEM-X (`jmx2_rmf_grp_0021.fits`), and the OSA 3.0 ISGRI matrices for IBIS (`isgr_rmf_grp_0010.fits`, `isgr_arf_rsp_0004.fits`). We retained the energy channels between 4 and 25 keV for JEM-X and those between 20 and 150 keV for ISGRI. Further rebinning of the JEM-X data was applied so that both ISGRI and JEM-X data give similar weight to the χ^2 statistics in the spectral fittings.

2.2. RXTE data

The field of IGR J19140+0951 has been observed 3 times with *RXTE* during pointed observations, the journal of which is summarised in Table 3. Two observations were truly dedicated to IGR J19140+0951, a public ToO, and an observation that is part of an on-going monitoring programme of the source. The third and oldest observation was dedicated to EXO 1912+097. Whether or not IGR J19140+0951 and the *EXOSAT* source are the same is beyond the scope of this paper, given that the best position of IGR J19140+0951 (Cabanac et al. 2004) is still consistent with the *EXOSAT* position of EXO 1912+097 (Lu et al. 1996). We assume in the following that the sources are the same.

Table 3. Journal of the *RXTE* observations discussed in the paper. † Net 3−25 keV mean count rate (cts/s)/PCU, only the top layers of PCUs are considered.

Obs. #	MJD	Exposure	# PCU	Count rate/PCU†
1	52 394.08	3248 s	2	6.8
2	52 708.79	2848 s	4	6.6
3	53 087.50	6496 s	3	11.8

The *RXTE* data have been reduced with the *LHEASOFT* package v5.3.1, following the standard procedures for both *Proportional Counter Array* (PCA, Jahoda et al. 1996), and *High Energy Timing Experiment* (HEXTE, Rothschild et al. 1998) data. See e.g. Rodriguez et al. (2003a, 2004b) for the procedure of spectral extraction, and 2–40 keV (channel 5−92) high time resolution light curves. In addition, and since the source is quite weak, we further rejected times of high electron background in the PCA (i.e. times when the electron ratio in Proportional Counter Unit (PCU) #2 is greater than 0.1), and time during the passage through the South Atlantic Anomaly (i.e. we retained the times since SAA > 30 or <0 min) to define the "good time intervals", and used the latest background files available for faint sources. The spectra were extracted from the top layer of all PCUs turned on during each observation. In order to account for uncertainties in the response matrix we added 0.8% systematics below 8 keV, and 0.4% above (Rodriguez et al. 2003a). Note that during the three observations, the data formats were different resulting in different time resolutions for the timing study. We could explore the source temporal behaviour up to 64 Hz, 4000 Hz, and 124 Hz in Obs. 1, 2, and 3 respectively. For HEXTE, we separated on and off source pointings and carefully checked for any background measurement pointing on GRS 1915+105, and other close-by sources (XTE J1908+094, X 1908+075, & 4U 1909+07). We only used the pointings which were not contaminated by other sources as background maps. However, due to either the weakness of IGR J19140+0951 or the limited number of background maps, no HEXTE data can sensibly be used in our analysis. We therefore focus on a comparison of the PCA spectra obtained during the 3 observations The spectra were fitted in XSPEC V11.3.1 (Arnaud 1996), between 3 and 25 keV.

3. Results

3.1. High resolution temporal analysis

We studied the PCA high resolution light curves in different frequency ranges given the different time resolution of the different data format, in order to investigate the time variability and search for Quasi-Periodic Oscillations. We produce 2−40 keV Power Density Spectra (PDS) on an interval length of 16 s. Our PDS were normalised according to Leahy et al. (1983). The lower boundary of the PDS is 0.0625 Hz in each case while the higher boundary is 64 Hz, 4000 Hz, and 128 Hz for Obs. 1, 2 and 3 respectively. The 3 PDSs are well fitted with constants with best values 1.999 ± 0.007 ($\chi^2_\nu = 1.10$ for 117 d.o.f.), 2.002 ± 0.001 ($\chi^2_\nu = 1.09$ for 199 d.o.f.) and 2.004 ± 0.004 ($\chi^2_\nu = 0.84$ for 139 d.o.f.) (error at the 90% confidence level), compatible with the expected value for purely Poisson noise. In case a High Frequency QPO (HFQPO) is present it usually has a higher rms amplitude at energy higher than ∼5−7 keV. We also produced a PDS in the 7−20 keV range from Obs. 2, and analysed it between 0.0625 Hz and 4000 Hz. A single constant fits the PDS well, with best value 2.000 ± 0.001 (at 90% confidence level), again indicative of purely Poisson noise.

Using

$$R = \sqrt{2 \times n_\sigma \times \frac{S+B}{S^2}} \sqrt{\frac{\Delta\nu}{T}} \quad (1)$$

where R is the fractional rms amplitude, S is the source net rate, B is the background rate, T and $\Delta\nu$ are the exposure time and the width of the QPO, one can estimate the 3σ upper limit on the detection of any QPO at any frequency, during the 3 observations. The limiting amplitude being proportional to the square root of the width, the limit for a sharp QPO will be lower than that of a broad feature. The most constraining results are obtained for Obs. 3, for which the limit on the presence of a $Q(=\nu/\Delta\nu) = 10$ low frequency feature is comprised between 1.5% ($\nu = 0.0625$ Hz) and 6.5% ($\nu = 20.0$ Hz). This puts tight constraints on the presence of such a feature since those low frequency QPOs are usually observed to have a rather high fractional amplitude (e.g. 5–30%, McClintock & Remillard 2004). For high frequency QPOs, however, the situation is reversed. With the help of Eq. (1), we obtain a limit of 17.4% for a 200 Hz QPO during Obs. 2. This means that if such a feature was present (in the 100−300 Hz range for a black hole and in the kHz range for a neutron star) then we would miss it. This is even true for a ∼15% rms HFQPO as sometimes detected in some Atoll sources (Swank 2004).

3.2. Spectral analysis

3.2.1. Simultaneous JEM-X/ISGRI spectral analysis

Over a total of 450 SCW, covering revolutions 48, 57, 59, 62, 67, 68, 69 and 70, IGR J19140+0951 is found in the "ultra faint" state during 271 SCW (60.2%), it is in the "faint state" during 130 SCW (∼28.9%), in the "bright state" during 37 SCW (8.2%), and in the "ultra bright" state during 12 SCW (∼2.7%). However, due to the 5×5 observing pattern (Courvoisier et al. 2003) and mean off axis angle during revolutions 67, 68, beginning of 69, and 70 (Table 1), the source is outside of the JEM-X FOV, during a large part of these revolutions. For the sake of consistency, we extracted mean spectra from the time when IGR J19140+0951 is in both the ISGRI and JEM-X FOV. However, in doing so some statistical sensitivity is lost especially at high energies, and we completely miss the flare occurring at the end of revolution 70 (Fig. 1). Finally, the selection based on the availability of JEM-X (good) data leads to effective exposures of ∼15 ks, ∼55 ks, ∼186 ks, and ∼400 ks for the "ultra bright", "bright", "faint", and "ultra faint" states respectively. In all our spectral fits a constant was included to take into account the cross calibration uncertainties, and was found at a similar value.

Table 4. Best fit parameters obtained for the "Faint state" observed with *INTEGRAL*. Errors are given at the 90% level. Fluxes are in units of erg cm^{-2} s^{-1}.

bbody+po	kT or kT_e	Γ or τ	χ^2_ν	Unabs. flux	
	(keV)		(d.o.f.)	1−20 keV	20−200 keV
	1.51 ± 0.07	$2.35^{+0.15}_{-0.08}$	1.36 (45)	2.24×10^{-9}	5.19×10^{-10}
bbody+comptt	21^{+1}_{-8}	$1.3^{+0.2}_{-1.0}$	1.07 (44)	1.83×10^{-9}	4.26×10^{-10}

Following the procedure presented in Paper I, we first fitted the spectra from both instruments simultaneously, with a simple model consisting of an absorbed power law. The value of N_H, was frozen to the value obtained with RXTE (Swank & Markwardt 2003), i.e. 6×10^{22} cm^{-2}, since the useful energy range of JEM-X does not allow us to obtain a better constraint on this parameter. We note, however, that this parameter may change from one observation to the other (see our *RXTE* spectral analysis below), but the results of our 4–150 keV spectral analysis remain largely unchanged, this energy range being largely unaffected by absorption.

Since significant evolution at least in terms of luminosity, and possibly in terms of spectral parameters (Paper I) is expected, we present here the results of the spectral fits to the different "states" separately.

"Ultra Faint State": the source is not detected in any of the spectral channels of our ISGRI mosaic. Therefore it is not possible to construct a spectrum. We therefore did not include these data in our analysis since consistent comparison with the other states was not possible (mainly due to the lack of constraints on the possible hard tail, cut-off etc.)

"Faint State": the simple power law model gives a poor fit to the data with a reduced chi square $\chi^2_\nu = 2.56$ (47 d.o.f.). Following the results from Paper I, we added a black body component to the power law. This component is required at more than 5σ. The best fit parameters are reported in Table 4. Replacing the power law by a cut-off power law (`cutoffpl` hereafter CPL) slightly improves the fit (the cut-off is required at just the 3σ level), but the cut-off energy is poorly constrained ($E_{\rm cut} = 44^{+44}_{-18}$ keV) (all along the text errors are given at the 90% confidence level). A good fit is also achieved with a simple power law and a Gaussian ($\chi^2_\nu = 1.26$ for 44 d.o.f.). The photon index is compatible ($\Gamma = 2.32^{+0.06}_{-0.08}$) with the value obtained with the former model. The line parameters are those reported in Table 8. Note that the large uncertainty on the line parameters, its large width and normalisation could indicate a possible mixing of line and the black body emission, as will be discussed in Sect. 3.2.4. This possibility could explain well the inability of our fits to converge to sensible results when trying to fit the data including both the black body and the Gaussian.

We tentatively replaced the phenomenological models with more physical models of Comptonisation. Using the `comptt` model (Titarchuk 1994) alone does not provide a good fit to the data. As in the previous case, adding a black body component improves the fit significantly. The temperature of the seed photon for Comptonisation tends to too low values to be constrained. It is therefore frozen to 0.3 keV. The black body temperature is consistent with that obtained with the phenomenological model ($kT = 1.42 \pm 0.06$ keV). Note that if a Gaussian instead of the black body is added to the `comptt`, a good fit can be achieved, but the parameters of the line are not physically acceptable (the centroid tends to too low a value, while the width is too high). The JEM-X and ISGRI spectra are plotted with the `comptt+bbody` model superimposed in Fig. 2, left panel.

"Bright State": here again the simple model of an absorbed power law does not fit the data well ($\chi^2_\nu = 2.78$ for 47 d.o.f.). A cut-off component is not required at a high level ($\gtrsim 3\sigma$). A black body and a simple power law does not provide a good fit to the data. In fact, an alternative model of a power law with high energy cut-off and a Gaussian line provides a good fit to the data. The addition of the Gaussian leads to an improvement $\Delta\chi^2 = 36$ for Δd.o.f. = 3. The best fit parameters for this state are reported in Table 5, while the line parameters are discussed in Sect. 3.2.4. Note that besides the presence of the line, the spectral parameters are consistent with those presented in Paper I.

Fitting the data with the `comptt` alone leads to $\chi^2_\nu = 2.04$ for 45 d.o.f. Again a black body component is marginally detected ($\gtrsim 3\sigma$). As with the phenomenological model, the fit is greatly improved if a Gaussian instead of the black body is added to the `comptt` model. The Gaussian parameters are compatible with those found with the phenomenological model. Note that the temperature of the seed photon for Comptonisation is too low to be well constrained. We therefore fixed it at 0.3 keV. The best fit parameters are reported in Table 5, while the spectra are shown in Fig. 2 middle panel.

"Ultra Bright State": as in the other "states" the single component model does not represent the data well ($\chi^2_\nu = 3.61$ for 47 d.o.f.). A high energy cut-off is required at more than 5σ. Adding a black body does not bring significant improvement. On the other hand, adding a Gaussian improves the fit slightly ($\Delta\chi^2 = 15$ for Δd.o.f. = 3). The best fit parameters are reported in Table 5, while the line parameters are discussed in Sect. 3.2.4. Note that alternative models involving black body emission (either with a Gaussian and/or a high energy cut-off) do not provide a good description of the data. As in the "Bright" state the `comptt` provides an acceptable fit if a Gaussian is added to the model. The temperature of the seed photons for Comptonisation is again fixed at 0.3 keV. The line parameters are consistent with those found with the phenomenological model. The best fit parameters are reported in Table 5, while the broad band spectrum is shown in Fig. 2 right panel.

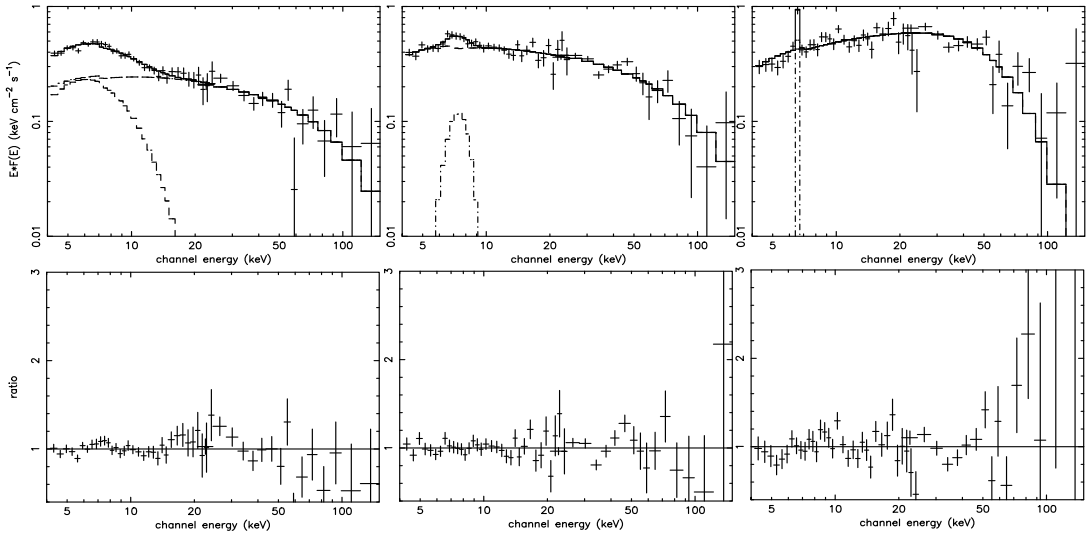

Fig. 2. *INTEGRAL*/JEM-X and ISGRI spectra with the best (physical) model superimposed in each case (see the text for details). The different component of the models (`comptt`, black body or Gaussian) are also plotted. From left to right, the panel correspond to the "Faint state", the "Bright state", the "Ultra bright state". The vertical axis is in $\nu - F_\nu$ units. The lower panels represent the ratio between the model and the data in each of the "states".

Table 5. Best fit parameters obtained with the different spectral model for the "Bright", and "Ultra Bright" states observed with *INTEGRAL*. Errors are given at the 90% level. Fluxes are in units of erg cm^{-2} s^{-1}. Note that a Gaussian line is included in the fit in all models. CPL stands for `cutoffpl` in XSPEC terminology

State	Model	Γ	$E_{\rm cut}$ or $kT_{\rm e}$	τ	χ^2_ν	Unabs. flux	
			(keV)		(d.o.f.)	1−20 keV	20−200 keV
Bright	CPL	$2.05^{+0.08}_{-0.14}$	71^{+29}_{-17}		1.48 (43)	2.52×10^{-9}	7.32×10^{-10}
	`comptt`		$22.0^{+15.6}_{-5.0}$	$1.2^{+0.5}_{-0.6}$	1.44 (43)	2.42×10^{-9}	7.12×10^{-10}
Ultra Bright	CPL	$1.37^{+0.14}_{-0.07}$	$27.1^{+6.7}_{-4.7}$		1.49 (43)	1.93×10^{-9}	9.54×10^{-10}
	`comptt`		$11.2^{+0.8}_{-0.5}$	$2.97^{+0.36}_{-0.15}$	1.75 (43)	2.09×10^{-9}	1.03×10^{-9}

3.2.2. PCA spectral analysis

During the 3 *RXTE* observations the source was dimmer than when detected with *INTEGRAL* (see e.g. the differences between Figs. 2 and 3). We fitted the spectra with the same spectral models, first a simple absorbed power law, or simple absorbed black body or disc black body. While the latter models give a poor description of the data, the former (after addition of a Gaussian at ∼6.4 keV to account for an excess due to Fe K complex emission) represents the data well for Obs. 1 and 2. The addition of the Gaussian leads to $\Delta\chi^2 = 56$, $\Delta\chi^2 = 101$ for Δd.o.f. = 3 in Obs. 1 and 2 respectively. The best fit parameters are reported in Table 6. The equivalent absorption column density ($N_{\rm H}$) was let free to vary in all spectral fits, and we note a slight decrease of $N_{\rm H}$ from Obs. 1 to Obs. 2, the latter being consistent with the results reported by Swank & Markwardt (2003).

The simple power law+Gaussian model fails to represent Obs. 3 ($\chi^2_\nu = 3.0$, 44 d.o.f.). Replacing the power law by a CPL leads to a good fit, an F-test indicates the cut-off is required at more than 5σ. Note that the CPL alone does not provide a good fit to the data ($\chi^2_\nu = 2.85$ for 46 d.o.f.). The value of $N_{\rm H}$ is slightly lower than during Obs. 2 (Table 6). Because a cut-off power law is usually interpreted as a signature of thermal Comptonisation, we replaced the phenomenological model by the `comptt` model. This more physical model represents the data well, but we note, however, that due to the 3 keV lower boundary of the PCA spectra, the input photon temperature is very poorly constrained (<1.12 keV at 90%, if it is left as a free parameter). We then froze this parameter to 0.3 keV in a second run. The best parameters are reported in Table 6. We note here that the value of $N_{\rm H}$ is more consistent with that obtained during Obs. 2. The line parameters are discussed in Sect. 3.2.4.

We then re-performed the fits to Obs. 1 and 2, either adding a high energy cut-off (with `highecut`) or replacing the power law by a CPL. The improvement to the fits is only marginal (just at the 3σ level) for Obs. 1, and $\gtrsim 3\sigma$ for Obs. 2, therefore

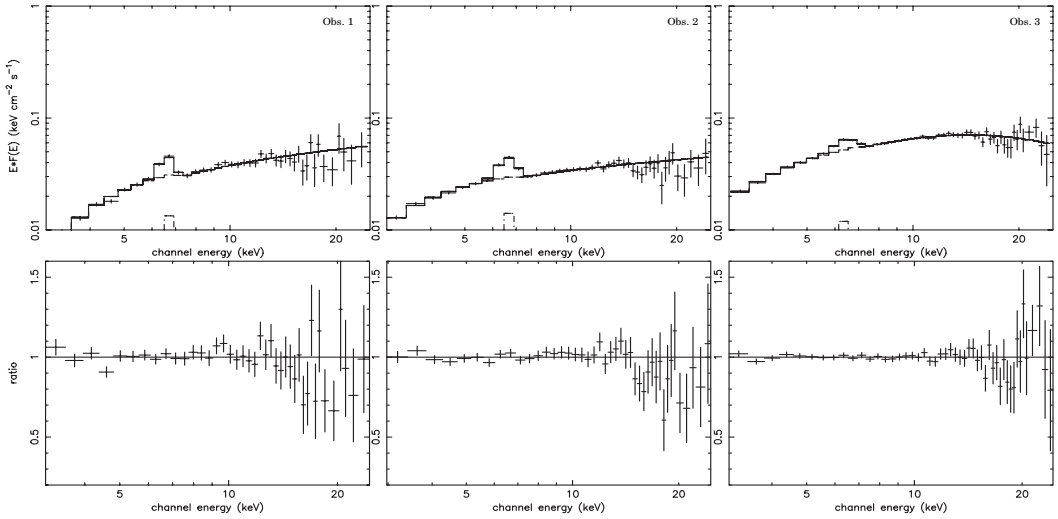

Fig. 3. *RXTE*/PCA spectra of EXO 1912+097/IGR J19140+0951 with the best fit model superimposed: a Gaussian at ∼6.5 keV, plus an absorbed power law for the left and middle one, and an absorbed power law with a high energy cut-off for the right one. The spectra are time ordered from left to right (1 year separation). The Gaussian is represented in all 3 spectra. Note that the same vertical scale as that of Fig. 2 is employed to facilitate the comparison. The lower panels represent the ratio between the best model and the data.

Table 6. Best fit parameters obtained from the spectral fits to the *RXTE*/PCA data. The errors are reported at the 90% confidence level. PL stands for power law, CPL for `cutoffpl` in XSPEC terminology.

Obs. Number	Model	$N_{\rm H}$	Γ	$E_{\rm cut}$ or $kT_{\rm e}$	τ	unabs. 1−20 keV flux	χ^2_ν
		$\times 10^{22}$ cm^{-2}		(keV)/(keV)	(keV)/	erg s^{-1} cm^{-2}	(d.o.f.)
1	PL	10.1 ± 2.0	1.64 ± 0.11			1.60×10^{-10}	0.95 (42)
2	PL	$5.8^{+1.4}_{-1.3}$	1.74 ± 0.08			1.47×10^{-10}	0.99 (42)
3	CPL	$3.85^{+1.2}_{-1.5}$	$0.98^{+0.17}_{-0.21}$	$13.7^{+3.9}_{-2.6}$		2.37×10^{-10}	0.95 (40)
	`comptt`	$5.8^{+0.9}_{-1.0}$		$5.0^{+0.5}_{-0.4}$	$5.3^{+0.5}_{-0.4}$	2.42×10^{-10}	0.99 (43)

not at high significance. We also replaced the phenomenological models by `comptt`, and although a good fit is achieved the parameters (especially the electron temperatures) are found to be quite high and very poorly constrained. The three spectra and the best fit models (simple power law for the first two and CPL for Obs. 3) are plotted in Fig. 3, together with the ratio between the model and the data.

Since the model parameters (especially the power law photon index) are strongly correlated to the value of $N_{\rm H}$, we represent the error contours of the photon index Γ vs. the value of $N_{\rm H}$, for the three observations in Fig. 4.

In addition to the simple power law fit, and in order to compare with the results from the fits to the *INTEGRAL* data, we tentatively fitted the spectra with the `comptt` model. The best fit parameters are reported in Table 6.

3.2.3. A closer look at RXTE observation 3

Since the 16 s PCA light curve shows that the source is very variable on short time scales, we separated the observation into two periods, one corresponding to the low and steady flux (second interval in Fig. 5 left), and the other one corresponding to the high flux and large variations (third interval in Fig. 5 left).

We applied the same (simple) models as discussed in the previous section. While for the first interval a simple absorbed power law (plus a Gaussian) fits the data well, the same model yields a poor fit for the second ($\chi^2_\nu = 3.48$ (44 d.o.f.)). A cut-off improves the fit, and is required at more than 5σ. The best fit results are reported in Table 7, while the spectra and best fit models are shown in Fig. 5. In this case again the `comptt` fits the data well. The temperature of the seed photons is again fixed at 0.3 keV. As for the global spectrum, we remark that the absorption column returned from the fit with this model is slightly higher than the value obtained with CPL.

We note a significant evolution of the absorption column density and of the power law photon index between the two intervals. In order to check whether the evolution of both was real, we re-performed the fits freezing $N_{\rm H}$ to its mean value (Table 6). The spectral parameters obtained for both fits are compatible with those found leaving all parameters free to vary,

Table 7. Best fit parameters to the PCA fits of the two intervals from Obs. 3.

Interval	Model	$N_{\rm H}$	Γ	$E_{\rm cut}$ or $kT_{\rm e}$	τ	unabs. 1–20 keV flux	χ^2_ν
		$\times 10^{22}$ cm^{-2}		(keV)		erg s^{-1} cm^{-2}	(d.o.f.)
1	PL	$2.5^{+1.0}_{-1.3}$	$1.86^{+0.06}_{-0.10}$			1.09×10^{-10}	0.87 (44)
2	CPL	$5.4^{+1.0}_{-1.2}$	$0.86^{+0.15}_{-0.18}$	$11.9^{+2.3}_{-1.8}$		3.45×10^{-10}	0.83 (43)
	comptt	$7.0^{+1.0}_{-1.2}$		4.7±0.3	$5.8^{+0.6}_{-0.4}$	3.84×10^{-10}	0.92 (43)

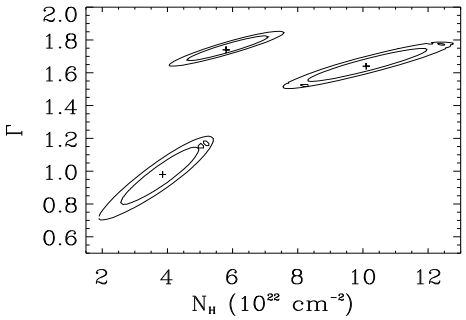

Fig. 4. Error contours for the column density ($N_{\rm H}$) and the power law photon index (Γ) derived from the fits to the three *RXTE*/PCA spectra. The crosses mark the location of the best fit values, and the 68% and 90% confidence contours are shown.

except the power law photon index which tends to a softer value in interval 1 ($\Gamma = 2.11 \pm 0.05$), and a to harder one for interval 2 ($\Gamma = 1.38 \pm 0.03$). Since $N_{\rm H}$ and Γ are tightly correlated, we also re-performed the fit freezing Γ to its mean value, and allowing $N_{\rm H}$ to vary. While for interval 2 the spectral parameters obtained in this case are close to the ones obtained when everything is free to vary, this method yields a poor fit for interval 1. We take these results as evidence that both Γ and $N_{\rm H}$ vary between both intervals. Note that this likely variation of the absorption is reinforced by the variations of $N_{\rm H}$ we observe between Obs. 1, 2 and 3 (Table 6).

3.2.4. The iron line

As mentioned previously in all the *INTEGRAL* and *RXTE* spectra, an iron Kα fluorescence line is required in the spectral fits. The parameters of the line obtained from the spectral fit to each observation are reported in Table 8. Note that these are obtained from the fits with the phenomenological models, but no significant differences are found in the spectra where a `comptt` model is used. One could wonder whether the line is intrinsic to IGR J19140+0951 itself, or whether it could originate from the Galactic background. The main argument that points towards an origin intrinsic to the system is that if the line was due to the Galactic ridge, we would expect its flux to be roughly constant. This is obviously not the case here.

It is interesting to note that in almost all cases, (except in the "Bright" and "Faint" states), the parameters inferred for the line could be indicative of a narrow line, rather than a broad line. In fact for both instruments the upper limit on the line width indicates that we are limited by the instrumental spectral resolution. The case of the faint and bright states seem different since our fits indicate a broad line (Table 8). Our spectral fits to the *INTEGRAL* data (Sect. 3.2.1) indicate that the "Bright" state is spectrally intermediate between the "Faint" state and the "Ultra-bright" one, as we will discuss further below. In particular in the soft X-rays (4–8 keV), a black body component could be present in the spectra of the "Bright" state, and represents the data well for the faint state. In both cases, a fit to the data with a black body and a Gaussian (besides the power law) does not converge on sensitive parameters for either of the components. The broad line we found instead could be indicative of a "mixture" of faint black body emission (poorly constrained given the 4 keV lower boundary of our fits) and a Gaussian line. This possibility is compatible with the evolution between the three *INTEGRAL* "states", as clearly seen of Fig. 2, where black body emission dominates the soft X-ray in the "Faint state" (when either no line is needed or a very broad one), to the "Ultra Bright" state, where no black body is detected, and with a good constraint on the line.

4. Discussion

4.1. A neutron star primary?

We performed a thorough spectral analysis of the *INTEGRAL* source IGR J19140+0951 using a well-sampled high energy monitoring with *INTEGRAL* in 2003 March–May, and adding 3 *RXTE* observations performed at different epochs. As already observed (Paper I), IGR J19140+0951 is highly variable on timescales from months down to hours, and it can show variations on shorter timescales as seen during *RXTE* observation 3 (Fig. 5). This behaviour is reminiscent of Galactic X-ray binaries (XRB), and our deep analysis further confirms the Galactic nature of IGR J19140+0951, already proposed in other publications (Paper I, Corbet et al. 2004).

When observed with *RXTE*, the source was dim, with a 1–200 keV (unabsorbed) luminosity of $\sim 3.4 \times 10^{36} \times (D/10 \text{ kpc})^2$ erg/s (Obs. 3), and a spectrum typical of Comptonisation of soft photons by a low temperature plasma ($kT \sim 5$ keV) with a relatively high optical depth ($\tau \sim 5$). This could correspond to the "ultra faint state" which seems to be the state in which the source spends most of its time as indicated by our *INTEGRAL* monitoring. During the *INTEGRAL* observations, the luminosity is up to about 10 times higher, with a maximum of $\sim 3.7 \times 10^{37} \times (D/10 \text{ kpc})^2$ erg/s. Here significant spectral evolution is observed since in one case a bright thermal component may be present in the soft X-rays while it is either marginal or not detected in the other "states" defined

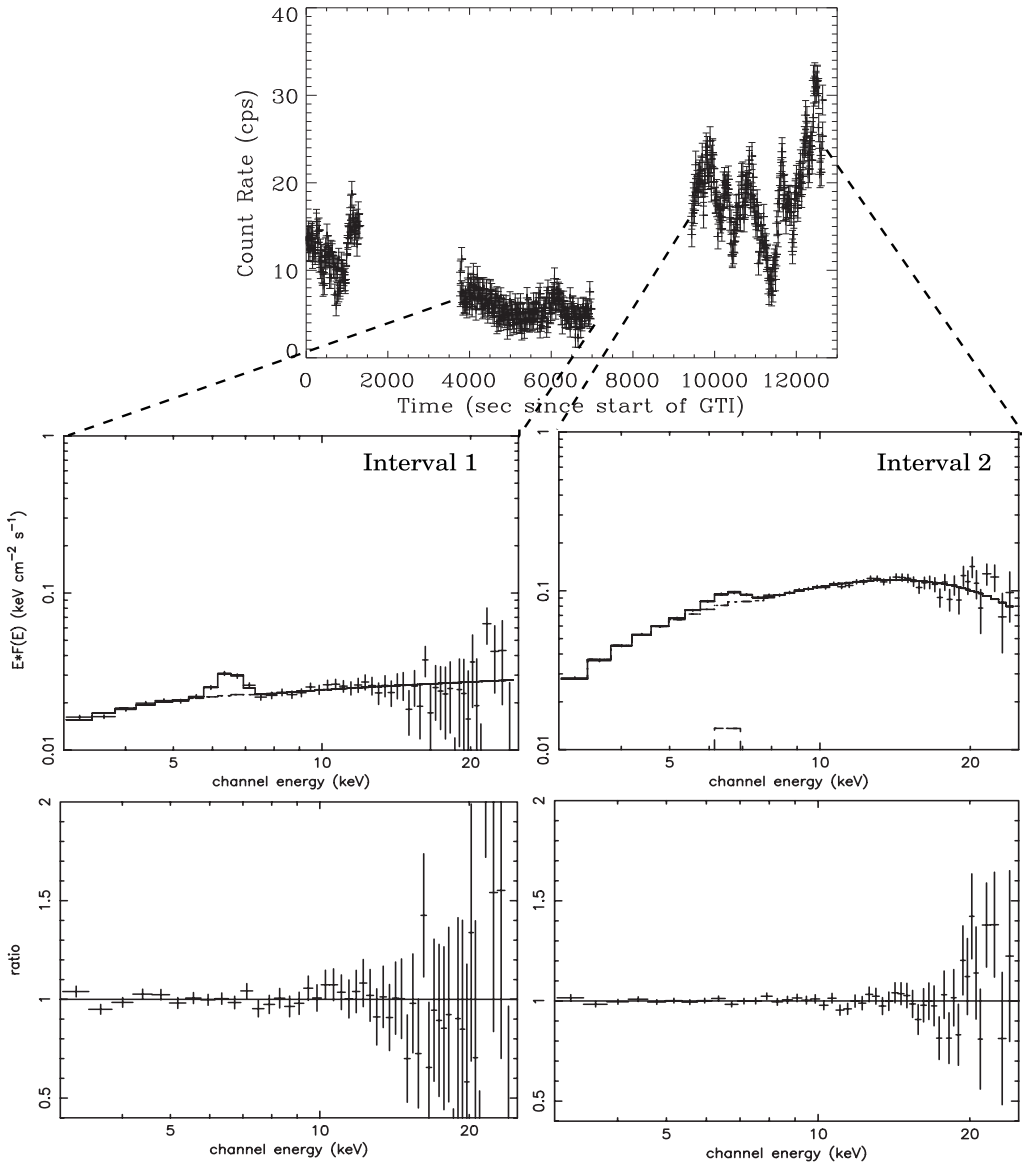

Fig. 5. *Top*: 2−40 keV PCA (Top Layer of PCU 2) light curve of Obs. 3. *Middle and bottom*: *left:* PCA 3−25 keV spectrum of interval 1, and its best fit model, the ratio between the model and the data is represented below. *Right:* same as left but for interval 2. Note that the same vertical scale is employed in both to facilitate the comparison.

from the ISGRI light curve. A clear pivoting between the three *INTEGRAL* spectra is clearly visible (Fig. 2). The phenomenological models may indicate a spectral transition from something resembling a standard soft state to a hard state (Tanaka & Shibazaki 1996), as seen in BHC, but the temperature of the black body, and the parameters of the Comptonisation, especially during the faint *RXTE* observations are more comparable to those of a neutron star primary. The spectral parameters obtained from our fits during the "Bright state" indicate that it is spectrally intermediate between the "Faint" state and the "Ultra bright" state (Tables 4 and 5). A hint for a black body component is indeed found here, although the best fit involves

Table 8. Parameters of the iron line obtained from the spectral fits to the *INTEGRAL* and *RXTE* data. Obs. 1, 2, 3 refer to the average *RXTE* spectra, while Obs. 3 low and high refer to the sub interval presented in Sect. 3.2.3. Errors are given at the 90% confidence.

Obs.	$E_{\rm centroid}$ (keV)	Width (σ) (eV)	Flux ($\times 10^{-4}$ ph/cm^2/s)	Eq. width (eV)
Faint State	$6.5^{+0.4}_{-0.8}$	1683^{+587}_{-445}	125^{+81}_{-39}	1560
Bright State	$7.2^{+0.4}_{-1.3}$	785^{+1299}_{-691}	50^{+112}_{-21}	535
Ultra Bright State	6.6 ± 0.2	<475	43^{+19}_{-17}	410
Obs. 1	6.53 ± 0.12	<518	$3.2^{+1.1}_{-0.9}$	385
Obs. 2	6.56 ± 0.10	375^{+211}_{-363}	$3.5^{+0.9}_{-0.8}$	469
Obs. 3	$6.37^{+0.13}_{-0.17}$	419^{+180}_{-181}	$3.5^{+1.6}_{-0.9}$	258
Obs. 3 low	$6.44^{+0.12}_{-0.15}$	<641	$2.1^{+0.8}_{-0.6}$	388
Obs. 3 high	$6.36^{+0.13}_{-0.08}$	460^{+276}_{-296}	$4.7^{+2.2}_{-1.4}$	213

an iron line. The large width of the latter, and the inability of our fits to converge when trying to model the spectra with both the line and the black body, tend to indicate that the huge line is in fact a mixture of a narrower feature with a fainter and cooler thermal component, for which no constraints can be obtained with the 4 keV lower boundary of our spectral analysis.

In order to try to constrain the primary type, we first compare the source luminosity with that of other known Galactic XRBs. To do so we plotted the 20−200 keV vs. 1−20 keV luminosities for the brightest *INTEGRAL* and *RXTE* states, at three different distances and over-plotted it with those presented in Barret et al. (1996) (Fig. 6).

It is clear from Fig. 6 that, unless the source is at a large distance of 20 kpc or beyond, it always falls in the "X-ray burster box", except for the *INTEGRAL* point at 10 kpc, which is exactly half way between the 2 standard states of Cyg X-1. However the delimitation between the two regions is purely empirical and based on measurements made up to 1996, on a sample of X-ray bursters only for the neutron stars (which at the time of writing were the only known neutron star X-ray binaries with hard X-ray tails extending to at least 100 keV). Since then, Di Salvo et al. (2001) have indeed shown that some neutron star systems, could definitely lie outside this so called "X-ray burster box". Therefore unless a very high luminosity hard tail is found, the fact that a source lies outside the "X-ray burster box" is not a definite proof for a black hole binary (Di Salvo et al. 2001). In addition, the spectral parameters we obtain from our spectral fits in all "states" are radically different from those usually observed in black hole binaries (e.g. McClintock & Remillard 2004), even in their quiescent states (e.g. Kong et al. 2002). This is particularly true for the parameters of the cut-off energy, or equivalently the electron temperature which are in agreement with those presented by Barret (2000) in the case of neutron star primaries.

As already pointed out in another system (4U 2206+54 Torrejón et al. 2004), we note that during the "Faint" state the black body temperature is high, while the source luminosity is not very high (although higher than in 4U 2206+054). Following the procedure presented by Torrejón et al. (2004),

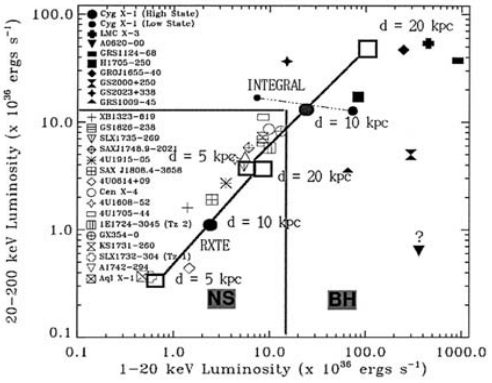

Fig. 6. IGR J19140+0951 luminosities as obtained from the spectral fits presented in this paper, and comparison with the "classification" proposed in Barret et al. (1996). The two continuous lines ending with squares indicate the positions of IGR J19140+0951 as obtained in this study with *INTEGRAL* and *RXTE* assuming three different distances (open squares are at 5 and 20 kpc, filled circles are at 10 kpc) for IGR J19140+0951. Based on Barret et al. (1996), systems with neutron star primaries would rather lie in the bottom left corner ("X-ray burster box") of the plot, whereas system with black hole binaries would lie outside this box (see however di Salvo et al. 2001).

we can estimate the radius of the black body emitter following $R_{\rm bb} = 3 \times 10^4 \times d_{\rm kpc} \sqrt{f^{\rm bol}/(1+y)}/kT_{\rm bb}$ (in't Zand et al. 1999), where y is the Compton parameter $y \propto kT_{\rm e}\tau^2$, $f^{\rm bol}$ the "bolometric" flux and $kT_{\rm bb}$ the black body temperature. Using the values found in our study (expanding the flux to the 0.1−200 keV range following in't Zand et al. 1999), we obtain $R_{\rm bb} = 0.999 \times d_{\rm kpc}$ km. We remark here a factor of 2 discrepancy between Torrejón et al. (2004) and in't Zand et al. (1999), the values given in the former are the diameter of the black body emitter, but this does not change their conclusions. This value implies that even at a very far distance (e.g. 20 kpc, therefore outside of our Galaxy, which appears rather unlikely), the black body radius is consistent with the radius of a neutron star.

4.2. Possible type of the system

The absorption column density ($N_{\rm H}$ =~3−10 × 10^{22} cm^{-2}) of IGR J19140+0951 derived from the spectral fits to the *RXTE* data is much higher than the Galactic absorption towards the source (1.26 × 10^{22} cm^{-2} Dickey & Lockman 1990). This favours an absorption intrinsic to the object, and therefore the presence of absorbing material in the vicinity of the compact object. The variations of the absorption (Fig. 4 and Table 7) also point toward an absorption intrinsic to the source. This is in fact similar to what is observed in IGR J16320-4751 (Rodriguez et al. 2003b), or 4U 1700−37 (Boroson et al. 2003), in which the absorption is seen to vary by a factor of about 2 in the former source (a most likely High Mass X-ray Binary HMXB; Rodriguez et al. 2003b) and 10 in the latter (a dynamically confirmed HMXB). The presence of absorbing material is consistent with the detection of a (cold) iron line. It is interesting to note that although when comparing Obs. 1, 2 and 3, the iron line fluxes are all comparable within the uncertainties (Table 8), while $N_{\rm H}$ varies significantly, the line flux is much stronger in Obs. 3 high (interval 2), than in Obs. 3 low (interval 1), i.e. it is stronger here when $N_{\rm H}$ is higher. In addition, there seems to be a tight correlation between the 1−200 keV (unabs.) flux of IGR J19140+0951 and the flux of the line although the case of the "Faint" state does not obey this relation, and the parameters of the line are poorly constrained in the "Bright" state. This relation, and the relative constancy of the line energy in most of the cases suggest that the line is produced through fluorescence in a cold medium as in e.g. Vela X-1 (Ohashi et al. 1984). In addition, the intensity of the iron line during the *INTEGRAL* observations is comparable to the intensity observed in the HMXB GX 301−2 at a similar flux (Saraswat et al. 1996). In the latter system the line width (measured with *ASCA*) was consistent with the instrumental spectral resolution, which seems to be the case in IGR J19140+0951, although the energy resolution of both *RXTE*/PCA and *INTEGRAL*/JEM-X is very poor in comparison to that of *ASCA*/SIS. These similarities between different systems would tend to indicate IGR J19140+0951 is an HMXB, rather than a system containing a low-mass secondary star (LMXB). Finally we observe that the hardest spectra (i.e. those for which the electron temperature or the cut-off energy is the highest) are observed at higher luminosities, which again is very similar to the HMXB 4U 2206+54 (Masetti et al. 2004), and rather contrary to what observed in the case of LMXB (Barret 2001).

Independently, the temporal variability on timescale ~1000 s is very similar to the HMXBs 4U 2206+054 (Nereguela & Reig 2001), 2S 0114+65 (Yamauchi et al. 1990), and Vela X-1 (Kreykenbohm et al. 1999). In these systems, this variability is commonly interpreted as due to random inhomogeneities in the accretion flow (e.g. Masetti et al. 2004 and references therein). The level of variability from 0.06 Hz on is compatible with what was found in 4U 1700-37 (Boroson et al. 2003) or 4U 2206+54 (Nereguela & Reig 2001), i.e. the variability is compatible with purely Poisson noise. In the former source significant aperiodic variability is detected only below 0.01 Hz, although a 13 mHz QPO is detected at a fractional amplitude 4.0% (Boroson et al. 2003). As discussed in Sect. 3.1, if such a feature was present in IGR J19140+0951, it should have been detected at least in *RXTE* Obs. 3. In 4U 2206+54, on the other hand, significant aperiodic variability is seen below ~0.06 Hz. However, no QPOs are detected in this system. Again the similarity of the behaviour of IGR J19140+0951 with that of confirmed HMXB, would tend to argue in favour of a high mass secondary star in IGR J19140+0951 and therefore X-ray luminosity due to wind accretion onto the compact object.

The hypothesis of IGR J19140+0951 being a HMXB is again in good agreement with the relatively large value of the orbital period of 13.55 days (Corbet et al. 2004), since HMXBs have usually higher orbital period than LMXBs. Note that this is not a definite proof since some LMXB can have large orbital period as e.g. GRS 1915+105 and GRO J1744-28 with ~33 days and ~12 days, respectively. The fact that the modulation is sinusoidal (Corbet et al. 2004) would tend to indicate a high inclination system (i.e. the orbital plane almost parallel to the line of sight) rather than variations of the X-ray flux due to perigee passage of the compact object in a highly eccentric orbit.

Finally, it should be noted that IGR J19140+0951 lies in the direction of the Sagittarius arm of our Galaxy, which is a region rich of high mass/young stars, and therefore HMXBs. This location could provide another indirect support for IGR J19140+0951 being a HMXB, as proposed for 3 similar sources lying in the Norma arm (Revnivtsev 2003). This arm is located about 2 kpc from the Sun, and if IGR J19140+0951 was associated with this region its luminosity as obtained from our spectral fit (10^{35}−10^{36} erg s^{-1}) would be completely consistent with that of the aforementioned HMXB/neutron star binaries, as Vela X-1.

5. Conclusion

We have presented a detailed study of the hard X-ray properties of IGR J19140+0951 observed at different times with *INTEGRAL* and *RXTE*. From a well-sampled monitoring of the source in 2003 March–May, we deduced that IGR J19140+0951 spends most of its time in a low luminosity state, which likely corresponds to the state observed with *RXTE* on three occasions. The source spectrum is characteristic for thermal Comptonisation, and on one occasion we have evidence for a black body component in the spectrum. From the comparison of the spectral properties of IGR J19140+0951 with those of other XRBs, we suggest that this system hosts a neutron star rather than a black hole.

The source spectra show evidence for a variable intrinsic absorption which indicate that the compact source is embedded in a dense cloud. This and the detection in all our spectra of a bright (and thin) iron line, whose flux is higher in the higher luminosity states points towards radial accretion from a stellar wind. Therefore it is very likely that IGR J19140+0951 is a HMXB, with properties similar to those of other well known HMXB.

The arguments presented in the present study are, however, only indicative, none of them being definite. In particular the identification of counterparts at other wavelengths

of the electromagnetic spectrum should allow one to truly confirm the nature of the system and/or the compact object. Such a study is, however, not possible at the moment given the relatively large error on the position of the source. Observations with high resolution X-ray satellites, such as *Chandra* or *XMM-Newton*, should permit a better position to be found, counterparts to be searched for, and possibly determine whether IGR J19140+0951 is indeed the same source as EXO 1912+097. In addition such a study should permit one to obtain much better constraints on the absorption and line parameters.

Acknowledgements. The authors acknowledge M. Cadolle-Bel, A. Goldwurm, A. Gros, P. Kretschmar, A. Paizis, S. Martínez Núñez & R. Walter for useful discussions and help with the INTEGRAL data reduction, and the anonymous referee for helpful comments, and the suggestion of describing the spectral extraction in more detail, which helped to improve the paper. We also acknowledge P. Lubinski for useful discussions on the spectral extraction methods, and for sharing some results with us prior to publication. JR is very grateful to T. E. Strohmayer and the RXTE help desk for appreciable help on the PCA confusion issue, and J. Swank for triggering the RXTE 2003 ToO. JR acknowledges financial support from the French space agency (CNES). DCH gratefully acknowledges a fellowship from the Academy of Finland. SES is supported by the UK PPARC. J.S. acknowledges the financial support of Vilho, Yrjö and Kalle Väisälä foundation and is grateful to the Finnish space research programme Antares and TEKES. This paper is based on observations with INTEGRAL, an ESA project with instruments and science data centre funded by ESA member states (especially the PI countries: Denmark, France, Germany, Italy, Switzerland, Spain), Czech Republic and Poland, and with the participation of Russia and the USA. This research has also made use of data obtained through the High Energy Astrophysics Science Archive Center Online Service, provided by the NASA Goddard Space Flight Center

Appendix A: ISGRI Spectral extraction from images

Principle of the method

Numerous issues with OSA, which remains under development, are reported on the ISDC website'[1] Of particular relevance to this work: "ii_spectra_extract runs per science window and in case of weak sources, addition of many spectra obtained for the different science windows may give a bad total spectrum. Spectral reconstruction is very sensitive to the background correction. In certain cases running the imaging procedure on several (large) energy bands can provide a better spectrum".

We therefore extracted the spectra of IGR J19140+0951 using a method based on the count rates extracted from the images. For the whole data set (only restricted to the SCW where the source is less than 5° from the center of the FOV), we ran the software up to the IMA level. We extracted the products 20 energy bins defined such that they match exactly the boundaries of the redistribution matrix file (rmf). The energy bands are 20.65−24.48, 24.48−28.31, 28.31−32.14, 32.14−35.97, 35.97−39.8, 39.8−43.36, 43.36−49.38, 49.38−53.21, 53.21−57.04, 57.04−60.87, 60.87−68.52, 68.52−76.18, 76.18−87.67, 87.67−99.16, 99.16−122.14, 122.14−150.86, 150.86−196.82, 196.82−300.22, 300.22−518.5, 518.5−1000 keV. Note that the energy ranges above ∼300 keV are of limited use for most of the sources.

Once this is finished, for each SCW, the intensity, exposure, variance and significance maps of the field are obtained in each of the aforementioned energy ranges. The average count rate, $F(E_i, \alpha, \delta)$, in the energy range E_i, over a list of p SCW, at the position (α, δ) of a given source is given by:

$$F(E_i, \alpha, \delta) = \frac{\sum_{j=1}^{p} \frac{F_j(E_i,\alpha,\delta)}{\mathrm{var}_j(E_i,\alpha,\delta)}}{\sum_{j=1}^{p} \frac{1}{\mathrm{var}_j(E_i,\alpha,\delta)}} \quad (2)$$

where $F_j(E_i, \alpha, \delta)$ is the count rate in SCW $\#j$, in the energy range E_i at a (sky) position (α, δ), and $\mathrm{var}_j(E_i, \alpha, \delta)$ is the associated variance value.

Repeating Eq. (2) from $i = 1$, to $i = 20$ (in our case) allowed us to obtain the source spectrum over the given list of SCW.

Validity of the method: Estimate of a Crab spectrum

In order to validate our method, we extracted a Crab spectrum following the same method. In order to be even more rigourous, we restricted our comparison to Crab observations performed with *the same observing pattern as most of our observations*, i.e. a hexagonal pattern. However we point out that a check on an arbitrary pattern gave similar and consistent results. The validation of the spectral extraction method is currently a work in progress and detailed results and issues will be presented in a forthcoming paper (Lubinski et al. in prep.). In general, and for what concerns this work, the discrepancy between the standard spectral extraction and this new method does not exceed 5% (Lubinski, priv. comm.). Our particular spectral analysis of the Crab using both methods showed that the spectral parameters were compatible within 1% for the photon index, within about 5% for the normalization, and the 20−200 keV flux discrepancy is about 2%.

[1] See the known issues at:
`http://isdc.unige.ch/Soft/download/osa/osa_sw/osa_sw-4.1/osa_issues.txt`.

References

Arnaud, K. A. 1996, in Astronomical Data Analysis Software and Systems V, ed. G. H. Jacoby, & J. Barnes, ASP Conf. Ser., 101, 17
Barret, D., McClintock, J. E., & Grindlay, J. E. 1996, ApJ, 473, 963
Barret, D. 2001, Adv. Space Res., 28, 307
Boroson, B., Vrtilek, S. D., Kallman, T., & Corcoran, M. 2003, ApJ, 592, 516
Cabanac, C., Rodriguez, J., Hannikainen, D., et al. 2004, ATel, 272
Corbet, R. H. D., Hannikainen, D. C., & Remillard, R. 2004, ATel, 269
Courvoisier, T. J.-L., Walter, R., Beckmann, V., et al. 2003, A&A, 411, L53
Dickey, J. M., & Lockman, F. J. 1990, ARA&A, 28, 215
Di Salvo, T., Robba, N. R., Iaria, R., et al. 2001, ApJ, 554, 49
Fuchs, Y., Rodriguez, J., Mirabel, I. F., et al. 2003, A&A, 409, L35
Hannikainen, D. C., Rodriguez, J., & Pottschmidt, K. 2003, IAUC, 8088

Hannikainen, D. C., Rodriguez, J., Cabanac, C., et al. 2004a, A&A, 423, L17, Paper I
Hannikainen, D. C., Vilhu, O., Rodriguez, J., et al. 2004b, Proc. of the 5th INTEGRAL workshop held in Munich, February 2004, ESA SP-552 [arXiv:astro-ph/0405349]
in't Zand, J. M., Verbunt, F., Strohmayer, T. E., et al. 1999, A&A, 345, 100
Jahoda, K., Swank, J. H., Gilmes, A. B., et al. 1996, Proc. SPIE, 2808, 59
Kong, A. K. H., McClintock, J. E., Garcia, M. R., Murray, S., & Barret, D. 2002, ApJ, 570, 277
Kreykenbohm, I., Kretschmar, P., Wilms, J., et al. 1999, A&A, 341, 141
Lebrun, F., Leray, J.-P., Lavocat, P., et al. 2003, A&A, 411, L141
Leahy, D. A., Darbro, W., Elsner, R. F., et al. 1983, ApJ, 266, 160
Lu, F. J., Li, T. P., Sun, X. J., Wu, M., & Page, C. G. 1996, A&AS, 115, L395
Lund, N., Budtz-Jørgensen, C., Westergaard, N. J., et al. 2003, A&A, 411, L231
Maccarone, T. J., & Coppi, P. S. 2003, MNRAS, 338, 189
Masetti, N., Dal Fiume, D., Amati, L., et al. 2004, A&A, 423, 311
McClintock, J. E., & Remillard, R. A. 2004, in Compact Stellar X-ray Sources (Cambridge Univ. Press), in press [arXiv:astro-ph/0306213]
Nereguela, I., & Reig, P. 2001, A&A, 371, 1056
Ohashi, T., Inoue, J., Koyama, K., et al. 1984, PASJ, 36, 699
Revnivtsev, M. 2003, Astron Lett., 2003 [arXiv:astro-ph/0304353]
Rodriguez, J., Corbel, S., & Tomsick, J. A. 2003a, ApJ, 595, 1032
Rodriguez, J., Tomsick, J. A., Foschini, L., et al. 2003b, A&A, 407, L41
Rodriguez, J., Fuchs, Y., Hannikainen, D. C., et al. 2004a, Proc. of the 5th INTEGRAL workshop held in Munich, February 2004a, ESA SP-552 [arXiv:astro-ph/0403030]
Rodriguez, J., Corbel, S., Kalemci, E., Tomsick, J. A., & Tagger, M. 2004b, ApJ, 612 [arXiv:astro-ph/0405398]
Rothschild, R. E., Blanco, P. R., Gruber, D. E., et al. 1998, ApJ, 496, 538
Saraswat, P., Yoshida, A., Mihara, T., et al. 1996, ApJ, 463, 726
Sunyaev, R. A., & Titarchuk, L. R. 1980, A&A, 86, 121
Swank, J. H., & Markwardt, C. B. 2003, ATel, 128
Swank, J. H. 2004, Proc. of X-Ray Timing 2003: Rossi and Beyond, ed. P. Kaaret, F. K. Lamb, & J. H. Swank [arXiv:astro-ph/0402511]
Tanaka, Y., & Shibazaki, N. 1996, ARA&A, 34, 607
Titarchuk, L. 1994, ApJ, 434, 313
Torrejón, J. M., Kreykenbohm, I., Orr, A., Titarchuk, L., & Nereguela, I. 2004, A&A, 423, 301
Ubertini, P., Lebrun, F., Di Cocco, G., et al. 2003, A&A, 411, L131
Vedrenne, G., Roques, J. P., Schöenfelder, V., et al. 2003, A&A, 411, L63
Winkler, C., Courvoisier, T. J.-L., Di Cocco, G., et al. 2003, A&A, 411, L1
Yamauchi, S., Asaoka, I., Kawada, M., et al. 1990, PASJ, 42, L53

9.2 L'éruption du trou noir IGR J17497−2721

THE ASTROPHYSICAL JOURNAL, 655: L97–L100, 2007 February 1

THE DISCOVERY OUTBURST OF THE X-RAY TRANSIENT IGR J17497−2821 OBSERVED WITH *RXTE* AND ATCA

JÉRÔME RODRIGUEZ,[1] MARION CADOLLE BEL,[1,2] JOHN A. TOMSICK,[3,4] STÉPHANE CORBEL,[1] CATHERINE BROCKSOPP,[5] ADA PAIZIS,[6] SIMON E. SHAW,[7,8] AND ARASH BODAGHEE[8,9]

Received 2006 November 10; accepted 2006 December 14; published 2007 January 11

ABSTRACT

We report the results of a series of *RXTE* and ATCA observations of the recently discovered X-ray transient IGR J17497−2821. Our 3–200 keV PCA+HEXTE spectral analysis shows very little variations over a period of ∼10 days around the maximum of the outburst. IGR J17497−2821 is found in a typical low-hard state (LHS) of X-ray binaries (XRBs), well represented by an absorbed Comptonized spectrum with an iron edge at about 7 keV. The high value of the absorption (∼4×10^{22} cm^{-2}) suggests that the source is located at a large distance, either close to the Galactic center or beyond. The timing analysis shows no particular features, while the shape of the power density spectra is also typical of the LHS of XRBs, with ∼36% rms variability. No radio counterpart is found down to a limit of 0.21 mJy at 4.80 and 8.64 GHz. Although the position of IGR J17497−2821 in the radio to X-ray flux diagram is well below the correlation usually observed in the LHS of black holes, the comparison of its X-ray properties with those of other sources leads us to suggest that it is a black hole candidate.

Subject headings: accretion, accretion disks — black hole physics — stars: individual (Cygnus X-1, IGR J17497−2821, SWIFT J1753.5−0127, XTE J1550−564)

1. INTRODUCTION

Transient X-ray binaries (XRBs) are known to show a series of different X-ray spectral states during their outbursts. A certain number of these objects, however, have undergone outbursts during which they remained in the low-hard state (LHS; e.g., Hynes et al. 2000; Brocksopp et al. 2004; Rodriguez et al. 2006a; Cadolle Bel et al. 2006b). A strong correlation exists between the radio and X-ray fluxes during this state (Corbel et al. 2003; Gallo et al. 2003). This may indicate some influence of the radio jet in the X-ray domain. The study of the LHS should therefore reveal important clues to the connection between the accretion and ejection processes. Interestingly, black hole (BH) transients are more radio-loud than neutron stars (NSs) by a factor of ∼30 (Migliari & Fender 2006) in the LHS.

IGR J17497−2821 was discovered with the *INTEGRAL* Soft Gamma-Ray Imager (ISGRI) on 2006 September 17, as a new hard XRB (Soldi et al. 2006) at Galactic coordinates $l = 0.97°$, $b = -0.46°$. Given that the line of sight to the source passes close to the Galactic center, and assuming a distance of 8 kpc, Kuulkers et al. (2006) estimated a 2–100 keV (unabsorbed) luminosity of ∼10^{37} ergs s^{-1}. The position and luminosity strongly indicate IGR J17497−2821 is a Galactic XRB. The preliminary spectral analysis of their *INTEGRAL* data led Kuulkers et al. (2006) to further suggest that the source was in a LHS typical of BH and NS XRBs. A follow-up observation with the *Chandra X-Ray Observatory* allowed a fine X-ray position to be given at $\alpha = 17^{h}49^{m}38.037^{s}$, $\delta = -28°21'17.37''$ ($\pm 0.6''$, at 90% confidence; Paizis et al. 2006). This refined X-ray position permitted Paizis et al. (2006) to identify the probable optical/IR counterpart and classify it as a red giant K-type star, making IGR J17497−2821 a low-mass X-ray binary.

Soon after the discovery, we triggered our *Rossi X-Ray Timing Explorer* (*RXTE*) program P92016 as well as radio observations with the Australian Telescope Compact Array (ATCA), aiming to identify the nature of the system. We report here the results of those campaigns.

2. OBSERVATIONS AND DATA ANALYSIS

2.1. *X-Ray Observations*

Our *RXTE* program has been divided into seven pointings, the details of which are reported in Table 1. Figure 1 shows the 3–30 keV *RXTE* Proportional Counter Array (PCA) and 15–50 keV *Swift* Burst Alert Telescope (BAT) light curves of IGR J17497−2821 over the outburst. The PCA data were reduced in the same way as the data in Rodriguez et al. (2003) but with the latest version of the HEASOFT software package. Since the source is located in a crowded area, standard background subtraction is not sufficient to remove the contribution of other sources and the Galactic bulge (about 10 mcrab between 2 and 10 keV; Markwardt & Swank 2006). In order to better estimate the sky background at the source position, we analyzed an *RXTE* observation of the nearby BH candidate XTE J1748−288 made at the end of its 1998 outburst, when the source flux was comparable with that of the Galactic background (ObsID 30185-01-20-00). The best-fitted model of this observation was then used as an extra background component for the spectral fittings of all our observations.

For the High-Energy X-Ray Timing Explorer (HEXTE), we extracted spectral data from the cluster B unit only, since cluster A no longer obtains a background measurement because the rocking has ceased. We checked that "plus" and "minus" offset pointings gave similar spectra (indicating that no active sources contributed to the background) and combined the two pointings to obtain background spectra. The remaining processes for HEXTE reduction are similar to the procedures presented in Rodriguez et al. (2003). The PCA and HEXTE spectra of each

[1] Astrophysique Interaction Multiéchelles CEA Saclay, DSM/DAPNIA/SAp, Gif-sur-Yvette, Cedex, France.
[2] European Space Astronomy Centre, Madrid, Spain.
[3] Space Sciences Laboratory, University of California, Berkeley, CA.
[4] Center for Astrophysics and Space Sciences, University of California at San Diego, La Jolla, CA 92093.
[5] Mullard Space Science Laboratory, University College London, Dorking, Surrey, UK.
[6] IASF Milano–INAF, Milano, Italy.
[7] School of Physics and Astronomy, University of Southampton, Southampton, UK.
[8] *INTEGRAL* Science Data Centre, Versoix, Switzerland.
[9] Observatoire Astronomique de l'Université de Genève, Sauverny, Switzerland.

TABLE 1
JOURNAL OF THE *RXTE* OBSERVATIONS ANALYZED IN THIS LETTER

Observation	ObsID (P92016)	MJD (days)	Good Time Interval (s)	Count Rates PCA	Count Rates HEXTE
1	01-01-00	53,998.2	6384	61.4	13.3
2	01-02-00	54,000.2	3200	67.5	14.5
3	01-01-02	54,001.3	3200	68.4	14.3
4	01-02-01	54,002.0	2368	66.7	14.3
5	01-02-02	54,003.2	3216	64.5	15.3
6	01-01-01	54,005.0	3232	60.8	13.0
7	01-03-00	54,007.1	6480	53.8	12.2

NOTES.—MJD 54,000 is 2006 September 22. The last two columns indicate the net count rates from PCA/PCU2 (3–30 keV) and HEXTE/cluster B (18–200 keV).

observation were fitted simultaneously in XSPEC version 11.3.2t between 3 and 200 keV. A normalization constant was introduced to account for calibration uncertainties between PCA and the single HEXTE cluster.

High-resolution light curves were extracted from Good Xenon and Event data with a time resolution of ~122 μs, allowing us to study the temporal properties of the source up to 4096 Hz. In order to restrict the background effects at low and high energies, we restricted the extraction to the ~5–40 keV range. Since quasi-period oscillations (QPOs) and coherent pulsations are usually stronger at these energies (e.g., Morgan et al. 1997; Rodriguez et al. 2004, 2006b), this ensures a higher sensitivity to any feature that might exist. We produced power density spectra (PDS) from each of the individual light curves between ~0.02 and 4096 Hz.

2.2. *Radio Observations*

IGR J17497−2821 was observed on 2006 September 26 and 27, with the ATCA, located at Narrabri, Australia. The array was in the H75 configuration (allowing a baseline as long as 6 km) with antennas 1 and 5 off-line due to maintenance. Observations were carried out simultaneously at 4.80 GHz (6 cm) and 8.64 GHz (3.5 cm), with a continuum bandwidth of 128 MHz, for a total of about 12.3 hr on-source. The amplitude and bandpass calibrator was PKS 1934−638, and the antennas' gain and phase calibration, as well as the polarization leakage, were derived from regular observations of the nearby calibrator TXS 1748−253. The editing, calibration, Fourier transformation, deconvolution, and image analysis were performed using the MIRIAD software package. No radio emission from IGR J17497−2821 was detected with ATCA on either date. Combining the two sets of observations resulted in the 3 σ upper limits for IGR J17497−2821 of 0.21 mJy at both frequencies.

3. RESULTS OF THE X-RAY ANALYSIS

Figure 1 shows the light curves seen by *Swift* BAT and *RXTE* PCA. In about 5 days the 15–50 keV BAT flux increased by a factor greater than 5, and remained around 0.02 counts s^{-1} until MJD 54,006. The BAT flux is not purely constant, however, since it showed the presence of two peaks. After MJD 54,006 a significant decrease is seen (Fig. 1). From the quality of the data, it is difficult to say whether the shape of the BAT light curve is like a fast rise, exponential decay or whether the decay is purely linear. In fact, fitting the decay with an exponential leads to an *e*-folding time of 16.9 days.

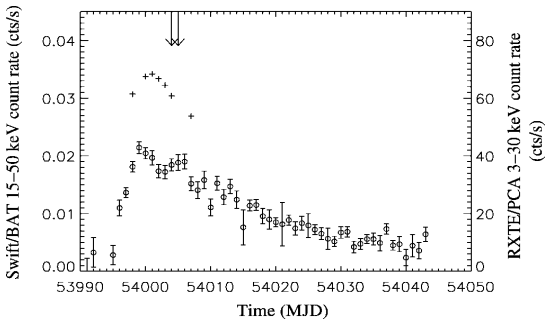

FIG. 1.—15–50 keV *Swift* BAT (*open circles*) and 3–30 keV *RXTE* PCA (*crosses*) light curves of IGR J17497−2821 during the outburst studied in this Letter. The vertical arrows represent the dates of our ATCA observations. For BAT 1 crab ~0.23 and ~1840 counts s^{-1} for PCA.

The spectra were first fitted with a simple absorbed power-law model. In all cases, the power-law photon index was hard (~1.56). Although the reduced χ^2 was relatively acceptable (1.5 for 96 degrees of freedom [dof] for observation 1), a slight deviation was visible at high energy. Adding a cutoff improved the fit. An *F*-test yielded a probability of 2.8×10^{-3} that the improvement was purely due to chance. In all observations except 4, 5, and 6 the cutoff was required at a high level of significance. This may indicate that it was either truly absent in observations 4, 5, and 6, or that the cutoff energy had increased closer to the upper boundary of our spectral analysis. Note that these three observations occur between the two peaks of the BAT light curve (Fig. 1).

Since a hard power law with an exponential cutoff is usually interpreted in XRBs as being due to thermal Comptonization, the pure phenomenological model was replaced by the `comptt` model (Titarchuk 1994). The same model was applied to all observations to ease the comparison. In all cases, a hint for an iron edge at ~7 keV was visible. Adding such a feature greatly improved the fits (1.7×10^{-9} chance improvement). The mention by Itoh et al. (2006) of such a feature in the *Suzaku* spectrum of the source lent further credibility to this detection. The optical depth of the edge ranges from 0.08 to 0.12, while the reduced χ^2 ranges from 0.97 to 1.14 for 93 dof. All other fit parameters are reported in Table 2, while Figure 2 shows the spectrum from observation 7. The source spectral parameters were relatively

TABLE 2
BEST-FIT PARAMETERS OBTAINED FROM THE COMBINED PCA+HEXTE SPECTRA

Observation	N_H ($\times 10^{22}$ cm^{-2})	Edge (keV)	kT_e (keV)	τ	Flux[a]
1	4.1 ± 0.4	6.8 ± 0.3	37^{+118}_{-7}	$1.6^{+0.3}_{-1.0}$	1.0
2	3.8 ± 0.4	6.6 ± 0.3	34^{+21}_{-6}	$1.8^{+0.3}_{-0.6}$	1.14
3	3.9 ± 0.4	6.7 ± 0.3	33^{+12}_{-5}	$1.8^{+0.2}_{-0.4}$	1.16
4	3.8 ± 0.5	$7.1^{+0.4}_{-0.3}$	33^{+16}_{-5}	$1.9^{+0.3}_{-0.5}$	1.13
5	3.3 ± 0.4	$6.8^{+0.4}_{-0.3}$	37^{+25}_{-6}	$1.7^{+0.3}_{-0.5}$	1.08
6	3.5 ± 0.4	$6.8^{+0.4}_{-0.3}$	40^{+22}_{-8}	$1.7^{+0.3}_{-0.5}$	1.02
7	3.6 ± 0.4	6.8 ± 0.3	$38^{+88.0}_{-7}$	$1.7^{+0.3}_{-1.1}$	0.91

NOTES.—The spectral model consists of `phabs*edge*comptt`. In all cases the reduced χ^2 is around 1. The seed photon temperature for Comptonization was frozen to 0.1 keV in all cases. Errors are given at the 90% confidence level.

[a] 3–20 keV unabsorbed $\times 10^{-9}$ ergs cm^{-2} s^{-1}.

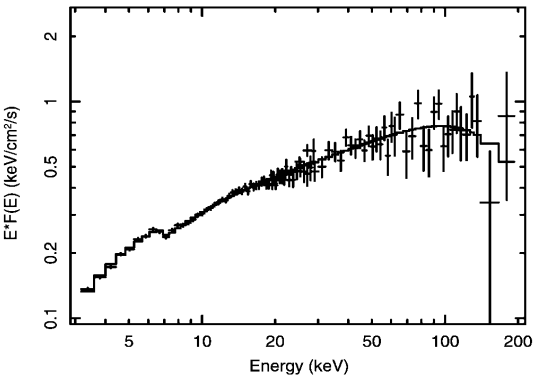

FIG. 2.—The 3–200 keV *RXTE* spectrum of observation 7. The best model is superposed as a line.

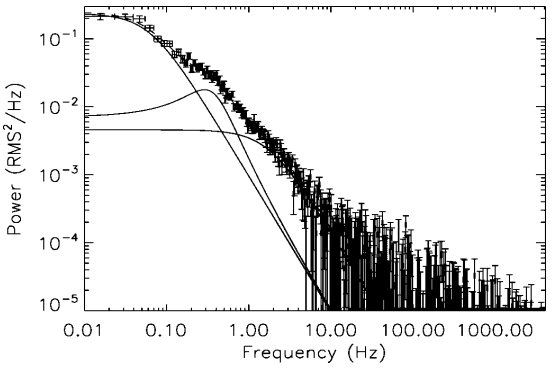

FIG. 3.—White-noise–corrected PDS from observation 1. The solid lines represent the three broad Lorentzians used to model the PDS. The dashed line is the best model.

stable over the period of observations. Slight differences are found only for observations 1 and 7, for which the electron temperatures seem higher, although poorly constrained.

The 1 s bin PCA light curves extracted from the seven observations showed no particular differences. No obvious dips, eclipses, or X-ray bursts were visible.[10] To quantify the degree of variability, we inspected each PDS individually. The variability of IGR J17497−2821 is dominated by frequencies lower than 1 Hz (Fig. 3 for observation 1). We modeled the PDSs with the help of broad Lorentzians (Belloni et al. 2002b). As in typical PDSs of XRBs, three such features are needed (van der Klis 2006), two with their centroid frozen to 0 and one representing the so-called low-frequency hump (LFH). Broad Lorentzians mimic a flat-top component and power-law decay above a break frequency. The analog of the break frequency is given by $\Delta = [(\sigma/2)^2 + \nu_0^2]^{1/2}$, with σ the full width at half maximum, and ν_0 the centroid frequency (Belloni et al. 2002b). The PDSs from the different observations showed very little variations. The three components were compatible (within the errors) with being constant through the outburst. As a reference the parameters we obtained for observation 1 are $\Delta = 0.06 \pm 0.01$ Hz, rms ~13% ± 2%, for the main component $\Delta = 1.8 \pm 0.7$ Hz, rms = 10% ± 2% for the second, and $\nu_0 = 0.30 \pm 0.07$ Hz, and $\Delta = 0.23 \pm 0.07$ Hz, rms = 13% ± 2% for the LFH. The total rms variability is then ~36% rms. The 3 σ upper limit for a 2 Hz FWHM QPO is 2%.

We searched for X-ray pulsations between ~0.2 ms and 256 s in the unbinned PDSs. We do not detect any coherent pulsations in any of them. While below 1 Hz the significant level of aperiodic noise renders our search less sensitive to the detection of a given feature, above 1 Hz a periodic signal would be more readily detectable out of the white noise. From the PDS of observation 1, and with a frequency resolution of 3.9×10^{-3} Hz, we could calculate 3 σ upper limits of 0.9% between 1 and 4096 Hz. Below 1 Hz, using a similar approach (assuming here that a pulsation should appear out of the level of aperiodic noise, and using the "flat-top" level below 0.3 Hz), we could calculate that the limit for a coherent pulsation ranges from ~2.4% at 0.4 mHz to ~1% at 1 Hz.

[10] In the PCU3 light curve of observation 2, however, a large flare was detected. This was not confirmed while inspecting all other active Proportional Counter Units (PCUs). This flare seems to be purely instrumental.

4. DISCUSSION

We analyzed a set of *RXTE* observations of the newly discovered source IGR J17497−2821. The PDSs of IGR J17497−2821 are typical of XRBs in the LHS (e.g., van der Klis 2006). Although the general shape of the PDSs makes it difficult to discriminate a NS from a BH (van der Klis 2006), the typical frequencies are believed to be lower in the case of the BH (the millisecond accreting pulsar IGR J00291+5934 being a recent counterexample). In fact, Sunyaev & Revnivtsev (2000) observed that in the LHS for BH systems no significant signal is detected above ~50 Hz, contrary to weakly magnetized NSs. In IGR J17497−2821 the lack of significant signal above ~10 Hz, above which the level of variability is compatible with being purely due to Poisson noise, and the high level of the flat-top noise, together with the low frequency of the break in the first Lorentzian component (0.06 Hz), are reminiscent of BH systems. Generally speaking, and although this is not a proof, none of the characteristics that would make IGR J17497−2821 a definite NS (kilohertz QPOs, X-ray bursts, coherent pulsations) are observed.

The source spectrum is well represented by a power law (with $\Gamma \sim 1.57$) convolved by interstellar absorption and a high-energy cutoff starting at $E_{\rm cut} \sim 50$ keV with a folding energy $E_{\rm fold} \sim 190$ keV, which are all typical of XRBs in the LHS. This is usually interpreted as due to thermal Comptonization of soft X-ray photons on a population of energetic electrons. Whether these electrons form a "corona" or the base of a compact jet is subject to debate (e.g., Markoff et al. 2005). A thermal Comptonization model represents the spectra well. The high value of the electron temperature and the optical depth suggest that the compact object is probably a BH. Indeed, with $E_{\rm cut} = 3kT_e$, we obtain an equivalent cutoff energy of about 100–120 keV, which is similar to, for example, Cyg X-1 while in the LHS (Cadolle Bel et al. 2006a), or XTE J1550−564 during its 2002 outburst (Belloni et al. 2002a), two well-known BHs. In addition, even if some extremely hard NS atoll sources can show similar spectra, the values of τ obtained in those cases are systematically higher (Barret 2001) than those of IGR J17497−2821.

The (unabsorbed) 1–20 and 20–200 keV luminosities are $1.1 \times 10^{37}(d/8\ {\rm kpc})^2$ ergs s^{-1} and $2.1 \times 10^{37}(d/8\ {\rm kpc})^2$ ergs s^{-1}.

At the distance of the Galactic center, these luminosities place the source outside the so-called burster box (Barret et al. 2000), in fact very close to Cyg X-1 in its LHS. Although several NS sources have been seen to lie outside this box, they all have their 20–200 keV luminosity lower than $\sim 10^{37}$ ergs s^{-1}. In this respect, if IGR J17497−2821 is located at a large distance, as possibly suggested by the high value of the equivalent absorption column density, its hard luminosity strongly suggests that it contains a BH.

Figure 4 shows the position of IGR J17497−2821 with respect to the radio–X-ray correlation. IGR J17497−2821 lies below the expected correlation for BHs. Figure 4 (see Corbel et al. 2004; Cadolle Bel et al. 2006b) shows that some black hole candidates (BHCs) have been observed to lie below the expected correlation. The nondetection of IGR J17497−2821 in radio is therefore not an argument against a BH primary. Given the results of our X-ray spectral analysis, we conclude that IGR J17497−2821 is a BHC in its LHS. The observations of sources for which the correlation between the radio and X-ray fluxes is not observed suggest that, contrary to other BHs in the LHS, the formation and/or emission from the jet may be prevented for some unknown reasons.

Recently, several sources have been observed to remain in the LHS during the whole duration of their outburst. These sources can either host a NS (e.g., Aql X-1), or a BH(C) (XTE J1550−564, SWIFT J1753.5−0127, GRO J0422+32, GRO J1719−24, and XTE J1118+480; Sturner & Shrader 2005; Cadolle Bel et al. 2006b; Brocksopp et al. 2004). Interestingly, Aql X-1 and XTE J1550−564 are also known to undergo major outbursts. The existence of LHS outbursts in XRBs brings interesting questions regarding the physics of accretion. In XTE J1550−564, Sturner & Shrader (2005) have suggested that this outburst could correspond to a discrete accretion event. Rodriguez et al. (2006a) have suggested the same could also occur in Aql X-1. In both these cases, the outbursts had a short duration (~30–40 days) compared to their previous outbursts. The similar duration of the outburst of IGR J17497−2821 could by comparison indicate that a similar event took place. As pointed out by Sturner & Shrader (2005) the LHS outburst in GRO J0422+32, GRO J1719−24, and XTE J1118+480 could (by opposition to at least XTE J1550−564) be explained by a lower reservoir of material, these sources having a short orbital periods. Although we cannot know whether IGR J17497−2821 will have a major outburst in the future, the fact that the companion of IGR J17497−2821 is a red giant K-type star (Paizis et al. 2006) rules out a system with a such a short orbital period.

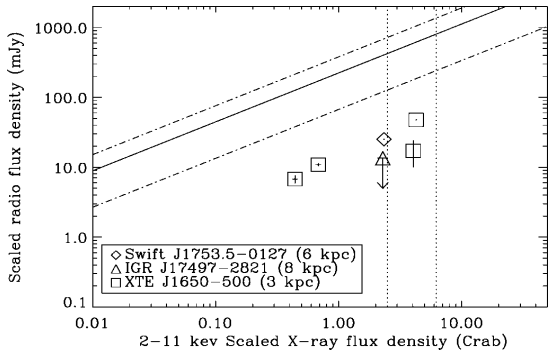

FIG. 4.—Plot of the radio vs. X-ray fluxes for the BH XTE J1650−500 (Corbel et al. 2004), the BHC SWIFT J1753.5−0127 (Cadolle Bel et al. 2006b), and IGR J17497−2821 with their (assumed) distances. All fluxes are normalized to a distance of 1 kpc. The range of correlated radio/X-ray fluxes is indicated by the dash-dotted lines, while the solid line indicates the best position. The vertical dotted lines indicate 2% and 5% of the Eddington luminosity.

We are especially grateful to J. H. Swank and the *RXTE* mission planers for having accepted our Target of Opportunity, and for their very rapid reaction to plan our observations. The *Swift* BAT transient monitor results are kindly provided by the *Swift* BAT team. J. R. would like to thank S. Chaty for useful discussions. This research has made use of data obtained through the High Energy Astrophysics Science Archive Center Online Service, provided by the NASA/Goddard Space Flight Center.

REFERENCES

Barret, D. 2001, Adv. Space Res., 28, 307
Barret, D., Olive, J.-F., Boirin, L., Done, C., Skinner, G. K., & Grindlay, J. E. 2000, ApJ, 533, 329
Belloni, T., Colombo, A. P., Homan, J., Campana, S., & van der Klis, M. 2002a, A&A, 390, 199
Belloni, T., Psaltis, D., & van der Klis, M. 2002b, ApJ, 572, 392
Brocksopp, C., Bandyopadhyay, R. M., & Fender, R. P. 2004, NewA, 9, 249
Cadolle Bel, M., et al. 2006a, A&A, 446, 591
———. 2006b, ApJ, in press (astro-ph/0612575)
Corbel, S., Fender, R. P., Tomsick, J. A., Tzioumis, A. K., & Tingay, S. 2004, ApJ, 617, 1272
Corbel, S., Nowak, M. A., Fender, R. P., Tzioumis, A. K., & Markoff, S. 2003, A&A, 400, 1007
Gallo, E., Fender, R. P., & Pooley, G. G. 2003, MNRAS, 344, 60
Hynes, R. I., Mauche, C. W., Haswell, C. A., Shrader, C. R., Cui, W., & Chaty, S. 2000, ApJ, 539, L37
Itoh, T., et al. 2006, Astron. Tel. 914
Kuulkeers, E., et al. 2006, Astron. Tel. 888
Markoff, S., Nowak, M. A., & Wilms, J. 2005, ApJ, 635, 1203
Markwardt, C. B., & Swank, J. H. 2006, Astron. Tel. 891
Migliari, S., & Fender, R. P. 2006, MNRAS, 366, 79
Morgan, E. H., Remillard, R. A., & Greiner, J. 1997, ApJ, 482, 993
Paizis, A., et al. 2006, ApJ, submitted (astro-ph 0611344)
Rodriguez, J., Corbel, S., Hannikainen, D. C., Belloni, T., Paizis, A., & Vilhu, O. 2004, ApJ, 615, 416
Rodriguez, J., Corbel, S., & Tomsick, J. A. 2003, ApJ, 595, 1032
Rodriguez, J., Shaw, S. E., & Corbel, S. 2006a, A&A, 451, 1045
Rodriguez, J., et al. 2006b, MNRAS, 366, 274
Soldi, S., et al. 2006, Astron. Tel. 885
Sturner, S. J., & Schrader, C. R. 2005, ApJ, 625, 923
Sunyaev, R., & Revnivtsev, M. 2000, A&A, 358, 617
Titarchuk, L. 1994, ApJ, 434, 570
van der Klis, M. 2006, in Compact Stellar X-Ray Sources, ed. W. Lewin & M. van der Klis (Cambridge: Cambridge Univ. Press), 39

9.3 2 ans de suivis de GRS 1915+105 : papier 1

The Astrophysical Journal, 675:1436–1448, 2008 March 10

2 YEARS OF *INTEGRAL* MONITORING OF GRS 1915+105. I. MULTIWAVELENGTH COVERAGE WITH *INTEGRAL*, *RXTE*, AND THE RYLE RADIO TELESCOPE

J. Rodriguez,[1] D. C. Hannikainen,[2] S. E. Shaw,[3] G. Pooley,[4] S. Corbel,[1] M. Tagger,[5] I. F. Mirabel,[6] T. Belloni,[7] C. Cabanac,[3] M. Cadolle Bel,[8] J. Chenevez,[9] P. Kretschmar,[8] H. J. Lehto,[10] A. Paizis,[11] P. Varnière,[12] and O. Vilhu[2]

Received 2007 July 2; accepted 2007 November 29

ABSTRACT

We report the results of simultaneous monitoring observations of the Galactic microquasar GRS 1915+105 with *INTEGRAL* and *RXTE* from 3 up to ∼300 keV, and the Ryle Telescope at 15 GHz. We first identify the classes of variability in which GRS 1915+105 is found, and report some direct transitions between them. The accretion ejection connections are studied in a model-independent manner through the source light curves, hardness ratio, and color-color diagrams. During a period of steady ''hard'' X-ray state (class χ) we observe a steady radio flux interpreted as the signature of a compact jet. We then turn to three particular observations during which we observe several types of soft X-ray dip and spike cycles, followed by radio flares, corresponding to classes ν, λ, and β types of variability. This is the first time ejections are reported during a class λ observation. We generalize the fact that a (nonmajor) discrete ejection always occurs, in GRS 1915+105, as a response to an X-ray sequence composed of a spectrally hard X-ray dip terminated by an X-ray spike marking the disappearance of the emission above 18 keV. We identify the trigger of the ejection as the X-ray spike. A possible correlation between the amplitude of the radio flare and the duration of the X-ray dip is found. The X-ray dips prior to ejections could thus represent the time during which the source accumulates energy and material that is ejected later. The fact that these results do not rely on any spectral modelling enhances their robustness.

Subject headings: accretion, accretion disks — black hole physics — radio continuum: stars — stars: individual (GRS 1915+105) — X-rays: binaries

1. INTRODUCTION

Microquasars are the Galactic scaled-down versions of active galactic nuclei (AGNs; Mirabel & Rodríguez 1998). In both classes of systems, the copious emission of energy is thought to originate from the accretion of matter onto the central black hole (BH), which occurs through an accretion disk. Relativistic ejections are observed in both classes of objects, either through discrete jets or in a self-absorbed compact jet. Apart from morphological similarities, the difference of the mass of the central object leads to a higher temperature of the inner regions of the accretion disk in the Galactic sources, smaller extent of the jets, and, of high importance, smaller timescales in any of the phenomena associated with either accretion or ejection processes (Mirabel & Rodríguez 1998). As a result, microquasars are excellent laboratories in which to study the accretion-ejection links on timescales from seconds to days. This is done by coupling the variations seen at X-ray energies (mapping the regions closest to the compact object) to those seen at radio and infrared (IR) wavelengths (representing the emission from the jets). Such a task has been initiated in GRS 1915+105 (Pooley & Fender 1997; Eikenberry et al. 1998; Mirabel et al. 1998; Fender & Pooley 1998), and pursued in a large number of systems since then.

An extensive review on GRS 1915+105 can be found in Fender & Belloni (2004). To summarize, GRS 1915+105 hosts a BH of $14.0 \pm 4.4\ M_{\odot}$ (Harlaftis & Greiner 2004), it is one of the brightest X-ray sources in the sky and a source of superluminal ejections (Mirabel & Rodríguez 1994), and it has a true bulk velocity $\geq 0.9c$. From these superluminal motions an upper limit on the distance to GRS 1915+105 of 11.2 kpc could be derived (on the assumption of intrinsic symmetry in the bipolar jets; Fender et al. 1999), although a distance as low as 6 kpc (Chapuis & Corbel 2004) cannot be excluded. The source is also known to show a compact jet during its periods of low and steady X-ray emission levels (Dhawan et al. 2000).

GRS 1915+105 has been extensively observed with the *Rossi X-ray Timing Explorer* (*RXTE*) since 1996. A rich pattern of variability has emerged from these data with timescales from years down to 15 ms (e.g., Morgan et al. 1997). Belloni et al. (2000), analyzing 163 *RXTE* observations from 1996 to 1997, classified all the observations into 12 separate classes (labeled with greek letters) based on count rates and color characteristics. This scheme has been widely used ever since and is also applied here. The classes could be interpreted as transitions between three basic states (A–B–C), A being equivalent to the soft state, B to the soft intermediate state, and C to the hard intermediate state in the classification of Homan & Belloni (2005). These spectral changes

[1] Laboratoire AIM, CEA/DSM-CNRS-Université Paris Diderot, DAPNIA/SAp, F-91191 Gif-sur-Yvette, France.
[2] Observatory, P.O. Box 14, FI-00014 University of Helsinki, Finland.
[3] School of Physics and Astronomy, University of Southampton, SO17 1BJ, UK.
[4] Astrophysics, Cavendish Laboratory, J. J. Thomson Avenue, Cambridge CB3 0HE, UK.
[5] Service d'Astrophysique (UMR AstroParticules et Cosmologie), CEA Saclay 91191 Gif-sur-Yvette, France.
[6] European Southern Observatory, Chile. On leave from CEA-Saclay, France.
[7] INAF-Osservatorio Astronomico di Brera, via Bianchi 46, 23807 Merate, Italy.
[8] European Space Astronomy Centre (ESAC) Apartado/P.O. Box 78, Villanueva de la Cañada, E-28691 Madrid, Spain.
[9] Danish National Space Center, Technical University of Denmark, Juliane Maries Vej 30, 2100 Copenhagen, Denmark.
[10] Tuorla Observatory and Department of Physics, University of Turku Väisäläntie 20, FI-21500 Piikkiö, Finland.
[11] IASF Milano-INAF, Via Bassini 15, 20133 Milano, Italy.
[12] LAOG, Université J. Fourier (UMR5571), Grenoble, France.

TABLE 1
JOURNAL OF ALL THE *INTEGRAL* OBSERVATIONS OF OUR CAMPAIGN

			MJD		RT RADIO OBSERVATIONS	
OBSERVATION NO.	REVOLUTION NO.	ObsID	Start	Stop	Start	Stop
1	246	02200280001	53296.3730	53297.5848	53296.710	53296.879
2	255	02200280002	53324.2773	53325.5107	53324.519	53324.803
3	295	02200280003	53442.9542	53444.1497	No coverage	No coverage
4	305	02200280004	53472.8673	53474.1419	53473.098	53473.417
	...	...	...	...	53474.085	53474.141
5	315	02200280005	53503.6328	53504.8691	53503.972	53504.353
6	356	03200200001	53626.3852	53627.5983	53626.853	53626.996
7	361	03200200002	53640.3856	53641.5803	53640.870	53640.946
8	367	03200200003	53659.9563	53660.3679	No coverage	No coverage
9	368	03200200004	53661.3222	53662.1313	53661.666	53661.879
10	373	03200200005	53676.2472	53677.4881	53676.562	53676.840
11	379	03200200006	53694.2739	53695.4691	No coverage	No coverage

NOTE.—The simultaneous RT observations are also indicated.

are, in most of the classes, interpreted as reflecting the rapid disappearance of the inner portions of an accretion disk, followed by a slower refilling of the emptied region (Belloni et al. 1997). Note that other possibilities, such as the disappearance of the corona (Chaty 1998; Rodriguez et al. 2002; Vadawale et al. 2003) or dissipation of magnetic energy (e.g., Tagger et al. 2004), have also been invoked in some models.

Multiwavelength coverages involving radio, IR, and X-ray telescopes have shown a clear but complex association between soft X-rays and radio emission, including radio quasi-periodic oscillations (QPOs) in the range 20–40 minutes that were associated with X-ray variations on the same timescale (Pooley & Fender 1997; Eikenberry et al. 1998; Mirabel et al. 1998; Fender & Pooley 1998). These oscillations were ascribed to small ejections of material from the system and were found to correlate with the disk instability, as observed in the X-ray band. This was the first time the disk-jet relation could be studied in detail. This kind of cycle could also reflect some magnetic flood scenario in which reconnection events would allow the ejection of blobs of material (Tagger et al. 2004).

While fine X-ray spectral and temporal analysis will be presented in a companion paper (Rodriguez et al. 2008), we analyze here, in a model-independent way, the multiwavelength data from our 2 yr monitoring campaign focusing on the observations during which correlated X-ray and radio variabilities are seen. We start with giving the basic properties of our *INTEGRAL* observations, i.e., we describe the campaign and the data-reduction processes in § 2. In §§ 3 and 4 we describe and discuss the four observations from which strong radio/X-ray connections are observed.

2. OBSERVATIONS AND DATA REDUCTION

2.1. *Journal of the Observations*

The journal of the *INTEGRAL* observations belonging to our monitoring campaign taken from 2004 October to 2005 December is given in Table 1, while Table 2 reports the details of our simultaneous *RXTE* monitoring. The daily multiwavelength light curves of GRS 1915+105 as seen by *RXTE* ASM (1.2–12 keV) and the Ryle Telescope (RT; 15 GHz) over the period of interest are reported in Figure 1 (January 1st 2004 is MJD 53,005). The days of our *INTEGRAL* pointings are shown as vertical arrows; the four bigger ones indicate the four observations whose accretion ejection properties are discussed in more detail in this paper.

2.2. *INTEGRAL Data Reduction*

Our monitoring makes use of the *INTEGRAL* Soft Gamma-Ray Imager (ISGRI; Lebrun et al. 2003)—the low-energy detector of the Imager On-Board *INTEGRAL* (IBIS)—to cover the 18 to ~300 keV energy range, and the X-ray monitors JEM-X (Lund et al. 2003) to cover the 3–30 keV energy range. Both

TABLE 2
JOURNAL OF THE *RXTE* OBSERVATIONS OF OUR CAMPAIGN

Observation No. (*INTEGRAL* Equivalent)	ObsID	MJD Start (MJD)	Date
1	90105-03-02-00	53296.387	2004 Oct 18
1	90105-03-02-01	53296.593	2004 Oct 18
1	90105-03-02-02	53296.661	2004 Oct 18
1	90105-03-02-03	53296.728	2004 Oct 18
1	90105-03-02-04	53296.794	2004 Oct 18
1	90105-03-01-000	53297.039	2004 Oct 19
1	90105-03-01-00	53297.370	2004 Oct 19
1	90105-03-03-00	53297.440	2004 Oct 19
1	90105-03-03-01	53297.508	2004 Oct 19
1	90105-03-03-02	53297.576	2004 Oct 19
2	90105-05-01-00	53324.261	2004 Nov 15
2	90105-05-02-00	53324.524	2004 Nov 15
2	90105-06-01-00	53325.180	2004 Nov 16
2	90105-06-02-00	53325.442	2004 Nov 16
3	90105-05-03-00	53442.968	2005 Mar 13
3	90105-05-03-01	53443.037	2005 Mar 14
3	90105-05-03-02	53443.105	2005 Mar 14
3	90105-05-03-03	53443.242	2005 Mar 14
3	90105-05-03-04	53444.019	2005 Mar 15
3	90105-05-03-05	53444.089	2005 Mar 15
4	90105-07-01-00	53472.921	2005 Apr 12
4	90105-07-02-00	53473.054	2005 Apr 13
4	90105-07-03-00	53473.972	2005 Apr 13
5	90105-08-01-00	53503.669	2005 May 13
5	90105-08-02-00	53503.870	2005 May 13
5	90105-08-03-00	53504.719	2005 May 14
7	90105-04-01-00	53640.390	2005 Sep 27
7	90105-04-02-00	53641.111	2005 Sep 28
7	90105-04-03-00	53641.439	2005 Sep 28
7	90105-04-03-01	53641.516	2005 Sep 28
11	90105-06-03-01	53694.908	2005 Nov 20
11	90105-06-03-00	53695.039	2005 Nov 21
11	90105-06-03-02	53695.308	2005 Nov 21

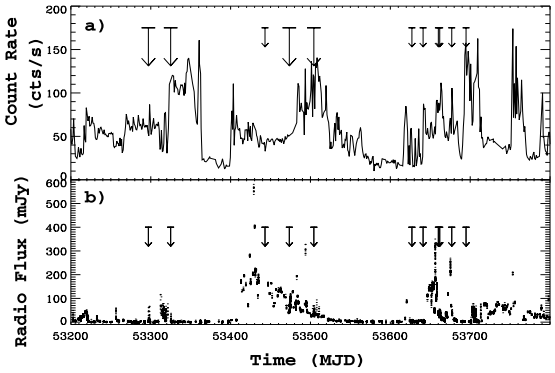

FIG. 1.—Light curves of GRS 1915+105 from MJD 53,200 to MJD 53,900 as seen (*a*) between 1.2 and 12 keV with the *RXTE* ASM, and (*b*) at 15 GHz with the RT. In each panel the vertical arrows show the dates of the *INTEGRAL* observations, and the longer arrows show the four particular observations whose accretion ejection properties are discussed in detail in this paper.

instruments see the sky through a coded mask. We reduced the *INTEGRAL* data using the Off Line Scientific Analysis (OSA) version 7.0. Apart from the different version of the software, the data from ISGRI and JEM-X were reduced in a way similar to that presented in Rodriguez et al. (2005) for another source present in the totally coded field of view (TCFOV) of ISGRI, IGR J19140+0951. Our first step was to produce ISGRI images in two energy bands, 20–40 and 40–80 keV, in order to detect the active sources of the FOV which have to be taken into account in the (spectral and temporal) extraction processes. All sources with a signal-to-noise ratio greater than 6 in the 20–40 keV ranges were considered. The list of sources found in each revolution is given in Table 3. Apart from a purely technical process of obtaining the cleanest data for the main target of our analysis (see, e.g., Goldwurm et al. [2003] for the details of the IBIS data reduction processes), this procedure also allows us to survey the brightest sources of this field and analyze their data (e.g., analysis of Aql X-1 during its faint 2005 April outburst can be found in Rodriguez et al. 2006).

Since GRS 1915+105 is the main target of all our observations, with a hexagonal dithering pattern it is always in the TCFOV of ISGRI and in the useful part of the FOV of JEM-X. We therefore did not include any restriction concerning the off-axis angle in selecting the data. The second step of our analysis was to produce JEM-X and ISGRI light curves with the view to identify the class and monitor the behavior of the source on short timescales. The JEM-X light curves were extracted with a time resolution of 1 s between ~3 and 13 keV, and further rebinned to 20 s. The ISGRI light curves were extracted between 18 and 50 keV with a time resolution of 20 s. They were further rebinned, as they can be quite noisy and hide interesting patterns when plotted on such a short time bin. The rebinning depended on the brightness of the source at energies above 18 keV and was usually in the range 50–200 s. The instrumental and sky background is estimated on the same time bins as the source raw count rate, from nonilluminated pixels. For ISGRI an additional step is to renormalize this background using background maps provided with the calibration tree. For each instrument, the light curves are corrected for background during the extraction process. From these background-corrected light curves we produced softness ratios (SRs) defined as SR = 3–13 keV/18–50 keV.

2.3. *RXTE Data Reduction*

The *RXTE* data were reduced with the LHEASOFT version 6.1.2. All data products were extracted from user's good times intervals (GTIs). GTIs corresponded to times when the satellite elevation was greater than 10° above the Earth limb, the offset pointing less than 0.02°, and proportional counter unit 2 was active. In order to identify the classes, we extracted 1 s resolution light curves in the 2–60 keV range and in the three energy bands defined in Belloni et al. (2000) from the Proportional Counter Array (PCA). These bands are 2–5.7 keV (channels 0–13, PCA epoch 5), 5.7–14.8 keV (channels 14–35), and >14.8 keV (channels 36–255). The colors were defined as HR1 = 5.7–14.8/2–5.7 keV and HR2 = 14.8–60/2–5.7 keV. The shift of gain between the different epochs of PCA leads to different absolute values of the count rates, hardness ratios (HRs), and position in the color-color (CC) diagrams, but the general shape of a given class is easily comparable to those of epoch 3 (Belloni et al. 2000), and therefore allowed us to easily identify the class of variability in each observation. Light curves with 16 s resolution were extracted from standard 2 data between 2 and 18 keV. These were directly compared to the 3–13 keV and 18–50 keV light curves extracted from the *INTEGRAL* data. All of these light curves were corrected for background, using the latest PCA background models available for bright sources.

2.4. *Ryle Telescope Observations*

The observations with the RT followed the scheme described by Pooley & Fender (1997). Observations of Stokes' $I + Q$ parameters were interleaved with those of a nearby phase calibrator (B1920+154); the flux-density scale was set by reference to 3C 48 and 3C 286 and is believed to be consistent with that defined by Baars et al. (1977). The data are sampled every 8 s, and 5 minute averages are displayed in this paper. Figure 1 shows the 15 GHz long-term light curve of GRS 1915+105.

3. ACCRETION EJECTION LINKS AND THE PRESENCE OF X-RAY CYCLES

Although the classification of the X-ray classes is purely phenomenological, we think it is rather important since it helps when referring to a given observation. Furthermore, the succession of classes, their relation with the radio behavior, and the pattern of state transition through a single class probably hides rich physical phenomena related to the accretion and ejection mechanisms. Hence, we feel it is important to report the identification of all classes and the possible transitions we observed during our campaign. Since it is not the core of our paper, however, this is given in the Appendix. The classes of variability identified during each observation are reported in Table 3. In the following we focus on the accretion ejection links of observations (Obs.) 1, 2, 4, and 5 with particular emphasis on the intervals that respectively belong to classes ν, λ, χ, and β during the times we have simultaneous radio and X-ray coverages (see Appendix).

3.1. *Observation 1: Class ν*

As can be seen on at least Figure 2 on two occasions, a sequence of a >100 s long X-ray dip ended by an X-ray spike (hereafter cycles) were followed by radio flares indicative of ejection of material (e.g., Mirabel et al. 1998). The cycles are all well defined above 18 keV (Fig. 2), with almost identical patterns as in the soft X-rays, although the dip and spike have a less marked amplitude. A notable difference with the soft X-ray light curve, however, is the presence of a short dip close to the spike. The shapes of the two radio flares are similar (Fig. 2). To estimate

TABLE 3
"Quick-look" Results of Our Campaign

Observation No.	Revolution No.	Source	Flux (counts s^{-1}) 20–40 keV	Flux (counts s^{-1}) 40–80 keV	20–40 keV Significance (σ)	Classes
1	246	GRS 1915+105	37.5	11.0	669	ν, ρ
		H 1907+097[a]	2.7	...	49	
		4U 1909+07	1.2	0.34	20	
		Ser X-1	1.4	...	13	
		XTE J1855−026	1.3	...	6.4	
		SS 433	0.4	...	6.1	
2	255	GRS 1915+105	19.5	5.4	355	μ, λ, δ
		H 1907+097[a]	1.8	...	30	
		IGR J19140+0951	1.7	0.64	29	
		4U 1909+07	1.4	0.4	24	
		XTE J1855−026	2.5	...	13	
		Ser X-1	1.2	...	11	
		IGR J18483−0311	2.5	...	9	
3	295	GRS 1915+105	37	7.7	646	χ
		4U 1909+07	1.6	...	26	
		H 1907+097[a]	1.4	0.43	24	
		Ser X-1	1.6	...	16	
		XTE J1855−026	2	1.4	7.4	
4	305	GRS 1915+105	26	5.2	476	χ
		Aql X-1[b]	15	6.6	152	
		H 1907+097[a]	3.1	...	57	
		4U 1909+07	1.5	0.54	24	
		IGR J19140+0951	1.3	0.48	23	
		Ser X-1	1.7	...	18	
		SS 433	0.7	...	10	
5	315	GRS 1915+105	22	5.5	297	μ, β
		4U 1909+07[a]	3	...	39	
		IGR J19140+0951	2.2	0.8	30	
		H 1907+097	2	0.7	26	
		Ser X-1	1.5	...	11	
		Ginga 1843+009	2.2	...	12	
		XTE J1855−026	1.7	...	7.6	
		Aql X-1[b]	0.8 1	6.1	...	
6	356[c]	GRS 1915+105	6.9	1.9	38	No JEM-X data
		H 1907+097	1.3	...	7	
		Ser X-1	2.3	...	7	
		IGR J19140+0951	1.1	...	6.1	
		4U 1909+07	1.3	...	6.1	
7	361	GRS 1915+105	15	3.5	268	ϕ, θ, δ
		H 1907+097[a]	3.2	...	57	
		IGR J19140+0951	2.4	0.8	43	
		4U 1909+07	2.1	0.6	35	
		Ser X-1	1.1	...	11	
		SS 433	0.6	...	9.0	
		XTE J1855−026	1.7	...	7.5	
8	367[d]	GRS 1915+105	22	4.7	242	χ
		H 1907+097[a]	1.3	...	14	
		4U 1909+07	1.3	...	13	
		Ser X-1	1.6	...	10	
9	368[d]	GRS 1915+105	27	5.5	420	χ
		4U 1909+07	1.2	0.6	17	
		H 1907+097[a]	0.9	...	13	
		SS 433	0.7	...	8.5	
		Ser X-1	1.0	...	9.0	
		XTE J1855−026	1.5	...	6.1	
10	373	GRS 1915+105	12	3.1	227	χ, μ, β
		H 1907+097[a]	1.3	...	23	
		Ser X-1	1.4	...	13	
		4U 1909+07	0.7	...	13	
		SS 433	0.6	...	9.8	
		IGR J19140+0951	0.43	...	7.7	

TABLE 3—*Continued*

Observation No.	Revolution No.	Source	Flux (counts s^{-1}) 20–40 keV	Flux (counts s^{-1}) 40–80 keV	20–40 keV Significance (σ)	Classes
11.....	379	GRS 1915+105	26	6.5	379	δ, μ, β
		Aql X-1[c]	7.1	3.5	60	
		IGR J19140+0951	1.7	0.5	24	
		H 1907+097[a]	0.9	...	12	
		4U 1909+07	0.95	...	13	
		Ser X-1	1.2	...	8.7	
		XTE J1855−026	1.9	...	8.1	

Note.—List of sources detected by ISGRI (with a signal-to-noise ratio greater than 6) and classes of variability of GRS 1915+105 in each observation.
[a] Detailed analysis of H 1907+097 (aka 4U 1907+09) during these observations is presented in Fritz et al. (2006).
[b] Analysis of Aql X-1 during these observations is reported in Rodriguez et al. (2006).
[c] Strong solar flares.
[d] These two observations were part of a huge multiwavelength campaign on GRS 1915+105 (Ueda et al. 2006).
[e] Rodriguez & Shaw (2005).

their true amplitude above a noise level, we estimated the variance of the radio light curve when in the nonflare intervals. The typical rms was 3.0 mJy. The flares reached maxima (calculated from the light curve with a temporal resolution of 5 minutes) of 62 ± 3 mJy and 60 ± 3 mJy on MJDs 53,296.76 and 53,296.83 respectively. Radio flares have been seen to occur as a response to each sequence of X-ray dips and spikes in this particular class (Klein-Wolt et al. 2002).

3.2. *Observation 2: Class λ*

As can be seen in Figures 3 and 4, on one occasion an X-ray cycle was followed by a radio flare indicative of an ejection event (e.g., Mirabel et al. 1998). The shape of the flare is rather symmetric. To estimate the statistical significance of the flare, we calculated the variance of the first part of the radio light curve. From this we can calculate a typical rms of 2.3 mJy. The flare thus had an amplitude of 40 ± 2.3 mJy (in the 5 minute bins light curve; Fig. 4). This observation of a radio flare during a class λ is the first ever reported. As for the other classes with cycles, e.g., class ν, the dips of class λ are known to be spectrally hard (Belloni et al. 2000). This is obvious in the SR of Figure 4. The dip, here mainly visible at soft X-rays, ended with a soft X-ray spike corresponding to a sudden decrease of the >18 keV emission (Fig. 4).

Interestingly, two small radio flares seem to have occurred prior to the main one around MJDs 53,324.68 and 53,324.75 (Fig. 4). They had respective amplitudes of 15.1 and 11.3 mJy. The flares were then significant at 6.5 and 4.9 σ, respectively. Deep inspection of the X-ray light curve shows that they followed short X-ray dips that occurred around MJD 53,324.66 and MJD 53,324.72 (Fig. 4). Unfortunately, during the first X-ray dip, for which the decrease of the 3–13 keV count rate is clearly visible (Fig. 4), *INTEGRAL* did a slew between two subsequent pointings that prevented a full coverage of this interval. We can only set a lower limit on the duration of the dip of 100 s. In the second case, the delay between the return to a high degree of variability at X-ray energies and the peak of the radio flare was 0.15 hr. Although the cycle was shorter than during the long one preceding the 40 mJy flare, a similar sequence of events can be seen here. The dip is really apparent below 13 keV and is spectrally hard, as illustrated by the SR in Figure 4. The cycle ended with a return to a high level at soft X-rays associated with a slight decrease of the hard X-ray emission. As in the previous cases the cessation of the dip manifested by a peak (although of much smaller amplitude than in the main cycle) in the SR in Figure 4.

3.3. *Observation 4: Class χ*

Contrary to the previous classes, GRS 1915+105 showed a relatively steady emission at all wavelengths, although some variations, in particular near the end of the observation, are visible (Fig. 5). In the radio domain the source had a mean flux of 44.9 mJy with a typical rms of 3.0 mJy (calculated from the radio light curve with a binning of 5 minutes) from MJD 53,473.10 to MJD 54,473.24.

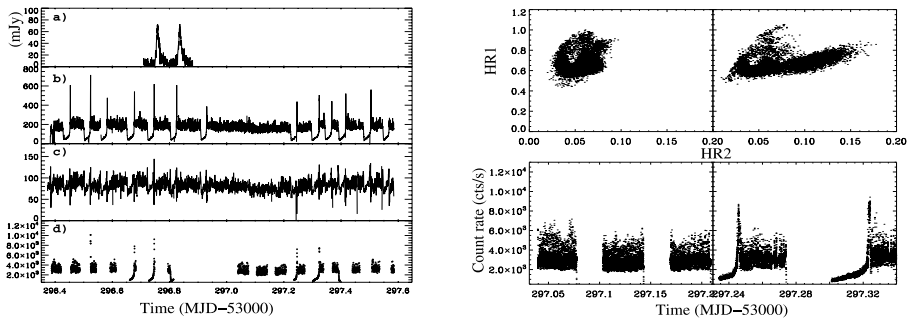

Fig. 2.—*Left*: Light curves of GRS 1915+105 during Obs. 1: (*a*) RT at 15 GHz; (*b*) JEM-X 3–13 keV binned at 20 s; (*c*) ISGRI 18–50 keV binned at 50 s; (*d*) *RXTE* PCA 2–18 keV binned at 16 s. *Right*: CC diagrams (*top*) and *RXTE* light curves (*bottom*) of two subintervals from Obs. 1, showing occurrences of class ρ (*left*) and class ν (*right*).

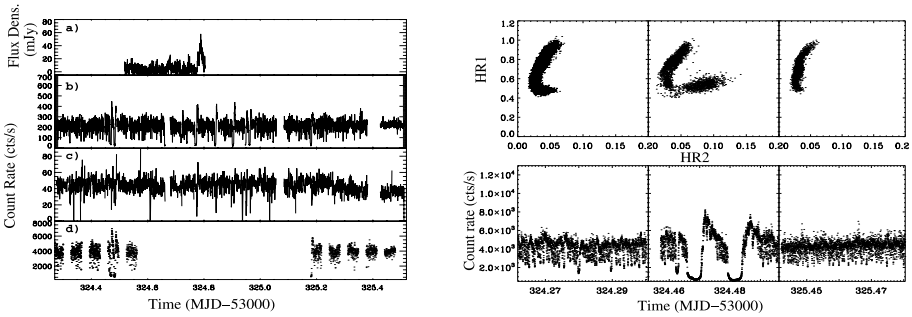

FIG. 3.—*Left*: Same as Fig. 2 for Obs. 2. *Right*: CC diagrams (*top*) and *RXTE* light curves (*bottom*) of three subintervals from Obs. 2, showing occurrences of class μ/κ (*left*), class λ (*middle*), and class γ (*right*).

It then slowly increased during ~4800 s to reach a mean flux of 70.4 mJy, with a rms of 4.4 mJy from MJD 53,473.30 to 53,473.42. The mean 3–13 keV JEM-X was 115.7 ± 6.8 counts s^{-1} from MJD 53,473.10 to 54,473.24 and 107.3 ± 6.5 counts s^{-1} later (MJD 53,473.30–53,473.42). The mean 18–50 keV ISGRI count rate was 55.3 ± 2.8 counts s^{-1} from MJD 53,473.10 to 54,473.24 and 58.4 ± 2.7 counts s^{-1} after (MJD 53,473.30–53,473.42).

Near the end of the observation (MJD 53,474.4), the radio flux was still around the same value as before the radio coverage was stopped (Fig. 5). It decreased for a short time to ~59 mJy and increased to ~110 mJy after MJD 53,472.2. Note that an inspection of the radio light curve the following days showed that the radio flux was at approximately the same level (120–130 mJy) on MJD 53,477 and had decreased to ~60 mJy on MJD 53,478. This may suggest that the radio emitter, the jet, has persisted over a long period, although it showed slight variations in its strength.

3.4. *Observation 5: Class μ and β*

During this observation, again on two occasions, the X-ray dips were followed by radio flares with symmetric shapes (Fig. 6).

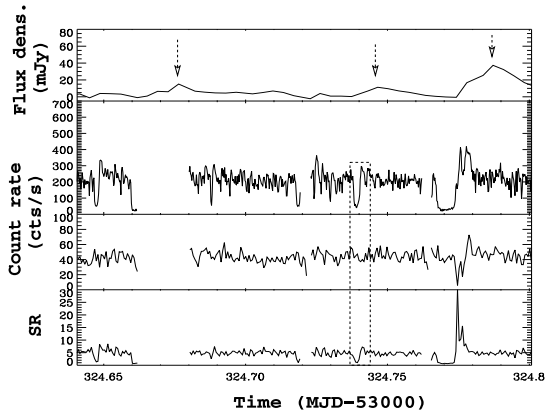

FIG. 4.—Zoom on a portion of Obs. 2 showing in the top panel three radio flares (indicated by the arrows). The other panels show, from top to bottom, the JEM-X 3–13 keV count rate, the ISGRI 18–50 keV count rate, and the 3–13 keV/18–50 keV SR. The box delimited with dashes shows the short cycle preceding the second radio flare.

The radio flares reached their maxima on MJDs 53,504.248 and 53,504.298, respectively, with absolute peak fluxes of 58.5 and 68.3 mJy (when using 5 minute bins to estimate them). However, unlike the two other classes, they sat on top of a nonzero radio flux. The mean radio flux prior to the two flares was 35.2 mJy with an rms of 3.4 mJy. The net amplitude of the flares above the continuum emission was therefore 23.3 ± 3.4 mJy and 33.1 ± 3.4 mJy, for the first and second flares respectively. The time delays between the X-ray spikes halfway through the dips (the triggers of the ejections; Mirabel et al. 1998; Chaty 1998), and the radio maxima were ~0.31 and ~0.34 hr, respectively. The presence of a relatively high radio flux prior to the ejections, when GRS 1915+105 was showing a high level of very variable X-ray emission (Fig. 6), is quite interesting. This kind of steady radio flux is usually indicative of the presence of a compact jet. However, the latter is usually seen when the source shows a steady X-ray flux dominated by hard X-ray emission, its spectrum then being indicative of a hard-intermediate state (state C of Belloni et al. 2000), similar to the one seen during Obs. 4. Klein-Wolt et al. (2002) also report the presence of radio emission during class μ observation with no oscillations of the radio flux. This could indicate that the cycles in class μ are too fast to be detected at radio wavelength. We should also note that the radio nonzero continuum seems to be the tail or exponential decay of a major flare that occurred some days before the observation, as can be seen in Figure 1. As in classes ν and λ, the cycles are also well defined above 18 keV. In particular, a dip can clearly be seen at hard X-ray energies during each cycle.

4. DISCUSSION

We have presented the results of 2 yr of simultaneous monitoring campaigns on the Galactic microquasar GRS 1915+105 made with several instruments. This has allowed us to follow the behavior of the source from radio wavelengths to hard X-ray energies. The *INTEGRAL* observatory, thanks to its large field of view, has allowed us to quickly monitor the behavior of sources that are in the vicinity of GRS 1915+105.

In the case of GRS 1915+105, we first classified the X-ray classes of variability of the source (Appendix), and saw that GRS 1915+105 could undergo transitions through many classes of variability on short timescales (few hundred seconds, Appendix). We report here the following specific and direct transitions: $\nu \leftrightarrow \rho$ (Obs. 1), $\mu \leftrightarrow \lambda$ and $\mu \rightarrow \delta$ (Obs. 2), $\mu \rightarrow \beta$ (Obs. 5), $\phi \rightarrow \theta \rightarrow \delta$ (Obs. 7), $\chi \leftrightarrow \theta$ (Obs. 8 and 9; Ueda et al. 2006), possibly $\delta(?) \rightarrow \mu \rightarrow \beta$ (Obs. 10), and $\delta \rightarrow \mu \rightarrow \beta$ (Obs. 11). We then focused more particularly on three observations showing the

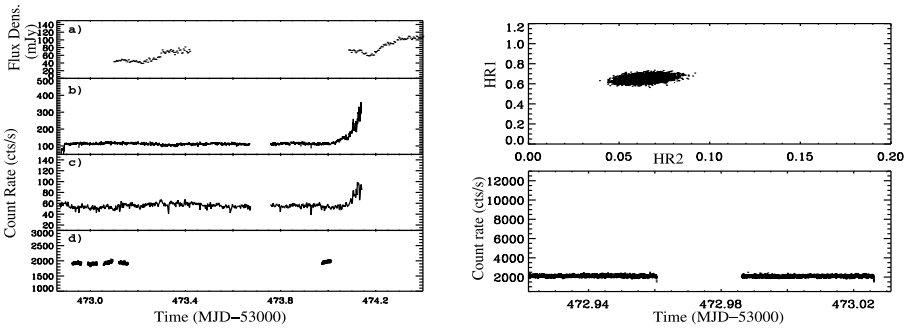

FIG. 5.—*Left*: Light curves of GRS 1915+105 during Obs. 4: (*a*) RT at 15 GHz; (*b*) JEM-X 3–13 keV binned at 50 s; (*c*) ISGRI 18–50 keV binned at 200 s; (*d*) *RXTE* PCA 2–18 keV binned at 16 s. *Right*: CC diagram (*top*) and *RXTE* light curve (*bottom*) of one subinterval from Obs. 4 showing the source was in class χ.

occurrences of X-ray cycles followed by radio flares. In a fourth observation the source was in its steady "hard" state accompanied by the presence of a persistent radio emission.

4.1. *Steady Radio and X-Ray Emission*

During Obs. 4, the persistent radio emission can be safely attributed to a steady compact jet, although the lack of simultaneous coverage at other radio wavelengths prevents us from precisely estimating the radio spectral index. GRS 1915+105 is in a class χ also known as being its "hard" state (in fact it rather corresponds to a hard-intermediate state in the recent classification of Homan & Belloni 2005), a state during which strong radio emission associated to a compact jet has been seen in the past (e.g., Fuchs et al. 2003). During this particular observation, the radio flux increased by a factor of 1.57 in a rather short time (less than an hour), while the 3–13 keV and the 18–50 keV count rates remained constant at the 1 σ level. The fact that the X-ray count rates do not follow the evolution of the radio flux may indicate that the jet has no influence on the X-ray emission at all. However, GRS 1915+105 is a source known to follow the radio to X-ray correlation seen in many microquasars (Corbel et al. 2003; Gallo 2006), which has been widely interpreted as evidence for an influence of the jet at X-ray energies. A way to reconcile our observation to the latter interpretation is to suppose that the X-ray count rates come from "competing" media emitting in the same energy ranges, e.g., a disk, and/or a standard corona and/or the jet. A model-dependent analysis is, however, beyond the scope of this paper.

4.2. *On the Generalization of the Radio to X-Ray Connection*

Focusing on the observations showing X-ray cycles, the observations of links between the X-ray cycles in class ν and β confirm previous findings that such events seem to be generic in those classes (Pooley & Fender 1997; Mirabel et al. 1998; Klein-Wolt et al. 2002). The observation of radio ejection in the λ class of variability is, however, the first ever reported. This may suggest a generalization of the fact that small-amplitude ejections in GRS 1915+105 always occur as a response to X-ray cycles, providing the X-ray hard dip is long enough (Klein-Wolt et al. 2002). The observation by Feroci et al. (1999) of an X-ray dip not followed by a radio flare during a *BeppoSAX* observation may be in contradiction with this generalization.

In fact, although some obvious morphological differences exist between the different classes, in terms of SR and colors they all undergo similar evolutions (Belloni et al. [2000] and Fig. 7). The cycles always begin with a transition to a low flux below 13 keV, the X-ray dip (interval I in Fig. 7), associated with a relatively bright flux above 18 keV. The 3–13 keV/18–50 keV SR has then a value of about 1. This indicates that the dip is spectrally hard. A short spike (interval II) occurs in the 3–13 keV range (it is very short in class λ). This spike seems to be the onset of a sudden and fast change, as the rising part is still hard (SR $\sim$ 1), although it

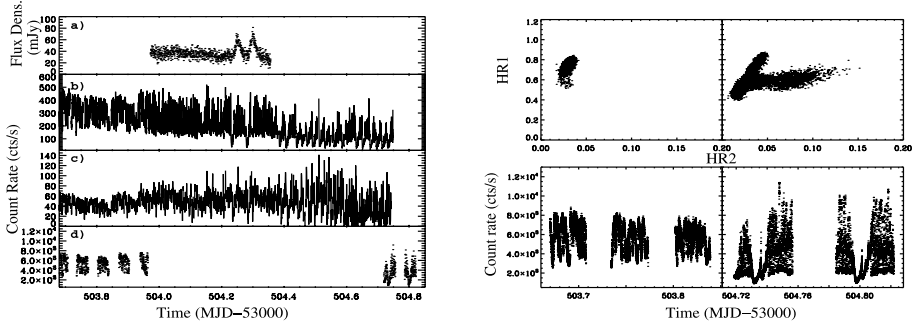

FIG. 6.—*Left*: Same as Fig. 2 for Obs. 5. *Right*: CC diagrams (*top*) and *RXTE* light curves (*bottom*) of two subintervals from Obs. 5 showing occurrences of class μ and β.

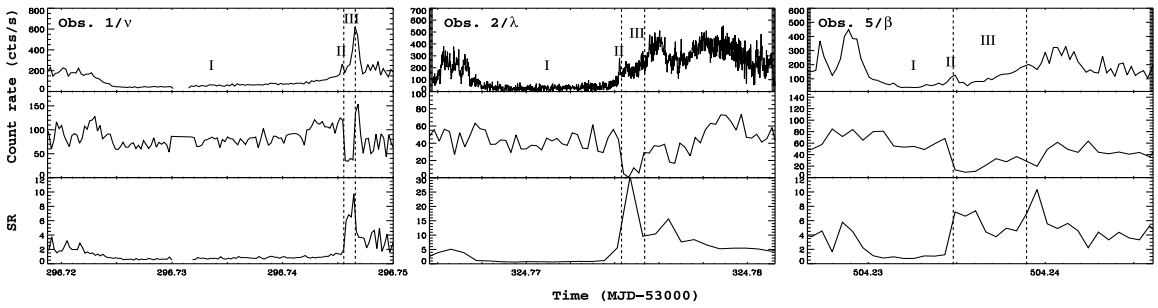

FIG. 7.—Zooms on portions of Obs. 2, 3, and 5 (*from left to right*). *Top*: JEM-X 3–13 keV light curves for each observation with the three intervals with specific properties discussed in the text. *Middle*: 18–50 keV ISGRI light curves. *Bottom*: 3–13 keV/18–50 keV SR. Note that different vertical scales of each individual plot.

smoothly evolves. After the spike, however, a fast and important decrease of the hard X-ray emission (interval III) during which the SR increases greatly indicates a much softer state is reached. In class ν, for example, the 18–50 keV count rate decreases by a factor $\sim$3. The evolution of the soft X-ray emission is less dramatic; although it decreases as well from intervals II to III in all classes, its evolution seems to be the continuation of the slow increase seen in each case at the end of interval I (Fig. 7). Mirabel et al. (1998) and Chaty (1998) identified the spike (II) in class β as the trigger to the ejection later seen in radio. In all three cases the delay between interval (Int.) II seen at X-ray energies and the peak of the radio flare is very similar. In class ν it is respectively $\sim$0.31 and $\sim$0.29 hr for the first and second flares, respectively. In class λ, it is $\sim$0.31 hr, while in class β it is respectively $\sim$0.31 and $\sim$0.34 hr for the first and second flare. This similarity may suggest that the same physical mechanism in the three classes give rise to the same phenomenon. Hence if the spike (Int. II) in class β is indeed the trigger of the ejection, it has the same role in classes ν and λ. This model-independent approach may suggest that the ejected material is the material responsible for the hard X-ray emission prior to the ejection occurring at Int. II. A similar interpretation was given by Chaty (1998) and Rodriguez et al. (2002) in the case of class β and α observations.

The lack of ejection after the X-ray dip reported by Feroci et al. (1999) can then easily be understood. In their case the dip in question is not followed by a spike, while an ejection they observe follows an X-ray spike, possibly following an X-ray dip (but missed due to occultation of GRS 1915+105 by the Earth). Interestingly, the approximate delay between the X-ray spike and the maximum of the radio flare in this observation (taken in 1996; Feroci et al. 1999) is $\sim$0.28 hr, and hence very similar to what we obtain in all our cases. In addition, the X-ray dip discussed in Feroci et al. (1999) seems much softer than the remaining intervals of their observation (see Table 1 of Feroci et al. 1999), as its photon index is the softest of the sequence. Putting everything together, then, it seems that we can generalize the following: plasmoid ejections *always* occur as response to an X-ray sequence composed of *a spectrally hard X-ray dip longer than 100 s terminated by a short X-ray spike*, the latter being the trigger of the ejection. This possible generalization is even reinforced by the observation of smaller amplitude ejections following short cycles during class λ. Although the shorter duration of the events prevented us from obtaining the same details as in the main cycles, it is obvious from Figure 4 that GRS 1915+105 undergoes similar evolution during one of the shorter dips. In particular, the dip is spectrally hard (SR $\sim$ 1), while it ends with a small 3–13 keV spike; it is also visible in the SR which increases to about 9, and therefore marks a transition to a much softer state.

4.3. *A Link between the Radio Amplitude and the Duration of the X-Ray Dip?*

Looking at class λ in more detail, we detected the presence of two small radio flares, each apparently following an X-ray dip of short duration. In order to study a possible dependence of the amplitude of the radio flare on the duration of the X-ray dip, we estimated the duration of the X-ray dips in each class. Since the dips have different shapes and the transition into the dip is quite smooth, the true starting time of the dip is quite difficult to estimate. To do so, we take as the starting point of the dip the mean time between the highest point immediately preceding the transition to the dip and the time at which the bottom of the dip is truly reached. The error here is the time difference between the highest point immediately preceding the transition to the dip and the bottom of the dip. The end time is taken as the "foot" of the X-ray spike, which renders its identification easier, given that the transition into the spike is quite sudden and rapid in all cases. The results are plotted in Figure 8. A positive correlation between the two quantities is quite obvious. The linear Spearman correlation coefficient is 0.93. The best linear fit leads to $F_{15\mathrm{GHz}}(\mathrm{mJy}) = 0.025t(\mathrm{s}) + 17.2$. Note, however, that a pure linear dependence of the radio amplitude versus the duration of the X-ray dip remains

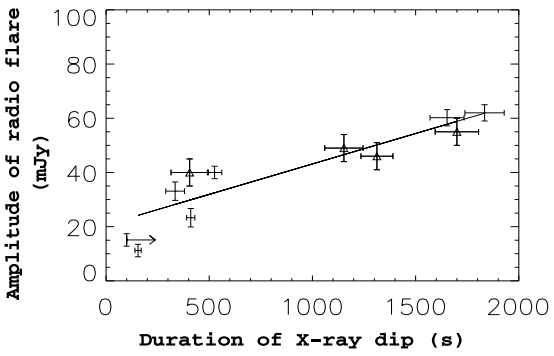

FIG. 8.—Evolution of the amplitude of the radio flares vs. the duration of the preceding X-ray dip. The points are from this study and the triangles come from Pooley & Fender (1997) and Klein-Wolt et al. (2002). The line represents the linear function that best fits the data.

unlikely as Klein-Wolt et al. (2002) remarked that for an ejection to take place a dip with a minimum duration of ~100 s is necessary.

In order to populate the region around 1000 s, we searched the literature for simultaneous radio (15 GHz) and X-ray data showing the occurrences of cycles and ejections. Some clear examples are given in Pooley & Fender (1997) and Klein-Wolt et al. (2002) for a total of eight cycles occurring around MJDs 50,381.6, 50,698.8, and 51,342.1. However, in four cycles (on MJDs 50,698.76 50,698.78, 51,342.06, and 51,342.12) the radio flares sat on top of nonzero (30–60 mJy) radio continuum, which renders the estimate of the radio amplitude very uncertain. Note that the binning of 32 s presented in Klein-Wolt et al. (2002) is also another source of uncertainty. These four cycles are not included here. The radio flares around MJD 50,381.6 (Pooley & Fender 1997) also sat on a nonzero continuum, but the latter is quite weak (~10 mJy), and therefore the amplitude of the radio flare can be estimated more accurately. Finally, the last radio flare occurs on MJD 50,698.83 just after a period of ~0 mJy level. These four additional cycles are added in Figure 8, and represented as triangles. With these new points, the general tendency remains the same. The linear Spearman correlation coefficient is 0.90, and the best linear fit leads to $F_{15\mathrm{GHz}}(\mathrm{mJy}) = 0.022t(\mathrm{s}) + 20.7$.

We also searched for other possible correlations between some properties of the cycles, and the amplitude of the radio flares such as, e.g., the amplitude of the spike (with respect to the bottom of the preceding dip), the amplitude of the variations of the SR after the spike, or the time delay between the X-ray spike and the peak of the radio flare. We do not find any obvious correlations between any of these quantities. The maximum variation for the SR is seen during the main λ cycle, while it corresponds to a rather low amplitude ejection. No correlation is found between the amplitude of the spike and the amplitude of the radio flare, either. The maximum amplitude of the spike occurs during the main cycle of class λ observation, for a relatively low amplitude radio flare. The spike with the minimum amplitude occurs during class β observation for a radio flare of similar amplitude to that of class λ.

The correlation of the radio amplitude with the duration of the X-ray dip brings up interesting possibilities regarding the accretion-ejection links. This may indicate, for example, that during the X-ray dip energy and matter, later used to power the ejection, are accumulated. The longer the X-ray dip, the more energy and/or matter are accumulated, and the higher the radio amplitude is. This is compatible with the fact that the ejected material is the matter responsible for the hard X-ray emission suggested by the sudden decrease of the 18–50 keV emission at the spike. In that case, a longer duration of the dip would indicate that more matter, later ejected, is accumulated during the dip.

Another possible explanation (not exclusive with the previous one) relies on the so-called magnetic floods scenario/model (Tagger et al. 2004). This model was recently proposed to account for the observed accretion-ejection and quasi-periodic variability properties during the cycles observed in a class-β observation. In this scenario, during the X-ray dip an accretion-ejection instability (AEI; Tagger & Pellat 1999) develops (and replaces the magneto-rotational instability [MRI] thought to occur during the preceding luminous soft X-ray state), because a poloidal magnetic field advected with the matter has accumulated in the inner region of the disk. If the magnetic configuration is favorable, a sudden reconnection event (producing the spike) can occur between magnetic fields of opposite polarities in the disk and in the magnetospheric structure of the black hole. This would then lead to the dissipation of the accumulated field in the inner regions, leading to the ejection (of the corona), and return to the MRI (Tagger et al. 2004). This scenario had some success in explaining all observational signatures (including QPOs) seen during the particular class β these authors dealt with. This interpretation is also compatible with the observed behavior we present here, andin particular with the possible correlation between the amplitude of the radio flare and the duration of the dip (Fig. 8). In that case, the longer the dip, the more magnetic flux can be accumulated in the inner region, and again the higher the available energetic reservoir used in energizing the ejection is. This interpretation is only tentative, however, and should not hide the fact that other models may explain these observations. However, the generalization of the X-ray cycles to radio ejections and the relation between the duration of the dip and the amplitude of the ejection bring strong constraints on any attempt to model the accretion-ejection behavior in GRS 1915+105 and other microquasars. Note that the possible correlation we found here clearly needs to be confirmed through systematic inspection of simultaneous radio and X-ray data, but also adding different frequencies (e.g., IR data).

J. R. would like to thank S. Chaty for useful discussions, C. A. Oxborrow for invaluable help with the ISGRI and JEM-X data reduction and calibration and A. Gros, A. Sauvageon, and N. Produit for help on specific aspects of the *INTEGRAL* software. J. R. also acknowledges E. Kuulkers, and more generally the *INTEGRAL* and *RXTE* planners for their great help in scheduling the observations. D. C. H. gratefully acknowledges a fellowship from the Finnish Academy. A. P. acknowledges the Italian Space Agency financial and programmatic support via contract ASI/INAF I/023/05/0. The authors thank the referee for his careful reading and valuable report, which helped to greatly improve the quality of this paper.

Based on observations with *INTEGRAL*, an ESA mission with instruments and science data center funded by ESA member states (especially the principle investigator countries: Denmark, France, Germany, Italy, Switzerland, Spain), Czech Republic, and Poland, and with the participation of Russia and the USA. This research has made use of data obtained through the High Energy Astrophysics Science Archive Center Online Service, provided by the NASA/Goddard Space Flight Center.

APPENDIX

IDENTIFICATION OF THE X-RAY CLASSES

In all cases the identification of states is based on the simultaneous inspection of the JEM-X light curves for the general shape, and PCA (when available) for confirmation through inspection of the CC diagrams. The different responses of JEM-X and PCA prevent direct comparison of the CCs produced with the two instruments, as they lead to completely different patterns. In some cases, especially when no simultaneous coverage by *RXTE* is available, we identify the class as the most likely based on the resemblance with the patterns identified by Belloni et al. (2000). The multiwavelength light curves and CC diagrams are reported in Figures 2–6 for the four observations discussed in detail in the paper and in Figures 10–14 for the others. As can be seen, while *RXTE* gives an easy access to

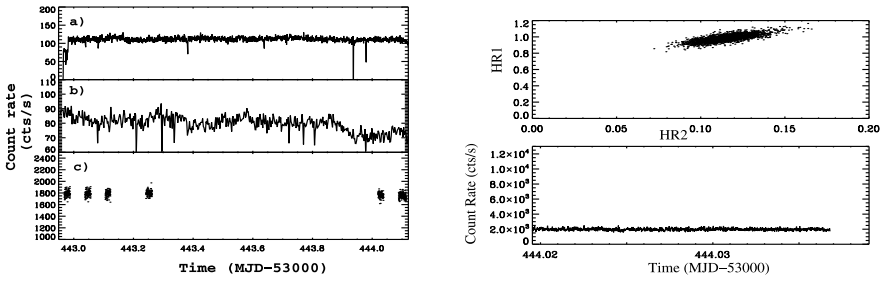

FIG. 9.—*Left*: Light curves of GRS 1915+105 during Obs. 3: (*a*) JEM-X 3–13 keV binned at 50 s; (*b*) ISGRI 18–50 keV binned at 200 s; (*c*) *RXTE* PCA 2–18 keV binned at 16 s. *Right*: CC diagram (*top*) and *RXTE* light curve (*bottom*) of a subinterval from Obs. 3 showing the source was in class χ.

high time resolution light curves and CC diagrams, *INTEGRAL* allows us to have a continuous coverage of the source and thus study the evolution of classes while witnessing transitions between some of them.

Obs. 1 (Fig. 2) shows alternating X-ray dips and spikes (cycles), followed by intervals of a high level of X-ray flux at all energies, and variability of different durations. Deep inspection of these behaviors shows that the source was in an alternation of class ν and class ρ heartbeat, as illustrated in Figure 2. As mentioned by Belloni et al. (2000), each ν-type cycle is separated by the preceding one by an interval of ρ-type behavior. This is illustrated by the fact that the CC diagram (Fig. 2) of class ν shows the same pattern as the one from class ρ with an extension toward higher values of HR2, corresponding to the dips. The radio light curve shows that at least after two sequences of X-ray dip/spike (hereafter cycles) radio flares occurred. In the past, similar radio flares have been seen to occur after each cycle (e.g., Klein-Wolt et al. 2002). This observation is one of the four whose deep analysis is presented in the core of this paper.

Obs. 2 (Fig. 3) shows a high level of very variable X-ray emission. On some occasions, one can see short dips in the soft X-ray light curves, each followed by a spike. A very variable behavior is also seen at hard X-ray energies, with occurrences of short dip clearly visible in the 18–50 keV light curve (Fig. 3). Looking more carefully at the source light curves, one can see that GRS 1915+105 seems to transit between different classes, as illustrated by the *RXTE* intervals (Fig. 3). Inspection of the CC diagrams shows that it started in class μ, transited to a class λ, transited back to μ, and evolved to a class γ. The presence of short $\sim$100 s long X-ray dips visible in the *INTEGRAL* JEM-X light curves indicates that the source transits continuously from μ to λ. Deep analysis of this observation is presented in the core of this paper.

In Obs. 3 (Fig. 9) GRS 1915+105 was in a low-luminosity steady state. The 3–13 keV JEM-X count rate was around 110 counts s^{-1}, while the 18–50 keV count rate was around 80 counts s^{-1}, with a slight decrease to about 70 counts s^{-1} near the end of the observation. The 2–18 keV PCA count rate was around 1800 counts s^{-1}. All light curves show a high degree of rapid variability. Both the light curve and the CC diagrams indicate the source was in class χ. No RTs were performed during this interval. The values of HR1 and HR2 are indicative of a very hard class χ (Fig. 9). In particular, the source is much harder here than during Obs. 4, although both observations belong to the same class.

Obs. 4 (Fig. 5) is very similar to Obs. 3, although GRS 1915+105 was slightly fainter at hard X-ray energies and showed lower values of the HRs. Near MJD 53,474.1 the source fluxes increased suddenly. This indicates that it underwent a transition to a brighter class, confirmed by the variations of the ASM light curve (Fig. 1). Simultaneous coverage at radio wavelengths shows a rather steady flux at around 50 mJy, although some variations are visible. In particular, the radio flux increased up to 100 mJy near the end of the observation (Fig. 5). The global X-ray behavior indicates that GRS 1915+105 was in a radio-loud class χ. This observation is one of the four that is deeply analyzed in this paper.

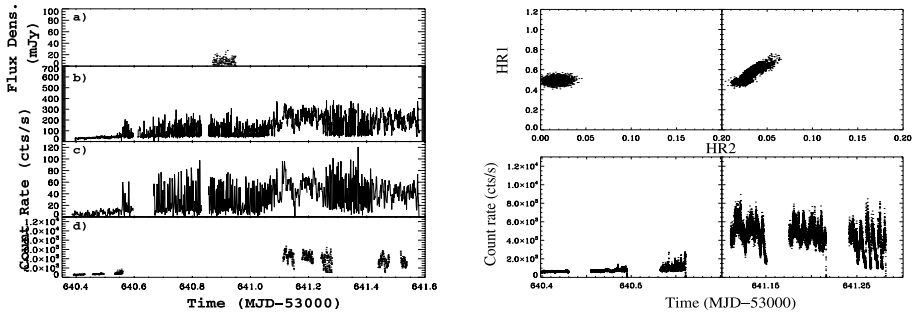

FIG. 10.—*Left*: Light curves of GRS 1915+105 during Obs. 7: (*a*) RT at 15 GHz; (*b*) JEM-X 3–13 keV binned at 20 s; (*c*) ISGRI 18–50 keV, binned at 100 s. *Right*: CC diagrams (*top*) and *RXTE* light curves (*bottom*) of two subinterval from Obs. 7 showing the source was in class ϕ at the beginning and class δ in the end. Note that between those two classes GRS 1915+105 transited through a class θ.

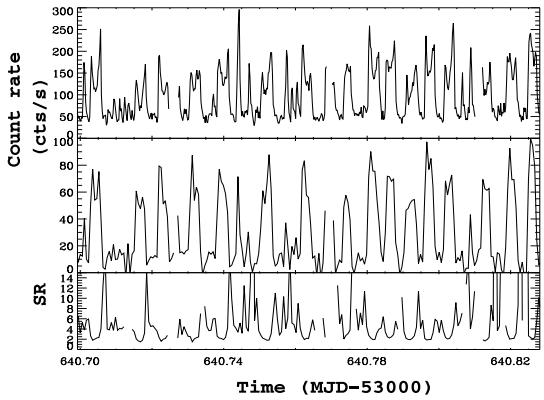

FIG. 11.— Zoom on a subinterval from Obs. 7. From top to bottom the plots respectively represent the JEM-X 3−13 keV, ISGRI 18−50 keV light curves, and the 3−13 keV/18−50 keV SR. Both light curves show "M-shaped" patterns typical of class θ.

Obs. 5 (Fig. 6) shows that GRS 1915+105 was in classes of high X-ray flux with a high degree of variability. It is interesting to note that the overall 18−50 keV variability increased during the observation. Although the mean 18−50 keV flux remained quite bright around 40−50 counts s^{-1}, significant dips and spikes can be seen, some in simultaneity with those seen at soft X-rays. It is clear from Figure 6 that it transited at least between two such classes. Inspection of the CC diagrams shows that it started in a class μ and finished in class β. Our radio observation shows a roughly constant flux of ∼40 mJy up to MJD 53,504.35, where two radio flares occurred after occurrences of dip-spike cycles in the X-ray domain. This observation is one of the four that is deeply analyzed in this paper.

Obs. 6 was of poor quality due to the effects of high solar activity and was therefore not considered in this analysis.

Obs. 7 (Fig. 10) shows a clear transition from a class with a very low level of X-ray emission to a class of high flux with high variability with similar evolving patterns at both soft and hard X-rays. The change from the first class to the last seems to occur through a third one, as illustrated by the differences in the JEM-X and ISGRI light curves, but the lack of *RXTE* data during this interval prevents us from obtaining any clear identification. A zoom on the intermediate part (Fig. 11) shows occurrences of 3−13 keV "M-shaped" patterns typical of class θ. In the mean time, the 18−50 keV light curve shows similar variability (the M can be seen in coincidence with those occurring at soft X-rays) and a high variability. The SR indicates the source was hard during the dips of the M, which is in agreement with the known behavior of class θ (Belloni et al. 2000). This class shows a behavior very similar to other classes with cycles, i.e., spectrally hard dips ended by a soft X-ray spike marking the disappearance of the hard X-ray emission (and transition to a soft state as illustrated by the variations of the SR visible in Fig. 11). The level of radio emission was quite low, with some variability, which is also in agreement with GRS 1915+105 being in class θ (Klein-Wolt et al. 2002). This may further corroborates the generalization of the X-ray to radio connection presented in this paper, although the resolution at radio wavelength do not allow us to identify any radio flares. The analysis of the *RXTE* data of the beginning and end of the *INTEGRAL* observations (Fig. 10) indicates that GRS 1915+105 started in class ϕ and ended in class δ.

Obs. 8 and 9 (Fig. 12) were part of a large multiwavelength campaign involving the *Suzaku* satellite at high energy. The *INTEGRAL* light curves are first very similar to the light curves of Obs. 4, which was indeed a class χ. The higher level of soft X-ray emission, and slightly lower level of hard X-ray emission tend to indicate a rather soft class χ. In the second part, a flare occurred at the beginning of the

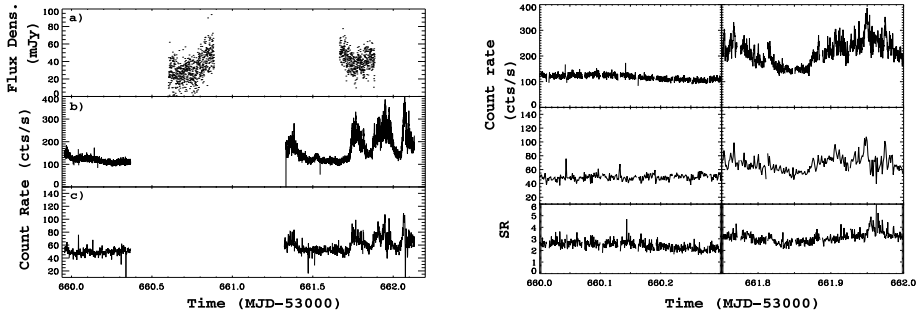

FIG. 12.— *Left*: Light curves of GRS 1915+105 during Obs. 8 and 9: (*a*) RT at 15 GHz; (*b*) JEM-X 3−13 keV binned at 20 s; (*c*) ISGRI 18−50 keV binned at 100 s. The source starts in class χ in the first part, transits to class θ (not visible here; see Ueda et al. 2006) and transits back in a likely class χ in the second interval visible here. *Right*: Zoom on two subintervals from Obs. 8 (*left*) and Obs. 9 (*right*). From top to bottom the plots respectively represent the JEM-X 3−13 keV, ISGRI 18−50 keV light curves, and the 3−13 keV/18−50 keV SR.

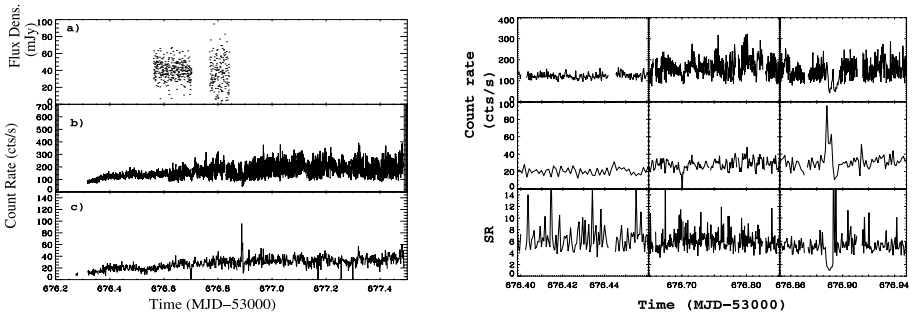

FIG. 13.—*Left*: Light curves of GRS 1915+105 during Obs. 10: (*a*) RT at 15 GHz; (*b*) JEM-X 3–13 keV; (*c*) ISGRI 18–50 keV. *Right*: Zoom on three subintervals of Obs. 10 showing (possible) occurrences of class δ, μ, and β. From top to bottom the panels respectively show the JEM-X 3–13 keV and ISGRI 18–50 keV light curves and the 3–13 keV/18–50 keV SR.

observing interval at both soft and hard X-rays. GRS 1915+105 then returned to a rather steady emission before transiting to a class that showed similar patterns at soft and hard X-rays. The lack of simultaneous *RXTE* coverage prevents us from securely identifying the class of variability. A zoom on the JEM-X light curve (Fig. 12) does not show any easily identifiable pattern. Furthermore, the 3–13 keV/18–50 keV SR has a value quite similar to that of Obs. 8 (Fig. 12) and even to Obs. 4 (not shown). Therefore, it seems the source was still in a class χ. Ueda et al. (2006) presented preliminary results of the whole campaign; they, in particular, showed that GRS 1915+105 started in a class χ showing the presence of a 6 Hz QPO, and transited in a class θ. The class θ, however, occurred between both *INTEGRAL* intervals. The mean level of radio emission was 31 mJy until MJD 53,660.7 and then increased to about 39 mJy during the first radio interval (Fig. 12). The mean level of radio emission during the second interval was about 40 mJy. The shape of the radio light curve may suggest that ejection had taken place between the two observing intervals. A simultaneous Very Large Array (VLA) light curve (Ueda et al. 2006) is also compatible with this interpretation. Ueda et al. (2006) suggested that ejection of material was triggered at the transition from spectral state C to spectral state A (hard intermediate to soft state), similar to our interpretation.

Obs. 10 (Fig. 13), shows a complex behavior made of several possible transitions. The radio light curve (Fig. 13) also indicates two different behaviors. In the first part (MJD 53,676.56–53,676.99), the mean 15 GHz flux was ~40.4 mJy with an rms of 10.4 mJy. In the second part (MJD 53,676.77–53,676.841), the mean flux was 36.5 mJy, and the variability of the radio emission had increased significantly with an rms of 19.6 mJy. This increase seems to be correlated to the X-ray behavior. Around MJD 51,678.9 a dip at soft X-ray energies associated to a 18–50 keV strong flare occurred. The identification of the classes is only based on the shape of the light curves and 3–13 keV/18–50 keV SR, since no *RXTE* data are available. We can distinguish three main periods in the light curves. Until MJD 53,676.6, the source flux gradually increased and so did the variability. The shape of the JEM-X light curve (Fig. 13, *right*) and the level of radio emission seem to indicate a class χ observation. The low level of hard X-ray emission and the SR, however, do not favor this identification. Figure 13 (*right*) shows that GRS 1915+105 was transiting between states with SR $\sim$ 4 and SR $\sim$ 14–15. This behavior is not what is observed in the other class χ observations. This would rather indicate a class with transitions between spectral state A and state B of Belloni et al. (2000) possibly class δ, although it was then fainter than the other class δ observations (e.g., Obs. 5) at both soft and hard X-rays. Note that the possible level of radio emission was not what is usually observed in this class (Klein-Wolt et al. 2002), which weakens the identification. After MJD 53,676.6, the shape resembles that of a class μ (Fig. 13, *right*), before undergoing a dip-spike sequence indicative of a class β. The identification of class μ is compatible with the level of radio emission (Klein-Wolt et al. 2002). It has to be noted that after the occurrence of this cycle, the level of X-ray emission was higher and more variable than before. Although there were no more occurrences of cycles toward the end of the observation, the X-ray behavior was similar to what is observed during class β between the occurrences of cycles (Belloni et al. 2000) with a high degree of variability.

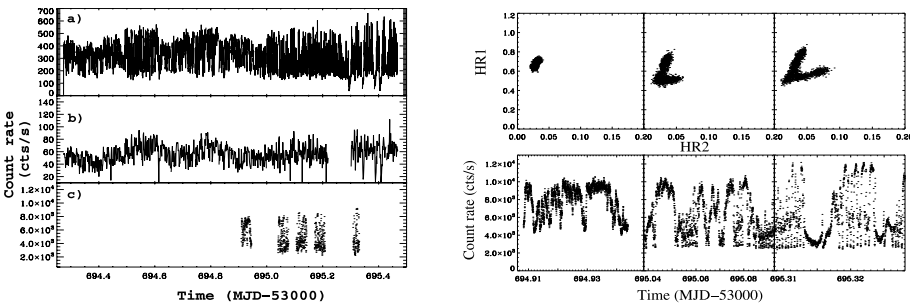

FIG. 14.—*Left*: Light curves of GRS 1915+105 during Obs. 11: (*a*) JEM-X 3–13 keV binned at 20 s; (*b*) ISGRI 18–50 keV binned at 100 s; (*c*) PCA 2–18 keV binned at 16 s. *Right*: Zoom on three subintervals showing occurrences of class δ (possibly), μ, and β.

Obs. 11 (Fig. 14) also shows several transitions. We do not have any radio coverage during this observation. Although our *RXTE* observations arrive late in the *INTEGRAL* coverage (Fig. 14), it seems that during the first part of the observation (up to about MJD 53,695), GRS 1915+105 was in the same type of variability. Zooms on the JEM-X and ISGRI light curves during this first part (not shown) indeed indicate similar morphologies. Inspection of the CC diagram of the first sample of the *RXTE* light curve shows the source was in a class δ (Fig. 14, *right*). The following samples show that GRS 1915+105 had changed class. This is especially indicated by the track in the CC diagram that shows an incursion in the low HR1 region, with an HR2 as high as 0.05. This pattern and the shape of the light curve is what is observed during class μ. However, typical class μ, such as the one observed during Obs. 3, show a longer extension toward higher value of HR1 (Fig. 3, *right*). This may simply indicate that while in the first hundred seconds of the interval the variations were still similar to δ, GRS 1915+105 evolved toward β in the end, and hence the CC diagram is a mixture of both, or simply that due to the short length of the interval ($\sim$2500 s) the high values of HR2 are less observed than in typical (>3000 s long) intervals. After that, around MJD 53,695.1, another transition occurred. GRS 1915+105 shows light curves with a high level of X-ray emission and a high degree of variability. The behavior was the same at soft and hard X-rays with occurrences of long dips in both light curves. This is reminiscent of what we saw during Obs. 5 (Fig. 6) with the occurrence of β-like cycles after some times (Fig. 14, *right*).

REFERENCES

Baars, J. W. M., Genzel, R., Pauliny-Toth, I. I. K., & Witzel, A. 1977, A&A, 61, 99

Belloni, T., Klein-Wolt, M., Méndez, M., van der Klis, M., & van Paradijs, J. 2000, A&A, 355, 271

Belloni, T., Mendez, M., King, A. R., van der Klis, M., & van Paradijs, J. 1997, ApJ, 488, L109

Chapuis, C., & Corbel, S. 2004, A&A, 414, 659

Chaty, S. 1998, Ph.D. thesis, Univ. Paris 7

Corbel, S., Nowak, M. A., Fender, R. P., Tzioumis, A. K., & Markoff, S. 2003, A&A, 400, 1007

Dhawan, V., Mirabel, I. F., & Rodríguez, L. F. 2000, ApJ, 543, 373

Eikenberry, S. S., Matthews, K., Morgan, E. H., Remillard, R. A., & Nelson, R. W. 1998, ApJ, 494, L61

Fender, R. P., & Belloni, T. 2004, ARA&A, 42, 317

Fender, R. P., Garrington, S. T., McKay, D. J., Muxlow, T. W. B., Pooley, G. G., Spencer, R. E., Stirling, A. M., & Waltman, E. B. 1999, MNRAS, 304, 865

Fender, R., & Pooley, G. 1998, MNRAS, 300, 573

Feroci, M., Matt, G., Pooley, G., Costa, E., Tavani, M., & Belloni, T. 1999, A&A, 351, 985

Fuchs, Y., et al. 2003, A&A, 409, L35

Fritz, S., Kreykenbohm, I., Wilms, J., Staubert, R., Bayazit, F., Pottschmidt, K., Rodriguez, J., & Santangelo, A. 2006, A&A, 458, 885

Gallo, E. 2006, in Proc. VI Microquasar Workshop: Microquasars and Beyond, ed. T. Belloni (Como: Proc. Science), 9.1

Goldwurm, A., et al. 2003, A&A, 411, L223

Harlaftis, E. T., & Greiner, J. 2004, A&A, 414, L13

Homan, J., & Belloni, T. 2005, Ap&SS, 300, 107

Klein-Wolt, M., Fender, R. P., Pooley, G. G., Belloni, T., Migliari, S., Morgan, E. H., & van der Klis, M. 2002, MNRAS, 331, 745

Lebrun, F., et al. 2003, A&A, 411, L141

Lund, N., et al. 2003, A&A, 411, L231

Mirabel, I. F., Dhawan, V., Chaty, S., Rodriguez, L. F., Marti, J., Robinson, C. R., Swank, J., & Geballe, T. 1998, A&A, 330, L9

Mirabel, I. F., & Rodríguez, L. F. 1994, Nature, 371, 46

———. 1998, Nature, 392, 673

Morgan, E. H., Remillard, R. A., & Greiner, J. 1997, ApJ, 482, 993

Pooley, G. G., & Fender, R. P. 1997, MNRAS, 292, 925

Rodriguez, J., Cabanac, C., Hannikainen, D. C., Beckmann, V., Shaw, S. E., & Schultz, J. 2005, A&A, 432, 235

Rodriguez, J., Durouchoux, Ph., Mirabel, I. F., Ueda, Y., Tagger, M., & Yamaoka, K. 2002, A&A, 386, 271

Rodriguez, J., & Shaw, S. E. 2005, Astron. Tel., 660

Rodriguez, J., Shaw, S. E., & Corbel, S. 2006, A&A, 451, 1045

Rodriguez, J., et al. 2008, ApJ, 675, 1449

Tagger, M., & Pellat, R. 1999, A&A, 349, 1003

Tagger, M., Varnière, P., Rodriguez, J., & Pellat, R. 2004, ApJ, 607, 410

Ueda, Y., et al. 2006, in Proc. VI Microquasar Workshop: Microquasars and Beyond, ed. T. Belloni (Como: Proc. Science), 23.1

Vadawale, S. V., Rao, A. R., Naik, S., Yadav, J. S., Ishwara-Chandra, C. H., Pramesh Rao, A., & Pooley, G. G. 2003, ApJ, 597, 1023

9.4 IGR J19294+1816 : SFXT ou système Be ?

June 22, 2009

The nature of the X-ray binary IGR J19294+1816 from *INTEGRAL*, *RXTE*, and *Swift* observations

J. Rodriguez[1], J.A. Tomsick[2], A. Bodaghee[2], J.-A. Zurita Heras[1], S. Chaty[1], A. Paizis[3], S. Corbel[1]

[1] Laboratoire AIM, CEA/DSM - CNRS - Université Paris Diderot (UMR 7158), CEA Saclay, DSM/IRFU/SAp, F-91191 Gif-sur-Yvette, France
[2] Space Science Laboratory, 7 Gauss Way, University of California, Berkeley, C1 94720-7450, USA
[3] INAF-IASF, Sezione di Milano, via Bassini 15, 20133 Milano, Italy

Preprint online version: June 22, 2009

ABSTRACT

We report the results of a high energy multi-instrumental campaign with *INTEGRAL*, *RXTE*, and *Swift* of the recently discovered *INTEGRAL* source IGR J19294+1816. The *Swift*/XRT data allows us to refine the position of the source to RA_{J2000}=19h 29m 55.9s, Dec_{J2000}=+18° 18′ 38.4″ (±3.5″), which permits us to identify a candidate infrared counterpart. The *Swift* and *RXTE* spectra are well fitted with absorbed power laws with hard ($\Gamma \sim 1$) photon indexes. We obtain evidence, in one case only, for absorption in true excess to the Galactic value, which may indicate some intrinsic absorption in this source. We detect a strong (P=40%) pulsation at ∼12.44 s that we interpret as the spin period of a pulsar. All these results, coupled with the possible 117 days orbital period point to IGR J19294+1816 being a HMXB with a Be companion star. However, while the long-term *INTEGRAL*/IBIS/ISGRI 18–40 keV light curve shows that the source spends most of its time in an undetectable state, we detect occurrences of short (∼ 2000 − 3000 s) and intense flares that are more typical of Supergiant Fast X-ray Transients. We therefore cannot conclude on the type of the system, and we discuss the possible implications of IGR J19294+1816 being a SFXT.

Key words. X-rays: binaries ; Accretion, accretion disks ; Stars: individual: IGR J19294+1816, IGR J11215−5952, IGR J18483−0311

1. Introduction

The INTErnational Gamma-Ray Astrophysics Laboratory (*INTEGRAL*) has permitted a large number of new sources to be discovered. Amongst the ∼ 250 new sources[1] *INTEGRAL* has unveiled two new or poorly known types of High Mass X-ray Binaries (HMXB): the very absorbed supergiant HMXBs, and the Supergiant Fast X-ray Transients (SFXT). While all types of HMXBs (including those hosting a Be star, Be-HMXBs) are powered by accretion of material by a compact object, understanding the nature of a system has a strong importance for the study of population of sources and their evolutionary path, and more globally the evolution of the Galaxy in terms of its source content.

IGR J19294+1816 was discovered by Tuerler et al. (2009) who first reported activity of this source seen with *INTEGRAL* during the monitoring campaign of GRS 1915+105 (e.g. Rodriguez et al. 2008a). Archival *Swift* data of a source named Swift J1929.8+1818 have allowed us to give a refined X-ray position of IGR J19294+1816 at RA_{J2000}= 19^h 29^m 55.9^s Dec_{J2000}=+18° 18′ 39″ (±3.5″) and find a possible infrared counterpart (Rodriguez et al. 2009). We also suggested that the *Swift* and *INTEGRAL* sources are the same, and that, activity from IGR J19294+1816 had been seen with *Swift* in the past. The temporal analysis of the XRT light curve showed the presence of a possible pulsation at 12.4 s (Rodriguez et al. 2009). Analysis of *Swift*/BAT archival data revealed that the source had been detected on many occurrences in the past, with a periodicity at 117.2 days (Corbet & Krimm 2009) interpreted as the orbital period of the system.

Soon after the discovery of the source with *INTEGRAL*, we triggered our accepted *RXTE* and *Swift* programs for follow-up observations of new *INTEGRAL* sources (PI Rodriguez). A preliminary analysis of the real time *RXTE* data have allowed us to confirm the presence of the pulsation in the signal from the source (Strohmayer et al. 2009) at a barycentred period of 12.44 s indicating that this object hosts an accreting X-ray pulsar. Here we report the detailed analysis of the *INTEGRAL*, *Swift*, and *RXTE* observations. We start this paper by detailing the procedures employed for the data reduction. We then describe the results (refined position, X-ray spectral and temporal analysis) in section 3, 4, 5 and 6, and discuss them in section 7.

2. Observations and Data Reduction

The log of the *Swift* and *RXTE* observations of IGR J19294+1816 is given in Table 1. The `LHEASOFT v6.6.2` suite was used to reduce the *Swift* and *RXTE* data. The *RXTE*/PCA data were reduced in a standard way, restricting to the times when the elevation angle above the Earth was above 10°, and the offset pointing less than 0.02°. We accumulated spectra from the top layer of proportional counter unit 2 (PCU 2), the only one that was active during all the observations, and therefore time-filtered the data for PCU 2 breakdown. The background was estimated using the faint model. In addition, we produced event files from `Good Xenon` data with `seextrct` with a time resolution of 2^{-12} s (∼ 250μs and 2–60 keV light curves with 1 s time resolution from standard 1 data for temporal

Send offprint requests to: J. Rodriguez e-mail: `jrodriguez@cea.fr`

[1] see http://isdc.unige.ch/∼rodrigue/html/igrsources.html for an up to date list of all sources and their properties.

Table 1. Journal of the *Swift* and *RXTE* dedicated observations. Obs. S3 and X5 were simultaneous with an *INTEGRAL* observation.

Satellite	Date start (MJD)	Exposure time (s)	Name
Swift	54443.051	7959	S1
Swift	54447.013	3457	S2
RXTE	54921.315	2600	X1
RXTE	54921.708	3344	X2
RXTE	54922.813	3344	X3
RXTE	54923.730	1440	X4
Swift	54925.814	2565	S3
RXTE	54925.826	3360	X5

studies. These were then corrected for the background.

The *Swift*/XRT data were first processed with the `xrtpipeline v0.12.2` tool to obtain standardly filtered level 2 event files. Images, light curves and spectra were extracted within `XSELECT V2.4a`. Source light curves and spectra were extracted from a circular region of 20 pixel radius centred on the best source position. We tested different regions of extraction for the background light curves and spectra, and obtained no significant differences. For the remainder of the analysis the background region is a circular region of 60 pixel radius centred at RA=19^h 29^m 41.8^s and DEC=+18° 21′ 11.5″. The ancillary response file was obtained with `xrtmkarf 0.5.6` after having taken the exposure map into account (see Rodriguez et al. 2008b, for more details).

We also analysed *all INTEGRAL* public pointings aimed at less than 10° from the position of IGR J19294+1816 plus all the still private data of our monitoring campaign on GRS 1915+105. The `Off-line Scientific Software (OSA) v7.0` was used for the *INTEGRAL* data reduction. We further filtered the list of science windows (SCW) to those where the good exposure time of ISGRI was greater than 1000 s. After omitting the bad pointings (e.g. first or last pointings before the instruments are switched off due to passage through the radiation belts) this resulted in a total of 1476 good SCWs. All these pointings were blindly searched for the presence of the source (see Rodriguez et al. (2008a), for the procedure of data reduction and source searching). An updated catalog containing IGR J19294+1816 with its best *Swift* position was given as an input to the software. Mosaics were accumulated on a revolution basis, but this results in mosaics of very different exposure times. Note that even in revolution 788, where we confirm the detection reported by Tuerler et al. (2009), the source is too dim for further spectral analysis.

3. IGR J19294+1816 as seen with *INTEGRAL*

IGR J19294+1816 was discovered on March 27, 2009 (revolution 788, MJD 54917 Tuerler et al. 2009). A re-analysis of the consolidated data has allowed us to confirm a clear detection of the source during this observation. The source is detected at 10.7 σ between 18 and 40 keV, with a flux of about 17 mCrab[2]. A re-analysis of the previous observation on March 21, 2009 (rev. 786, MJD 54911) led to a detection in the 18–40 keV with a significance of 4.5 σ and a flux of about 7.2 mCrab. IGR J19294+1816 is not detected on April 4, 2009 (rev 790, MJD 54925) with a 18–40 keV 3-σ upper limit of about 5 mCrab. The source is not detected in any of the mosaics from the previous revolution. However, given the very different exposure times we used in building the mosaics and the periodicity of the source activity seen with *Swift*/BAT (Corbet & Krimm 2009), this may simply indicate that the periods of activity of the source are short.

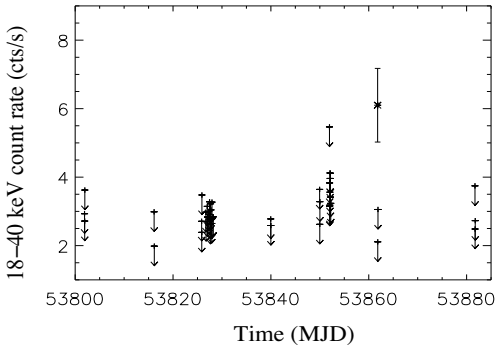

Fig. 1. *INTEGRAL*/IBIS 18–40 keV light curve of IGR J19294+1816 showing the flare of MJD 53861.

Looking at these data on a SCW basis shows that the source is detected on a few occurrences. It is in particular clearly detected during an observation in rev. 435 (MJD 53861) and during another pointing in rev. 482 (MJD 54004). In the former, IGR J19294+1816 is detected in SCW 9 (19.17–19.77 h UTC) with a 18–40 keV flux of about 33.7 mCrab. It is not detected in the following SCW (19.85–20.50 h) with a 3 σ upper limit of 11.6 mCrab. There is no pointing available before. The 18–40 keV light curve of this period is reported in Fig. 1. In rev. 482 the source is detected in SCW 51 (1.05–2.03 h UTC) at a 18–40 keV flux of 22 mCrab (5.4 σ). It is not detected in the previous and following SCWs with respective 3 σ upper limits of 11.0 and 13.9 mCrab.

4. Refining the X-ray position, and the search for counterparts

We added all *Swift* observations to create a mosaic image of the field. As can be seen on Fig. 2 a single bright X-ray source is found within the ∼ 5′ 90% error circle of the *INTEGRAL* position given in Tuerler et al. (2009). This source lies at (as obtained with `xrtcentroid`) RA_{J2000}=19h 29m 55.9s Dec_{J2000}=+18° 18′ 38.4″ with an uncertainty of 3.5″. Note that this is slightly different from the preliminary position given in Rodriguez et al. (2009), but the two positions are clearly compatible. Given the addition, here, of an additional *Swift* pointing to obtain this position, we consider this one as the most precise one.

We browsed the online catalogs, such as the 2 Micron All Sky Survey point source and extended source catalogs[3] (2MASS and 2MASX, Skrutskie et al. 2006), the National Radio Astronomy Observatory VLA Sky Survey (NVSS, Condon et al. 1998), the US Naval Observatory (USNO[4]) to search for counterparts. We also made use of images from the Second Palomar

[2] The count rate to Crab conversion is based on an analysis of the Crab observation performed during rev. 774, with 1 $Crab_{18-40keV}$ = 181.1 cts/s.

[3] http://www.ipac.caltech.edu/2mass/

[4] http://www.usno.navy.mil/USNO/astrometry/optical-IR-prod/icas

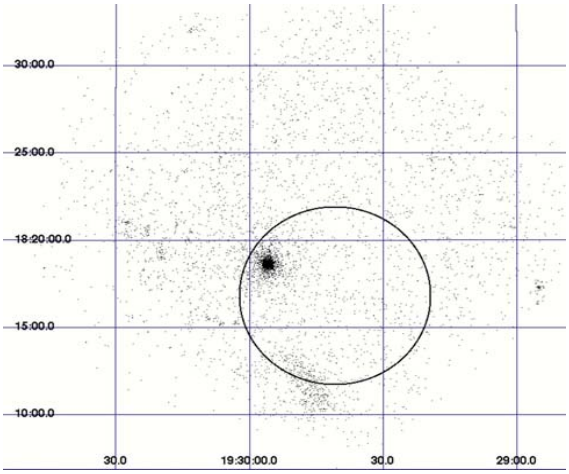

Fig. 2. *Swift*/XRT mosaic of the field around IGR J19294+1816. The circle represents the error box from *INTEGRAL*.

Table 2. Infrared magnitudes dereddened with different values of the absorption.

N_H $\times 10^{22}$ cm^{-2}	A_V	$J_{der.}$	$H_{der.}$	$K_{s,der.}$	J-H	H-K_s
2.0	11.20	11.32	11.04	10.86	0.28	0.18
2.73	15.29	10.14	10.32	10.40	−0.18	−0.08
4.0	22.40	8.08	9.09	9.53	−1.01	−0.44

Observatory Sky Survey obtained through the STScI Digitized Sky Survey (DSS[5]). The 2MASS IR and DSS finding charts are shown in Fig. 3.

A clear infrared counterpart is found in the 2MASS catalog. 2MASS J19295591+1818382 has magnitudes J=14.56 ±0.03, H=12.99 ±0.02 and K_s=12.11 ±0.02. No optical or radio counterpart is found in either of the other catalogs, although a faint object may be present in the "infrared" (7000-9700Å) POSS II image (Fig. 3). The infrared magnitudes were dereddened using $A_\lambda = C(\lambda) \times A_V$, with $C(\lambda)$ the wavelength dependent coefficients obtained by Cardelli et al. (1989) (see Table 4 in Rahoui et al. 2008, for the values adopted), and $A_V = 5.6 \times 10^{22} \times N_H$ (Predehl & Schmitt 1995). The value of the total absorbing column density on the line of sight was obtained from the LAB survey of Galactic HI (Kalberla et al. 2005), and the CO survey of Dame et al. (2001) for the value of molecular H_2. Therefore $N_H = N_{HI} + 2N_{H_2} = 1.23 + 2 \times 0.75 = 2.73 \times 10^{22}$ cm^{-2}. We also used the value of N_H obtained through the X-ray spectral fits to the data, $N_{HX,bbody} = 2.0 \times 10^{22}$ cm^{-2}, and $N_{HX,po} = 4.0 \times 10^{22}$ cm^{-2} (see Sec. 5). The dereddened magnitudes are reported in Table 2.

5. X-ray spectral analysis

5.1. Correction of the Galactic Ridge emission in the PCA spectra

Since IGR J19294+1816 is faint and located in the Galactic plane (its Galactic coordinates are l=53.5400°, b=0.1150°), the Galactic ridge can contribute a significant amount of the flux collected by the PCA. We estimated the level of emission using the results from Valinia & Marshall (1998), and first corrected the spectra from the Galactic ridge emission in a similar way as done for IGR J19140+0951 by Prat et al. (2008), ie adding the Galactic ridge spectrum to the instrumental background spectrum.

The simultaneous fit to the S3 and X5 spectra showed a large offset in the normalizations of the spectra: when including a constant in the fit and freezing it to 1 for the S3 spectrum it systematically tended to low value (~0.45) for the X5 spectrum. This may indicate that either the source has varied during the non-simultaneous part of these observations, or that we over corrected the emission of the Galactic ridge in the PCA spectrum. We consider this last hypothesis as the most likely given that the spectrum of the Galactic ridge obtained from Valinia & Marshall (1998) is just an average spectrum covering the central regions of the Galaxy, i.e. $-45° < l < 45°$ and $-1.5° < b < 1.5°$, and that IGR J19294+1816 is slightly outside this region. Although it is right in the Galactic ridge, we may expect local variations in the ridge, and/or slight changes (lower intensity for example) at high longitude (as also mentioned in Valinia & Marshall 1998).

In a second run, we did not correct the X5 spectrum for the contribution of the Galactic ridge. During the fit we did not include any normalization constant between the S3 and X5 spectra (we therefore made the assumption that *Swift* and *RXTE* are perfectly cross calibrated), and fitted them with a model including both an absorbed power law and the best model for the Galactic ridge spectrum obtained by Valinia & Marshall (1998), with the parameters of the latter frozen. A multiplicative constant was included before this spectral component. The spectral model is therefore `phabs*powerlaw+constant*(wabs*(raymond+powerlaw))` in the `XSPEC` terminology. We first fitted the S3 spectrum alone (with the constant frozen to 0) to obtain the parameters of the source. We then added the X5 spectrum and only left the normalization constant to the X5 data free to vary while it was frozen to 0 for the S3 data. We therefore assume that the average spectral parameters obtained in the $-45° < l < 45°$ are still valid at the position of IGR J19294+1816 and that only the overall flux of the ridge emission changes. The best value obtained for the constant is 0.85±0.04 (at 90%), and in all subsequent analysis we used this value to correct all PCA spectra following:

$$\mathrm{BGD_{tot}} = \mathrm{BGD_{instr}} + 0.85 \times \mathrm{Ridge} \quad (1)$$

5.2. Results of the spectral analysis

The *Swift*/XRT spectra were rebinned so as to have a minimum of 20 cts per channel, except the channels below about 1.2 keV that were grouped in 2 bins: one below 0.2 keV that was not considered further for the spectral fitting, and one between 0.2–1.2 keV to obtain an additional spectral point to better constrain the absorption column density N_H. We fitted each individual spectrum alone in `XSPEC 11.3.2ag`, except the spectra from observations S3 and X5 that were fitted simultaneously. Different spectral models were used to fit the spectra. The *Swift* spectra are well fitted using either an absorbed blackbody, or an absorbed power law, while only the latter model provides a good fit to the *RXTE* spectra, and joint *Swift* and *RXTE* spectra. This and the detection at energies greater than 20 keV with *INTEGRAL* and *Swift* probably indicates that the true origin of the emission is not a blackbody. We, however, report the parameters of the black-

[5] http://archive.stsci.edu/cgi-bin/dss_form

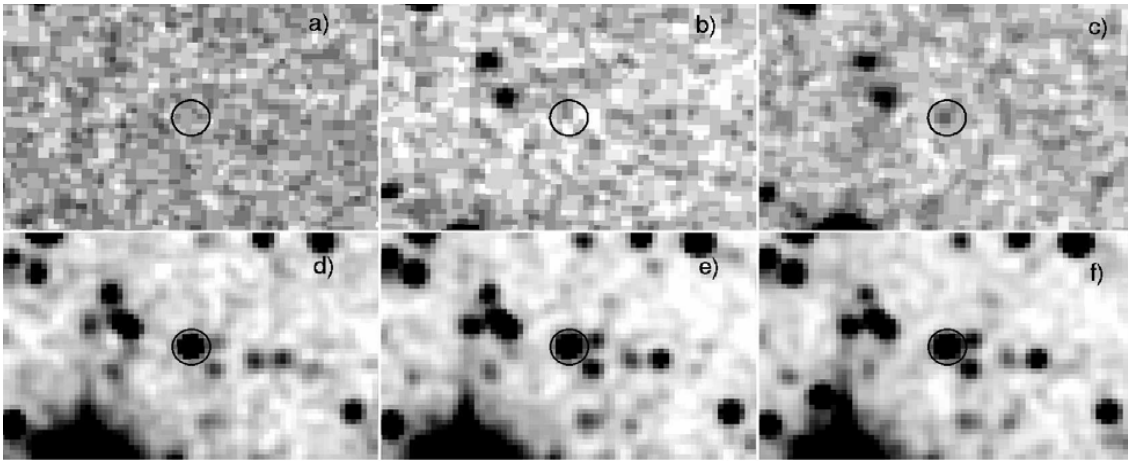

Fig. 3. 1.14′×0.73′ POSS II optical (top) and 2MASS infrared (bottom) images of the field around IGR J19294+1816. The black circle is the *Swift* error box. a) " Blue", b) "Red", c) "infrared", d) J filter e) H filter, f) K_s filter .

Table 3. Results of the X-ray spectral fitting. The errors are at the 90% confidence level.

Obs	N_H ($\times 10^{22}$ cm^{-2})	Γ	kT_{bb} (keV)	$F_{2-10,unabs.}$ (erg cm^{-2} s^{-1})
S1	$4.0^{+0.9}_{-0.8}$	0.9±0.2		3.6×10^{-11}
	2.0±0.4		2.1±0.2	3.0×10^{-11}
S2	$3.4^{+1.0}_{-0.8}$	1.0±0.3		3.8×10^{-11}
	1.8±0.5		$1.8^{+0.3}_{-0.2}$	3.0×10^{-11}
X1	3.4 (Frozen)	$1.17^{+0.14}_{-0.11}$		2.65×10^{-11}
X2	3.4 (Frozen)	$1.0^{+0.3}_{-0.2}$		0.9×10^{-11}
X3	3.4 (Frozen)	1.2±0.1		2.6×10^{-11}
X4	3.4 (Frozen)	1.1±0.4		1.1×10^{-11}
S3+X5	$3.4^{+1.5}_{-1.6}$	$1.2^{+0.3}_{-0.4}$		0.74×10^{-11}

body together with those obtained with the power law model in Table 3. Observations S3 and X5 were simultaneous with an *INTEGRAL* observation, but the source is not detected by the latter satellite with a 18–40 keV 3 σ upper limit of 5 mCrab with IBIS.

Since the PCA is well calibrated only above 3 keV, it is not adapted for proper measures of N_H, especially in such a dim source. In fact, leaving all parameters free to vary during the spectral fits leads to poorly constrained values for this parameter ($N_H < 5.4 \times 10^{22}$ cm^{-2} in obs. X1). We therefore froze the value of N_H to the value returned by the fit to the closest *Swift* data (obs. S3 which, simultaneously fitted with X5, leads to 3.4×10^{22} cm^{-2} for a power law model).

6. X-ray temporal analysis

Although the first hint for the presence of a pulsation came from *Swift*/XRT data (Rodriguez et al. 2009), we focus here only on the data from *RXTE*/PCA which is the instrument dedicated to the timing analysis of astrophysical sources. We also only consider, here Obs. X1 and X3, that both have 2 PCUs on and exposure times longer than 2.5 ks, in order to increase the statistical significance of the pulse. We first produced power spectral density (PSD) between 0.00785 and 1024 Hz with `powspec v1.0` averaging all sub-intervals of 128 s long of each of the two observations. The continuum of the 0.00785–1024 Hz PSD is equally well represented by a model consisting of a constant (to account for the contribution of Poisson noise), and either a power law (of index $\Gamma = -1.67 \pm 0.14$) or a zero-centred Lorentzian (with a width of $2.2^{+1.3}_{-0.8} \times 10^{-2}$ Hz). In both cases, a strong peak at around 0.08 Hz and its first harmonic can be seen. At this frequency resolution the fundamental may appear as genuinely broad. Higher resolution PSDs show that the peak is one bin large, and sits on top of a rather broad complex (not shown). The ∼0.08 Hz feature is, therefore, indicative of a coherent pulsation. To study the properties of this pulsation, we barycentred the 1 s light curves with `barycorr v1.8` using the orbit ephemeris of the satellite, and background corrected the light curves. The period of the pulsation was searched using a Lomb-Scargle periodogram as described in Press & Rybicki (1989) with the errors calculated from the periodogram following Horne & Baliunas (1986). This is the same method used by Rodriguez et al. (2006) to find the pulse best period in IGR J16320−4751. The light curves were folded with `efold v1.1`. We combined obs. X1 & X3 to obtain the most precise measure of the pulsation. A very prominent peak is visible in the periodogram (Fig. 4), together with its first harmonic. We derive a pulse period of P=12.43781(3) s. The light curve, folded at a period of 12.44 s, is shown in Fig. 4) as an insert. The pulse fraction was calculated in a standard way ($P = \frac{I_{max}-I_{min}}{I_{max}+I_{min}}$, see e.g. Rodriguez et al. 2006). Without taking the emission of the Galactic ridge into account, we estimate a pulse fraction $P = 28 \pm 2.3\%$. As the source lies in the Galactic plane which has a non-negligible contribution to the total flux, this value is an underestimate of the true pulse fraction, and should be considered as a lower limit. According to the results of the spectral analysis presented in the previous section, we obtained the "true" background following Eq. 1, which includes the estimated contribution from the Galactic ridge at the position of IGR J19294+1816. With the light curves corrected for this total background we obtain $P = 40 \pm 4.4\%$.

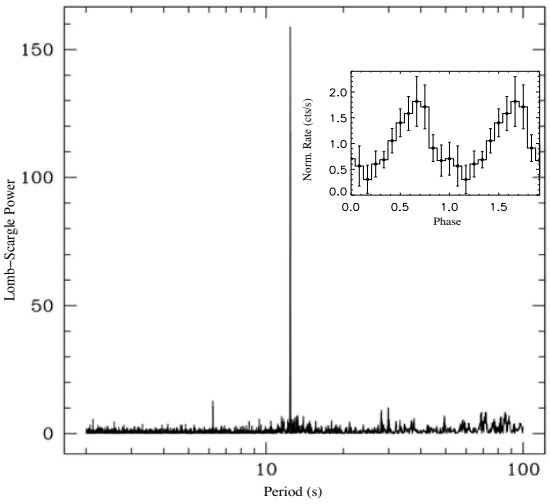

Fig. 4. Lomb-Scargle periodogram of *RXTE* obs. 1 & 2. The prominent peak is found at a best period of ~ 12.44 s. The insert shows the light curve folded at 12.44 s.

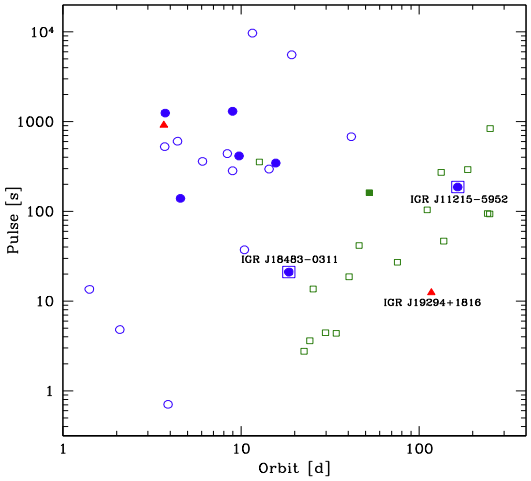

Fig. 5. Most recent version of the "Corbet diagram" including all sources detected with *INTEGRAL* (Bodaghee et al. 2009 in prep.). Squares represent Be-HMXBs, circles Supergiant-HMXBs (Sg-HMXB), circles in squares are SFXTs, filled symbols stands for sources discovered by *INTEGRAL*. The triangles are HMXB of unknown nature (including IGR J19294+1816). The positions of IGR J19294+1816 and of the two SFXTs lying in the Be region of the plot are highlighted.

7. Discussion and conclusions

We have reported here the results obtained from a multi-instrumental campaign dedicated to the X-ray properties of new *INTEGRAL* sources. The refinement of the X-ray position provided by the *Swift*/XRT observations have allowed us to identify a possible counterpart at infrared wavelengths. The differences of dereddened magnitudes (Table 2) do not lead to any of the spectral type tabulated in Tokunaga (2000). With N_H=2.0×10^{22} cm^{-2}, J-H=0.28 would indicate an F7 V or F8 I star. However the value of H-K_s is inconsistent with both possibilities. With N_H=2.73×10^{22} cm^{-2}, J−H seems too high to any spectral type, although we remark a marginal compatibility (at the edge of the errors on the magnitude) with an O9.5 V star (J−H=−0.13, H−K_s=−0.04 Tokunaga 2000). It is, however, likely that the value of the absorption on the line of sight is lower, and we, in particular, note that with N_H=2.5×10^{22} cm^{-2} we obtain J−H=−0.04 and H−K_s=0.05, which is very close to the values tabulated for a B3 I star (J−H=−0.03, H−K_s=0.03 Tokunaga 2000). In that case, the source would lie at a distance $d \gtrsim 8$ kpc.

The X-ray behaviour of the source is indicative of an HMXB: the X-ray spectra are power law like in shape with hard photon index. One of the spectrum shows evidence for absorption in clear excess to the absorption on the line of sight, which may indicate some intrinsic absorption in this source. The evidence is however marginal in the other spectra, which may indicate that variations of the intrinsic absorption takes place in this system, as observed in a number of HMXBs. A long term periodicity is found in the *Swift*/BAT data which confirms the binarity of the source (Corbet & Krimm 2009). We clearly detect an X-ray pulse at a period 12.44 s, indicating the presence of an X-ray pulsar. We estimate a pulse fraction P = 40%. Apart from millisecond X-ray pulsars, found in systems that are at the end of the evolutionary path of X-ray binaries (and are LMXBs), pulsars are young objects that are usually found in HMXBs.

In fact, IGR J19294+1816 clearly lies in a region populated by Be-HMXB in the so-called "Corbet Diagram" (Corbet 1986; Corbet & Krimm 2009), as can be seen in Fig. 5. Note that this plot is the most recent update of the Corbet diagram as of June 2009 (Bodaghee et al. 2009 in prep.). Recently Bodaghee et al. (2007) further explored the parameter spaces occupied by high energy sources. They remarked that Be-HMXB and supergiant HMXB also segregate in different parts in the N_H vs. Orbital period and N_H vs. spin period diagrams. The value of the absorption we obtained through our spectral analysis and both the values of the spin and orbital periods make IGR J19294+1816 lie in a region populated by Be-HMXBs in those diagrams as well. At first order, one can easily understand the segregation in those three different diagrams as results of the age, type of accretion, and probable type of orbit. Be systems are younger, and hence have eccentric orbits, longer orbital period, and shorter spin periods, while supergiant systems are older, are mostly circularised with shorter orbital period and longer spin periods. In those latter systems, in addition, the compact object is embedded in the wind of the companion (the feed matter for accretion) which explains their (usually) higher intrinsic absorption. In this respect, all our results point towards IGR J19294+1816 being a Be-HMXB (the same conclusion, although only based on the Corbet diagram, was presented by Corbet & Krimm 2009) .

INTEGRAL has unveiled a new (sub-)type of supergiant HMXBs, characterised by short (~hours) and intense flares seen at X-ray energies, the so-called SFXTs. Models of SFXTs involve stochastic accretion of clumps from the (heterogenous) wind of the supergiant (e.g. in't Zand 2005; Negueruela et al. 2006), on-top of longer but fainter periods of activity (e.g. Sidoli et al. 2007). In this respect, the detection of periods of short and intense flares in IGR J19294+1816 with *INTEGRAL* (Fig. 1), a behaviour typical of SFXTs, raises the possibility that

this source finally belongs to this new class. Its position in the Corbet and the N_H vs. spin or orbital period diagrams (Fig. 5) is not a definitive contradiction to this hypothesis, since systematic X-ray studies of SFXTs have shown that, contrary to other HMXBs, they seem to populate any part of the diagrams. In particular, IGR J18483−0311, and IGR J11215−5952, the only two SFXTs for which both orbital and pulse periods are known, lie in the region of Be-systems in these representations (Fig. 5). The former source has a pulse period of 21.05 s, an orbital period of 18.5 d, and has an B0.5 Ia companion (see Rahoui & Chaty 2008, and references therein). The latter has a pulse period of about 187 s, an orbital period of about 165 d (e.g. Sidoli et al. 2007; Ducci et al. 2009), and is associated with a B supergiant (Negueruela et al. 2005). To reconcile the fact that they are long period systems with a rather low absorption, an eccentric orbit is invoked. IGR J19294+1816 could be the third member of SFXTs (with a known pulse period) having a long and eccentric orbit. In this case, this may point towards the existence of an evolutionary link between Be-HMXBs and eccentric SFXTs (Liu et al. 2009 in prep.). The quality of the data does not allow us to conclude on the nature of the system, and only an identification of the type of the counterpart will allow this question to be answered.

Acknowledgements. JR acknowledges useful and productive discussions with Farid Rahoui. AP acknowledges the Italian Space Agency financial and programmatic support via contract I/008/07/0. We would like to warmly thank the RXTE and Swift PIs and mission planners for having accepted to perform these observations, and the efficient scheduling in simultaneity with one of the INTEGRAL pointings. This research has made use of the USNOFS Image and Catalogue Archive operated by the United States Naval Observatory, Flagstaff Station (http://www.nofs.navy.mil/data/fchpix/) This research has made use of the SIMBAD database, operated at CDS, Strasbourg, France. It also makes use of data products from the Two Micron All Sky Survey, which is a joint project of the University of Massachusetts and the Infrared Processing and Analysis Center/California Institute of Technology, funded by the National Aeronautics and Space Administration and the National Science Foundation. The Digitized Sky Surveys were produced at the Space Telescope Science Institute under U.S. Government grant NAG W-2166. The images of these surveys are based on photographic data obtained using the Oschin Schmidt Telescope on Palomar Mountain and the UK Schmidt Telescope. The plates were processed into the present compressed digital form with the permission of these institutions. The Second Palomar Observatory Sky Survey (POSS-II) was made by the California Institute of Technology with funds from the National Science Foundation, the National Geographic Society, the Sloan Foundation, the Samuel Oschin Foundation, and the Eastman Kodak Corporation.

References

Bodaghee, A., Courvoisier, T. J.-L., Rodriguez, J., et al. 2007, A&A, 467, 585
Cardelli, J. A., Clayton, G. C., & Mathis, J. S. 1989, ApJ, 345, 245
Condon, J. J., Cotton, W. D., Greisen, E. W., et al. 1998, AJ, 115, 1693
Corbet, R. H. D. 1986, MNRAS, 220, 1047
Corbet, R. H. D. & Krimm, H. A. 2009, The Astronomer's Telegram, 2008, 1
Dame, T. M., Hartmann, D., & Thaddeus, P. 2001, ApJ, 547, 792
Ducci, L., Sidoli, L., Mereghetti, S., Paizis, A., & Romano, P. 2009, ArXiv e-prints
Horne, J. H. & Baliunas, S. L. 1986, ApJ, 302, 757
in't Zand, J. J. M. 2005, A&A, 441, L1
Kalberla, P. M. W., Burton, W. B., Hartmann, D., et al. 2005, A&A, 440, 775
Negueruela, I., Smith, D. M., & Chaty, S. 2005, The Astronomer's Telegram, 470, 1
Negueruela, I., Smith, D. M., Reig, P., Chaty, S., & Torrejón, J. M. 2006, in ESA Special Publication, Vol. 604, The X-ray Universe 2005, ed. A. Wilson, 165–+
Prat, L., Rodriguez, J., Hannikainen, D. C., & Shaw, S. E. 2008, MNRAS, 389, 301
Predehl, P. & Schmitt, J. H. M. M. 1995, A&A, 293, 889
Press, W. H. & Rybicki, G. B. 1989, ApJ, 338, 277
Rahoui, F. & Chaty, S. 2008, A&A, 492, 163
Rahoui, F., Chaty, S., Lagage, P.-O., & Pantin, E. 2008, A&A, 484, 801
Rodriguez, J., Bodaghee, A., Kaaret, P., et al. 2006, MNRAS, 366, 274
Rodriguez, J., Hannikainen, D. C., Shaw, S. E., et al. 2008a, ApJ, 675, 1436
Rodriguez, J., Tomsick, J. A., & Chaty, S. 2008b, A&A, 482, 731
Rodriguez, J., Tuerler, M., Chaty, S., & Tomsick, J. A. 2009, The Astronomer's Telegram, 1998, 1
Sidoli, L., Romano, P., Mereghetti, S., et al. 2007, A&A, 476, 1307
Skrutskie, M. F., Cutri, R. M., Stiening, R., et al. 2006, AJ, 131, 1163
Strohmayer, T., Rodriguez, J., Markwardt, C., et al. 2009, The Astronomer's Telegram, 2002, 1
Tokunaga, A. T. 2000, Infrared Astronomy, ed. A. N. Cox, 143–+
Tuerler, M., Rodriguez, J., & Ferrigno, C. 2009, The Astronomer's Telegram, 1997, 1
Valinia, A. & Marshall, F. E. 1998, ApJ, 505, 134

Troisième partie

Quelques études de la physique des phénomènes liés à l'accrétion et aux éjections de matière

Chapitre 10
Quelques aspects de la physique des systèmes accrétant par vent

10.1 Introduction

Le but de ma recherche est de comprendre la physique responsable des divers phénomènes observés au sein des systèmes accrétants, et des binaires X en particulier. L'approche phénoménologique a évidemment ses limites inhérentes à la manière même dont on considère les paramètres que l'on étudie : une loi de puissance ne sera jamais qu'une approximation locale (en terme de longueur d'onde) d'un spectre. Ce ne sera donc pas un processus d'émission même s'il est possible, en se plaçant dans un cadre particulier, de l'interpréter comme tel. Les diverses corrélations permettent de discriminer entre différents types de sources ; cela représente une base solide pour les études ultérieures : elle permettent en effet de se placer dans un cadre théorique de base. L'analyse physique pure servira à comprendre les détails fins (mécanismes, géométries, propriétés, environnement, composition chimique, ...), des objets observés. Comme nous n'avons accès qu'a un certains nombres d'observables, bien souvent, plusieurs explications, plusieurs modèles, peuvent expliquer le même p-uplet de paramètres. Toute nouvelle observation mettra ainsi en compétition divers modèles pour ne retenir que celui ou ceux qui représentent le mieux les résultats observés. Les petites fluctuations à des modèles devront aussi servir de nouvelles contraintes aux théoriciens pour affiner leur théories. Ce sont ces aspects d'approches physiques, dans le cadre de modèles théoriques que je veux illustrer dans cette partie.

10.2 Une radiographie du système permise par les rayons X

Dans ce chapitre nous allons nous concentrer sur les Sg-HMXB. L'origine des rayons X émis vient de l'accrétion du vent de l'étoile Sg compagnon ; différents modèles concurents présentent les détails possibles de la physique à l'origine des émissions X et gamma. En ce qui nous concerne nous ne pourrons, à partir des X seuls, distinguer entre les différentes possibilités (polar cap, slot gap,

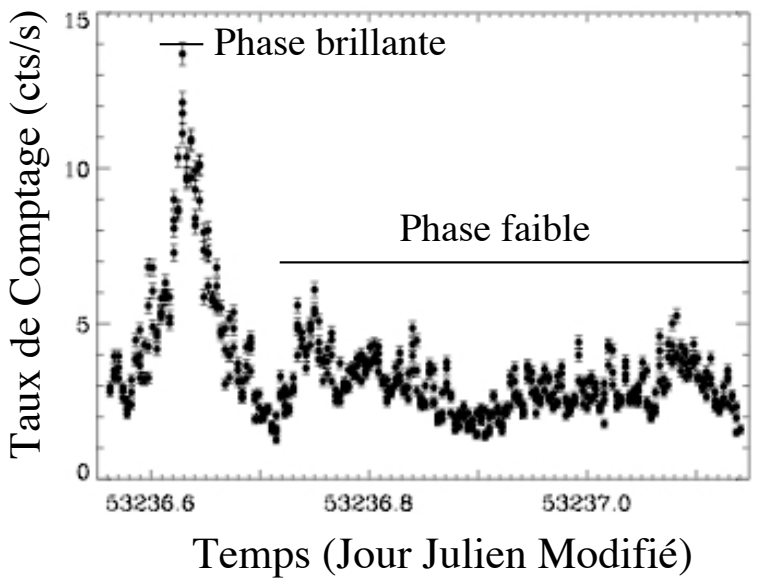

FIG. 10.1 – Courbe de lumière *XMM–Newton* (0,5–10 keV) de IGR J16320−4751. Cette observation est entièrement simultanée avec une observation *INTEGRAL*. Les deux phases distinctes pour l'accumulation des spectres discutés ici sont indiquées. Adapté de Rodriguez et al. (2006a).

outer gap). Nous supposerons que, dans les sg-HMXB, la matière accrétée suit les lignes de champs et est accrétée aux pôles du pulsar. Cette interprétation explique relativement bien la détection de pulsations périodiques dans certains de ces objets si l'on admet que, comme sur Terre, l'axe magnétique et l'axe de rotation du pulsar ne sont pas confondus. La pulsation provient d'un effet de type "phare". D'autres observables sont compatibles avec cette interprétation. C'est le cas de la détection de raies de résonnance cyclotron, indiquant un fort champ magnétique dans ces objets. Les variations de la fréquence de ces raies sont, généralement en bon accord avec une interprétation d'accrétion polaire dans ces systèmes (voir le chapitre 1 et les références citées).

Bien que d'une manière générale, j'étudie la physique menant à l'émission de rayons X à proximité de l'objet compact, je ne développerai pas cet aspect ici. Nous admettrons que l'émission X provient de la chute de matière, et est émise sous forme thermique par la surface de l'étoile à neutron, et qu'une partie de cette émission subit un processus Compton inverse dans le flot d'accrétion (fig. 1.1 et chap. 1). Je me concentrerai, en revanche, sur l'un des avantages des rayons X : leur pouvoir de pénétration. En effet, avant de nous parvenir, ce rayonnement X issus de l'accrétion et émis à proximité de l'objet compact doit traverser un certain nombre de milieux, en particulier, le milieu interne au système binaire. On a donc un moyen de sonder l'environnement immédiat de l'objet compact et son interaction avec le compagnon. J'illustre ici plus particulièrement ces points en présentant l'étude *XMM–Newton-INTEGRAL* de IGR J16320−4751 et le suivi *RXTE-INTEGRAL* de IGR J19140+0951.

10.3 IGR J16320−4751 : excès mou et raie du fer

Les résultats des analyses temporelles de la longue (50 ks) observation strictement simultanée *XMM–Newton-INTEGRAL* sont déjà décrit dans la partie II, au chapitre 6. Cette observation nous a permis d'obtenir une position X plus fine de cet objet, levant ainsi le doute quant à l'identification de

la contrepartie infrarouge, permettant ensuite l'identification du type de système (chapitre 4). J'ai pu conduire une étude très complète des propriétés X de la source, à partir des analyses temporelles, spectroscopiques, et de spectroscopie résolue en phase. L'article (Rodriguez et al. 2006a, MNRAS, 366, 274) est inclus au chapitre 14 à la fin de la partie III. Je présente ici deux aspects liés à la matière contenue dans le système.

La courbe de lumière *XMM–Newton* (fig. 10.1) montre que l'observation débute par un pic d'émission, avant de revenir à un niveau de flux plus faible et calme. J'ai donc séparé les observations en deux portions, la première contient les 3,6 ks les plus brillante du pic initial, la seconde les 30 ks finales de l'observation (fig. 10.1). J'ai extrait les spectres *XMM–Newton* et *INTEGRAL* en respectant cette séparation en deux phases, une faible et une brillante. Les spectres sont ajustés avec un modèle standard pour ce type d'objet : tout d'abord une loi de puissance avec coupure exponentielle modifiée par l'absorption à basse énergie. Ce modèle est couramment associé à un modèle de comptonisation inverse, et, dans un second temps, les spectres sont ajustés avec un modèle de comptonisation (absorbé). Dans les deux cas il est nécessaire d'ajouter une raie d'émission à 6,4 keV, attribuée à la fluorescence du fer (raie Kα), et une composante de front d'absorption due au fer au-delà de 8 keV. Les spectres combinés *XMM–Newton* et *INTEGRAL* acummulés lors des deux phases, et les meilleurs ajustements obtenus avec ce modèle sont reportés en figure 10.2. Le premier point notable est la forte absorption vue dans ce système ($N_H > 10^{23}$ cm^{-2}) qui semble être une caractéristique des Sg-HMXB découvertes par *INTEGRAL*. De plus, ce modèle seul ne donne pas une représentation parfaite des spectres, en particulier de celui de la période faible, ou un large excès est vu sous 2 keV (fig. 10.2).

Par analogie avec ce qui est vu dans d'autres IGR absorbées le modèle final employé pour ajuster les spectres contiendra deux composantes d'absorption, l'une représentant l'absorption sur la ligne de visée, l'autre l'absorption locale au système pour laquelle j'ai laissé l'abondance du fer varier, puisque cet élément semble être présent en quantité importante, comme l'atteste la détection de la raie à 6,4 keV. Un corps noir est aussi inclu pour représenter l'excès mou.

10.3.1 Origine possible de l'excès mou

Dans la période de faible luminosité l'absorption intrinsèque vaut $N_H = 1,2 \times 10^{23}$ cm^{-2}, et la température de l'excès mou vaut 0,07 keV. La première conclusion est que l'excès mou ne peut pas provenir de la surface de l'objet compact (du polar cap par exemple) puisque la grande absorption intrinsèque bloque tout photon < 1 keV. De plus, il n'est pas détecté lors de la période brillante initiale. Ceci peut indiquer deux choses ; ou bien il est vraiment absent, ou, ce que je pense être plus probable, ses paramètres (température, flux) son constants et il est donc "noyé" dans le flux global provenant de l'objet compact. Cette dernière possibilité indique encore que l'excès mou est découplé de l'émission provenant de l'accrétion, et que son orgine est autre, puisque s'il était lié à l'accrétion nous pourrions nous attendre à ce que son flux augmente de manière corrélée au flux global.

Des excès mous on été vus dans un certains nombre de binaires X (Hickox et al. 2004), y compris des IGR (Bodaghee et al. 2006; Zurita Heras et al. 2006). Hickox et al. (2004) ont étudié en détails l'origine possible de ces excès, et suggèrent des mécanismes différents dans différentes sources. Dans le cas de IGR J16320−4751 le fait que l'on ne détecte pas de pulsations sous 2 keV exclut que la colonne d'accrétion soit à l'origine de l'excès. Cet excès pourrait alors soit provenir de la rediffusion des photons mous absorbés par un milieu diffusant (qui serait alors le milieu absorbant), ou encore l'émission due à un "nuage énergetisé par collision" . Dans ce dernier cas, l'émission X du pulsar ionise le vent de l'étoile. Ce dernier est alors ralenti lors de son passage à proximité de l'objet compact, et la densité locale est donc accrue. Une queue de surdensité est ainsi formé lorsque l'étoile à neutron

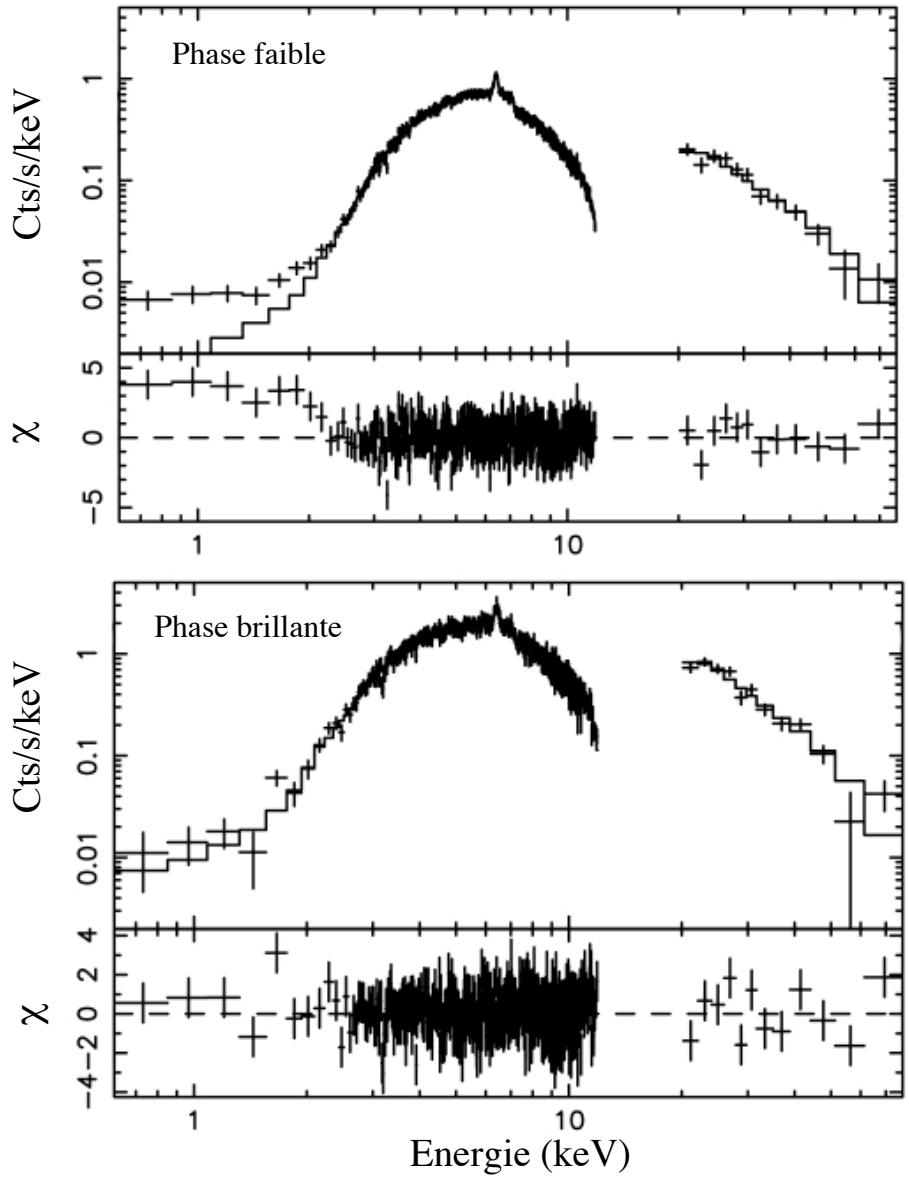

FIG. 10.2 – Spectres combinés *XMM–Newton* et *INTEGRAL* tirés de la phase faible (panneau du haut) et de la phase brillante (panneau du bas). Le sous panneau représente, dans chaque cas, l'écart en valeur de χ^2 entre le spectre et l'ajustement. Adapté de Rodriguez et al. (2006a).

évolue sur son orbite. L'excès mou résulte alors de l'émission due au choc entre le vent stellaire rapide et cette queue dense.

Dans le cas de la rediffusion des photons absorbés, en raison de la conservation de l'énergie, on devrait avoir $F_{\rm corpsnoir} \lesssim \Delta F_{\rm continuum}$, où $F_{\rm corpsnoir}$ est le flux (bolométrique) de l'excès mou ajusté avec un modèle de corps noir, et $\Delta F_{\rm continuum}$ est la différence entre les flux ($\sim$ bolométriques) non-absorbés et absorbés du continuum modélisé avec un processus de comptonisation thermique. Nous obtenons en fait le contraire, ce qui nous permet de réfuter une rediffusion des photons absorbés comme origine de l'excès mou. Nous en concluons donc que l'excès mou est, dans IGR J16320−4751, est probablement dû à l'émission d'un milieu énergétisé par collision.

10.3.2 La raie du fer et les diagnostiques associés

L'observation longue faite avec *XMM–Newton* m'a permis de détecter une raie en émission à $\sim 6,41$ keV due à la fluorescence K_α du fer. La finesse de la raie permet déjà de conclure que ce fer se trouve dans le vent, ou dans de la matière circum-stellaire, et exclut très certainement la présence d'un disque d'accrétion, puisqu'alors la raie sera naturellement élargie, notamment par le mouvement de rotation du disque autour de l'objet compact.

La valeur du centre de la raie traduit la présence de fer XIII. En utilisant $\xi = L/(\rho \times R^2)$, avec ξ paramètre de ionisation, L la luminosité de la source, ρ la densité de la coquille irradiée, R la distance entre la source X, et le fait que $\rho \times R = N_{\rm H}$, on en déduit $R = \frac{L}{N_{\rm H} \times \xi}$. En utilisant Kallman et al. (2004) on obtient $log(\xi) < 2 \Leftrightarrow \xi < 100$ et donc $R > 0,07$ ua pour une distance de la source de 5 kpc. Evidemment cette taille augmente en raison du carré du distance de la source.

La conclusion est que le bord intérieur du milieu ou le fer est irradié se trouve relativement loin de la source de rayons X. Ceci va de pair avec la conclusion présentée à la section précédente quant à l'origine de l'excès mou, qui provient d'un milieu indépendant du flot d'accrétion. Une remarque concerne l'abondance de fer qui semble être bien supérieure à l'abondance solaire. Ceci pourrait être lié à l'origine même du milieu ; le fer pourrait y avoir été produit lors de l'évolution du protopulsar.

10.4 L'évolution orbitale de IGR J19140+0951 dévoile sa géométrie

Les premières observations *RXTE* et *INTEGRAL* de IGR J19140+0951 montraient que cette source semblait occuper plusieurs états spectraux dont l'un, au moins, laissait apparaître une émission de type thermique (chapitre 6). En regard des conclusions obtenues pour IGR J16320−4751 et dans le but de mieux comprendre ces objets, il était important de se pencher plus avant sur cet aspect. De plus, j'avais alors la chance d'être PI de nombreuses observations simultanées *RXTE* et *INTEGRAL* (33 pointés *RXTE* et 29 avec *INTEGRAL* fin 2007). Connaissant la période orbitale de la source, cela pouvait permettre d'étudier l'évolution de ses caractéristiques spectrales le long de son orbite. C'était le but du stage de master que je proposai, et qui fut effectué par Lionel Prat.

Evidemment la sensibilité et le domaine spectral couvert par *RXTE* sont loin des capacités de *XMM–Newton*, et l'on ne peut attendre le même degré de détails ni la même précision dans les mesures, notamment en ce qui concerne l'absorption et le potentiel excès mou. Néanmoins IGR J19140+0951 est une source relativement brillante et absorbée, ce qui laissait espérer des résultats concluants. Nous avons donc fait l'analyse spectrale de toutes les observations en incluant les spectres *RXTE*/PCA et *INTEGRAL*/IBIS pour les observations simultanées. Nous avons commencé les ajustements avec des modèles phénoménologiques (loi de puissance, absorption, coupure à haute énergie, raie du fer et corps noir), et avons aussi remplacé la loi de puissance coupée par un modèle de comptonisation thermique, pour obtenir des paramètres plus physiques.

L'une des difficultés, dans le cadre d'une source du plan Galactique observée avec le PCA (un

collimateur) vient de la correction de l'émission du fond. Pour des sources extrêmement brillantes comme GRS 1915+105 cette correction est inutile, en revanche il faut en tenir compte dans le cadre de IGR J19140+0951. Cette émission du fond Galactique a un impact très fort sur les observations les plus faibles notamment pour la mesure de l'absorption et celle de la raie du Fer. Nous avons corrigé tous les spectres à l'aide du modèle moyen d'émission trouvé par Valinia & Marshall (1998) pour la région $-45^\circ < l < 45^\circ$ and $-1.5^\circ < b < 1.5^\circ$. Ce modèle fait intervenir une emission de plasma chaud type Raymond-Smith et une loi de puissance absorbés avec les paramètres suivants : N_H= 1.8, kT = 2.9 keV $\mathrm{Norm_{Raymond}} = 0.021$ pour l'émission du plasma, et $\Gamma = 1.8$, $\mathrm{Norm_{lp}} = 3.91 \times 10^{-3}$.
Cette correction fait évidemment intervenir une incertitude supplémentaire. En particulier, et parce que ce modèle inclue une émission due au fer (et le fait que la résolution spectrale du PCA est relativement mauvaise), on ne pourra faire une étude précise des propriétés du milieu émetteur du fer.

10.4.1 Variations spectrales

Les résultats obtenus ne montrent aucune relation particulière entre l'indice de photon, l'énergie de coupure, la température de comptonisation, l'épaisseur optique de comptonisation et la phase orbitale. La figure 10.3 (gauche) montre l'exemple particulier de la variation de l'indice de photon de la loi de puissance. De même le paramètre indicatif de l'efficacité du processus de comptonisation, dit aussi paramètre de Kompaneets, $y = \tau^2 \times (4kT_e)/(m_e c^2)$ ne présente pas de variations particulières par rapport à la position orbitale. La valeur trouvée, 0,5–1, indique un processus moyennement efficace, ce qui est en accord avec le type d'accrétion (par vent, et donc moins efficace) ayant lieu dans ce système. Ce qui pourrait paraître étonnant, à première vue, est l'absence de relation entre la luminosité X et la phase orbitale. La luminosité de la source est très variable, et l'on aurait pu s'attendre à ce que cela soit corrélé d'une manière ou d'un autre avec l'orbite, notamment du fait de la détection de la période à partir des X mous avec *RXTE*/ASM. En fait, ceci indique que l'orbite du système est très proche d'une orbite circulaire. Les variations sont alors probablement dues à des inhomogenéités du vent du compagnon. Ce modèle d'accrétion de grumeaux dans les systèmes à supergéante connaît en effet un certain succès ces dernières années notamment pour les SFXTS (par exemple Negueruela et al. 2006; Walter & Zurita Heras 2007), mais pourrait aussi expliquer les variations de luminosité des sg-HMXB (Walter et al. 2006).

Nous trouvons, en revanche, une relation entre N_H et la phase orbitale, comme nous pouvons le voir sur la figure 10.3. Comme N_H et Γ sont relativement influencés l'un par l'autre lors des ajustements, nous avons tout d'abord confirmé la véracité de ces variations en produisant des diagrammes de contours statistiques des valeurs de Γ par rapport à N_H. Les variations de l'absorption sont vraies et non pas dues à une possible dégenerescence de ces paramètres. En définissant la phase 0 comme la conjonction inférieure du système (la phase 0,5 étant la conjonction supérieure), alors nous observons que N_H atteint son minimum en conjonction inférieure et son maximum en conjonction supérieure (fig. 10.3). Ces variations peuvent ainsi facilement expliquer comment la période orbitale est détectée dans le ASM de *RXTE* : cet instrument couvre en particulier les X mous (1,2–12 keV), et est donc très influencé dans ses canaux les plus bas par la valeur de l'absorption. Cette dernière étant liée à la période orbitale, le flux X-mou brut (i.e. en taux de comptage) va suivre la même tendance.

10.4.2 Excès mou

Dans IGR J19140+0951 un excès mou est parfois détecté. La bande spectrale couverte par *RXTE* n'en permet une détection que lorsqu'il est le plus brillant, et dans ces cas une étude fine

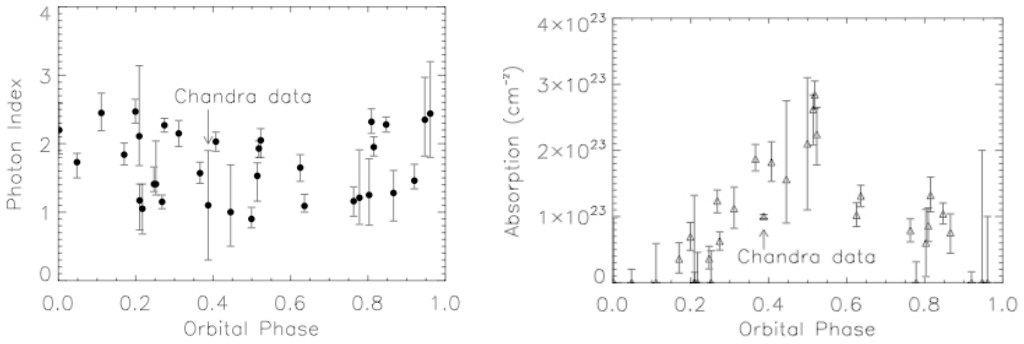

FIG. 10.3 – Evolution de Γ (gauche) et de N_H (droite) en fonction de la phase orbitale dans IGR J19140+0951. Tiré de Prat et al. (2008).

n'est pas possible. Il est néanmoins important de remarquer que les détections ont toutes lieu à proximité de la conjonction supérieure. Comme dans le cas de IGR J16320−4751, nous pouvons exclure un disque d'accrétion comme origine de cet excès : en premier lieu, et vu la température de l'excès ($\sim 0,5$ keV), et en raison de la forte absorption locale, un tel disque ne serait pas détecté ; de plus nous estimons que le point de Lagrange dans ce système est dans l'intervalle 34–56 $R_\odot$ pour un rayon stellaire de 30 $R_\odot$ pour une supergéante B 1. Il est donc extrêmement improbable que le compagnon remplisse son lobe de Roche et qu'un disque soit formé. De manière plus générale, nous pouvons aussi exclure la colonne d'accrétion sur l'objet compact comme origine de l'excès, puisque, là encore, la forte absorption ne permettrait pas de voir cette émission.

Deux possibilités restent (Hickox et al. 2004) donc comme origine de l'excès mou dans cette source : la rediffusion des photons absorbés par un milieu environnant l'objet compact et/ou le système, et l'émission due à l'interaction du vent stellaire et du milieu englobant l'objet compact (nuage énergétisé). Malheureusement les limitations de *RXTE*/PCA en terme de spectromètre ne permettent pas de distinguer entre les deux modèles. Nous avons demandé du temps avec *XMM–Newton* lors du dernier AO, mais ne l'avons pas obtenu ; nous reproposerons des observations avec ce satellite lors du prochain AO.

10.4.3 Les variations de N_H et le vent de l'étoile

Nous avons immédiatement pensé au vent comme possible origine des variations de N_H. Naivement lorsque l'étoile à neutrons est derrière le compagnon l'émission X doit traverser plus de matière que lorsqu'elle se trouve en conjonction inférieure. Sans rentrer totalement dans les détails de modélisation du vent, qui sont tous reportés dans Prat et al. (2008, MNRAS, 389, 301) inclus au chapitre 14, nous utilisons une loi dite de type β pour représenter l'évolution de la vitesse du vent en fonction de la distance r à l'étoile. On a (Castor et al. 1975) :

$$V(r) = V_0 + (V_\infty - V_0)(1 - \frac{R_\star}{r})^\beta \tag{10.1}$$

où $R_\star$ est le rayon de l'étoile, V_∞ la vitesse terminale du vent. On peut montrer que :

$$N_H = N_{H,ISM} + \frac{\dot{M}_\star}{4\pi\mu m_H V_\infty} \int_0^\infty \frac{ds}{r^2(1 - \frac{R_\star}{r})^\beta} \tag{10.2}$$

où $\mathrm{N_{H,ISM}}$ est l'absorption interstellaire, $\dot{M}_\star$ le taux de perte de masse du compagnon, m_H la masse de l'atome d'hydrogène, et μ le poid atomic moyen des particules en unité de m_H, et r la distance étoile à neutrons observateur. Ce modèle, relativement simple, ne fait en particulier pas intervenir la structure grumeleuse du vent. Nous pouvons fixer certains de ses paramètres et ajuster les autres. Le fait de connaître le type du compagnon (Sg 0.5-1), permet en effet d'utiliser des valeurs tabulées pour sa masse (10–30 $\mathrm{M_\odot}$), son rayon (10–30 $\mathrm{R_\odot}$), son taux de perte de masse (10^{-6} $\mathrm{M_\odot}$/an) , la valeur terminale du vent (~ 1000 km/s), et le paramètre β (0.5–1). Le meilleur ajustement est obtenu pour M$= 20$ $\mathrm{M_\odot}$, $\beta = 0,5$ pour lesquels nous avons R$= 21$ $\mathrm{R_\odot}$ et $38° < i < 43°$.

10.4.4 Conclusions : une vision schématique de la binaire dans IGR J19140+0951

L'étude de IGR J19140+0951 sur son orbite nous a permis d'accéder à certains paramètres du systèmes habituellement obtenus grâce à des observations dans le visible, comme par exemple l'inclinaison. En combinant tous nos résultats, dont la présence de l'excès mou, on peut construire une représentation schématique du système dans laquelle une queue (type cométaire) suit le passage de l'étoile à neutrons. Cette queue pourrait être responsable de l'excès mou. Certaines questions se posent alors naturellement comme par exemple les raisons de la non détection de l'excès dans les phases autre que la conjonction supérieure. Je pense que dans ces cas là la raison principale est instrumentale : ces phases correspondent aux moments où l'absorption est moindre et donc le flux émis par l'accrétion est dominant et noie probablement l'émission de l'excès. Ici encore des suivis avec *XMM–Newton* ou *Chandra*, seraient d'une grande utilité pour affiner notre modélisation. Ce sera très certainement le sujet de propositions à venir.

10.5 Conclusions du chapitre : pour aller plus loin

Les études de deux sg-HMXB nous ont permis d'avancer dans notre compréhension de ces systèmes. L'accrétion de matière par l'objet compact est responsable de l'émission primaire dans ces objets. Cette émission est très absorbée, et la valeur de $\mathrm{N_H}$, bien supérieure à la valeur de l'absorption interstellaire, indique une composante locale, qui peut être attribuée au vent de l'étoile compagnon dans lequel baigne l'objet compact. Le fort rayonnement X interagit avec le vent stellaire, et contribue à créer une zone localement plus dense pouvant être comparée à une queue suivant l'étoile à neutron sur son orbite. le choc produit entre cette queue et le vent rapide produit un excès mou observé dans les spectres. Dans IGR J16320−4751 j'ai pu détecter une émission due à la fluorescence du fer d'un milieu se trouvant à environ 0,07 ua de l'objet compact. Cette distance n'est pas incompatible avec une origine se trouvant, la encore, dans cette queue responsable de l'émission de haute énergie. Cette distance est en effet équivalente à 1.4 $\mathrm{R_\odot}$ et donc clairement à proximité de l'objet compact (rappelons que la distance entre les deux composantes dans IGR J19140+0951 est d'au moins 51 $\mathrm{R_\odot}$).

Pour continuer dans cette direction nous (PI Zurita Heras) avons demandé et obtenu du temps d'observation *XMM–Newton* pour suivre IGR J16320−4751 au long de son orbtie (8 pointés) et ainsi pouvoir mener une étude des propriétés spectrales de cet objet sur son orbite. Le travail est en cours, et même si il est évident que l'utilisation d'un satellite plus performant dans les X mous va devoir nous pousser à mener une modélisation plus précise du vent, les premiers résultats montrent que $\mathrm{N_H}$ est maximum à la conjonction supérieure. Nous avons aussi du temps d'observation d'une autre source IGR J16393−4643 toujours avec *XMM–Newton*. Les observations n'ont pas eu lieu. Notons dans ces deux cas que *XMM–Newton*, outre la mesure précise de $\mathrm{N_H}$, permettra de suivre l'évolution de l'excès mou.

Une autre manière d'aborder l'analyse des matériaux locaux aux systèmes (par exemple les absorbants) est d'étudier les propriétés du complexe du fer, et notamment la présence d'une "épaule Compton" (CS *Compton Shoulder*). C'est un point d'étude auquel j'ai participé dans Ibarra et al. (2007) lors d'observations *XMM–Newton* de IGR J16318−4848, même si mon implication dans ces travaux se trouvait plutôt au niveau de l'analyse des données de haute énergie. En reprenant les données présentées dans ces travaux je me suis rendu compte que la présence d'un CS était relativement incertaine et extrêmement dépendante de la manière d'aborder les ajustements. De plus, l'effet maximum pour la raie à 6.40 keV est un CS de pic à $\Delta E = 0,150$ keV ce qui est exactement la résolution d'*XMM–Newton* à cette énergie. Pour aller plus loin, j'ai proposé des observations avec *Chandra*. Ma proposition n'a malheureusement pas été retenue lors du dernier AO de cet instrument.

Chapitre 11
La couronne : origine de la matière éjectée dans les microquasars ?

11.1 Éruptions des microquasars et liens accrétion-éjections

J'ai présenté au chapitre 7 quelques résultats relatifs au microquasar GRS 1915+105, sans rentrer dans les détails relatifs aux processus physiques en jeu dans cet objet. Dans un microquasar, contrairement aux HMXB que j'ai présentées jusque là, l'accrétion se fait notamment via un disque qui rayonne la majorité de son énergie dans les rayons X mous (typiquement $0.1 - 10$ keV). Ces sources sont très brillantes et bien souvent transitoires. Je montre, en figures 11.1 et 11.2, les courbes de lumière multi-longueurs d'ondes (radio et X) des microquasars XTE J1748−248 et XTE J1859+226, ainsi que les HR entre différentes bandes spectrales. On voit clairement sur ces figures :

- Une éruption vue dans les rayons X (la dénomination 'XTE' indique que ces sources ont été découvertes par *RXTE*).
- Un sursaut radio
- Le maximum des pics X mous (< 10 keV) est précédé par un pic X dur (> 20 keV)
- Les pics X mous et X durs interviennent avant le maximum radio
- Même si les constantes de temps sont différentes dans les deux sources, une décroissance du HR a lieu avant le sursaut radio
- Le sursaut radio semble débuter après une décroissance du flux X-dur dans chacun des cas

Il est important de remarquer que ces deux objets ne sont pas uniques. GRS 1915+105, bien qu'étant brillant depuis plus de 15 ans, montre de telles propriétés (comme l'illustre la figure 7.5 au chapitre 7 par exemple). Il semble bien, en effet, que les microquasars débutent tous leurs éruptions par un état dur. Les éjections, lorsqu'elles ont lieu, interviennent lorsque la source a déjà transité depuis cet état vers un état plus mou (état intermédiaire ou état mou). Cet aspect est illustré schématiquement par le diagramme en Q (figure 1.2, chapitre 1) tout d'abord proposé par R. Fender et ses collaborateurs pour représenter les éruptions de GX 339−4, et depuis généralisé à d'autres sources (par exemple Fender et al. 2004). L'une des grandes questions actuelles concerne les mécanismes

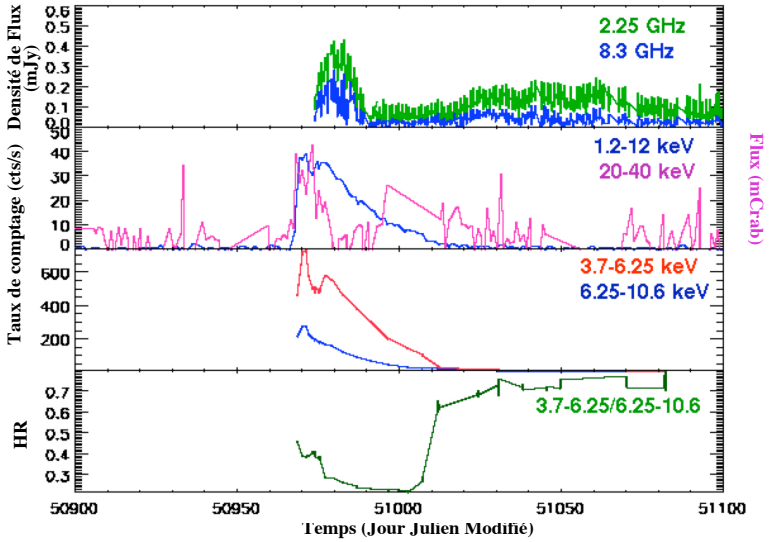

FIG. 11.1 – Vue multi-longueurs d'onde du microquasar XTE J1748−248. De haut en bas, courbes de lumière radio (2.25 et 8.3 GHz), et X obtenues par *RXTE*/ASM et CGRO/BATSE. Courbes de lumière obtenues à partir des ajustements des spectres *RXTE*, et le HR associé.

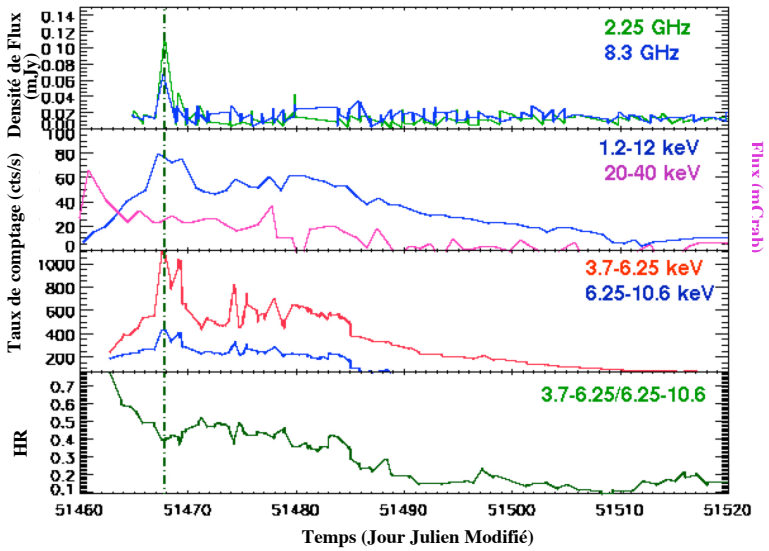

FIG. 11.2 – Vue multi-longueurs d'onde du microquasar XTE J1859+226. De haut en bas, courbes de lumière radio (2.25 et 8.3 GHz), et X obtenues par *RXTE*/ASM et CGRO/BATSE. Courbes de lumière obtenues à partir des ajustements des spectres *RXTE*, et le HR associé.

d'évolution entre états spectraux au cours d'une éruption. Il est aujourd'hui clair, notamment, que le taux d'accrétion seul ne peut paramétrer les transitions spectrales (Homan et al. 2001). Dans une étude récente, Yu et al. (2009 accepté dans ApJ), propose, à partir d'une étude exhaustive des courbes de lumière *RXTE*/ASM et *Swift*/BAT de 15 étoiles à neutrons et 5 trous noirs, que le taux de variation du taux d'accrétion pourrait être ce paramètre lors de la montée de l'éruption.

Depuis la fin de ma thèse je m'intéresse aux aspects d'évolutions des microquasars du point de vue spectral aussi bien que temporel. A travers mes travaux et collaborations j'aborde différents aspects de la physique de ces objets, comme, par exemple, la nature de la queue de haute énergie notamment détectée avec *INTEGRAL*/SPI dans Cyg X-1 (Cadolle Bel et al. 2006). Je me concentre cependant plus particulièrement sur l'interaction disque-couronne, à partir de la grande base de données *RXTE*, qui permet des études spectro-temporelles, et des observations *INTEGRAL*, lorsqu'elles sont disponibles. Une des grandes questions concerne le lien entre le système disque-couronne et le jet compact, et/ou les éjections discrètes ; en d'autres termes les liens accrétion-éjections. C'est ce thème que je veux aborder dans ce chapitre.

En 2002–2003 il était relativement clair que les éjections discrètes avaient lieu à la transition etat dur→état mou, sans plus de précision (par exemple Corbel et al. 2001, dans le cas de XTE J1550−564). Les variations rapides du flux X-mou ($\lesssim 10$ keV) dans GRS 1915+105 avaient été interprétées comme résultantes de vidages et remplissages rapides des régions internes du disque (Belloni et al. 1997a,b). Mirabel et al. (1998) suggéraient, après avoir observé de forts liens entre comportements X et radio, que la disparition des régions internes du disque déclenchait l'éjection, ce qui laissait supposer que la matière éjectée provenait du disque. En 2002, lors d'une très large campagne multi-longueurs d'onde de GRS 1915+105 (Ueda et al. 2002), l'étude des courbes de lumière X (dans différentes bandes) et l'étude des variations de HR dans la classe α, m'avait conduit à proposer une possible éjection de la couronne (Rodriguez et al. 2002a). Un pivotement spectral ne pouvait cependant pas être exclu, et la couronne éjectée ne restait qu'une possibilité intéressante mais non-totalement prouvée. En faisant une étude spectro-temporelle détaillée de l'éruption de 2000 de XTE J1550−564, j'apportai une première preuve observationnelle de l'éjection probable de la couronne (Rodriguez et al. 2003a). Dans cet article, inclus à la fin de ce chapitre, mon approche était relativement basique, et basée sur l'évolution des flux relatifs des composantes spectrales précédant l'éjection. Comme il n'est, néannmoins, pas possible de tirer des conclusions générales à partir d'un seul objet, il était nécessaire de se tourner vers d'autres microquasars pour confirmer ou infirmer cette proposition.

11.2 GRS 1915+105 et la campagne *INTEGRAL* : approche physique

GRS 1915+105 est un objet naturel vers lequel se tourner : il est le premier dans lequel des liens entre accrétion et éjection ont été vus (Mirabel et al. 1998). Il est extrêmement variable, et est connu pour ses oscillations radio quasi-périodiques (Pooley & Fender 1997, et chapitre 7). Je mène depuis 2003 la campagne d'observations *INTEGRAL*, conjointement à des observations radio au Ryle (en collaboration avec Guy Pooley). Je menais aussi une campagne simultanée avec *RXTE* au cours des trois premières années (2003–2006). L'avantage de l'utilisation d'*INTEGRAL* est que la durée d'observation est plus longue (qu'avec *RXTE*) et la simultanéité avec les observations au sol (fondamentale vue la grande variabilité de GRS 1915+105) est plus facile à organiser. En outre, la grande sensibilité d'IBIS/ISGRI, sa plus large couverture spectrale et sa meilleure résolution temporelle (pour l'analyse spectrale résolue en temps) par rapport à *RXTE*/HEXTE, permettait des études spectrales large bande (jusqu'à environ 200 keV), et donc l'utilisation de modèles physiques

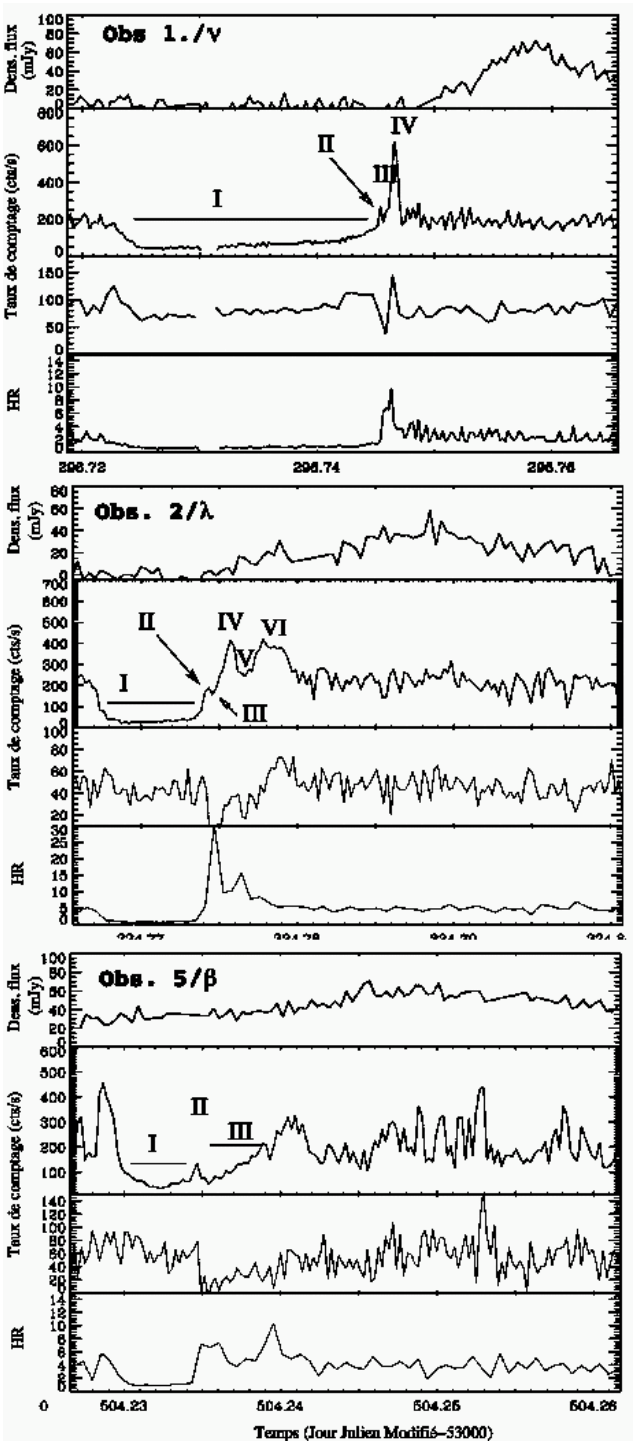

FIG. 11.3 – Zoom sur un cycle de chacune des classes observées avec *INTEGRAL*. Tiré de Rodriguez et al. (2008b).

pour étudier les propriétés de la queue de haute énergie. Quatres observations dans les AO 2 et 3 m'ont permis d'obtenir des résultats importants. L'approche ne dépendant d'aucun modèle est présentée au chapitre 7, et je résume ci-après les résultats de l'analyse physique des ces observations. L'article (Rodriguez et al. 2008b) est inclus à la fin du chapitre.

11.2.1 La couronne éjectée dans GRS 1915+105

L'analyse phénoménologique de la campagne m'a permis de généraliser un comportement qualitatif menant aux éjections dans GRS 1915+105 : les cycles X vus dans les classes $\alpha, \beta, \lambda, \nu, \theta$ (Belloni et al. 2000, et figures 7.2 et 7.3) précèdent toujours une éjection. La durée du creux X (spectralement dur) pourrait même avoir une influence sur l'amplitude de l'éjection (Rodriguez et al. 2008a, chapitre 7).

Pour tenter de comprendre le comportement physique de GRS 1915+105 lors des cycles, j'ai séparé chacun des cycles observés avec *INTEGRAL*, à savoir les cycles ν, λ, et β en séquences d'intensités et de "saveurs" spectrales identiques. Cette séparation est donc exempte de tout a-priori. Selon la classe de variabilité cette étape résulte donc en trois, quatre ou cinq intervalles différents ; ceux-ci sont illustrés sur la figure 11.3. Dans le cas des classes ν et β j'ai ensuite accumulé des spectres pour chacun des intervalles en utilisant tous les cycles observés lors de l'observation. Cette approche est justifiée par le fait que ces classes sont connues pour manifester des éjections en réponse à chaque cycle (Pooley & Fender 1997; Mirabel et al. 1998; Eikenberry et al. 1998a; Klein-Wolt et al. 2002). En revanche, l'éjection radio suivant le cycle λ étant la première jamais observée, j'ai préféré accumuler les spectres à partir de cet unique cycle. Ceci permet de concentrer l'analyse spectrale sur la seule certitude que l'on a : ce cycle est suivi d'une éjection. J'ai bien entendu commencé les ajustements avec des modèles phénoménologiques, mais, même dans les cas où aucune coupure n'était visible, je les ai remplacés par un modèle de comptonisation thermique. L'avantage est que la bosse compton à basse énergie est bien représentée (le modèle est de ce point de vue auto-cohérent), ce qui n'est pas le cas d'une loi de puissance qui diverge à basse énergie, et donc donne une surestimation de sa contribution relative. Les mesures des paramètres du disque sont aussi faussés dans cette modélisation. Enfin, il faut tout de même ajouter que la moins bonne qualité statistique du spectre λ ne m'a permis d'utiliser qu'une loi de puissance pour les ajustements. La figure 11.4 montre les spectres *INTEGRAL*/JEM-X et *INTEGRAL*/ISGRI, accumulés à partir des intervalles I à IV lors de la classe ν. La représentation de ces spectres est en $\nu-\mathrm{F}_\nu$ (dans laquelle une loi de puissance d'indice spectral 2 est une droite constante) qui permet de voir directement les influences relatives des diverses composantes spectrales. Le résultat notable, valable dans toutes les classes étudiées, et directement visible sur la figure 11.4 peut être résumé de la manière suivante :

- Intervalle I : le spectre est dur, et les ajustements montrent que la source est dans un état de pure comptonisation thermique, même si les paramètres physiques de la couronne sont peut-être différents entre la classe ν ($kT_e = 33$ keV, $\tau = 0.6$), et la classe β ($kT_e = 15$ keV, $\tau = 1.5$, avec de grandes incertitudes dans ce dernier cas). Le disque est marginalement présent, et clairement froid ($\lesssim 0.8$ keV).
- Intervalle II : Ici l'évolution est moins claire. En effet, cet intervalle correspond au pic terminant brusquement chacun des creux X ; or ce pic a une durée différente dans chacune des classes, ce qui ajoute une difficulté supplémentaire à la spectroscopie résolue en temps. Ce qui est notable, en revanche, est que, dans les trois classes, le flux associé à la couronne (sous forme de comptonisation, ou de loi de puissance pour λ) a augmenté par rapport à l'intervalle I. La même remarque est valable pour le flux du disque, lorsque ce dernier est détecté (ν, β).
- Intervalle III : Dans les trois cas la composante associée à la couronne évolue de manière drastique. Elle est à peine détectée dans la classe λ, alors que son flux chute brutalement d'un

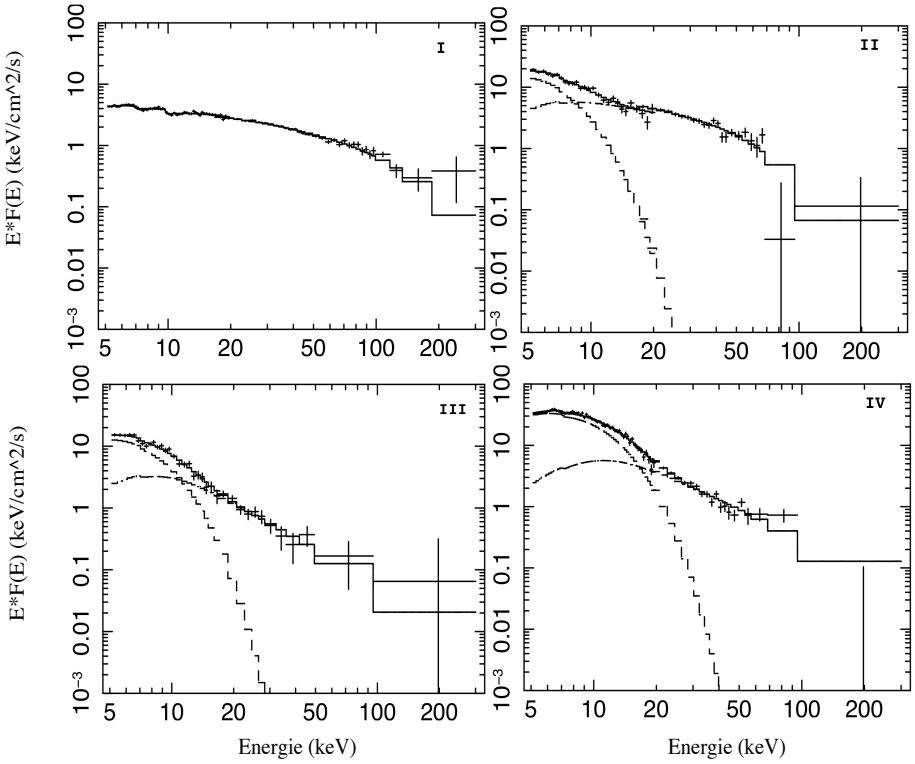

FIG. 11.4 – Spectres large bande (5–300 keV) des quatres intervalles I, II, III, IV identifiés sur la figure 11.3 dans le cas du cycle ν. Les deux composantes spectrales, le disque d'accrétion et la couronne comptonisante, sont aussi representées. Le spectre est en représentation "ν-F$_\nu$" permettant une comparaison directe des contributions relatives de ces composantes. Tiré de Rodriguez et al. (2008b).

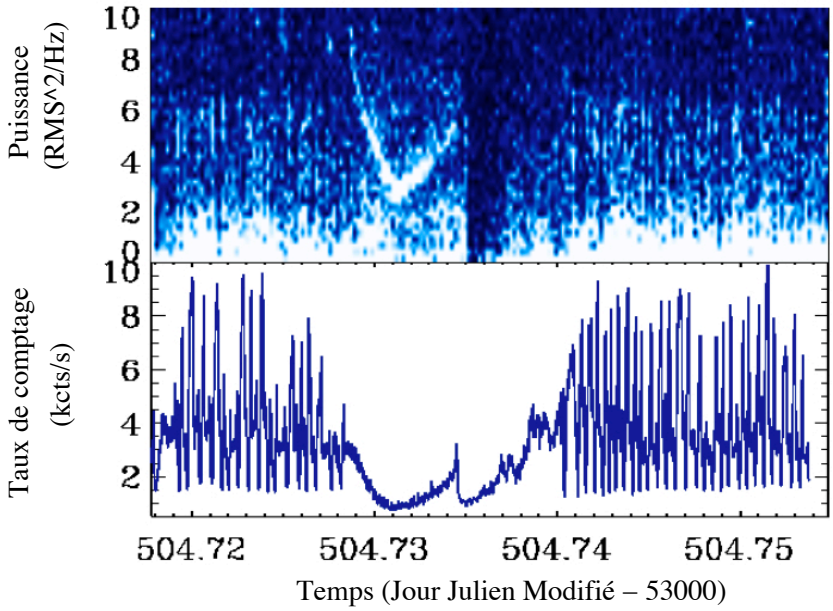

FIG. 11.5 – Spectre de puissance dynamique (panneau du haut) et courbe de lumière (panneau du bas) montrant un cycle de la classe β. Sur le spectre de puissance la couleur code la puissance associée à chaque fréquence (et à chaque moment). Plus la couleur est claire plus la puissance associée est élevée. Adapté de Rodriguez et al. (2008b).

facteur > 5 dans la classe β et > 2 dans la classe ν. Dans le même temps, la température et le flux du disque ont continué à augmenter.

Comme au chapitre 7, nous voyons, ici encore, que le pic (ou intervalle II) marque un changement majeur au niveau des propriétés de la matière dans GRS 1915+105. La source change d'état spectral à ce moment, ce qui se traduit (outre l'évolution des paramètres associés au disque et à la couronne) par la disparition d'une partie de la couronne, que l'on mesure grâce aux variations de flux. Étant donné la détection d'une éjection dans tous les cas, très peu de temps après, j'en ai conclu que dans GRS 1915+105, comme probablement dans XTE J1550−564 (Rodriguez et al. 2003a), la matière éjectée avait pour origine très probable la couronne.

Bien que je parlerai de l'analyse temporelle et des QPO au chapitre suivant, il est très intéressant de noter que dans toutes les classes à cycles, y compris la classe λ, les creux des cycles sont associés à un fort niveau de "bruit" (grande variabilité de la source), ainsi qu'un QPO de (basse) fréquence variant de manière corrélée au flux X[1]. Cet aspect est illustré sur la figure 11.5 où un spectre de puissance dynamique est représenté. Un changement clair est visible sur le spectre de puissance dynamique au moment du pic intermédiaire : le bruit global et le QPO (codé par une couleur claire) disparaissent brusquement. Il est aujourd'hui relativement bien admis que les signatures temporelles (notamment les QPO) ont une forte puissance lorsque la couronne est présente (chapitre 12). La forte diminution du bruit, et la disparition des QPO au pic (intervalle II) est, ici encore, compatible avec l'éjection de la couronne.

[1]La fréquence des QPO est en fait correlée au flux X mous ($\lesssim 10$ keV) dans GRS 1915+105 (Rodriguez et al. 2002a) et XTE J1550−564 (Rodriguez et al. 2004b).

11.2.2 Une influence du jet compact dans les X durs ?

La quatrième observation d'importance est une observation de classe χ faite le 13 avril 2005. Nous avons eu la chance d'avoir une simultaneité parfaite entre la radio et les rayons X durant environ 34 ks pour cette observation. Les courbes de lumière correspondant à cette portion sont représentées en figure 11.6. Durant cette observation GRS 1915+105 a un flux X relativement stable, et son spectre est plutôt dur. C'est durant cette classe que des jets compacts peuvent être présents (Klein-Wolt et al. 2002; Fuchs et al. 2003). Le niveau et la stabilité de l'émission radio (figure 11.6) indiquent que tel est bien le cas lors de notre observation. L'intérêt de ce suivi est l'augmentation notable du flux radio au cours de l'observation. Durant les 13000 premières secondes d'observation le flux radio moyen est de 44,9 mJy (intervalle I sur la figure 11.6) ; le niveau d'émission radio atteint un niveau moyen de 70,4 mJy lors des $\sim$ 10000 s finales (intervalle III).

De manière à étudier les connexions possibles avec les rayons X (et donc l'accrétion), j'ai séparé les observations X selon les trois intervalles définis par les niveaux d'émission radio, comme indiqué sur la figure 11.6, et en ai extrait des spectres. Il faut remarquer que l'analyse phénoménologique préalable des courbes de lumière X ne montre aucune corrélation évidente (Rodriguez et al. 2008a) entre X et radio. Les spectres (3–250 keV) sont bien ajustés avec une composante de comptonisation thermique, et une loi de puissance additionnelle représentant une queue de haute énergie, visible notamment après la coupure thermique du spectre. Le disque d'accrétion n'est détecté dans aucun des spectres. Les paramètres obtenus lors des ajustements montrent que durant l'augmentation de flux radio (d'un facteur $1,57 \pm 0,14$), seul le flux (2–200 keV, non absorbé) associé à la queue de haute énergie suit une évolution similaire, puisque il augmente d'un facteur $1,61 \pm 0,13$. L'indicateur statistique de Pearson donne un facteur de corrélation de $0,93$ entre les deux composantes, en tenant compte des flux obtenus dans les trois intervalles. Cette corrélation, bien que fondée sur trois points, pourrait indiquer un lien fort entre la loi de puissance et le jet compact. Il est intéressant de remarquer que les paramètres spectraux obtenus ici sont très similaires à ceux présentés lors d'une autre observation par Vadawale et al. (2003). Ces auteurs, à partir d'une modélisation simple du jet compact, montrent que la loi de puissance pourrait être l'émission synchrotron directe du jet compact. La ressemblance de mes résultats avec les leurs, et la possible corrélation des flux me pousse à conclure dans ce sens.

Ce résultat et l'interprétation que j'en tire sont sujets à discussions, notamment en raison du faible nombre de points d'observations. Il faut cependant remarquer que GRS 1915+105, comme bien d'autres microquasars, suit la corrélation entre flux X et flux radio (Corbel et al. 2001; Gallo et al. 2003). Il n'est donc pas étonnant d'y trouver une influence du jet compact dans les X durs. L'avantage de GRS 1915+105 réside dans sa variabilité rapide : c'est en effet la première fois que la corrélation X-radio peut être suivie en direct. La simultanéité des événements est importante puisque c'est un argument supplémentaire en faveur d'un lien direct entre le jet compact et la queue de haute énergie. Pour aller plus loin, une modélisation précise de la répartition spectrale d'énergie est nécessaire. Avec S. Markoff nous nous penchons actuellement sur cet aspect, en utilisant notamment le modèle de jet compact développé par ses soins, et qui fait intervenir différents processus physiques : l'émission synchrotron directe provenant du jet, l'émission synchro-self Compton des électrons du jet, la comptonisation des photons du disque sur la base du jet et la reflexion d'une partie de toute ces émissions sur le disque.

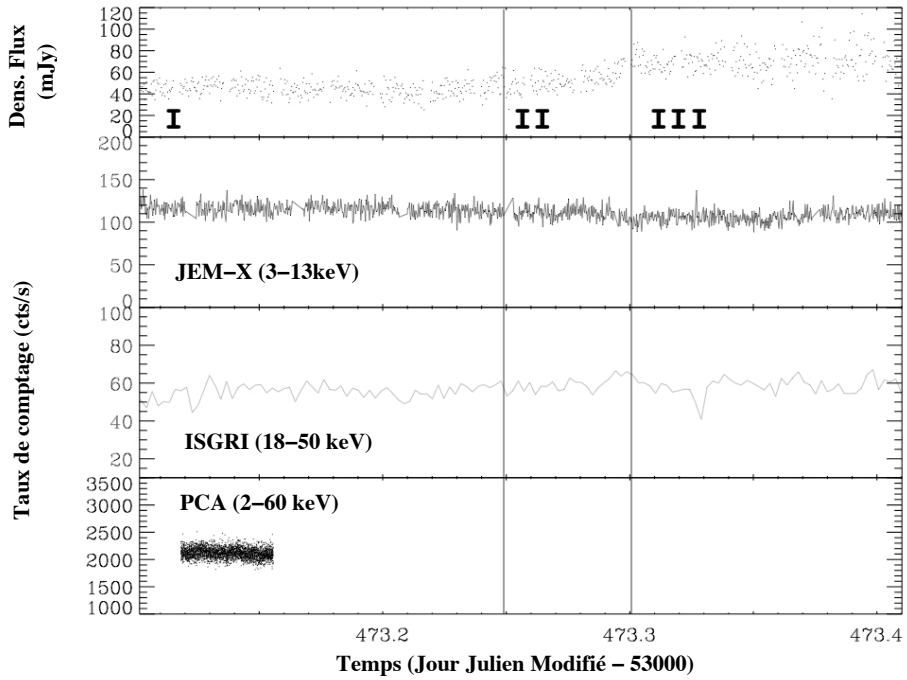

FIG. 11.6 – Courbes de lumière multi-longueurs d'onde de GRS 1915+105 lors de l'observation du 13 Avril 2005. Les trois intervalles I, II, et III sont discutés dans le texte. Adapté de Rodriguez et al. (2008a).

11.3 L'éjection de la couronne est-elle un phénomène général dans les microquasars ?

Afin d'étudier l'universalité du lien couronne-jet vu dans GRS 1915+105 et XTE J1550−564, L. Prat et moi-même nous sommes lancés, depuis fin 2007, dans un travail de longue haleine. Nous avons recherché tous les objets pour lesquels existaient des observations X et radio quasi simultanées dans le but d'étudier l'évolution spectrale des objets ayant montré des phases d'éjections discrètes. Aujourd'hui nous avons identifié les sources suivantes : XTE J1550−564, H1743−322, GX 339−4, GRO J1655−40, 4U 1630−47 qui ont fait plusieurs éruptions, et XTE J1748−288, XTE J1859+226 (fig. 11.1 et 11.2), 4U1543−47. Nous avons, pour ce faire, considéré uniquement les archives *RXTE* et *INTEGRAL* en X, et Green Bank Interferometer (GBI, 2,25 et 8,3 GHz) et Ryle Telescope (RT, 15 GHz) en radio.

Nous avons considéré, dans nos analyses, les spectres large bande (3–200 keV), en utilisant le PCA et HEXTE lors d'observations *RXTE*, ou bien JEM-X et ISGRI lors d'observation *INTEGRAL*. Ces spectres sont ajustés avec un modèle impliquant une composante thermique due au disque et une composante de comptonisation due à la couronne. Les premières sources que nous avons étudiées sont XTE J1748−288, et XTE J1859+226 pour lesquelles j'ai présenté les résultats prélimaires au 6ème workshop *INTEGRAL* (Rodriguez & Prat 2008), et GX 339−4 présenté par L. Prat lors du second symposium SIMBOL-X (Prat & Rodriguez 2009).

L'évolution des flux des composantes du système accrétant, disque et couronne, ainsi que le flux radio à 2,25 GHz sont reportés sur les figures 11.7 pour XTE J1748−288 et 11.8 pour XTE J1859+226. Dans le cas de la première source, j'ajoute aussi le flux à 1,46 GHz tel que vu avec le VLA (obtenu à partir de Hjellming et al. 1998b,a; Rupen et al. 1998). L'évolution du flux du disque

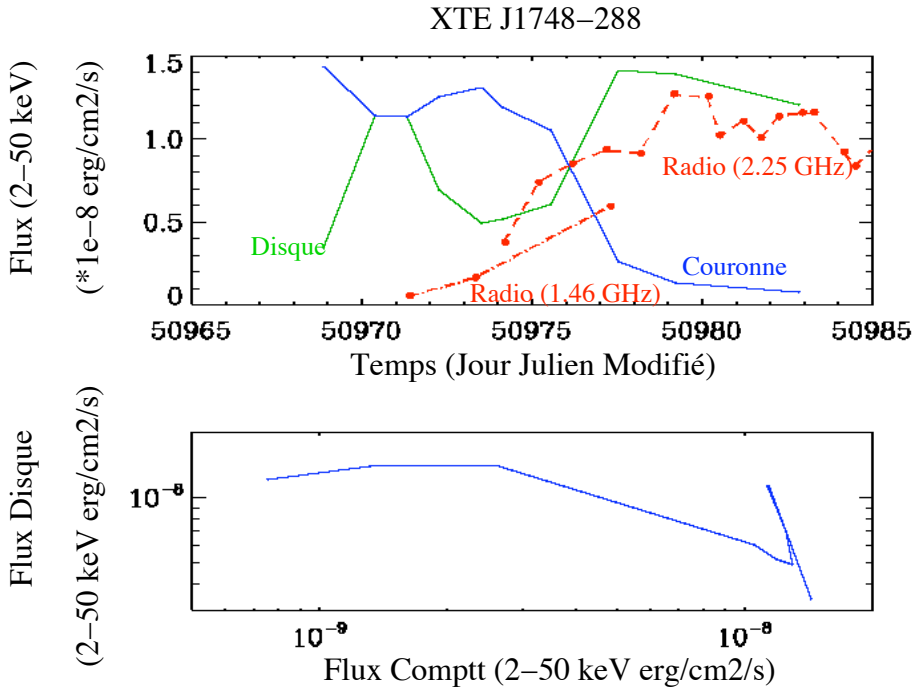

FIG. 11.7 – **Panneau du haut :** Evolution des flux du disque (vert), de la couronne (bleu) et du jet (rouge à deux fréquences) en fonction du temps pour XTE J1748−288. Le flux radio n'est pas à l'échelle. **Panneau du bas :** Evolution du flux du disque en fonction de celui de la couronne.

en fonction du flux de la couronne est aussi représentée sur ces figures. Les indices spectraux radio donnés par les mesures au deux fréquences sont négatifs (le flux radio diminue avec la fréquence) au moment des maxima dans les deux sources ; ceci est indicatif d'éjections discrètes type bulle de matière (van der Laan 1966).

Dans XTE J1748−288 une décroissance du flux de la couronne est vue avant la détection radio du VLA. Il est, de plus, clair que le disque subit relativement moins de variation de flux que la couronne (panneau du bas de la figure 11.7) ; il diminue au plus d'un facteur ~ 2 au long de cette séquence de l'éruption, alors que le flux de la couronne diminue d'un facteur ~ 15. Il peut sembler que la décroissance du flux du disque et la détection radio soient contemporaines. Le cas de XTE J1859+226 est encore plus problématique puisque les deux composantes spectrales voient leur flux respectifs croître avant la détection radio le Jour Julien Modifié (JJM) 51465 (figure 11.8). Remarquons que dans XTE J1859+226 lors des premières détections, le spectre radio est inversé et plutôt typique d'un jet compact que d'une éjection discrète. Ceci est confirmé par les suivis avec le VLA, Merlin, RATAN, et le Ryle présentés dans Brocksopp et al. (2002). L'éjection discrète débute réellement en JJM 50467,5 (Brocksopp et al. 2002).

Dans le cadre de la comptonisation thermique, le paramètre de Kompaneets $y = \frac{kT_e}{m_e c^2} \times max(\tau, \tau^2)$ caractérise en quelque sorte l'éfficacité du processus de comptonisation et sera le premier paramètre à étudier. Il est important de remarquer que y peut être décomposé en deux termes : le premier, $\frac{kT_e}{m_e c^2}$, est le gain moyen d'énergie par interaction et le second est relié au nombre moyen d'interactions. Il est relié à l'épaisseur optique $\tau \propto \rho \times R$, où ρ est la densité du milieu, et R son rayon ($\rho \times R$ a la dimension d'une densité surfacique). L'évolution du paramètre y et de τ dans le

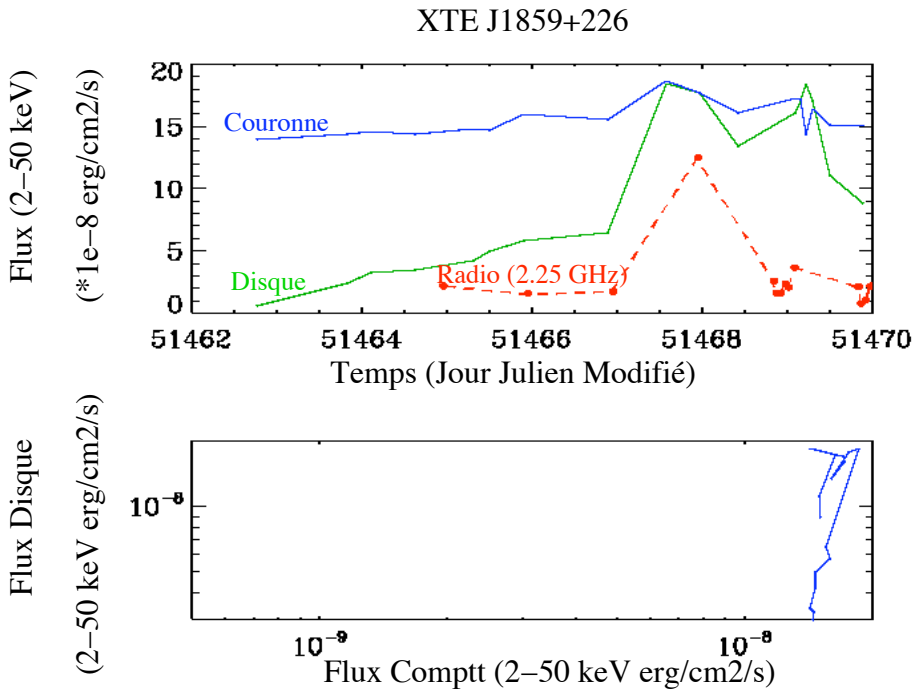

FIG. 11.8 – **Panneau du haut :** Evolution des flux du disque (vert), de la couronne (bleu) et du jet (rouge) en fonction du temps pour XTE J1859+226. Le flux radio n'est pas à l'échelle. **Panneau du bas :** Evolution du flux du disque en fonction de celui de la couronne.

cas de XTE J1859+226, est représentée en figure 11.9. Nous voyons sur cette figure q'une brusque variations des paramètres de comptonisation précède le début de l'éjection discrète. τ diminue notamment d'un facteur > 10. Dans l'interprétation présentée précédemment ceci implique que le milieu comptonisant a vu sa densité ou son rayon diminuer (ou les deux). Dans tous ces cas cela traduit une perte de matière. On aboutit donc à une disparition (partielle) de la couronne précédent immédiatement le jet.

Le cas de XTE J1748−288 est de ce point de vue un peu plus complexe. En effet, les détections radio montrent qu'il est fort probable que le sursaut radio (l'éjection discrète) ait débuté après la première observation X. Les ajustements spectraux semblent bien indiquer une décroissance des paramètres de comptonisation. Mais il n'existe qu'une seule observation X avant l'allumage radio ; Il n'est donc pas possible d'obtenir de conclusions dans cet objet.

Enfin les premiers résultats obtenus lors de l'éruption de 2002 de GX 339−4 indiquent dans cet objet aussi une forte décroissance de τ immédiatement avant la détection de la source en radio. Ici encore les variations de τ peuvent donc s'interpréter aisemment dans le cadre d'une disparition partielle de la couronne. Malheureusement nous n'avons pas de suivis radio pour cet objet mais uniquement quelques pointés discrets montrant alors simplement une détection ou non. Il n'est donc pas possible de remonter précisemment au début de l'éruption radio.

11.4 Conclusions du chapitre

Dans ce chapitre j'ai présenté quelques résultats notables que j'ai obtenus dans le cadre de mes études des phénomènes d'accrétion-éjection et de leurs liens possibles. Dans GRS 1915+105 j'ai mis

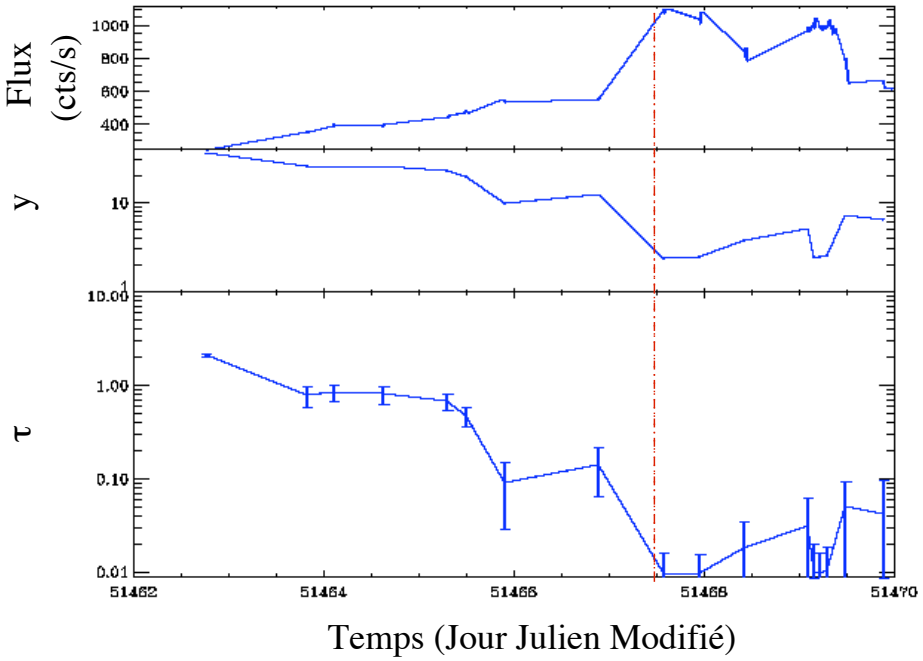

FIG. 11.9 – De haut en bas, évolution du taux de comptage, du paramètre y, et de l'épaisseur optique τ dans XTE J1859+226. La ligne verticale rouge représente le début de l'éjection radio, telle qu'observée par Brocksopp et al. (2002).

en avant une probable émission du jet dans les X-durs. La corrélation flux X–flux radio n'est pas nouvelle (même si les intervalles spectraux X sont en général plus restreints et à plus basse énergie), mais, pour la première fois, j'observe une évolution corrélée des flux en direct. Pour aller plus loin il faudrait évidemment plus d'observations de ce type. Ceci est néanmoins difficile à prévoir ; j'ai eu beaucoup de chance avec cette observation, et il n'est pas du tout sûr que cela se reproduise. Une autre approche est la modélisation théorique de ces observations. La modélisation de la répartition spectrale d'énergie que nous effectuons avec S. Markoff devrait nous apporter plusieurs éléments de réponses sur l'interaction du jet et de son environnement immédiat.

L'autre aspect présenté ici concerne l'évolution spectrale X (et donc les comportements du flot d'accrétion) des microquasars précédent les éjections discrètes. Vu les similarités de comportements entre XTE J1550−564 et GRS 1915+105 nous pouvons légitimement nous poser la question de l'universalité de l'éjection de la couronne comme origine des jets discrets dans les microquasars. Cette étude est en cours, et les premiers résultats semblent prometteurs. L'approche physique permet de circonvenir à quelques problèmes liés aux études basées uniquement sur les flux relatifs des composantes spectrales. Dans XTE J1859+226 et GX 339−4 la matière coronale semble bien disparaître juste avant la détection d'une éjection. Notons que d'autres objets semblent aussi aller dans ce sens ; dans H 1743−322 (parfois appelé IGR J17464−3213) l'analyse spectrale *RXTE* et *INTEGRAL* (impliquant un modèle de comptonisation) montre une forte décroissance de l'épaisseur optique τ juste avant la détection radio : τ passe d'une valeur de ~ 3.4 quelques jours avant à 0.25 juste après (Joinet et al. 2005). A partir d'observation simultanées *XMM–Newton* et *INTEGRAL*de l'éruption de 2007 de GX 339−4, Caballero-García et al. (2009) observent aussi une disparition de matière coronale peu de temps avant la détection d'un sursaut radio. Ces auteurs mentionnent clairement le passage d'un état à couronne compacte, à un état quasiment sans couronne. L'intérêt de ces travaux est l'utilisation de modèles de comptonisation hybrides permettant une modélisation plus précise des couronnes "thermiques" (vitesse des électrons Maxwellienne) et "non-thermiques".

Tous ces résultats semblent donc aller dans le même sens, à savoir que la couronne est la source de la matière éjectée. Pour aller plus loin, il nous faut évidemment augmenter notre échantillon d'étude, et inclure toutes les éruptions pour les objets récurrents. De plus nous pensons aussi utiliser des modèles plus performants de comptonisation, notamment les modèles hybrides qui permettent d'accéder aux composantes thermiques et non-thermiques de la comptonisation. Une fois l'éjection de la couronne confirmée, ceci devrait nous permettre de mieux contraindre la part éjectée. Enfin, dans tous les cas il semble que la disparition de la couronne s'accompagne d'un échauffement du disque, et d'une diminution de son rayon interne (le bord du disque se rapproche du trou noir). Nous pouvons alors nous demander si la couronne est éjectée par un phénomène dû au disque approchant, ou bien si le disque peut s'approcher parce que la couronne disparaît. Répondre à cette question devrait permettre d'affiner les modèles d'éjections, puisque dans un cas le disque initierait clairement l'éjection, alors que dans l'autre il pourrait n'être qu'observateur du phénomène.

Chapitre 12
Etudes des propriétés temporelles rapides : Oscillations Quasi-Périodiques dans les microquasars

12.1 Introduction

Nous avons vu au chapitre 6 comment la détection de pulsations strictement périodiques était indicative de la présence d'une étoile à neutron au sein d'un système binaire. Dans IGR J16320−4751 l'étude de la dépendance en énergie de la pulsation nous a, de plus, permis d'obtenir des contraintes concernant la nature de l'excès mou (Rodriguez et al. 2006a) : celui-ci ne peut être le "polar cap" puisque l'amplitude de la pulsation à basse énergie, où le polar cap aurait son pic d'émission, est indétectable.

Dans les trous noirs accrétants, le niveau de variabilité rapide (typiquement > 0.1 Hz) est clairement lié à la présence d'une forte composante de comptonisation thermique. La définition de l'état dur est aujourd'hui aussi basée sur le niveau de variabilité (Homan et al. 2005), la forme du spectre de puissance (PSD pour *Power Spectral Density* dans la suite), et la présence d'oscillations quasi-périodiques (QPO) de basses fréquences (0.1–10 Hz). L'état mou, dominé par le disque d'accrétion, est quand à lui caractérisé dans le domaine temporel par un faible niveau de variabilité, et les PSD sont en loi de puissance d'indice ~ -1 (voir chapitre 1). Même si l'origine physique des différentes composantes est inconnue, ces premières discriminations permettent d'établir de possible liens avec les différents milieux émetteurs (disque, couronne, jet). Pour aller plus loin dans la compréhension de ces phénomènes temporels diverses approches sont possibles (chap. 1) ; toutes tentent de connecter l'approche temporelle à l'approche spectrale. Une des questions sur lesquelles je me suis penché est de connaître l'origine des émissions quasi-périodiques de basses fréquences (0.1–10 Hz). Dans la

suite de ce chapitre QPO se rapportera par défaut aux oscillations de basses fréquences. Avant de présenter mes travaux (originaux par rapport à ma thèse) relatifs à cet aspect, il est important de rappeler quelques unes des connexions spectro-temporelles (chap. 1).

12.2 QPO et connexions spectro-temporelles

Il est important de remarquer que les QPO ne sont vus que dans les systèmes à disque. Ce dernier étant la seule source de périodicité rapide (la rotation quasi-képlérienne de la matière) dans le système, il est tentant de lui associer les manifestations quasi-périodiques (comme dans l'exemple de la bulle chaude de Sunyaev 1973, chap. 1). Les connexions spectro-temporelles présentées au chapitre 1 semble effectivement indiquer que le disque fixe d'une certaine manière la fréquence des QPO. Mais, comme pour la variabilité globale, les QPO sont forts dans les états durs et dur-intermédiaires ($15-30\%$) ; ils sont faibles dans l'état mou-intermédiaire ($5-10\%$), et absents (ou non-détectés) dans l'état mou (par exemple Homan & Belloni 2005; McClintock & Remillard 2006, pour des revues). En d'autres termes, une forte composante de comptonisation est toujours associée à leur détection. Les QPO de hautes fréquences sont, eux, détectés dans certains états intermédiaires, et ont des puissances plutôt faibles ($\sim 1\%$ par exemple pour le QPO de 67 Hz de GRS 1915+105).

12.3 Dépendances énergétiques des QPO : première étape avec XTE J1550−564

Depuis la fin de ma thèse, je m'intéresse, en ce qui concerne les QPO, à une signature qui pourrait permettre de mieux les comprendre. Pour aller plus loin que les corrélations spectro-temporelles, certes importantes et contraignantes, je pense qu'il faut étudier les propriétés spectrales des QPO. Si nous pouvions en établir des spectres en énergie fins, nous pourrions, à terme, tenter des ajustements de ces spectres avec des modèles physiques. C'est une approche que je tente depuis de nombreuses années.

La première source pour laquelle j'ai tenté cette approche de manière systématique (c'est-à-dire au long de toute une éruption) est XTE J1550−564. Le faible flux de la source lors de son éruption de 2000, ne m'a cependant permis d'obtenir que des spectres de très faible résolution (4 points spectraux, figure 12.1). De plus, la faible significativité des points spectraux ne permet, au mieux, qu'un ajustement des spectres avec une constante pour le QPO de l'état dur (fig. 12.1). Lors de l'état intermédiaire, les spectres des QPO sont plus significatifs ; ils sont clairement croissants avec l'énergie, et montrent un aplatissement au-delà de 10 keV. Remarquons le bas niveau total des QPO des JJM 51675 et 51676. La raison de la faiblesse des oscillations ces deux jours n'est pas claire. Sans rentrer dans les détails de la classifications des différents types de QPO (les types A, B ou C, voir par exemple Remillard et al. 2002; Casella et al. 2005), il est possible que les QPO soient d'un type différent ces jours-ci.

Le résultat principal de cette analyse spectrale des QPO est, qu'ici encore, il est clair que le flux émis par le disque n'est pas le flux oscillant. Les spectres des QPO de l'état dur montrent une puissance comparable à basse et haute énergie, lors d'observations où l'analyse spectrale de la source ne montre pas de disque d'accrétion[1]. Au contraire, lorsque ce dernier devient suffisamment brillant et domine les spectres en énergie de XTE J1550−564 sous 5–6 keV (lors de l'état intermédiaire, Rodriguez et al. 2003a), l'amplitude des oscillations à basse énergie (sous 5 keV), est bien plus faible (fig. 12.1).

[1] l'analyse spectrale de l'éruption est décrite en détail dans l'article Rodriguez et al. (2003a), inclus au chapitre 14.

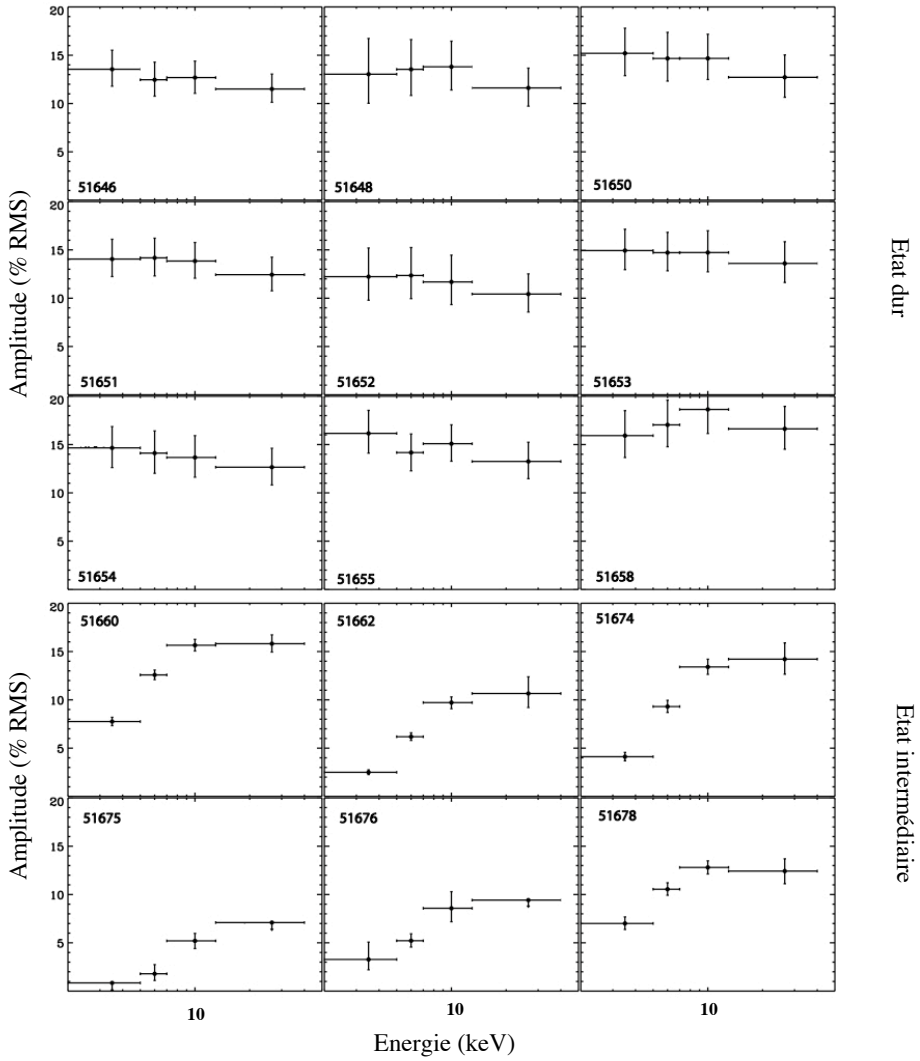

FIG. 12.1 – Dépendances énergétiques (spectres) du QPO lors de l'éruption de 2000 de XTE J1550−564. La source montre une transition état dur→état intermédiaire entre les JJM 51658 et 51660. Les nombres reportés dans chaque panneau indiquent la date de l'observation en JJM. Adapté de Rodriguez et al. (2004b).

12.4 Dépendance énergétique des QPO BF dans GRS 1915+105

12.4.1 Ajustement des spectres des QPO

Au cours des premières années de la campagne *INTEGRAL* (chap. 7 et 11) j'ai eu la chance de mener de front une campagne d'observations simultanées avec *RXTE*. Lors de la première année du suivi *INTEGRAL*, GRS 1915+105 est dans la classe χ (spectre dur et flux constant, fig. 7.3) durant trois observations *INTEGRAL*. Dans le même temps, *RXTE* a observé GRS 1915+105 au cours de huit pointés. J'ai étudié les propriétés spectrales et temporelles de chacun de ces pointés. Je résume ici quelques résultats et leur interprétation présentés dans un article (Rodriguez et al. 2004a, ApJ, 2004, 615) inclus au chapitre 14, à la fin de la partie III.

Les séquences dont les QPO ont des fréquences voisines, ont été réunies pour l'extraction des spectres de QPO. La luminosité de GRS 1915+105 et les longs temps d'exposition m'ont permis d'obtenir, pour la première fois, des spectres de QPO sur plus de 20 canaux spectraux ; cela m'a conduit à les qualifier de "spectres de haute résolution". Ceux-ci sont reportés en figure 12.2. Des différences entre les différents spectres sont visibles : le QPO à 2.498 Hz montre notamment une coupure au-delà de 20 keV, alors que celui à 1.04 Hz semble être simplement croissant avec l'énergie.

Afin d'étudier les propriétés des spectres de QPO et pour éviter tout à-priori physique, j'ai utilisé

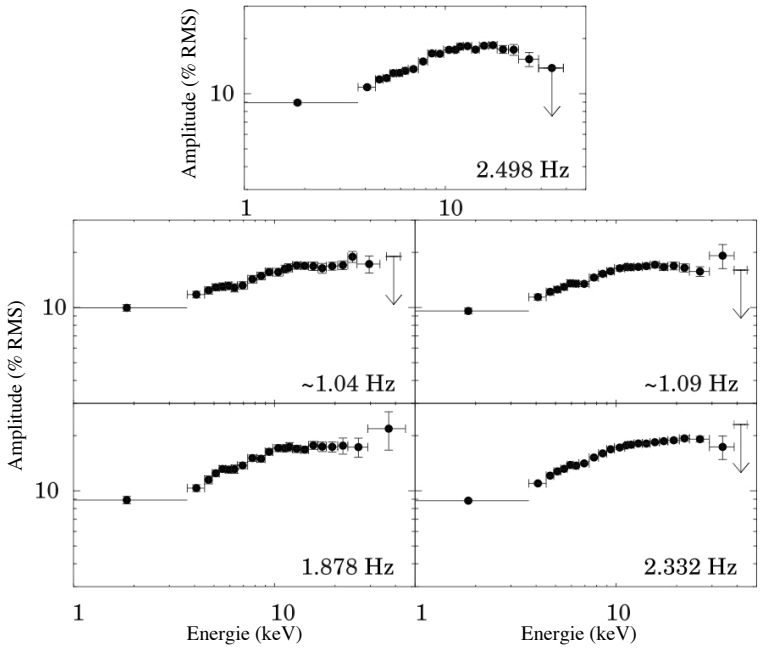

FIG. 12.2 – Spectres en énergie des 5 QPO de fréquences différentes obtenus lors des observations de classe χ de la première année de notre suivis simultané avec *INTEGRAL*. Adapté de Rodriguez et al. (2004a).

des modèles simples lors des ajustements. Notons que des ajustements avec des modèles physique ne sont pas appropriés ici, puisque l'unités des spectres est l'amplitude (% RMS/canal spectral). Pour utiliser des modèles physiques, il faudra transformer le spectre en amplitude en spectre en photons ou en coups. Les spectres sont bien représentés par une loi de puissance, avec, pour certains, une coupure à haute énergie. Le modèle employé ici est `cutoffpl` dans `XSPEC`, où $F(E) = F_0 \times E_{1\mathrm{keV}}^{-\Gamma} \times e^{-E/E_c}$, où Γ est l'indice de photon, et E_c l'énergie de coupure. Les paramètres obtenus sont reportés dans la table 12.1. Les ajustements spectraux confirment la présence d'une coupure dans les spectres de

Fréquence (Hz)	Indice de la loi de puissance (Γ)	Energie de coupure (keV)
$1.04^{\ddagger}$	-0.26 ± 0.02	> 40
1.09	-0.59 ± 0.05	$29.5^{+5.2}_{-3.9}$
1.878	-0.70 ± 0.07	$25.6^{+6.5}_{-4.4}$
2.332	-0.71 ± 0.05	$26.7^{+4.4}_{-3.3}$
2.498	-0.77 ± 0.04	$21.9^{+2.7}_{-2.2}$

TAB. 12.1 – Résultats des ajustements spectraux des spectres des 5 QPO obtenus lors de la première année de la campagne de suivi de GRS 1915+105. ‡Aucune coupure n'est nécessaire lors de l'ajustement du spectre sur l'intervalle 2–40 keV pour le QPO à 1,04 Hz.

QPO. Une coupure est même nécessaire pour représenter de manière satisfaisante tous les spectres sauf celui du QPO de plus basse fréquence. Ceci montre clairement que l'énergie de la coupure du spectre des QPO varie selon le QPO. Il semble même que cette coupure tend à décroître lorsque la fréquence du QPO augmente ; cependant, en raison des grandes incertitudes, cette tendance n'est que marginale. Il est, en revanche, clair que le spectre des QPO durcit lorsque leur fréquence augmente (table 12.1).

12.4.2 Forme spectrale des QPO : une influence du jet compact à haute énergie ?

Souvenons-nous que les spectres des QPO sont en amplitudes relative et non en flux. Puisque la fréquence des QPO est corrélée aux propriétés du disque (température, flux X-mou, et taille, par exemple Muno et al. 1999; Rodriguez et al. 2002a,b, et chapitre 1), une augmentation de la fréquence du QPO indique une probable croissance de la température et du flux du disque (et une probable diminution de son rayon interne). Nous pouvons en déduire que sa contribution relative au flux total de la source augmente dans le même temps (même si le disque reste trop froid pour être détecté lors des ajustements des spectres en énergie). Il est, d'autre part, possible de voir sur la figure 12.2 que l'amplitude dans les premiers canaux en énergie est plus basse pour les QPO de plus hautes fréquences. Ceci résulte en un durcissement des spectres pour des QPO de fréquences croissantes, qui indique donc, comme dans XTE J1550−564, que le disque d'accrétion ne participe pas à l'oscillation.

L'origine et les variations d'énergie de la coupure des spectres de QPO sont plus énigmatiques. Nous pourrions penser à un éventuel lien avec une coupure dans les spectres en énergie de GRS 1915+105. Les spectres *RXTE*/PCA (3–25 keV) sont effectivement bien ajustés par un modèle de loi de puissance coupée (ou de comptonisation thermique) d'énergie 20–25 keV. La bonne correspondance est, contrairement à ce que nous pourrions penser, troublante. En effet, si les émissions X de GRS 1915+105 n'étaient dues qu'à un disque et une couronne comptonisante, sachant qu'au-delà de 10 keV la contribution du disque au flux global est négligeable, la coupure dans les spectres de QPO indiquerait que le flux modulé ne provient pas de la couronne. En effet si le QPO provenait d'une modulation du flux compton, nous pourrions nous attendre à ce que l'amplitude du QPO devienne constante avec l'énergie dans le domaine spectral où la comptonisation domine (au-delà d'environ 10 keV).

En étudiant les spectres en énergie s'étendant sur une bande spectrale plus large (3–400 keV *RXTE*/PCA, *RXTE*/HEXTE et *INTEGRAL*/IBIS), je me suis rendu compte qu'une troisième composante spectrale était nécessaire pour bien représenter les spectres. La figure 12.3 montre un exemple de spectre PCA–HEXTE ajusté par un simple modèle de comptonisation absorbée et une raie du fer.

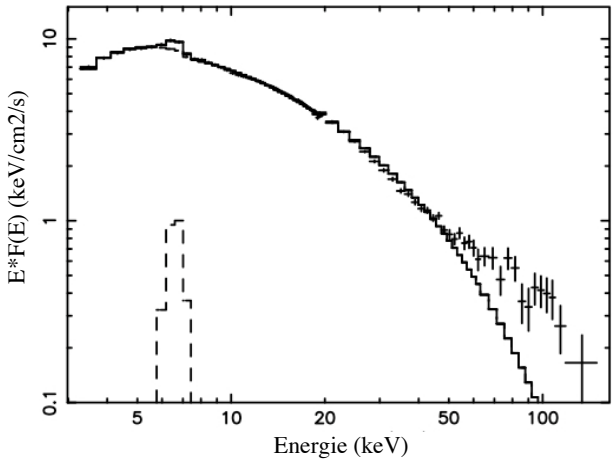

FIG. 12.3 – Spectre en énergie *RXTE*/PCA+*RXTE*/HEXTE (3–150 keV) de GRS 1915+105. Un modèle consistant en une loi de puissance avec coupure exponentielle à haute énergie, convoluée à de l'absorption, et une raie du fer est superposé au spectre. Ce modèle fournit une bonne représentation du spectre jusqu'à environ 25 keV. Une grande déviation est vue au-delà de cette énergie, montrant le besoin d'une composante additionnelle. Adapté de Rodriguez et al. (2004a).

Un excès à haute énergie y est évident, même si le modèle de comptonisation représente parfaitement le spectre en deça de ∼25 keV. La présence de cette composante spectrale dans les spectres de GRS 1915+105 avait été discutée dans de précédents travaux (par exemple Muno et al. 1999; Trudolyubov 2001), et pouvait sembler liée à la présence d'un jet compact. Mon approche spectrale et multi-longueur d'onde publiée plus tard (en 2008, chapitre 11, section 11.2.2) semble effectivement indiquer que l'extension de haute énergie pourrait être due au jet.

En 2004, lors de ces travaux, je n'avais pas de preuve aussi directe, même si un jet compact était détecté lors de toutes les observations. Pour comprendre l'évolution des spectres du QPO, je proposais que l'extension de haute énergie soit l'émission directe du jet compact. Ainsi les spectres en énergie pouvaient s'interpréter comme provenant de la contribution d'une couronne (Comptonisation), et de la contribution directe synchrotron du jet compact. Le spectre en énergie résultant dépendra donc fortement de la contribution relative de chacune de ces composantes. Dans cette interprétation, en admettant que le QPO provient du flot d'accrétion et non du jet, la coupure dans le spectre du QPO est liée à l'énergie à laquelle la contribution relative du jet devient prépondérante. Ainsi, plus la contribution du jet au spectre en énergie est forte, plus la fréquence de coupure dans le spectre du QPO est basse.

Cette inteprétation est en bon accord qualitatif avec les observations :

- Le modèle de jet compact, avec extension dans les X durs, a été appliqué avec succès dans un certain nombre de microquasars (Markoff et al. 2001, par exemple).
- Un jet compact est clairement détecté dans l'observation montrant la coupure la plus claire (Fuchs et al. 2003).
- L'émission radio à 15 GHz est forte (> 100 mJy) lors des observations montrant une coupure dans le spectre du QPO, et bien plus faible (~ 40 mJy) lors de l'observation du QPO à 1.04 Hz, qui n'a pas de coupure.

Cette approche est originale dans le sens où elle permet de montrer d'une manière totalement indépendante de la modélisation du jet compact, que ce dernier pourrait avoir une influence jusque dans les X-durs. Au-delà même de l'implication au niveau de la compréhension des phénomènes

d'éjections (par exemple l'énergétique du jet compact), ceci montrerait clairement que le QPO n'est alors pas relié à des oscillations du flux du jet. Pour terminer cette analyse, j'ajouterai que cette interprétation est totalement compatible avec mes résultats récents ; j'ai, en effet, montré, par une méthode indépendante, que le jet compact était probablement détecté dans les X durs (Rodriguez et al. 2008b, inclus au chapitre 14 et décris au chapitre 11).

12.5 QPO : oscillations de la couronne ?

Les résultats précédents ainsi que toutes les (cor)relations entre QPO et comportements spectraux (chap. 1) indiquent un lien, certes fort, avec le disque (qui fixerait la fréquence de l'oscillation), mais surtout une connexion avec la couronne (ou milieu comptonisant). Il est clair que le disque n'est pas à l'origine des QPO, ou du moins les oscillations ne proviennent pas de son flux. Les connexions que je présente dans la section précédente semblent indiquer que le jet n'est, lui non plus, pas à l'origine du QPO. Il est donc naturel de se tourner vers le "dernier" milieu émetteur du système : la couronne. Bien entendu l'origine exacte, et surtout la géométrie de cette couronne sont inconnues (chap. 1). Néanmoins il existe des modèles prédisant que les QPO sont produits à une interface disque-couronne lors de chocs oscillants[2]. Indépendamment de la modélisation théorique des flots d'accrétion que je discuterai brièvement au prochain chapitre en guise de conclusion de cette partie, il est naturel de se demander si la couronne peut être à l'origine des QPO.

L'observation jointe *INTEGRAL–RXTE* du JJM 53473 présentée au chapitre 11 (et discutée en détails dans Rodriguez et al. 2008b, inclus au chapitre 14) est idéale pour étudier plus avant l'origine possible des QPO. Tout d'abord un QPO de fréquence $3,77$ Hz et de puissance 10.9% y est détecté. Comme lors des observations présentées précedemment, le spectre du QPO est de bonne qualité et fin (fig. 12.4). Ce spectre est mal représenté par une loi de puissance, et une coupure exponentielle à haute énergie est nécessaire pour en obtenir un bon ajustement (fig. 12.4). L'énergie de coupure que j'obtiens est $E_c = 11.3$ keV, pour un indice $\Gamma = -0.53$. Notons que le modèle utilisé pour les ajustements est différent de celui présenté à la section précédente. Une comparaison directe n'est donc pas possible. Je confirme néanmoins la présence d'une coupure (d'énergie variable) dans les spectres (en amplitude) des QPO.

Comme nous l'avons vu au chapitre 11 le flux radio est élevé durant cette observation, et l'utilisation simultanée de *RXTE* et *INTEGRAL* m'a permis de bien contraindre les processus et paramètres spectraux : le spectre en énergie peut être décomposé en une composante de comptonisation thermique dominant les émission sous ~ 25 keV et une loi de puissance à plus haute énergie. La première conclusion de l'étude de cette observation est que l'extension de haute énergie pourrait être l'émission directe du jet compact. Nous pouvons établir le spectre des dépendances relatives des différentes composantes spectrales (exprimé en % par rapport au flux total dans un canal spectral). Les spectres en énergie et en amplitude relative de GRS 1915+105 entre 3 et 25 keV (bande spectrale utile sur laquelle le spectre du QPO est obtenu) sont représentés en figure 12.4 (panneau de droite).

Le spectre du QPO ne ressemble à aucun des spectres en amplitude relative des différentes composantes spectrales. A haute énergie, la loi de puissance voit son amplitude augmenter alors que celle du QPO décroît. Cela confirme, ici encore, que le QPO n'est pas associé au milieu dont la signature spectrale est la loi de puissance. Si, comme je le suggère, cette loi de puissance est associée au jet, le QPO n'est pas produit par le jet. Le résultat nouveau ici est que le spectre du QPO ne suit pas la distribution d'amplitude relative de la couronne. Cela tendrait à prouver qu'une couronne oscillante n'est pas à l'origine du QPO. Remarquons cependant qu'à partir de 10 keV la forme des spectres du QPO et de la couronne semblent relativement similaires. Ceci pourrait donc indiquer que, bien que

[2]par exemple le *CENtrifugal BOundary Layer* (CENBOL Chakrabarti 1996) ; voir aussi chapitre 1 et 13.

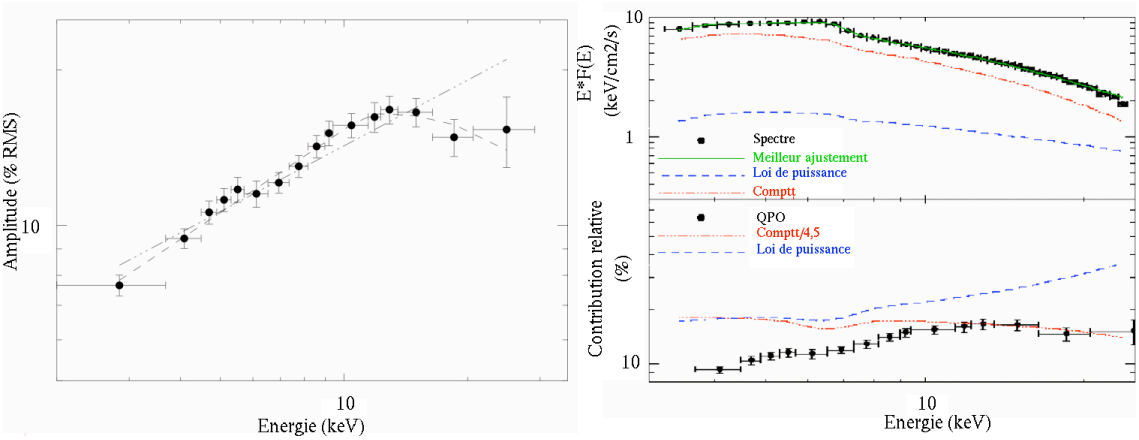

FIG. 12.4 – **Gauche :** Spectre du QPO de GRS 1915+105 lors de l'observation du JJM 53473. **Droite :** Le spectre en énergie de GRS 1915+105 est reporté dans le panneau du haut. Les différentes composantes spectrales sont représentées avec des symboles et des couleurs différentes. Le panneau du bas montre les amplitudes relatives des diverses composantes, ainsi que le spectre du QPO. Adapté de Rodriguez et al. (2008b).

la couronne n'émette pas l'oscillation, l'émission quasi-périodique subit la comptonisation, d'où son spectre semblable (en forme) à la couronne à plus haute énergie.

12.6 Conclusions

L'étude des spectres de QPO dans GRS 1915+105 est riche d'enseignements. La forte luminosité de la source, couplée à l'amplitude élevée des QPO permet d'obtenir des spectres des QPO très fins. Pour la première fois j'ai pu donc mener une étude spectrale des QPO, et en tirer des contraintes sur leur origine. Le QPO n'est pas émis par le disque, mais il n'est pas lié à la composante de haute énergie non plus. Cette composante étant très probablement le jet, j'en conclus que le QPO n'est pas émis par le jet. Par une approche détournée, dans le sens où je ne fais pas un ajustement direct des spectres du QPO, mais les compare aux contributions relatives des différentes composantes spectrales, j'ai montré que le flux comptonisé n'est pas à l'origine du QPO, même si le flux oscillant pourrait subir la comptonisation.

Ces résultats sont extrêmement contraignants puisqu'ils n'associent le QPO à aucune des composantes d'accrétion-éjection évidentes, et donc tendent à me faire rejeter des modèles basés sur des oscillations de ces milieux. Nous pourrions ainsi être tentés d'imaginer un milieu additionnel comme origine du QPO, par exemple un point chaud dans le disque. Nous pourrions aussi envisager le QPO comme signature d'interactions au sein du système accrétant, comme des chocs issus d'instabilités.

Pour aller plus loin dans l'étude des phénomènes temporels il faudra produire et étudier systématiquement les spectres des QPO dans GRS 1915+105 mais aussi d'autres sources brillantes, comme par exemple GRO J1655−40, et d'autres microquasars transitoires. Dans le futur je compte aussi m'attacher à comprendre le fond de variabilité (les différentes composantes du continuum des PSD) de ces sources. Ces études constituent le sujet de thèse — que j'ai proposé dans le cadre du réseau Européen "Black Hole Universe" (financement Marie Curie FP7/ITN) dont je fais partie —, et sur lequel T. Chen va travailler à partir d'octobre 2009.

Chapitre 13
Conclusions de la partie III : modélisation théorique des phénomènes d'accrétion-éjection et de leur évolution dans les microquasars

13.1 Que doit prendre en compte un "bon" modèle d'accrétion-éjection ?

Nous avons vu dans cette partie plusieurs aspects concernant les phénomènes d'accrétion dans les binaires X en général, et leurs relations avec les éjections dans les microquasars. Dans le cadre des binaires X massives j'ai présenté les études permettant de sonder la matière interne au système, le vent de l'étoile compagnon et son interaction avec les forts flux de rayons X émis par l'accrétion sur l'étoile à neutron. Les rayons X m'ont, en quelque sorte, permis d'effectuer une radiographie du système. Je n'ai pas développé l'étude de l'accrétion, même si nous avons pu voir qu'elle se traduisait par de fortes signatures spectrales (émission Compton), mais aussi temporelles (pulsations périodiques, chap. 6, 10).

Bien que j'aie choisi de séparer les aspects temporels et spectraux, il est cependant évident que ces phénomènes sont liés ! Toute modélisation théorique des microquasars et de leur évolution au cours d'une éruption devra prendre en compte toutes les connexions spectro-temporelles et multi-longueurs d'onde observées ces dernières années. Ceci concerne en particulier l'accrétion et ses différents régimes (états spectraux), les éjections et leurs différents types, leurs liens avec le régime d'accrétion, et enfin les propriétés temporelles, QPO de toutes fréquences, et niveau de variabilité global. Ces différents aspects reportés en fonction de l'évolution d'une source au cours de son éruption, sont reportés de

manière schématique sur le diagramme intensité-dureté (ou diagramme en "Q") présenté en figure 1.2 au chapitre 1.

Résumons les différents points "critiques" :

- Existence de 2 états spectraux canoniques, l'état dur et l'état mou, ainsi que d'états intermédiaires, et d'un état de quiescence.
- Les transitions entre états peuvent avoir lieu à différentes luminosités : existence d'une hysteresis dans l'évolution d'une source au cours de son éruption : ceci induit la nécéssité d'un paramètre additionnel au taux d'accrétion pour totalement paramétrer l'éruption.
- L'état dur est associé à une forte couronne, un jet puissant continu et compact, un niveau élevé de bruit temporel, et des QPO BF. Le disque est très probablement tronqué loin de sa dernière orbite stable[1]
- L'état mou est associé à un disque brillant à sa dernière orbite stable. Il n'y a pas de jet, pas de couronne, peu de bruit temporel, et pas de QPO.
- Les états intermédiaires mous et durs sont des mixtures de ces deux états, avec observations de QPO HF. La transition entre les deux croise la ligne de jet qui s'accompagne d'une éjection discrète. Le jet compact est éteint durant la transition état dur→état mou.
- Présence d'une composante de réflexion dans les spectres en énergie, qui semble corrélée à la luminosité du disque.
- La fréquence typique des QPO augmente avec le flux X d'une source, mais leur amplitude décroît avec le flux X-mou (< 10 keV).
- La fréquence des QPO BF croît lorsque le rayon interne du disque diminue. Cette tendance s'inverse pour un disque approchant de la dernière orbite stable.
- La fréquence des QPO BF est corrélée à l'indice de photon de la loi de puissance. Cette tendance s'inverse pour les grandes valeurs de Γ ($\Gamma \sim 2.5$).

J'ai, de plus, montré que :

- Le disque semble se rapprocher de façon monotone lors de l'évolution vers les états plus mous dans les microquasars étudiés (GRS 1915+105, XTE J1550−564, XTE J1859+226, XTE J1758−288, et aussi probablement GX 339−4).
- C'est la couronne qui est éjectée au moment de l'éjection discrète.
- Le jet compact est détecté dans les X durs dans GRS 1915+105.
- Les QPO sont liés au disque par leur fréquence, mais ont un spectre dur.
- Les QPO ne proviennent pas d'oscillations de flux du disque, ni du jet, ni de la couronne.
- Certains trous noirs restent dans l'état dur au cours de leur éruption. Ils peuvent montrer alors un niveau d'émission radio bien plus faible que les autres sources.

Un "bon" modèle théorique devra donc tenir compte et expliquer ou prédire ces différents points.

Certains de ces aspects sont liés et relativement aisés à interpréter et mènent au scenario qualitatif d'évolution présenté à la section 1.5.4 du chapitre 1.

13.2 L'instabilité magnéto-rotationnelle dans l'état mou

Le modèle α (Shakura & Sunyaev 1973) est la référence couramment admise pour modéliser le disque dans l'état mou. C'est sur la base d'ajustements spectraux de cet état que certains auteurs

[1]Cette interprétation ne fait plus consensus ces derniers temps, même si elle reste l'hypothèse la plus valable. Le lecteur intéressé pourra lire une argumentation sur cet aspect dans Tomsick (2008), qui favorise cependant le modèle de disque tronqué. Notons que Cabanac et al. (2009) propose une alternative aux problèmes de disques froids et proches de leur dernière orbite stable ; ces auteurs montrent, en laissant l'absorption libre de varier, que le disque est tronqué et que son rayon interne varie au cours de l'eruption.

tentent de mesurer le spin de certains trous noirs même si la méthode et surtout les résultats ne font pas toujours l'unanimité (McClintock et al. 2006; Middleton et al. 2006). Parmi les nombreuses hypothèses sous-jacentes figure celle d'une viscosité anormale due à une turbulence à petite échelle (comparable à l'épaisseur du disque) et entraînant un transport d'énergie et de moment cinétique. Il est également largement admis que cette turbulence est due à l'instabilité magnéto-rotationnelle (Balbus & Hawley 1991). Cette instabilité se dévellope pour une faible magnétisation du disque (ie $\beta \propto p/B^2 >> 1$ où β est le rapport des pressions thermiques et magnétiques) et entraîne un fort transport radial d'énergie et de moment cinétique : l'énergie libérée lors de l'accrétion de la matière au bord interne du trou noir ne sert donc qu'au chauffage du disque. La luminosité du système ne va, ici, dépendre que du taux d'accrétion.

Cette instabilité n'est clairement pas appropriée dans les autres états. Dans l'état dur notamment, la présence de jets collimatés suppose une composante de champ magnétique perpendiculaire au disque (B_z) importante (notamment pour la collimation). De plus la présence de jets, compacts ou discrets, impose, qu'à un certain moment, une partie de l'énergie de l'accrétion soit redirigée verticalement dans ou vers ce jet (à moins qu'il n'existe une source d'énergie extérieure à l'accrétion qui pourrait fournir l'énergie des éjections). Dans ces états la présence même d'une couronne modifie très probablement les propriétés du disque, lequel dévie alors d'une structure pure α. Enfin la MRI ne fait aucune prédiction quant à la présence de QPO.

13.3 Différentes prescriptions des régions centrales

Je ne vais pas faire une revue de tous les modèles proposés mais vais me concentrer sur trois qui, à mon avis, sont les plus complets du point de vue de l'explication de tous les phénomènes précédemment cités. Le CENBOL (Chakrabarti 1996, 1997), le paradigme JED-SAD (Ferreira et al. 2006, *Jet-Emitting Disc/Standard Accretion Disc)* et l'AEI, pour *Accretion Ejection Instability* dévellopée par Tagger & Pellat (1999), et à laquelle je collabore activement sur l'aspect confrontation théorie-observations. Remarquons tout de même que l'AEI est plus une instabilité pouvant expliquer les états durs et dur-intérmédiaires, alors que le JED-SAD et le CENBOL sont définis comme pouvant représenter la totalité de l'évolution. Je discuterai certains aspects du développement de l'AEI et d'instabilités voisines et leur application possible à l'évolution des microquasars en section 13.4. Les configurations schématiques de ces trois modèles sont reportées sur la figure 13.1.

13.3.1 Le CENBOL

Le CENBOL postule l'existence d'un disque d'accrétion standard, d'une composante secondaire d'accrétion quasi-sphérique en chute libre, et d'une région interne au disque supporté par une barrière centrifuge : le CENBOL à proprement parler (fig. 13.1). Le rayon de transition CENBOL-disque est le paramètre régissant l'évolution du système au cours de l'éruption. Un jet compact peut être produit, et sera collimaté par la compression due au choc à la transition disque-CENBOL. De nombreux articles de S. Chakrabarti et ses collaborateurs présentent les développements liés à ce modèle. Chakrabarti (1996) et Chakrabarti (1999) présentent la base du modèle et les prédictions liées aux jets.

Les points forts de ce modèle peuvent se résumer comme suit :

- Bonne représentation qualitative de l'évolution et des transitions spectrales. Le paramètre de base est le rayon de transition CENBOL-disque.
- Les X-durs sont émis par la région post-choc, c'est-à-dire le CENBOL lui-même.
- Prédiction de l'existence de l'état dur et de l'état mou (Chakrabarti & Mandal 2006).

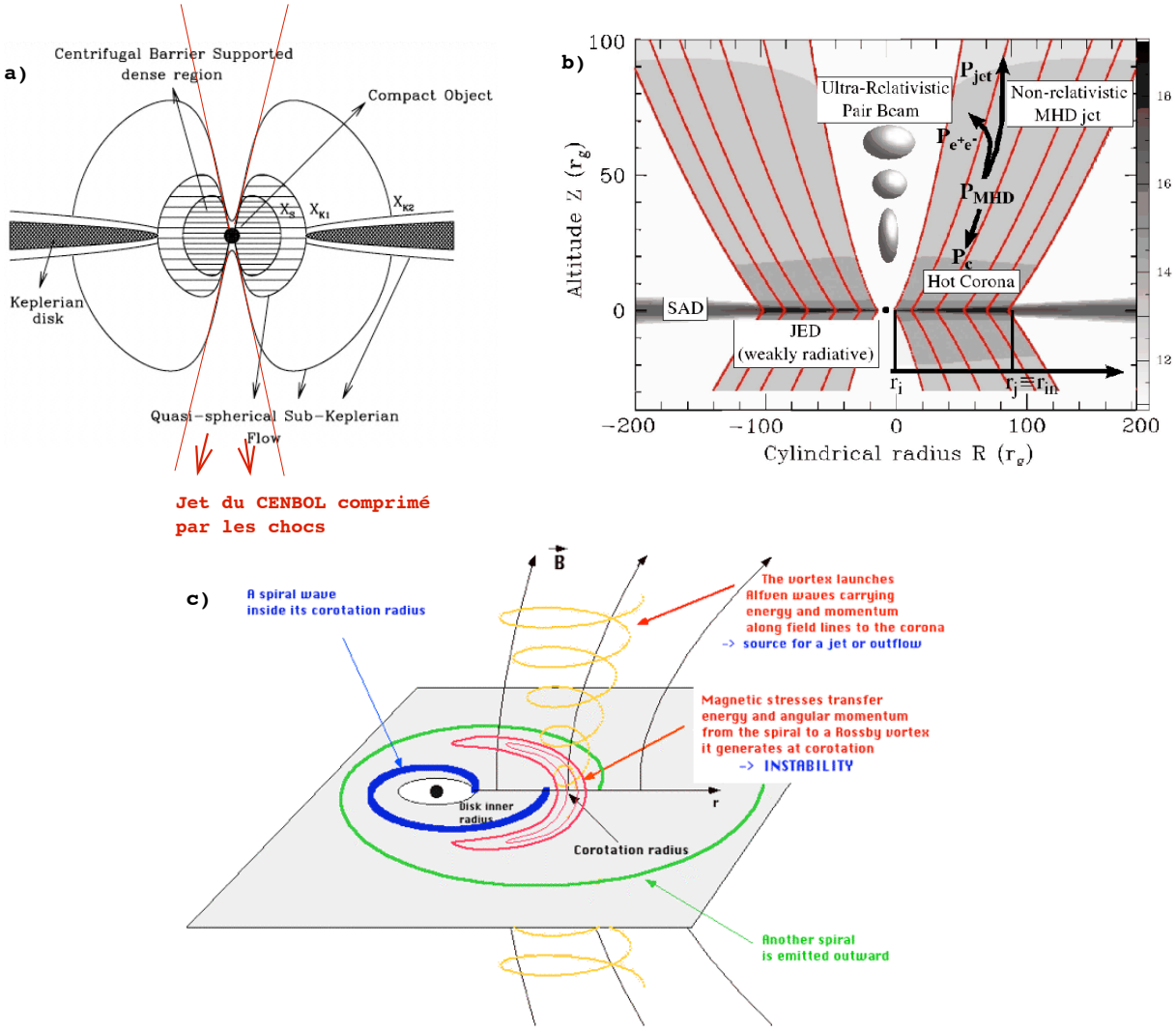

FIG. 13.1 – Représentations schématiques des trois modèles 'globaux' d'accrétion-éjection. a) le CENBOL (tiré de Chakrabarti 1996, 1999), b) le SAD-JED (tiré de Ferreira et al. 2006), c) l'AEI (tiré de Tagger & Pellat 1999; Varnière & Tagger 2002).

- Différents temps caractéristiques ont été mis en évidence lors des éruptions, et pourrait montrer la coexistence de deux flots d'accrétion : l'un en chute libre, l'autre étant le disque.
- Prédit l'existence des jets.
- Prédit l'existence de QPO BF. Ceux-ci sont dus aux oscillations des chocs créés à l'interface disque-CENBOL (Molteni et al. 1996).
- Prédit une dépendance de la fréquence des QPO avec la taille du disque (Molteni et al. 1996; Mondal & Chakrabarti 2006).
- Prédit l'existence d'une émission synchrotron due aux électrons de la region post-choc (Mondal & Chakrabarti 2006, par exemple).

Voici quelques points faibles, ou du moins peu clairs, qui, à mon avis, diminuent la crédibilité de ce modèle[2] :

- Un champ magnétique global n'est pas pris en compte. Or celui-ci semble être nécessaire/présent dans tous les systèmes astrophysiques présentant des jets.
- L'hysteresis n'est pas expliquée.
- Le paramètre additionnel au taux d'accrétion n'est pas précisé.
- L'origine des éjections discrètes n'est pas claire.
- L'inversion de la corrélation rayon du disque-fréquence des QPO BF n'est pas prédite. Au contraire Mondal & Chakrabarti (2006) semblent favoriser une augmentation de cette fréquence jusqu'à la production de QPO HF.
- Le spectre des QPO est un spectre de Comptonisation dû à l'oscillation du CENBOL.
- Le champ magnétique est inclus et supposé être stochastique dans la région post-choc.
- Il est difficile de reproduire les variations de la composante de réflexion de photons durs sur le disque d'accrétion.

13.3.2 SAD-JED

Dans cette prescription co-existent un disque d'accrétion standard (disque α, le SAD) et un disque interne, radiativement peu efficace, et responsable de la production du jet (le JED). Le rayon de transition SAD-JED, R_j, est équivalent au rayon interne du disque d'accrétion et est déterminé par le rapport de la pression thermique à la pression magnétique due à la composante verticale (B_z, perpendiculaire au disque) du champ magnétique. R_j est le lieu où $\beta = 1$. Le JED fournit un jet MHD non-relativiste ($\Leftrightarrow$jet compact), dont la base est la couronne. Pour une certaine configuration du taux d'accrétion (et de R_j) un jet relativiste est créé (les éjections discrètes). Ces éjections sont constituées de paires $e^+ - e^-$. Le lecteur intéressé par les détails peut se reporter à Ferreira et al. (2006) et Petrucci et al. (2008) pour les détails théoriques et certaines implications observationnelles.

Les points forts de ce modèles sont, à mon avis, les suivants :

- Prise en compte du champ magnétique (nécessaire dans tous les modèles de jets).
- Identification du paramètre additionnel au taux d'accrétion : R_j.
- Deux types de jets co-existent.
- Interprétation simple des états spectraux X, et de leurs corrélations avec la radio.
- Phénomène d'hysteresis prévu.
- QPO prédits et de fréquences en accord avec les constantes de temps à R_j.

Ce modèle est relativement récent (pour les microquasars) même si certains développements théoriques remontent au début des années 90. Il ne bénéficie (ou au contraire ne pâtit) pas d'une (trop) abondante littérature. Il me paraît séduisant dans le sens où il permet de répondre à des questions très

[2] j'ajouterai aussi volontiers le trop grand nombre d'articles cherchant à tout prix à justifier ce modèle, et qui au final, en diminue la crédibilité en le faisant paraître *ad-hoc*.

actuelles en se basant sur peu de paramètres.

Il y a, je pense, néanmoins quelques points qui mériteraient d'être approfondis :

- Toute la connexion spectro-temporelle devrait être développée. A l'heure actuelle la présence de QPO n'est que supposée et non forcément prédite.
- Le jet discret (jet de paires $e^+ - e^-$) ne semble exister que lorsque qu'un jet compact (certes plus faible que dans l'état dur) est présent dans l'état intermédiaire. Dans GRS 1915+105, au moins, les éjections discrètes peuvent avoir lieu sans observation préalable de jet compact.
- Devrait-on s'attendre à une émission typique autour de 511 keV due au jet de paires ? Celle-ci n'a encore été vue que dans un système (Nova Musca 1991). Existe-t-elle sous la limite de sensibilité des instruments actuels ?
- Une forte émission devrait être vue au-delà du MeV, et Ferreira et al. (2006) mentionnent le domaine du TeV comme possibilité. Cette émission n'aurait aujourd'hui été vue que dans Cyg X-1 (à seulement 4 σ), en admettant que LS 5039 et LSI +61303 ne sont pas des microquasars.

13.4 L'AEI

Je sépare l'AEI des deux autres modèles car j'ai plus activement participé à certains travaux reliés à son développement. C'est un modèle récent, puisque ses fondements remontent à 1999 (Tagger & Pellat 1999). Comme dans le modèle précédent c'est la valeur du champ magnétique vertical, ou du moins le rapport β des pressions thermiques à magnétiques qui va jouer un rôle crucial. L'AEI est une instabilité magnétique qui se développe dans le disque lorsque $\beta \sim 1$. Une onde spirale va se développer entre le bord interne du disque et le rayon de corotation. Cette onde va contribuer à transporter énergie et moment cinétique dus à l'accrétion vers la corotation. A la corotation un vortex magnétique, dit vortex de Rossby, est généré. Energie et moment cinétique pourront alors être émis verticalement (dans la couronne par exemple) sous forme d'onde d'Alfvén (fig. 13.1). Le lecteur intéressé par les détails théoriques pourra se référer à Tagger & Pellat (1999), Varnière et al. (2002) et Varnière & Tagger (2002).

13.4.1 AEI = états durs

L'instabilité AEI a en fait été développée comme un modèle de QPO BF. C'est une instabilité dont nous pensons qu'elle se développe dans les états durs. En effet, il faut d'une part que la pression thermique ne soit pas trop importante sinon le système n'est plus à l'équipartition. D'autre part Varnière & Tagger (2002) ont montré qu'en présence d'une couronne une fraction significative de l'énergie du disque servait à énergiser la couronne : le disque chauffe donc moins au profit d'une couronne plus énergétique.

Ce modèle permet d'interpréter certains phénomènes avec succès. Les points forts sont les suivants :

- Le disque est tronqué à un certaine distance R_{in} du trou noir, et ce rayon interne est un paramètre évolutif au cours d'une éruption.
- L'AEI prédit les QPO : ils sont la signature de l'instabilité.
- La fréquence du QPO BF est environ $0,1 \times F_{in}$, ou F_{in} est la fréquence Képlerienne à R_{in}.
- La fréquence du QPO est corrélée au bord interne du disque. Cependant, Varnière et al. (2002) ont montré que des effets relativistes modifiaient cette dépendance pour des rayons faibles. Ceci corrobore les observations d'inversion de relation entre fréquence du QPO et taille du disque (Rodriguez et al. 2002b; Mikles et al. 2009), fréquence de QPO et flux X mou (< 10 keV, Rodriguez et al. 2004b), fréquence du QPO et indice de photon (Vignarca et al. 2003).
- Les simulations numériques 2-D montrent la présence de la spirale (Caunt & Tagger 2001).

– Le QPO peut être identifié à la spirale qui est elle même un choc. Le spectre en énergie du QPO est donc celui de ce choc. Vu la position de la spirale, il est aisé d'admettre son émission n'est ni celle du disque, ni celle de la couronne, mais qu'elle subit de la comptonisation.

L'AEI est, je le pense, un modèle très séduisant. Néanmoins sa principale limitation est la suivante : l'AEI pure n'explique que les états durs. Il est nécessaire de l'inclure dans une prescription plus vaste.

13.4.2 Le scenario de crues magnétiques

Pour aller dans le sens d'une généralisation de ce modèle, nous avons proposé un scenario qualitatif qui, partant de l'hypothèse que l'AEI explique bien les QPO BF, se fonde sur la physique de l'instabilité et ses conditions d'apparition pour tenter d'interpréter/expliquer les cycles durant la classe β de GRS 1915+105 (chap. 7, 11). Dans ce scénario l'advection de flux magnétique avec le gaz du disque, puis sa destruction par reconnexion magnétique, créent et suppriment les conditions d'instabilité de l'AEI. Un cycle peut alors être compris comme suit : à la transition dans le creux dur β devient de l'ordre de 1, l'AEI s'allume, un QPO de fréquence variable est visible. Durant ce cycle l'accrétion amène du champ magnétique vers le bord interne du disque. Tant que le champ advecté est de même signe que le champ au bord interne, l'état dur persiste. Le pic, signature de l'éjection, arrive lorsque du champ de signe opposé est advecté. Un phénomène de reconnexion va alors être responsable de la violence des processus d'accrétion et d'éjection (Tagger et al. 2004).

Ce scenario est sujet à caution. Il ne résulte pas de calculs théoriques, mais est qualitatif. Même si de nombreuses inconnues restent (origine du changement de signe du champ magnétique, et surtout de sa quasi-fréquence), certains de mes travaux ultérieurs sont compatibles avec cette interprétation et pourraient même permettre certains raffinements du scenario. En supposant vrai le scenario de crues magnétiques dans la classes β, mes récents travaux (chap. 7, 11, Rodriguez et al. 2008a,b) permettent :

1. Une généralisation du scenario. J'ai en effet montré que toutes les classes à cycles présentaient les mêmes phénomènes d'accrétion-éjection. Si les crues magnétiques sont vraies dans l'une, elles sont alors vraies dans toutes.
2. De comprendre la corrélation entre le temps passé dans le creux X-dur et l'amplitude de l'éjection suivante. En effet le creux est le moment durant lequel l'énergie et de la matière sont accumulées. Nous pouvons donc penser que plus ce temps est long plus l'éjection sera importante en raison d'un grand stockage de matière et de flux magnétique.

13.4.3 Développements ultérieurs

Comme je l'ai mentionné plus haut la limite principale de l'AEI est qu'elle ne s'applique qu'aux états durs. Même si le scenario de crues magnétiques présente une explication tentante aux transitions vers états mous, il ne reste qu'un scenario qualitatif, et ne permet pas, de plus, d'aisément comprendre le diagramme en Q et l'hysteresis (notamment la décroissance des éruptions). Il faut ajouter que lors de nos travaux, qu'ils soient théoriques ou observationnels, nous nous sommes principalement concentrés sur GRS 1915+105. Il est donc nécessaire d'inclure des systèmes "plus normaux" à nos travaux.

Le travail de développement continue donc sous plusieurs aspects. Le plus importants pour l'aspect évolution globale est la piste que nous suivons sous l'impulsion de P. Varnière et qui consiste à étudier différentes instabilités pouvant se développer dans le disque d'accrétion (Varniere et al. 2008, et Varnière et al. 2009, soumis à A&A). Deux des instabilités considérées sont la MRI et l'AEI. Une troisième, l'instabilité d'ondes de Rossby (RWI pour *Rossby Wave Instability* Tagger & Varnière 2006), est une instabilité "cousine" de l'AEI qui se développe dans les régions internes

du disque lorsque celui-ci est à sa dernière orbite stable. Les signatures temporelles (et spectrales) alors produites lors de la manifestation de ces instabilités nous permettent d'identifier des états spectraux-temporels. Ainsi nous pouvons distinguer les cas suivants :

1. $\beta \sim 1$ et $\dot{m}$ peu important, le disque est froid (< 0.5 keV, et loin de la dernière orbite stable) : le système est dans un état pur AEI. La caractéristique temporelle principale est la présence d'un très fort QPO BF. L'état spectral est identifié comme étant l'état dur.
2. $\beta > 1$ et $\dot{m}$ grand, le disque est chaud ($1 - 2$ keV, et à sa dernière orbite stable) : le système est dans un état RWI (*Rossby Wave Instability*). Des QPO HF sont produits. L'état spectral est intermédiaire mou.
3. $\beta > 1$ et $\dot{m}$ peu important, pas de couronne et le disque est chaud (~ 1 keV, et peut être proche de sa dernière orbite stable) : le disque est pur α, l'instabilité s'y développant est la MRI. Nous sommes dans l'état mou.
4. $\beta \sim 1$ et $\dot{m}$ important, disque chaud ($1 - 2$ keV et à sa dernière orbite stable) : AEI et RWI se développent de concert. Le résultat est la production de QPO HF et BF. Nous proposons que cet état soit l'état intermédiaire dur.

Cette approche est prometteuse car basée sur des développements théoriques solides, et des confrontations fortes aux observations de plusieurs microquasars (par exemple XTE J1550−564 et GRO J1655−40). Une conséquence intéressante est la prédiction, dans l'état intermédiaire dur, de la présence simultanée de QPO BF (dus à l'AEI) et de QPO HF (dus à la RWI). Enfin, même si cet aspect, n'est pas au coeur de cette interprétation, le paramètre additionnel au taux d'accrétion est ici β qui va paramétrer l'état d'instabilité du disque.

13.5 Conclusions

Dans cette dernière partie j'ai présenté des travaux se focalisant plus sur la physique des systèmes accrétant. Je suis un observateur et j'interprète les diagnostiques observationnels (astrométrie, photométrie, spectroscopie, analyse de Fourier) dans le cadre de modèles physiques. Chaque nouvelle observation apporte de nouvelles données qui doivent servir à contraindre les modèles et/ou discriminer entre différentes propositions théoriques.

Je travaille en étroite collaboration avec des théoriciens et modélisateurs dans le cadre du développement d'un modèle d'évolution des microquasars. En confrontant nos idées, les prédictions mathématiques, les prédictions numériques nous tentons de comprendre l'origine des mécanismes régissant l'évolution de ces systèmes. Bien entendu ce modèle n'est pas unique et j'ai présenté dans ce chapitre trois propositions pouvant expliquer globalement les microquasars et leurs comportements.

Mes travaux ainsi que ceux d'autres chercheurs de la communauté m'ont permis d'établir une sorte de carte de visite d'un bon modèle. Nous avons cependant bien vu qu'aucun des trois modèles présentés ici ne satisfaisait tous les points. Et même si le modèle CENBOL me paraît plus en difficulté que les deux autres[3], aucun de ces trois modèles ne peut être totalement rejeté ou accepté. Il faut donc continuer l'interaction proche observations-théorie de manière à obtenir, par les observations, des paramètres toujours plus contraignants pour les théories, et par les développement théoriques des prédictions précises et "facilement" vérifiables. Le futur réside aussi dans la modélisation numérique,

[3]Le fait que le champ magnétique ne soit considéré que comme paramètre externe est je pense son plus gros défaut. Il semble, en effet, que pour obtenir des jets astrophysiques dans tout type de système, AGN comme étoiles jeunes, un champ magnétique soit invoqué voire nécessaire.

sur laquelle un grand effort devra être mis pour vérifier les prédictions sans être tributaire du bon vouloir d'une source. Pour revenir à l'AEI, ou bien plus généralement aux disques d'accrétion, le futur est la modélisation 3-D ; dans l'AEI elle devrait, par exemple, permettre de vérifier si le disque s'épaissit bien au niveau de la spirale et si, donc, cette spirale est vraiment une bonne explication pour le QPO.

Chapitre 14

Articles de recherche liés à la partie III

14.1 IGR J16320−4751 vu par *XMM–Newton* et *INTEGRAL*

Mon. Not. R. Astron. Soc. **366,** 274–282 (2006) doi:10.1111/j.1365-2966.2005.09855.x

INTEGRAL and XMM–Newton observations of the X-ray pulsar IGR J16320−4751/AX J1631.9−4752

J. Rodriguez,[1,2,3⋆] A. Bodaghee,[3,4] P. Kaaret,[5] J.A. Tomsick,[6] E. Kuulkers,[7] G. Malaguti,[8] P.-O. Petrucci,[9] C. Cabanac,[9] M. Chernyakova,[3] S. Corbel,[1,2] S. Deluit,[10] G. Di Cocco,[8] K. Ebisawa,[11] A. Goldwurm,[1,12] G. Henri,[9] F. Lebrun,[1,12] A. Paizis,[3,13] R. Walter[3,4] and L. Foschini[8]

[1]*CEA Saclay, DSM/DAPNIA/Service d'Astrophysique, 91191 Gif sur Yvette, France*
[2]*Unité mixte de recherche CEA/CNRS/Université Paris 7 UMR AIM/7158*
[3]*ISDC, Chemin d'Ecogia, 16, 1290 Versoix, Switzerland*
[4]*Observatoire de Genève, Chemin des Maillettes 51, 1290 Sauverny, Switzerland*
[5]*Department for Physics and Astronomy, University of Iowa, Iowa City, IA 52242, USA*
[6]*Center for Astrophysics and Space Science, University of California at San Diego, MS 0424, La Jolla, CA 92093 USA*
[7]*ISOC, ESA/ESAC, Urb. Villafranca del Castillo, PO Box 50727, 28080 Madrid, Spain*
[8]*INAF/IASF, Via Gobetti 101, 40129 Bologna, Italy*
[9]*Laboratoire d'Astrophysique de l'Obesrvatoire de Grenoble, BP 53X, 38041 Grenoble, France*
[10]*Centre d'Etude Spatiale des Rayonnements 9, avenue du Colonel Roche - Boite postale 4346 31028 Toulouse Cedex 4, France*
[11]*NASA Goddard Space Flight Center, Code 661, Greenbelt, MD 20771, USA*
[12]*Unité mixte de recherche APC, 11 place Berthelot 75005 Paris, France*
[13]*INAF/IASF sezione di Milano, Via Bassini 15, 20133 Milano, Italy*

Accepted 2005 November 10. Received 2005 November 9; in original form 2005 September 19

ABSTRACT

We report on observations of the X-ray pulsar IGR J16320−4751 (also known as AX J1631.9−4752) performed simultaneously with International Gamma-Ray Astrophysics Laboratory (*INTEGRAL*) and *XMM–Newton*. We refine the source position and identify the most likely infrared counterpart. Our simultaneous coverage allows us to confirm the presence of X-ray pulsations at ∼1300 s, that we detect above 20 keV with *INTEGRAL* for the first time. The pulse fraction is consistent with being constant with energy, which is compatible with a model of polar accretion by a pulsar. We study the spectral properties of IGR J16320−4751 during two major periods occurring during the simultaneous coverage with both satellites, namely a flare and a non-flare period. We detect the presence of a narrow 6.4 keV iron line in both periods. The presence of such a feature is typical of supergiant wind accretors such as Vela X-1 or GX 301−2. We inspect the spectral variations with respect to the pulse phase during the non-flare period, and show that the pulse is solely due to variations of the X-ray flux emitted by the source and not due to variations of the spectral parameters. Our results are therefore compatible with the source being a pulsar in a High Mass X-ray Binary. We detect a soft excess appearing in the spectra as a blackbody with a temperature of ∼0.07 keV. We discuss the origin of the X-ray emission in IGR J16320−4751: while the hard X-rays are likely the result of Compton emission produced in the close vicinity of the pulsar, based on energy argument we suggest that the soft excess is likely the emission by a collisionally energized cloud in which the compact object is embedded.

Key words: stars: neutron – pulsars: general – stars: individual: IGR J16320-4751, AX J1631.9-4752 – X-rays: binaries.

1 INTRODUCTION

The International Gamma-Ray Astrophysics Laboratory (*INTEGRAL*) was set up on 2002 October 17 (Winkler et al. 2003). Since then, through regular scans of our Galaxy and guest observers'

⋆E-mail: rodrigue@discovery.saclay.cea.fr

Table 1. Journal of the observations analysed in this paper.

Satellite	Revolution no	Start day	Date obs. Stop day	(MJD 53000)	Prop. Id	Total duration ($\times 10^3$ s)
INTEGRAL	226	2004 Aug 19	2004 Aug 20	236.57–237.94	0220014&0220007	∼118
XMM–Newton	860	2004 Aug 19	2004 Aug-20	236.55–237.14	0201700301	∼51

observations, about 75 new sources[1] have been discovered mainly with the IBIS telescope (Ubertini et al. 2003), thanks to its low-energy camera ISGRI (Lebrun et al. 2003). Because of its energy range (from 15 keV to ∼1 MeV), its high angular resolution (12 arcmin), good positional accuracy (down to ∼0.5 arcmin for bright sources) and its unprecedented sensitivity, between 20 and 200 keV, IBIS/ISGRI has helped us to answer the question of the origin of the hard X-ray background in the Galaxy (Lebrun et al. 2004). These capacities have helped us to discover many peculiar X-ray binaries characterized by a huge equivalent absorption column density ($N_{\rm H}$), as high as a few times 10^{24} cm^{-2} in IGR J16318−4848 (Matt & Guainazzi 2003; Walter et al. 2003), the first source discovered by *INTEGRAL*. Due to the high absorption, most of these sources were not detected during previous soft X-ray scans of the Galaxy [see e.g. Kuulkers (2005) for a review].

IGR J16320−4751 was detected on 2003 February 1 with ISGRI (Tomsick et al. 2003) as a hard X-ray source. The source was observed to vary significantly in the 15–40 keV energy range on time-scales of ∼1000 s, and was sometimes detected above 60 keV (Tomsick et al. 2003; Foschini et al. 2004). The inspection of the X-ray archives revealed that IGR J16320−4751 is the hard X-ray counterpart to AX J1631.9-4752, observed with *ASCA* in 1994 and 1997 (Sugizaki et al. 2001). The analysis of archival BeppoSAX-WFC data showed that this source was persistent for at least 8 yr (in't Zand et al. 2003). Soon after the discovery of IGR J16320−4751 by *INTEGRAL*, an *XMM–Newton* Target of Opportunity was triggered. This allowed us to obtain the most accurate X-ray position to date (Rodriguez et al. 2003), which in particular led to the identification of two possible infrared counterparts (Tomsick et al. 2003; Rodriguez et al. 2003) (hereafter source 1 and 2). From this analysis, we suggested that IGR J16320−4751 is probably a High Mass X-ray Binary (HMXB) hosting a neutron star (Rodriguez et al. 2003). This last point has been reinforced since the discovery of X-ray pulsations from this source in both *XMM–Newton* and *ASCA* observations (Lutovinov et al. 2005) with a pulse period of about 1300 s. Aharonian et al. (2005), reporting results of the survey of the inner regions of the Galaxy at very high energy with the High Energy Stereoscopic System (HESS), found a new source, HESS J1632−478, at a position coincident with IGR J16320−4751, but the authors suggest that this could be simply a chance coincidence. Very recently, Corbet et al. (2005) reported the discovery of strong modulations of the X-ray flux seen with Swift, that they interpreted as revealing the orbital period of the system. The period of 8.96 d that they find is compatible with the system containing an early-type supergiant (Corbet et al. 2005).

Here, we report on observations of IGR J16320−4751 performed simultaneously with *INTEGRAL* and *XMM–Newton* in 2004 August. The sequence of observations is introduced in the following section together with technical information concerning the data reduction. Section 3 of this paper describes the results which are commented and discussed in the last part of the paper.

[1] An updated list of all *INTEGRAL* sources can be found at http://isdc.unige.ch/∼rodrigue/html/igrsources.html.

2 OBSERVATIONS AND DATA REDUCTION

The journal of the observations can be found in Table 1. The *INTEGRAL* observation results from an amalgamation of the observation of IGR J16318−4848 (PI Kuulkers, programme no 0220007) with that of IGR J16320−4751 (PI Foschini, programme no 0220014). IGR J16320−4751, however, remained the on-axis target for this observation.

2.1 *INTEGRAL* Data Reduction

Our *INTEGRAL* observation was performed with the so-called hexagonal dithering pattern (Courvoisier et al. 2003), which consists of a sequence of seven pointings (called science windows, hereafter: SCW) following a hexagonal dithering on and around the position of the source. Being the on-axis target, IGR J16320−4751 is always in the fully coded field of view of the IBIS and SPI instruments, where the instrumental response is optimal. The *INTEGRAL* data were reduced using the Off-line Scientific Analysis (OSA) v 5.0, with specificities for each instrument described below.

The data from IBIS/ISGRI were first processed until the production of images in the 20–40 and 40–80 keV energy ranges, with the aim of identifying the most active sources in the field. From the results of this step, we produced a catalogue of active sources which was given as an input for a second run producing images in the 20–60 and 60–200 keV energy ranges. In the latter, we forced the extraction/cleaning of each of the catalogue sources in order to obtain the most reliable results for IGR J16320−4751 [see Goldwurm et al. (2003) for a detailed description of the IBIS software]. In order to check for the presence of the 1300-s X-ray pulsations in the IBIS range, we also produced light curves with a time bin of 250 s (with the OSA 5.0/III_LC_EXTRACT V2.4.3 module) in the same energy ranges.

We produced spectra using two alternative methods. The first method is to use the standard spectral extraction from the OSA pipeline. The second method uses the individual images produced in 20 energy bins to estimate the source count rate and build the spectrum as explained in Rodriguez et al. (2005). This second method can be used to crosscheck the results obtained with the standard spectral extraction. Comparison of the spectra obtained with the two methods showed no significant differences, we therefore used the spectra obtained with the standard procedure in our spectral fits. We used the standard response matrices provided with OSA 5.0, i.e. ISGR_ARF_RSP_0010.FITS and ISGR_RMF_GRP_0016.FITS, the latter rebinned to 20 spectral channels.

The source is not spontaneously detected by the JEM-X detector. We tentatively forced the extraction of science products at the position of IGR J16320−4751, but a rapid comparison with the *XMM–Newton* data showed that the JEM-X products were very likely to be contaminated by the nearby black hole candidate 4U 1630−47 that was in a bright soft state outburst at the time of the observation (Tomsick et al. 2005). These data were not considered further. We did not use the data from the spectrometer SPI because the

2.5 angular resolution did not allow to discriminate the emission of IGR J16320−4751 from that of e.g. 4U 1630−47 (the angular separation between the two sources is ∼40 arcmin), or IGR J16318−4848 (∼55 arcmin).

2.2 *XMM–Newton* data reduction

The *XMM–Newton* data were reduced with the Science Analysis System (SAS) v6.1.0. Event lists for EPIC MOS (Turner et al. 2001) and EPIC PN (Strüder et al. 2001) cameras were obtained after processing the Observation Data Files with EMCHAIN and EPCHAIN. During the processing, the data were screened by rejecting periods of high background, and by filtering the bad pixels. The EPIC MOS were both operating in timing mode allowing one to obtain light curves from the central chip with 1.5-ms resolution. The EPIC PN was operating in full frame mode, allowing light curves with a time resolution as high as 73.4 ms to be obtained. For the PN camera, we extracted the spectra and light curves from a 35-arcsec radius circle centred on the source, while background products were extracted from a 60-arcsec circular region free of sources (from the same chip).

Because of the operating mode of the MOS cameras, no background estimate can be obtained from the central chip where the source lies. A 'quick look' at the lateral MOS chips shows that the background remained negligible during the whole observation. The latter could therefore be neglected in the analysis of the MOS data. MOS light curves were hence extracted from the central chip of both cameras. For the three EPIC cameras, light curves were extracted in different energy ranges (2–12, 0.6–2, 2–5, 5–8, 8–12 keV) with the highest time resolution achievable. Barycentric correction was applied to all light curves. The MOS light curves were then summed using the FTOOLS LCMATH.

A redistribution response matrix and an ancillary response file for the PN spectral products were generated with RMFGEN and ARFGEN. The resulting spectrum was fitted in XSPEC v11.3.1 (Arnaud 1996) simultaneously with the spectrum obtained with *INTEGRAL*/ISGRI.

3 RESULTS

3.1 Refining of the X-ray position

Given the long exposure time (Table 1) and the high flux from the source, we tried to obtain a better estimate on the position in order to possibly discriminate between the two candidate counterparts (Rodriguez et al. 2003). For this purpose, we used the EDETECT_CHAIN task after having extracted PN images in five energy ranges. The latter were further rebinned so that an image pixel had a physical size of 4.4 arcmin. The best position obtained with this method is RA$_{J2000}$ = 248.0077 and Dec.$_{J2000}$ = −47.8742 with a nominal uncertainty of ∼4 arcmin. This is about 1.9 arcmin from the position reported by Rodriguez et al. (2003). To cross check, we re-analysed the 2003 *XMM–Newton* observation with the latest calibration files available, and using the same EDETECT_CHAIN in the same energy ranges. As explained in Rodriguez et al. (2003), only MOS data are available, and the data need to be filtered for soft proton flares. The best position we obtained is RA$_{J2000}$ = 248.0081° and Dec.$_{J2000}$ = −47.8741. We can therefore refine the X-ray position to RA$_{J2000}$ = $16^h32^m01^s.9$ Dec.$_{J2000}$ = −47°52′27″ with an uncertainty of ∼3 arcmin at 90 per cent confidence. This new position more strongly suggests that the source labelled as no 1 in Fig. 1 is the genuine counterpart of IGR J16320−4751, since source 2 is now outside the 90 per cent error box on the X-ray position.

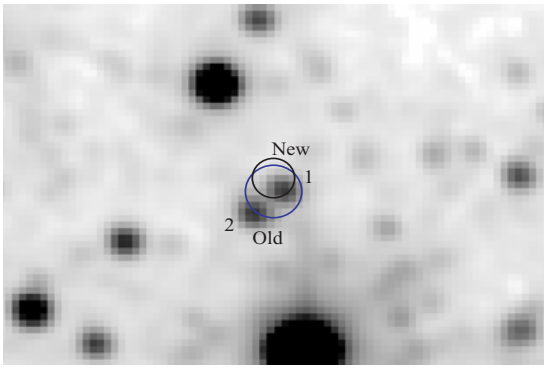

Figure 1. 2MASS K_S 1.3 × 0.9 arcsec^2 image of the field around IGR J16320−4751. The two circles respectively represent the *XMM–Newton* position given in Rodriguez et al. (2003, large circle), and the refined position discussed in the text. Infrared sources 1 and 2 are the candidate counterparts.

We compared the X-ray source positions for high significance sources (likelihood ⩾200) with infrared sources from the Two Micron All Sky Survey (2MASS) catalogue. We found a match within 0.4 arcsec between the *XMM–Newton* source at RA$_{J2000}$ = $16^h32^m12^s.306$, Dec.$_{J2000}$ = −47°44′59.″32 and a bright 2MASS source with a K magnitude of 9.3 located at RA$_{J2000}$ = $16^h32^m12^s.339$ and Dec.$_{J2000}$ = −47°44′59.″45. We found a second close match between the *XMM–Newton* source at RA$_{J2000}$ = $16^h31^m35^s.642$, Dec.$_{J200}$ = −47°51′27.″42 and a bright 2MASS source with a K magnitude of 9.3 located at RA$_{J2000}$ = $16^h31^m35^s.634$, Dec.$_{J2000}$ = −47°51′27.″89. Allowing a 1-arcsec error circle for the *XMM–Newton* source, and taking into account the surface density of *XMM–Newton* sources and 2MASS sources at appropriate magnitude limits, we find that the chance probability of occurrence of these X-ray/IR source coincidences is 0.3 per cent. This increases our confidence that the astrometry of the X-ray is correct and that we have identified the correct infrared (IR) counterpart to IGR J16320−4751.

3.2 Timing analysis

The light curves of IGR J16320−4751 obtained in different energy ranges with the different instruments are presented in Fig. 2. As already reported, IGR J16320−4751 is a variable source on various time-scales, from seconds–minutes (Rodriguez et al. 2003; Fig. 2) to days–months (e.g. Foschini et al. 2004). During our observations, the source shows a prominent flare around MJD 53236.6, visible in both light curves (Fig. 2). A second similar flare is visible in the ISGRI 20–60 keV light curve around MJD 53237.3. Unfortunately, our *XMM–Newton* observation does not cover this period.

We used the EPIC cameras to study the pulsations of IGR J16320−4751 already reported in Lutovinov et al. (2005). We performed a period search on the MOS and PN light curves using the XRONOS tool EFSEARCH. Because the source is highly absorbed (Rodriguez et al. 2003), and in order to improve the detection of the pulsation we restricted our period search to the 2–12 keV range for all EPIC cameras. The Lomb–Scargle of the PN 2–12 keV light curve is reported in Fig. 3.

A very prominent peak is visible with both PN and MOS detectors. Fitting the peak with Gaussian profiles led to best values of 1303.8 ± 0.9 s (7.669 ± 0.005 × 10^{-4} Hz) and 1302.0 ± 1.1 s (7.680 ±

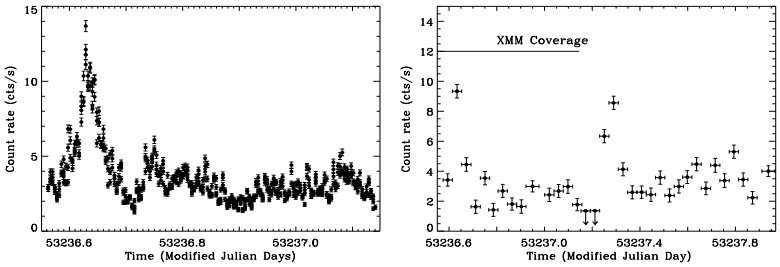

Figure 2. Left-hand side: the 2–12 keV *XMM–Newton*/PN light curve of IGR J16320−4751. Right-hand side: the 20–60 keV *INTEGRAL*/ISGRI light curve of IGR J16320−4751. Note that the two data sets have different lengths, and the light curves have different time resolutions. The time bin of the *XMM–Newton* light curve is 100 s, while that of *INTEGRAL*/ISGRI is about 3200 s (length of a SCW). Upper limits are given at the 3σ level.

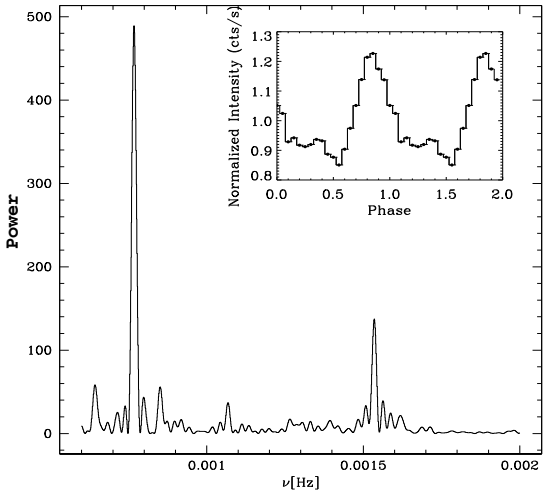

Figure 3. Lomb–Scargle periodogram of the 2–12 keV PN light curve. The insert shows the pulse profile of the 2–12 keV light curve obtained by folding the PN light curve at a period of 1303 s.

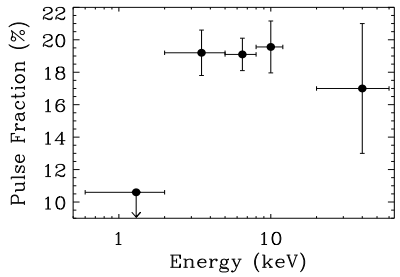

Figure 4. Energy dependence of the pulse fraction, obtained after folding the *XMM–Newton* and *INTEGRAL* light curves. The upper limit at low energy is given at the 3σ level.

0.006×10^{-4} Hz) for MOS and PN, respectively. The errors are calculated from the periodograms using the method developed by Horne & Baliunas (1986). These values are in complete agreement with the best value reported by Lutovinov et al. (2005), therefore confirming the identification of the pulsation at ∼1300 s. A fainter peak is found at a period half that of the main feature (Fig. 3) that identifies it as a first harmonic of the pulse period. We then folded the PN light curve with a period of 1303 s (the mean of the PN and MOS values). The folded light curve is shown in Fig. 3 (insert). The pulse fraction (defined as $P = \frac{I_{\max} - I_{\min}}{I_{\max} + I_{\min}}$, where $I_{\max}$ and $I_{\min}$ respectively represent the intensities at the maximum and the minimum of the pulse profile) is 18.11 ± 0.7 per cent between 2 and 12 keV for the main pulse. The pulsation is also visible in the ISGRI 20–60 keV light curve. Folding the light curve at a period of 1303 s leads to a pulse fraction between 20 and 60 keV of 17 ± 4 per cent. We produced light curves in several energy ranges and folded them with a period of 1303 s in order to study the energetic dependence of the pulse fraction. As can be seen in Fig. 4 apart from the possible non-detection of pulsations below 2 keV, the pulse amplitude is compatible with being flat from 2 to 60 keV. The reported upper limit below 2 keV is 10.5 per cent.

3.3 Spectral analysis

In order to avoid mixing different spectral properties together, we separated the observation in two different time regions, the first corresponding to the first flare (where we isolated ∼3.6 ks), and the second corresponding to the end of the simultaneous coverage by *XMM–Newton* and *INTEGRAL*, i.e. the last ∼30 ks of the *XMM–Newton* observation. The spectra were fitted between 0.6 and 12 keV (*XMM–Newton*), and 20 and 80 keV (*INTEGRAL*). No relative normalization constant was included in any of the fits.

3.3.1 Spectral analysis of the non-flaring period

Several models were tested in the course of the analysis starting first with phenomenological models. A single absorbed power law leads to a poor reduced χ^2 (in the remaining of the paper χ^2_ν stands for reduced χ^2). In fact, a large deviation is seen at high energy, indicative of a high energy cut-off. Replacing the single (absorbed) power law by a power law with a high energy cut-off improves the fit, although the χ^2_ν is still poor, and high residuals are found around 6.4 keV. We obtain a relatively acceptable fit with a model consisting of an absorbed power law with a high energy cut-off, and a Gaussian emission line at ∼6.4 keV. The χ^2_ν is 1.48 for 441 degrees of freedom (d.o.f.). This value and some remaining significant residuals indicate that an improvement is achievable. This is particularly true below

278 *J. Rodriguez et al.*

Table 2. Best-fitting parameters obtained from the fit to the 0.6–12 and 20–80 keV *XMM–Newton* and *INTEGRAL* flare and non-flare spectra with the simple phenomenological model consisting of an absorbed power law with a high energy cut-off, a Gaussian and an iron edge. Errors and limits are given at the 90 per cent confidence level.

Spectra	$N_{\rm H}$ ($\times 10^{22}$ cm^{-2})	Cut-off energy (keV)	e-folding (keV)	Γ	Line (centroid) (keV)	Line width (keV)	Line eq. width (eV)	Edge (keV)	Max τ
Non-flare	$15.5^{+0.1}_{-0.6}$	7.1 ± 0.4	$13.4^{+0.7}_{-0.9}$	$0.24^{+0.02}_{-0.12}$	$6.409^{+0.027}_{-0.005}$	<0.03	100^{+20}_{-14}	7.21 ± 0.04	0.14 ± 0.04
Flare	11.5 ± 0.5	$11.4^{+0.9}_{-0.5}$	10.1 ± 0.7	$0.28^{+0.07}_{-0.03}$	6.419 ± 0.014	$0.046^{+0.025}_{-0.029}$	116^{+39}_{-37}	$7.3^{+0.3}_{-0.1}$	$0.15^{+0.02}_{-0.05}$

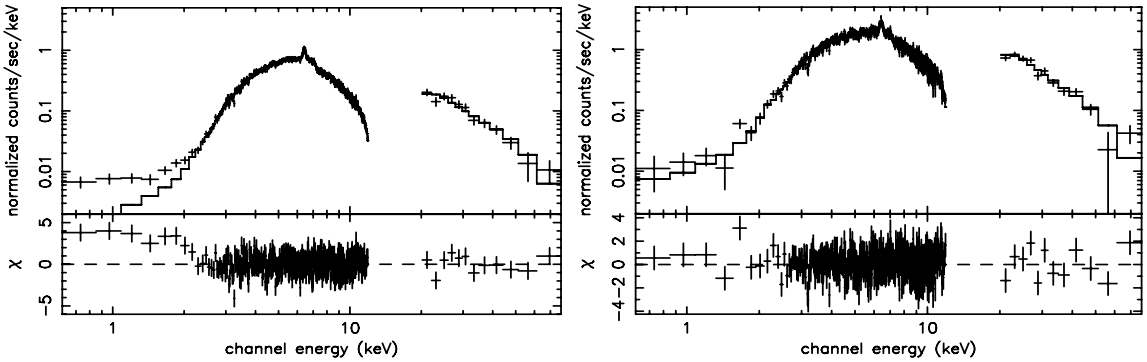

Figure 5. *XMM–Newton*/PN and *INTEGRAL*/ISGRI count spectra. Left-hand side: non-flare spectra. Right-hand side: Flare spectra. In both the cases, the continuous line represents the best-fitting model (EDGE*WABS*HIGHECUT*(POWERLAW+GAUSS), see the text for the details of the fitting). Note that the same vertical scale is used for both the cases.

2 keV, where a significant excess is detected, and around 7 keV. To account for the latter, we included an iron edge in the model. The fit is significantly improved with $\chi^2_\nu = 1.20$ (for 439 d.o.f.). The best-fitting parameters are reported in Table 2 (all errors on the spectral parameters are given at the 90 per cent confidence level). The 2–10 keV unabsorbed flux is 9.22×10^{-11} erg cm^{-2} s^{-1}, and the 20–100 keV flux is 2.33×10^{-10} erg cm^{-2} s^{-1}.

The large excess still visible below 2 keV (Fig. 5) seems to be reminiscent of several of the so-called highly absorbed sources detected by *INTEGRAL* (e.g. IGR J17252−3616; Zurita et al. 2005, IGR J16393−4643, Bodaghee et al. 2005), and has been seen in other X-ray Binaries containing pulsars (e.g. Hickox, Narayan & Kallman 2004). In order to try to understand its origin, we fitted the spectra with different types of absorption. The first one ($N_{\rm H_{ext}}$) corresponds to the absorption on the line of sight by the Galaxy and was modelled with the PHABS model in XSPEC, while the second ($N_{\rm H}$) is modelled by photoelectric absorption with variable abundance cross-sections. All the abundances were frozen to the solar values except that of iron given the presence of an emission line and an absorption edge in the simple model presented earlier. The soft excess is modelled by a blackbody emission. The spectral model is PHABS*(BBODY+VPHABS*HIGHECUT*(POWERLAW+GAUSS)) in the XSPEC terminology. The value of the interstellar absorption ($N_{\rm H_{ext}}$) was fixed to the value obtained from Dickey & Lockman (1990) in the direction of the source, i.e. $N_{\rm H_{ext}} = 2.1 \times 10^{22}$ cm^{-2} while the abundances of elements are set to solar values. The fit is good with $\chi^2_\nu = 1.13$ (438 d.o.f.). The intrinsic absorption is $11.8^{+0.5}_{-0.4} \times 10^{22}$ cm^{-2}, the blackbody temperature is $0.07^{+0.04}_{-0.01}$ keV and the iron abundance is $Z_{\rm Fe} = 1.50^{+0.25}_{-0.15}\ Z_\odot$. The other parameters are compatible with those returned from the previous fit. The (extrapolated) 0.01–10 keV unabsorbed flux of the blackbody (soft excess) is 3.7×10^{-10} erg cm^{-2} s^{-1}, while the 0.01–100 keV unabsorbed flux of the power-law component is $\sim 4.7 \times 10^{-10}$ erg cm^{-2} s^{-1}.

Since a cut-off power law is usually interpreted as a signature for thermal Comptonization, we replaced the phenomenological model by a more physical model of Comptonization (COMPTT, Titarchuk 1994). The choice of this model is also dictated by the fact that it gave a good representation of the *XMM–Newton* spectrum of a previous observation Rodriguez et al. (2003), although the lack of high energy data had prevented us from obtaining a good constraint on the temperature of the electrons. A simple absorbed COMPTT model (plus a Gaussian) represents the data rather well ($\chi^2_\nu = 1.54$ for 442 d.o.f.), although the soft excess and an iron edge are here again clearly visible. We therefore fitted the data with a model consisting of an (externally) absorbed blackbody plus intrinsically absorbed Comptonization (all abundances are set to solar values except the iron density of the local (vphabs) absorption that was left as a free parameter) and a Gaussian line (PHABS(BBODY+VPHABS(COMPTT+GAUSS)) in XSPEC). Similar to the previous case, $N_{\rm H_{ext}}$ is frozen to the Galactic value along the line of sight. We obtain a good representation of the spectrum with $\chi^2_\nu = 1.15$ for 438 d.o.f. The best-fitting parameters are reported in Table 3, while the '$\nu - F_\nu$' spectrum is presented in Fig. 6. The blackbody (unabsorbed) bolometric flux is 2.2×10^{-10} erg cm^{-2} s^{-1}, while the 0.01–100 keV unabsorbed (i.e. external plus intrinsic absorption corrected) COMPTT flux is 4.4×10^{-10} erg cm^{-2} s^{-1}.

We also tried an alternative model involving partial covering by an ionized absorber (PCFABS in XSPEC). When leaving the disc temperature free to vary, non-realistic values are obtained for its normalization. We then froze $kT_{\rm bb}$ to the best value obtained with

Table 3. Best-fitting parameters obtained from the fit to the 0.6–12 and 20–80 keV *XMM–Newton* and *INTEGRAL* flare and non-flare spectra with the physical models involving thermal Comptonization. $N_{\rm H}$ is the absorption intrinsic to the source, $kT_{\rm bb}$ represents the temperature of the soft excess, kT_{inj} represents the temperature of the injected photon for Comptonization and $kT_{\rm e}$ is the temperature of the Comptonizing cloud. Errors represent the 90 per cent confidence level.

Spectra	$N_{\rm H}$ ($\times 10^{22}$ cm^{-2})	$Z_{\rm Fe}$ $Z_{\odot}$	$kT_{\rm bb}$ (keV)	kT_{inj} (keV)	$kT_{\rm e}$ (keV)	τ_{ρ}	Line (centroid) (keV)	Line width (keV)	Line e.q. width (eV)
Non-Flare	$8.9^{+0.2}_{-0.7}$	$1.83^{+0.30}_{-0.26}$	$0.075^{+0.024}_{-0.018}$	$1.98^{+0.15}_{-0.10}$	$8.0^{+1.0}_{-0.7}$	$4.9^{+0.5}_{-0.4}$	6.411 ± 0.006	<0.03	100^{+24}_{-20}
Flare	$7.6^{+1.2}_{-1.4}$	$2.2^{+0.9}_{-0.6}$	0.075 *frozen*	$1.30^{+0.31}_{-0.24}$	$6.5^{+0.4}_{-0.3}$	$9.8^{+1.2}_{-1.4}$	$6.419^{+0.014}_{-0.015}$	0.04 ± 0.02	112^{+42}_{-44}

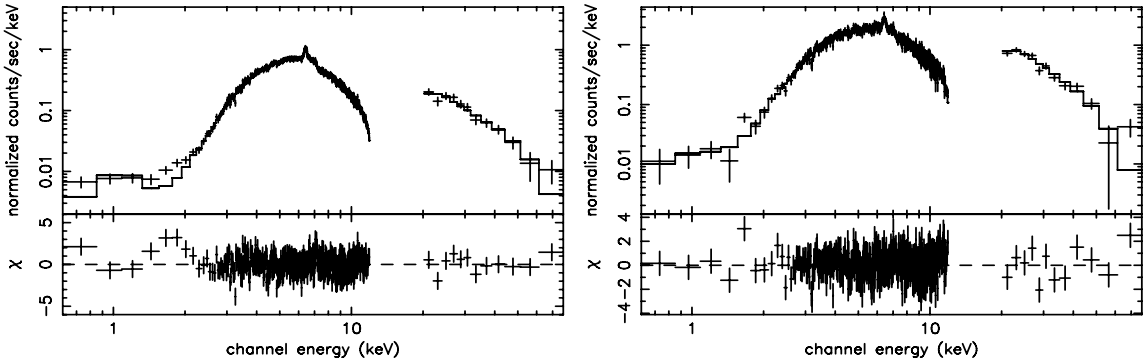

Figure 6. *XMM–Newton*/PN and *INTEGRAL*/ISGRI unfolded spectra. Left-hand side: non-flare spectra. Right-hand side: flare spectra. In both the cases, the continuous line represents the best-fitting model (PHABS*(BBODY+VPHABS*(COMPTT+GAUSS)), see the text for the details of the fitting). Individual components are also represented. Note that the same vertical scale is used for both the cases.

Table 4. Best-fitting parameters from the thermal Comptonization model, modified by a partial-covering absorber applied to the 0.6–12 and 20–80 keV *XMM–Newton* and *INTEGRAL* flare and non-flare spectra. Errors and limits denote the 90 per cent confidence level. In both the cases, the blackbody temperature of the soft excess is frozen to 0.075 keV.

Spectra	$N_{\rm H}$ ($\times 10^{22}$ cm^{-2})	kT_{inj} (keV)	$kT_{\rm e}$ (keV)	τ_{ρ}	Covering fraction per cent
Non-flare	12.2 ± 0.6	$1.5^{+0.05}_{-0.11}$	$7.0^{+0.5}_{-0.4}$	6.4±0.7	$98.4^{+0.3}_{-0.7}$
Flare	$9.2^{+1.1}_{-1.3}$	1.0 ± 0.2	6.6 ± 0.2	$9.9^{+0.5}_{-0.7}$	$98.0^{+1.8}_{-0.5}$

the other models, i.e. 0.075 keV. The fit is good with $\chi^2_{\nu} = 1.17$ for 444 d.o.f. The spectral parameters are compatible with those obtained with the previous model except that the intrinsic absorption is slightly higher here (Table 4). Note that the fit indicates that the central source is almost completely covered by the absorber.

3.3.2 *The initial flare*

We started to fit the spectra with the best (first) phenomenological model obtained in the previous case, namely an absorbed power law with a high energy cut-off, a Gaussian line and an iron edge. The χ^2_{ν} is 1.06 for 439 d.o.f. The best-fitting parameters are reported in Table 2, while the spectra are shown in Fig. 5 with those of the non-flare period. The 2–10 keV unabsorbed flux is 2.39×10^{-10} erg cm^{-2} s^{-1}, and the 20–100 keV flux is 4.20×10^{-10} erg cm^{-2} s^{-1}. It is interesting to note that no soft excess is obvious here, while the value of $N_{\rm H}$ has significantly decreased. It is possible that the soft excess is still present, although at a level compatible with the emission from the source (Fig. 5). This could then affect the results of the fits, in particular the value of the absorption. In order to compare with the non-flare period, we fitted the data with the same types of models. We first started with the PHABS*(BBODY+VPHABS*HIGHECUT*(POWERLAW+GAUSS)) model, fixing $N_{\rm H_{ext}}$ to the Galactic value along the line of sight. Given the presence of an iron edge in the simple previous fit, we also left the iron abundance free to vary. As one could expect, the parameters of the blackbody are poorly constrained, and the values of the parameters are close to those found without the inclusion of the blackbody. In a second run, we fixed the blackbody temperature to the value found during the non-flare period (0.07 keV, with the phenomenological model). A good fit is achieved with $\chi^2_{\nu} = 1.06$ (439 d.o.f). The value of the intrinsic absorption is still lower than in the non-flare case with $N_{\rm H} = 7.8^{+0.9}_{-0.8} \times 10^{22}$ cm^{-2}. The cut-off energy is now $16.2^{+1.6}_{-1.7}$ keV, while the folding energy is $11.8^{+1.2}_{-1.1}$ keV. The iron abundance is quite higher (although compatible within the errors) than in the non-flare case with $Z_{\rm Fe} = 1.97^{+0.64}_{-0.52}$. The other parameters are compatible with those obtained with the simple model. We also allowed the temperature of the blackbody to vary while fixing

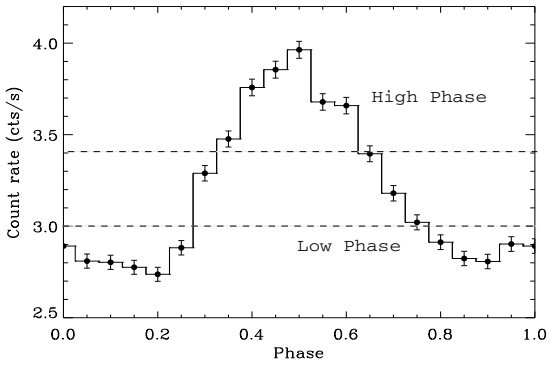

Figure 7. Phase diagram of the non-flare period. Only one cycle is represented. The horizontal lines represent the limit above (respectively below) which the high phase (resp. low phase) PN spectrum has been extracted.

the value of the intrinsic absorption to that found during the non-flare period (11.8×10^{22} cm^{-2}). In this case, however, non-credible parameters are obtained for the blackbody.

Replacing the phenomenological model by a COMPTT also leads to a good representation of the spectra with $\chi^2_\nu = 1.07$ for 438 d.o.f. In a first fit, the blackbody parameters are left free to vary. We obtain an upper limit on the temperature of 0.11 keV (90 per cent confidence), but the normalization is poorly constrained. We therefore froze the temperature to the best value obtained during the non-flare period (0.075 keV) and refitted the spectra. The χ^2_ν is 1.07 for 439 d.o.f. The best-fitting parameters are almost identical to those obtained when $kT_{\rm bb}$ is free to vary, and are reported in Table 3. Contrary to the phenomenological case, the $N_{\rm H}$ value obtained is marginally compatible with the value obtained from the fit to the non-flare period.

As in the non-flare case, we replaced the previous model by a model involving partial covering. Here again, to fit the soft excess well, a blackbody component is required. Since no constraints are obtained on the blackbody parameters if the blackbody temperature is left free to vary, we froze the latter to 0.075 keV. The fit is good with $\chi^2_\nu = 1.11$ for 442 d.o.f., and the best-fitting parameters are reported in Table 4.

3.4 Phase resolved spectroscopy

To study the dependence of the spectrum along the phase, we extracted PN spectra from the non-flare period in the low part of the phase diagram (hereafter low phase) and from the high part of the phase diagram (hereafter high phase) as illustrated in Fig. 7, i.e. the high phase corresponds to the time when the count rate is higher than 3.4 cts s^{-1}, while the low phase corresponds to the time when the count rate is lower than 3 cts s^{-1}. The origin of the phase is taken here as the start of the non-flare period, which we consider as the start of the good time intervals for the phase resolved spectroscopy. The shift of the phase diagram of Fig. 7 as compared to that of Fig. 3 is simply due to the fact that the origin of the phase in the former is equal to the beginning of the entire observation. Also in Fig. 7, the vertical axis is 'real' mean counts per second rather than normalized ones as it is the case in Fig. 3.

We focus on the 2–12 keV energy range, since the 0.6–2 keV does not show the presence of the pulsation with a rather constraining 3σ upper limit of 10.5 per cent. We fitted the spectra directly with the PHABS(VPHABS(COMPTT+GAUSS)) model. The Galactic absorption ($N_{\rm H_{ext}}$) was again fixed to 2.1×10^{22} cm^{-2}. Since we only consider the *XMM–Newton* spectra here, no constraint can be obtained for the temperature of the Comptonizing electrons. We therefore fixed $kT_{\rm e}$ to the value obtained during the fit to the entire non-flare spectra, i.e. 7.8 keV. In both the cases, the fits are good with $\chi^2_\nu = 1.18$ and $\chi^2_\nu = 1.01$ (422 d.o.f.) for the low and high phases, respectively. The best-fitting parameters are reported in Table 5.

It is obvious from Table 5 that the spectral parameters of both the high and the low phase are completely compatible. The only change is clearly related to a change of the source flux. Although the errors on the line equivalent width may indicate that this parameter does not evolve with the pulse, it is interesting to note the possible decrease of this parameter by ∼30 per cent between the low and high phase. This may suggest that the iron is unpulsed.

4 DISCUSSION

We report here on the analysis of simultaneous *XMM–Newton* and *INTEGRAL* observations of the enigmatic source IGR J16320−4751. We focus on the time of strict simultaneous coverage by both satellites. We detect very significant X-ray pulsations at a period of around 1300 s confirming previous findings (Lutovinov et al. 2005). The pulsation is seen in the *INTEGRAL*/ISGRI light curve above 20 keV. Apart from the non-detection of the pulsation below 2 keV, no particular dependence of the pulse amplitude with the energy is seen. When studying the phase-dependent *XMM–Newton* spectra of the source (in the non-flare) period, we observe no particular spectral differences between the high-phase and low-phase spectra. In particular, the intrinsic absorption, temperature of seed photons for Comptonization and plasma optical depth remain relatively constant. This is compatible with a model of polar accretion by a pulsar. The modulation of the X-ray flux is due to the misalignment of the pulsar spin axis and the pulsar magnetic axis. When the pulsar magnetic axis points towards us, the X-ray flux we detect is enhanced. The pulse period would then be the spin period as already suggested by Lutovinov et al. (2005). The weak amplitude of the pulse (as compared to other absorbed source as e.g. IGR J16393−4643; Bodaghee et al. 2005)

Table 5. Best-fitting parameters obtained from the fit to the 2–12 keV high and low phase PN spectra, with the PHABS(VPHABS(COMPTT+GAUSS)) model. Errors are given at the 90 per cent level.

Spectra	$N_{\rm H}$ ($\times 10^{22}$ cm^{-2})	$Z_{\rm Fe}$ $Z_\odot$	kT_{inj} (keV)	τ_ρ (keV)	Fe centroid (keV)	E.q. width (eV)	2-10 unabs. Flux ($\times 10^{-10}$ erg cm^{-2} s^{-1})
Low phase	$9.2^{+0.4}_{-0.8}$	1.7 ± 0.3	$1.93^{+0.17}_{-0.11}$	$5.1^{+0.4}_{-0.6}$	6.411 ± 0.006	104^{+20}_{-17}	0.86
High phase	9.4 ± 1.4	$1.8^{+0.3}_{-0.5}$	1.9 ± 0.3	$4.8^{+1.0}_{-1.5}$	6.44 ± 0.02	72^{+38}_{-31}	1.04

may indicate that the spin axis and the magnetic axis are not highly misaligned, or simply that the angle of the pulsar equator with the line of sight is quite low. The constancy of the pulse amplitude above 20 keV indicates that the Comptonized component is also pulsed. This shows that Comptonization occurs very close to the site of production of the soft photons.

Using two independent *XMM–Newton* observations, we could refine the X-ray position to the source. This allowed us to further suggest that the infrared source labelled as no 1 in Rodriguez et al. (2003), and in Fig. 1 here, was the most likely counterpart to IGR J16320−4751. As discussed in Rodriguez et al. (2003), the magnitudes of this object could be indicative of some infrared excess possibly due to circumstellar matter, either a hot plasma or some dust.

We provide for the first time a spectral analysis of IGR J16320−4751 up to 80 keV, with significant detection by *INTEGRAL*/ISGRI. The hard X-ray spectrum of the source is indicative of a high energy cut-off, whose parameters cannot be constrained when focusing on the soft X-rays only (Rodriguez et al. 2003). The main emission mechanism in the source seems to be Compton upscattering of soft X-ray photons by a hotter plasma. The spectral parameters we obtained either with phenomenological fits (Table 2) or more physical fits to the data are similar to those obtained for several HMXB (e.g. 4U 1700−37; Boroson et al. 2003). If we assume that the source is associated with the Norma arm located between 5 and 10 kpc from the Sun, with a tangent at 8 kpc, we can estimate its bolometric luminosity. During the non-flare period, the extrapolated bolometric flux of the source is 4.12×10^{-10} erg cm^{-2} s^{-1}. This leads to a luminosity of 3.15×10^{36} erg s^{-1} at 8 kpc, and 1.23×10^{36} (resp. 4.92×10^{36}) for a distance of 5 (resp. 10) kpc. We note that this estimate of the luminosity is compatible with the typical ionizing luminosity of accretion driven X-ray (1.2×10^{36} erg s^{-1}) pulsars suggested by Bildsten et al. (1997).

Our spectral analysis allowed us to reveal the presence of a soft excess that may be indicative of an additional medium. This soft excess is well fitted with a blackbody with temperature quite low and found around 0.07 keV. Such a soft excess seems to be commonly observed in X-ray binaries (Hickox et al. 2004), and some other highly absorbed *INTEGRAL* sources (Bodaghee et al. 2005; Walter et al. 2005; Zurita et al. 2005). This soft excess can have different origins from one system to another (Hickox et al. 2004). It could be, for example, the signature of thermal reprocessing of the harder X-rays produced by the accretion of material on to the pulsar either by the inner boundary of an optically thick accretion disc or by an optically thin diffuse cloud. Whatever is the exact origin of the medium responsible for the soft excess, the fact that the temperature of the soft excess is different than that of the seed photon for Comptonization rules out a model where this medium would be contained in the Comptonizing cloud. It seems difficult to consider that this medium could be the Comptonizing medium giving birth to the hard X-ray emission. Given that the Comptonized component shows the pulsation with an amplitude similar to that of the soft X-rays, it is very likely that Comptonization occurs in the close vicinity of the pulsar, the seed photons being then probably emitted by the hot surface of the compact object, and the up-scattered pulsed Comptonized component emitted by the channelled accretion flow.

Given the high quality of our data and the long exposure time, we detect for the first time a narrow iron line in IGR J16320−4751. This kind of feature is again reminiscent in many HMXB, and is also detected in most of the highly absorbed sources unveiled by *INTEGRAL*, the extreme case being IGR J16318−4848 (Matt & Guainazzi 2003; Walter et al. 2003, 2004; Kuulkers 2005). The presence of a narrow fluorescence line, as in e.g. Vela X-1, GX 301−2, 4U 1700−37, or even Cen X-3 (e.g. Boroson et al. 2003; Wojdowski et al. 2003), is usually interpreted as fluorescence of iron in a wind or circumstellar matter. This indicates that accretion occurs (at least partly) through a wind. This points towards a high mass companion in IGR J16320−4751 rather than a low mass one. The value of the centroid obtained during the fit to the non-flare spectra corresponds to Fe XIII (House 1969). We can estimate the distance R between the irradiating source and the inner radius of the fluorescent shell using $\xi = L/(\rho \times R^2)$, with L the luminosity of the source, ρ the density of the gas and ξ the ionization parameter. From fig. 5 of Kallman et al. (2004), we can estimate $\log(\xi) < 2$ therefore $\xi < 100$. Knowing that $\rho \times R = N_{\rm H}$, we obtain

$$R > \frac{L}{N_{\rm H} \times \xi} = 10^{11}\,{\rm cm} \sim 0.07\,{\rm au}$$

using the value of the luminosity found assuming a distance of 5 kpc, i.e. 1.23×10^{36} erg s^{-1}, and $R > 0.18$ au (resp. 0.28 au) for a distance of 8 (resp. 10) kpc. The inner edge of the fluorescent shell seems therefore quite far from the inner accretion flow which is again compatible with the presence of an additional medium responsible for the soft excess. It is interesting to note that when leaving the iron abundance free to vary, it tends to values greater than the solar abundance [using the values of the abundance of Anders & Grevesse (1989)]. This could be indicative of the iron origin and the cloud itself since both seem linked. Iron could have been produced by the evolution of the protopulsar in IGR J16320−4751.

Given the fact that in all the energy ranges the pulse fraction is roughly constant, it is very probable that the non-detection of the pulsation below 2 keV indicates that the X-ray flux below 2 keV, and consequently the soft excess, does not pulsate. As discussed in Hickox et al. (2004), this clearly rules out the accretion column as the origin of the soft excess. This property would suggest that the soft excess is either the emission by a collisionally energized cloud or simply the reprocessing of the hard X-rays by a diffuse cloud. In the latter case, it seems quite natural to think that the absorbing material is the cloud itself. Because of the energy conservation, $F_{\rm bb} \lesssim \Delta F_{\rm comptt}$ where $F_{\rm bb}$ is the unabsorbed bolometric flux of the blackbody and $\Delta F_{\rm comptt}$ the difference of the unabsorbed to the absorbed ($\sim$bolometric) flux of the Comptonized component. In the non-flare case (when the blackbody components are well constrained), our fits lead to $\Delta F_{\rm comptt} \sim 0.4 \times 10^{10}$ erg cm^{-2} s^{-1}. The unabsorbed bolometric flux of the blackbody component is 2.2×10^{-10} erg cm^{-2} s^{-1}. Hence, the origin of the blackbody emission cannot be due to reprocessing of the hard X-rays. The soft excess would rather be the signature of a collisionally energized cloud.

We also studied the spectral properties of the source during a flare period and compared it to the non-flare period. Although a strict comparison is rendered delicate by the presence of the soft excess which is very poorly constrained during the flare, it seems that the change during the flare is accompanied by a slight decrease of the absorption column density, while the injected temperature of the photons for Comptonization and that of the Comptonizing electrons decreases significantly. Given the degeneracy of those two parameters, the contour plots of τ versus $kT_{\rm e}$ are reported in Fig. 8 for both periods. This plot shows that the evolution of the Comptonizing plasma optical depth and temperature is genuine. The ratio of the $y(\propto kT_{\rm e}\tau^2$, e.g. Titarchuk 1994) parameters between the flare and

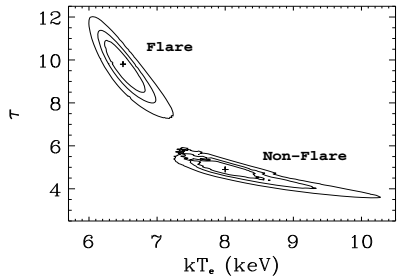

Figure 8. Error contour for the optical depth τ versus the electron temperature kT_e from the fit with the COMPTT model and the absorption with variable abundances. The crosses mark the location of the best values, while the contour are the 68, 90 and 99 per cent confidence region.

non-flare spectra is $y_{\rm noflare}/y_{\rm flare} = 0.30$, indicating a much more efficient Compton up-scattering in the case of the flare period. The short time-scale on which the flare occurs is more compatible with free-falling phenomena, rather than phenomena occurring in an accretion disc where times are of the order of the viscous time-scale. This argument again points to radial accretion in IGR J16320−4751, therefore further suggesting that the system is a HMXB.

We note that in order to test other possibilities and explain the soft excess, a model involving partial covering was tested in the course of the analysis. However, although it can lead to good results, it has to be noted that this model requires the addition of the blackbody to account for the soft excess. The result of the fits indicates that the covering of the central source of X-ray is quite high and close in both cases to its maximum value. The high values of the covering fraction would tend to confirm a picture in which the X-ray source is embedded in a dense material responsible for the soft X-ray. The fact that this covering fraction undergoes few variations between the flare and the non-flare periods seems to suggest that the flare is not caused by a huge geometrical change of this medium. This does not exclude that the flare is powered by inhomogeneities in the density of the stellar wind close to the neutron star. As the size of the region responsible for the absorption and fluorescence is of the order of the orbital radius, this is where such inhomogeneities in the wind are in fact expected. The evolution of the absorbing column density in the model involving partial covering would tend to be in agreement with a picture, where variations of the local wind density are responsible for both the variations of the column density and of the hard X-ray flux. Clearly, more observations on this and other highly absorbed sources will shed light on the origin of the soft excess in accreting X-ray pulsars.

ACKNOWLEDGMENTS

JR is specially grateful to J. Zurita for his great help with the timing analysis. JR acknowledges G. Bélanger, M. Cadolle-Bel, T. Courvoisier, A. Lutovinov, G. Palumbo and M. Revnivtsev for useful discussions on various aspects of the work and analysis presented here. The authors thank the anonymous referee for his/her very useful comments. This work is based on observations with *INTEGRAL*, an ESA mission with instruments and science data centre funded by ESA member states (especially the PI countries: Denmark, France, Germany, Italy, Switzerland, Spain), Czech Republic and Poland, and with the participation of Russia and the USA, and observations obtained with *XMM–Newton*, an ESA science mission with instruments and contributions directly funded by ESA member states and NASA.

REFERENCES

Aharonian et al. (the HESS collaboration), 2005, ApJ, in press (astro-ph/0510397)
Anders E., Grevesse N., 1989, GeCoA, 53, 197
Arnaud K. A., 1996, in Jacoby G. H., Barne J., eds, ASP Conf. Ser. Vol. 101, Astronomical Data Analysis Software an Systems V. Astron. Soc. Pac., San Francisco, p. 17
Bodaghee A., Walter R., Zurita, Heras J. A., Bird A. J., Courvoisier T. J.-L., Malizia A., Terrier R., Ubertini P., 2005, A&A, in press (astro-ph/0510112)
Bilsten L. et al., 1997, ApJS, 113, 367
Boroson B., Vrtilek S. D., Kallman T., Corcoran M., 2003, ApJ, 592, 516
Corbet R. et al., 2005, Atel, 649
Courvoisier T. J.-C. et al., 2003, A&A, 411, L53
Dickey J. M., Lockman F. J., 1990, ARA&A, 28, 215
Foschini L., Tomsick J. A., Rodriguez J., Walter R., Goldwurm A., Corbel S., Kaaret P., 2004 in Schönfelder V., Lichti G., Winkler C., eds, Proc. V *INTEGRAL* Workshop: The *INTEGRAL* Universe. ESA-SP552, p. 247
Goldwurm A. et al., 2003, A&A, 411, L223
Hickox R. C., Narayan R., Kallman T. R., 2004, ApJ, 614, 881
Horne J. H., Baliunas S. L., 1986, ApJ, 302, 757
House L. L., 1969, ApJS, 18, 21
in't Zand J. J. M., Ubertini P., Capitanio F., Del Santo M., 2003, IAUC, 8077
Kallman T. R., Palmeri P., Bautista M. A., Mendoza C., Krolik J. H., 2004, ApJS, 155, 675
Kuulkers E., 2005, in Antonelli L. A. et al., eds, Interacting Binaries: Accretion, Evolution and Outcomes. AIP, New York, in press (astro-ph/0504625)
Lebrun F. et al., 2003, A&A, 411, L141
Lebrun F. et al., 2004, Nat, 428, 293
Lutovinov A. A., Rodriguez J., Revnivtsev M., Shtykovskiy P., 2005, A&A, 433, L41.
Matt G., Guainazzi M., 2003, MNRAS, 343, L13.
Rodriguez J., Tomsick J. A., Foschini L., Walter R., Goldwurm A., Corbel S., Kaaret P., 2003, A&A, 407, L41
Rodriguez J., Cabanac C., Hannikainen D. C., Beckmann V., Shaw S. E., Schultz J., 2005, A&A, 432, 235
Strüder L. et al., 2001, A&A, 365, L18
Sugizaki M., Mitsuda K., Kaneda H., Matsuzaki K., Yamauchi S., Koyama K., 2001, ApJS, 134, 77
Tomsick J. A., Rodriguez J., Foschini L., Walter R., Goldwurm A., 2003, IAUC, 8096
Tomsick J. A., Corbel S., Goldwurm A., Kaaret P., 2005 ApJ, 630, 413
Titarchuk L., 1994, ApJ, 434, 570
Turner M. et al., 2001, A&A, 365, L27
Ubertini P. et al., 2003, A&A, 411, L131
Walter R. et al., 2003, A&A, 411, L427
Walter, R. et al., 2004, in Schönfelder V., Lichti G., Winkler C., eds, Proc. V *INTEGRAL* Workshop: The *INTEGRAL* Universe. ESA-SP552, p. 417
Walter R. et al., 2005, A&A, submitted
Winkler C. et al., 2003, A&A, 411, L1
Wojdowski P. S., Liedahl D. A., Sako M., Kahn S. M., Paerels F., 2003, ApJ, 582, 959
Zurita J., De Cesare G., Walter R., Bodaghee A., Belanger G., Courvoisier T. J.-L., Shaw S. E., Stephen J. B., 2005, A&A, in press (astro-ph/0511115)

This paper has been typeset from a TEX/LATEX file prepared by the author.

14.2 Le vent de la surpergéante dans IGR J19140+0951

Mon. Not. R. Astron. Soc. **389,** 301–310 (2008) doi:10.1111/j.1365-2966.2008.13558.x

Peering through the stellar wind of IGR J19140+0951 with simultaneous *INTEGRAL*/*RXTE* observations

L. Prat,[1⋆] J. Rodriguez,[1] D. C. Hannikainen[2,3] and S. E. Shaw[4]

[1]*DSM/IRFU/Service d'Astrophysique, CEA/Saclay, F-91191 Gif-sur-Yvette, France*
[2]*Observatory, PO Box 14, FI-00014 University of Helsinki, Finland*
[3]*Metsähovi Radio Observatory, Helsinki University of Technology TKK, Metsähovintie 114, FI-02540 Kylmälä, Finland*
[4]*School of Physics and Astronomy, University of Southampton, Southampton S017 1BJ*

Accepted 2008 June 10. Received 2008 May 14; in original form 2007 October 15

ABSTRACT

We have used the *RXTE* and *INTEGRAL* satellites simultaneously to observe the high-mass X-ray binary (HMXB) IGR J19140+0951. The spectra obtained in the 3–80 keV range have allowed us to perform a precise spectral analysis of the system along its binary orbit. The spectral evolution confirms the supergiant nature of the companion star and the neutron star nature of the compact object. Using a simple stellar wind model to describe the evolution of the photoelectric absorption, we were able to restrict the orbital inclination angle in the range 38°–75°. This analysis leads to a wind mass-loss rate from the companion star of $\sim 5 \times 10^{-8}\,\mathrm{M}_{\odot}\,\mathrm{yr}^{-1}$, consistent with an OB I spectral type. We have detected a soft excess in at least four observations, for the first time for this source. Such soft excesses have been reported in several HMXBs in the past. We discuss the possible origin of this excess, and suggest, based on its spectral properties and occurrences around the superior conjunction, that it may be explained as the reprocessing of the X-ray emission originating from the neutron star by the surrounding ionized gas.

Key words: accretion, accretion discs – stars: individual: IGR J19140+0951 – X-rays: binaries.

1 INTRODUCTION

High-mass X-ray binaries (HMXBs) are binary systems consisting of a compact object orbiting a massive companion star. Prior to the launch of the INTErnational Gamma-ray Astrophysics Laboratory (*INTEGRAL*) in 2002, a large majority of the known HMXBs contained a Be companion. In Be-type HMXBs, the compact object emits strong X-ray flashes when it crosses the equatorial plane of the companion star, where a thick disc of matter originating from the stellar wind is present. Supergiant O- and B-type stars have more isotropic stellar winds which absorb the X-ray emission of the compact object, rendering them almost undetectable below a few keV. Thanks to its sensitivity in the soft gamma-ray range, however, *INTEGRAL* has found many such systems in the past few years (see e.g. Liu et al. 2006; Bodaghee et al. 2007). In this perspective, the use of X-ray spectroscopy at different orbital phases makes it possible to probe the stellar wind, providing two-dimensional information on the density and ionization structure of the wind. For instance, the soft excess that is present in the soft X-ray spectra of many HMXBs, whose origin is still quite mysterious, is linked to the physics of the wind close to the compact object, especially the region where the fast moving stellar wind collides with the slow moving and highly ionized gas surrounding the compact object (Hickox, Narayan & Kallman 2004).

IGR J19140+0951 was discovered by *INTEGRAL* in 2003 March (Hannikainen, Rodriguez & Pottschmidt 2003), during the first observation of the nearby microquasar GRS 1915+105[1] (Hannikainen et al. 2004). Corbet, Hannikainen & Remillard (2004) and Wen et al. (2006) analysed archival *RXTE*/All-Sky Monitor (ASM) data from 1996 onwards and discovered a 13.552 ± 0.006 d periodicity in the X-ray light curve. They associated it with the orbital period of the system, identified as an X-ray binary. An early analysis of the first *RXTE* and *INTEGRAL* data is presented in Rodriguez et al. (2005, hereafter Paper I). These observations were not simultaneous, but the study of the spectral evolution of the source allowed them to classify it as a probable HMXB hosting a neutron star, which captures matter from the stellar wind without Roche lobe overflow. In this paper, we confirm this classification for IGR J19140+0951. There is no evidence in the *RXTE* data of an eclipse of the compact object by its companion star, which gives an upper limit to the inclination of the system (see Section 4.3). After the refinement

⋆E-mail: lionel.prat@cea.fr

[1] IGR J19140+0951 lies ∼1.°1 from GRS 1915+105.

of the X-ray position with *Chandra*, in't Zand et al. (2006) identified the infrared counterpart with Two-Micron All-Sky Survey (2MASS) 19140422+0952577. Nespoli, Fabrega & Mennickent (2007) later estimated the spectral type of the companion star to be B1 I. Hannikainen et al. (2007) made further observations, narrowing the spectral type to B0.5 I, confirming the HMXB nature of IGR J19140+0951. IGR J19140+0951 is situated in the direction of the Sagittarius arm, a site of active stellar formation. Given that HMXBs are young systems and that the Sagittarius arm already hosts several HMXBs, it is reasonable to think that IGR J19140+0951's distance lies between 2 and 6 kpc. This is further supported by the upper limit of 5 kpc obtained from the *K* magnitudes of the source (Hannikainen et al. 2007).

In this paper, we present several *RXTE* and *INTEGRAL* observations of IGR J19140+0951, most of them taken simultaneously with the two s. The sequence of observations and data reduction process are described in Section 2. In Section 3, we present the spectral analysis and its main results. In Section 4, we discuss these results and use a simple stellar wind model to calculate some characteristics of the source.

2 OBSERVATIONS AND DATA REDUCTION

We have been monitoring GRS 1915+105 (and therefore IGR J19140+0951) since 2003 March with *INTEGRAL*, and made simultaneous *RXTE* observations as often as possible. Our data cover the period 2004 March–2007 September with 32 observations, the log of which is reported in Table 1. We also used one public *RXTE* observation performed in 2003 March, and used the results from in't Zand et al. (2006) based on one *Chandra* observation taken in 2004 May.

2.1 *INTEGRAL*/IBIS data

To study the properties of the hard (>20 keV) X-ray emission from the source, we used the data from the Imager on Board the *INTEGRAL* Satellite (IBIS; Ubertini et al. 2003). This instrument uses a coded mask, which allows imaging over a large Field of View (FOV), $\sim 30^\circ \times 30^\circ$ up to zero response. The Totally Coded FOV (TCFOV), where the sensibility is uniform, is $9^\circ \times 9^\circ$. The *INTEGRAL* Soft Gamma-Ray Imager (ISGRI; Lebrun et al. 2003) is the upper layer of the IBIS detection unit, covering the range between 13 keV and a few hundred keV. Its angular resolution is 12 arcmin.

The *INTEGRAL* campaign was aimed at studying the microquasar GRS 1915+105, but also allows observations of every other source that lies in the IBIS TCFOV, including IGR J19140+0951. Since 2004 October, our *RXTE* observations were made simultaneously with the *INTEGRAL* observations. Following the method used in Paper I, the data were reduced using the standard OFF-LINE SCIENTIFIC ANALYSIS (OSA) v. 7.0 software package provided by the *INTEGRAL* Science Data Centre (http://isdc.unige.ch). First, we ran the software up to the production of images and mosaics in the 20–40 and 40–80 keV range, using only the science windows simultaneously with the *RXTE* observations. The software was left free to find the most significant sources in the images, which means that faint sources like IGR J19140+0951 were not always detected. Then, we used a catalogue containing the seven most luminous sources of the field for spectral extraction, in order to 'force' the program to extract the spectrum of our source from the images. Given the faintness of the source, we rebinned the redistribution matrix file provided with OSA to obtain six energy bins in the range 18–110 keV.

Table 1. List of the observations.

Observation ID	*INTEGRAL* revolution	Date[a] (MJD)	*RXTE* exposure (s)	Orbital phase[b] (cycles)
P80404-01-01-00	0049	52708.847	2864	0.815
P90112-01-01-00		53087.593	7760	0.763
P90112-01-02-00	0246	53296.931	8752	0.210
P90112-01-03-00	0295	53443.185	1936	0.002
P90112-02-01-00	0305	53473.889	5808	0.268
P90112-02-01-01	0305	53473.202	3232	0.217
P90112-02-02-00	0361	53641.355	2016	0.625
P90112-02-03-00		53676.250	3216	0.199
P90112-03-01-00	0373	53677.239	9152	0.274
P90112-03-02-00	0431	53852.034	2352	0.170
P91083-01-01-00	0478	53990.140	1776	0.361
P91083-01-01-01	0478	53990.207	2176	0.366
P91083-01-02-00	0480	53996.118	2416	0.803
P91083-01-03-00	0481	54001.625	2272	0.209
P91083-01-04-00	0486	54016.558	1488	0.311
P91083-01-05-00	0489	54025.374	2176	0.961
P91083-01-06-00	0493	54037.379	1408	0.847
P91083-01-06-01	0495	54040.956	1520	0.111
P91083-01-07-00		54049.996	4816	0.778
P91083-02-01-00	0501	54059.039	3200	0.445
P91083-02-02-00	0537	54166.928	1680	0.406
P91083-02-03-00	0539	54173.148	1520	0.865
P91083-02-04-00	0542	54181.948	4336	0.514
P91083-02-05-00	0544	54187.806	6064	0.947
P91083-02-06-00	0546	54195.604	1904	0.523
P91083-02-06-01	0546	54195.537	1504	0.518
P91083-03-01-00	0549	54202.729	6832	0.048
P91083-03-02-00	0551	54208.841	3216	0.499
P91083-03-03-00	0553	54214.537	1920	0.920
P91083-03-04-00	0557	54226.594	3040	0.809
P91083-03-05-00	0559	54232.526	2160	0.247
P91083-03-05-01	0559	54232.594	2528	0.252
P91083-04-01-01		54373.323	2720	0.636
Chandra		53136.732		0.387

[a]Mid-point of observations.
[b]The orbital phases are calculated using an orbital period of 13.552 d, and a phase 0.5 in MJD 51593.4 (Corbet et al. 2004).

2.2 *RXTE*/PCA data

For our analysis of the *RXTE* data, we used the top layers of the Proportional Counter Units (PCUs) 2 and 3 of the Proportional Counter Array (PCA), which were turned on in every observation. The data were reduced using LHEASOFT package v6.4. We restricted the study to the time when the elevation angle was above 10° and the offset pointing was less than $0.^\circ02$, as recommended by the Guest Observer Facility (GOF) to avoid Earth contamination and errors due to slew motion. In addition, and since the source is quite weak, we further rejected times of high electron background in the PCA (i.e. times when the electron ratio in one of the PCUs is greater than 0.1). The response and background were generated using PCARSP version 10.1, and PCABACKEST version 3.1, respectively, with the latest calibration files provided by the *RXTE* GOF. These files include the corrections applied to the PCA Background since 2007 September 18. We verified for IGR J19140+0951 that the impact of these corrections on the background is typically 5 per cent below 5 keV, and 2 per cent above, which is what is expected for a faint source. The source is faint and the errors dominated by statistical effects (Jahoda et al. 2006), so we did not include any systematic error. We, however, checked that the results remained the

same when adding a 'standard' systematic error of 0.6 per cent to the data, with only a slight and non-significant decrease in the reduced χ^2. In addition, the default spectral binning of the PCA detector is too fine for this dim source, so we rebinned all our *RXTE*/PCA spectra above 8 keV to make one bin out of four native bins between 8.1 and 16.5 keV, and one bin out of 10 bins between 16.5 and 26.6 keV. This slightly improves the precision on the parameters.

We also checked the data from the High-Energy Timing Experiment (HEXTE), the second instrument onboard *RXTE*. However, as already pointed out in Paper I, no HEXTE data can sensibly be used in our analysis because of the faintness of the source.

The PCABACKEST software computes the total instrument and cosmic X-ray background. Since IGR J19140+0951 is a faint source, and lies in the Galactic ridge, we also corrected the spectra for the Galactic X-ray background (GXB). Valinia & Marshall (1998) quantified the diffuse GXB in several regions of the Galactic ridge, including one with Galactic Latitude in the range $-1\overset{\circ}{.}5$–$1\overset{\circ}{.}5$ and Galactic Longitude in the range -40°–40°, which corresponds to our source. They used a three-component model in the 3–35 keV range: a Raymond–Smith model and a power law, attenuated by interstellar absorption with a column density of $N_{\rm HIS} \sim 1.5\,10^{22}\,{\rm cm}^{-2}$. Note that the model absorption measures the Galactic column density through the whole Galaxy in a given direction, so it overestimates the absorption experienced by IGR J19140+0951 which is most probably situated between 2 and 6 kpc. As we are interested in the relative variations of the absorption, and since the Galactic absorption in the direction of the source is constant, the precise value of the latter is not needed as it just adds a constant to the absorption intrinsic to the source.

Moreover, the smallest measurement of the absorption we have near phase 0 with a meaningful error bar is $3.9 \pm 2.3 \times 10^{22}\,{\rm cm}^{-2}$, once the Galactic contribution has been removed. This means that, even if we assume the minimum intrinsic absorption is $\sim$1.6 $\times$ $10^{22}\,{\rm cm}^{-2}$, this is still bigger than the Galactic absorption in the direction of the source. So, we can reasonably consider the absorption we measure as highly dominated by intrinsic absorption. In the following, we assume that what we measure is the local absorption, which is, hereafter, referred to as $N_{\rm H}$. The *RXTE*/PCA spectra were fitted in XSPEC version 11.3.2, between 3 and 25 keV. A joint *RXTE-INTEGRAL* spectrum is shown in Fig. 1 (right-hand panel).

3 RESULTS

3.1 Spectral analysis

We used the ephemeris of Corbet et al. (2004) to fold the spectra, starting at phase 0 when the flux is at a minimum. The analysis of the absorption done by the X-ray flux along the orbit shows that phase 0 also corresponds to a minimum of the absorption (see Section 4.3). Thus, phase 0 corresponds to when the compact object is located between the Earth and the companion star (hereafter inferior conjunction): in this case, the X-ray flux coming from the compact object travels a shorter distance in the companion stellar wind. Phase 0.5 is therefore when the compact object is behind the companion star (superior conjunction). The fact that a minimum flux corresponds to a minimum absorption may be puzzling, but actually these two effects act on two different energy ranges: indeed, the modulation of the ASM flux is seen only in the 5–12 keV range (Wen et al. 2006), where the photoelectric absorption has no influence. Qualitatively, when the neutron star is behind the companion star, we directly see the shock between the stellar wind and the ionized gas surrounding the compact object, where the high-energy emission is produced. At inferior conjunction however, the high-energy-emitting region is partially occulted by the neutron star: thus, this moment appears as a minimum flux in the ASM.

The phases are calculated at the mid-point of the observations. One observation typically lasts 0.005 phase. The 0.003 d uncertainty in the period determination of 13.552 d by Wen et al. (2006) leads to an uncertainty of 0.02 on the phase determination over the 4 yr of observations.

We tested several models in analysing the spectra, starting with phenomenological models. The data were well fitted using an absorbed power law combined with a high-energy cut-off. An iron fluorescent line at 6.4 keV is present in the observations where the source is detected at a high enough significance (see Fig. 1, right-hand panel). Note that the high-energy cut-off is only detected in the

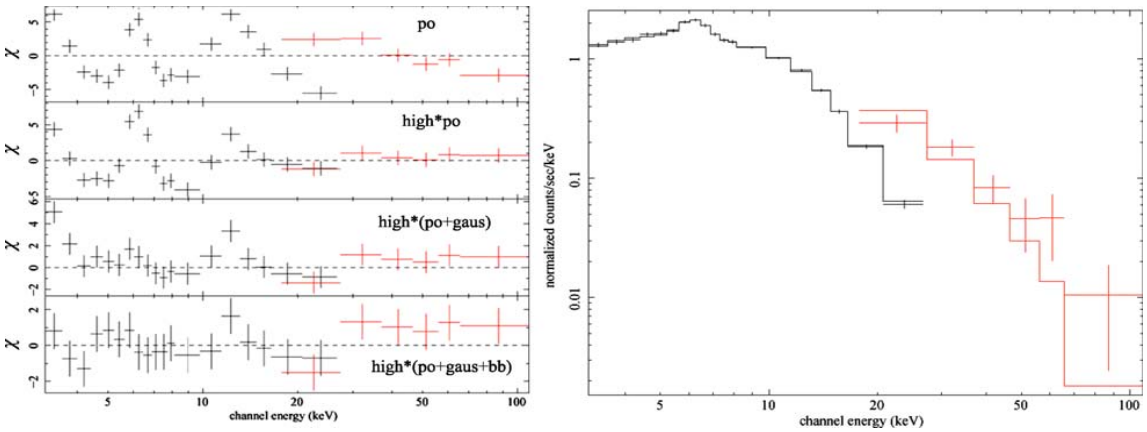

Figure 1. Left-hand panel: residuals in terms of σ between the models used to fit the *INTEGRAL* +*RXTE* spectra. In each case, the model mentioned in the panel is convolved with interstellar absorption. 'Po' stands for power law, 'high' stands for high-energy cut-off, 'gaus' stands for Gaussian and 'bb' stands for blackbody. Right-hand panel: joint *INTEGRAL* +*RXTE* spectrum from Obs ID P91083-03-02-00, corresponding to the residuals on the left-hand side. *RXTE*/PCA data are from 3 to 25 keV and *INTEGRAL*/ISGRI data from 20 to 100 keV. The best model is superposed on the spectrum.

304 *L. Prat et al.*

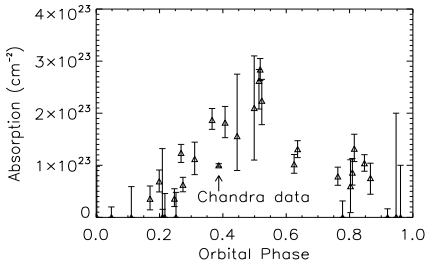

Figure 2. Evolution of the absorbing column density along the orbital phase of the system. Error bars are shown at the 90 per cent confidence level. 'Chandra data' refer to the value of $N_{\rm H}$ measured by in't Zand et al. (2006).

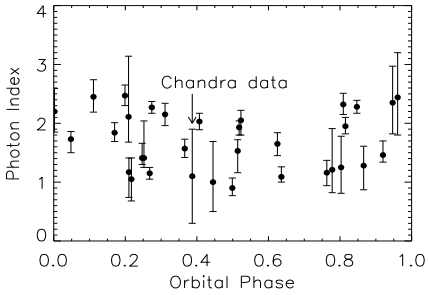

Figure 4. Evolution of the photon index along the orbital phase of the system. Error bars are shown at the 90 per cent confidence level. 'Chandra data' refer to the value of Γ measured by in't Zand et al. (2006).

observations where the source flux is sufficiently high, thus giving enough precision at the high-energy end of the spectra. Fig. 1 (left-hand panel) shows the residuals from the fit procedure when we add successively each component of the model. Note that for this observation, we need an additional component to accurately describe the spectrum below 6 keV. The spectrum shows a 'soft excess' feature in this range, which is discussed below. The best-fitting spectral parameters deduced from this phenomenological model are reported in Table 2 (left part).

3.2 Absorption evolution

The most important feature that we found is a strong evolution of $N_{\rm H}$ along the orbit (Fig. 2). In order to check whether the evolution of $N_{\rm H}$ was genuine or not, we produced power-law photon index (Γ) versus $N_{\rm H}$ contour plots for all observations. Eight typical observations are reported in Fig. 3. These correspond to spectra whose parameters are well constrained. The outer contour represents the 99 per cent confidence level. The parameters Γ and $N_{\rm H}$ are correlated: any variations of $N_{\rm H}$ will have a strong impact on the measure of Γ and vice versa. The elliptical elongation of each individual contour is the result of this link in the fitting process. The contours are clearly distinct from one observation to the next, which clearly indicates that the evolution of $N_{\rm H}$ and Γ is genuine. If this were not the case, the contours would overlap. The detailed study of the evolution of $N_{\rm H}$ along the orbital phase is presented in Section 4.3.

The absorption measured by *Chandra* is more precisely determined because of the better spectral resolution and the lower energy boundary of this instrument in the soft X-ray range. It is ~ 40 per cent lower than the general tendency observed by *RXTE* around the same phase. The discrepancy may have two origins. First, there may be a difference of calibration between the two instruments. Secondly, the *Chandra* high-energy range is limited to 10 keV, so it gives bad constraints on the index of the power law, as can be seen in Fig. 4 [in't Zand et al. (2006) obtained $N_{\rm H} = 1.0 \pm 0.3 \times 10^{23}$ cm^{-2} and $\Gamma = 1.1 \pm 0.8$)]. Since increasing Γ would increase $N_{\rm H}$, confidence levels in the $N_{\rm H} - \Gamma$ plane could increase the value of the error on $N_{\rm H}$. Given these uncertainties, the value of $N_{\rm H}$ obtained with the *Chandra* observation was excluded from our wind model fits.

The absorption measured using the Comptonization model differs from the phenomenological model for some observations, especially in the observations where a soft excess is detected, but its overall evolution remains the same. It confirms the reality of this evolution, and the discrepancy is inherent to the differences between the models. Because the phenomenological model fits all the spectra, and in a view to obtain a consistent analysis, we used only the values of $N_{\rm H}$ obtained from the phenomenological model in our studies.

3.3 Thermal Comptonization

Since a cut-off power law is usually interpreted as a signature of thermal Comptonization, we replaced this simpler model with a more physical Comptonization model (COMPTT; Titarchuk 1994). In IGR J19140+0951, neither stable accretion disc nor thermal component has been detected, so we fixed the disc temperature parameter kT_0 at 0.1 keV. The χ^2_ν obtained when fitting with this model

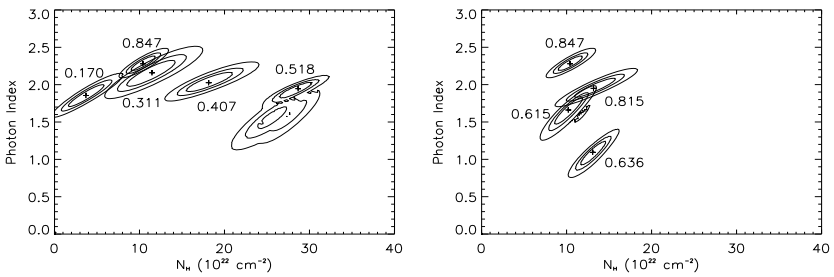

Figure 3. Contour plots of χ^2 in the $N_{\rm H} - \Gamma$ plane from fits of eight spectra. The contours correspond to the 68, 90 and 99 per cent confidence limit, the central cross being the most probable value. The numbers next to the contours are the orbital phase of each observation. Left-hand panel: five observations with different $N_{\rm H}$ values and similar Γ. Right-hand panel: four observations with similar $N_{\rm H}$ values and different Γ.

(modified by photoelectric absorption) were comparable to those of the phenomenological models (see Table 2). Since the parameters are constrained by the high-energy end of the spectra, only observations with a relatively high flux, hence a relatively good signal-to-noise ratio at high energies, are suitable for the Comptonization model.

3.4 Soft excess detection

In some observations, the χ^2_ν was far higher than for the other observations, the discrepancy between the model and the data being particularly important at low energies. In those cases, the residuals between the model and the spectrum show that some soft excess is present (see Fig. 1, left-hand panel). This feature has already been observed in many X-ray binaries (see Hickox et al. 2004, for a review). We tried to systematically add a blackbody component at low energies to all our observations, obtaining a better χ^2_ν for several of them. In four observations, an F-statistic test indicated values greater than 99.9 per cent for a true improvement of the fit with the blackbody, giving a very good confidence in this detection. In one more observation, the test gave a value greater than 90 per cent. The spectral characteristics of these observations are given in Table 3.

Note that other models, such as the Raymond–Smith model, could also account for the soft excess, but we lack the resolution at low energies to discriminate between the different possibilities, so we kept the simplest one, i.e. the blackbody model. Besides, since the blackbody and the absorption models influence the spectra mostly below 5 keV where the PCA coverage and resolution are moderate (only six spectral channels cover the range 3–6 keV), it is difficult to separate their respective contributions, and hence we obtain large uncertainties for $N_{\rm H}$. Similarly, the blackbody temperature that we found in the range 0.3–0.6 keV must be treated with caution. Other X-ray binaries have soft excess temperatures in the range 0.1–0.2 keV; a blackbody with this temperature has weak influence above 3 keV where *RXTE* is sensitive, so the values we obtain should be regarded more as an order of magnitude than absolute values.

Adding a blackbody at low energy increases the uncertainties as it adds a degeneracy in the fitting process: increasing the blackbody flux compensates for a decrease in the absorption level. Therefore, we verified, by drawing confidence levels in the $kT - N_{\rm H}$ plane, that the blackbody temperature is clearly determined. Given the high uncertainties on this latter parameter, however, the contours of several observations in which the soft excess is detected overlap. We, therefore, cannot conclude on any evolution and/or relation of the temperature with orbital phase.

4 DISCUSSION

4.1 Comparison with previous work

A comprehensive analysis of the very first X-ray observations of IGR J19140+0951 is reported in Paper I. The goal of this study was to try to understand the nature of this, then newly discovered source. At that time only, a set of three *RXTE* observations and a limited number of simultaneous JEM-X and ISGRI data were available. Instead of performing an orbital phase resolved study, and in order to improve the signal-to-noise ratio of the *INTEGRAL* data, we performed a time-resolved spectroscopy based on the 20–40 keV luminosity level of the source. As a result, it is very likely that we mixed the spectra extracted at different orbital positions. This is particularly obvious if one tries to compare the results obtained in Paper I and the ones we report here. Although qualitatively they match quite well, i.e. the spectral models are similar, and the sets of parameters are compatible, none of the 'states' identified through the *INTEGRAL* data in Paper I was observed here.

First of all, it has to be noted that during the fitting of the *INTEGRAL* spectra in Paper I, the value of $N_{\rm H}$ was frozen to that found in Swank & Markwardt (2003), i.e. 6×10^{22} cm^{-2}, while it is clear from the present study that $N_{\rm H}$ is tightly linked to the orbital phase. Secondly, the procedure of summing spectra taken at similar fluxes in Paper I may have allowed us to pick up peculiar phases of accretion, as, for example, flares due to enhanced accretion. The analysis reported here focuses more on a global and 'normal' behaviour of IGR J19140+0951. Finally, since the analysis of the *INTEGRAL* data in Paper I was based on the detection by ISGRI, it is clearly biased towards states that are bright at hard X-rays. Our orbital-phase-dependent analysis showed us that there was not necessarily a connection between the level of hard X-rays and the position on the orbital phase. Note also that although IGR J19140+0951 and GRS 1915+105 are 1.°1 apart, some confusion is still possible in the JEM-X data.

Two of the *RXTE* observations presented here were already analysed in Paper I. They respectively correspond to phase 0.763 (Obs. 3 in Paper I) and 0.815 (Obs. 2 in Paper I). One can immediately see that the results obtained in both analyses clearly differ, in particular in the value of the absorption (and consequently the unabsorbed fluxes). There are two reasons that are the very probable origin of the discrepancies. First, the analysis presented in Paper I was made with old versions of the software and history file that could cause errors on the background estimation of up to 10 per cent. This problem has been solved since then. The second origin, which is probably the main reason for the differences, is that in Paper I the Galactic background was not taken into account in correcting the data. This has a strong effect at low energies, and hence influences highly on the determination of the absorption.

Qualitatively, however, the spectral behaviour of IGR J19140+0951 is confirmed. We confirm that an iron Kα fluorescence line is present in most of the spectra. This line is intrinsic to the source, since if it were due to the Galactic background, we would expect its flux to be roughly constant, which is not the case here. We measure upper limits on its width in the range 300–1000 eV, depending on the line flux. This could be indicative of a narrow line, rather than a broad line, but actually we are mainly limited by the instrumental spectral resolution.

4.2 Spectral evolution

4.2.1 Comptonization model

Our first spectral analysis showed that a simple cut-off power-law model could accurately fit all the spectra. Therefore, we applied a thermal Comptonization model, as this is the usual physical model that explains this feature. We obtained the parameters kT_e and τ reported in Table 2, which are consistent with similar observations of other HMXBs and absorbed sources detected by *INTEGRAL* (e.g. IGR J16320−475; Rodriguez et al. 2006). The Comptonization parameter $y = \frac{4kT_e}{m_e c^2}\tau^2$ (also known as the Kompaneets parameter) determines the efficiency of the Comptonization process, and thus the shape of the spectrum (Titarchuk 1994). In our case, this parameter is ≈0.5–1, indicating a moderately efficient process. It corresponds to a rather low accretion rate, which is consistent with the supposed nature of the system: wind-fed accretion is less efficient than Roche lobe overflow. Our estimation of this mass-loss

Table 2. Best-fitting parameters. The errors and upper limits are given at the 90 per cent confidence level.

Phase	$N_{\rm H}$ (10^{22} cm^{-2})	Γ	$E_{\rm cut}$ (keV)	Unabs. flux (10^{-11} erg cm^{-2} s^{-1})	χ^2_ν	$N_{\rm H}$ (10^{22} cm^{-2})	kT_e (keV)	τ_p (keV)	y ($\frac{4kT_e}{m_ec^2}\tau^2$)	χ^2_ν
	Phenomenological model					Comptonization model				
0.002	<9.8	2.2 ± 0.37		2.6 ± 0.6	1.79					
0.048	<2	1.68 ± 0.18	7.5 ± 2.1	6.2 ± 2.2	1.19					
0.111	<5.9	2.45 ± 0.29		4.2 ± 1	1.19					
0.170	3.9 ± 2.3	1.84 ± 0.16		9.5 ± 1	1.42					
0.199^R	6.9 ± 2.1	2.47 ± 0.17		6.5 ± 0.5	1.20					
0.209	< 13.2	2.35 ± 0.75		0.8 ± 0.1	1.00					
0.210	< 1.6	1.25 ± 0.3	6.4 ± 0.6	3 ± 2	1.39	<4.5	3.7 ± 0.7	6.4 ± 1.5	1.1 ± 0.6	1.23
0.217	< 4.6	1.05 ± 0.36	6.2 ± 0.7	9.2 ± 0.8	1.01	6.1 ± 2.0	3.6 ± 0.8	5.9 ± 1.2	1.0 ± 0.5	1.63
0.247	3.8 ± 1.6	1.35 ± 0.15	6.3 ± 0.5	19 ± 5	1.80					
0.252	< 4.8	1.60 ± 0.35	< 18	5.2 ± 2	1.61	<4.0	5.5 ± 1.6	4.6 ± 1.3	0.8 ± 0.5	1.56
0.268	12.4 ± 1.7	1.15 ± 0.1	9.2 ± 0.6	67 ± 3	1.08	34.3 ± 1.8**	13.3 ± 2.6	2.0 ± 0.4	0.4 ± 0.2	1.12
0.274	6.3 ± 1.4	2.3 ± 0.1		12 ± 2	1.29					
0.311	11.2 ± 3.1	2.15 ± 0.19		7.6 ± 1	1.13					
0.366	18.7 ± 2.0	1.57 ± 0.15	6.1 ± 0.8	27 ± 2	1.62	27.1 ± 5.0**	13. ± 4	2.6 ± 0.5	0.6 ± 0.3	1.00
0.387^C	10. ± 0.3	1.1 ± 0.8		35 ± 5	1.01					
0.407	18.2 ± 3.0	2.03 ± 0.14		12 ± 1	1.27	17. ± 3.0	11.5 ± 7.0	< 4.66	0.4 ± 0.8	1.30
0.445	17.6 ± 8.0*	1.0 ± 0.6	< 10.4	32 ± 1.5	1.18	32. ± 4.5*	10.7 ± 4.1	3.6 ± 0.8	0.7 ± 0.5	1.04
0.499	21. ± 10.**	0.9 ± 0.15	12.2 ± 0.8	13 ± 2.5	1.27	<26.6	5.1 ± 0.5	9.5 ± 4.5	3.0 ± 3.0	1.41
0.514	24.5 ± 3.9	1.45 ± 0.27	9.3 ± 1.	14 ± 3	1.15	28.3 ± 2.5	4.9 ± 0.3	5.5 ± 1.0	0.9 ± 0.4	1.74
0.518	28.4 ± 2.1	1.93 ± 0.12	10.2 ± 2	48 ± 5	1.60	25. ± 2.2	5.5 ± 0.7	4.8 ± 0.8	0.9 ± 0.3	1.66
0.523	22.4 ± 4.3	2.02 ± 0.2	< 30	15 ± 4	1.34	21.6 ± 3.8	15 ± 10	2.2 ± 1.2	0.5 ± 0.8	1.30
0.625	10.2 ± 1.8*	1.6 ± 0.2	6.6 ± 0.9	27 ± 5	1.16	13.4 ± 1.0**	13 ± 5.0	2.5 ± 0.7	0.5 ± 0.4	1.87
0.636^R	13.1 ± 1.6	1.14 ± 0.13	6.3 ± 0.5	47 ± 5	1.38	14.2 ± 1.5	4.9 ± 0.4	6.0 ± 0.6	1.4 ± 0.3	1.04
0.763^R	7.9 ± 1.7	1.16 ± 0.2	6.2 ± 0.5	16 ± 3	1.67	9.1 ± 1.5	4.3 ± 0.3	6.0 ± 0.7	1.2 ± 0.3	1.05
0.778^R	<3.2	1.35 ± 0.55	< 9.2	6 ± 2	1.75	3.2 ± 2.2	4.9 ± 0.8	5.0 ± 1.2	0.9 ± 0.5	1.95
0.803	6.0 ± 5.0	1.25 ± 0.45	6.2 ± 1.5	5.6 ± 1	1.67					
0.809	8.7 ± 2.5	2.32 ± 0.18		5.8 ± 1	1.78					
0.815	13.2 ± 2.5	1.95 ± 0.14		13.2 ± 2	1.68					
0.847	10.4 ± 1.6	2.28 ± 0.11		18 ± 2	1.12					
0.866	7.6 ± 2.9	1.25 ± 0.37	6.4 ± 0.8	18 ± 2	1.48	8.7 ± 2.4	4.3 ± 1.0	5.6 ± 1.2	1.1 ± 0.5	1.49
0.920	<1.7	1.52 ± 0.18	6.2 ± 0.7	9.6 ± 2	1.27	2.3 ± 1.7	4.0 ± 0.9	5.6 ± 0.9	0.8 ± 0.4	1.79
0.947	<20	2.3 ± 0.5		0.3 ± 0.2	1.75					
0.961	<10	2.4 ± 0.7		1.1 ± 0.5	1.23					

*Observations where a soft excess is detected with a 90 per cent confidence level; **With a 99.9 per cent confidence level. The reduced χ^2 are calculated for 16 degrees of freedom (d.o.f.) for observations with both *RXTE* and *INTEGRAL*, and 11 d.o.f. otherwise. The unabsorbed flux is calculated in the range 2–20 keV. *C* marks the *Chandra* data and *R* marks the four observations for which *INTEGRAL* data are missing.

Table 3. Spectral characteristics of the five soft excess observations.

Phase	kT	$N_{\rm H}{}^a$	Γ	$\chi^{2\,b}_{\nu}$	y^c
0.268	0.27 ± 0.02	12.4 ± 1.7	1.15 ± 0.1	1.08	0.4
0.366	0.27 ± 0.10	18.7 ± 2.0	1.57 ± 0.2	1.62	0.6
0.445	0.22 ± 0.04	17.6 ± 8.0	1.00 ± 0.6	1.18	0.7
0.499	0.46 ± 0.25	$21. \pm 10.$	0.90 ± 0.2	1.27	3.0
0.625	0.27 ± 0.08	10.2 ± 1.8	1.60 ± 0.2	1.16	0.5

[a]Phenomenological model.
[b]Calculated for 15 d.o.f. for the phenomenological model. The Comptonization model gives χ^2_ν values with differences of ± 0.15.
[c]Kompaneets parameter obtained from the Comptonization model.

Table 4. Typical parameter values for a B1I star.

Parameter	Value
$R_\star$	10– 30 $R_\odot$
$M_\star$	10– 30 $M_\odot$
$\dot{M}_\star$	$10^{-6}\,M_\odot\,yr^{-1}\,a$
V_∞	$\approx$1000 km s$^{-1}\,b$
β	0.5–1

[a]Lamers (1981).
[b]Haberl et al. (1989).

rate (Section 4.3.2) in the range $4–7 \times 10^{-8}\,M_\odot\,yr^{-1}$ corroborates the B-type nature of the companion. Note that it has no significant evolution along the orbital phase, showing that the emission process is remarkably stable along the orbit. This suggests a rather stable accretion rate, and therefore would tend to favour a circular orbit for the system.

4.2.2 Phenomenological model

Several observations show a photon index $\Gamma \sim 1$, for instance 1.15 ± 0.1 at phases 0.268 and 0.636, or 1.05 ± 0.36 at phase 0.217. This is consistent with a neutron star nature of the compact object, as these hard spectra are typical of saturated Comptonization found in binary systems containing a neutron star (Di Salvo, Santangelo & Segreto 2004).

Having identified the emission process as thermal Comptonization, we returned to the phenomenological model, which allows all the spectra to be fitted and permits a true study of the absorption evolution to be done. Before studying the evolution of $N_{\rm H}$, we can draw some conclusions from the other parameters.

The unabsorbed flux undergoes strong variations that are not correlated with the orbital phase. The variations probably arise from the details of the accretion process. The stellar wind is not perfectly homogeneous and the accretion on to the neutron star, following the magnetic field line to the magnetic poles, is a highly unstable and complicated process (see e.g. Takata et al. 2006, and references therein, for a review of the emission processes). Since our observations are spread over several years, it is not surprising that the source flux is highly variable. However, if the orbit of the neutron star were eccentric, when the compact object approaches the companion star where the stellar wind density is higher, we would see an increase in the source flux. Such evolution is marginally visible, the unabsorbed flux being smaller between phases 0.9 and 0.2. However, as this is only marginal, we interpret it as another point in favour of a circular orbit for the system.

The photon index of the power-law component undergoes strong variations as well (Fig. 4). These variations are not correlated with the flux evolution or the orbital phase, which means that this is probably just another effect of the high variability of the accretion process.

4.2.3 Origin of the soft excess

During our study, some spectra exhibited an excess in the soft X-ray part of the spectra, which we modelled by adding a blackbody component to the model. Following Hickox et al. (2004), we can look for possible mechanisms explaining this feature. Using the parameters listed in Table 4, the orbital separation between the two objects a ($a = [\frac{GM_\star P^2_{\rm orb}}{4\pi^2}]^{1/3}$) is in the range 51– 74 $R_\odot$. If we assume a mass for the neutron star of $\sim 2\,M_\odot$, then the Lagrange point L_1 is located at a distance from the companion star in the range 34–56 $R_\odot$. Thus, it is very unlikely that the companion star overflows its Roche lobe, which is confirmed by the fact that we do not observe any accretion disc. This rules out explanations for the soft excess feature involving an accretion disc or a gas stream flowing from the companion to the compact object (Fahlman & Walker 1980). We can also rule out soft emission from the accretion column, as it would imply soft pulses in the spectra.

According to Hickox et al. (2004), this leaves two possible processes which involve the immediate surroundings of the compact object, characterized by the influence of the compact object X-ray emission. The stellar wind of massive stars is mostly accelerated by bound–bound transitions of atoms. The neutron star, due to its high energy emission, ionizes the surrounding material, so the already-ionized gas around the neutron star is no longer accelerated by the stellar radiation field (Fransson & Fabian 1980). When the compact object moves along its orbit, the hot gas will gradually be overtaken by the stellar wind. This will lead to the formation of a 'tail' trailing the neutron star.

The stellar wind collides with this tail, transforming a fraction of its kinetic energy into X-ray emission. This results in a shock located between the compact object and the secondary. According to Hickox et al. (2004), this could explain the soft excess of faint sources ($L_{\rm X} \lesssim 10^{36}\,{\rm erg\,s^{-1}}$), which is the case of IGR J19140+0951 ($L_{\rm X} \approx 3.10^{35}\,{\rm erg\,s^{-1}}$ for a distance of $\sim$5 kpc and a characteristic X-ray flux of $\sim 10^{-10}\,{\rm erg\,cm^{-2}\,s^{-1}}$). Finally, the last process involves the 'tail' itself: the diffuse cloud around the neutron star may reprocess the hard X-rays coming from the compact object.

However, to differentiate between emission produced in collisionally or photoionized plasma, high-resolution grating spectra are required, which is unfortunately beyond the possibilities of *RXTE*. Still, the fact that the soft excess was only seen around the superior conjunction may be of some importance. Until now, only a handful of soft excess detections have been reported and among them two detections, reported for 4U 1700−37 by Haberl, White & Kallman (1989) and for Centaurus X-3 by Burderi et al. (2000), both sources for which the orbital position is known, fall during phase 0.5–0.75. However, this is too small a sample to draw any definite conclusion.

4.3 Wind model

4.3.1 Description of the model

Since the orbit of the X-ray source is probably almost circular, one possible explanation for the observed change in $N_{\rm H}$ relies on an

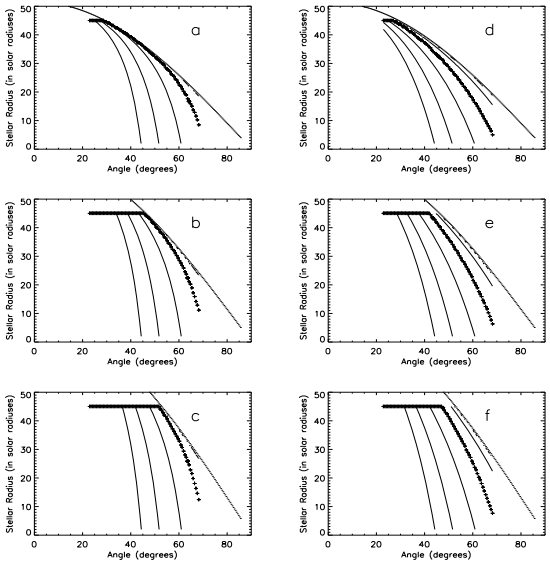

Figure 5. Most probable orbital inclination, as a function of the companion radius, for various $M_\star$ and β. (a) $\beta = 0.5, M_\star = 10\,\mathrm{M}_\odot$. (b) $\beta = 0.5, M_\star = 20\,\mathrm{M}_\odot$. (c) $\beta = 0.5, M_\star = 30\,\mathrm{M}_\odot$. (d) $\beta = 1, M_\star = 10\,\mathrm{M}_\odot$. (e) $\beta = 1, M_\star = 20\,\mathrm{M}_\odot$. (f) $\beta = 1, M_\star = 30\,\mathrm{M}_\odot$. The '+' symbols correspond to the most probable orbital inclination, confidence contours are drawn at the 25, 68 and 90 per cent confidence levels. The dotted line is the 'eclipse limit': points above this line are excluded as it would imply an eclipse of the neutron star by its companion, which is not observed.

inclined orbit for the system. Qualitatively, when the neutron star is behind its companion, its light has to travel a longer distance in the stellar wind, so the absorption in the soft X-rays increases. Therefore, at the superior conjunction we should observe a maximum in the absorption, which is indeed the case (Fig. 2). Following this hypothesis, we used a simple wind model in order to constrain several parameters for the system, following the method already used by Levine et al. (2004). A B-type star emits a strong stellar wind, usually taken to be stationary and spherically symmetric (e.g. Castor, Abbott & Klein 1975). Its velocity is given by a β-law:

$$V(r) = V_0 + (V_\infty - V_0)\left(1 - \frac{R_\star}{r}\right)^\beta, \tag{1}$$

where r is the distance from the companion star, $R_\star$ its radius, V_0 the wind velocity at the photosphere and V_∞ the terminal wind velocity. Observations show that V_∞ typically lies in the range 1000–1500 km s^{-1} for a B1 star (Gathier, Lamers & Snow 1981). For early-type stars, β is in the range 0.7–1.2 (e.g. Puls et al. 1996). We have $V_0 \ll V_\infty$, so for our purposes we can take

$$V(r) \simeq V_\infty \left(1 - \frac{R_\star}{r}\right)^\beta. \tag{2}$$

The equation of mass conservation then gives

$$\dot{M}_\star = 4\pi r^2 V(r)\rho(r), \tag{3}$$

where $\dot{M}_\star$ is the mass-loss rate of the star and $\rho(r)$ the density. The number density $n(r)$ of hydrogen atoms is in turn given by $\rho(r) = \mu m_\mathrm{H} n(r)$, where μ is the mean atomic weight of the particles expressed in units of the hydrogen atom mass m_H ($\mu = 0.602$ for solar composition material). The instantaneous equivalent absorbing column density of hydrogen N_H between the neutron star and the observer is given by

$$\begin{aligned} N_\mathrm{H} &= N_{\mathrm{H_{ISM}}} + \int_0^\infty n[r(s)]\,\mathrm{d}s \\ &= N_{\mathrm{H_{ISM}}} + \frac{\dot{M}_\star}{4\pi\mu m_\mathrm{H} V_\infty} \int_0^\infty \frac{\mathrm{d}s}{r^2\left(1 - \frac{R_\star}{r}\right)^\beta}, \end{aligned} \tag{4}$$

where N_HISM is the contribution from the interstellar medium, and s is the distance along the line joining the neutron star and the observer. s is given by

$$r^2 = a^2 + s^2 - 2as\cos(\psi), \tag{5}$$

where ψ is the angle subtended at the neutron star between the radial and the observer directions, and a is the orbital separation. Finally, for a circular orbit with orbital inclination i, the angle ψ is related to the inclination angle and the orbital phase ϕ by

$$\cos(\psi) = -\sin i \cos[\phi(t) - \phi(\tau_{90})] \tag{6}$$

where τ_{90} is the instant of the superior conjunction. Since no eclipse is visible in the system's light curve, we can restrict the inclination angle to

$$i < \arccos\left(\frac{R_\star}{a}\right). \tag{7}$$

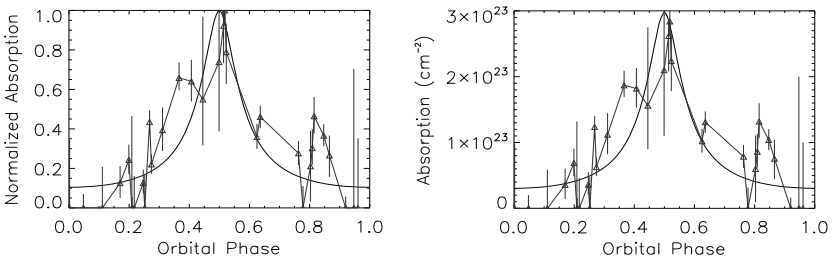

Figure 6. Model absorption (continuous line) and experimental absorption (△ symbols), for the stellar model with parameters $M_\star = 20\,\mathrm{M}_\odot, R_\star = 21\,\mathrm{R}_\odot$ and $\beta = 0.5$. Left-hand panel: result obtained with data and model normalized ($\chi^2_\nu = 1.440$). Right-hand panel: same as left-hand side, but without normalization ($\chi^2_\nu = 1.432$).

4.3.2 Parameter fitting

Our model needs four parameters, $R_\star, M_\star, \beta$ and the ratio $\dot{M}_\star/V_\infty$, and computes the most probable orbital inclination i. We first verified the consistency of the ephemeris. We fixed every parameter to the typical values listed in Table 4, and let the program adjust the maximum of the absorption for several i. We obtained maxima between phases 0.49 and 0.5, thus confirming the value of τ_{90}. Then, fixing the maximum to phase 0.5, we left free the inclination i and the stellar radius $R_\star$, set $M_\star$ to 10, 20 and 30 $M_\odot$, β to 0.5 and 1, and the ratio $\dot{M}_\star/V_\infty$ normalized to the data.

The results are shown in Fig. 5. The outer contour lines correspond to the 90 per cent confidence levels. The two lines at 2 $R_\odot$ and 45 $R_\odot$ are artefacts caused by the artificial constraint of $R_\star$ between these two values. For the most probable stellar radius of 21 $R_\odot$, the lower inclination limit is constrained between 38° and 43°, with χ^2 being at a minimum in the range 60°–67°. Fig. 6 (left-hand panel) shows the best-fitting model against the experimental normalized data, with a good agreement.

We can also determine the ratio $K = \frac{\dot{M}_\star}{4\pi\mu m_H V_\infty}$. Using the values given in Table 4, the predicted value of K is $K_0 = 5.0 \times 10^{34}$ atoms cm^{-1}. An estimate of the experimental value of K can be obtained using the best model, whose parameters are $M_\star = 20\,M_\odot$, $R_\star = 21\,R_\odot$ and $\beta = 0.5$. We let the program adjust the normalization of the model, and obtain $K = 0.045\,K_0$ (Fig. 6, right-hand panel). The observations predict V_∞ in the range 1000–1500 km s^{-1} for a B1I star (Gathier et al. 1981), which give $\dot{M}_\star$ in the range 4–7 $\times 10^{-8}\,M_\odot$ yr^{-1}. This is consistent with the expected value, and retrospectively corroborates the model. However, the wind model used in this analysis is really simple, it does not take into account, for example, a clumping of the wind, since our data are not sufficiently precise to allow a refinement the model. Therefore, our numerical results should remain mostly indicative of the evolution of the system.

5 CONCLUSIONS: SIMPLE REPRESENTATION OF THE SYSTEM

Fig. 7 schematically summarizes our main results. We found that photoelectric absorption highly correlates with the orbital phase of the system. Using a simple stellar wind model, we found a rather high orbital inclination, ∼65°. We have detected a soft excess in some observations, just before the superior conjunction, in the area indicated on the figure. This may be explained by a cloud of highly ionized gas surrounding the neutron star. Because of its ionization, this gas is less accelerated by the stellar wind and, while being gradually overtaken by the wind, tends to form a 'tail'. For typical parameters for the secondary star, the neutron star velocity V_{NS} on its orbit is ∼100 km s^{-1} and the wind velocity at the position of the orbit is ∼0.8 V_∞. Therefore, as the diagram shows, the angle between the 'tail' and a vector normal to the orbit is $\theta = \arcsin(\frac{V_{NS}}{0.8V_\infty}) \approx 10°$. This tail could scatter the hard X-ray emission from the compact object and thus explain the soft excess feature. However, these results remain qualitative, as a precise determination of the geometry of the stellar wind would require a better sensitivity in the soft X-ray range, which could be achieved, for instance, with the use of the *XMM* or *Chandra* satellites.

The study of X-ray binaries is challenging since it is often difficult if not impossible to identify their visible and infrared counterparts. Even if an infrared counterpart were observed, the distance to some systems prohibits the measurement of the orbital characteristics. Our study shows that X-ray observations can overcome these limitations and produce very precise inferences. The *RXTE* and *INTEGRAL* observations of IGR J19140+0951 have led to good measurements of the orbital period of the system and constraints on its inclination angle.

Moreover, we can use the compact object to probe the stellar wind of the companion. In the case of IGR J19140+0951, we diagnosed the type of the companion (supergiant O or B), the wind density

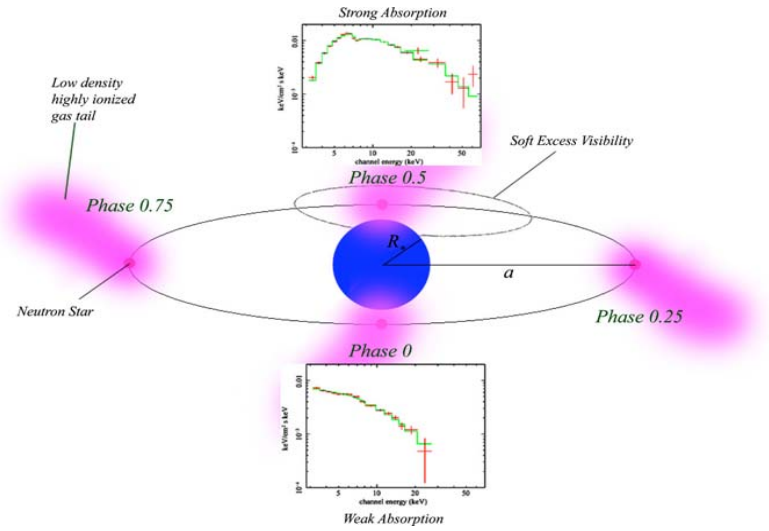

Figure 7. Diagram of IGR J19140+0951 as it could be seen from the Earth. The orbital inclination of the system is taken to be ∼65°.

and its structure around the neutron star. More precise observations could lead to constraints on the mass and radius of the companion, and better constraints on the stellar wind. This allows the study of new *INTEGRAL* sources, either distant or highly absorbed, and ultimately the determination of new useful data for X-ray binary evolution scenarios.

ACKNOWLEDGMENTS

We thank T. Foglizzo for useful discussions on the soft excess interpretation. We are grateful to an anonymous referee for a careful reading of the manuscript and constructive comments that significantly improved this paper. The authors warmly thank the *RXTE* and *INTEGRAL* planners for having scheduled the observations in simultaneity. DCH gratefully acknowledges a Fellowship from the Academy of Finland. This research has made use of data obtained through the High Energy Astrophysics Science Archive Research Centre and quick-look results provided by the ASM/RXTE team. Based on observations with *INTEGRAL*, an ESA project with instruments and science data centre funded by ESA member states (especially the PI countries: Denmark, France, Germany, Italy, Switzerland, Spain), Czech Republic and Poland, and with the participation of Russia and the United States.

REFERENCES

Bodaghee A. et al., 2007, A&A, 457, 585
Burderi L., Di Salvo T., Robba N. R., La Barbera A., Guainazzi M., 2000, ApJ, 530, 429
Castor J. I., Abbott D. C., Klein R. I., 1975, ApJ, 195, 157
Corbet R., Hannikainen D., Remillard R., 2004, Astron. Telegram, 269
Di Salvo T., Santangelo A., Segreto A., 2004, Nucl. Phys. B, 132, 446
Fahlman G. G., Walker G. A. H., 1980, ApJ, 240, 169
Fransson C., Fabian A., 1980, A&A, 87, 102
Gathier R., Lamers H. J. G. L. M., Snow T. P., 1981, ApJ, 247, 173
Haberl F., White N., Kallman T., 1989, ApJ, 343, 409
Hannikainen D., Rodriguez J., Pottschmidt K., 2003, IAU Circ., 8088
Hannikainen D., Rodriguez J., Cabanac C., Lund N., Vilhu O., Petrucci P., Henri G., 2004, A&A, 423, L17
Hannikainen D., Rawlings M. G., Muhli P., Vilhu O., Schultz J., Rodriguez J., 2007, MNRAS, 380, 665
Hickox R. C., Narayan R., Kallman T. R., 2004, ApJ, 614, 881
In't Zand J., Jonker P., Nelemans G., Steeghs D., O'Brien K., 2006, A&A, 448, 1101
Jahoda K., Markwardt C. B., Radeva Y., Rots A. H., Stark M. J., Swank J. H., Strohmayer T. E., Zhang W., 2006, ApJS, 163, 401
Kitamoto S., Miyamoto S., Tanaka Y., Ohashi T., Kondo Y., Tawara Y., Nakagawa M., 1984, Publ. Astron. Soc. Japan, 36, 731
Lamers H. J. G. L. M., 1981, ApJ, 245, 593
Lebrun F. et al., 2003, A&A, 411, L141
Levine A. M., Rappaport S., Remillard R., Savcheva A., 2004, ApJ, 617, 134
Liu Q. Z., Paradijs J., van, Heuvel E. P. J. van den, 2006, A&A, 455, 1165
Nespoli E., Fabrega J., Mennickent R., 2007, Astron. Telegram, 983
Puls J. et al., 1996, A&A, 305, 171
Rodriguez J., Cabanac C., Hannikainen D., Beckmann V., Shaw S., Schultz J., 2005, A&A, 432, L17 (Paper I)
Rodriguez J. et al., 2006, MNRAS, 366, 274
Swank J. H., Markwardt C. B., 2003, Astron. Telegram, 128
Takata J., Shibata S., Hirotani K., Chang H.-K., 2006, MNRAS, 366, 1310
Titarchuk L., 1994, ApJ, 434, 570
Ubertini P. et al., 2003, A&A, 411, L131
Valinia A., Marshall F. E., 1998, ApJ, 505, 134
Wen L., Levine A., Corbet R., Bradt H., 2006, ApJS, 163, 372

This paper has been typeset from a TEX/LATEX file prepared by the author.

14.3 L'éruption de 2000 de XTE J1550−564 vue par *RXTE*

The Astrophysical Journal, 595:1032–1038, 2003 October 1

SPECTRAL EVOLUTION OF THE MICROQUASAR XTE J1550−564 OVER ITS ENTIRE 2000 OUTBURST

J. Rodriguez,[1,2] S. Corbel,[1,3] and J. A. Tomsick[4]
Received 2003 May 5; accepted 2003 June 11

ABSTRACT

We report on *RXTE* observations of the microquasar XTE J1550−564 during a ∼70 day outburst in 2000 April–June. We present the PCA+HEXTE 3–200 keV energy spectra of the source and study their evolution over the outburst. The spectra indicate that the source transited from an initial low hard state (LS) to an intermediate state (IS) characterized by a ∼1 crab maximum in the 1.5–12 keV band and then went back to the LS. The source shows a hysteresis effect such that the second transition occurs at a 2–200 keV flux that is half of the flux at the first transition. This behavior is similar to what is observed in other sources and favors a common origin for the state transitions in soft X-ray transients. In addition, the first transition occurs at an approximately constant 2–200 keV flux, which probably indicates a change in the relative importance of the emitting media, whereas the second transition occurs during a time when the flux gradually decreases, which probably indicates that it is driven by a drop in the mass accretion rate. In both LSs, the spectra are characterized by the presence of a strong power-law tail (Compton corona) with a variable high-energy cutoff. During the IS, the spectra show the presence of a ∼0.8 keV thermal component, which we attribute to an optically thick accretion disk. The inner disk radius as inferred from disk blackbody fits to the energy spectrum remains relatively constant throughout the IS. This suggests that the disk may be close to its last stable orbit during this period. We discuss the apparently independent evolution of the two media and show that right after the X-ray maximum on MJD 51,662 the decrease of the source luminosity is due to a decrease of the power-law luminosity, at a constant disk luminosity. The detection of radio emission with a spectrum typical of optically thin synchrotron emission soon after the X-ray peak and the sudden decrease of the power-law luminosity at the same time may suggest that the corona is ejected and further detected as a discrete radio ejection.

Subject headings: accretion, accretion disks — black hole physics — stars: individual (XTE J1550−564) — X-rays: bursts

1. INTRODUCTION

Soft X-ray transients (SXTs) are accretion-powered binary systems, hosting a compact object (either a neutron star or a black hole), that spend most of their lives in quiescence and are detected in X-rays as they undergo episodes of outburst. Their X-ray spectra are usually dominated by two components representing different physical processes acting in the close vicinity of the accreting object. The soft X-rays are likely the spectral signature of an optically thick, geometrically thin accretion disk, whereas the hard X-rays are interpreted as the inverse Compton scattering of the soft photons from the accretion disk on hot electrons present in an optically thin coronal medium. Depending on whether the electrons have a thermal velocity distribution or not, this "hard tail" can be characterized by the presence or absence of an exponential cutoff at a given threshold energy. On the basis of the shape and strength of the spectra one can distinguish between five common spectral states thought to be linked to the accretion rate of the source (see, e.g., Belloni 2001 for a recent review):

1. The quiescent state (QS) is the "off" state in which SXTs spend most of their lives. The observations of SXTs in such a state have shown that the spectrum was power law–like, with a photon index that could be either soft or hard (e.g., Kong et al. 2002). The luminosity is several orders of magnitude below that of the other states. The accretion disk is undetectable in the X-rays.
2. In the low hard state (LS), the ν-f_ν spectrum is peaked in the hard X-rays and characterized by a strong power law with a photon index $\Gamma \sim 1.5$–1.9 and a cutoff around 100 keV. The disk emission remains weak, and its innermost part has a temperature $kT \leq 0.5$ keV.
3. During the intermediate state (IS) the contribution of the two spectral components to the overall luminosity is of the same order. The disk reaches a temperature of ∼1 keV, and the hard tail has a photon index of $\Gamma \sim 2.5$.
4. In the high soft state (HS) the soft ($\leq$10 keV) luminosity is high, and the spectrum is dominated by a thermal component in that range. The temperature of the disk is ∼1–1.5 keV. The power law is faint with a steep photon index $\Gamma \geq 2.5$.
5. In the very high state (VHS) the overall luminosity is close to the Eddington luminosity. The disk has a temperature $kT \sim 1$–2 keV, and the power law is steep with $\Gamma \sim 2.5$, although both components contribute significantly to the luminosity. It should be noted that the VHS is spectrally intermediate between the LS and the HS (Rutledge et al. 1999), thus making the IS and VHS similar states observed at different luminosities (Homan et al. 2001; see also Méndez & van der Klis 1997).

A summary of the source history can be found in Rodriguez et al. (2003, hereafter Paper I). XTE J1550−564 is a

[1] DSM/DAPNIA/Service d'Astrophysique (CNRS URA 2052), CEA Saclay, 91191 Gif-sur-Yvette, France.
[2] Integral Science Data Center, Chemin d'Ecogia, 16, CH-1290 Versoix, Switzerland.
[3] Université Paris VII Fédération APC, 2 Place Jussieu, 75005 Paris, France.
[4] Center for Astrophysics and Space Sciences, Code 0424, University of California at San Diego, La Jolla, CA 92093.

microquasar (Hannikainen et al 2001; Corbel et al. 2002) hosting a black hole of $10.5 \pm 1.5\ M_{\odot}$ (Orosz et al. 2002), lying at a distance of 3.2 kpc $\leq D \leq$ 10.8 kpc, with a preferred distance of 5.3–5.9 kpc (Orosz et al. 2002). Extensive spectral and timing analysis of its 1998–1999 outburst has shown the need of an additional parameter beside the accretion rate $\dot{M}$ to account for the X-ray state transitions (Homan et al. 2001). Renewed X-ray activity of XTE J1550−564 was reported by Smith et al. (2000). The source underwent a ~70 day outburst starting on 2000 April 6 (Paper I and references therein). Corbel et al. (2001) report the detection of a radio emission with a negative spectral index on MJD 51,665. They attribute it to optically thin synchrotron emission from a discrete ejection. The date of the ejection event is, however, hard to constrain and may correspond to the state transition occurring a few days before (Corbel et al. 2001). These authors also point out the absence of radio emission on MJD 51,670, indicating that no jet feature is present during that time, and they detect radio emission with an inverted spectrum on MJD 51,697, which they attribute to a compact jet. The outburst initiates in the IR and optical (Jain et al. 2001) ~10 days before the X-rays, and a second IR-optical maximum occurs as the source has returned to the LS around MJD 51,690. This second IR-optical peak is possibly related to the compact jet synchrotron tail (Corbel et al. 2001), as its inverted spectrum can extend up to the near-IR range (Corbel & Fender 2002). Tomsick, Corbel, & Kaaret (2001, hereafter TCK01) report spectral (*RXTE*+*Chandra*) observations during the very last part of the outburst, as XTE J1550−564 is returning to quiescence. We have studied the behavior of a low-frequency QPO in Paper I, and we focus here on the X-ray spectral behavior of XTE J1550−564 from the very beginning of the PCA+HEXTE pointed observations from MJD 51,644 until MJD 51,698, when the observations are contaminated by both the Galactic ridge diffuse emission and the close outbursting transient pulsar XTE J1543−568 (TCK01). We perform an analysis similar to that reported in TCK01 (covering MJD 51,680–51,698) and add the whole *RXTE* data set publicly available in the archives covering this outburst. We thus present for the first time the entire PCA+HEXTE spectral analysis of XTE J1550−564 over its 2000 outburst. The organization of the paper is as follows. We start by presenting the data reduction and analysis method used and then present the spectral evolution of the source. We discuss our results in the last part of the paper.

2. OBSERVATIONS

2.1. *Data Reduction*

XTE J1550−564 has been observed continuously with *RXTE* over all its outburst, i.e., from MJD 51,644 (April 10) to MJD 51,741 (July 16). Since the background in the Galactic ridge is difficult to estimate with a nonimaging instrument, we restrict our study to the interval between MJD 51,644 and MJD 51,698 and refer the reader to the study of TCK01 for the following period. We have reduced and analyzed the data using the LHEASOFT package version 5.2, which includes new response matrices and new background files for the PCA. We use here the maximum number of proportional counter units (PCUs) turned on over an observation and both clusters of HEXTE. We restricted ourselves to the time when the elevation angle was above 10° and the offset pointing was less than 0°.02, and we also rejected the data taken while crossing the South Atlantic Anomaly. In addition, the good time intervals were defined as when the number of PCUs turned on was constant and equal to the maximum available over a given observation; for most of them, at least three PCUs were turned on. 2000 May 12 corresponds to the abrupt loss of xenon layer in PCU 0, which renders its use for spectral analysis difficult and uncertain. We therefore extracted all the spectra from the top layer of all available PCUs except PCU 0. All spectra from individual PCUs were summed during the extraction. Background spectra were estimated using *pcabcakest* version 3.0. The responses were generated with *pcarsp* version 8.0. HEXTE spectra were extracted from both clusters in the standard mode data. We followed the "cook book" procedures for separating the ON and OFF positions before extracting the raw spectra (source and background), and then we corrected them for dead time. Responses were estimated with *hxtrsp* version 3.1. The PCA+HEXTE resultant spectra of a single observation were then analyzed together in XSPEC version 11.1.0. We retain in our fits the energy channels between 3 and 30 keV for the PCA and between 18 and 200 keV for the HEXTE. Furthermore, in order to accommodate the uncertainties in the PCA response matrix, we included 0.8% systematic errors from 3 to 8 keV and 0.4% from 8 to −30 keV (see TCK01).

2.2. *Spectral Analysis*

Several models were tested in the course of the spectral analysis. In every fit, a multiplicative constant representing the normalization between the instruments was added to the spectral model in order to take into account the uncertainties in the PCA-HEXTE cross calibration. To determine the spectral models, we first fitted PCA+HEXTE from MJD 51,646 and MJD 51,648 with a simple model consisting of interstellar absorption (*wabs* in XSPEC terminology) plus a power law. The resultant χ^2 is poor (1191 for 142 degrees of freedom [dof]), with large residuals around 6.5 keV and a broad minimum around 10 keV. As the *RXTE* bandpass is not ideally suited for the determination of the interstellar absorption, we applied the equivalent hydrogen column density value $N_{\rm H}$ returned from recent *Chandra* observations (Kaaret et al. 2003), i.e., $N_{\rm H} = 0.9 \times 10^{22}$ cm^{-2}, and froze it in all our fits. Adding iron-edge absorption (smedge) improves the fits significantly with $\chi^2 = 942$ (139 dof). Following Sobczak et al. (1999) and TCK01, we froze the width of the smedge model to 10 keV. In order to accommodate for the high-energy behavior (HEXTE band), an exponential cutoff at higher energy is needed and gives satisfactory fits with $\chi^2 = 137$ (138 dof) for MJD 51,646 and 144 (138 dof) for MJD 51,648. Adding a Gaussian emission line around 6.5 keV gives only a marginal improvement to our fits. We also tentatively included a multicolor disk blackbody (Mitsuda et al. 1984), thought to represent the emission coming from the optically thick accretion disk, but our fits failed to achieve convergence, at least from MJD 51,644 to MJD 51,655. The spectral parameters returned from the fits are shown for the entire outburst in Table 1, and the spectrum of MJD 51,644 is represented in the left-hand panel of Figure 1. From MJD 51,658 a soft excess is detectable in the spectra (Fig. 1 shows the example of

TABLE 1
BEST-FIT PARAMETERS RETURNED FROM THE FITS OVER THE WHOLE OUTBURST

Date (MJD)	Photon Index	Color Radius (km)	Disk Temperature (keV)	$E_{\rm cutoff}$ (keV)	$E_{\rm fold}$ (keV)	Reduced χ^2 (dof)
51,644.4	1.49 ± 0.01	...	...	$33.8^{+2.0}_{-2.1}$	165 ± 7	1.10 (138)
51,646.3	1.46 ± 0.01	...	...	$33.6^{+2.8}_{-3.0}$	137^{+8}_{-7}	0.99 (138)
51,646.6	1.48 ± 0.01	...	...	$35.9^{+2.3}_{-2.5}$	127^{+6}_{-5}	1.26 (138)
51,648.7	1.47 ± 0.01	...	...	33.3 ± 1.6	123^{+4}_{-3}	1.04 (138)
51,650.7	1.47 ± 0.01	...	...	30.3 ± 1.8	120 ± 4	1.24 (138)
51,651.4	1.48 ± 0.01	...	...	$31.9^{+1.7}_{-1.5}$	122^{+3}_{-4}	1.34 (138)
51,652.2	1.47 ± 0.01	...	...	$33.6^{+1.6}_{-2.0}$	111 ± 4	1.11 (138)
51,653.5	1.50 ± 0.01	...	...	$32.1^{+1.2}_{-1.3}$	109 ± 3	1.00 (138)
51,654.7	1.51 ± 0.01	...	...	29.7 ± 1.5	109 ± 3	0.96 (138)
51,655.7	1.55 ± 0.01	...	...	$30.7^{1.7}_{-2.1}$	111 ± 5	0.97 (138)
51,658.6	1.70 ± 0.01	146^{+1413}_{-108}	0.37 ± 0.014	$19.4^{+1.6}_{-1.5}$	115 ± 5.6	0.98 (136)
51,660.0	2.05 ± 0.02	47^{+19}_{-12}	0.60 ± 0.06	$18.7^{+1.1}_{-0.7}$	144^{+8}_{-7}	0.92 (136)
51,662.2	2.33 ± 0.02	$32.5^{+2.5}_{-1.3}$	0.95 ± 0.04	$17.7^{+4.3}_{-2.0}$	422^{+216}_{-80}	0.86 (136)
51,664.4	2.37 ± 0.02	$45.6^{+0.9}_{-1.5}$	0.86 ± 0.01	...	...	1.05 (138)
51,664.6	2.35 ± 0.02	42.4 ± 1.5	0.89 ± 0.01	...	...	1.43 (138)
51,665.4	2.38 ± 0.02	$52.0^{+2.7}_{-1.9}$	0.80 ± 0.01	...	...	1.00 (138)
51,667.7	2.28 ± 0.02	$47.8^{+2.4}_{-1.3}$	0.82 ± 0.02	...	...	0.95 (138)
51,668.8	2.28 ± 0.02	$47.8^{+1.4}_{-1.3}$	0.80 ± 0.01	...	...	1.07 (138)
51,669.2	2.30 ± 0.01	$49.5^{+1.9}_{-1.7}$	0.78 ± 0.01	...	...	1.18 (138)
51,670.5	2.28 ± 0.01	$53.0^{+2.2}_{-1.5}$	0.77 ± 0.02	...	...	1.02 (138)
51,670.8	2.26 ± 0.02	$49.7^{+1.9}_{-2.3}$	0.78 ± 0.01	...	...	0.87 (138)
51,671.4	2.30 ± 0.02	$50.8^{+1.8}_{-2.0}$	0.75 ± 0.01	...	...	1.06 (138)
51,672.4	2.27 ± 0.02	55.2 ± 2.2	0.75 ± 0.02	...	...	1.08 (138)
51,672.9	2.32 ± 0.01	$51.0^{+3.0}_{-1.7}$	0.77 ± 0.02	...	...	1.20 (138)
51,673.4	2.31 ± 0.01	$39.4^{+2.5}_{-2.0}$	0.77 ± 0.02	...	...	1.28 (138)
51,674.7	2.16 ± 0.02	45.0 ± 2.4	0.77 ± 0.02	...	...	1.52 (133)
51,675.4	2.22 ± 0.01	43.8 ± 1.8	0.67 ± 0.02	...	...	0.92 (138)
51,676.4	2.18 ± 0.01	$46.1^{+5.1}_{-4.9}$	0.65 ± 0.03	...	...	1.16 (138)
51,678.5	2.06 ± 0.01	$46.5^{+6.3}_{-4.7}$	0.54 ± 0.05	...	...	1.23 (138)
51,680.4	2.01 ± 0.01	$53.5^{+17.8}_{-14.0}$	0.56 ± 0.06	...	...	1.16 (138)
51,682.3	1.76 ± 0.01	39^{+20}_{-12}	0.5 ± 0.1	$30.3^{+6.2}_{-4.9}$	198^{+37}_{-32}	0.93 (136)
51,683.8	1.638 ± 0.005	...	...	$60.5^{+7.4}_{-6.6}$	197^{+38}_{-31}	0.84 (138)
51,684.8	1.647 ± 0.007	...	...	$59.2^{+23.1}_{-9.9}$	185^{+63}_{-55}	0.91 (138)
51,686.3	1.60 ± 0.01	...	...	$76.4^{+12.6}_{-11.6}$	302^{+257}_{-108}	1.00 (138)
51,687.2	1.53 ± 0.01	...	...	$55.84^{+11.0}_{-11.5}$	202^{+78}_{-52}	1.17 (138)
51,688.8	1.49 ± 0.01	...	...	$31.8^{+11.7}_{-17.8}$	338^{+114}_{-65}	0.78 (138)
51,690.7	1.48 ± 0.02	...	...	...	...	1.05 (140)
51,690.9	1.53 ± 0.01	...	...	...	...	1.32(140)
51,692.5	1.48 ± 0.01	...	...	...	...	1.17 (140)
51,693.4	1.50 ± 0.02	...	...	...	...	1.07 (140)
51,695.2	1.50 ± 0.02	...	...	...	...	0.87 (140)
51,696.4	1.53 ± 0.01	...	...	...	...	1.04 (140)
51,698.9	1.59 ± 0.05	...	...	...	...	0.90 (140)

[a] $R_{\rm col}/1\ {\rm km} = \sqrt{{\rm norm}/\cos i} \times D/6\ {\rm kpc}$, where $i = 73.^{\circ}1$ (see Orosz et al. 2002).

MJD 51,662). Using the model consisting of an absorbed (H+Fe edge) power-law cut at high energy leads to poor χ^2 (153 for 138 dof, and even worse for the following days). The addition of a multicolor disk blackbody model (Mitsuda et al. 1984) to the fits greatly improves their quality ($\chi^2 = 134$ for 136 dof on MJD 51,658, although the disk radius parameter is difficult to constrain that day). Note that during IS/VHS, the multicolor disk model can give unreliable values of the inner radius (Sobczak et al. 1999; Merloni, Fabian, & Ross 2000), especially when the ratio of the disk flux to the total flux is low (Merloni et al. 1999). The high-energy cutoff is still needed until MJD 51,662 (it is significant at the 99.5% level using an *F*-test). We have checked for its presence on the following days by systematically adding an exponential cutoff in our fits, but it gave no improvement to the fits (see Table 1). Over that period, the hard X-ray contribution has significantly decreased (Fig. 2) and the photon index ranges from $\simeq$2.0 to $\simeq$2.4. The iron line may still be present, but for the same reasons as explained above we did not include it in our analysis.

Around MJD 51,683 the fits fail to converge if the blackbody component is kept in the model. From MJD 51,682 until MJD 51,688, an exponential cutoff is needed in the fits. We note, however, that for MJD 51,686, 51,687, and 51,688 the resultant improvement in the fits becomes only marginal; we nonetheless kept this additional component. After MJD 51,688 there is no convergence when the exponential cutoff is included in the model (see also TCK01), so that the last observations are fitted with a simple model consisting of interstellar and smeared edge ($\geq$7 keV) absorptions and a power law. Two of the observations were already reported by Miller et al. (2003; MJD 51,667 and 51,670). Although

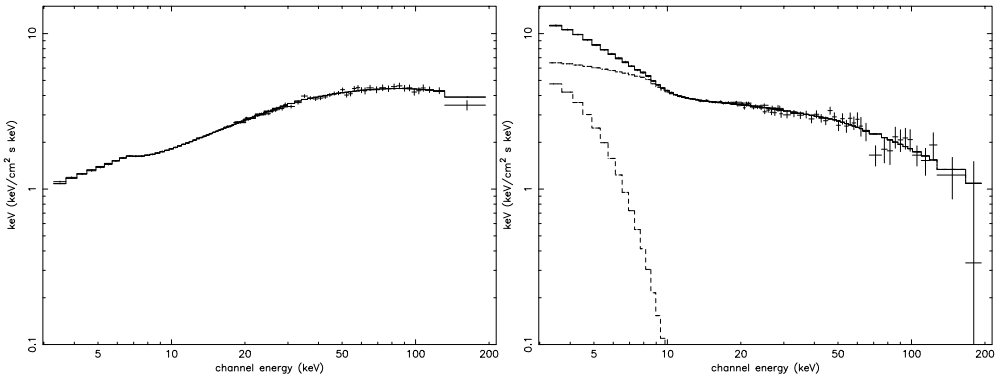

FIG. 1.—PCA (3–30 keV) and HEXTE (18–200 keV) unfolded spectra. The left-hand panel shows a typical LS spectrum with the best-fit model (see the text for the details of the modeling) overplotted (*line*). The right-hand panel is an IS spectrum showing the different spectral components (*dashed line*) used in the fits, i.e., a multicolor disk blackbody plus a power law. The best-fit model is overplotted as a line. The spectra are in "νF_ν" units.

they included a Gaussian feature in their fit, we note the relatively good agreement between their results and ours for both dates. The small differences might be due to the fact that they have used a value of 0.8×10^{22} cm^{-2} for the $N_{\rm H}$ parameter and have made joint *Chandra*+*RXTE* spectral fits.

3. SPECTRAL EVOLUTION: GLOBAL BEHAVIOR AND STATE IDENTIFICATION

The evolution of the spectral parameters are reported in Table 1, and they are plotted in Figure 2. The source spectral behavior over the outburst can be divided into two distinct states, as illustrated in Figure 2. On the basis of the spectral parameters returned from the fits (Table 1), we identify, without any ambiguities, the initial rise as a standard LS (from MJD 51,644 to MJD 51,658). The evolution of the source is rather slow here; the photon index rises from 1.49 ± 0.01 to 1.70 ± 0.01 (Fig. 2) as the 2–60 keV flux slowly rises from 1.3×10^{-8} ergs cm^{-2} s^{-1} (MJD 51,644) to 2.0×10^{-8} ergs cm^{-2} s^{-1} (MJD 51,658). The exponential cutoff ranges from $\sim$20 to $\sim$36 keV and presents no obvious correlation with the flux, whereas the folding energy decreases from $\simeq$165 keV on MJD 51,644 to $\simeq$115 keV on MJD 51,658, with an increasing soft flux. MJD 51,658 is still typical of a LS, with a photon index of less than 2, but here the spectrum has already started to soften (Fig. 2). The state transition occurs on MJD 51,660, where the hard tail steepens significantly with a photon index $\geq$2. On MJD 51,660 and 51,662; however, a cutoff at high energy is still needed in the fits. We note that the folding energy increases up to $\simeq$144 keV on MJD 51,660 and to $\simeq$422 keV on MJD 51,662. On the basis ofthe spectral parameters, we can identify this new state as an intermediate/very high state. It is difficult to distinguish between these two states since both have similar spectral and temporal behaviors (and may be the same state observed at different luminosities (Homan et al. 2001; Méndez & van der Klis 1997). The presence of high-frequency QPOs (Miller et al. 2001) over the period of IS/VHS does not help much in lifting the ambiguity. It is usually assumed that the VHS has a luminosity close to $L_{\rm Edd}$, which in our case, assuming a 10 $M_\odot$ black hole at 6 kpc (although the uncertainties are large), is $\sim 1.3 \times 10^{39}$ ergs s^{-1}. Here at the maximum (MJD 51,662), the bolometric disk flux is 2.1×10^{-8} ergs cm^{-2} s^{-1} and the 2–500 keV (extrapolated) power-law flux is 3.35×10^{-8} ergs cm^{-2} s^{-1}, giving a bolometric luminosity close to $\sim 2.3 \times 10^{38}$ ergs s^{-1}. Given the flux and in comparison with the previous outburst (Sobczak et al. 1999), we will refer to this state as an IS. The spectral evolution from MJD 51,660 to MJD 51,662 is rather abrupt (Fig. 2) and suggests that the source has undergone dramatic evolution. Indeed, the power-law tail is now much steeper, the disk temperature is higher, and the folding energy of the cutoff has increased by a factor of $\sim$3. The (color) radius obtained from the spectral fits (Fig. 2) varies between $\simeq$32 and $\simeq$146 km (assuming a distance of 6 kpc, for 73°.1 inclination). Its value remains constant around 45–55 km over 13 observations. The disk reaches its highest temperature on MJD 51,662, and from MJD 51,665 until

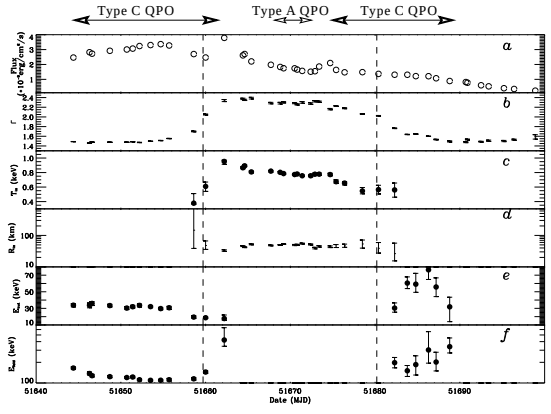

FIG. 2.—Evolution of the spectral parameters over the outburst. (*a*) 2–200 keV light curve of the outburst. (*b*) Power-law spectral index Γ. (*c*) Inner disk temperature (keV). (*d*) Inner disk radius (assuming $D = 6$ kpc and $i = 73°.1$). (*e*) Cutoff energy (keV). (*f*) The *e*-folding of the cutoff (keV). The vertical dashed lines represent the dates of state transitions. The arrows on top of the plot show the dates where QPO are detected and to which type they belong (see Paper I).

MJD 51,674 its color temperature is around 0.75–0.8 keV and is fairly constant (Fig. 2). After that, it starts to decrease down to ~0.5 keV on MJD 51,682. We note here that although the color temperature decreases, the color radius seems to decrease also. This may be due to the difficulty in determining this parameter from spectral fits starting above 3 keV at times when the source count rate starts to be low (compared to, e.g., MJD 51,658, where although the disk has a lower color temperature, the counting statistics allow a better estimate of the parameters). After MJD 51,680, the source slowly returns into a LS (see TCK01 for the spectral analysis of the observations after MJD 51,680). Although the transition to the final low state is not as sharp as in the initial stage, there is a clear evolution in terms of spectral parameters between MJD 51,680 and MJD 51,682, where the spectrum gets harder (Fig. 2) and manifests a cutoff at high energies (Table 1). From MJD 51,682 to 51,698 the source is in a LS, which first shows the presence of an exponential cutoff at high energy (MJD 51,682–MJD 51,688), while the following observations do not show any cutoff up to 200 keV. Our timing analysis (Paper I) further confirms the nature of the states. During both states, we detect low-frequency QPOs in the range 0.1–10 Hz. Two types of LFQPOs seem to be present over the outburst. The first type resembles the type C QPO (Remillard et al. 2002), and the other is more likely a type A. Interestingly, the presence of type C QPO is not related to the spectral state of the source, since it disappears after the X-ray peak on MJD 51,662 (Fig. 2), well after the first transition, and reappears after the secondary peak, on MJD 51,674, before the second transition. During the LS, however, it has a high amplitude (10%–16% rms), and during the IS it is fainter (5%) as usually observed.

4. DISCUSSION

4.1. *Hard-Component Evolution during the Initial Hard State*

Although recent studies have shown that the high-energy emission could originate in a compact jet (Markoff, Falcke, & Fender, 2001; Markoff et al. 2003), the results we present here will be discussed in the context of the standard Comptonization model involving a corona. We note, however, that the coronal geometry is unclear and that the corona could be seen as the base of the jet. In the standard Comptonization picture, the folding energy of the cutoff is close to the electron temperature. The slight decrease of the folding energy between MJD 51,644 and MJD 51,658 may indicate that the Compton cloud is cooled more efficiently. This might correspond to the approach of the accretion disk (decreasing inner radius) while its inner temperature and the soft X-ray flux increase. This interpretation is in good agreement with the state transition observed on MJD 51,660 and the presence of a thermal component in our fits from MJD 51,658. This is also in good agreement with the observation of an infrared-optical luminosity peak with a spectrum that is compatible with a thermal emission, occurring 10 day before that in the X-ray (Jain et al. 2001). In that case, the 10 day delay between the infrared/optical and the X-rays would indicate that the accretion disk fills on a viscous timescale, suggesting that it is truncated at a certain distance from the black hole. The fact that the photon index evolves from $\Gamma = 1.57$ on MJD 51,655 to $\Gamma = 1.74$ on MJD 51,658 (Fig. 2) may indicate that the state transition initiates first by a change in the Compton medium. As already suggested from the analysis of the Unconventional Stellar Aspect (USA) data (Reilly et al. 2001), the situation could be similar to the two-component accretion flow proposed in the case of other sources (Smith, Heindl, & Swank, 2002). In that case, both flows possess their own response timescale to any external perturbation (of the accretion rate). In a standard thin disk it corresponds to the viscous timescale $t_{\rm visc} \sim R^2/\nu$ (R being the radial distance to the black hole and ν being the kinematic viscosity, usually parameterized with the α-prescription), which is then of the order of days (Frank, King, & Raine, 1992). The coronal timescale is the free-fall timescale, which is much shorter. In this picture, any external change in the accretion rate would first occur on the corona and then on the disk. We should note here that the evolution of XTE J1550−564 during this LS is very similar to that of the 1998 outburst (Wilson & Done 2001; Wu et al. 2002). This suggests a common evolution for both outbursts, although XTE J1550−564 did not reach the same X-ray luminosity during the 2000 outburst.

4.2. *State Transitions and Hysteresis Effect between the Two LSs*

The first transition occurs at a total 2–200 keV flux of $\sim 2.3 \times 10^{-8}$ ergs cm^{-2} s^{-1} on MJD 51,660, and the second occurs on MJD 51,682, with a total 2–200 keV flux of 1.1×10^{-8} ergs cm^{-2} s^{-1}. The first transition is rather abrupt and occurs at a roughly constant flux, whereas the second is smoother and occurs while the source flux is monotonically decreasing, at a flux half that of the first one. We have plotted in Figure 3 (*left*) the evolution of the spectral index versus the 2–200 keV flux over the outburst. The figure shows an hysteresis, similar to what is observed in other black hole sources (Miyamoto et al. 1995; Nowak, Wilms, & Dove 2002) and possibly in the neutron star Aql X-1 (Maccarone & Coppi 2003). In order to have a direct comparison with the latter source, we have plotted in Figure 3 (*right*) the ratio of the 2–50 keV power-law (corona) flux to the 2–50 keV disk blackbody flux versus the 2–50 keV source flux. The behavior of XTE J1550−564 is here similar to that of Aql X-1, shown in Figure 1 of Maccarone & Coppi (2003). In addition, Maccarone & Coppi (2003) have shown that the evolution of the hardness ratio versus the soft (1–12 keV) X-ray flux, i.e., the evolution of a given source in terms of spectral states versus source flux, was very similar for at least four black hole SXTs (XTE J1550−564, XTE J1859+326, XTE J2012+381, and probably XTE J1748−288, in addition to those previously reported by Miyamoto et al. 1995, i.e., GX 339−4, GS 1124−683, and Cyg X-1, and by Nowak et al. 2002, i.e., GX 339−4), with the occurrence of a hysteresis loop. This similarity, with both black hole systems and at least one neutron star system, suggests that the state transitions and the spectral evolution of those sources over their outbursts obey similar mechanisms. The fact that the first transition occurs at constant flux is not what is expected if we assume that the increase of the luminosity is due to an increase of the accretion rate alone. This behavior more likely reflects a change in the relative importance of the emitting media, as pointed out by Zhang et al. (1997) in the case of Cyg X-1. This would further confirm the need of an additional parameter (beside the accretion rate) to model the state evolutions of LMXBs in outburst, as already pointed out by Homan et al. (2001)

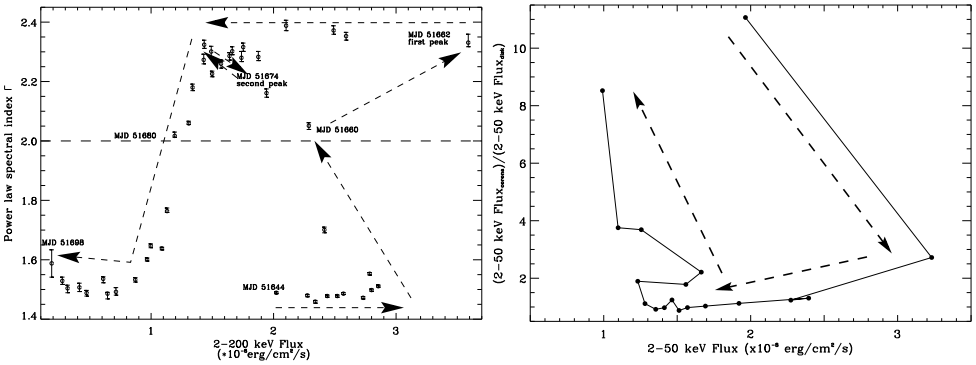

FIG. 3.—*Left:* Evolution of the power-law photon index Γ vs. the 2–200 keV flux for the whole period of outburst. The hysteresis discussed in the text is clearly visible in this figure. The horizontal line separates the two states, and the arrows indicate the chronology of the events. Some dates, showing special events, have been reported. *Right:* Ratio of the fluxes of the power-law component (corona) to the multicolor disk component versus the source flux. The errors are left unplotted for the sake of clarity. This plot allows for a direct comparison with the neutron star system Aql X-1 (Maccarone & Coppi 2003). The arrows indicate the chronology of the outburst.

during the previous outburst of XTE J1550−564 and by Smith et al. (2002) for other sources. The additional parameter beside the accretion rate may then be related to the relative geometry disk-corona (e.g., the corona size, as suggested by Homan et al. 2001). In that case a stable accretion rate will produce the same amount of energy and the relative geometry of the disk-corona system will modify the spectral energy distribution. During the decline of the outburst, the transition toward the LS occurs while the flux is dropping similarly in all spectral bands (Fig. 2). This behavior is what expected if the state transition is driven only by variations of the accretion rate. In addition, when comparing the two different LSs, one can see that the folding energy of the cutoff is systematically higher during the second LS (when present). This indicates that the coronal temperature is higher during the second LS. If we assume that the electron temperature depends on the flux of soft photons from the disk, the higher folding energy after the outburst may indicate that the disk recedes faster than it approaches the black hole. Although our observations seem to indicate rather constant physical parameters for the disk (Fig. 2), the fact that the disk is suddenly not detected soon after the transition, at times where the cutoff reappear in the spectra, provides evidence for this possibility. The recession of the disk is compatible with the observation of a 65 Hz QPO by Kalemci et al. (2001), which seems to be of the same type as the HFQPO previously seen during the brightest part of the outburst (Miller et al. 2001).

4.3. *The Intermediate State: Accretion-Disk Behavior*

The presence of a cutoff in the spectra of MJD 51,660 and MJD 51,662 suggests that the coronal electrons have still a thermalized velocity distribution, although the photon index is soft. On those days also the disk starts contributing significantly to the overall luminosity. So, in the standard picture of Comptonization, as the amount of cool thermal photons increases, the coronal electron temperature should decrease because of the higher cooling rate. The observation of an increasing folding energy for the cutoff between MJD 51,658 and MJD 51,662 argues, on the contrary, for coronal heating. This behavior is similar to what is observed by TCK01, although it occurs during the decay. They suggest that this might be the signature of the onset of different emission mechanism (e.g., bulk motion Comptonization). According to Merloni et al. (2000), low values of the disk radius and flux ratio hide some failures in the basic multicolor disk blackbody model. In a previous work (Rodriguez et al. 2002b), we have retained the radius values in our analysis only when $F_{\rm bbody}/F_{\rm tot} > 0.5$, with the fluxes estimated between 2 and 50 keV. This criterion is more stringent than that of Merloni et al. (2000), and it has allowed us to study the disk radius behavior with high accuracy (Rodriguez et al. 2002b). On MJD 51,662, the ~2–50 keV disk unabsorbed flux is 8.4×10^{-9} ergs cm^{-2} s^{-1}, giving a ~25% contribution to the total flux. It is very likely, then, that the disk parameters returned from the fit on this day are unreliable. The disk behavior over the 2000 outburst resembles that of the 1998 outburst (at least during the first part of the latter reported in Sobczak et al. 1999). Although the peak temperatures and the luminosities of the two outbursts differ significantly, there are in both cases periods of relatively constant disk parameters. During these, the temperatures are in the same ranges (0.5–0.9 keV) (Table 1 in Sobczak et al. 1999; Table 1 in the current study). Given the constancy of the disk parameters, especially the inner radius over the IS (Fig. 2), and the similarity with the huge 1998–1999 outburst, it is tempting to consider that the disk is close to the last stable orbit. The presence, over this period, of high-frequency QPOs (251–276 Hz; Miller et al. 2001), almost the highest values as yet observed in this source (285 Hz) (Remillard et al. 1999; Homan et al. 2001), may further support this assumption (see also Kalemci et al. 2001).

4.4. *Ejection of the Corona?*

Corbel et al. (2001) report the detection of radio emission with a flux density $\propto \nu^{-0.46}$. The negative spectral index is indicative of optically thin synchrotron emission, which Corbel et al. (2001) attribute to a discrete ejection of material from the system. This detection of a discrete ejection, which might be associated with the state transition (Corbel et al. 2001), raises the question of the origin of the ejected material. If the ejection is associated with the

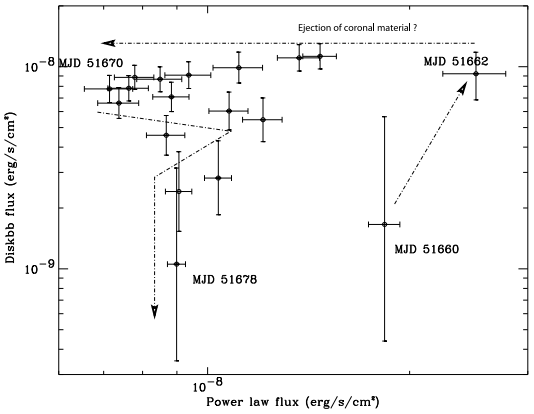

FIG. 4.—Evolution of the disk-blackbody 2–50 keV flux vs. the power-law 2–50 keV flux. The arrows indicate the chronology of the events starting at the first transition on MJD 51,660 and lasting until MJD 51,678. Because of high uncertainties on the disk parameters, the points corresponding to MJD 51,658, 51,680, and 51,682 are not represented here for the sake of clarity.

transition, this may indicate that the Comptonizing medium is the source of the ejection of the material as suggested in GRS 1915+105 (Rodriguez et al. 2002a). The ejection may also be triggered at the peak of luminosity, soon after MJD 51,662. Indeed, if we plot the 2–50 keV unabsorbed blackbody flux versus the 2–50 keV unabsorbed power-law flux (Fig. 4), it appears that after the 1 crab flare (the extreme right-hand point in Fig. 4), as the total luminosity is decreasing (Fig. 2), the disk-blackbody flux remains approximately constant during an initial period, while it is the power-law flux that decreases significantly. Given the relative constancy of the photon index on those days (Figs. 2 and 3), this may suggest that there is less Compton upscattering of the soft photons. A possible reason is that a part of the Compton medium is ejected. Given the detection of ejected material, it is tempting to consider that the Compton medium may be blown away, not, as usually assumed, the innermost part of the disk. Here again it is interesting to compare this outburst with the 1998–1999 one. During the latter outburst a discrete ejection of relativistic plasma (with apparent superluminal motion) was also detected right after the X-ray peak luminosity (Hannikainen et al. 2001). Both outbursts have very similar initial stages, starting with the LS, reaching a peak in luminosity soon after a state transition, and a discrete ejection coincident with the spike in the 1998 outburst and possibly coincident with the spike during the 2000 outburst. It is very interesting to note the similarities in the behavior of the source during both outbursts. In 1998 the huge X-ray spike it is associated with large superluminal ejection (Hannikainen et al. 2001; Corbel et al. 2002), and during the 2000 outburst the X-ray spike is associated with a discrete ejection of smaller amplitude. This may point out a strong coupling between the X-ray behavior and ejection of material in XTE J1550−564. However, the observation of Corbel et al. (2001) does not allow us to determine the date of ejection. Future multiwavelength monitoring of SXTs in outburst should allow us to study better the accretion-ejection coupling, as has been done for jet sources, e.g., GRS 1915+105 and GX 339−4. In the near future, this can be done also by including in multiwavelength studies the high-energy broadband spectra from the soft X-rays with *RXTE*, up to the gamma rays with *INTEGRAL*.

J. R. would like to thank D. Barret, Ph. Durouchoux, J.-M. Hameury, G. Henry, E. Kalemci, M. Tagger, and P. Varnière for useful discussions. J. R. acknowledges financial support from the French spatial agency (CNES). J. A. T. acknowledges partial support from NASA grant NAG 5-13055. The authors thanks the anonymous referee for useful comments. This research has made use of data obtained through the High Energy Astrophysics Science Archive Center Online Service, provided by the NASA Goddard Space Flight Center.

REFERENCES

Belloni, T. 2001, preprint (astro-ph/0112217)
Corbel, S., & Fender, R. P. 2002, ApJ, 573, L35
Corbel, S., Fender, R. P., Tzioumis, A. K., Tomsick, J. A., Orosz, J. A., Miller, J. M., Wijnands, R., & Kaaret, P. 2002, Science, 298, 196
Corbel, S., et al. 2001, ApJ, 554, 43
Frank, J., King, A., & Raine, D. 1992, Accretion Power in Astrophysics (Cambridge: Cambridge Univ. Press)
Hannikainen, D., Campbell-Wilson, D., Hunstead, R., McIntyre, V., Lovell, J., Reynolds, J., Tzioumis, T., & Wu, K. 2001, Ap&SSS, 276, 45
Homan, J., Wijnands, R., van der Klis, M., Belloni, T., van Paradijs, J., Klein-Wolt, M., Fender, R. P., & Méndez, M. 2001, ApJS, 132, 377
Jain, R. K., Baylin, C. D., Orosz, J. A., McClintock, J. E., & Remillard, R. A. 2001, ApJ, 554, L181
Kaaret, P., Corbel, S., Tomsick, J. A., Fender, R., Miller, J. M., Orosz, J. A., Tzioumis, T., & Wijnands, R. 2003, ApJ, 582, 945
Kalemci, E., Tomsick, J. A., Rothschild, R. E., Pottschmidt, K., & Kaaret, P. 2001, ApJ, 563, 239 (K01)
Kong, A. K. H., McClintock, J. E., Garcia, M. R., Murray, S. S., & Barret, D. 2002, ApJ, 570, 277
Maccarone, T. J., & Coppi, P. S. 2003, MNRAS, 338, 189
Markoff, S., Falcke, H., & Fender, R. 2001, A&A, 372, L25
Markoff, S., Nowak, M. A., Corbel, S., Fender, R. P., & Falcke, H. 2003, A&A, 397, 645
Méndez, M., & van der Klis, M. 1997, ApJ, 479, 926
Merloni, A., Fabian, A. C., & Ross, R. R. 2000, MNRAS, 313, 193
Miller, J. M., et al. 2001, ApJ, 563, 928
———. 2003, MNRAS, 338, 7
Mitsuda, K., et al. 1984, PASJ, 36, 741
Miyamoto, S., Kitamoto, S., Hayashida, K., & Egoshi, W. 1995, ApJ, 442, L13
Nowak, M. A., Wilms, J., & Dove, J. B. 2002, MNRAS, 332, 856
Orosz, J. A., et al. 2002, ApJ, 568, 845
Reilly, K. T., et al. 2001, ApJ, 561, L183
Remillard, R. A., McClintock, J. E., Sobczak, G. J., Bailyn, C. D., Orosz, J. A., Morgan, E. H., & Levine, A. M. 1999, ApJ, 517, L127
Remillard, R. A., Muno, M. P., McClintock, J. E., & Orosz, J. A. 2002, ApJ, 580, 1030
Rodriguez, J., Corbel, S., Kalemci, E., Tomsick, J. A., & Tagger, M. 2003, ApJ, submitted (Paper I)
Rodriguez, J., Durouchoux, P., Mirabel, F., Ueda, Y., Tagger, M., & Yamaoka, K. 2002a, A&A, 386, 271
Rodriguez, J., Varnière, P., Tagger, M., & Durouchoux, P. 2002b, A&A, 387, 487
Rutledge, R. E., et al. 1999, ApJS, 124, 265
Smith, D. A., Levine, A. M., Remillard, R., Fox, D., Schaefer, R., & *RXTE*/ASM Team. 2000, IAU Circ. 7394
Smith, D. M., Heindl, W. A., & Swank, J. H. 2002, ApJ, 569, 362
Sobczak, G. J., McClintock, J. E., Remillard, R. A., Levine, A. M., Morgan, E. H., Baylin, C. D., & Orosz, J. A. 1999, ApJ, 517, L121
Tomsick, J. A., Corbel, S., & Kaaret, P. 2001, ApJ, 563, 229
Wilson, C. D., & Done, C. 2001, MNRAS, 325, 167
Wu, K., et al. 2002, ApJ, 565, 1161
Zhang, S. N., Harmon, B.A., Paciesas, W. S., Remillard, R. E., & van Paradijs, J. 1997, ApJ, 477, L95

14.4 2 ans de suivis de GRS 1915+105 : papier 2

The Astrophysical Journal, 675:1449–1458, 2008 March 10

2 YEARS OF *INTEGRAL* MONITORING OF GRS 1915+105. II. X-RAY SPECTRO-TEMPORAL ANALYSIS

J. Rodriguez,[1] S. E. Shaw,[2] D. C. Hannikainen,[3] T. Belloni,[4] S. Corbel,[1] M. Cadolle Bel,[5] J. Chenevez,[6] L. Prat,[1] P. Kretschmar,[5] H. J. Lehto,[7] I. F. Mirabel,[8] A. Paizis,[9] G. Pooley,[10] M. Tagger,[11] P. Varnière,[12] C. Cabanac,[2] and O. Vilhu[3]

Received 2007 October 22; accepted 2007 November 27

ABSTRACT

This is the second paper presenting the results of 2 yr of monitoring of GRS 1915+105 with *INTEGRAL*, *RXTE*, and the Ryle Telescope. We present the X-ray spectral and temporal analysis of four observations showing strong radio to X-ray correlations. During one observation GRS 1915+105 was in a steady state, while during the three others it showed cycles of X-ray dips and spikes (followed by radio flares). Through time-resolved spectroscopy of these cycles, we suggest that the soft X-ray spike is the trigger of the ejection. The ejected medium is then the coronal material responsible for the hard X-ray emission. In the steady state observation, the X-ray spectrum is indicative of the hard-intermediate state, with the presence of a relatively strong emission at 15 GHz. The X-ray spectrum is the sum of a Comptonized component and an extra power law extending to energies >200 keV without any evidence for a cutoff. We observe a possible correlation of the radio flux with that of the power law component, which may indicate that we see direct emission from the jet at hard X-ray energies. We study the energy dependence of a ~4 Hz QPO during the hard-intermediate state observation. The QPO "spectrum" is well modeled by a power law with a cutoff at an energy of about 11 keV, and clearly differs from the relative contribution of the Comptonized component to the overall flux. This may rule out models of global oscillations of the Compton corona.

Subject headings: accretion, accretion disks — black hole physics — stars: individual (GRS 1915+105, XTE J1550−564) — X-rays: stars

1. INTRODUCTION

X-ray binaries and microquasars are known to be sources of copious X-ray emission from a few hundred eV up to the MeV range in some cases. This high-energy emission is commonly attributed to a thermal accretion disk for the softer X-rays (below approximately 10 keV), while no real consensus has yet been found for the so-called hard X-ray tails that can be detected up to the MeV range (e.g., Grove et al. 1998). This emission is usually attributed to an inverse Compton process of the soft (disk) photons on a distribution of electrons thought to represent a corona whose geometry is a matter of debate. The electrons can have a Maxwellian distribution of their velocity (thermal Comptonization), or not. They can represent a hybrid population (thermal and nonthermal Comptonization, e.g., Poutanen & Svensson 1996), or be in free-falling inflow with bulk motion (e.g., Laurent & Titarchuk 1999). Alternatives to pure Comptonization exist. In states showing the presence of an optically thick compact jet, the high-energy emission could also originate from synchrotron self-Compton (SSC) radiation from the jet (e.g., Markoff et al. 2005). The relative strength of the spectral components together with the behavior of microquasars in the temporal domain at frequencies typically >0.1 Hz led to the identification of the so-called spectral states (see, e.g., Remillard & McClintock [2006] and Homan & Belloni [2005] for recent definitions). Following the changes of spectral states in these sources using a multiwavelength approach is the only way to probe the physics of accretion and its connection with the jets.

In this respect, GRS 1915+105 is probably one of the best microquasars to perform such studies. It is one of the brightest X-ray sources in the sky and it is a source of superluminal ejections (Mirabel & Rodríguez 1994), with a true velocity of the jets $\geq 0.9c$. It is also known to have a strong compact jet during its periods of "hard" and steady X-ray states (e.g., Fuchs et al. 2003), while multiwavelength approaches have shown a clear connection between the presence of soft X-ray dip/spike sequences (hereafter X-ray cycles) followed by plasma ejections (Mirabel et al. 1998; Fender & Pooley 1998). A complete review on GRS 1915+105 can be found in Fender & Belloni (2004). GRS 1915+105 has been extensively observed with the *Rossi X-ray Timing Explorer* (*RXTE*) since 1996. A rich pattern of variability has emerged from these data with timescales ranging from years down to 15 ms (e.g., Morgan et al. 1997). Belloni et al. (2000) classified all the observations into 12 separate classes, which could be interpreted as transitions between three basic spectral states: a hard intermediate one (State C) and two soft intermediate ones (State A and State B) following the classification of Homan & Belloni (2005). Note that State A is much dimmer and softer than State B, which is the brightest state of the three.

This is the second of two papers reporting the results of 2 yr of an extensive monitoring campaign involving several instruments,

[1] Laboratoire AIM, CEA/DSM-CNRS-Université Paris Diderot, DAPNIA/SAp, F-91191 Gif-sur-Yvette, France.
[2] School of Physics and Astronomy, University of Southampton, SO17 1BJ, UK.
[3] Observatory, P.O. Box 14, FI-00014 University of Helsinki, Finland.
[4] INAF-Osservatorio Astronomico di Brera, via Bianchi 46, 23807 Merate, Italy.
[5] European Space Astronomy Centre (ESAC) Apartado/P.O. Box 78, Villanueva de la Cañada, E-28691 Madrid, Spain.
[6] Danish National Space Center, Technical University of Denmark, Juliane Maries Vej 30, 2100 Copenhagen, Denmark.
[7] Tuorla Observatory and Department of Physics, University of Turku Väisäläntie 20, FI-21500 Piikkiö, Finland.
[8] European Southern Observatory, Chile. On leave from CEA-Saclay, France.
[9] IASF Milano-INAF, Via Bassini 15, 20133 Milano, Italy.
[10] Astrophysics, Cavendish Laboratory, J. J. Thomson Avenue, Cambridge CB3 0HE, UK.
[11] Service d'Astrophysique (UMR AstroParticules et Cosmologie), CEA Saclay 91191 Gif-sur-Yvette, France.
[12] LAOG, Université J. Fourier (UMR5571), Grenoble, France.

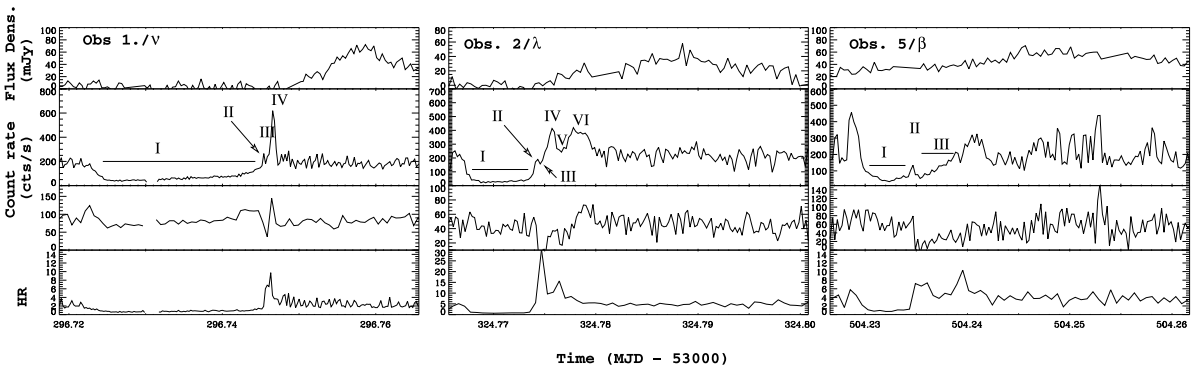

FIG. 1.—Zoom on one cycle from each of the three observations with cycles. From top to bottom, the panels respectively represent the Ryle 15 GHz, the JEM-X 3–13 keV, the ISGRI 18–50 keV light curves, and the 3–13 keV/18–50 keV HR. The different intervals from which spectra were extracted are indicated with roman numerals on the JEM-X light curve.

namely *RXTE*, the Ryle Telescope (RT), and *INTEGRAL*, the latter being the main observatory of our campaign. In Rodriguez et al. (2008, hereafter Paper 1) we presented the results of the multiwavelength analysis. In particular, we focused on four particular observations. These four observations were chosen because of the availability of simultaneous radio and X-ray observations. In all four of them the radio to X-ray connections could then be studied in great detail, and show interesting links. In three of them we found clear associations between the X-ray behavior of the source and the occurrence of radio flares. In the fourth one, the level of radio emission was rather steady and indicative of a compact jet. In Paper 1, we generalized the fact that (nonmajor) discrete ejections always occur as a response to an X-ray cycle composed of an X-ray dip longer than 100 s ending in an X-ray spike. Based on a model-independent analysis, we also suggested that the spike was the trigger of the ejection. We also found a possible correlation between the duration of the X-ray dip and the amplitude of the radio ejection, which may suggest that energy and/or matter accumulated during the dip are later ejected.

In this paper we focus on the X-ray spectral and temporal analysis of those four particular observations. We start by describing the methods of data reduction in § 2. In § 3, we present the results, which are discussed in the last part of the paper.

2. OBSERVATIONS AND DATA REDUCTION

The log of all observations can be found in Paper 1. In this paper we focus on observations (Obs.) 1, 2, 4, and 5, and particularly on the intervals that we identified as belonging to classes ν, λ, χ, and β, respectively (Belloni et al. 2000). To summarize, classes ν, λ, and β show occurrences of spectrally hard X-ray dips of several hundred seconds ended by a very bright X-ray spike, marking the return to a softer state (State A). These are followed by periods of intense and very variable X-ray activity indicative of State A to State B transition. We refer to these intervals (hard dips to soft spike) as cycles. Figure 1 shows zooms on cycles from each of the three observations. During class χ, GRS 1915+105 has a relatively steady level of X-ray emission over long times. In that case it is in the hard-intermediate state, and usually shows rapid (>1 s) variability and presence of low-frequency QPOs.

2.1. *INTEGRAL Data Reduction*

The data were reduced with the Off Line Scientific Analysis (OSA) version 7.0 software. Our first step was to produce ISGRI images in two energy bands, 20–40 keV and 40–80 keV, in order to detect the active sources of the field of view which have to be taken into account in the (spectral and temporal) extraction processes. This list of "bright" sources was then given as an input for the extraction of IBIS/ISGRI spectra and light curves. This is a necessary process since all bright sources in the field of view can be considered as contributing to the background for the others. This means that we extracted spectra and light curves from between five and eight sources. In the case of JEM-X the spectra were extracted from unit 1 of the detector.[13] For both detectors (IBIS and JEM-X) the latest versions (provided with OSA 7.0) of the response matrices were used in the spectral fitting. Note that due to the high variability of GRS 1915+105 accumulating spectra over the entire observation is meaningless most of the time. In the four observations we discuss here, we extracted time-resolved spectra based on selected good time intervals. The JEM-X light curves were extracted with a time resolution of 1 s between ~3 and 13 keV, and further rebinned to 20 s. The ISGRI light curves were extracted between 18 and 50 keV with a time resolution of 20 s, and further rebinned to 100 or 200 s.

We should remark here that since GRS 1915+105 is very bright in the soft X-rays good quality spectra are obtained even with short accumulation times. This is, however, not the case above 20 keV. We therefore used different binning of the redistribution matrix file during the extraction process to obtain the spectra of the best possible quality.

The resultant spectra were fitted in XSPEC version 11.3.2t, between 5 and 20 keV for JEM-X,[14] and 18 and 300 keV for ISGRI. In most cases the spectra were further rebinned so as to obtain good quality spectra (especially in the case of short accumulation times). We added 3% systematics to the uncertainties in the JEM-X spectra, and 2% to the ISGRI ones before the fitting process. In all fits a normalization constant was added to account for uncertainties in the cross calibration of the instruments. If frozen to 1 for the ISGRI spectrum, it is usually found to be between 0.9 and 1.1 for JEM-X. Since SPI is less sensitive than ISGRI below 200 keV we do not analyze SPI data in the study presented here.

2.2. *RXTE Data Reduction*

The *RXTE* data were reduced with LHEASOFT version 6.1.2. following standard criteria for the definition of good time intervals

[13] JEM-X unit 2 has been switched off since March 08, 2004.

[14] Except in the case of Obs. 4, where the JEM-X spectra were fitted between 3 and 20 keV since comparison with a simultaneous PCA spectrum showed a good agreement between both detectors.

(elevation above Earth limb greater than 10° and offset pointing less than 0.02°). We first produced light curves in several energy ranges to produce color-color diagrams, hardness ratio, and hardness intensity diagrams (HIDs). For the latter purpose, we extracted 16 s light curves from the top layer of PCU 2 in four energy ranges, namely 2–126 keV (channels 0–255), band 1 = 3.28–6.12 keV (channels 8–14), band 2 = 6.12–10.22 keV (channels 15–24), and band 3 = 14.76–40.41 keV (channels 36–95). These light curves were background corrected before producing hardness ratio (or colors) defined as follows: HR1 = band 2/band 1 and HR2 = band 3/band 1. Note that the background files were produced with the latest version of the saa-history file, released after the discovery of gaps in the former file.

In the case of Obs. 4 (the steady state observation; Paper 1), we extracted PCA and HEXTE spectra from the unique interval that was simultaneous with *INTEGRAL* observation and observation from the RT. The procedure is the same as that described in Rodriguez et al. (2003) again apart from the newer version of the reduction software and the background maps used here, which are the latest made available by the *RXTE* Science Operations Facilities (SOF).

For the production of high temporal resolution light curves and Fourier analysis of the PCA data, the data were reduced in the same way as presented in Rodriguez et al. (2004; except for the different versions of the software). We extracted ~4 ms resolution light curves from Binned data format covering the 2–15 keV energy range and ~1 ms light curves from Single Bit and Event data format, respectively, covering the ~5–15 keV and 15–60 keV energy ranges (we restricted the highest absolute spectral channel to 150 for the latter). We then produced power density spectra (PDS) from the combined 2–60 keV (Nyquist frequency of 128 Hz) and 5–60 keV light curves (Nyquist frequency of 512 Hz) to study the presence of low- and high-frequency quasiperiodic oscillations (LFQPO, HFQPO). Note that for the production of dynamical PDS, or PDS from a large energy range, the background correction can be neglected for the estimate of the fractional rms variability.

For Obs. 4 we also produced energy-dependent PDSs in a manner similar to that presented in Rodriguez et al. (2004), i.e., extracting a ~4 ms light curve from about 20 spectral channels covering the 2–40 keV range. In that case the rms amplitudes have to be corrected for the energy-dependent background level. This has been done according to Berger & van der Klis (1994), i.e., $\mathrm{rms}_{\mathrm{corr}} = \mathrm{rms}_{\mathrm{leahy}}(S + B)/S$, where $\mathrm{rms}_{\mathrm{leahy}}$ is the rms obtained from the Leahy normalized PDS (non–background corrected), $S + B$ is the raw count rate, and S the net count rate of the source.

3. RESULTS OF THE HIGH ENERGY OBSERVATIONS

We focus here on the observations for which we obtained simultaneous X-ray and radio observations (Paper 1). Among them, we distinguish Obs. 1, 2, and 5, for which we observed sequences of X-ray cycles followed by radio flares, and Obs. 4, during which GRS 1915+105 is found in the steady χ class and shows a relatively steady level of radio emission around 40–80 mJy (Paper 1).

3.1. *Time-resolved Spectroscopy and Models for the Spectral Fittings of the Cycles*

All cycles from all classes show similar repeating patterns, although their time constants are different. For example, class λ looks very much like class β, except that the sequences in the cycle seem to occur faster (Belloni et al. 2000). We can distinguish in each cycle at least three intervals (Fig. 1) with common characteristics (Paper 1). Interval I is the spectrally hard X-ray dip, interval II corresponds to a precursor spike ending the dip, and interval (Int.) III is spectrally a very soft dip immediately following the precursor spike. In the case of class ν we identified an additional interval (Int. IV) corresponding to the major spike following the whole sequence (Fig. 1, *left*), while in class λ three more intervals have been identified (Fig. 1, *middle*). There is a major soft X-ray spike of about 600 counts s^{-1} (Int. IV) followed by a dip in both soft and hard X-rays (Int. V) and a return to a high degree of soft and hard X-ray emission (Int. VI). Since ejections seem to always occur after such cycles during classes ν and β (e.g., Klein-Wolt et al. 2002), we extracted time-resolved spectra from all cycles, and further averaged those belonging to the same type of interval in those two observations. On the other hand it is the first time a radio flare has been observed in class λ (Paper 1). Since we cannot, a priori, know whether radio flares occur in response to each of these cycles, we extracted time-resolved spectra from this particular cycle only. Note that the ubiquity of the accretion-ejection links during cycles seen in all other classes indicates that each λ cycle is probably followed by an ejection.

During the spectral fittings, we tested several models, starting with the phenomenological family based on a power-law tail at high energy plus a thermal component at low energy modified by interstellar absorption. Note that in all fits the absorption column density, N_{H}, was frozen to 5.7×10^{22} cm^{-2}, a value well within the $(5–6) \times 10^{22}$ cm^{-2} range of value usually found in the literature (e.g., Belloni et al. 2000). Note that varying N_{H} within this range does not affect the results of the spectral analysis significantly. This is especially true when considering the spectra above 5 keV. Because of a more accurate treatment of the inner regions of the disk, we used the `ezdiskbb` model (Zimmerman et al. 2005), which assumes zero torque at the inner boundary of the disk. For Obs. 2 the statistics are not good enough to find other spectral features or fit the data with more sophisticated models. A high-energy cutoff is needed in intervals I_{ν} and I_{β}. Since a power law with an exponential cutoff is usually interpreted as being due to thermal Comptonization, we then fitted all spectra of classes ν and β with a model consisting of interstellar absorption, a thermal component (`ezdiskbb` when needed), and a Comptonized component (`comptt`; Titarchuk 1994). The temperature of the seed photons for Comptonization was set equal in all cases to that of the inner disk (except when the disk is not needed, and was then frozen to 0.7 keV, the temperature below which no disk component can be detected in JEM-X above 5 keV). In some cases the optical depth of the Comptonized component tends to very low values, while the electron temperature is quite high and poorly constrained. In this range of parameters we are outside the range of validity for this particular model. They correspond to spectral states A and B (in the classification by Belloni et al. 2000), which are equivalent to steep power law/soft intermediate states, in which the coronal medium is very tenuous, and the population of electrons is probably nonthermal. The shape of the spectrum is then equivalent to a power law with no cutoff. In those cases the τ-parameter was frozen to 0.01, which is the value toward which the parameter usually tended, the smallest value allowed in XSPEC. Note that despite these caveats concerning the model used for the fitting, we preferred it to the phenomenological one because (1) it avoids the mixing of the two components at low energy (i.e., no overestimate of the contribution of the corona below $3kT_{\mathrm{seed}}$) that is unavoidable with a simple power law model; (2) we are interested in the relative

TABLE 1
BEST PARAMETERS OBTAINED FROM THE FITS TO THE JEM-X+ISGRI DATA OF THE SEVERAL INTERVALS OF OBS. 1, 2, AND 5

INTERVAL	kT[a] (keV)	$R_{\rm in}$[b] ($\times R_G/[\cos(i)]^{1/2}$)	kT_e (keV)	τ	χ^2_ν (dof)	UNABS. FLUXES ($\times 10^{-8}$ erg cm^{-2} s^{-1}) 3–50 keV disk	3–50 keV comptt	3–50 keV PL	POWER LAW INDEX (Γ)
				Obs. 1, class ν					
I_ν	0.7 (frozen)	...	33^{+6}_{-4}	0.6 ± 0.1	1.49 (88)	...	1.4	...	...
II_ν	1.33 ± 0.09	$12.1^{+2.2}_{-1.7}$	14^{+8}_{-3}	$1.5^{+0.6}_{-0.7}$	1.42 (44)	2.42	1.9	...	...
III_ν	$1.5^{+0.3}_{-0.2}$	$7.6^{+2.0}_{-0.6}$	90^{+57}_{-12}	0.01 (frozen)	1.30 (31)	2.66	0.86	...	...
IV_ν	$2.10^{+0.06}_{-0.07}$	6.2 ± 0.3	110^{+17}_{-14}	0.01 (frozen)	1.52 (68)	7.9	1.5	...	...
				Obs. 5, class β					
I_β	0.8 ± 0.2	28^{+64}_{-14}	15^{+32}_{-5}	$1.5^{+0.5}_{-1.2}$	1.11 (43)	0.77	1.2	...	...
II_β	0.9 ± 0.4	21^{+100}_{-13}	181^{+65}_{-31}	0.01 frozen	1.20 (39)	0.89	1.6	...	...
III_β	1.5 ± 0.1	$6.2^{+1.2}_{-1.4}$	> 124[c]	0.01 frozen	1.13 (31)	1.4	0.24	...	...
				Obs. 2, class λ					
I_λ	...	...	...	...	1.14 (48)	...	...	0.95	$2.51^{+0.09}_{-0.11}$
II_λ	...	...	...	...	0.95 (37)	...	...	1.2	2.6 ± 0.2
III_λ	1.83 ± 0.09	7^{+1}_{-2}	...	...	0.88 (29)	4.4	...	<0.29	2 frozen
IV_λ	$2.11^{+0.08}_{-0.07}$	6 ± 1	...	...	0.88 (31)	7.3	...	<0.43	2 frozen
V_λ	2.05 ± 0.07	$5.1^{+0.9}_{-0.5}$	...	...	1.08 (33)	4.8	...	<0.49	2 frozen
VI_λ	1.97 ± 0.06	5.9 ± 0.6	...	...	1.49 (41)	5.4	...	1.9	2.9 ± 0.3

NOTES.—The fits of Obs. 1 correspond to the interval represented in Fig. 2. For Obs. 1 and 5 the best-fit model is `phabs(ezdiskbb+comptt)` (in XSPEC notation), while for Obs. 2 it is `phabs(ezdiskbb+powerlaw)`. The errors are given at the 90% confidence level. The upper limits on the fluxes are at the 3 σ (99.73%) level.

[a] This is the seed value for Obs. 1 and 5 and the disk value for Obs. 2.

[b] We take a correction factor $f = 1.9$ (Shimura & Takahara 1995), $M = 14\ M_\odot$, and $D = 10$ kpc to convert the model normalization to R_G, $R_{\rm in} = 0.859\sqrt{K}\{R_G/[\cos(i)]^{1/2}\}$, with K the model normalization and i the inclination angle.

[c] The limit on this parameter is given at the 90% confidence level.

variations of the 3–50 keV flux, which is thus well below the supposed kT_e, in other words where the shape of the spectrum is power law–like; (3) the use of the same model allows a true and robust comparison of the fluxes in the different intervals. Although when τ is very low and kT_e is very high the interpretation in terms of thermal Comptonization is thus dubious, in terms of fluxes the relative contributions of each model component to the total flux are, therefore, more reliable. Note that similar evolutions of the fluxes are seen when fitting with the phenomenological model. This shows that our method is valid. The best-fit parameters for all intervals of the three observations are reported in Table 1, while Figure 2 shows particular examples of the four spectra from Obs. 1/class ν with the best model and individual spectral components superposed.

In all three observations the disk temperature increased smoothly through the cycle, with a simultaneous decrease of its inner radius (Table 1). Its overall contribution to the total 3–50 keV flux also increased accordingly. On the other hand, the 3–50 keV contribution of the Comptonized component was never so monotonic. In class ν it first increased from I_ν to II_ν, and was then reduced by a factor of 2.2 from II_ν to III_ν. It recovered at a higher level (a factor of approximately 1.7 higher) in IV_ν. A very similar evolution is seen in Obs. 5/class β where the Comptonized component sees its 3–50 keV flux reduced by a factor 6.7 between II_β and III_β. During Obs. 2/class λ the disk appeared during III_λ and remained at a high temperature and low radius over the remaining intervals. The flux of the hard tail (assumed to be the emission of the Comptonizing corona) first increased from I_λ to II_λ, with a small decrease in the photon index. It was not statistically required in the fit to III_λ, which likely indicates that it had disappeared. Nevertheless, we added a power law to the disk component with a photon index frozen to 2.0[15] and estimated the upper limit on its flux. We find that from II_λ to III_λ the power-law contribution to the 3–50 keV flux was suppressed by a factor greater than 4.2 (at 3 σ), and remained at a low flux until VI_λ, where it reached its highest flux over the entire cycle (Table 1).

[15] This value is a quite standard value for BHs in general. Note that freezing the photon index to values greater than two results in even lower limits on the flux of the hard tail component.

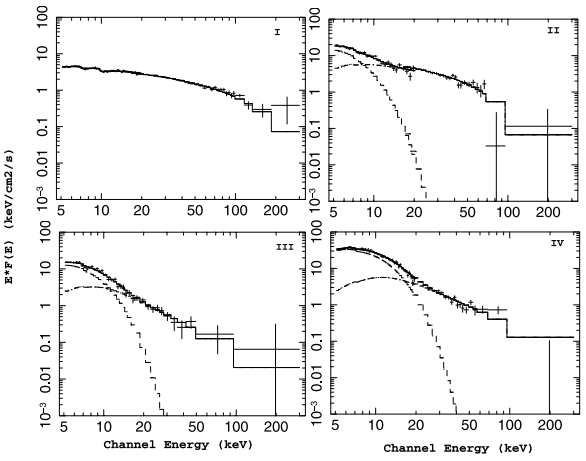

FIG. 2.—Joint JEM-X and ISGRI spectra from the four intervals of Obs. 1/class ν. The best-fit model is superposed onto the spectra, as are the individual components, a disk and a Comptonized tail. The best-fit parameters are given in Table 1.

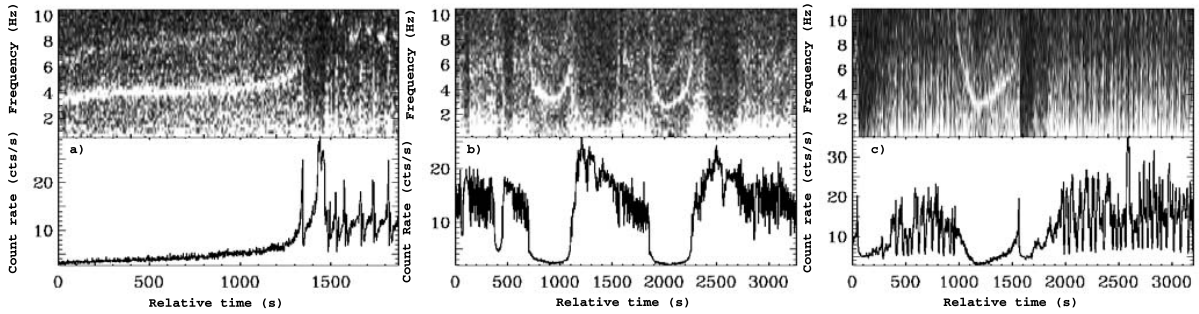

FIG. 3.—Dynamical power spectrum (*top*) and PCA light curve (*bottom*) from the three observations with cycles. (*a*) ν-type cycle simultaneously observed with *RXTE* and *INTEGRAL*. (*b*) λ-type cycles observed with *RXTE*. (*c*) β-type cycle observed with *RXTE*. The gray scale represents the rms power of the variability, with white having a higher power than dark points.

3.2. *Temporal Analysis of the Cycle*

The dynamical power spectra of all three observations showing X-ray cycles are shown in Figure 3. In the case of type ν, this corresponds to a cycle that is simultaneously covered with *INTEGRAL* and *RXTE*, and followed by a radio flare. Although the dip is not entirely covered by *RXTE*, a strong feature, a LFQPO, of variable frequency can be seen. The frequency of the LFQPO seems to follow the evolution of the X-ray flux, as observed in other classes (e.g., Markwardt et al. 1999; Rodriguez et al. 2002a, 2002b), namely β and α.

Very similar behavior is seen during λ- and β-type cycles: a strong LFQPO of variable frequency appears the moment GRS 1915+105 enters the dip (Fig. 3). The frequency rapidly decreases, in (cor)relation with the X-ray flux. The feature ceases at the end of the dip. Because of the short timescales of the events occurring at the end of the dip in class λ and the 16 s step on which the dynamical PDS is calculated, the precise moment of the cessation of the LFQPO is quite difficult to estimate. It seems to occur somewhere between the equivalent of Ints. II–IV (Fig. 3). In class β the QPO is cut at the maximum of the precursor spike, and so seems to be the overall noise (Fig. 3). Note that for the two latter cycles, we do not have simultaneous *RXTE* coverage to the cycles which were followed by the radio flares. Hence, we can hypothesize that GRS 1915+105 undergoes the same behavior concerning the LFQPO during all cycles, and thus also showed a LFQPO prior to the ejections during classes λ and β. Given that this is commonly observed in GRS 1915+105 and that it has already been seen in class β (e.g., Markwardt et al. 1999; Rodriguez et al. 2002a) in simultaneity with radio flares (Mirabel et al. 1998), this hypothesis seems quite reasonable.

3.3. *Observations 4: Class χ*

3.3.1. *X-Ray Spectral Analysis*

During the *INTEGRAL* coverage of Obs. 4, we obtained two observing intervals with the RT and five with *RXTE* (Paper 1). The second coverage with the RT overlapped only very briefly with *INTEGRAL* and we will not discuss it further here. During the first, however, the multiwavelength coverage (Fig. 4) shows that the radio flux, while being rather steady during the first 13 ks at a mean value of 44.9 mJy, increased slightly between MJD 53,473.25 and 5,3473.30. It reached a mean level of 70.4 mJy after 53,473.30 up to the end of the radio coverage on MJD 53,474.42. We separated this observation into three intervals (I_χ, II_χ, III_χ) based on the radio behavior of the source from which we extracted *INTEGRAL* spectra. In the case of I_χ, an *RXTE* pointing is also available and was added to the spectral fit.

As in the previous observations, we started with different combinations of phenomenological models. It has to be noted that none of the spectra is well represented by the standard model composed of an accretion disk and a power-law tail. A single absorbed power law is a very poor representation of the spectra. Figure 5 shows the residuals in terms of number of σ between the model and the spectra. Adding a multicolor disk blackbody in either of its forms (`diskbb, ezdiskbb`) still leads to a poor representation of the spectrum (even with a Gaussian, see below). In I_χ, for example, the reduced χ^2 is 10.4 for 124 degrees of freedom (dof). Since the simple power law overestimates the spectrum at high energies, we replaced it by a cutoff power law. This provides a much better representation of the spectrum, although it is still not satisfactory. Again adding a disk emission does not provide a good description of the spectrum. In I_χ, for example, even after having included a Gaussian around 6.5 keV, the reduced χ^2 is 12.6 for 123 dof. The emission above >40 keV is still underestimated. Instead of a disk emission, an extra power law improves the fit significantly (F-test probability of $\sim 7 \times 10^{-19}$ chance improvement). Some residuals are still visible in the iron Kα region at 6.5 keV. We therefore added a Gaussian to account

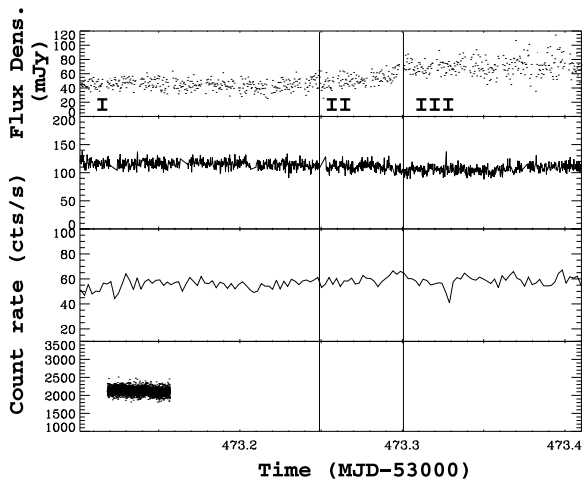

FIG. 4.—Zoom on the interval of Obs. 4. from which we extracted the time-dependent spectra. From top to bottom, the panels respectively represent the Ryle 15 GHz, the JEM-X 3–13 keV, the ISGRI 18–50 keV, and the PCA 2–60 keV light curves. The different intervals from which spectra were extracted are indicated with the roman numeral on the light curves. The best-fit parameters are given in Table 2.

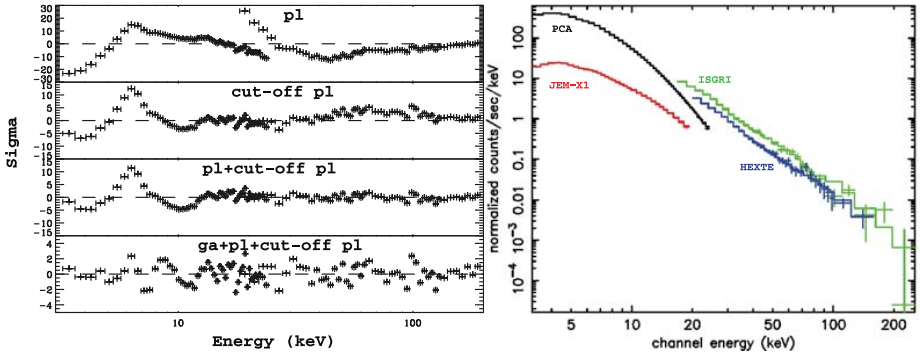

FIG. 5.—*Left*: Residuals in terms of σ between the models used to fit the *RXTE* spectra. In each case the model mentioned in the panel is convolved with interstellar absorption. Pl stands for power law and ga stands for Gaussian. From top to bottom the reduced χ^2 are the following: 25.2 (132 degrees of freedom; dof), 7.3 (131 dof), 5.5 (129 dof), and 1.8 (126 dof). *Right*: Joint *INTEGRAL*+*RXTE* spectra from Obs. 4 Int. I. The best model (consisting of a `comptt`, a power law, and a Gaussian convolved by absorption) is superposed on the spectra.

for this feature. The reduced χ^2 is 1.73 (123 dof) in I_χ with this model. The cutoff power law was then replaced by the `comptt` model (Titarchuk 1994). This model provided very good fits to the data and gives a better χ^2 (Table 2). All spectral parameters are reported in Table 2.

A clear evolution in terms of spectral parameters is seen between the three intervals of Obs. 4 (Table 2), especially for the power-law component. The temperature of the seed photons for Comptonization is rather stable around 0.3 keV and the Kompaanets parameter $[y = kT_e/m_ec^2 \max(\tau, \tau^2)]$, which roughly characterizes the efficiency of Comptonization, is multiplied by a factor of about 1.1 between I_χ and III_χ. In the mean time the power-law photon index of the hard tail gets softer. In terms of fluxes (unabsorbed 2–200 keV), that of the Comptonized component is divided by a factor of about 1.2 between I_χ and III_χ, while that of the hard tail is multiplied by a factor of about 1.6. The power-law fluxes are significant at more than 10 σ in each intervals. Based on the errors of the power-law parameters we can estimate a ratio 1.61 ± 0.13 (1 σ error) increase of the power-law flux between I_χ and III_χ.

3.3.2. *Timing Analysis: LFQPOs*

We first analyzed the 2–60 keV PDS of the unique ~3000 s *RXTE* pointing that was simultaneous with both *INTEGRAL* and the RT. The PDS was computed between 0.03125 and 124 Hz. The PDS is composed of a flat top component up to a break frequency above which a power-law decrease can be seen. On top of this continuum a strong LFQPO is detected. Above about 20 Hz the PDS is compatible with Poissonian noise. We modeled it with the sum of a broad zero-centered Lorentzian, a narrow one (the LFQPO), and a constant to account for the white noise. The fractional rms amplitude of the continuum of the PDS above 0.03125 Hz is $13.1\% \pm 0.4\%$. The QPO centroid frequency is 3.77 ± 0.01 Hz, its quality factor Q ($=\nu_{\rm centroid}/{\rm FWHM}$) is 7.7, and its fractional rms amplitude $10.9^{+0.6}_{-0.7}$ (%).

This best model was used to fit the energy-dependent PDSs. Note that given their poorer statistics and the fact that we are interested in the parameters of the LFQPO, we subtracted the white noise and restricted the frequency range to 0.03125–10 Hz. The energy dependence of the LFQPO (hereafter QPO spectrum) is plotted in Figure 6. The QPO spectrum is hard in the sense that it increases with energy. A plateau and possible following decrease can be seen from 10–15 keV. Such behavior has already been reported for LFQPOs from class χ observations (Rodriguez et al. 2004). We first fitted the QPO spectrum with a simple power law model. The statistics of the fit is poor with $\chi^2_\nu = 2.05$ for 14 dof. In order to account for the deviation from a simple power law (Fig. 6), we added an exponential cutoff to the power law (see Rodriguez et al. 2004). We obtained a good representation of the spectrum with $\chi^2_\nu = 0.41$ for 12 dof. The best parameters are a power-law index of 0.53 ± 0.04, a cutoff energy $E_{\rm cut} = 11.3 \pm 1.3$ keV, and a folding energy for the cutoff $E_{\rm fold} = 23 \pm 6$ keV.

4. DISCUSSION

4.1. *Model-independent Evolution, Hardness Intensity Diagrams*

Figure 7 shows two HIDs of all the *RXTE* pointings of the four observations presented in this paper (see Table 2 of Paper 1 for

TABLE 2

BEST PARAMETERS OBTAINED FROM THE FITS TO THE JEM-X+ISGRI (AND PCA+HEXTE WHEN AVAILABLE) SPECTRA OF OBS. 4/CLASS χ

INTERVAL	$kT_{\rm seed}$ (keV)	kT_e (keV)	τ	Γ	χ^2_ν (d.o.f.)	2–200 keV UNABS. FLUXES[a] ($\times 10^{-8}$ erg cm^{-2} s^{-1}) comptt	PL
I_χ[b]	0.32 ± 0.01	6.66 ± 0.03	2.084 ± 0.008	2.62 ± 0.01	1.60 (122)	2.70	0.77
II_χ	$0.33^{+0.06}_{-0.03}$	$6.66^{+0.34}_{-0.07}$	$2.22^{+0.2}_{-0.02}$	$2.74^{+0.02}_{-0.04}$	0.92 (52)	2.65	1.09
III_χ	$0.26^{+0.04}_{-0.2}$	7.0 ± 0.1	$2.16^{+0.03}_{-0.02}$	$2.81^{+0.02}_{-0.07}$	1.25 (51)	2.32	1.24

NOTE.—The best-fit model is `phabs(comptt+ga+powerlaw)` in `XSPEC` notation. The errors on the parameters are given at the 90% confidence level.

[a] The fluxes are those from *INTEGRAL* ISGRI (extrapolated to 2–200 keV).

[b] Fits of this interval also include simultaneous *RXTE* data. Note that if the normalization constant is frozen to 1.0 for PCA, the one we obtain from the fit for ISGRI is 0.952 and that for JEM-X is 1.016.

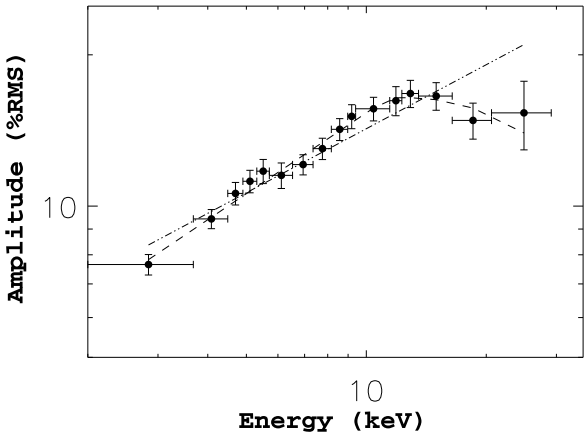

FIG. 6.—Spectrum of the LFQPO from the unique *RXTE* observation that was simultaneous to *INTEGRAL* Obs. 4 and the RT. The best model obtained from fits with power law and power law with an exponential cutoff are respectively overplotted as a dash-double-dotted and a dashed line. A better fit is obtained with the power law with cutoff.

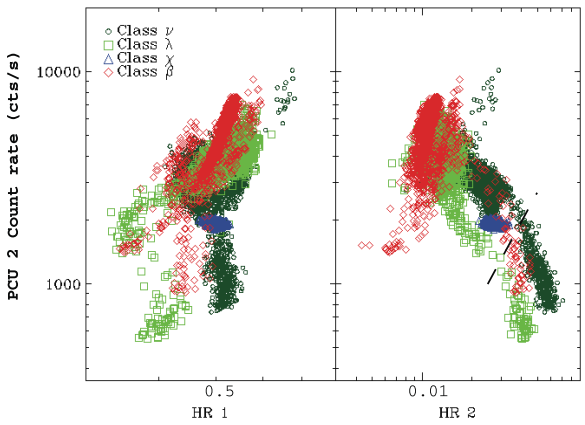

FIG. 7.—Hardness-intensity diagrams of the four observations discussed in the paper. Each point represents 16 s. *Left*: PCU 2 count rate vs. (6.1–10.2) keV/(3.3–6.1) keV. *Right*: PCU 2 count rate vs. (14.8–40.4) keV/(3.3–6.1) keV. The dashed line is roughly indicative of the position of the jet line: each time GRS 1915+105 transits from the dip through this line an ejection occurs.

the journal of all the observations). The first one, representing the PCU2 intensity versus HR1 [(6.12–10.22) keV/(3.28–6.12) keV; hereafter HID1] exactly matches the colors commonly used in the literature for the production of HIDs (e.g., Belloni 2005; Fender et al. 2004). However (as clearly mentioned in Fender et al. 2004), since the thermal disk component in GRS 1915+105 is always brighter than in any other BH, using the same colors results in having the hard C state lying in a softer part of the HID than the soft B state (Fig. 7, *left*). The second HID (HID2) makes use of colors [HR2 = (14.76–40.41) keV/(3.28–6.12) keV] well separated so that the disk component can clearly be separated from any other component. Although the values of the HR are quite different between the three classes with cycles, the general pattern shows striking similarities in both plots. They all have in common a "parallel" trend from the low values of intensity and HR1 $\sim$ 0.5, (respectively HR2 $\sim$ 0.03) to intermediate values of the intensity, and HR1 $\sim$ 0.5, (respectively HR2 $\sim$ 0.01). This corresponds to the dips of the cycle (at the bottom right of the tracks), and the spikes that end them. This parallel track also corresponds to the temporal evolution of GRS 1915+105 when going through the cycle. It first evolves in intensity at a high value of HR2 (or roughly constant value of HR1), and after the spike it falls to the left part of the plots (low values of HR2 and decrease in intensity). Note that, as we show in the next section, the spike is very likely the trigger of the ejection; hence the HR2 of the spike could represent the jet line of Fender et al. (2004). Its precise value is, however, quite difficult to estimate in the three classes, as just before the ejection the values of HR2 are clustered in a region they can reach even in the flaring state. This is quite well illustrated in Figure 7 in the case of class λ around HR2 = 0.02. However, we remark that each time GRS 1915+105 exits the dip of a cycle, an ejection occurs (Paper 1). The approximate position of the jet line is represented in the right panel of Figure 7. The flaring states of the observations correspond to oscillations between the points that lie on the left of this jet line.

4.2. *Ejection of Coronal Material?*

In Paper 1 we have shown that the same sequence of events will lead to the ejection of material. Namely, an X-ray dip of duration longer than 100 s terminated by an X-ray spike always precedes a radio flare. We have argued, in a model-independent way, that the X-ray spike terminating the sequence was the trigger of the ejection. This was based on the similarity of the sequence of events, and that in class β the spike had been identified by Mirabel et al. (1998) as the trigger of the ejection. Here we followed a different approach, and performed fits to each remarkable interval of the cycles.

Although the precise spectral parameters returned from the fits (Table 1) show differences between the cycle of each class, a similar evolution can be seen in all. As presented in § 3, while the evolution of the disk along the cycles is monotonic and may indicate a disk that slowly reaches its last stable orbit around the BH, the evolution of the Comptonized component or the power-law component (the corona) is quite different. While it entirely dominates the spectra during the hard dips (Int. I), it disappears after the spike labeled II in all cases, and seems absent in the soft dips (Int. III). Its relative contribution to the source flux in the same band as that of the disk decreases by a minimum factor of 2.2 (in class ν).

In the case of class β Mirabel et al. (1998) demonstrated that the X-ray spike was the trigger of the ejection. In Paper 1, based on the similarities of the sequences seen during the three classes, shape, evolution of the source fluxes in different X-ray bands, and delays between the X-rays and the radio peak, we argued that the spike (II_ν, II_λ, and II_β) is very likely the trigger of the ejection. Our spectral analysis is compatible with such an interpretation, since in all cases the spectra greatly evolve after the spike and show a transition to a state dominated by the disk component. In that case, the quantitative evolution of the coronal flux shows that this component disappears between Ints. II and III. Given the detection of ejected material at approximately the same time delay in all three classes, it is tempting to believe that the corona is ejected at the spike, decoupled from the central system, and is further detected at radio wavelengths.

One could argue that the spike is not the real trigger. The other remarkable moment of each cycle (at least from the spectral point of view) is the entrance into the dip. Here the spectrum becomes hard, which likely indicates that the inner regions of the disk either recede from the BH or disappear. Several arguments do not favor this moment as being the trigger of the ejection. First the radio flares—the signature of the ejections—have similar profiles (Paper 1), while the transitions to the dip at X-ray energies are

quite different, especially in their temporal evolutions. The decrease of the X-ray count rate is quite slow in ν and β, while it is quite sudden in λ. If this moment were the signature of the ejection at X-ray energies, it is reasonable to think that its temporal evolution would influence the subsequent ejection. Secondly, during class β, a 0.8 keV disk is clearly detected during the dip, while the amplitude of the ejection is higher than in class λ (no disk in the dip), and the duration of the dip is longer. This is in contradiction to a model where the longer duration dip associated with a higher amplitude ejection would indicate that more disk material is ejected, and hence it would take longer for it to be refilled. Finally, the delay between the peak in radio and the spike terminating the cycle is similar in all classes (Paper 1), while the duration of the dip, and hence the delay between the transition into the dip and the radio peak, is quite different between the three classes. It is around 0.8 hr in class ν, while it stays around 0.4 hr in the other two classes.

We therefore favor an interpretation where the coronal material is ejected from the system at the spike terminating the hard dips of the cycle. It is interesting to note that in another class with a cycle (class α), Rodriguez et al. (2002b) had come to the same conclusion, although based on the inspection of the evolution of HRs and light curves only (see also Vadawale et al. 2003). Further strengthening this interpretation is the case of another microquasar, XTE J1550−546, where Rodriguez et al. (2003) arrived at the same conclusion studying the evolution of this source's outburst in 2000. The similar conclusions reached in two different sources may indeed indicate that the discrete ejections in (all) microquasars are composed of coronal material.

4.3. *Steady Hard* (*Intermediate*) *State*

During one of our observations, GRS 1915+105 was found in the so-called χ class of variability in the X-rays, which corresponds to its hardest steady state.[16] In the radio domain a relatively bright and steady emission is detected and attributed to the presence of a compact jet (e.g., Fuchs et al. 2003). As mentioned in Vadawale et al. (2003), the spectrum of this radio-loud χ observation indicates the presence of a Comptonizing component and an extra power law (Table 2). We do not need any thermal component at low energy, which indicates that the accretion disk is quite cold (at least it has no effect above 3 keV), and indeed the temperature of the seed photons for Comptonization is quite low, around 0.3 keV. It is interesting to note that when separating the observation into three noticeable intervals based on differences in the radio fluxes, we clearly see the spectral evolutions of the two X-ray spectral components (Table 2). While the 15 GHz flux increases, the 2–200 keV flux of the Compton component decreases, while that of the extra power-law component seems to increase as well in coordination with a softening of the tail.

The spectral characteristics of radio-loud χ classes in GRS 1915+105 have been shown to always imply Comptonization by a corona of a few keV and optical depth of the order of several units (Trudolyubov 2001; Vadawale et al. 2003). This either results in spectra of shape similar to the ones we observed here (Vadawale et al. 2003), or phenomenologically with breaks at 12–20 keV (Trudolyubov 2001). Several competing models may explain the simultaneous presence of thermal Comptonization and of an additional power law. This may be the signature of Comptonization on a hybrid thermal/nonthermal population of electrons (e.g., Poutanen & Svensson 1996). This family of models has been successfully applied to the modeling of microquasars in steep power law/soft intermediate/very high states showing power laws with no cutoff up to the MeV domain (e.g., Cadolle Bel et al. 2006), or even to some peculiar classes of GRS 1915+105 (Hannikainen et al. 2005). These states were, however, never associated to a strong radio emission. Trudolyubov (2001) argued that differences between the radio-loud and radio-quiet χ states are related to different structures of the accretion flow around the black hole, the obvious difference being the presence or absence of a compact jet. The fact that the flux of the power-law component increased in simultaneity with the radio flux from the compact jet seems to indicate a link between the hard tail and the radio emission. This correlation between the evolution of both components leads to the tempting conclusion that the hard tail seen at X-ray energies is emitted by the jet itself. This possibility may be further reinforced by the very similar evolution of both components: the 2–200 keV flux of the hard tail increased by a factor 1.61 ± 0.13 between I_χ and III_χ when at the same time the radio flux increased by a factor 1.57 ± 0.14. The Pearson correlation factor between the radio and power-law fluxes of the three intervals is 0.93, which suggests that the radio and power-law fluxes are strongly correlated. In this case emission from the compact jet the radio emission would lie in the optically thick spectral domain, while the X-ray emission would lie in the optically thin one. Therefore a direct linear relation may appear as a special case. It has to be noted that the parameters of the power law we find here are very similar to the one reported by Vadawale et al. (2003). In the latter work these authors suggested, based on a simple modeling of a compact jet, that this additional power law could be direct synchrotron emission from the jet. The similarity of their results and ours may also favor the same interpretation. The origin or possible link of the Comptonized component with the jet is less clear, as inverse Comptonization can occur either on the base of the jet or in the form of SSC of the jet photons (Markoff et al. 2005). The fact that the temperature for the seed photons remains constant at a low value rather suggests that the seed photons for Comptonization probably come from the cold disk.

As expected during class χ, a strong LFQPO is detected during the unique interval that is simultaneous to the RT and *INTEGRAL*. We confirm previous findings that the QPO spectrum shows a cutoff (Rodriguez et al. 2004), and by comparing with previous observations, we can see that the cutoff energy is clearly not constant and may evolve from one observation to another (Rodriguez et al. 2004). In Rodriguez et al. (2004) we suggested that the spectrum of the QPO could be understood if one assumed that the high-energy component was not modulated and came from a jet. Here the same conclusion holds when observing a cutoff, while the power law may extend to much higher energies than the QPO does (Figs. 6 and 5). The presence of a LFQPO is always contemporaneous to the presence of a Comptonized component in the energy spectra of the source. Whether this component is thermal or not (i.e., whether it shows a cutoff or not when modeled with power laws) depends on the source and the spectral state. Several models have attempted to explain the QPOs. One can distinguish between models based on instabilities in the disk (e.g., the accretion ejection instability [AEI]; Tagger et al. 2004), oscillations of the boundary between the accretion disk and an inner postshock region (e.g., Chakrabarti & Titarchuk 1995), or even global oscillations of the disk itself (e.g., Nowak & Wagoner 1992). The correlations seen between some of the spectral parameters and those of the LFQPO as well as their intrinsic properties (e.g., Markwardt et al. 1999; Rodriguez

[16] Note that as GRS 1915+105 is never observed to be in the canonical hard state seen in other microquasars, "hard" is taken here as relative to its other spectral states. The so-called χ class/state corresponds to the hard-intermediate state in the other sources, following the definition of Homan & Belloni (2005).

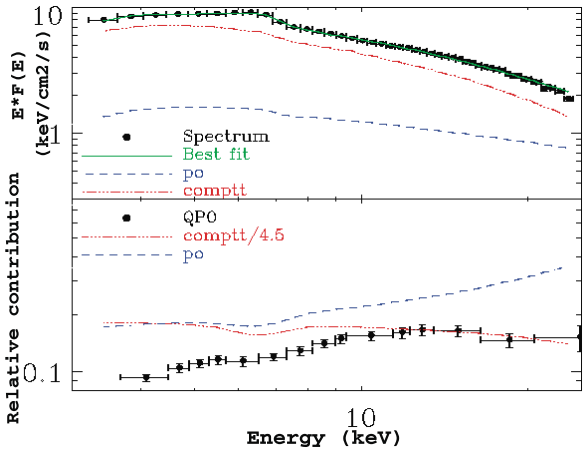

FIG. 8.—*Top*: *RXTE* PCA spectrum of Obs. 4 Int. I (*filled circle*). The best-fit model, the power-law component, and the `comptt` component are overplotted. *Bottom*: Relative contribution of the `comptt` component and spectrum of the QPO.

et al. 2002a, 2002b, 2004; Vignarca et al. 2003) indicate that they are tightly linked to the Keplerian orbit of the accretion disk, and to the corona itself. In order to study the possibility that the QPO represents some oscillation of the corona, we plotted in Figure 8 the *E*-F_E PCA spectrum from I_χ with the different contributions superposed on it. In the bottom panel we compared the relative contribution of the `comptt` and power-law components to the QPO spectrum. The QPO spectrum is clearly not power law–like, further indicating that its origin does not lie in the hard tail. The fact that this hard tail is likely the direct emission from the jet at high energy gives more strength to the suggestion of Rodriguez et al. (2004) that the jet emissions do not contain any quasi-periodic modulation. Furthermore, the QPO spectrum and the relative contribution of the Comptonized component, even scaled down, are clearly not compatible (Fig. 8). This may rule out models based on the oscillation of the corona, and would rather favor models of disk instability (as, e.g., the AEI; Tagger et al. 2004), or global oscillations of the disk (Nowak & Wagoner 1992). The presence of strong QPO together with a strong corona may simply indicate that the corona either enhances the modulation, or simply that the QPO needs the corona to develop. In that case one has to note that whatever produces the QPO, its emission necessarily undergoes Compton up-scattering. Note that if the Compton component comes from SSC from the jet, then the large differences between two spectra (QPO and Compton) further indicates that the jet is not at the origin of the LFQPO.

5. SUMMARY

We have presented the X-ray spectral analysis of four *INTEGRAL* and *RXTE* observations of the microquasar GRS 1915+105. In this analysis we focused on intervals that were strictly simultaneous to radio observations taken with the Ryle Telescope. The results of the multiwavelength approach are reported in Paper 1, where we showed that bubble ejections always follow a sequence of a hard dip terminated by a sudden spike at X-ray energies (referred to as a cycle). We performed a fine spectral analysis of the entire cycles from a few keV up to about 100 keV for the first time in three different classes. We then presented a spectral and timing analysis of the unique observation, during which GRS 1915+105 is found in a steady hard-intermediate state, and for which a strong and rather steady jet is detected in radio. The main results of our analysis can be summarized as follows:

1. In all classes with cycles (ν, λ and β) we showed that the ejection seen in radio is triggered at the spike terminating the cycle. By comparison with other such classes, which always end with a large X-ray spike (e.g., θ and α), we suggest that this is a very generic behavior in GRS 1915+105.
2. In the same observations, we showed that each spike is indicative of the disappearance of the Compton component from the X-ray spectra. We interpreted this as the evidence that the ejected material was the corona responsible for the Comptonized component. Again comparing with the behavior seen during other classes (Rodriguez et al. 2002b; Vadawale et al. 2003) or in other sources (e.g., Rodriguez et al. 2003) leads us to suggest that this phenomenon is very generic in microquasars.
3. In all cycles a strong LFQPO with variable frequency shows up at the transition into the dip and is quenched at the X-ray spike ending the cycle. This phenomenon may indicate a strong link between the QPO, the X-ray behavior, and the subsequent ejection. In a model-dependent interpretation, this is compatible with the prediction of the AEI and the magnetic flood proposed to explain the behavior of GRS 1915+105 during class β (Paper 1; Tagger et al. 2004).
4. The X-ray behavior of GRS 1915+105 during a radio-loud χ observation shows the presence of two emitting media, one responsible for thermal Comptonization, and another emitting a hard X-ray tail modeled with a power law extending up to 200 keV without any break.
5. We find a correlation between the radio flux and the 2–200 keV flux of the hard tail. The very similar evolution of both the radio flux and the flux of the hard tail may suggest that this component is direct emission from the jet.
6. The energy dependence of a LFQPO does not follow the energy dependence of the relative contribution of the Comptonized component, nor that of the hard tail. This indicates that the QPO does not have its origin in the jet, and may also rule out models based on oscillations of a Compton corona. Globally the behavior of the LFQPO is more compatible with models of disk instabilities.

All these points tend to show GRS 1915+105 behaves in a way very similar to other microquasars, and is certainly compatible with the generic model of Fender et al. (2004). The main difference is that its disk is never completely emptied and hence GRS 1915+105 never reaches true quiescence and undergoes cycles between bright hard intermediate and soft intermediate states. The similarity of all cycles, the possible correlation between the amplitude of the ejections and the duration of the dip at X-ray energies (Paper 1), the repeating scenario of ejection of the coronal medium, and the correlated presence of LFQPO indicate a that unique mechanism may be at the origin of all cycles. In the case of a β cycle, Tagger et al. (2004) proposed a magnetic flood scenario compatible with these observed properties. Our monitoring campaign will continue with the goal of covering many more of those cycles and better understanding the origin of the hard X-ray emitters and their connections to those of the radio jet.

J. R. would like to thank A. Gros for invaluable help with the ISGRI data reduction software, and C. A. Oxborrow for precious help with the JEM-X data reduction and calibration. D. C. H. gratefully acknowledges the Academy of Finland. A. P. acknowledges

the Italian Space Agency financial and programmatic support via contract ASI/INAF I/023/05/0.

Based on observations with *INTEGRAL*, an ESA mission with instruments and science data centre funded by ESA member states (especially the principal investigator countries: Denmark, France, Germany, Italy, Switzerland, Spain), Czech Republic, and Poland, and with the participation of Russia and the USA. This research has made use of data obtained through the High Energy Astrophysics Science Archive Center Online Service, provided by the NASA/Goddard Space Flight Center.

REFERENCES

Belloni, T. 2005, in Proc. Interacting Binaries Meeting, Interacting Binaries: Accretion, Evolution and Outcomes, ed. L. A. Antonelli et al., preprint (astro-ph/0504185)
Belloni, T., Klein-Wolt, M., Méndez, M., van der Klis, M., & van Paradijs, J. 2000, A&A, 355, 271
Berger, M., & van der Klis, M. 1994, A&A, 292, 175
Cadolle Bel, M., et al. 2006, A&A, 446, 591
Chakrabarti, S. K., & Titarchuk, L. G. 1995, ApJ, 455, 623
Fender, R. P., & Belloni, T. 2004, ARA&A, 42, 317
Fender, R. P, Belloni, T., & Gallo, E. 2004, MNRAS, 355, 1105
Fender, R., & Pooley, G. 1998, MNRAS, 300, 573
Fuchs, Y., et al. 2003, A&A, 409, L35
Grove, J. E., Johnson, W. N., Kroeger, R. A., McNaron-Brown, K., Skibo, J. G., & Phlips, B. F. 1998, ApJ, 500, 899
Hannikainen, D. C., et al. 2005, A&A, 435, 995
Homan, J., & Belloni, T. 2005, Ap&SS, 300, 107
Klein-Wolt, M., Fender, R. P., Pooley, G. G., Belloni, T., Migliari, S., Morgan, E. H., & van der Klis, M. 2002, MNRAS, 331, 745
Laurent, P., & Titarchuk, L. 1999, ApJ, 511, 289
Markoff, S., Nowak, M. A., & Wilms, J. 2005, ApJ, 635, 1203
Markwardt, C. B., Swank, J. H., & Taam, R. E. 1999, ApJ, 513, 37
Mirabel, I. F., Dhawan, V., Chaty, S., Rodriguez, L. F., Marti, J., Robinson, C. R., Swank, J., & Geballe, T. 1998, A&A, 330, L9
Mirabel, I. F., & Rodríguez, L. F. 1994, Nature, 371, 46
Morgan, E. H., Remillard, R. A., & Greiner, J. 1997, ApJ, 482, 993
Nowak, M. A., & Wagoner, R. V. 1992, ApJ, 393, 697
Poutanen, J., & Svensson, R. 1996, ApJ, 470, 249
Remillard, R. A., & McClintock, J. E. 2006, ARA&A, 44, 49
Rodriguez, J., Corbel, S., Hannikainen, D. C., Belloni, T., Paizis, A., & Vilhu, O. 2004, ApJ, 615, 416
Rodriguez, J., Corbel, S., & Tomsick, J. A. 2003, ApJ, 595, 1032
Rodriguez, J., Durouchoux, Ph., Mirabel, I. F., Ueda, Y., Tagger, M., & Yamaoka, K. 2002b, A&A, 386, 271
Rodriguez, J., Varnière, P., Tagger, M., & Durouchoux, P. 2002a, A&A, 387, 487
Rodriguez, J., et al. 2008, ApJ, 675, 1436 (Paper 1)
Shimura, T., & Takahara, F. 1995, ApJ, 445, 780
Tagger, M., Varnière, P., Rodriguez, J., & Pellat, R. 2004, ApJ, 607, 410
Titarchuk, L. 1994, ApJ, 434, 570
Trudolyubov, S. P. 2001, ApJ, 558, 276
Vadawale, S. V., Rao, A. R., Naik, S., Yadav, J. S., Ishwara-Chandra, C. H., Pramesh Rao, A., & Pooley, G. G. 2003, ApJ, 597, 1023
Vignarca, F, Migliari, S., Belloni, T., Psaltis, D., & van der Klis, M. 2003, A&A, 397, 729
Zimmerman, E. R., Narayan, R., McClintock, J. E., & Miller, J. M 2005, ApJ, 618, 832

14.5 Propriétés spectrales des QPO dans GRS 1915+105

The Astrophysical Journal, 615:416–421, 2004 November 1

SPECTRAL PROPERTIES OF LOW-FREQUENCY QUASI-PERIODIC OSCILLATIONS IN GRS 1915+105

J. Rodriguez,[1,2] S. Corbel,[1,3] D. C. Hannikainen,[4] T. Belloni,[5] A. Paizis,[2] and O. Vilhu[4]
Received 2004 April 19; accepted 2004 July 2

ABSTRACT

We report on the timing analysis of *RXTE* observations of the Galactic microquasar GRS 1915+105 performed in 2003. Out of a total of six ∼20 ks observations, we focus here only on the three during which GRS 1915+105 is found in a steady C-state (referred to as class χ), resulting in a total of ∼50 ks. During these observations, we detect low-frequency quasi-periodic oscillations (QPOs) with high (∼14%) rms amplitude in the 2–40 keV energy range. Contrary to what is usually observed in GRS 1915+105, in most of our observations the QPO frequency presents no correlation with the *RXTE* PCA count rate, nor with the *RXTE* ASM count rate. We present, for the first time, high-resolution (22 spectral channels) 2–40 keV spectral fits of the energy dependence of the QPO amplitude ("QPO spectra"). The QPO spectra are well modeled with a cutoff power law except on one occasion in which a single power law gives a satisfactory fit (with no cutoff at least up to ∼40 keV). The cutoff energy evolves significantly from one observation to another, from a value of ∼21.8 to ∼30 keV in the other observations in which it is detected. We discuss the possible origin of this behavior and suggest that the compact jet detected in the radio contributes to the hard X-ray (≥20 keV) mostly through synchrotron emission, whereas the X-rays emitted below 20 keV would originate through inverse Compton scattering. The dependence of the QPO amplitude on the energy can be understood if the modulation of the X-ray flux is contained in the Comptonized photons and not in the synchrotron ones.

Subject headings: accretion, accretion disks — black hole physics — stars: individual (GRS 1915+105) — X-rays: stars

1. INTRODUCTION

GRS 1915+105 was discovered by the WATCH instrument on board *Granat* in 1992 (Castro-Tirado et al. 1992). It is the first Galactic source observed to have apparent superluminal motion in radio (Mirabel & Rodrìguez 1994), corresponding to the ejection of plasma at a speed of ∼92%–98% of the speed of light. It distance is estimated to be 9 ± 3 kpc (Chapuis & Corbel 2004), and the mass of the compact object in GRS 1915+105 is estimated to be 14.0 ± 4.4 $M_{\odot}$ (Harlaftis & Greiner 2004).

Systematic monitoring in the X-rays (mainly with the *Rossi X-Ray Timing Explorer* [*RXTE*]) revealed a rich pattern of variability on all timescales. GRS 1915+105 is a source of low- and high-frequency quasi-periodic oscillations (LFQPOs, HFQPOs; Morgan et al. 1997), whose properties (frequency, rms amplitude) are tightly correlated with the spectral parameters (Morgan et al. 1997; Muno et al. 1999; Markwardt et al. 1999; Rodriguez et al. 2002a, 2002b; Vignarca et al. 2003). When analyzing data of black hole binaries, the frequencies of LFQPOs have been shown to be best correlated with the slopes of the high-energy tails of the energy spectra (Vignarca et al. 2003). It should be noted that the LFQPO frequency is usually correlated with the soft X-ray flux, thought to originate from the accretion disk.

Belloni et al. (2000; hereafter B00), analyzing 163 *RXTE* observations, have shown that, although complex, the behavior of GRS 1915+105 could be understood as spectral transitions between three basic states A, B, and C. They identified 12 recurrent classes of variability on a timescale of ∼3000 s. GRS 1915+105 spends most of the time in the so-called χ class of variability that corresponds to a steady state in the X-rays, lying in a rather hard part of the color-color diagram (state C or hard state). Based on the X-ray (spectral end temporal) and radio properties of GRS 1915+105, four subclasses (χ_1, χ_2, χ_3, χ_4) can be distinguished. Two of them have a high level of radio emission with a flat spectrum, LFQPOs, and a high-energy tail (B00; Trudolyubov 2001; Muno et al. 2001; Klein-Wolt et al. 2002).

We monitored GRS 1915+105 with the *International Gamma-Ray Astrophysics Laboratory* (*INTEGRAL*) during its first AO, for a total of 6 × 100 ks (Hannikainen et al. 2003, 2004), and obtained 120 ks divided into six sequences of simultaneous observations with *RXTE*. One of our *RXTE* observations was planned during an *INTEGRAL* target of opportunity on GRS 1915+105, and it allowed wideband simultaneous spectral and temporal coverage to be performed (Fuchs et al. 2003, hereafter F03). The global analysis of the whole campaign is reserved for a future publication. Here we focus on the timing analysis of the three steady C-state *RXTE* observations. The data reduction methods are described in § 2, while the results are presented in § 3 and discussed in § 4.

2. OBSERVATIONS AND DATA REDUCTION

The log of the observations analyzed in this paper can be found in Table 1. Each observation covers several satellite orbits. The analysis was first performed on each single revolution, and when no noticeable (spectral or temporal) evolution was found, the different orbits were further averaged to increase the statistics.

We extracted light curves from the Proportional Counter Array (PCA) following the standard method described in the

[1] DSM-DAPNIA, Service d'Astrophysique, CNRS FRE 2591, CEA Saclay, 91191 Gif-sur-Yvette, France.
[2] INTEGRAL Science Data Centre, Chemin d'Ecogia, 16, 1290 Versoix, Switzerland.
[3] Université Paris 7 Denis Diderot, 2 Place Jussieu, 75005 Paris, France.
[4] Observatory, University of Helsinki, P.O. Box 14, Tähtrtornimäki 00014, Finland.
[5] Osservatorio Astronomico di Brera, INAF, via E. Bianchi 46, 23807 Merate (LC), Italy.

TABLE 1
LOG OF THE *RXTE* OBSERVATIONS USED IN THE PRESENT ANALYSIS

Observation	Observation Date (MJD)	Observation ID (P80127-)	Good Time (s)	PCU	Net Count Rate per PCU[a] (counts s^{-1})
1	52,731	01-03-00	9300	4	1737.5
2	52,738	02-01-00	5400	3	1700.8
3	52,739	02-02-02	1800	3	1675.8
4		02-02-01	1800	4	1666.9
5		02-02-00	2060	3	1660.4
6		02-03-00	11,100	3–4	1674.7
7		02-01-01	3200	3	1677.0
8	52,768	03-01-00	14,000	3–4	1460.2

NOTE.—The first of these observations was performed simultaneously with the multiwavelength campaign discussed in Fuchs et al. (2003). Observations are time ordered.
[a] Measured as counts s^{-1} in the top layer of PCU 2, both anodes.

Cook Book and ABC of *RXTE*,[6] with the LHEASOFT version 5.3 package. Good time intervals are defined as follows: satellite elevation over the Earth limb is >10°, offset pointing is <0°.02, and PCUs 0 and 2 are turned on. Light curves were extracted from "binned" and "event" data. We first accumulated a broadband 2–40 keV (absolute channels 0–94, epoch 5) light curve with the highest time resolution allowed by the (binned) data format (∼4 ms). We then extracted light curves in small-energy bins, with the highest spectral resolution allowed by the (binned) data (16 energy bins from 2 to 14.8 keV), and over seven additional spectral bins for the event data (from 15 to ∼40 keV). Power density spectra (PDSs) were produced using POWSPEC version 1.0 and corrected for white noise. In the case of the 2–40 keV light curves, PDSs were produced on an interval length of 64 s between 15.625 mHz and 64 Hz. All intervals were averaged together. The energy-dependent PDSs were produced on an interval of 160 s length, between 6.25 mHz and 12.8 Hz. Figure 1 shows, as an example, the PDSs extracted in three energy bands, for observation 1. We extracted background light curves in all these energy ranges and used their count rate to obtain the true rms amplitude following Berger & van der Klis (1994). In addition, to check for short-term evolution of the QPO frequency, we produced dynamical power spectra with ∼16 s resolution between absolute channels 0 and 35 (∼2–14.8 keV).

[6] See http://heasarc.gsfc.nasa.gov/docs/xte/abc/contents.html.

3. RESULTS

The preliminary spectral analysis (in a multiwavelength context) of the first observation is presented in F03. The eight other sequences presented here show similar steady light curves (see Hannikainen et al. 2004, hereafter H04, for details on the *INTEGRAL/RXTE* campaign). The *RXTE* ASM light curve, showing the dates of our pointed *INTEGRAL/RXTE* observations, is represented in Figure 2. While the long-term evolution

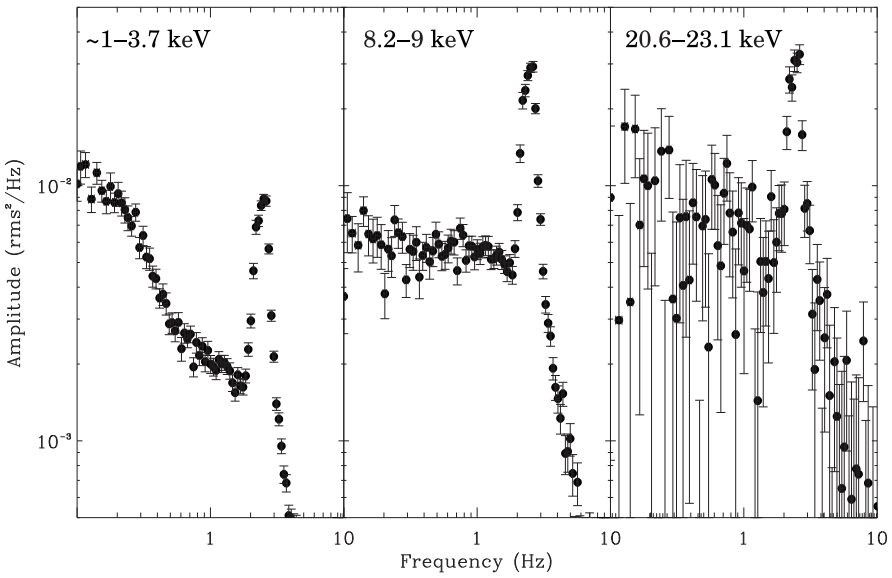

FIG. 1.—Example of PDSs extracted in three energy bands (1–3.7 keV, 8.2–9 keV, and 20.6–23.1 keV), as described in the text. These PDSs are from observation 1. The 2.498 Hz LFQPO is obvious in each panel. The same vertical scale is used for each PDS and allows for a direct comparison of the source behavior in those energy bands.

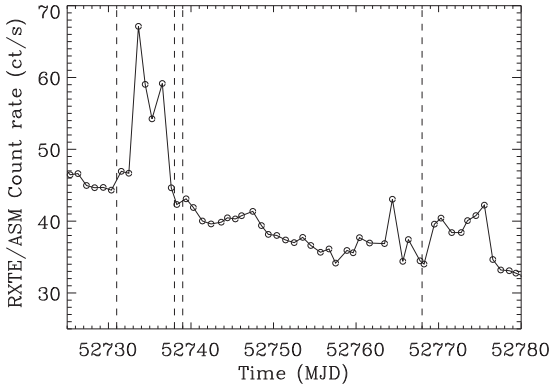

FIG. 2.—*RXTE* All Sky Monitor 1.2–12 keV light curve of GRS 1915+105. The vertical dashed lines show the days our observations took place. The 1.2–12 keV ~1 crab flare is obvious here. A radio flare is detected at the same time, with its maximum occurring 2 days later (F03).

shows a slow decay, a double flare occurs between observation 1 and observations 2–7. This X-ray flare is associated with a radio flare (F03), probably indicative of a discrete ejection. We identify the class of variability of our observations as class χ of B00. The high level of radio emission detected during each of these observations (F03, H04) allows us to further classify the observations as class χ_1-χ_3, also known as the radio-loud hard state (Muno et al. 2001) or type II hard state (Trudolyubov 2001). It should be noted, however, that such a long-term decay with the source mostly in class χ is rather peculiar, and had never been seen previously. A preliminary spectral analysis (F03; H04) shows that the common model of black hole X-ray binaries, i.e., a multicolor disk blackbody and a power law, represents the data well. As mentioned for such classes (Muno et al. 2001), however, the disk temperature returned from the fit is too high (3–4 keV), and the inner radius far too small. Alternative models of broken power law or broken power law plus disk component fit the data well and lead to parameters closer to what is seen in other systems (H04). We also successfully fitted the *RXTE* PCA 3–25 keV spectra with a cutoff power law with a high-energy cutoff of about 20–25 keV (Rodriguez et al. 2004; Fig. 3). When adding higher-energy spectra, such as those extracted with *RXTE* HEXTE, a large deviation to the spectrum is seen at high energy, indicating the need for an additional spectral component to the model, e.g., an extra power law (Zdziarski et al. 2001; D. C. Hannikainen et al., in preparation). This is illustrated in Figure 3 (*left panel*) with the particular example of observation 1.[7] Furthermore, Rodriguez et al. (2004) have shown that the 20–400 keV combined *RXTE* HEXTE and *INTEGRAL* IBIS and SPI spectra could be fitted with a power law of photon index ~3.5. Note that similar results were found from the OSSE spectral analysis of Zdziarski et al. (2001).

For all sequences, the 2–40 keV PDSs were fitted between ~15 mHz and 10 Hz with a sum of two or three Lorentzians (depending on the energy range), to account for the wideband variability (Belloni et al. 2002). A strong LFQPO is detected in all the PDSs and is modeled with an additional Lorentzian (harmonics are also detected, especially during intervals with the longest exposures). A first analysis of observation 8 showed a rather broad QPO, with parameters poorly constrained. As the dynamical power spectrum showed two distinct features, we separated this observation into subintervals and averaged those showing the QPO at the same frequency. This resulted in two distinct sets of data, for which we identified two different QPOs. The LFQPO parameters are reported in Table 2.

At first glance, there is apparently no obvious correlation between the QPO frequency and the PCA 2–60 keV count rate (Tables 1 and 2). To further verify this, we fitted each of the ~2–15 keV 16 s PDSs used to construct our dynamical power spectra with a Lorentzian around the average QPO frequency (Table 2), and could therefore obtain the variations of the QPO frequency with a time resolution of 16 s. No correlation is found between the QPO frequency and the PCA 2–15 keV count rate

[7] Note that the details of the *RXTE* and *INTEGRAL* spectral analysis will be given in a forthcoming paper, dedicated to the spectral analysis of the whole campaign. However, the *RXTE* (PCA and HEXTE) spectra have been extracted in the same way as in, e.g., Rodriguez et al. (2003).

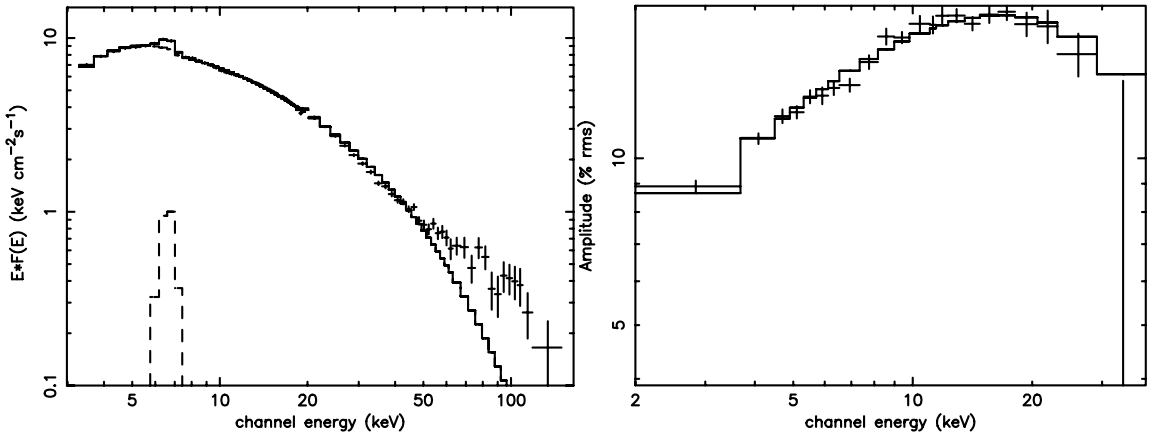

FIG. 3.—*Left panel*: PCA+HEXTE 3–150 keV ν-f_ν spectra from observation 1. A model consisting of an absorbed power law with a high-energy cutoff of about 25 keV (plus a Gaussian at 6.4 keV) is superimposed. The deviation from this model at high energy is obvious here. This likely reflects the need for an additional component to account for the high-energy emission from GRS 1915+105. *Right panel*: Energy dependence of the QPO amplitude observed during the same observation. The best-fit model, a power law with a high-energy cutoff of ~22 keV, is superimposed.

TABLE 2
PARAMETERS OF THE LFQPO DETECTED IN EACH OF THE EIGHT SEQUENCES

Observation Sequence	QPO Frequency (Hz)	Q^a	rms Amplitude (%)
1	2.498 ± 0.005	5.0	12.6 ± 0.3
2	1.040 ± 0.004	3.8	13.5 ± 0.6
3	1.081 ± 0.004	7.2	$13.2^{+1.0}_{-0.9}$
4	1.039 ± 0.004	7.2	$12.7^{+1.2}_{-1.3}$
5	1.097 ± 0.005	10.0	11.5 ± 1.0
6	1.096 ± 0.002	6.4	13.4 ± 0.4
7	1.060 ± 0.003	6.4	13.0 ± 0.9
8_QPO1	$1.878^{+0.005}_{-0.003}$	6.8	12.9 ± 0.5
8_QPO2	2.332 ± 0.005	5.3	14.9 ± 0.5

[a] Q is defined as Q = Centroid frequency/FWHM.

from observations 1–7, whereas we do find a correlation in observation 8.

We further averaged sequences showing the QPO at a similar frequency (observation 7, showing the QPO at 1.06 Hz is averaged with observations 2 and 4, whereas observations 3, 5, and 6 are averaged together) and produced PDSs in the 22 energy bins described in § 2. These energy-dependent PDSs were fitted between 6.25 mHz and 10 Hz. The energy dependences of the amplitude of the four distinct features are reported in Figure 4.

A clear difference in the shape of the energy dependence of the amplitude of the QPO appears in Figure 4. A clear turnover in the amplitude versus energy relation is visible for the ~2.48 Hz QPO detected on MJD 52,731, and another one is visible for the ~1.09 Hz QPO from the observation of MJDs 52,738–52,739, although it is not as clear as for the first QPO. For the three other features we do not see any clear turnover (Fig. 4), although a flattening is obvious at energies above 10 keV. This may suggest that the turnover energy evolves from one observation to another, and is above the upper energy limit of our QPO "spectra." To further test this hypothesis, we fitted the QPO spectra in XSPEC version 11.3.0. For all QPOs but the 1.04 Hz one, the spectra are well fitted by a cutoff power law (*cutoffpl* in XSPEC). The fit parameters are reported in Table 3, while the right panel of Figure 3 shows the QPO spectrum of observation 1 with the best-fit model superimposed. It should be added here that a single power law gives a rather good representation of the 1.878 Hz QPO detected in observation 8, with a reduced χ^2 of 1.89 (20 degrees of freedom). A cutoff power-law model improves the fit (Table 3), although the cutoff energy is poorly constrained (4.7 σ significance on this

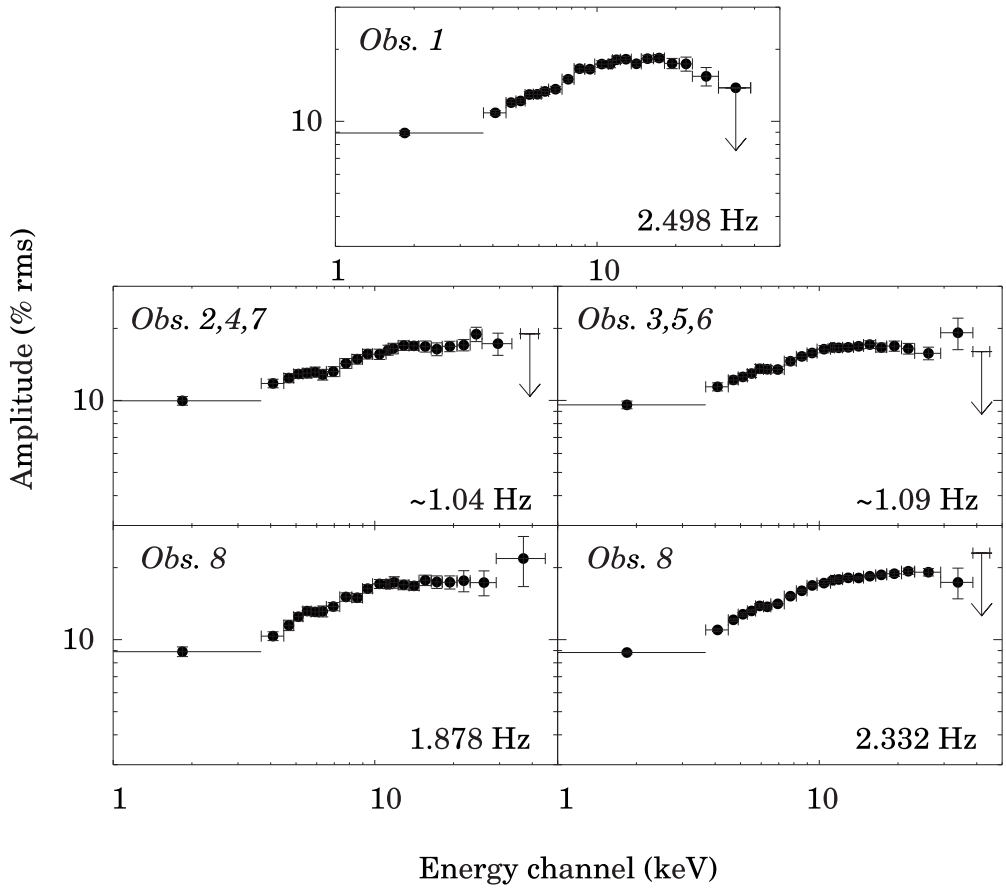

FIG. 4.—Energy dependence of the LFQPO amplitude. The frequency (or mean frequency) of the feature and the observation numbers are written in each panel.

TABLE 3
PARAMETERS OF THE FITS TO THE ENERGY DEPENDENCE OF THE QPO AMPLITUDE

QPO Frequency (Hz)	Power-Law Slope (Γ)	Cutoff Energy (keV)	Reduced χ^2 (dof)
2.498	-0.77 ± 0.04	$21.9^{+2.7}_{-2.2}$	1.0 (19)
1.04	-0.26 ± 0.02	No cutoff[a]	0.92 (21)
1.09	-0.59 ± 0.05	$29.5^{+5.2}_{-3.9}$	0.37 (20)
1.878	-0.70 ± 0.07	$25.6^{+6.5}_{-4.4}$	0.5 (19)
2.332	-0.71 ± 0.05	$26.7^{+4.4}_{-3.3}$	0.28 (20)

NOTE.—Fits to the energy dependence of the QPO amplitude are also referred to as QPO spectra in the text. The errors are given at the 1 σ level.
[a] No cutoff is detected in this observation at least up to ~40 keV.

parameter). It is interesting to note that the break energy seems anticorrelated with the QPO frequency, i.e., the lowest break energy is observed for the highest QPO frequency (Table 3). Caution has to be expressed, however, since the statistical uncertainties on the break energies do not allow us to draw a firm conclusion.

4. DISCUSSION

The presence of LFQPO in GRS 1915+105 during class χ (as well as during other classes) is a known fact (e.g., Muno et al. 1999; Rodriguez et al. 2002a, 2002b). It is also known that QPO parameters depend on spectral parameters in black hole binaries (BHBs) in general. Here we present observations taken during the same state, with few differences between the spectral parameters returned from the spectral fits. The parameters of the QPO change dramatically from one observation to another. Except in observation 8, the frequency of the QPO does not seem to correlate to the PCA 2–15 keV flux or the ASM 1.2–12 keV flux, either (although the highest frequency is observed when the ASM flux is the highest; Fig. 2 and Table 2), contrary to what is usually claimed/observed. This could indicate some definite peculiarities in observations 1–7, which are taken just before and after the X-ray/radio flare (Fig. 2, F03). On the other hand, observation 8 occurs later, after GRS 1915+105 apparently went off the linear decay phase, after the ASM light curve showed some variability again.

The most striking behavior appears when studying the energy dependence of the QPO amplitude. It is expected and a known fact that it presents a turnover at some point (e.g., Tomsick & Kaaret 2001; Rodriguez et al. 2002a). We report here, for the first time, a clear evolution of the turnover energy between states that are spectrally similar and have similar PCA fluxes. This "cutoff" energy has an origin that is unclear. It could represent, for example, some specific temperature at which the QPO is produced, either through oscillations of a shocked boundary layer between the accretion disk and a hot inner flow (e.g., Chakrabarti & Titarchuk 1995), or by a hot spot orbiting at some specific radius in the disk (e.g., Rodriguez et al. 2002a; Tagger et al. 2004). In these two cases, however, we would expect the frequency of the QPO to scale with the inner radius of the accretion disk and thus the soft X-ray flux (Molteni et al. 1996; Tagger & Pellat 1999), unless the soft X-rays are not uniquely produced by the accretion disk, but by another physical medium, as, e.g., a compact jet (see Markoff & Nowak 2004). The variations of the soft X-ray flux could be due to variations of the compact jet flux (with a steady thermal flux from the accretion disk), as we discuss below.

The spectral approach presented in H04 and Rodriguez et al. (2004), the systematic analysis of type II states (Trudolyubov 2001), and the detection of a hard tail up to (at least) 600 keV with OSSE (Zdziarski et al. 2001) raise the challenging question of the origin of the third spectral component needed to fit the high-energy spectra well. Models of jet emission (e.g., Markoff et al. 2003; Markoff & Nowak 2004) propose a jet model in which the X-ray spectrum of an X-ray binary would represent the sum of thermal emission from the accretion disk, direct synchrotron from the jet, Comptonization (either through synchrotron self-Compton from the jet, and/or Comptonization on the basis of the jet, the "corona"), and reflection of these radiations on the accretion disk. This proposition has found an echo with the radio flux/X-ray flux correlation found in several BHBs when in the low hard state (when the compact jet is present, e.g., Corbel et al. 2003; Gallo et al. 2003) and also in the case of radio-loud active galactic nuclei (e.g., Merloni et al. 2003; Falcke et al. 2004). Our *RXTE* observation of MJD 52,731 occurred at a time when the radio flux was high and indicative of the presence of the compact jet (F03). The level of radio emission as measured by the Ryle telescope at 15 GHz is about 130–150 mJy during this observation, with a spectrum extending up to the near infrared range (F03). Unfortunately, we do not have such nice coverage for the following observations, but the observation of MJDs 52,738–52,739 indicates a higher level of 15 GHz emission (~250 mJy, F03) that is dropping rapidly. We remark that this observation occurred just after a radio flare indicative of a discrete ejection. It is thus very likely that the radio emission this day partly originates from the discrete ejection (with a different spectrum). During the last observation, the radio flux is very low compared with the two previous dates, with a level dropping from 107 mJy on MJD 52,767 to 44 mJy on MJD 52,769 (H04). Both our spectral analysis (H04, Rodriguez et al. 2004) and the properties of the QPOs (present work) can be understood easily if the X-ray emission in GRS 1915+105 during radio-loud/type II/class χ_1-χ_3 observations originate (as proposed by Markoff & Nowak 2004) from two different physical processes (besides the thermal emission of the accretion disk): Comptonization and synchrotron radiation. The high-energy spectrum of a source with a compact jet thus represents the sum of these different emission processes. As a result, the spectrum will strongly depend on the relative contribution of each of these emission processes. The break in the energy spectrum could be representative of the energy at which the relative contributions of these components cross each other. Above the break the contribution of the synchrotron radiation would be the dominant process to the spectrum. Then, the higher the relative contribution of the synchrotron component (to the overall spectrum), the lower the break energy is. In this case, to understand the energy dependence of the QPO amplitude, one has to assume that

the QPO is contained in the Comptonized flux and not in the synchrotron flux. Then the position of the cutoff in the energy dependence of the QPO amplitude would be linked to the synchrotron flux emitted by the jet. We find this interpretation at least qualitatively in good agreement with several observational facts:

1. The compact jet model has successfully been used in the fitting of different BHBs (e.g., Markoff et al. 2001).
2. Type II states show a 2–30 keV level of variability lower than that of type I (radio-quiet) states (Trudolyubov 2001).
3. A compact jet is detected during the observation showing the clear and well-constrained cutoff in the energy dependence of the QPO amplitude (observation 1, Fig. 4).
4. A high level of radio emission is detected during the observation taken on MJDs 52,738–52,739, and a turnover in the energy dependence of the $\sim$1.09 Hz QPO is detected (Fig. 4, Table 3, although it is absent in the spectrum of the $\sim$1.04 Hz QPO), while for the last observation (MJD 52,768) the radio flux is much lower, a single power law can fit the first QPO spectrum, and the turnover is poorly constrained (Fig. 4, Table 3).

We should add that the optical/UV/X-ray variability (and presence of LFQPO in those bands) seen in XTE J1118+480 (Hynes et al. 2003), a black hole X-ray transient in which the compact jet model has been shown to fit the broadband spectra well (Markoff et al. 2001), is also compatible with our interpretation. Hynes et al. (2003) pointed out that the variability could not originate from the disk itself, but involved another nonthermal source of photons.

The lack of complete simultaneity between the radio and X-ray observations prevents us from drawing any firmer conclusions. In addition, a cutoff in the spectrum of the compact jet is expected in the near infrared domain. Knowing its exact position would allow us to estimate the flux expected from the jet in the hard X-rays accurately and thus test our hypothesis. We hope to obtain such simultaneous coverages in the near future, with *INTEGRAL* and *RXTE* for the high energies, but also the Ryle telescope and the VLA in the radio domain, and the *Spitzer Space Telescope* and ground-based telescopes in the infrared domain.

The authors would like to thank G. Henri for useful discussions and G. Pooley for kindly providing the Ryle data to our group. J. R. acknowledges financial support from the French Space Agency (CNES). D. C. H. acknowledges the Finnish Academy.

REFERENCES

Belloni, T., Klein-Wolt, M., Méndez, M., van der Klis, M., & van Paradijs, J. 2000, A&A, 355, 271 (B00)
Belloni, T., Psaltis, D., & van der Klis, M. 2002, ApJ, 572, 392
Berger, M., & van der Klis, M. 1994, A&A, 292, 175
Castro-Tirado, A. J., Brandt, S., & Lund, N. 1992, IAU Circ., 5590, 2
Chakrabarti, S. K., & Titarchuk, L. G. 1995, ApJ, 455, 623
Chapuis, C., & Corbel, S. 2004, A&A, 414, 659
Corbel, S., Nowak, M., Fender, R. P., Tzioumis, A. K., & Markoff, S. 2003, A&A, 400, 1007
Falcke, H., Körding, E., & Markoff, S. 2004, A&A, 414, 895
Fuchs, Y., et al. 2003, A&A, 409, L35 (F03)
Gallo, E., Fender, R. P., & Pooley, G. G. 2003, MNRAS, 344, 60
Hannikainen, D. C., et al. 2003, A&A, 411, L415
———. 2004, in Proc. 5th *INTEGRAL* Workshop (ESA SP-552; Noordwijk: ESA), in press (H04)
Harlaftis, E. T., & Greiner, J. 2004, A&A, 414, L13
Hynes, R. I., et al. 2003, MNRAS, 345, 292
Klein-Wolt, M., Fender, R. P., Pooley, G. G., Belloni, T., Migliari, S., Morgan, E. H., & van der Klis, M. 2002, MNRAS, 331, 745
Markoff, S., Falcke, H., & Fender, R. P. 2001, A&A, 372, L25
Markoff, S., & Nowak, M. 2004, ApJ, 609, 972
Markoff, S., Nowak, M., Corbel, S., Fender, R., & Falcke, H. 2003, A&A, 397, 645
Markwardt, C. B., Swank, J. H., & Taam, R. E. 1999, ApJ, 513, L37
Merloni, A., Heinz, S., & di Matteo, T. 2003, MNRAS, 345, 1057
Mirabel, I. F., & Rodriguez, L. F. 1994, Nature, 371, 46
Molteni, D., Sponholz, H., & Chakrabarti, S. K. 1996, ApJ, 457, 805
Morgan, E. H., Remillard, R. A., & Greiner, J. 1997, ApJ, 482, 993
Muno, M. P., Morgan, E. H., & Remillard, R. A. 1999, ApJ, 527, 321
Muno, M. P., Remillard, R. A., Morgan, E. H., Waltman, E. B., Dhawan, V., Hjellming, R. M., & Pooley, G. 2001, ApJ, 556, 515
Rodriguez, J., Corbel, S., & Tomsick, J. A. 2003, ApJ, 595, 1032
Rodriguez, J., Durouchoux, P., Mirabel, F., Ueda, Y., Tagger, M., & Yamaoka, K. 2002a, A&A, 386, 271
Rodriguez, J., Fuchs, Y., Hannikainen, D. C., Vilhu, O., Shaw, S.E., Belloni, T., & Corbel, S. 2004, in Proc. 5th *INTEGRAL* Workshop (ESA SP-552; Noordwijk: ESA), in press (astro-ph/0403030)
Rodriguez, J., Varnière, P., Tagger, M., & Durouchoux, P. 2002b, A&A, 387, 487
Tagger, M., & Pellat, R. 1999, A&A, 349, 1003
Tagger, M., Varnière, P., Rodriguez, J., & Pellat, R. 2004, ApJ, 607, 410
Tomsick, J. A., & Kaaret, P. 2001, ApJ, 548, 401
Trudolyubov, S. 2001, ApJ, 558, 276
Vignarca, F., Migliari, S., Belloni, T., Psaltis, D., & van der Klis, M. 2003, A&A, 397, 729
Zdziarski, A. A., Grove, E. J., Poutanen, J., Rao, A. R., & Vadawale, S. V. 2001, ApJ, 554, L45

Quatrième partie

Conclusions générales, originalité de mon travail et perspectives

Conclusions

J'ai présenté dans cette HDR mes principales activités de recherche. Le cœur de mon activité scientifique concerne l'étude des binaires X en général. Dans ce document je me suis focalisé sur deux sous-types de cette famille : les binaires X de fortes masses contenant une supergéante et les micro-quasars. Les programmes scientifiques que j'ai organisés, les analyses que j'en ai faites et les résultats que j'ai obtenus ont permis d'avancer quelque peu dans la compréhension de certains aspects de ces systèmes. J'apporte ainsi quelques éléments de réponses aux questions de la liste (non-exhaustive) présentée au chapitre 1.

• Les trous noirs existent-ils ? Ont-ils une signature particulière ?
Sans avoir traité directement cette question, je suis convaincu de l'existence de ces objets. Ou du moins, d'astres extrêmement denses, dont la densité dépasse celle d'une étoile à neutrons. La physique actuelle ne prédit aucun astre dégénéré pour de telles densités. D'un point de vue plus observateur, il est intéressant de remarquer que les binaires X à trous noirs sont moins lumineuses en quiescence que les binaires X à étoiles à neutrons. Ceci est couramment interprété comme la signature d'une surface dans un cas (le peu de matière accrétée libère son énergie lorsqu'elle heurte la surface), alors que cette énergie d'accrétion est advectée et perdue dans le trou noir dans l'autre cas. Enfin, même si aucune signature claire n'a été découverte à partir des X seuls, il faut bien avouer que les systèmes à trous noirs (c'est-à-dire les binaires X dont la présence d'un astre compact de masse > 3 M$_\odot$ a été démontrée par la mesure de la fonction de masse) ont des comportements assez différents de ceux des étoiles à neutrons. Ils sont, en général, plus brillants, et peuvent largement dépasser la luminosité d'Eddington d'une étoile à neutrons ($L_{edd} \propto 10^{38} \times M/M_\odot$).

Bien que convaincu de leur existence, je pense que ces objets sont probablement différents de l'idée parfaite du trou noir de Schwarzschild. Les trous noirs dits de masses stellaires sont issus de l'évolution d'un étoile massive. La conservation du moment cinétique de l'étoile (en rotation) fait que ce sont probablement des astres en rotation (trous noirs de Kerr). Celle-ci va donc d'une certaine manière contrebalancer l'effondrement "infini" de l'astre.

• Influence de l'étude des populations de source sur les modèles d'évolution
Cet aspect est relativement délicat car l'évolution de ces systèmes, bien que rapide à l'échelle de l'Univers, est extrêmement lente à l'échelle de notre vie. Néanmoins, dans les cas des HMXB, la découverte récente des SFXT, dont certaines pourraient avoir de longues périodes orbitales (signes d'orbites excentriques), pourrait indiquer un lien d'évolution entre Be-HMXB et Sg-HMXB (chapitre 8). De ce point de vue, l'identification des sources et de leurs paramètres (périodes orbitales, pulsations, mais aussi jets, absorption locale) est de première importance car elle permet l'étude des familles, de leur liens et comportements. Par exemple, des systèmes comme IGR J19294+1816 s'ils se généralisaient, prouveraient que la frontière entre sg-HMXB et Be-HMXB est plus tenue que l'on ne le pensait.

De même en étudiant la répartition spatiale de ces objets, il est possible de se rendre compte que les systèmes jeunes n'ont pas eu le temps de migrer à travers la Galaxie. Ils restent près de leur lieu de naissance. La répartition spatiale des HMXB apporte donc une cartographie de notre Galaxie telle qu'elle était il y a quelques millions d'années. Ce sont donc de nouvelles contraintes qui peuvent être utilisé dans la modélisation de l'évolution de notre Galaxie au cours du temps (rotation, lieux de for-

mation stellaire, ...). Nous pouvons nous poser la question de savoir s'il existe une différence notable entre sg-HMXB et Be-HMXB en terme de repartition céleste. Si elle existait, cette différence serait riche d'enseignements sur une région donnée, puisqu'elle permettrait de tracer très précisemment son histoire récente.

• Quelle est l'origine de la forte absorption et de ses variations dans les sg-HMXB ?
Nous avons montré, à travers l'étude de IGR J19140+0951 (chapitre 10) par comparaison avec un modèle simple de vent, que cette absorption provenait du vent du compagnon. Un travail similaire en cours sur IGR J16320−4751 semble mener à la même conclusion, même si, dans ce système, un modèle de vent plus précis devra être pris en compte. Enfin, il est important de noter que dans des systèmes Compton-épais, cette explication n'est probablement pas suffisante. Dans IGR J16318−4848 un cocon additionnel a été invoqué dans certaines études. Les variations de N_H que nous avons vues avec *XMM–Newton* (Ibarra et al. 2007) semblent cependant indiquer une influence de la position orbitale de l'objet compact, et donc possiblement du vent.

• Quelle est l'origine de l'excès mou dans les sg-HMXB ?
Ici encore, les études de IGR J19140+0951 et IGR J16320−4751 favorisent une interaction entre le vent de la supergéante et le fort afflux de rayons X provenant de l'accrétion. De ce point de vue (en ajoutant l'étude de l'absorption, et des raies de fluorescence) les rayons X issus de l'accrétion permettent une certaine radiographie de la matière interne au système. L'utilisation du modèle de vent simple, couplée à l'étude de l'excès mou nous a permis de contraindre certains paramètres de la binaire dans IGR J19140+0951 (chapitre 10), alors que dans IGR J16320−4751 nous avons pu mettre une limite inférieure sur la taille de la coquille contenant le fer irradié. Dans le futur, nous devrons incorporer des inhomogénéités dans le vent, et prendre en compte l'effet de l'excès mou pour obtenir une modélisation plus propre. Les observations *XMM–Newton* de deux systèmes que nous avons récemment obtenues nous aideront dans ce sens.

L'étude de ces objets et de l'environnement immédiat est important. Ils peuvent donner des indications sur la matière circum-système présente, et par la même sur l'évolution du couple lui-même. Enfin le complexe absorbant dans ces systèmes ressemble fortement au complexe absorbant vu dans les AGN de type 2 (du moins les phénomènes physiques sont similaires). En observant des objets proches, brillants et variant plus rapidement nous pourrons obtenir des indications/réponses sur les processus physiques applicables ensuite aux AGN.

• Origine de la queue de haute énergie dans les microquasars ?
Il n'est pas question, à partir des seules analyses présentées ici, de répondre totalement à cette question. Remarquons cependant que dans les creux durs de GRS 1915+105 aucun jet compact n'est détecté (chapitres 7, 11), alors qu'une composante spectrale dure domine le spectre. Dans IGR J17497−2721 aucun jet n'est détecté alors que la source est dans un état dur (chapitre 6). L'origine de l'émission de haute énergie ne peut alors provenir du jet compact. L'interprétation en termes de couronne comptonisante est clairement favorisée.

Dans d'autres cas, cependant, j'ai montré que le jet compact avait une influence probable dans les rayons X durs (> 20 keV) émis par GRS 1915+105 (chapitres 11, 12). J'ai de plus montré dans GRS 1915+105 que la composante X dure attribuée au jet s'accompagnait d'une composante de comptonisation, clairement détectée dans les spectres en énergie. Nous pouvons alors nous poser la question de l'origine de la composante de comptonisation dans ces cas particuliers. Provient-elle du jet par effet synchroton-self Compton, par comptonisation sur la base du jet, ou bien d'une couronne indépendante ?

• Quelle est l'origine des QPO ?

J'ai montré, grâce notamment aux spectres en énergie des QPO BF, que ceux-ci ne provenaient ni d'oscillations de la queue de haute énergie (et donc pas du jet), ni d'oscillations de flux du milieu comptonisation (donc pas de la couronne). Il est de plus clair que les QPO BF ne proviennent pas d'oscillations du flux du disque (et donc pas du disque). La partie haute énergie de leur spectre ressemble cependant à la partie haute énergie du spectre de la couronne. Le QPO subirait-il alors la comptonisation ? Vu les dépendances entre la fréquence des oscillations et les paramètres du disque d'accrétion, cela pourrait indiquer que le QPO est produit d'une certaine manière à une interface disque-couronne.

• Quelle est l'origine des variabilités de tous types ?

Cette question est extrêmement vaste car les causes de variations temporelles dépendent probablement des fréquences auxquelles nous les étudions. Les phénomènes de chute libre (couronne par exemple) sont bien plus rapides (secondes) que les phénomènes liés à la viscosité dans le disque (minutes–jours). Concentrons nous sur les variabilités rapides ($\gtrsim 0.1Hz$). En présentant les spectres de puissance dans différentes bandes d'énergies (Rodriguez et al. 2004a, chapitre 14), il est possible de voir que les composantes du continuum de variabilité ont clairement des dépendances énergétiques différentes : la composante de basse fréquence s'exprime fortement à basse énergie, alors que la composante de fréquence $5 - 10$ Hz a un spectre dur. Nous (dans le cadre de la thèse de T. Chen débutant en octobre 2009) allons nous pencher sur cet aspect en produisant systématiquement les spectres en énergie des différentes composantes.

• Origine des transitions spectrales ?

Cette question est le pendant de la question précédente pour des temps relativement longs. Il semble clair que la taille et la température du disque d'accrétion jouent un rôle fondamental dans les transitions. Dans une modélisation basique (disque α), ces paramètres sont directement liés au taux d'accrétion. Néanmoins un paramètre additionnel est nécessaire pour pouvoir reproduire les évolutions au cours d'une éruption. Différents modèles prédisent différents paramètres. Yu & Yan (2009) proposent que ce paramètre soit le taux de croissance du taux d'accrétion. Mais la question réelle reste : qu'est ce qui règle ce taux de croissance ? D'autres pensent que la taille de la couronne pourrait être ce paramètre (par le taux de comptonisation par exemple), ou bien la magnétisation, ou un rayon de transition disque α–disque non-α/JED/Flot d'accrétion dominé par l'advection (ADAF)....

La question reste posée. J'ai néanmoins montré que la transition état dur→état dur, ou du moins le passage de la ligne de jet s'accompagnait d'une disparition d'une partie de la couronne dans cinq microquasars. Comment celle-ci se reconstruit-elle subitement lors de la transition inverse ? Et quelle est l'exacte relation entre le disque et la couronne ? La couronne est-elle éjectée par l'approche du disque, ou bien le disque peut-il s'approcher parce que la couronne disparaît ?

• Origine de la matière éjectée dans les microquasars ?

La disparition d'une partie de la matière comptonisante précède les éruptions radio dans cinq microquasars. Dans le même temps les paramètres liés au disque montrent que celui-ci semble s'approcher de l'objet compact de manière monotone. Ceci m'a conduit à suggérer que dans ces systèmes la matière éjectée provenait de la couronne. Il est intéressant de remarquer que dans GRS 1915+105 il existe une possible corrélation entre l'état dur précédant l'éjection et l'amplitude de celle-ci. L. Prat, dans le cadre de sa thèse, investigue cet aspect plus avant. Les résultats préliminaires sont relativement concluants, et semblent indiquer une corrélation entre la durée du creux dur et l'énergie (la fluence) totale du sursaut radio. Cette étude considère tous les cycles de GRS 1915+105 ayant

eu des suivis radio (mono-fréquences pour l'instant). Cette corrélation pourrait signifier que durant l'état dur précédant l'éjection matière et/ou énergie libérées lors de l'éjection sont accumulées.

• Peut-on tirer un modèle global d'évolution des microquasars ?
J'ai présenté en fin de partie III trois modèles tentant de relier une majorité de ces points. Même si je pense que le CENBOL est probablement celui qui a le plus de mal à répondre à tous ces points, chacun présente des limitations. Il n'est donc pas possible de conclure même s'il est certain que chaque nouvelle observation apporte de nouvelles contraintes.

Bien entendu je me suis concentré dans ces différents points sur l'aspect purement physique des phénomènes. Mon travail de recherche est de ce point de vue original puisqu'il apporte à la communauté scientifique des éléments de réponse neufs. Ceux-ci sont utilisés pour avancer dans la compréhension des phénomènes, notamment du point de vue théorique, puisque j'intéragis constamment avec des théoriciens comme P. Varnière et M. Tagger. Ces collaborations donnent un échange fort et privilégié permettant des avancées rapides dans différentes directions. Les observations nous indiquent les fausses pistes et les développements théoriques montrent de nouveaux diagnostics à tester.

Ce que j'ai voulu montrer à travers ce document et son organisation est l'aspect astronome-astrophysicien dont je pense qu'il se manifeste fortement dans ma recherche. Du fait de ma spécialisation en tant qu'astronome de haute énergie et ma participation aux suivis du ciel avec *INTEGRAL*, j'ai eu la chance de connaître les étapes de découvertes de nouvelles sources de rayonnement. J'ai donc très tôt mis en place des programmes de suivis permettant l'identification possible de ces objets. Outre la réponse à l'énigme de l'origine d'une nouvelle source, l'identification a une importance capitale pour la compréhension de nos cieux, de l'évolution des étoiles, de notre Galaxie, et de notre Univers lorsque l'on se penche sur des objets dits cosmologiques. Ceci est rendu possible par l'étude des populations de sources, leur évolution, leur répartition spatiale. C'est ces aspects que j'ai voulus illustrer notamment dans les deux premières parties de cette HDR.

Il est évident que le travail n'est pas terminé ! J'ai présenté dans cette HDR différentes analyses qui ne sont que préliminaires, d'autres tout juste soumises à publication. Le futur immédiat est donc de terminer ces analyses. Je mentionnerai à ce titre l'étude spectrale de tous les microquasars dans les phases précédant les éjections. Cet aspect rejoint le travail de thèse de L. Prat concernant la corrélation etat-dur/énergie du jet qui doit être étendue et terminée. Du point de vue temporel, comme je le mentionne plus haut, un travail de longue haleine constituant le sujet de thèse de T. Chen, sera d'étudier les propriétés spectrales des composantes temporelles des spectres de puissance des microquasars. Le travail d'interaction observations-théorie bénéficiera de ces résultats. En étant à l'interface observations-théorie, il m'est extrêmement facile de communiquer les nouvelles contraintes observationnelles à mes collègues.

L'étude des populations de sources X-dures est un aspect sur lequel nous (en collaboration avec A. Bodaghee) avons commencé à nous pencher. L'idée est de mettre à jour le travail préliminaire de 2007, en incluant les sources vues par *Swift*. L'identification des nouvelles sources en est un préliminaire fondamental. Comme je le mentionne plus haut dans cette conclusion, il sera intéressant d'étudier une possible dichotomie entre les répartitions spatiales des sg-HMXB et Be-HMXB.

Comme corolaire (puisque ceux-ci forment une grande partie des sources X-dures) j'aimerais me pencher sur l'étude des AGN, avec un intérêt plus particulier pour les AGN absorbés et compton épais. Cet aspect me permettra d'étudier les similitudes pouvant exister avec les microquasars, bien sur, mais aussi de déterminer les parallèles qui pourront être établis avec la physique des binaires ab-

sorbées. Pour ce faire il existe de nombreuses bases de données, *INTEGRAL XMM–Newton Chandra*. L'étude des AGN sera aussi possible grâce à SVOM, satellite dédié aux GRB et dont je suis Co-I, et particulièrement intéressé par les aspects science hors sursaut. Après la préparation du segment sol de SIMBOL-X, et la participation au segment sol/centre de données de *INTEGRAL*, je fais aussi partie du centre de données Français de SVOM. Ceci consiste à préparer les infrastructures (informatiques entre autres), et, pour ma part, je me concentre sur tout ce qui concerne la science hors sursaut. Le premier document de préparation/définition des produits scientifiques vient d'être livré au CNES. La majeure partie du travail reste à faire et cet aspect est un gros projet dans mon travail pour l'horizon 2013, date prévue de lancement de la mission. La suite consistera alors en l'analyse et l'interprétation des données.

J'aurai aussi une place privilégiée pour étudier les GRB. Outre l'interêt personnel pour ces objets, le parallèle avec les microquasars est évident : les GRB sont issus de l'effondrement d'un astre massif en un trou noir (pour certains), ou de la coalescence d'objets compacts. Outre les tests de relativité en champ fort (par exemple l'émission d'ondes gravitationnelles), leur fonctionnement implique la présence d'un disque d'accrétion et d'éjections relativistes.

Enfin le futur passe aussi par l'étude de nouveaux diagnostiques. De ce point de vue, et pour rejoindre l'aspect d'étude des sources de rayonnements de haute énergie, j'aimerais confronter les catalogues X-durs avec les catalogues de sources Fermi, HESS, Magic, ... Ceci pourrait, d'une part permettre l'identification de certains de ces objets, mais aussi apporterait de nouvelles contraintes/questions sur la physique des binaires X. Par exemple, certains modèles de jets prédisent effectivement des émissions dans les domaines $>$GeV. Observer une telle émission serait donc une signature forte.

S'il m'est difficile d'envisager participer directement à des observations de neutrinos ou d'ondes gravitationnelles, les études de polarimétrie en X sont, je pense, tout à fait envisageables. Si pour l'instant la polarisation n'est détectée que dans peu de sources, il est clair que les détecteurs futurs, et une astronomie dédiée devrait permettre d'ouvrir une nouvelle fenêtre d'étude à travers laquelle j'aimerais observer les sources accrétantes.

A plus long terme le satellite IXO apportera, espérons-le, de nombreuses possibilités entre ~ 0.1 et 40 keV. Outre ses capacités d'imageur et de spectromètre, un aspect important concernera ses capacités temporelles rapides. La grande surface collectrice (3 m^2 à 1,2 keV, 0.6 m^2 à 6 keV, 150 cm^2 à 30 keV) en fait un instrument de premier ordre pour les études temporelles. Avec l'instrument collecteur à haute résolution temporelle (HTRS), installé au plan focal, il sera possible d'étudier tout type de variations sur une plage spectrale la plus large jamais explorée. La grande surface collectrice permettra aussi de repousser les limites de sensibilité atteintes par *RXTE* à haute fréquence, et peut-être de détecter des oscillations de très hautes fréquences. De ce point de vue, je fais partie d'un vaste groupe de travail pour un tel détecteur. Mes préoccupations concernent plus l'approche résolue en énergie des variabilités temporelles. Un observatoires tel que IXO devrait nous permettre d'obtenir des spectres larges bandes, à haute résolution, et de grande qualité statistique de toutes les variabilités vues dans les binaires X et autres objets accrétants. IXO me permettra donc d'éffectuer une analyse spectrale extrêmement précise de la variabilité.

Bibliographie

Balbus, S. A. & Hawley, J. F. 1991, *Astrophys. J.*, 376, 214

Barret, D., McClintock, J. E., & Grindlay, J. E. 1996, *Astrophys. J.*, 473, 963

Belloni, T., Klein-Wolt, M., Méndez, M., van der Klis, M., & van Paradijs, J. 2000, *Astron. & Astrophys.*, 355, 271

Belloni, T., Mendez, M., King, A. R., van der Klis, M., & van Paradijs, J. 1997a, *Astrophys. J.*, 488, L109+

Belloni, T., Mendez, M., King, A. R., van der Klis, M., & van Paradijs, J. 1997b, *Astrophys. J.*, 479, L145+

Bird, A. J., Barlow, E. J., Bassani, L., et al. 2006, *Astrophys. J.*, 636, 765

Bird, A. J., Barlow, E. J., Bassani, L., et al. 2004, *Astrophys. J.*, 607, L33

Bird, A. J., Malizia, A., Bazzano, A., et al. 2007, *Astrophys. J. Suppl. Ser.*, 170, 175

Bodaghee, A., Courvoisier, T. J.-L., Rodriguez, J., et al. 2007, *Astron. & Astrophys.*, 467, 585

Bodaghee, A., Walter, R., Zurita Heras, J. A., et al. 2006, *Astron. & Astrophys.*, 447, 1027

Boroson, B., Vrtilek, S. D., Kallman, T., & Corcoran, M. 2003, *Astrophys. J.*, 592, 516

Brocksopp, C., Fender, R. P., McCollough, M., et al. 2002, *Mon. Not. R. Astron. Soc.*, 331, 765

Butler, S. C., Tomsick, J. A., Chaty, S., et al. 2009, ArXiv e-prints

Caballero-García, M. D., Miller, J. M., Trigo, M. D., et al. 2009, *Astrophys. J.*, 692, 1339

Cabanac, C., Fender, R. P., Dunn, R. J. H., & Körding, E. G. 2009, *Mon. Not. R. Astron. Soc.*, 396, 1415

Cadolle Bel, M., Prat, L., Rodriguez, J., et al. 2009, *Astron. & Astrophys.*, 501, 1

Cadolle Bel, M., Ribó, M., Rodriguez, J., et al. 2007, *Astrophys. J.*, 659, 549

Cadolle Bel, M., Rodriguez, J., Sizun, P., et al. 2004, *Astron. & Astrophys.*, 426, 659

Cadolle Bel, M., Sizun, P., Goldwurm, A., et al. 2006, *Astron. & Astrophys.*, 446, 591

Casella, P., Belloni, T., & Stella, L. 2005, *Astrophys. J.*, 629, 403

Castor, J. I., Abbott, D. C., & Klein, R. I. 1975, *Astrophys. J.*, 195, 157

Castro-Tirado, A. J., Brandt, S., & Lund, N. 1992, *IAU Circ.*, No. , 5590, 2

Caunt, S. E. & Tagger, M. 2001, *Astron. & Astrophys.*, 367, 1095

Chakrabarti, S. K. 1996, *Astrophys. J.*, 464, 664

Chakrabarti, S. K. 1997, *Astrophys. J.*, 484, 313

Chakrabarti, S. K. 1999, *Astron. & Astrophys.*, 351, 185

Chakrabarti, S. K. & Mandal, S. 2006, *Astrophys. J.*, 642, L49

Chapuis, C. & Corbel, S. 2004, *Astron. & Astrophys.*, 414, 659

Chaty, S., Rahoui, F., Foellmi, C., et al. 2008, *Astron. & Astrophys.*, 484, 783

Corbel, S., Fender, R. P., Tomsick, J. A., Tzioumis, A. K., & Tingay, S. 2004, *Astrophys. J.*, 617, 1272

Corbel, S., Fender, R. P., Tzioumis, A. K., et al. 2000, *Astron. & Astrophys.*, 359, 251

Corbel, S., Kaaret, P., Jain, R. K., et al. 2001, *Astrophys. J.*, 554, 43

Corbel, S., Nowak, M. A., Fender, R. P., Tzioumis, A. K., & Markoff, S. 2003, *Astron. & Astrophys.*, 400, 1007

Corbet, R. H. D. 1986, *Mon. Not. R. Astron. Soc.*, 220, 1047

Corbet, R. H. D. & Krimm, H. A. 2009, The Astronomer's Telegram, 2008, 1

Courvoisier, T. J.-L., Walter, R., Rodriguez, J., Bouchet, L., & Lutovinov, A. A. 2003, *IAU Circ.*, No. , 8063, 3

Del Santo, M., Rodriguez, J., Ubertini, P., et al. 2003, *Astron. & Astrophys.*, 411, L369

Dhawan, V., Mirabel, I. F., & Rodríguez, L. F. 2000, *Astrophys. J.*, 543, 373

Di Salvo, T., Robba, N. R., Iaria, R., et al. 2001, *Astrophys. J.*, 554, 49

Dickey, J. M. & Lockman, F. J. 1990, *Annu. Rev. Astron. Astrophys.*, 28, 215

Ebisawa, K., Tsujimoto, M., Paizis, A., et al. 2005, *Astrophys. J.*, 635, 214

Eikenberry, S. S., Matthews, K., Morgan, E. H., Remillard, R. A., & Nelson, R. W. 1998a, *Astrophys. J.*, 494, L61+

Eikenberry, S. S., Matthews, K., Murphy, Jr., T. W., et al. 1998b, *Astrophys. J.*, 506, L31

Fender, R. & Belloni, T. 2004, *Annu. Rev. Astron. Astrophys.*, 42, 317

Fender, R., Corbel, S., Tzioumis, T., et al. 1999a, *Astrophys. J.*, 519, L165

Fender, R. P. 2001, *Mon. Not. R. Astron. Soc.*, 322, 31

Fender, R. P., Belloni, T. M., & Gallo, E. 2004, *Mon. Not. R. Astron. Soc.*, 355, 1105

Fender, R. P., Garrington, S. T., McKay, D. J., et al. 1999b, *Mon. Not. R. Astron. Soc.*, 304, 865

Fender, R. P. & Pooley, G. G. 2000, *Mon. Not. R. Astron. Soc.*, 318, L1

Feroci, M., Matt, G., Pooley, G., et al. 1999, *Astron. & Astrophys.*, 351, 985

Ferreira, J., Petrucci, P.-O., Henri, G., Saugé, L., & Pelletier, G. 2006, *Astron. & Astrophys.*, 447, 813

Frank, J., King, A., & Raine, D. J. 2002, Accretion Power in Astrophysics : Third Edition (Accretion Power in Astrophysics, by Juhan Frank and Andrew King and Derek Raine, pp. 398. ISBN 0521620538. Cambridge, UK : Cambridge University Press, February 2002.)

Fuchs, Y., Rodriguez, J., Mirabel, I. F., et al. 2003, *Astron. & Astrophys.*, 409, L35

Gallo, E., Fender, R. P., & Pooley, G. G. 2003, *Mon. Not. R. Astron. Soc.*, 344, 60

Giacconi, R., Gorenstein, P., Gursky, H., & Waters, J. R. 1967, *Astrophys. J.*, 148, L119+

Giacconi, R., Gursky, H., Paolini, F. R., & Rossi, B. B. 1962, Physical Review Letters, 9, 439

Greiner, J., Cuby, J. G., & McCaughrean, M. J. 2001, *Nature*, 414, 522

Gros, A., Goldwurm, A., Cadolle-Bel, M., et al. 2003, *Astron. & Astrophys.*, 411, L179

Grove, J. E., Johnson, W. N., Kroeger, R. A., et al. 1998, *Astrophys. J.*, 500, 899

Haberl, F., White, N. E., & Kallman, T. R. 1989, *Astrophys. J.*, 343, 409

Hannikainen, D. C., Rawlings, M. G., Muhli, P., et al. 2007, *Mon. Not. R. Astron. Soc.*, 380, 665

Hannikainen, D. C., Rodriguez, J., Cabanac, C., et al. 2004, *Astron. & Astrophys.*, 423, L17

Hannikainen, D. C., Rodriguez, J., & Pottschmidt, K. 2003a, *IAU Circ.*, No. , 8088, 4

Hannikainen, D. C., Rodriguez, J., Vilhu, O., et al. 2005, *Astron. & Astrophys.*, 435, 995

Hannikainen, D. C., Vilhu, O., Rodriguez, J., et al. 2003b, *Astron. & Astrophys.*, 411, L415

Hickox, R. C., Narayan, R., & Kallman, T. R. 2004, *Astrophys. J.*, 614, 881

Hjellming, R. M., Rupen, M. P., Ghigo, F., et al. 1998a, *IAU Circ.*, No. , 6937, 1

Hjellming, R. M., Rupen, M. P., & Mioduszewski, A. J. 1998b, *IAU Circ.*, No. , 6934, 1

Homan, J. & Belloni, T. 2005, *Astro. & Space Sc.*, 300, 107

Homan, J., Buxton, M., Markoff, S., et al. 2005, *Astrophys. J.*, 624, 295

Homan, J., Wijnands, R., van der Klis, M., et al. 2001, *Astrophys. J. Suppl. Ser.*, 132, 377

Ibarra, A., Matt, G., Guainazzi, M., et al. 2007, *Astron. & Astrophys.*, 465, 501

Joinet, A., Jourdain, E., Malzac, J., et al. 2007, *Astrophys. J.*, 657, 400

Joinet, A., Jourdain, E., Malzac, J., et al. 2005, *Astrophys. J.*, 629, 1008

Kallman, T. R., Palmeri, P., Bautista, M. A., Mendoza, C., & Krolik, J. H. 2004, *Astrophys. J. Suppl. Ser.*, 155, 675

Klein-Wolt, M., Fender, R. P., Pooley, G. G., et al. 2002, *Mon. Not. R. Astron. Soc.*, 331, 745

Krivonos, R., Revnivtsev, M., Lutovinov, A., et al. 2007, *Astron. & Astrophys.*, 475, 775

Kuulkers, E., Chenevez, J., Shaw, S., et al. 2006, The Astronomer's Telegram, 888, 1

Labanti, C., Di Cocco, G., Ferro, G., et al. 2003, *Astron. & Astrophys.*, 411, L149

Lebrun, F., Leray, J. P., Lavocat, P., et al. 2003, *Astron. & Astrophys.*, 411, L141

Lund, N., Budtz-Jørgensen, C., Westergaard, N. J., et al. 2003, *Astron. & Astrophys.*, 411, L231

Lutovinov, A., Revnivtsev, M., Gilfanov, M., et al. 2005, *Astron. & Astrophys.*, 444, 821

Markoff, S., Falcke, H., & Fender, R. 2001, *Astron. & Astrophys.*, 372, L25

Markoff, S., Nowak, M., Corbel, S., Fender, R., & Falcke, H. 2003, *Astron. & Astrophys.*, 397, 645

Mas-Hesse, J. M., Giménez, A., Culhane, J. L., et al. 2003, *Astron. & Astrophys.*, 411, L261

Masetti, N., Bassani, L., Bazzano, A., et al. 2006a, *Astron. & Astrophys.*, 455, 11

Masetti, N., Mason, E., Bassani, L., et al. 2006b, *Astron. & Astrophys.*, 448, 547

Masetti, N., Mason, E., Morelli, L., et al. 2008, *Astron. & Astrophys.*, 482, 113

Masetti, N., Morelli, L., Palazzi, E., et al. 2006c, *Astron. & Astrophys.*, 459, 21

Masetti, N., Palazzi, E., Bassani, L., Malizia, A., & Stephen, J. B. 2004, *Astron. & Astrophys.*, 426, L41

Masetti, N., Parisi, P., Palazzi, E., et al. 2009, *Astron. & Astrophys.*, 495, 121

Masetti, N., Pretorius, M. L., Palazzi, E., et al. 2006d, *Astron. & Astrophys.*, 449, 1139

Matt, G. 2002, *Mon. Not. R. Astron. Soc.*, 337, 147

Matt, G. & Guainazzi, M. 2003, *Mon. Not. R. Astron. Soc.*, 341, L13

McClintock, J. E. & Remillard, R. A. 2006, Black hole binaries, ed. W. H. G. Lewin & M. van der Klis, 157–213

McClintock, J. E., Shafee, R., Narayan, R., et al. 2006, *Astrophys. J.*, 652, 518

McConnell, M. L., Zdziarski, A. A., Bennett, K., et al. 2002, *Astrophys. J.*, 572, 984

Middleton, M., Done, C., Gierliński, M., & Davis, S. W. 2006, *Mon. Not. R. Astron. Soc.*, 373, 1004

Migliari, S., Fender, R. P., & van der Klis, M. 2005, *Mon. Not. R. Astron. Soc.*, 363, 112

Mikles, V. J., Varniere, P., Eikenberry, S. S., Rodriguez, J., & Rothstein, D. 2009, *Astrophys. J.*, 694, L132

Mirabel, I. F., Dhawan, V., Chaty, S., et al. 1998, *Astron. & Astrophys.*, 330, L9

Mirabel, I. F., Dhawan, V., Mignani, R. P., Rodrigues, I., & Guglielmetti, F. 2001, *Nature*, 413, 139

Mirabel, I. F., Mignani, R., Rodrigues, I., et al. 2002, *Astron. & Astrophys.*, 395, 595

Mirabel, I. F. & Rodrigues, I. 2003, Science, 300, 1119

Mirabel, I. F. & Rodriguez, L. F. 1994, *Nature*, 371, 46

Miyamoto, S., Kitamoto, S., Hayashida, K., & Egoshi, W. 1995, *Astrophys. J.*, 442, L13

Molkov, S. V., Cherepashchuk, A. M., Lutovinov, A. A., et al. 2004, Astronomy Letters, 30, 534

Molteni, D., Sponholz, H., & Chakrabarti, S. K. 1996, *Astrophys. J.*, 457, 805

Mondal, S. & Chakrabarti, S. K. 2006, *Mon. Not. R. Astron. Soc.*, 371, 1418

Morgan, E. H., Remillard, R. A., & Greiner, J. 1997, *Astrophys. J.*, 482, 993

Mowlavi, N., Kreykenbohm, I., Shaw, S. E., et al. 2006, *Astron. & Astrophys.*, 451, 187

Muno, M. P., Bauer, F. E., Baganoff, F. K., et al. 2009, *Astrophys. J. Suppl. Ser.*, 181, 110

Muno, M. P., Morgan, E. H., & Remillard, R. A. 1999, *Astrophys. J.*, 527, 321

Muno, M. P., Remillard, R. A., Morgan, E. H., et al. 2001, *Astrophys. J.*, 556, 515

Negueruela, I., Smith, D. M., Reig, P., Chaty, S., & Torrejón, J. M. 2006, in ESA Special Publication, Vol. 604, The X-ray Universe 2005, ed. A. Wilson, 165–+

Paizis, A., Beckmann, V., Courvoisier, T. J.-L., et al. 2003, *Astron. & Astrophys.*, 411, L363

Paizis, A., Ebisawa, K., Tikkanen, T., et al. 2005a, *Astron. & Astrophys.*, 443, 599

Paizis, A., Farinelli, R., Titarchuk, L., et al. 2006, *Astron. & Astrophys.*, 459, 187

Paizis, A., Nowak, M. A., Chaty, S., et al. 2007, *Astrophys. J.*, 657, L109

Paizis, A., Nowak, M. A., Wilms, J., et al. 2005b, *Astron. & Astrophys.*, 444, 357

Petrucci, P.-O., Ferreira, J., Henri, G., & Pelletier, G. 2008, *Mon. Not. R. Astron. Soc.*, 385, L88

Pooley, G. G. & Fender, R. P. 1997, *Mon. Not. R. Astron. Soc.*, 292, 925

Porquet, D., Reeves, J. N., O'Brien, P., & Brinkmann, W. 2004, *Astron. & Astrophys.*, 422, 85

Pottschmidt, K., Kreykenbohm, I., Wilms, J., et al. 2005, *Astrophys. J.*, 634, L97

Prat, L. & Rodriguez, J. 2009, in American Institute of Physics Conference Series, Vol. 1126, American Institute of Physics Conference Series, ed. J. Rodriguez & P. Ferrando, 177–180

Prat, L., Rodriguez, J., Cadolle Bel, M., et al. 2009, *Astron. & Astrophys.*, 494, L21

Prat, L., Rodriguez, J., Hannikainen, D. C., & Shaw, S. E. 2008, *Mon. Not. R. Astron. Soc.*, 389, 301

Rahoui, F., Chaty, S., Lagage, P.-O., & Pantin, E. 2008, *Astron. & Astrophys.*, 484, 801

Remillard, R. A., Sobczak, G. J., Muno, M. P., & McClintock, J. E. 2002, *Astrophys. J.*, 564, 962

Rodriguez, J. & Bodaghee, A. 2008, in American Institute of Physics Conference Series, Vol. 1010, A Population Explosion : The Nature & Evolution of X-ray Binaries in Diverse Environments, ed. R. M. Bandyopadhyay, S. Wachter, D. Gelino, & C. R. Gelino, 225–229

Rodriguez, J., Bodaghee, A., Kaaret, P., et al. 2006a, *Mon. Not. R. Astron. Soc.*, 366, 274

Rodriguez, J., Cabanac, C., Hannikainen, D. C., et al. 2005a, *Astron. & Astrophys.*, 432, 235

Rodriguez, J., Cadolle Bel, M., Tomsick, J. A., et al. 2007a, *Astrophys. J.*, 655, L97

Rodriguez, J., Chenevez, J., & Hannikainen, D. 2009a, The Astronomer's Telegram, 1977, 1

Rodriguez, J., Corbel, S., Hannikainen, D. C., et al. 2004a, *Astrophys. J.*, 615, 416

Rodriguez, J., Corbel, S., Kalemci, E., Tomsick, J. A., & Tagger, M. 2004b, *Astrophys. J.*, 612, 1018

Rodriguez, J., Corbel, S., & Tomsick, J. A. 2003a, *Astrophys. J.*, 595, 1032

Rodriguez, J., Del Santo, M., Lebrun, F., et al. 2003b, *Astron. & Astrophys.*, 411, L373

Rodriguez, J., Durouchoux, P., Mirabel, I. F., et al. 2002a, *Astron. & Astrophys.*, 386, 271

Rodriguez, J., Hannikainen, D. C., & Mowlavi, N. 2004c, The Astronomer's Telegram, 280, 1

Rodriguez, J., Hannikainen, D. C., Shaw, S. E., et al. 2008a, *Astrophys. J.*, 675, 1436

Rodriguez, J., Paizis, A., Cadolle-Bel, M., Hannikainen, D. C., & Shaw, S. E. 2005b, The Astronomer's Telegram, 464, 1

Rodriguez, J. & Prat, L. 2008, ArXiv e-prints

Rodriguez, J., Prat, L., Shaw, S. E., & Hannikainen, D. C. 2007b, The Astronomer's Telegram, 1079, 1

Rodriguez, J. & Shaw, S. E. 2005, The Astronomer's Telegram, 660, 1

Rodriguez, J., Shaw, S. E., & Corbel, S. 2006b, *Astron. & Astrophys.*, 451, 1045

Rodriguez, J., Shaw, S. E., Hannikainen, D. C., et al. 2008b, *Astrophys. J.*, 675, 1449

Rodriguez, J., Shaw, S. E., Prat, L., & Hannikainen, D. C. 2007c, The Astronomer's Telegram, 1229, 1

Rodriguez, J., Tomsick, J., Beckmann, V., et al. 2008c, The Astronomer's Telegram, 1554, 1

Rodriguez, J., Tomsick, J. A., & Chaty, S. 2008d, *Astron. & Astrophys.*, 482, 731

Rodriguez, J., Tomsick, J. A., & Chaty, S. 2009b, *Astron. & Astrophys.*, 494, 417

Rodriguez, J., Tomsick, J. A., Foschini, L., Walter, R., & Goldwurm, A. 2003c, *IAU Circ.*, No. , 8096, 1

Rodriguez, J., Tomsick, J. A., Foschini, L., Walter, R., & Goldwurm, A. 2003d, *IAU Circ.*, No. , 8096, 2

Rodriguez, J., Tomsick, J. A., Foschini, L., et al. 2003e, *Astron. & Astrophys.*, 407, L41

Rodriguez, J., Tuerler, M., Chaty, S., & Tomsick, J. A. 2009c, The Astronomer's Telegram, 1998, 1

Rodriguez, J., Varnière, P., Tagger, M., & Durouchoux, P. 2002b, *Astron. & Astrophys.*, 387, 487

Rupen, M. P., Hjellming, R. M., & Mioduszewski, A. J. 1998, *IAU Circ.*, No. , 6938, 2

Rykoff, E. S., Miller, J. M., Steeghs, D., & Torres, M. A. P. 2007, *Astrophys. J.*, 666, 1129

Saraswat, P., Yoshida, A., Mihara, T., et al. 1996, *Astrophys. J.*, 463, 726

Shakura, N. I. & Sunyaev, R. A. 1973, *Astron. & Astrophys.*, 24, 337

Shaposhnikov, N. & Titarchuk, L. 2007, *Astrophys. J.*, 663, 445

Shaposhnikov, N. & Titarchuk, L. 2009, ArXiv e-prints

Stirling, A. M., Spencer, R. E., de la Force, C. J., et al. 2001, *Mon. Not. R. Astron. Soc.*, 327, 1273

Strohmayer, T., Rodriguez, J., Markwardt, C., et al. 2009, The Astronomer's Telegram, 2002, 1

Sugizaki, M., Mitsuda, K., Kaneda, H., et al. 2001, *Astrophys. J. Suppl. Ser.*, 134, 77

Sunyaev, R. & Revnivtsev, M. 2000, *Astron. & Astrophys.*, 358, 617

Sunyaev, R. A. 1973, Soviet Astronomy, 16, 941

Sunyaev, R. A., Grebenev, S. A., Lutovinov, A. A., et al. 2003, The Astronomer's Telegram, 190, 1

Sunyaev, R. A. & Titarchuk, L. G. 1980, *Astron. & Astrophys.*, 86, 121

Tagger, M. & Pellat, R. 1999, *Astron. & Astrophys.*, 349, 1003

Tagger, M. & Varnière, P. 2006, *Astrophys. J.*, 652, 1457

Tagger, M., Varnière, P., Rodriguez, J., & Pellat, R. 2004, *Astrophys. J.*, 607, 410

Tomsick, J. A. 2008, in Proceedings of the VII Microquasar Workshop : Microquasars and Beyond. September 1 - 5, 2008. Foca, Izmir, Turkey. Published online at http ://pos.sissa.it/cgi-bin/reader/conf.cgi ?confid=62, p.4, 4–+

Tomsick, J. A., Chaty, S., Rodriguez, J., et al. 2006, *Astrophys. J.*, 647, 1309

Tomsick, J. A., Chaty, S., Rodriguez, J., Walter, R., & Kaaret, P. 2008, *Astrophys. J.*, 685, 1143

Tomsick, J. A., Chaty, S., Rodriguez, J., Walter, R., & Kaaret, P. 2009a, *Astrophys. J.*, 701, 811

Tomsick, J. A., Chaty, S., Rodriguez, J., et al. 2009b, *Astrophys. J.*, 694, 344

Tomsick, J. A., Lingenfelter, R., Walter, R., et al. 2003, *IAU Circ.*, No. , 8076, 1

Trudolyubov, S. P. 2001, *Astrophys. J.*, 558, 276

Tuerler, M., Rodriguez, J., & Ferrigno, C. 2009, The Astronomer's Telegram, 1997, 1

Ubertini, P., Lebrun, F., Di Cocco, G., et al. 2003, *Astron. & Astrophys.*, 411, L131

Ueda, Y., Yamaoka, K., Sánchez-Fernández, C., et al. 2002, *Astrophys. J.*, 571, 918

Vadawale, S. V., Rao, A. R., Naik, S., et al. 2003, *Astrophys. J.*, 597, 1023

Valinia, A. & Marshall, F. E. 1998, *Astrophys. J.*, 505, 134

van der Klis, M. 2006, Rapid X-ray Variability, ed. W. H. G. Lewin & M. van der Klis, 39–112

van der Laan, H. 1966, *Nature*, 211, 1131

Varnière, P., Rodriguez, J., & Tagger, M. 2002, *Astron. & Astrophys.*, 387, 497

Varniere, P., Rodriguez, J., & Tagger, M. 2008, in Proceedings of the VII Microquasar Workshop : Microquasars and Beyond. September 1 - 5, 2008. Foca, Izmir, Turkey. Published online at http ://pos.sissa.it/cgi-bin/reader/conf.cgi ?confid=62, p.117, 117–+

Varnière, P. & Tagger, M. 2002, *Astron. & Astrophys.*, 394, 329

Vedrenne, G., Roques, J.-P., Schönfelder, V., et al. 2003, *Astron. & Astrophys.*, 411, L63

Vignarca, F., Migliari, S., Belloni, T., Psaltis, D., & van der Klis, M. 2003, *Astron. & Astrophys.*, 397, 729

Walter, R., Rodriguez, J., Foschini, L., et al. 2003, *Astron. & Astrophys.*, 411, L427

Walter, R. & Zurita Heras, J. 2007, *Astron. & Astrophys.*, 476, 335

Walter, R., Zurita Heras, J., Bassani, L., et al. 2006, *Astron. & Astrophys.*, 453, 133

Watanabe, S., Sako, M., Ishida, M., et al. 2003, *Astrophys. J.*, 597, L37

Watson, M. G., Schröder, A. C., Fyfe, D., et al. 2009, *Astron. & Astrophys.*, 493, 339

Weidenspointner, G., Skinner, G., Jean, P., et al. 2008, *Nature*, 451, 159

Winkler, C., Courvoisier, T. J.-L., Di Cocco, G., et al. 2003, *Astron. & Astrophys.*, 411, L1

Yu, W. & Yan, Z. 2009, ArXiv e-prints

Zurita Heras, J. A., de Cesare, G., Walter, R., et al. 2006, *Astron. & Astrophys.*, 448, 261